IMAGE PROCESSING AND INFORMATICS LABORATORY

Department of Radiology
University of Southern California

2007 Annual Report

SUMMARY

"It was the best of times, it was the worst of times" – Charles Dickens

Amidst the bleak outlook across the National scientific research community with regards to NIH research support, the Image Processing and Informatics Laboratory (IPI) during year 2006 experienced growth in numbers and continued its major emphasis in education, new expansion in International liaisons, and the realization of new research directions and industrial collaborations. In order to handle these additional loads, Brent Liu has assumed the responsibility of Deputy Director; and Michael Zhou, Manager of IPI. Some of the accomplishments are detailed:

1. Education and Expansion

We completed year one of a five year T32 Training Grant from the National Institute of Biomedical Imaging and Bioengineering (NIBIB), National Institutes of Health (NIH), DHHS entitled: "Biomedical Imaging Informatics Training Program" effective September, 1, 2005 – August 31, 2010, totaling about US$1.6 million. The PI and Co-PI are Dr. H.K. Huang of Radiology and Dr. Michael Khoo of BME, respectively. We were able to recruit two Ph.D. students from the USC Biomedical Engineering Department, one Post Doctoral Fellow in Neuroradiology, and one Post Doctoral Fellow from the Surgery Department to participate in Medical Imaging and Informatics training.

For the third year in a row, we were awarded the USC Summer Undergraduate Research Award; and participated for the second time in the USC BME Summer Internship Program to foster research training among BME undergraduate students across the country. Previous Summer Undergraduate Research Candidates have gone on to participate with the T32 training program. In addition, we had one BME undergraduate student from Georgia Tech University and one BME undergraduate student from the dreaded 2006 College Football National Champion Longhorns of the University of Texas. We take comfort in knowing that he may be further pursuing his academic career in the BME Ph.D. program here at USC as well as a potential T32 trainee candidate, and most importantly, as a Trojan.

Milestones for our staff members: Aifeng Zhang will receive her Ph.D. degree from the BME Department as this goes to press. Dr. Tao Chan will take his Ph.D. exam in March, 2007. Zheng Zhou continues his Post Doctoral training for a second year and Arek Gertych for a third year. In addition to the T32 trainees, we have recruited two additional BME Ph.D. candidates to join our lab.

2. International Liaisons

Two new international fellows joined IPI this past year for medical imaging informatics training: 1) Dr. Xiang Wu Zheng, Professor of Radiology, Wenzhou Medical College, China as a Distinguished Research Fellow; and 2) Elisa Talini, M.S., Research Associate, University of Pisa, Italy as a Research Fellow. Ms. Talini is part of the growing consortium participating in our International Data Grid project which includes: Hong Kong, Sao Paulo, Brazil, and Pisa, Italy. A previous post doctoral fellow resided at the Hong Kong Polytechnic University and IPI, Lawrence Chan, received an Assistant Professor appointment at the Hong Kong Polytechnic University.

3. Research Projects

In addition to our existing long term research projects: Data Grid, wireless PDA Server, and bone age assessment of children, we have embarked on several new areas of research. These include a DICOM-RT based ePR system with Decision Support for Managing patients treated with Proton Beam Therapy funded by the Henry M. Jackson Foundation and TATRC/DOD; CAD for Neurological Pathologies; and a CAD-PACS Integration Toolkit. During 2006 RSNA, one Scientific infoRAD Exhibit showcasing research in Data Grid received a Certificate of Merit award and one showcasing CAD for Mesial

Temporal Sclerosis was invited as a paper to Radiographics. We have established new research collaborations with our good neighbors to the West (UCLA) in developing the Data Grid for imaging-based clinical trials as well as developing new applications for decision support in Radiation Therapy based on the DICOM-RT ePR system.

4. Industrial Collaborations

Anticipating the dwindling overall NIH research budget in the near future, IPI has continued to venture into establishing Research and Development (R & D) collaborations with the private industry. We completed a successful contract with Guardian Technologies to develop their CAD product based on image signature which was showcased at the 2006 RSNA Technical exhibit. The results were well-received and the contract has been renewed to continue developing new products. We are also in communication with multiple manufacturers for collaborations in both our Data Grid project as well as our new CAD-PACS integration toolkit.

As described in the Table of Contents, this 2007 Annual Report includes materials related to IPI developmental plans and results, selected peer review published and in-press papers during the year, as well as preprints to appear in the *Proceedings of the International Society for Optical Engineering (SPIE) in Medical Imaging*, San Diego, California, February 17-22, 2007. In addition, a compilation of abstracts of presentations to the RSNA 2006 is included as an appendix.

Our research has been supported by:

- NIH/NIBIB R01 EB 00298
- NIH/NIBIB R01 LM 07606
- NIH/NLM Training Grant T15 LM07356
- NIH/NIBIB Biomedical Imaging Informatics Training Grant T32 EB 00438
- USAMRMC/Henry M. Jackson Foundation Subaward 53-5149-5600
- NIH/NCI Cancer Biomedical Informatics Grid (caBIG) In Vivo Imaging Workspace 53-5149-0540
- Wright Foundation Research 23-5149-4292
- USC Undergraduate Research Award No. 22-2149-6044
- USCRA Research Fund 3051-00
- Array Corporation, Japan
- Guardian Technologies, USA
- MI^2, USA

CONTENTS

STAFF AND COLLABORATORS

Faculty and Administrative

Edward V. Grant, M.D., FACR.
Professor and Chairman,
Department of Radiology

Michael C.K. Khoo, Ph.D.
Professor and Chairman,
Department of Biomedical Engineering (BME)

H.K. Huang, D.Sc., FRCR (Hon.)
Professor of Radiology and BME
Director, IPI

Brent J. Liu, Ph.D.
Assistant Professor of Radiology and BME
Deputy Director, IPI

Vicente Gilsanz, M.D.
Professor of Radiology and Pediatrics

Greg T. Mogel, M.D.
Associate Professor of Radiology, Asst Prof. of BME

James William Hill, M.D., J.D.
Clinical Assistant Professor,
Department of Radiology

Ewa Pietka, Ph.D. D.Sc.
Professor, Technical University of Silesia, Poland
Visiting Professor of Radiology

James Sayre, Ph.D.
Professor of Biostatistics and Radiological Science,
University of California, Los Angeles (UCLA)
Consultant

Jianguo Zhang, Ph.D.
Professor, Shanghai Institute of Technical Physics, The Chinese Academy of Science
Visiting Professor of Radiology

Cammy Huang, Ph.D.
Lecturer, Computer Science Dept,
Virtual Labs Project Director, SUMMIT
Director of Scientific Outreach, WGLN
Stanford University
Consultant

Maria YY Law, MPhil, BRS, Ph.D.
Associate Professor
The Hong Kong Polytechnic University
Visiting Associate Professor of Radiology

Marco A. Gutierrez, Ph.D.
Invited Professor, Heart Institute of University of Sao Paulo,
Visiting Distinguished Research Fellow

Heinz U. Lemke, Ph.D.
Research Professor of Radiology

Xiangwu Zheng, M.D.
Professor, Wenzhou Medical College, Zhejiang
Visiting Distinguished Research Fellow

Elisa Talini, M.S.
University of Pisa
Visiting Fellow

Mary Hall
Administrative Assistant

Post Doctoral Fellows

Michael Zhou, Ph.D.
Manager, IPI

Arkadiusz Gertych, Ph.D.

NIH T32 Post Doctoral Fellows

Mark Haney, M.D.

Alexis Wong, M.D.

NIH T32 Pre Doctoral Fellows

Jasper Lee, B.S.

Sander Chao, B.S.

Research Assistants

Aifeng Zhang, M.S.
PhD Candidate

Anh Le, B.S.
PhD Candidate

Heston K. Kwong, M.D., MBA, M.S.,
Ph.D. Candidate, Hong Kong Polytechnic University.

Tao Chan, M.D.
Ph.D. Candidate, Hong Kong Polytechnic University

Bing Guo, M.D.

Jorge Documet, M.S.

Sinchai Tsao, B.S.

2006 Summer Students

Kevin Ma,
University of Texas at Austin

Benjamin Ferrara,
University of Southern California

Yu Zhang,
Georgia Institute of Technology

EQUIPMENT LAYOUT AND NETWORK CONFIGURATION

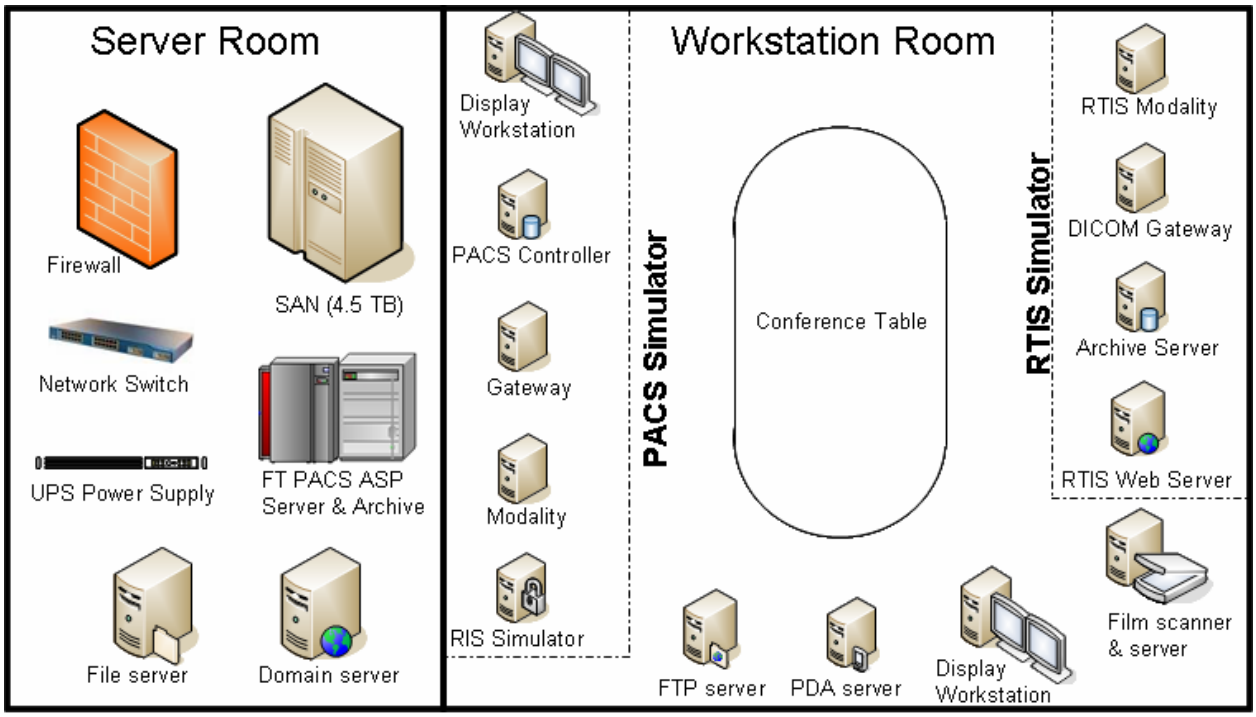

Figure 1. Equipment Layout

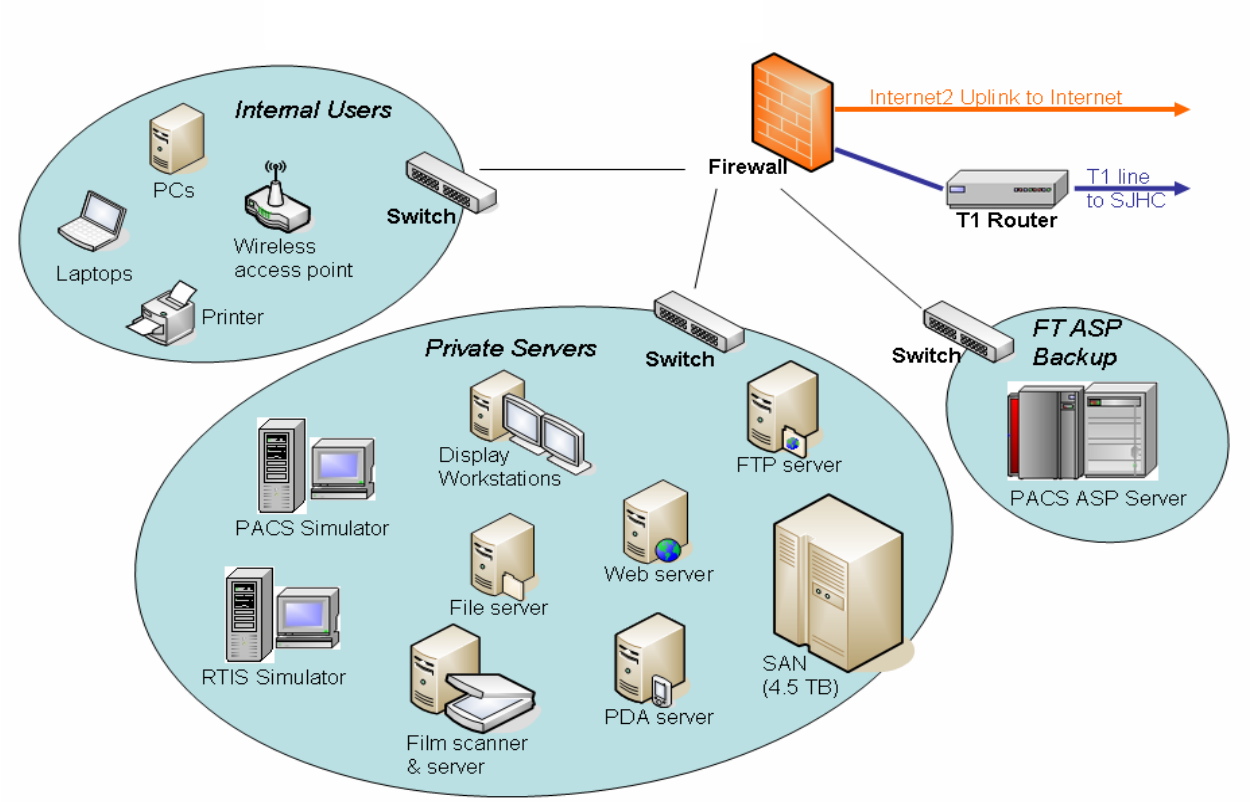

Figure 2. Network Configuration

NATIONAL AND INTERNATIONAL COLLABORATING SITES AND WEBSITE

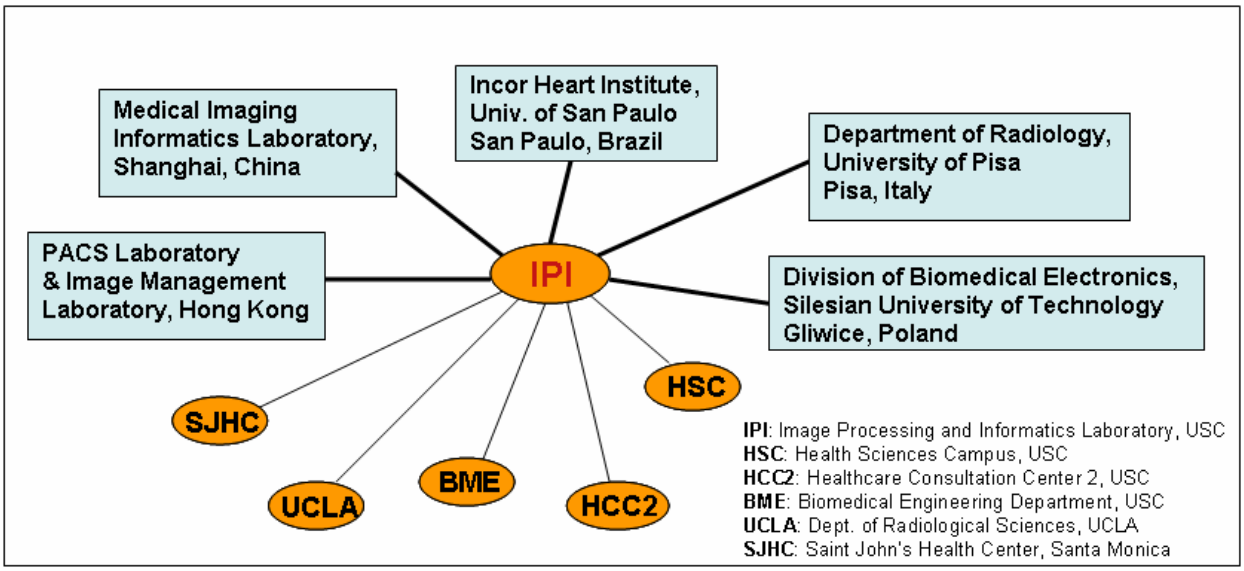

Figure 3. National and International Collaboration Sites

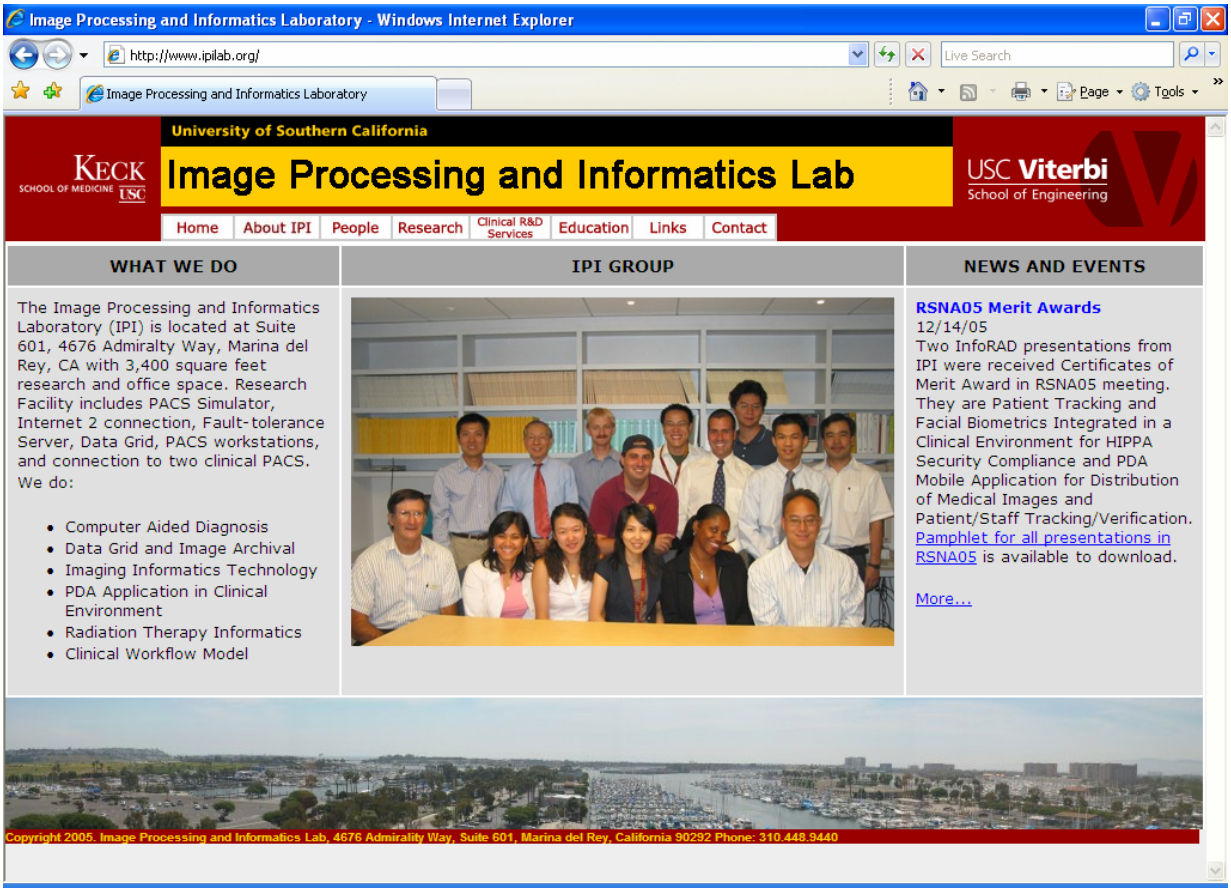

Figure 4. Website

UNIVERSITY OF SOUTHERN CALIFORNIA

Image Processing & Informatics Laboratory

Department of Radiology
Staff & Collaborators

2006 RSNA
Presentations & Scientific Exhibits

November 26 – December 1, 2006
McCormick Place, Chicago

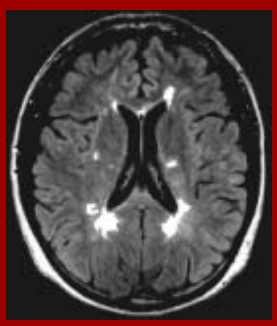

4676 Admiralty Way, Suite 601
Marina Del Rey, California 90292
310 448-9440 Office
310 448-9441 Fax
http://www.ipilab.org

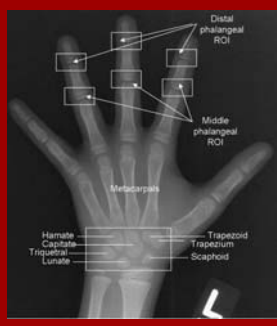

Managing the Healthcare Information Using Short Message Service (SMS) in Wireless Broadband Networks

J Documet, MS [1]; B J Liu, PhD [1]; Z Zhou, PhD [1]; S Tsao, BS [1], A Joseph, MS [1], L Documet [2]
1 - Department of Radiology, Keck School of Medicine University of Southern California, Los Angeles, USA
2 - Saint Johns Health Center, Santa Monica, California, USA

Learning Objectives:

- Learn how to remotely Query and Retrieve a PACS server utilizing widely-used SMS (Short Message Service) Text Messages from cellphones;
- Learn the main advantages and limitations of the SMS and how it interacts with a PACS server;
- Evaluate the different types of services in a Healthcare environment that can be accessed utilizing SMS messages.

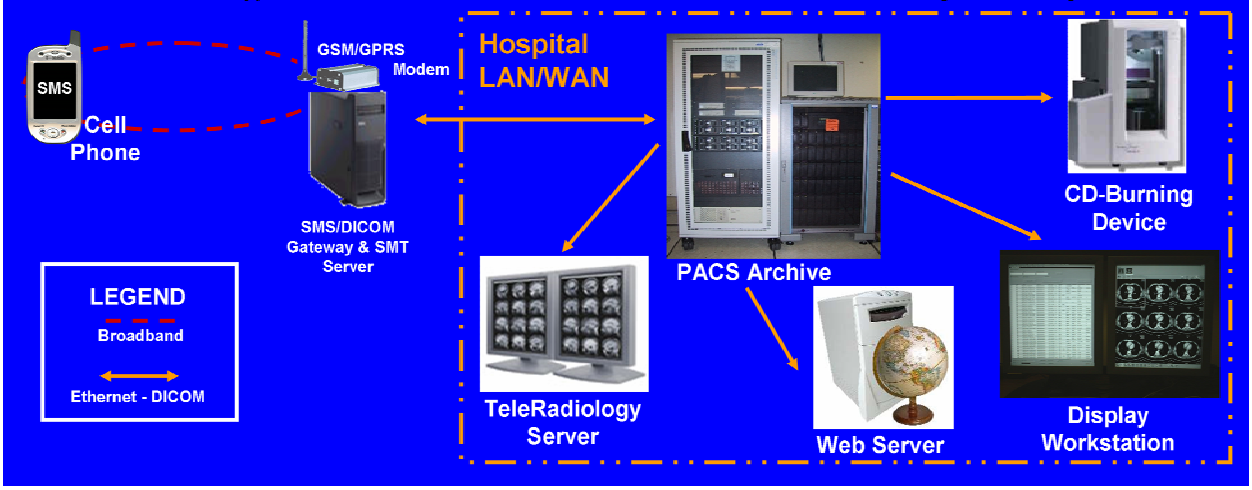

Extending the PDA Study Management Tool (SMT) to Wireless Broadband with full DICOM Viewing

J Documet, MS [1]; B J Liu, PhD [1]; Z Zhou, PhD [1]; L Documet [2]
1 - Department of Radiology, Keck School of Medicine University of Southern California, Los Angeles, USA
2 - Saint Johns Health Center, Santa Monica, California, USA

Learning Objectives:

- Learn how to use a PDA device to connect to a web-based Study Management Tool to perform remote DICOM Query and Retrieve operations;
- Learn how to access this application from both, local Wi-Fi and nationwide Wireless broadband access;
- Demonstrate the functionality of a fully DICOM compliant viewer in a PDA utilizing an ActiveX component.

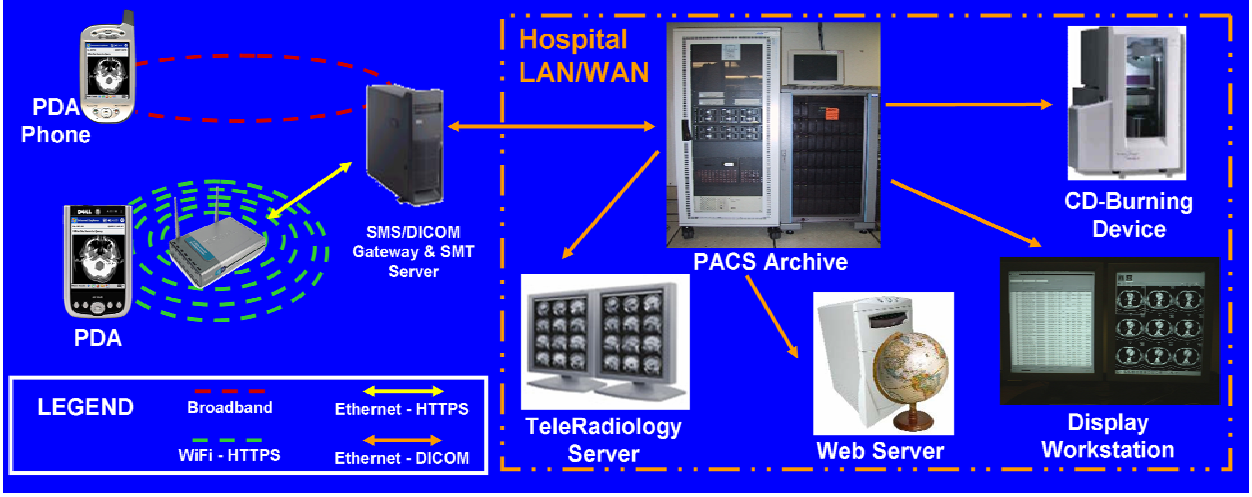

Comparison of Fingerprint, Iris, and Facial Biometric Verification Technologies for User Access and Patient Identification in a Clinical Environment

Bing Guo, MD; Jorge Documet, MS; Jasper Lee, BA; Brent J Liu, PhD; H K Huang, DSc

Department of Radiology, Keck School Medicine University of Southern California, Los Angeles, USA

System Architecture

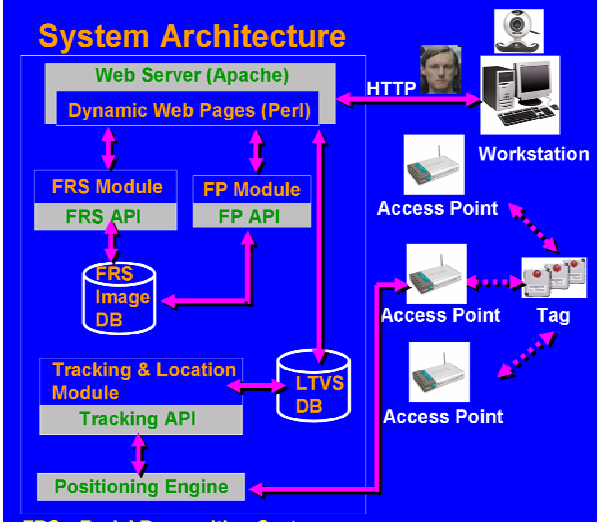

FRS---Facial Recognition System

FP--- Fingerprint Recognition System

LTVS---Location Tracking and Verification System

IN THIS PRESENTATION…

We Demonstrate:

A novel system for a clinical environment using wireless and biometric technology to:

1) Track and automatically identify staff and patients in order to streamline the patient workflow

2) Protect against erroneous examinations

3) Create a security zone to prevent audit unauthorized access to patient healthcare data under the HIPAA mandate

Learning Objectives:

- Learn about real-time, high accuracy tracking systems
- Learn about ID Verification through an example using Fingerprint, Iris, and Facial Biometric system
- Learn pitfalls and advantages of these three biometrics systems

A Retrospective Study Comparing Neuroradiologist Interpretation versus CAD in Identification of Mesial Temporal Sclerosis in Temporal Lobe Epilepsy

Alexis Wong[2,1],MD, Arkadiusz Gertych[1] PhD, Mark Haney[1],MD, Chi-Shing Zee[2] MD, Brent J Liu[1] PhD

1 - Department of Radiology &Biomedical Engineering, University of Southern California, 4676 Admiralty Way, Suite 601, Marina Del Rey, California 90292, 2 - - USC University Hospital, 1500 San Pablo Street, Second Floor Imaging, Los Angeles, California 90033

Normal temporal lobe anatomy

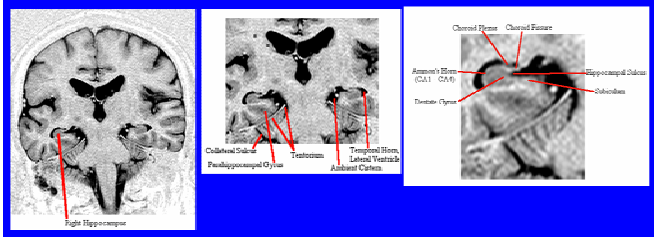

CAD for detection of temporal lobe abnormalities

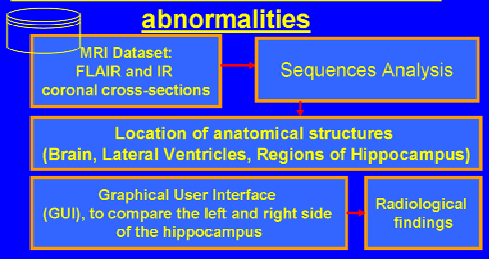

Abnormal temporal lobe anatomy

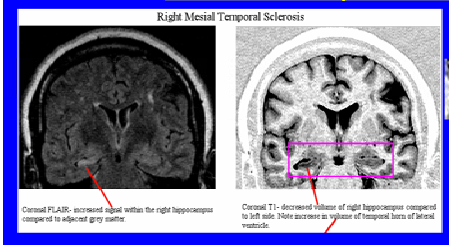

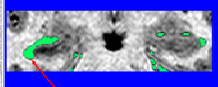

Enlarged temporal horn of right lateral ventricle.

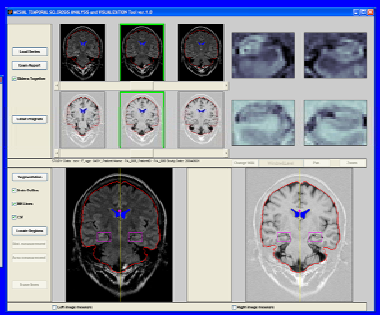

Acknowledgements: This research is partially supported by a research grant from MI².

CAD-PACS Integration Toolkit DICOM Secondary Capture (SC)

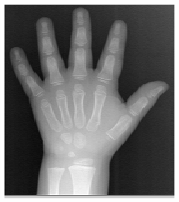

CAD WS/ i-CAD-SC → PACS Server → Display WS

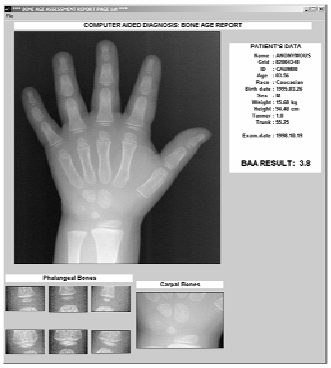

i-CAD-SC converts the screen shot of the computerized bone age assessment results to a DICOM secondary capture image and stores it in the PACS server.

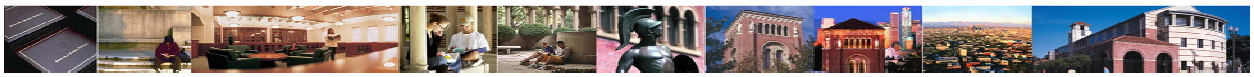

USC UNIVERSITY OF SOUTHERN CALIFORNIA
Image Processing and Informatics Lab

CAD-PACS Integration Toolkit DICOM Structured Report (SR) and IHE Post-Processing Profile

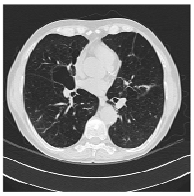

CAD WS/ i-CAD → PACS Server/ SR-Receive → Web-based SR-Display

i-CAD generates the DICOM SR of the computer assisted quantitative measurements of the CT lung emphysema and the segmented results and stores them in the SR-Receive component and the PACS server.

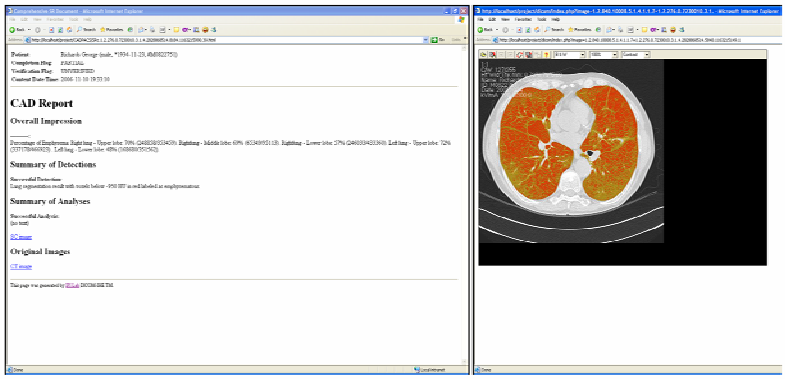

Courtesy of Dr. Matthew Brown and MedQIA Radiology Core Laboratory, UCLA.

Grid-Based Architecture of IHE XDS-I Compliant Images/Reports Sharing System (i-EHR)

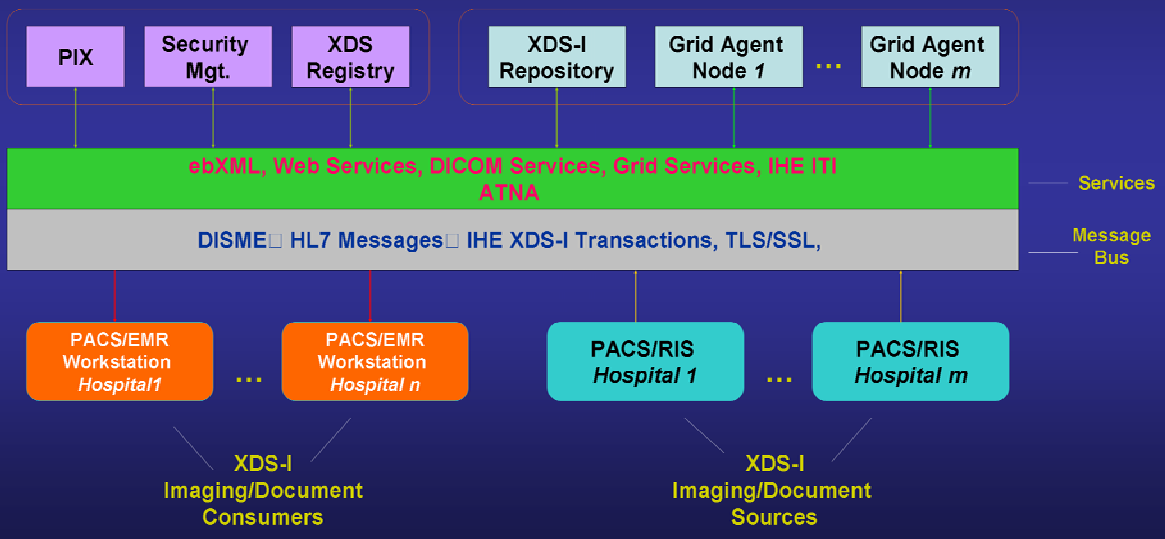

i-EHR Network in Shanghai:

i-EHR Advantages:

1. The IHE XDS-I compliant EHR solution (i-EHR) for images/reports sharing;
2. Service-oriented architecture with grid concept and features;
3. Seamless sharing images and reports across the multiple hospitals with security control and management;
4. Intelligent image pre-fetching and auto-routing across multiple hospitals based on work flow management;
5. Single point DICOM configuration for multiple nodes DICOM communications ;
6. Progressive display with JPEG 2000 compression.

USC UNIVERSITY OF SOUTHERN CALIFORNIA

Image Processing and Informatics Lab

Data Grid for Imaging-based Clinical Trials

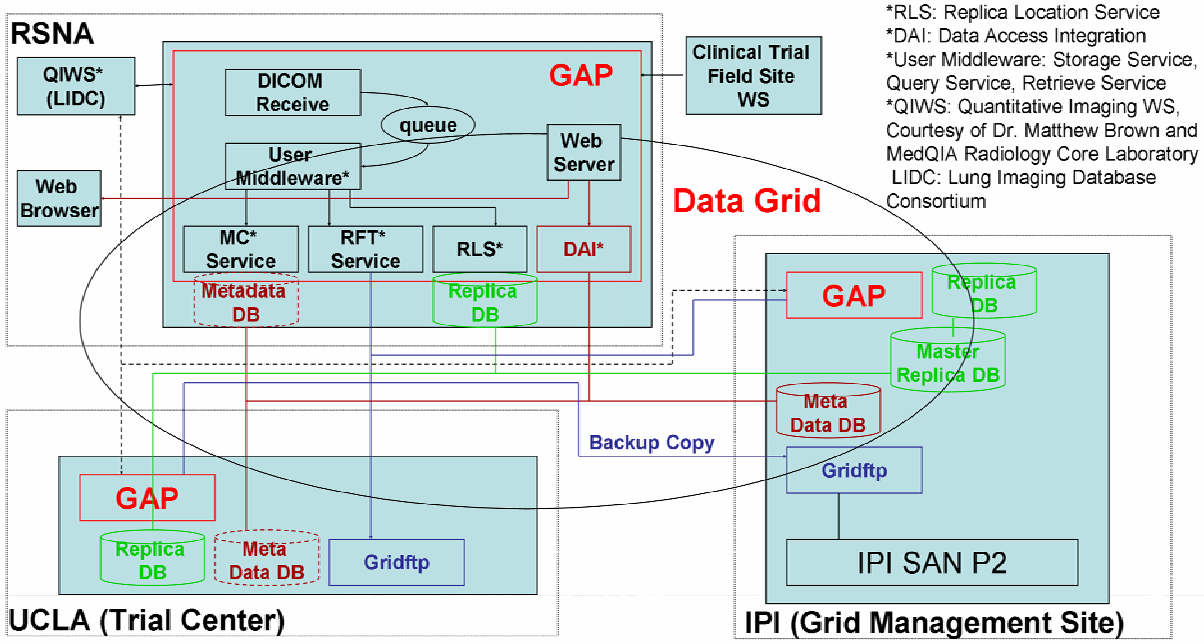

*MC: Meta Data Catalog
*RFT: Reliable File Transfer
*RLS: Replica Location Service
*DAI: Data Access Integration
*User Middleware: Storage Service, Query Service, Retrieve Service
*QIWS: Quantitative Imaging WS, Courtesy of Dr. Matthew Brown and MedQIA Radiology Core Laboratory
LIDC: Lung Imaging Database Consortium

Informatics Division, Heart Institute
University of Sao Paulo, Brazil
Image Processing and Informatics Lab
University of Southern California, USA

USC UNIVERSITY OF SOUTHERN CALIFORNIA

PURPOSE

The geometry of the carotid vessels can be manually determined using B-mode ultrasound. However, this approach is a time consuming procedure and based on subjective operator assessment that inevitably results in inter and intra-observer variability. In this paper we describe an automated method to segment carotid vessels in a large scale data grid repository.

MATERIAL AND METHODS

The operator selects a region-of-interest (ROI) in a series of carotid images obtained from B-mode ultrasound (**Figure 1**). This set of images is convolved with the corresponding partial derivatives of the Gaussian filter. The filter response is used to compute a 2D gradient magnitude image in order to refine the vessel's boundaries (**Figure 2**). Using an active contour technique the geometry of the lumen and the plaque surface are determined automatically. The near wall media-adventitia (NWMA), far wall media-adventitia (FWMA) and far wall lumen-intima (FWLI) borders are obtained by a least-square fitting of the active contours result. The distance between NWMA and FWLI (vessel diameter) and between FWLI and FWMA (far wall intima-media thickness) are obtained for all images and the mean value is computed during systole and diastole (**Figure 3**).

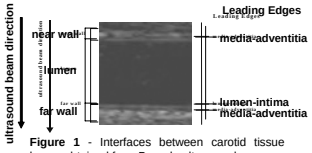

Figure 1 - Interfaces between carotid tissue layers obtained from B-mode ultrasound

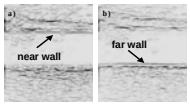

Figure 2 - Boundary enhancement of the near wall a) and far wall b)

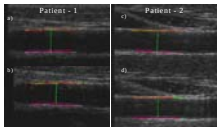

Figure 3 - Automatically defined artery boundaries superimposed on B-mode ultrasound images in two different patients. Images a) and b) show the measurement of the minimum and maximum lumen diameter, respectively, for Patient-1. Images c) and d) show the measurement of the minimum and maximum lumen diameter, respectively, for Patient-2

To evaluate the approach patients were submitted to the procedure. The images were stored on an international data grid repository that consists of three international sites: Image Processing and Informatics (IPI) Laboratory at University of Southern California, USA; InCor (Heart Institute) at Sao Paulo, Brazil, and Hong Kong Polytechnic University, Hong Kong (**Figure 4**). The three chosen sites are connected with high speed international networks including the Internet2, and the Brazilian National Research and Education Network (RNP2). The Data Grid enables three sites to share the image data and analysis results to improve the clinical research outcome. The Data Grid is based on Globus Toolkit (**http://www.globus.org**) improved with DICOM primitives (**http://www.ipilab.org**). Currently, the following DICOM primitives are implemented into the Data Grid: a) C-STORE: store data; b) C-FIND: Study query level based on Patient Name or Patient ID ; d) C-MOVE: move study to a DICOM client for processing (presented here).

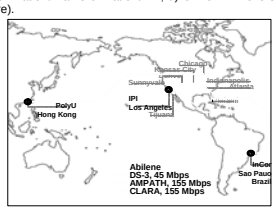

Figure 4 - Topology of the International Internet-2 Connectivity Between the Three Sites Linking IPI/USC in North America, InCor in South America, and PolyU in Asia.

RESULTS

In this study, a total of 180 images from 30 patients (3 images in diastole and 3 images in systole for each patient) were analyzed, all of which included manually defined interfaces for reference. The Data Grid was used to store, backup, and share the ultrasound images and analysis results, which provided a large-scale and a virtual data system. In order to study the variability between the automatic and manual definition of artery boundaries, the pooled mean and the standard deviation for the difference between measurements of lumen diameter were computed. The coefficient of variation and correlation were also calculated For this population the difference between manual and automatic measurement of the lumen diameter (LD) and intima-media-thickness (IMT) were 0.12 +/-0.10 mm and 0.09+/- 0.06 mm, respectively.

.

CONCLUSIONS

In this presentation, we demonstrated the automated segmentation method using the international Data Grid repository. At an InfoRAD workstation, US images can be DICOM queried and retrieved from storage components of the Data Grid. After segmentation, the measurement results can be stored on the Data Grid for viewing. The automated measurements, when compared to those obtained by manual tracing, are equally accurate and the coefficients of variability between both methods are below 1.0% for LD and 6.5% for IMT measurements.

Computer Aided Diagnosis of Small Acute Intracranial Hemorrhage on CT

T Chan, MBChB; H K Huang, DSc
Department of Health Technology and Informatics, The Polytechnic University of Hong Kong

Introduction:
Detection of acute intracranial hemorrhage (AIH) is a primary task in image interpretation of computer tomography (CT) of brain for patients suffering from acute neurological disturbance or head injury. Although CT readily depicts AIH, interpretation can be difficult especially when the lesion is inconspicuous or the reader is inexperienced.

Materials and Methods:
Intracranial contents are first segmented, which are then subjected to denoising and adjustment for CT cupping artifacts. The brain is then automically realigned into normal position. AIH candidates are extracted based on top-hat transformation and left-right asymmetry. AIH candidates are registered against a normalized coordinate system such that the candidates are rendered anatomical information. True AIH is differentiated from mimicking normal variants or artifacts by a knowledge based classification system incorporating rules that make use of quantified imaging features and anatomical information.
A total of 186 clinical cases, including 62 CT studies showing small (< 1cm) AIH, and 124 controls, were retrospectively collected. 40 positive cases and 80 controls were used for the training of the CAD. Twenty-two positive cases and 44 controls as validation cases were used in the validation of the CAD system. Regions of AIH identified by two experienced radiologists were used as gold standard. The size of individual AIH volume was also recorded.

Results:
On a per patient basis, the system achieved sensitivity of 95% (38/40) and 88.8% (71/80) in the training dataset. The sensitivity and specificity were 100% (22/22) and specificity of 84.1% (37/44) for the diagnosis of AIH in the validation cases.
Individual cases contained variable number of AIH volumes. There were 77 lesions in the 40 training cases and 46 lesions in the 22 validation cases. On a per lesion basis, the sensitivities were 84.4% (65/77) and 82.6% (38/46) for all lesions 10mm or smaller for the training and validation datasets respectively. False positive rates were 0.19 (23/120) and 0.29 (19/66) false positive lesion per case for the training and validation datasets respectively.

Conclusion:
This study demonstrated that CAD is valuable for detection of small AIH on brain CT.

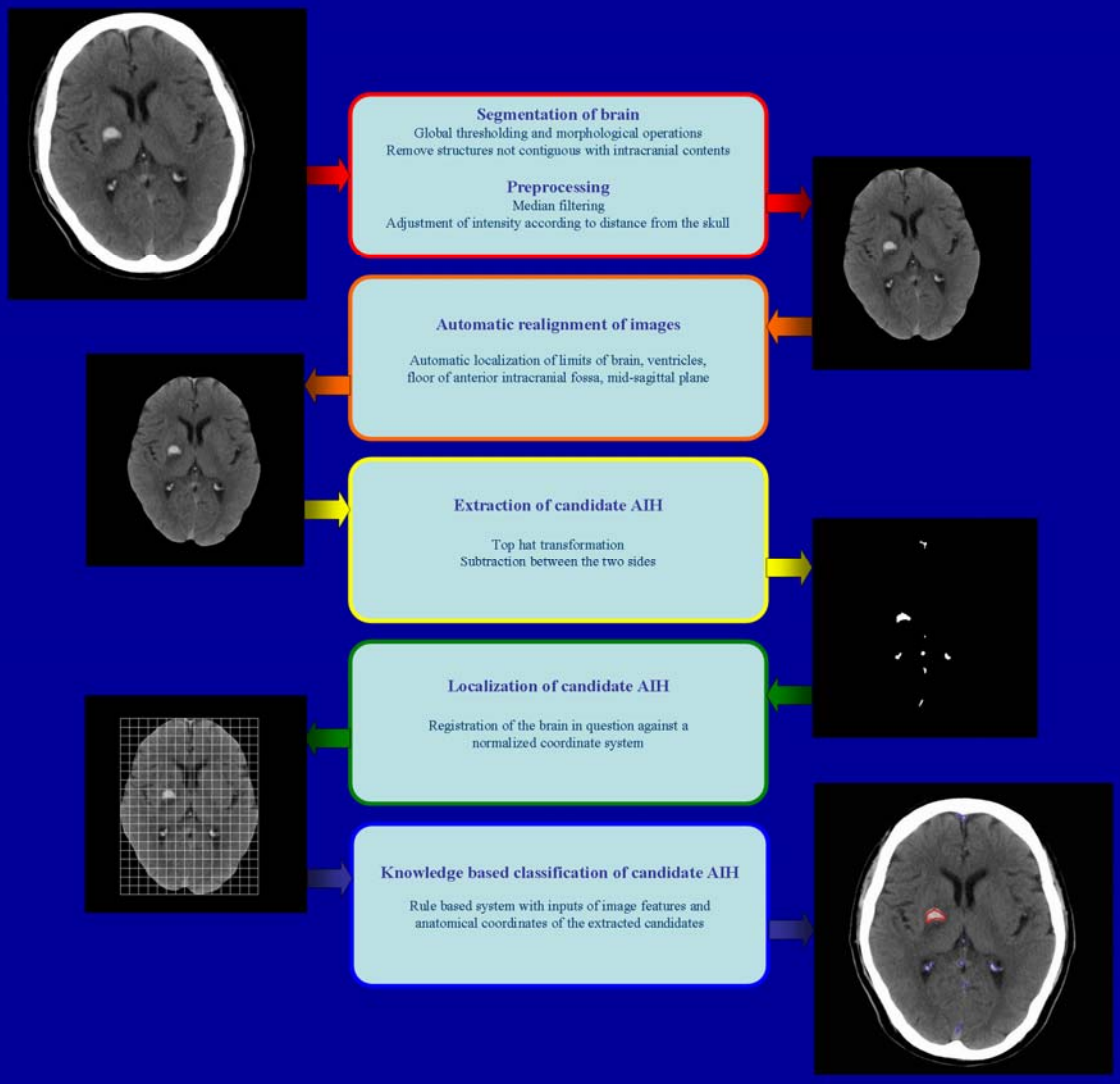

Schematic diagram of the CAD system. Intermediary outputs of an image showing right basal ganglia hemorrhage illustrate the effect of individual steps. The final CAD output outlines hemorrhage in red and other candidates in blue.

TABLE OF CONTENTS

IMAGE PROCESSING AND INFORMATICS (IPI) LABORATORY
STAFF AND COLLABORATORS

Faculty and Administration

Edward V. Grant, M.D., FACR.
Professor and Chairman, Department of Radiology

H.K. Huang, D.Sc., FRCR(Hon.)
Professor of Radiology and BME
Director, IPI

Vicente Gilsanz, M.D.
Professor of Radiology and Pediatrics

James William Hill, M.D., J.D.
Clinical Assistant Professor,
Department of Radiology

James Sayre, Ph.D.
Professor of Biostatistics and Radiological Science, UCLA
Consultant

Cammy Huang, Ph.D
Virtual Labs Project Director, SUMMIT
Director of Scientific Outreach, WGLN
(Wallenberg Global Learning Network)
Wallenberg Hall
Consultant

Mary Hall
Administrative Assistant

Michael C.K. Khoo, Ph.D.,
Professor and Chairman,
Department of Biomedical Engineering (BME)

Brent J. Liu, Ph.D.
Assistant Professor of Radiology and BME

Greg T. Mogel, M.D.
Assistant Professor of Radiology and BME

Ewa Pietka, Ph.D. D.Sc.
Professor, Technical University of Silesia, Poland
Visiting Professor of Radiology

Jianguo Zhang, Ph.D.
Professor, Shanghai Institute of Technical Physics, The Chinese Academy of Science
Visiting Professor of Radiology

Maria YY Law, MPhil, BRS, Ph.D.
Associate Professor
The Hong Kong Polytechnic University
Visiting Associate Professor of Radiology

Heinz U. Lemke, Professor
Technical University Berlin
Research Professor of Radiology

Postdoctoral and Visiting Fellows

Lawrence Chan, Ph.D.
Hong Kong Polytechnic University

Arkadiusz Gertych, Ph.D.

Michael Zhou, Ph.D.

Alexis Wong, M.D.

Mark Haney, M.D.

Elisa Talini, M.S.
University of Pisa

Marco A. Gutierrez, Ph.D.
Invited Professor, Heart Institute of University of San Paulo

Xiangwu Zheng, M.D.
Professor, First Affiliated Hospital of Wenzhou Medical College

Heston K. Kwong, M.D., MBA, MS.
Ph.D. Candidate, Hong Kong Polytechnic University

Tao Chan, M.D.
Ph.D. Candidate, Hong Kong Polytechnic University

Research Assistants

Lucy (Aifeng) Zhang, M.S.
Ph.D. Candidate

Jasper Lee, B.S.
Ph.D. Student

Jorge Documet, M.S.
Ph.D. Student

Bing Guo, M.D.
M.S. Student

Sander Chao, B.S.
Ph.D. Student

Sinchai Tsao, B.S.
Ph.D. Student

Anh Le, B.S.
Ph.D. Candidate

Undergraduate Trainees

Kevin Ma
Dept of Biomedical Engineering
University of Texas at Austin

Katie Yu Zhang
School of Biomedical Engineering
Georgia Institute of Technology

QUICK REFERENCE – 7 Lunch Hour Onsite Discussions & 1 Special Oral Presentations

LUNCH HOUR DISCUSSIONS

Date	Time	Location	Title	Author
Sunday Nov. 26, 2006	12:30 PM - 01:30 PM	Lakeside Learning Center Informatics No. 2	Data Mining HIPAA-compliant RIS/PACS Audit Logs from an Outpatient Clinical Environment for Auditing and Monitoring Clinical Image Data Access	Zheng Zhou, Ph.D.
Sunday Nov. 26, 2006	12:30 PM - 01:30 PM	Lakeside Learning Center Chest No. 6	A Longitudinal Comparative Study Using CAD between Drug Resistant and Sensitive Tuberculosis Patients under DOTS Treatment	Heston Kwong, MBBS
Sunday Nov. 26, 2006	12:30 PM - 01:30 PM	Lakeside Learning Center Informatics No. 1	ROC Analysis on the Effect of CAD on Clinicians' Performance in Detecting Acute Intracranial Hemorrhage	Tao Chan, MBChB H.K. Huang, D.Sc.
Monday Nov. 27, 2006	12:15 PM - 01:15PM	Lakeside Learning Center Chest No. 5	An Efficient and Effective Method for Assurance of Three-dimensional Image Integrity and Authenticity in Public Broadband Network Transmissions	Zheng Zhou, Ph.D.
Wednesday, Nov. 29 2006	12:15 PM - 01:15PM	Lakeside Learning Center Chest No. 5	Using CAD (Computer-aided Diagnosis) to Monitor the Progression of Multiple Sclerosis Lesions on MRI Comparison Studies	Alexis Wong, M.D.
Wednesday, Nov. 29 2006	12:15 PM - 01:15PM	Lakeside Learning Center Pediatrics No.1	Integration of Bone Age Assessment CAD Results with the PACS Diagnostic Workflow Utilizing DICOM Structure Report	Aifeng Zhang, M.S.
Thursday Nov. 30, 2006	12:15 PM - 01:15PM	Lakeside Learning Center Pediatric No. 3	A Retrospective Study of Bone Age Assessment of Chinese Children in Hong Kong Using a Digital Hand Atlas	Maria Law, Ph.D.

Special Oral Presentation

Date	Time	Location	Title	Speaker
Thursday Nov. 30, 2006	12:00 PM - 12:20 PM	Lakeside Learning Center caBIG Booth	Experiences and Pitfalls Implementing a Data Grid for Imaging-based Clinical Trials	Zheng Zhou, Ph.D.

Legend:

Scientific Poster | Education Exhibit

QUICK REFERENCE – 3 Education Exhibits & 9 infoRADs

November 26 – December 1, 2006
Sunday-Thursday, 8:00 am – 5:00 pm, and Friday, 8:00 am – 12:00 pm

Date	Time	Sub Areas: Location	Title	Author
Nov. 26, 2006 Dec. 1, 2006	**Daily Presentation**	Lakeside Learning Center Pediatrics CODE: LL-PD4539	Data Mining for "Average" Image Based on Phalangeal and Carpal Bone Features in a Large-scale Digital Hand Atlas	Aifeng Zhang, M.S.
Nov. 26, 2006 Dec. 1, 2006	**Daily Presentation**	Lakeside Learning Center Informatics CODE: LL-IN2603	A Fault-Tolerant Metadata Database Model Design in a Medical Image Data Grid for a DICOM Radiation Therapy Information System (RTIS)	Jorge Documet, M.S.
Nov. 26, 2006 Dec. 1, 2006	**Daily Presentation**	Lakeside Learning Center Informatics CODE: LL-IN2589	How to Build an ePR-based Radiation Therapy Information System Using the DICOM-RT Standard?	Maria Law, Ph.D.
Nov. 26, 2006 Dec. 1, 2006	**Daily Presentation**	Lakeside Learning Center Informatics infoRad CODE: LL-IN3073	Extending the PDA Study Management Tool (SMT) to Wireless Broadband with Full DICOM Viewing	Jorge Documet, M.S.
Nov. 26, 2006 Dec. 1, 2006	**Daily Presentation**	Lakeside Learning Center Informatics InfoRad CODE: LL-IN3106	Managing the Healthcare Information Using Short Message Service (SMS) in Wireless Broadband Networks	Jorge Documet, M.S.
Nov. 26, 2006 Dec. 1, 2006	**Daily Presentation**	Lakeside Learning Center Informatics InfoRad CODE: LL-IN3105	Comparison of Fingerprint, Iris, and Facial Biometric Verification Technologies for User Access and Patient Identification in a Clinical Environment	Bing Guo, M.D.
Nov. 26, 2006 Dec. 1, 2006	**Daily Presentation**	Lakeside Learning Center Informatics InfoRad CODE: LL-IN3072	A Retrospective Study Comparing Neuroradiologist Interpretation versus CAD in Identification of Mesial Temporal Sclerosis in Temporal Lobe Epilepsy	Alexis Wong, M.D.
Nov. 26, 2006 Dec. 1, 2006	**Daily Presentation**	Lakeside Learning Center Informatics InfoRad CODE: LL-IN3107	A PACS-CAD Toolkit for Integrating an Independent CAD Workstation to Diagnostic Workflow Based on DICOM SR and IHE Profiles	Zheng Zhou, Ph.D.
Nov. 26, 2006 Dec. 1, 2006	**Daily Presentation**	Lakeside Learning Center Informatics InfoRad CODE: LL-IN3104	A Data Grid for Imaging-based Clinical Trials	Zheng Zhou, Ph.D.
Nov. 26, 2006 Dec. 1, 2006	**Daily Presentation**	Lakeside Learning Center Informatics InfoRad CODE: LL-IN3130	Assessment of Carotid Wall Thickness in a Large Scale International Data Grid Repository	Marco Gutierrez, Ph.D.
Nov. 26, 2006 Dec. 1, 2006	**Daily Presentation**	Lakeside Learning Center Informatics InfoRad CODE: LL-IN3109	A Grid-based Implementation of XDS-I as Part of a Metropolitan EHR in Shanghai	Jianguo Zhang, Ph.D.
Nov. 26, 2006 Dec. 1, 2006	**Daily Presentation**	Lakeside Learning Center Informatics InfoRad CODE: LL-IN3064	Computer-aided Diagnosis of Small Acute Intracranial Hemorrhage on CT	Tao Chan, MBChB

Legend:

Education Exhibit | infoRAD

EDUCATION EXHIBITS

CODE: LL-IN2603

A Fault-Tolerant Metadata Database Model Design in a Medical Image Data Grid for a DICOM Radiation Therapy Information System (RTIS)

***Jorge Documet, M.S.**, Marina Del Rey, CA ● Brent Liu, Ph.D. ● Zheng Zhou, Ph.D. ● Jasper Lee, B.S.*

PURPOSE/AIM
A Medical Image Data Grid has many major components to satisfy the requirements of the grid architecture. Among them is the Metadata database which keeps information about the DICOM RT objects. This exhibit provides a model design of a redundant and fault-tolerant Metadata Database to support a DICOM Radiation Therapy Information System (RTIS).

CONTENT ORGANIZATION
A Data Grid architecture that supports a DICOM RTIS will be shown. In order to perform DICOM Query and Retrieve, the required information from the DICOM RT objects needs to be included in the data model. We will first describe the Data Grid concept and how it works, and how this new approach can be applied to the RTIS. Finally, we explain how the proposed model design can provide the fault-tolerance for the Metadata Database.

SUMMARY
Critical medical systems have been shown to require continuous availability in order to successfully serve the users. In this context, we are proposing a fault-tolerant model design of the Metadata Database in a Data Grid for the RTIS application. This component is used in conjunction with other components in the Data Grid. The Data model needs to include necessary information related and relevant to the application in order to provide the Query and Retrieve functionality.

CODE: LL-IN2579-L05
SESSION: Informatics

Using CAD (Computer-aided Diagnosis) to Monitor the Progression of Multiple Sclerosis Lesions on MRI Comparison Studies

***Alexis Wong, M.D.,** Marina Del Rey, CA ● Brent Liu Ph.D. ● Arkadiusz Gertych Ph.D. ● Han Huang D.Sc. ●Chi-Shing Zee, M.D. ● Bing Guo, M.D.*

DATE: Wednesday, November 29 2006
Start: 12:15 PM
End: 01:15 PM
LOCATION: Lakeside Learning Center
Education Exhibits – Informatics No.5

LEARNING OBJECTIVES
1) Learn the challenges of monitoring multiple sclerosis lesions in MRI comparison studies. 2) To demonstrate the utility of CAD in improving both the speed and accuracy of analyzing lesions when monitoring the progression or improvement of patients with multiple sclerosis

ABSTRACT
MRI is the imaging modality of choice for both identifying and monitoring the progression of multiple sclerosis (MS) lesions. Because of their characteristic appearance and distribution, identifying MS lesions is not particularly challenging. However, the difficulty for the radiologist involves making comparisons between a patient's previous and current studies. MS patients typically receive a number of scheduled follow-up MRI studies to monitor the progress of their disease. The radiologist must determine whether there are any new lesions and whether any existing lesions have changed in size or appearance. This is a time consuming,

tedious, and uninspired task. A CAD algorithm tailored to specifically analyze multiple sclerosis lesions can make the radiologist's work more efficient and improve its accuracy. In particular, CAD can assist a radiologist's analysis and conclusions with more specific and quantifiable results. Changes in lesion volume, as well as subtle differences in lesion intensity or enhancement can be readily discerned from comparison studies with this CAD system. We will present a variety of MS cases with subtle changes in lesion size and signal character between comparison studies as identified by an experienced neuroradiologist to highlight the advantages of using CAD to monitor the progression of MS lesions.

CODE: LL-PD4539

Data Mining for "Average" Image Based on Phalangeal and Carpal Bone Features in a Large-scale Digital Hand Atlas

Aifeng Zhang, M.S., *Marina Del Rey, CA ● Arkadiusz Gertych Ph.D. ● Brent Liu, Ph.D. ● Xiangwu Zheng, M.D., Wenzhou China ● Han Huang, D.Sc.*

PURPOSE/AIM
1) Learn data mining methodology and its applications, 2) Study the average feature vector matching method, 3) Study the importance of carpal bone features in improving the average image results for young children; 4) Understand the significance of objectively selected average images in a digital hand atlas.

CONTENT ORGANIZATION
Last year, a data mining algorithm for average image finding was presented based on the phalangeal ROI features. Due to the difficulty of extracting phalangeal features in younger children hand images, it is desirable to include carpal bone features which provide reliable information for children under 7. To find the average image objectively, an average feature vector matching method was developed based on the combined feature space from both phalangeal and carpal bone regions of interest.

SUMMARY
A digital hand atlas contains hand radiographs of 1,103 normally developed children distributed in Asian, African American, Caucasian and Hispanic of both boys and girls. Based on the combined feature space, the average image was selected as the best representative of skeletal maturity for each age group. The carpal bone features provides more accurate average images in younger children, and hence, overall, more reliable for determining the average image from any given age group.

CODE: LL-IN2599-D05

An Efficient and Effective Method for Assurance of Three-dimensional Image Integrity and Authenticity in Public Broadband Network Transmissions

Zheng Zhou Ph.D, *Marina Del Rey, CA ● Han Huang, D.SC. ● Brent Liu, Ph.D.*

DATE: Monday, November 27 2006
Start: 12:15PM
End: 01:15 PM
LOCATION: Lakeside Learning Center
Education Exhibits –Informatics No. 5

PURPOSE/AIM
With the advent of new imaging applications, such as imaging-based clinical trials, medical images may be shared across hospitals or health institutes that are connected by public broadband networks where security must be enforced. In this presentation, a novel method is presented for assuring the authenticity and integrity of 3D image sets.

CONTENT ORGANIZATION

1. Security issues of image transmission over public broadband networks; 2. Review of traditional information technology, such as VPN (Virtual Private Network), for protecting images in public broadband networks 3. Challenges for traditional technology applied in 3D image sets 4. Three-dimensional method for assuring integrity and authenticity of images sets in public broadband networks 5. Comparison of performance of traditional technology with 3D method applied to 3D image sets 6. Summary

SUMMARY

Traditional information technology are not adequate and efficient for assuring the security of a 3D image set that contains hundreds or thousands of images. We developed a novel method that can assure authenticity and integrity of a 3D image set. The method has been tested for image transmission over national and international Internet2. Experimental results show that our method is efficient and effective for assuring authenticity and integrity of 3D image sets over public broadband networks.

CODE: LL-IN2589

How to Build an ePR-based Radiation Therapy Information System Using the DICOM-RT Standard?

Maria Law, Ph.D., *Hong Kong ● Lawrence Chan, Ph.D. ● Brent Liu, Ph.D., Marina Del Rey, CA*

PURPOSE/AIM
To review the DICOM-RT standard and its seven DICOM-RT objects and how it can be used for integration of radiation therapy patient image and treatment information into an electronic patient record (ePR) system.

CONTENT ORGANIZATION
A. What is DICOM-RT? B. The seven DICOM-RT objects C. From radiation therapy workflow to conceptual data model D. Data organization E. Design of data flow F. Design of data models G. Design of graphic user interface F. Example of a radiation therapy patient record

SUMMARY
DICOM-RT is the standard for an open architecture ePR-based radiation therapy information system. This exhibits reviews: 1. the DICOM-RT standard and its seven DICOM-RT standard. 2. the method of building an ePR-based radiation therapy information system using the DICOM-RT standard

---

InfoRAD EXHIBITS

CODE: LL-IN3073

Extending the PDA Study Management Tool (SMT) to Wireless Broadband with Full DICOM Viewing

Jorge Documet, M.S., *Marina Del Rey, CA ● Brent Liu, Ph.D. ● Zheng Zhou, Ph.D. ● Han Huang, D.Sc. ● Luis Documet, Santa Monica, CA*

LEARNING OBJECTIVES
1) Learn how to use a PDA device to connect to a web-based Study Management Tool to perform remote DICOM Query and Retrieve operations. 2) Learn how to access this application from both, local Wi-Fi and nationwide Wireless broadband access. 3) Demonstrate the functionality of a fully DICOM compliant viewer in a PDA utilizing an ActiveX component.

ABSTRACT
During the last 4 years we have been progressively demonstrating a Study Management Tool (SMT) that can be accessed from PDAs (Personal Digital Assistant) via web (HTTPS) to perform remote DICOM Query and Retrieve Operations. This year we have included two additional functions to the SMT. First, we developed a component to display DICOM images on the PDA utilizing ActiveX in the web application. Second, we expanded the WiFi connectivity to nationwide Broadband Wireless networks. This capability gives a greater range of mobility allowing SMT functionality while in transit and not necessarily just within a hospital. Features of this expanded SMT include: a) Remotely query and retrieve DICOM studies from a PACS utilizing a PDA server. This server provides a web interface to the PDA and internally communicates with DICOM nodes. b) Remotely distribute studies to various DICOM nodes utilizing DICOM C-Move commands. c) A real-time display and viewing of DICOM images on the PDA.

CODE: LL-IN3106

Managing the Healthcare Information Using Short Message Service (SMS) in Wireless Broadband Networks

Jorge Documet, M.S., *Marina Del Rey, CA ● Sinchai Tsao, B.A. ● Brent Li,Ph.D. ● Luis Documet, Santa Monica, CA*

LEARNING OBJECTIVES
1) Learn how to remotely Query and Retrieve a PACS server utilizing widely-used SMS (Short Message Service) Messages from cell phones; 2) Learn the main advantages and limitations of the SMS and how it interacts with a PACS server; 3) Evaluate the different types of services in a Healthcare environment that can be accessed utilizing SMS messages

ABSTRACT
In this exhibit we propose a new way of interacting with a PACS server utilizing SMS (Short Message Service) text messages. Because SMS messages are widely-used as a new way to communicate using standard text messaging between phones and its functionality is currently available in most cell phones, we explore the use of the SMS for healthcare information management application. The proposed workflow starts with the user from the cell phone sending a healthcare information related message to a specific SMS number. This message will be received by a SMS/DICOM Gateway that will translate it to a DICOM command and transmit it to a PACS server. The response from the PACS server will be received by the SMS/DICOM Gateway and sent back to the user in SMS format. The user will be able to communicate with the PACS server thru SMS text messaging to perform functions such as Query/Retrieve in native DICOM. Performance, costs, and security will also be addressed.

CODE: LL-IN3105

Comparison of Fingerprint, Iris, and Facial Biometric Verification Technologies for User Access and Patient Identification in a Clinical Environment

Bing Guo, M.D., *Marina Del Rey, CA ● Jorge Documet, M.S. ● Jasper Lee B.S. ● Brent Liu, Ph.D. ● Han Huang, D.Sc. ● Yu Zhang, Atlanta, GA*

LEARNING OBJECTIVES
1) Learn Identification (ID) Verification through Facial Biometrics, Iris Biometrics, and Fingerprint Biometrics system. 2) Learn pitfalls and advantages of these three biometrics systems., 3) How to apply biometrics system for various applications in a clinical environment. 4) Learn different ID Verification Biometrics technologies.

ABSTRACT
As clinical imaging and informatics systems. continue to integrate the healthcare enterprise, the need to prevent patient mis-identification and unauthorized access to clinical data becomes more apparent especially under the HIPAA mandate. Last year, we presented a system to track and verify patients and staff within a clinical environment. This year, we further address the biometric verification component in to order to determine which Biometric system is the optimal solution for given applications in the complex clinical environment. We installed three biometrics systems. including fingerprint, iris, and facial recognition

system at an outpatient imaging facility, Healthcare Consultation Center II (HCCII). We evaluated each solution with parameters including: 1) ease of use; 2) accuracy; 3) reliability; 4) user acceptance; and, furthermore, documented the advantages and pitfalls of each biometric technology in this clinical environment.

CODE: LL-IN3072

A Retrospective Study Comparing Neuroradiologist Interpretation versus CAD in Identification of Mesial Temporal Sclerosis in Temporal Lobe Epilepsy

Alexis Wong, M.D., *Marina Del Rey, CA ● Brent Liu, Ph.D. ● Han Huang, D.Sc. ● Arkadiusz Gertych, Ph.D. ● Chi-Shing, Zee, M.D. ● Mark Haney M.D., Los Angeles, CA*

LEARNING OBJECTIVES
1) Learn the challenges of identification of mesial temporal sclerosis in temporal lobe epilepsy. 2) Demonstrate the utility of CAD in improving both the speed and accuracy of analyzing. 3) Investigate the impact of CAD in diagnosis at different Radiology training levels.

ABSTRACT
Diagnosing mesial temporal (hippocampal) sclerosis, a common but sometimes elusive cause of temporal lobe seizures, can be difficult for the radiologist. We have developed a computer-aided detection (CAD) algorithm which analyzes the hippocampi using both volumetric and intensity measurements to aid the radiologist in identifying their subtle findings. Introduction to the difficulty of diagnosis of subtle lesions as well as the utility of a CAD algorithm is presented. The user is invited to diagnose mesial temporal sclerosis on sample cases without CAD results first. Then, with CAD results, these cases are diagnosed again. Cases will be reviewed with the retrospective diagnoses by radiologists at various levels of training: resident, neuroradiology fellow, and neuroradiology attending. Finally, the user will complete an online survey to document impact of the CAD results.

CODE: LL-IN3107

A PACS-CAD Toolkit for Integrating an Independent CAD Workstation to Diagnostic Workflow Based on DICOM SR and IHE Profiles

Zheng Zhou, Ph.D., *Marina Del Rey, CA ● Brent Liu, Ph.D. ● Han Huang, D.Sc. ● Arkadiusz Gertych, Ph.D. ● Anh Le*

LEARNING OBJECTIVES
1. Gain knowledge in DICOM Structured Report and IHE Post-Processing Workflow Profile; 2. Convert CAD workstation results into DICOM Structured Report; 3. Use IHE Post-Processing workflow profile to integrate independent CAD workstations with diagnostic workflow; 4. Retrieve and Display CAD results in a PACS workstation.

ABSTRACT
Computer Aided Diagnosis (CAD) coupled with physician's knowledge can improve the accuracy of clinical decision. However, although DICOM and IHE provide protocols using Structured Reports (SR) and Post-Processing Workflow Profile as a means for integration, its implementation by individual CAD developers remains difficult because of the challenges of integrating this new workflow with various PACS manufacturers. This obstacle hinders the extensive use of independent CAD results in clinical diagnosis. In this presentation, we demonstrate an open and universal PACS-CAD toolkit that can seamlessly integrate independent CAD results with a clinical PACS based on DICOM SR and IHE Post-Processing Workflow Profile. In the demonstration, the CAD results generated in a CAD workstation is transferred to a PACS archive server and is further displayed in a PACS workstation. The successful implementation of this toolkit can greatly ease the extensive use of various CAD results in clinical diagnosis.

CODE: LL-IN3104

A Data Grid for Imaging-based Clinical Trials

Zheng Zhou, Ph.D., *Marina Del Rey, CA ● Brent Liu, Ph.D. ● Han Huang, D.Sc. ● Jorge Documet, M.S. ● Matthew Brown, Ph.D. , Westwood, CA ● Der-Ming Liou et al, Ph.D.*

LEARNING OBJECTIVES
1. Learn Concepts and Workflow of imaging-based clinical trials; 2. Gain knowledge of Grid Computing; 3. Learn infrastructure design of the Data Grid; 4. Use the Data Grid for imaging-based clinical trials; 5. How to establish a Data Grid testbed; 6. Use grid computing for medical imaging applications.

ABSTRACT
Imaging based clinical trials play a crucial role in testing new drugs or devices in modern clinical practice because images provide a unique and fast diagnosis with visual observance and quantitative assessments. A typical imaging-based clinical trial includes a radiology core that has a quality control mechanism and a server for storing and distributing data and analysis results. With the ever-increasing number of clinical trials, it becomes a great challenge for a radiology core to have a robust server to administrate multiple trials and to quickly distribute information to participating clinicians worldwide to assess trial results. In this presentation, we demonstrate a DICOM-based Data Grid architecture that provides storing and sharing of images and analysis results for a clinical trial radiology core. In the demonstration, the trial workstation can retrieve DICOM images from the Data Grid to perform data analysis and store the analysis results back to the Data Grid for sharing.

CODE: LL-IN3130

Assessment of Carotid Wall Thickness in a Large Scale International Data Grid Repository

Marco Gutierrez, Ph.D.*, Brazil ● Edward Grant, M.D., Los Angeles, CA ● Zheng Zhou, Ph.D., Marina Del Rey, CA ● Brent Liu, Ph.D. ● Silvia Lage, M.D., Ph.D. ● Paulo Pilon, Beng*

LEARNING OBJECTIVES
1)Gain knowledge of assessment of carotid wall thickness using B-mode US imaging; 2)Learn automatic segmentation of carotid arteries; 3)Learn infrastructure design of the international Data Grid with Internet2 connectivity; 4)Establish an international Data Grid for medical imaging applications using the Internet2 to facilitate clinical research

ABSTRACT
The geometry of the carotid vessels can be manually determined using B-mode US. However, this approach is a time consuming task and based on subjective operator assessment that results in inter and intra-observer variability. We have developed an automated method to segment carotid vessels and measure the lumen diameter and plaque thickness. The evaluation of this method is being conducted worldwide with the facilitation of an international Data Grid repository. Currently, the Data Grid consists of three international sites: IPI Lab, University of Southern California, USA; InCor, University of Sao Paulo, Brazil, and the Hong Kong Polytechnic University, Hong Kong. In this presentation, we will demonstrate the automated segmentation method using the international Data Grid repository. At an InfoRAD workstation, US images can be DICOM queried and retrieved from storage components of the Data Grid. After segmentation, the measurement results can be stored on the Data Grid for viewing.

CODE: LL-IN3064

Computer-aided Diagnosis of Small Acute Intracranial Hemorrhage on CT

Tao Chan, MBChB , *Hong Kong ● Han Huang, D.Sc., Marina Del Rey, CA*

LEARNING OBJECTIVES
1. To learn the use of CAD in detecting small intracranial hemorrhage. 2. To learn the usefulness of anatomical information in the development of CAD. 3. To appreciate the application of CAD in emergency conditions.

ABSTRACT
Small volume of acute intracranial hemorrhage (ICH) can be missed on CT with dire consequences. This CAD system aims. to detect small (< 1cm) ICH and differentiate them from mimicking variants and artifacts. Intracranial contents and candidate ICH are successively segmented from the DICOM images, using morphological operations and regional thresholding. Image features of the candidates are quantified. The candidates are given anatomical context by registration against a normalized coordinate system. The features and coordinates are subsequently used in the rule-based classification system to remove false positives. The CAD was tested with 120 cases, each with a series of images. There were 40 cases showing a total of 77 small ICH and 80 control cases. Sensitivity on per lesion basis varies according to size of lesion: 100% for ICH >5mm, 84% for ICH >2.5mm and ≤5mm, and 53% for ICH ≤2.5mm. Specificity on per case basis: 89%. False positive rate: 0.18 per case.

CODE: LL-IN3109

A Grid-based Implementation of XDS-I as Part of a Metropolitan EHR in Shanghai

Jianguo Zhang, Ph.D., *China ● Zhuowei Yu, M.D. ● Zhongze Fan, M.D. ● Huanrong Qin, M.D., Ph.D. ● Jianyong Sun, Ph.D. ● Yuanyuan Yang, M.S. et al*

LEARNING OBJECTIVES
1.The XDS-I compliant EHR solution (i-EHR) for images/reports sharing based on a grid concept with a SOA 2.Progressive display with JPEG 2000 compression in i-EHR; 3.Access controlling and monitoring in i-EHR for security management.

ABSTRACT
A number of hospitals in Shanghai are piloting the deployment of an EHR solution based on a grid concept with a service-oriented architecture (SOA). The first phase of the project targets the Diagnostic Imaging domain and allows seamless sharing of images and reports across the multiple hospitals. The EHR solution is fully aligned with the IHE XDS-I integration profile and consists of three components: Master Node, Agent Node and User Node, which are synonymous with the XDS-I registry, repository, source and consumer actors. By using a SOA, the solution uses ebXML over secured http for all transactions within the grid. However, communication with the PACS and RIS is DICOM and HL7 v3.x The solution was installed in four hospitals in Shanghai and tested for performance of data publication, user querying and image retrieval. The results are extremely positive and demonstrate that an EHR solution based on a SOA with grid concept can scale effectively to serve a regional EHR implementation.

SCIENTIFIC POSTERS

CODE: LL-PD4023-L01
SESSION: Pediatrics

Integration of Bone Age Assessment CAD Results with the PACS Diagnostic Workflow Utilizing DICOM Structure Report

Aifeng Zhang, M.S., *Marina Del Rey, CA ● Zheng Zhou, Ph.D. ● Arkadiusz Gertych, Ph.D. ● Brent Liu, Ph.D. ● Xiangwu Zheng,M.D., Wenzhou China ● Han Huang, D.Sc.*

DATE: Wednesday, November 29 2006
START TIME: 12:15 PM
END TIME: 01:15 PM
LOCATION: Lakeside Learning Center –
Electronic Computer Exhibit - Pediatrics No.1

PURPOSE
A computer-aided diagnosis (CAD) method for bone age assessment has been developed based on a large-scale digital hand atlas. The CAD procedure on each pediatric hand and wrist hand image yields a list of results including assessed bone age, abnormality, extracted bony features and region of interest (ROI) sub-images. But how to integrate these CAD results seamlessly into the PACS diagnosis workflow remains a challenge. This poster provides a solution utilizing DICOM Query/Retrieve Services as well as DICOM structure reports (SR) to integrate results in a PACS archive.

METHOD AND MATERIALS
A DICOM software package with query, retrieval and storage of hand images is integrated with the bone age CAD workstation. The CAD workstation queries/retrieves DICOM images from PACS archive server and performs. automatic bone age assessment based on phalangeal and carpal bone features. The CAD results include: 1) The assessed bone age or some error messages; 2) Abnormality of subject's skeletal development; 3) Extracted Phalangeal and carpal bone features; 4) The average image for the assessed chronological age group; and 5) Sub-images of phalangeal and carpal bone ROI. We use the DICOM SR as a means to integrate the CAD result in a standard DICOM display workstation. It can incorporate the numeric results such as bone age, text results abnormality, and also provides a link to the average image and sub-images by creating a new series for the average image and sub-images. The CAD results in SR were stored in the PACS server database which has the SR support and viewed on a PACS display workstation.

RESULTS
We have tested our digital hand atlas database which contains 1,103 digitized hand images. The PACS workstation can query and retrieve the CAD results from the PACS server and display them.

CONCLUSION
This paper presents a method to integrate the bone age assessment CAD results from a stand-alone CAD workstation with the PACS diagnosis workflow. The successful implementation can greatly facilitate the extensive use of bone age assessment CAD results in clinical diagnosis workflow.

CLINICAL RELEVANCE/APPLICATION
A method to integrate CAD-based Bone age assessment results within a PACS is important for distribution and review for PACS users.

CODE: LL-IN2052-B02
SESSION: Informatics

Data Mining HIPAA-compliant RIS/PACS Audit Logs from an Outpatient Clinical Environment for Auditing and Monitoring Clinical Image Data Access

Zheng Zhou, Ph.D., *Marina Del Rey, CA ● Brent Liu, Ph.D. ● Han Huang, D.Sc. ● Aifeng Zhang, M.S. ● Kevin Wang, Los Angeles, CA, ● Rasu Shrestha, M.D.*

DATE: Sunday, November 26 2006
START TIME: 12:30 PM
END TIME: 01:30 PM
LOCATION: Lakeside Learning Center –
Education Exhibits - Informatics No. 2

PURPOSE
HIPAA compliance requires healthcare providers to monitor and prevent unauthorized image data access in daily clinical operation. However, current RIS/PACS lack the ability to automatically detect such violations. In this presentation, a novel method is presented to audit and monitor clinical image data access by mining HIPAA-compliant RIS/PACS audit logs.

METHOD AND MATERIALS
A HIPAA compliant auditing system (HCAS) has been developed for auditing clinical image data access which was presented in 2005 RSNA. This year, a new component, Audit Analysis Tool using data mining technology, is added to the HCAS. In the HCAS, a log collector software module collects HIPAA compliant audit logs generated by daily PACS workflow and stores them in a centralized database for mining. The

data mining process starts by preprocessing the log data to select features for data modeling. Then, a statistical model is built based on these features and a clustering analysis is performed to estimate the model by mining the data. Finally, the modal is interpreted and the conclusions are drawn. In this case, the conclusions are various HIPAA violated image access cases.

RESULTS
An outpatient facility that generates about 1300 patient exams. per month has been chosen as a test bed. The audit log data is created everyday to record PACS image data access events. A four-gigabyte log data containing one week long audit events was collected and fed into the HCAS as the initial training set. After the data mining model was established, audit logs containing three-months image data access events was collected and analyzed. The analysis results were tabulated and presented.

CONCLUSION
It is extremely difficult for healthcare administrators to detect HIPAA violated image data access from the HIPAA compliant PACS audit logs because the logs contain a huge amount of data that is difficult to audit manually. We present a novel method to automatically analyze the log data to detect HIPAA violated image access using data mining technology. Experimental results show that the method is effective for auditing and monitoring the clinical image access.

CODE: LL-CH4030-B06
SESSION: Chest

A Longitudinal Comparative Study Using CAD between Drug Resistant and Sensitive Tuberculosis Patients under DOTS Treatment

Heston Kwong, MBBS, *Hong Kong ● Grace Zhang, BS ● Han Huang, D.Sc., Marina Del Rey, CA*

DATE: Sunday, November 26 2006
START TIME: 12:30 PM
END TIME: 01:30 PM
LOCATION: Lakeside Learning Center –
Electronic Computer Exhibits – Chest No. 6

PURPOSE
To identify discriminating parameters based on CAD on pixels of digital chest films. of drug resistant and sensitive tuberculosis patients under DOTS treatment.

METHOD AND MATERIALS
Two groups of 100 patients respectively from drug sensitive and drug resistant tuberculosis patients were selected from government tuberculosis clinics in Hong Kong. Each patient has six longitudinal A-P chest films. which were digitized to DICOM format. Lung fields were extracted through knowledge-based method. The lung fields were aligned after ribs, clavicles and mediastinum were removed. Longitudinal ROIs of the retrospectively identified pathological regions were compared in cascade with the initial value using three parameters: (1) mean grey value of pixels; (2) ratio of overlapping areas of histogram of grey value to overall areas: The histogram of grey value of the improved ROIs is distinctively different from the initial ROIs while the histograms. are mostly overlapping in drug resistance group; (3) temporal image subtraction with images of previous cross-sectional time points. The improvement of the testing parameters was plotted against the duration of treatment in weeks. A least square method and a higher polynomial equation fitting were used to describe the changes.

RESULTS
First set of 100 patients data were used to train the CAD. Improvement in mean grey value of pixels, ratio of overlapping and temporal subtraction all showed linear relationship with time in the drug sensitive group but not the drug resistance group. A linear equation with the slope representing the rate of improvement was constructed by half the dataset. Higher order polynomial relationship was also observed. The equations were validated by the second 100 patients of the dataset.

CONCLUSION
Linear improvement of mean grey value of pixel, ratio of overlapping histogram, and temporal subtraction were observed in drug sensitive but not resistant group. Further CAD methods, non-linear relationship and additional parameters will be explored.

CODE: LL-PD4020-R03
SESSION: Pediatric

A Retrospective Study of Bone Age Assessment of Chinese Children in Hong Kong Using a Digital Hand Atlas

***Maria Law, Ph.D.**, Hong Kong ● Tao Chan, MBChB ● Fuk Hay Tang, Ph.D. ● Thomas Yue-Huen Lau, Ph.D. ● Han Huang, D.Sc. , Marina Del Rey, CA ● Aifeng Zhang ,M.S.*

DATE: **Thursday, November 30 2006**
START TIME: **12:15 PM**
END TIME: **01:15 PM**
LOCATION: **Lakeside Learning Center-**
Electronic Computer Exhibit, Pediatric No. 3

PURPOSE
Contrary to the use of the traditional Greulich and Pyle atlas for bone age assessment, this project performed a retrospective bone age assessment of the Chinese children in Hong Kong using the computer-assisted detection (CAD) method of a digital hand atlas.

METHOD AND MATERIALS
Existing hand films. of normal children with known age and between 0 and 18 years were collected and digitized. Five images from each gender and each age group were collected. Two pediatric radiologists with experience in reading pediatric hand images were invited to read the bone age of the images. The CAD algorithm already developed in the US for bone age assessment and tested on four racial groups was deployed at our Laboratory for assessment of the images collected on their bone age. Results of the bone age from the radiologists' reading and that of the CAD were compared.

RESULTS
Except for the first age group, i.e. age 0-1, for which insufficient numbers were collected, the CAD method in general produced results close to the chronological age of the children as those of the radiologists' readings even though the CAD digital atlas does not include Chinese children in Hong Kong.

CONCLUSION
The CAD hand atlas, trained for a specific racial group, can accurately assess the bone age of children. It also has the prospect of hooking up with the PACS for more efficient bone age assessment.

CODE: LL-IN2051-B01
SESSION: Informatics

ROC Analysis on the Effect of CAD on Clinicians' Performance in Detecting Acute Intracranial Hemorrhage

***Tao Chan, MBChB,** Hong Kong ● Chi-Ming Chan, MBChB ● Han Huang, D.Sc., Marina Del Rey, CA*

DATE: Sunday, November 26 2006
START TIME: **12:30 PM**
END TIME: **01:30 PM**
LOCATION: **Lakeside Learning Center –**
Education Exhibits, Informatics No.1

PURPOSE
The authors have developed a CAD system of acute intracranial hemorrhage (ICH) on CT with very encouraging results, which was demonstrated in RSNA 05. This system is developed for acute care physicians, who often need to make immediate management decision based on imaging findings, before expert opinion is available. To validate the effect of CAD on clinicians' performance in detecting ICH, a multiple reader multiple case (MRMC) ROC analysis was performed.

METHOD AND MATERIALS
50 sets of brain CT examinations, each with multiple images and some with multiple lesions, including 25 cases showing ICH and 25 control cases, were used in the evaluation. Seven emergency physicians, of ER experience between 4 to 8 years, were invited to read these examinations, first on their own and then with support by CAD system. They recorded their confidence in diagnosis of ICH on a scale of 1 (definite absence of ICH) to 10 (definite presence of ICH) for each case. The subjects were also interviewed to determine how the CAD output has affected their decision making for individual case. The same evaluation is being conducted with radiology residents and specialists.

RESULTS
As a group, area under ROC curve showed significant increase from 0.896 to 0.971 ($p<0.05$), when emergency physicians read brain CT examinations with support from the CAD output. Almost every individual improves his/her performance with the CAD. Preliminary results of the same analysis on radiology residents showed consistent but less conspicuous improvement in performance.

CONCLUSION
CAD significantly improves emergency physicians' performance in detecting acute intracranial hemorrhage on brain CT.

Special Oral Presentation

Experiences and Pitfalls Implementing a Data Grid for Imaging-based Clinical Trials

***Z Zhou, PhD**, Marina del Rey, CA; B J Liu, PhD; H K Huang, DSc; M S Brown, PhD; J Documet; D Liou, PHD*

LEARNING OBJECTIVES
1. Learn Concepts and Workflow for imaging-based clinical trials;
2. Gain knowledge of Grid Computing;
3. Learn infrastructure design of the Data Grid;
4. Use the Data Grid imaging-based clinical trials;
5. Understanding the challenges of implementing the Data Grid for imaging-based clinical trials (eg, legacy storage systems and data migration, unique and complex workflow management of imaging data in clinical trials, integration of QC components, security and access).
6. How to establish a Data Grid testbed;
7. Use grid computing for medical imaging applications.

ABSTRACT
Imaging based clinical trials play a crucial role in testing new drugs or devices in modern clinical practice because images provide diagnosis with visual observance and quantitative assessments. A typical imaging-based clinical trial includes a radiology core that has a quality control mechanism and a server for storing, distributing, and analyzing data results. It becomes a great challenge for a radiology core to have a robust server to administrate multiple trials and to quickly distribute information to participating clinicians worldwide to assess trial results. In this presentation, we demonstrate a DICOM compliant Data Grid architecture that provides storing and sharing of images and analysis results for a clinical trial radiology core. Experiences and lessons learned in overcoming challenges such as data migration and federation of legacy storage systems, unique and complex imaging trial workflow, data security and accessibility will also be discussed.

PREPRINTS FROM SPIE 2007

PACS-CAD Toolkit for Integrating an Independent CAD Workstation to Diagnostic Workflow

Zheng Zhou[a], Anh Le[b], Brent Liu [a], HK Huang[a]

[a]Dept. of Radiology, USC, 4676 Admiralty Way Ste 601, Marina del Rey, CA, USA 90292;
[b]Dept. of Biomedical Engineering, USC, 4676 Admiralty Way Ste 601, Marina del Rey, CA, USA 90292

ABSTRACT

Computer Aided Diagnosis (CAD) coupled with physician's knowledge can improve accuracy of clinical decision. However, many developed CAD software have no features to integrate its results with a picture archive and communication system (PACS). This obstacle hinders the extensive use of independent CAD results within a more streamlined diagnosis workflow. In this paper, we demonstrate a universal PACS-CAD toolkit that can seamlessly integrate independent CAD results with a clinical PACS. The PACS-CAD toolkit consisted of two versions, a DICOM Secondary Capture (DICOM-SC™) version and a DICOM-IHE™ version to accommodate various PACS. The DICOM-SC™ version toolkit installed on a CAD workstation converts the screen shot of CAD results to a DICOM image file for storing in a PACS server and displaying on PACS workstations. The DICOM-IHE™ version toolkit follows DICOM and IHE standards using DICOM Structured Report and Post-Processing Workflow Profiles; thus, results from various CAD software can be integrated into diagnosis workflow of a PACS having DICOM and IHE-compliance and, most importantly, these quantified CAD results can be directly queried for and retrieved from within PACS for future data mining applications. The successful implementation of this toolkit can greatly ease the extensive use of various CAD results in the clinical diagnosis workflow.

Keywords: PACS, DICOM, Structured Report, Integrating the Healthcare Enterprise, CAD

INTRODUCTION

Computer technology has had a tremendous impact on medical imaging; furthermore, with the use of the computer detection and analysis, computer aided detection/diagnosis (CAD) yields clinically valuable information. CAD quantification coupled with automatically detection of abnormalities and/or pathologies in medical imaging becomes feasible and helpful for physicians to determine the extent and progression of a disease more accurate and efficient.

For last two decades, many research and commercial CAD companies have devoted their time and effort to develop more accurate CAD applications with very robust algorithms [1-3]. However, little effort is put into system integration between the CAD application and a picture archive and communication system (PACS) to make CAD results become widely used and faster to access [4,5]. In current clinical practice and workflow, the CAD results are limited at the independent CAD workstation (WS), these results have not been integrated with PACS. Figure 1 shows the current workflow: as the CAD process for an exam is ordered through RIS, the technologist or radiologist sends the original image from PACS server or PACS WS to CAD WS for processing. The CAD result is reviewed and kept on the CAD WS.

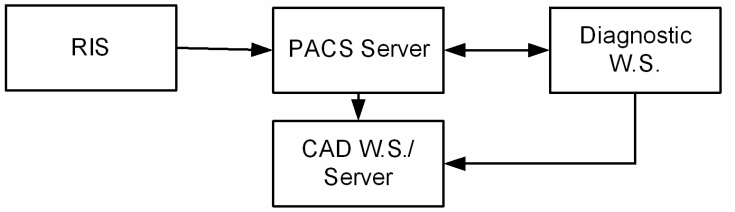

Figure 1. Current CAD Clinical Workflow

Although the Digital Imaging and Communications in Medicine (DICOM) standard [6] and the Integrating the Healthcare Enterprise (IHE) [7] provide protocols using DICOM Structured Report (SR) and Post-Processing Workflow Profiles as a means for integration, its implementation by individual CAD developer remains difficult because of the complexity of integrating this new workflow with various manufacturers. Even many commercial companies are extending their application to integrate their CAD results with PACS [8,9]; however, their add-on feature is limited to their CAD only. Therefore, it is not a solution for integration of a third party CAD application with PACS.

As CAD research grows and becomes a new trend in medical imaging, a larger number of CAD applications are made available for clinical use. However, CAD results still reside in the independent CAD WS, CAD server or diagnosis WS, which becomes a drawback of using CAD. Therefore, the need for an integrating toolkit to deliver these findings into clinical workflow becomes more urgent for clinical CAD usage.

The purpose of this paper is to present an open and universal PACS-CAD toolkit that can seamlessly integrate independent CAD results with a clinical PACS based on DICOM SR and IHE Post-Processing Workflow Profile.

METHODS

The ultimate purpose of the PACS-CAD toolkit is to convert CAD results to DICOM compliant files to store on PACS server and integrate the CAD workstation to diagnosis workflow. The PACS-CAD toolkit consisted of two versions, a DICOM Secondary Capture (DICOM-SC™) version and a DICOM-IHE™ version, shown in Figure 2. The DICOM-SC™ version installed on a CAD workstation uses the DICOM (Digital Imaging and Communications in Medicine) secondary capture object model to convert CAD results into a DICOM image file which is stored in a PACS server and displayed on a PACS workstation. The DICOM-IHE™ version follows DICOM SR function and IHE (Integrating the Healthcare Enterprise) Post-Processing Workflow Profiles that make a CAD application developed by any manufacturer become DICOM and IHE compliant; therefore, results from various CAD applications can be integrated into the clinical diagnosis workflow of a PACS having DICOM and IHE-compliance and, most importantly, these quantified CAD results can be directly queried and retrieved within PACS for future data mining applications. Both versions of PACS-CAD are developed under Windows environment and using DCMTK-DICOM library. The PACS-CAD toolkit is evaluated on a PACS simulator running computer bone age assessment CAD.

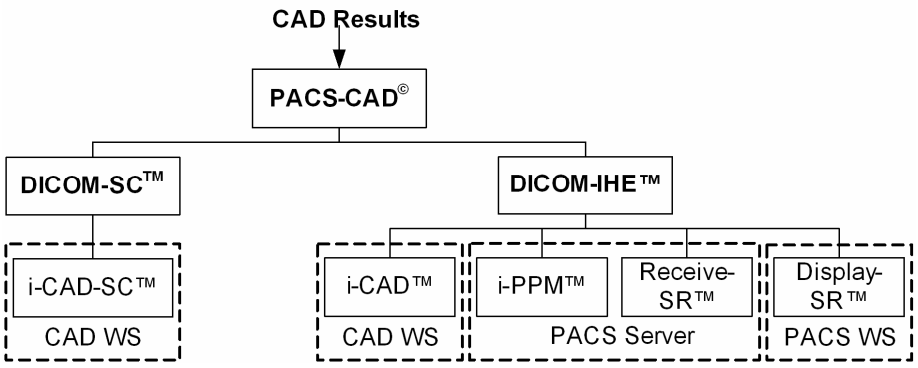

Figure 2. PACS-CAD Model

2.1 The DICOM-SC Version

The PACS-CAD DICOM-SC software can directly communicate with the PACS server without any new configurations. This version provides a simple and low cost solution for PACS workstation to query and retrieve CAD results and reports. The DICOM-SC captures the CAD result window and converts it to DICOM secondary capture file which will be sent automatically to a PACS server for storage. This DICOM image can be queried and retrieved from a PACS display workstation for viewing. The required input of the DICOM-SC version includes patient demographic information, study information and a screenshot of CAD result in BMP, JPEG or TIFF format. If the CAD application cannot provide the screenshot, the DICOM-SC has a module to create screenshot.

The DICOM-SC version has three modules: i-CAD Screen Capture module to create the screenshot for any CAD application, i-CAD Covert module to convert the CAD screenshot to DICOM file and the DICOM C-Store SCU to automatically send the DICOM file to PACS for storage

The workflow to integrating CAD results with PACS is shown in Figure 3.

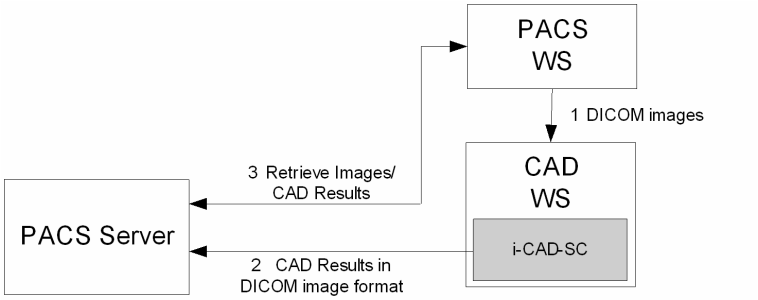

Figure 3. DICOM-SC Workflow

1. The PACS WS sends DICOM files to CAD WS for process. The CAD WS receives DICOM files and performs the CAD process.
2. The DICOM-SC with i-CAD-SC package installed in CAD WS converts the screen shot of CAD results to DICOM files and sends it to PACS Server. If the CAD cannot provide screenshot, the i-CAD Screen Capture is used to capture the CAD windows creating the screen shot. This output image is created as a DICOM secondary capture image having the same patient information of the original DICOM image with a new generated series information in DICOM header. Therefore, it will be stored as additional series under the same study of patient data model in PACS server.
3. When the PACS WS queries the PACS Server, the new series containing the CAD results will appear as a series under the study of patient. Radiologists can retrieve the CAD results with the study to their WS. The CAD results are shown as a DICOM image.

2.2 The DICOM-IHE Version

The DICOM-IHE™ version is based on the DICOM Structured Report (SR) standard (DICOM Working Group 15, CAD template Supplement 50) [6], and the IHE Key Image Note (IHE Profile 6), Simple Image and Numeric Report (IHE Profile 7) and Post-Processing Workflow Profiles (IHE Profile 10) [7]. Therefore, the DICOM-IHE is the correct method of approach for long term usage and integrity of its integration of the CAD WS with PAC systems. CAD schedule and management developed in this version allows CAD results to be archived in the PACS server in DICOM format. The DICOM SR data can be converted into structured data which allows further data analysis and data mining application of the CAD results.

As shown in Figure 2, the DICOM-IHE version has 4 modules. The i-CAD and the Post-Processing Manager (i-PPM) are for general PACS integration. The Receive-SR and Display-SR are for CAD WS and/or PACS Server not supporting DICOM structured report (SR) which is required by DICOM-IHE for PACS-CAD integration. The function of i-CAD is to convert CAD results to DICOM SR and DICOM CAD images which can be stored in the PACS server and retrieved by PACS WS for viewing. This module resides in CAD WS. The Receive-SR and Display-SR are for storing and displaying DICOM SR files. The i-PPM functions is a tool to manage the CAD process workflow and integrate it with RIS/PACS workflow. Receive-SR and i-PPM reside in PACS server and Display-SR resides in PACS WS.

The i-CAD module uses the Key Image Note (IHE Profile 6) and the Post-Processing Workflow (IHE Profile 10). The i-PPM and Receive-SR use Post-Processing Workflow Profiles (IHE Profile 10). The Display-SR uses Simple Image and Numeric Report (IHE Profile 7).

a. The i-CAD module

The i-CAD module resides in CAD WS and has six sub-modules, providing key functions for PACS-CAD integration. The function of each module is described as following:

1. DICOM-SR Module creates the DICOM SR objects from information given by CAD results. This object is created based on tree level model defined in DICOM SR general templates, shown in Figure 6, with the root node defined as CAD Document Root (Level 1). The first generation sub-tree (Level 2) contains four nodes: Summary of Detections, Summary of Analysis, Overall Impression/Finding Summary and Image Library. The structure of first two nodes is similar. Each node contains one or n nodes (Level 3), each of which presents one detection/analysis method running by CAD either successful or failed. The number of nodes in Level 3 is determined by CAD developers.
2. CAD-SR Module gets the DICOM SR objects from Module 1 to create DICOM SR file.
3. DICOM SR C-Store SCU sends the DICOM SR file to PACS server for archive.
4. DICOM C-Find SCU queries the CAD worklist in post-processing manager (iPPM) module (which will be discussed later). The CAD worklist is similar to DICOM worklist in the diagnosis WS. and retrieve DICOM image files from PACS server to CAD WS.
5. DICOM C-Move SCU retrieves DICOM study/images from PACS server.
6. i-CAD Messenger exchanges general purpose scheduled procedure object for claiming Scheduled Work Item(s), Work Item PPS (Purpose Procedure Step), or Work Item Complete message between i-CAD and i-PPM.

b. The Post-Processing Manager (i-PPM)

The i-PPM residing in PACS server provides the function to schedule or track the status of PACS-CAD workflow. This module is also used as a supplement for those PACS, which do not support post-processing management, to be DICOM and IHE-compliant for PACS-CAD integration.

The i-PPM consists of 4 modules:

1. Worklist Receiver gets a list of available DICOM studies from the PACS server or PACS WS, or query the list from the PACS server.
2. Worklist Startup creates CAD worklist.
3. DICOM C-Find SCP queries worklist from CAD WS.
4. i-PPM Messenger acts as a messenger to exchange to status message with the i-CAD (as mention in i-CAD module).

c. The Receive-SR

The Receive-SR also resides in PACS server and consists of three sub-modules: DICOM SR Database, DICOM SR C-Find SCP and DICOM SR C-Store SCP.

1. The DICOM SR Database module stores the results SR in database.
2. The DICOM SR C-Find SCP supports DICOM SR query from PACS WS.
3. The DICOM SR C-Store SCP receives the DICOM SR.

d. The Display-SR

The Display-SR resides in PACS WS. This module is used when PACS do not support DICOM SR C-Store SCU and C-Find. It is built as a Display Web-Server with DICOM SR C-Store and C-Find features.

2.3 Process of Integrating DICOM-IHE Version with PACS

Figure 4 shows the workflow of DICOM-IHE integrating with PACS. The number (1-7) is referred by each step respectively.

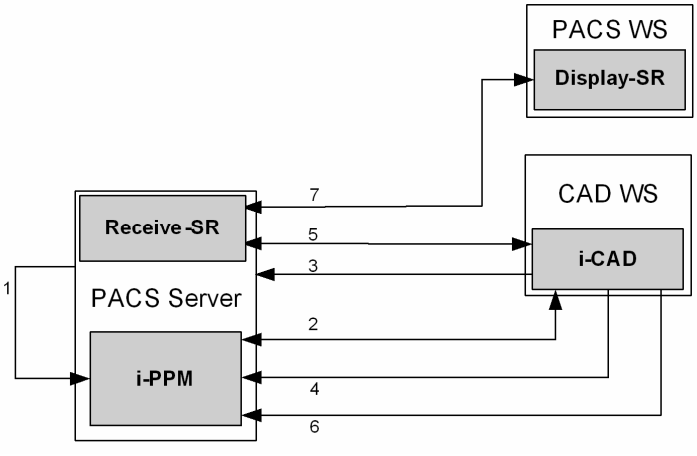

Figure 4. DICOM-IHE Workflow

1. PACS server pushes a DICOM worklist to i-PPM to requesting a CAD process for the studies. If PACS server cannot push the worklist, the i-PPM can query the PACS server for DICOM worklist automatically.
2. The CAD WS queries the CAD worklist from i-PPM. The CAD claims work items to be performed.
3. The CAD WS queries/retrieves DICOM images from the PACS server for CAD process.
4. The CAD WS sends "work item in progress" message to the Post-Processing Manager (i-PPM).
5. The CAD Workstation performs CAD process and stores the CAD results in the Receive-SR installed in the PACS server.
6. The CAD WS reports Work Item PPS & Work Item Completed Message to the i-PPM.
7. The PACS WS retrieves the DICOM SR CAD results for physicians' review. The web-based Display-SR can be used in the PACS WS to view the CAD results.

RESULTS

By using PACS-CAD toolkit, the results from CAD applications have been successfully integrated within the laboratory environment utilizing the PACS simulator developed at Image Processing and Informatics Laboratory, USC [10,11]. The CAD report is converted to a DICOM image file (using DICOM-SC™ version) or DICOM SR (using DICOM-IHE™ version) that is stored in the PACS server. The DICOM image file or DICOM SR file is retrieved and displayed on the PACS workstation or a web-based structure report viewer. Various CAD applications have been used for evaluation of the toolkit.

Figure 5 shows an example of integration the computer bone age assessment (BAA) CAD [12,13] with PACS using DICOM-SC version toolkit. Figure (a) shows the 3.8 year-old Caucasian boy's original hand image which resides in the PACS server before CAD evaluation. Figure (b) shows the screen-captured computer assisted BAA result and seven images segmented from the left hand radiography image of the boy. The segmented images show the region of interests (ROI) in phalangeal and carpal bones where multiple features are extracted for BAA. Figure (c) display the image of both original hand image and the CAD result in DICOM format of the same study on the display workstation.

Figure 6 shows an example of the DICOM SR CAD result depicting the bone age assessment results. Figure (a) shows the DICOM SR result that contains the CAD findings and detection process on the web browser. Figure (b) shows the result when the user clicks on the link "SC_image" to see a DICOM segmentation image the Summary of Analysis of the report.

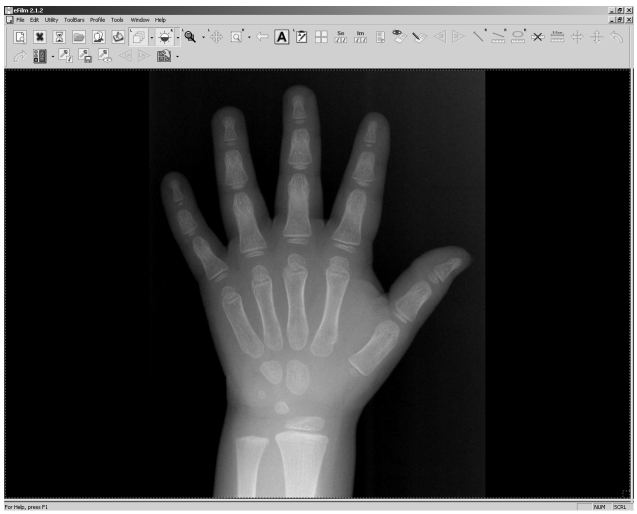

(a)

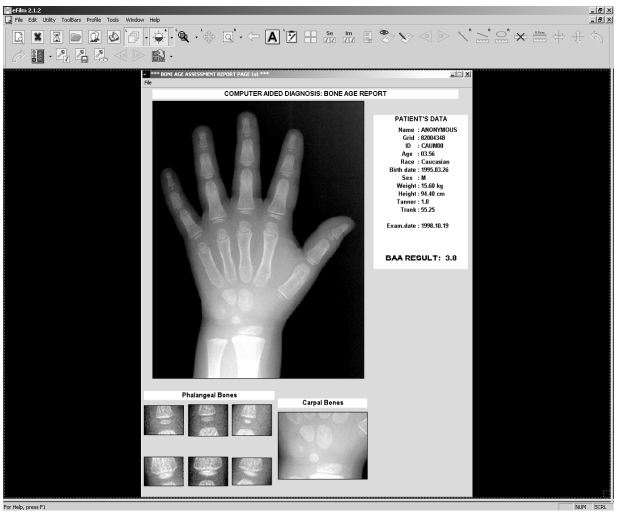

(b)

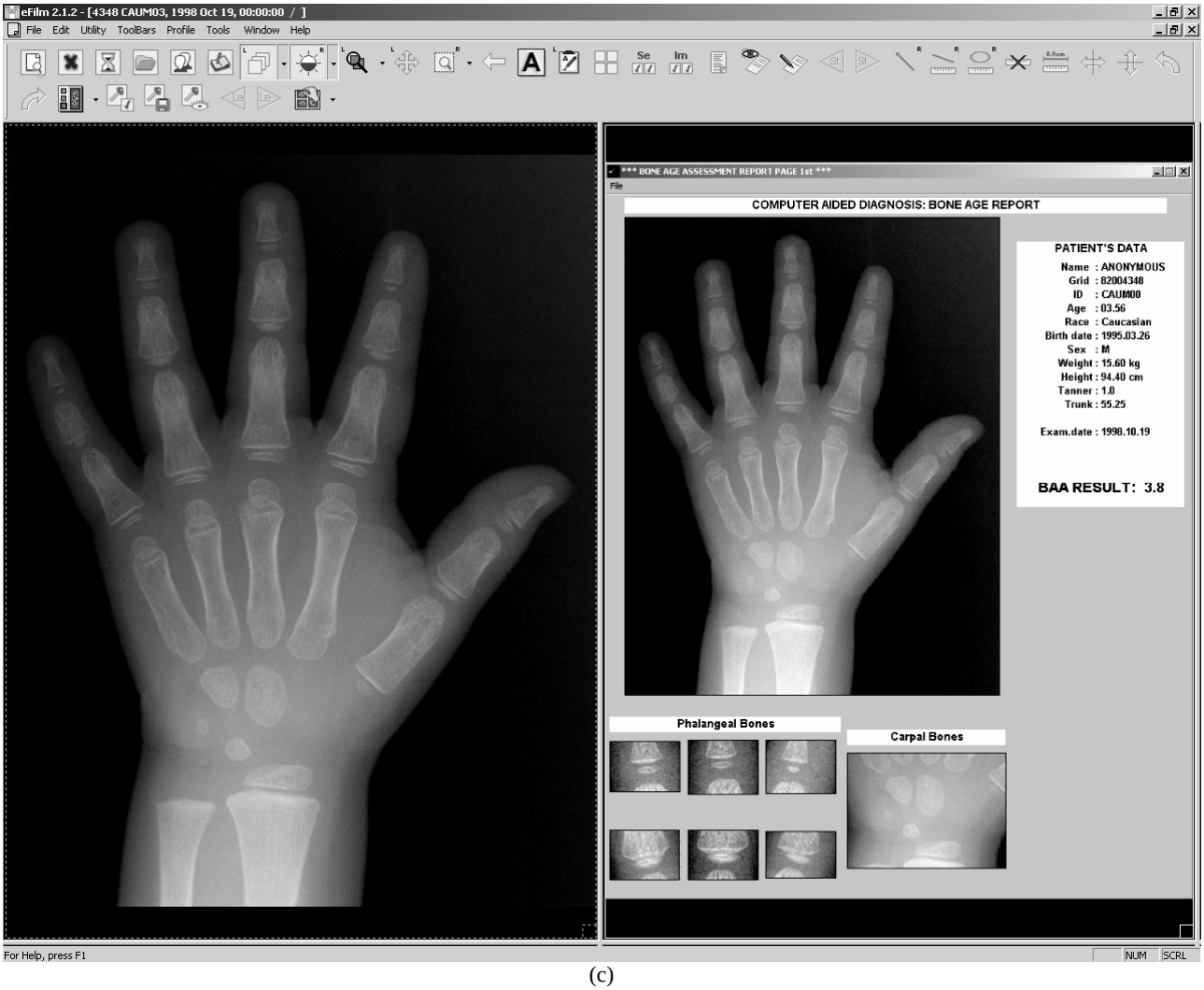

(c)

Figure 5. Example of DICOM-SC Result

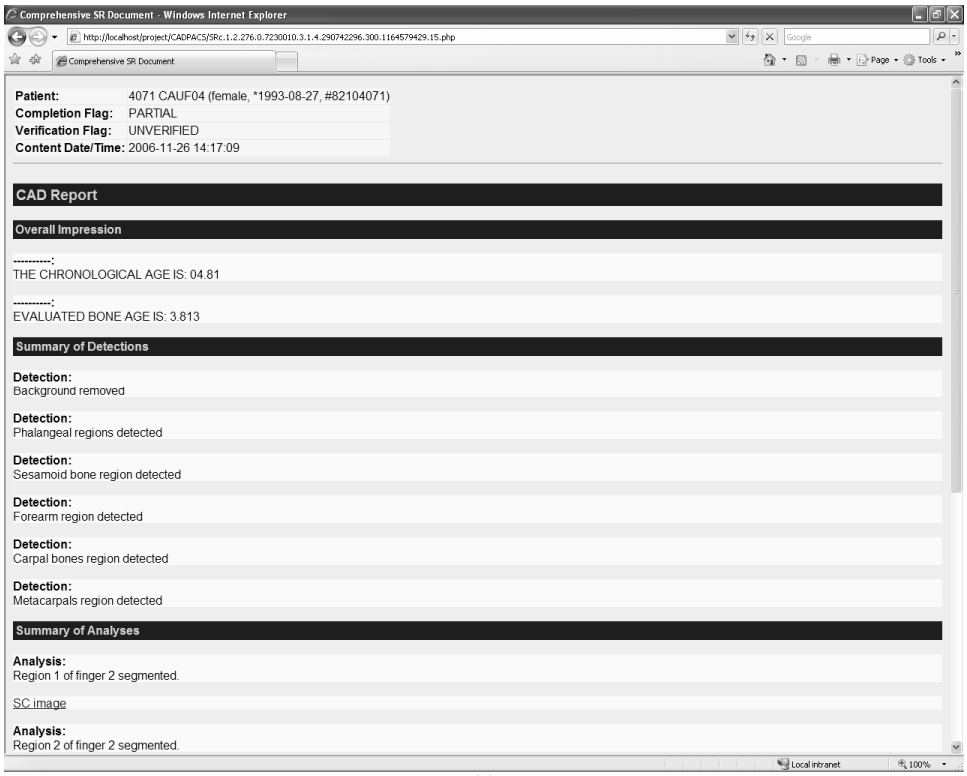

(a)

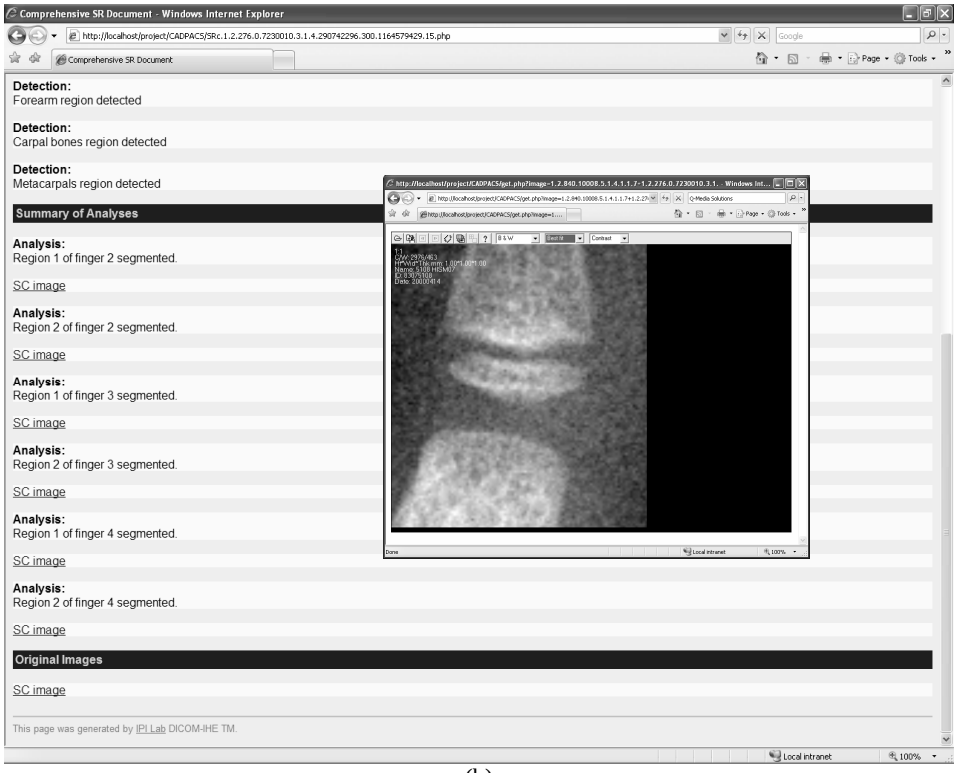

(b)

Figure 6. Example of DICOM-IHE Result

DISCUSSION

In two versions, PACS-CAD i-CAD-SC (Secondary Capture) version is simple and straightforward. Its integration, implementation and evaluation is low cost and requires no special methodology or addition modules to develop. The disadvantages of i-CAD-SC are that (1) it does not allow data analysis and further data mining to CAD results and (2) it does not support CAD workflow schedule and management.

In contrast, PACS-CAD DICOM-IHE version uses structured reporting which is more complex requiring more understanding of IHE profiles and its implementation is more costly. Furthermore, the implementation requires the cooperation of CAD developers to define templates accommodating special requirements for each CAD application. The development of i-PPM/Receive-SR also needs the cooperation of PACS manufacturers to open system software of PACS server for installing the i-PPM/Receive-SR. However, i-PMM/Receive-SR can be run in an additional computer that is connected to PACS network until the manufacturer can support IHE Post-Processing Workflow Profile and DICOM Structured Report store in their PACS. The Display-SR is web-based and can be run in a PACS WS or a client computer connected to the PACS network. This implementation gives physicians the ability to query and retrieve CAD results, including key image and quantitative report, from their workstation.

SUMMARY

The PACS-CAD toolkit has been proposed and developed for integrating various CAD results with clinical PACS. The PACS-CAD toolkit contains two different integration methods, DICOM-SC and DICOM-IHE. The former is simple and low cost solution which is easy to implement and the latter is a DICOM and IHE compliant solution for long-term use with ability to do further data analysis and data mining of CAD results. Our experimental integration of CAD application to diagnosis workflow shows efficiency of two methods to integrate independent CAD results with a PACS seamlessly. The PACS-CAD toolkit is a solution for more accurate analysis and faster assessment in the clinical decision-making process.

REFERENCES

1. M.L. Giger, K. Doi, H. MacMahon, Image feature analysis and computer-aided diagnosis in digital radiography: 3. Automated detection of nodules in peripheral lung fields, Med. Phys. 15 (1988) 158-166.
2. M. McNitt-Gray, Lung nodules and beyond: approaches, challenges and opportunities in thoracic CAD, CARS 2004, 896-091.
3. K. Doi, et al., Computer-Aided Diagnosis in Medical Imaging, Elsevier, New York, 1999.
4. H. K. Huang, A. W. K. Wong, S. L. Lou, and T. M. Bazzil, et al, Clinical experience with a second generation PACS, J Digital Imaging, vol. 9, no. 4, pp. 151-66, 1996.
5. Huang HK, PACS and imaging informatics. Hoboken, NJ: John Wiley & Sons, 2004.
6. DICOM, http://medical.nema.org/, accessed on November 18 2006.
7. IHE, http://www.ihe.net/, accessed on November 18 2006.
8. P. Heffernan, H. Zhang, Software architecture for a CAD server, CARS 2004, 861-866.
9. R2 Technology Inc., http://www.r2tech.com/main/home/index.php, accessed on November 18 2006.
10. Z. Zhou, H. K. Huang, F. Cao, B. J. Liu, J. Zhang, and G. T. Mogal, Educational RIS/PACS Simulator, SPIE Medical Imaging, vol. 4, pp. 139-147, 2003.
11. M. Y. Y. Law, Z. Zhou, New direction in PACS education and training, J. Computerized Medical Imaging and Graphics, vol. 27, pp. 147-156. 2003.
12. E. Pietka, A. Gertych, S. Pospiech, F. Cao, H.K. Huang, V. Gilsanz, Computer Assisted Bone Age Assessment: Image Processing and Epiphyseal/Metaphyseal ROI Extraction, IEEE Trans. Medical Imaging, 20, 715-729, 2001.
13. E. Pietaka, S. Pospiech, A. Gertych, F. Cao, H.K. Huang, V. Gilsanz, Computer Automated Approach to the Extraction of Epiphyseal Regions in Hand Radiographs, Journal of Digital Imaging, 14, 165-172, 2002.

A CAD system and Quality Assurance Protocol for Bone Age Assessment utilizing Digital Hand Atlas

Arakadiusz Gertych, Aifeng Zhang, Benjamin Ferrara and Brent J.Liu

Image Processing and Informatics Laboratory, Department of Radiology, University of Southern California, 4676 Admiralty Way, Suite 601, Marina Del Rey, California 90292

ABSTRACT

Determination of bone age assessment (BAA) in pediatric radiology is a task based on detailed analysis of patient's left hand X-ray. The current standard utilized in clinical practice relies on a subjective comparison of the hand with patterns in the book atlas. The computerized approach to BAA (CBAA) utilizes automatic analysis of the regions of interest in the hand image. This procedure is followed by extraction of quantitative features sensitive to skeletal development that are further converted to a bone age value utilizing knowledge from the digital hand atlas (DHA). This also allows providing BAA results resembling current clinical approach. All developed methodologies have been combined into one CAD module with a graphical user interface (GUI). CBAA can also improve the statistical and analytical accuracy based on a clinical work-flow analysis. For this purpose a quality assurance protocol (QAP) has been developed. Implementation of the QAP helped to make the CAD more robust and find images that cannot meet conditions required by DHA standards. Moreover, the entire CAD-DHA system may gain further benefits if clinical acquisition protocol is modified. The goal of this study is to present the performance improvement of the overall CAD-DHA system with QAP and the comparison of the CAD results with chronological age of 1390 normal subjects from the DHA. The CAD workstation can process images from local image database or from a PACS server.

Keywords: Imaging Informatics, Computer Aided Diagnosis, Quality control, Bone Age Assessment

1. INTRODUCTION

Bone age assessment is a procedure frequently performed in pediatric radiology and the goal is to determine the stage of skeletal maturity of a patient based on detailed analysis of left hand X-ray ossification centers. Currently used, manual method of BAA based on a book atlas[1] is a time consuming procedure and requires clinical experience. Additionally, subjectivity and inter and intra observer variability of assessment results has also been reported. To increase the objectivity of the BAA a semiautomatic method[2] has been developed, however it is seldom used in clinical practice, particularly in the US.

The main idea of the computerized approach to BAA is to perform an automatic image analysis with minimized user's interaction and to provide radiologist a second and objective opinion in the form of bone age value and closest hand image match. It may be clinically important when large amount of images have to be processed in relatively short time. It utilizes knowledge about skeletal development derived from the Digital Hand Atlas (DHA) containing 1390 hand images. Such approach also reduces subjectivity of the diagnosis.

The CAD for BAA has been implemented and is being tested. It has been found that performance and development of the CAD strongly depends on image data quality. Current results show that there is a deficiency in the clinical work-flow that needs be refined by incorporating a data quality control procedure. Then, both the CAD and the DHA will be improved. In this paper one specific example of methodology and implementation of quality assurance protocol (QAP) built over the CAD utilizing (DHA) is presented. Ultimately, this methodology can be applied to other CAD systems. The QAP consist of the visual and automatic image control steps resulting in a CAD correction and selection of hand images of good quality. Some of the QAP steps are permanently built-in the CAD. In addition benefits gained by the entire CAD-DHA system are also discussed.

Corresponding author: A.Gertych; gertych@usc.edu; phone: (310) 448 9442, fax: (310) 448 9440

2. MATERIALS: DIGITAL HAND ATLAS

The DHA consists of 1390 left hand images of normally developed individuals of four races: African-American, Caucasian, Asian and Hispanic, boys and girls respectively collected during the last two decades. Subjects age is spanned between 0 and 18 years, that approximately yields 135 cases per gender within one race.[3] The data has also been split into age groups yielding 5 or 10 images per age group if age of a subject was lower than 10 or more than 10 years respectively. This data have been collected accordingly to a clinical protocol approved by the institutional review board. The protocol required also the following patient demographic data to be collected: race, sex, age, date of birth, date of examination, Tanner maturity index and heights of trunk and body[4] respectively. Additionally, the bone age of each subject was blindly assessed by clinical experts (1103 images were evaluated by two experts and 287 were evaluated by four experts) using book atlas method,[1] and the bone age values were attached to the patient data record. Each hand image was digitized and saved as a DICOM file. Patient data were included in the DICOM header. At present, the DHA and patient data are stored in a data base that can be browsed using: `http://www.ipilab.org/BAAweb/` link.

3. METHODS

3.1. The CAD with Graphical User Interface

The CAD methods for BAA have been developed and presented.[5–11] The overall idea of the CAD utilizing DHA is shown in Figure 1. A left hand image that is subjected to the analysis is loaded by the CAD engine. Quantitative features are derived from automatically located regions of interest and bone age is assessed by decision making module utilizing the fuzzy logic technique. All image processing results are presented in the CAD-GUI window utilized by a CAD operator. The GUI can also provide messages about feasibility of current image analysis step. Ultimately a summary of the CAD processing is provided via a BAA Report Page (GUI-RP). This page contains ossification centers, patient data and CBAA results. The CBAA results can be further supported by a Comparison Sheet (GUI-CS) when closest matches[8] fetched from DHA are displayed. It is similar to the current clinical scheme of BAA and may be helpful in making of final diagnosis. For research and teaching purposes CAD fuzzy results can also be displayed. This property is intended to use in the CAD results verification and improvement. In Figure 1 dashed box shows CAD components that can be affected by the QAP. The QAP is used to improve reliability of the DHA and robustness of the CAD based on incoming information in the form of digitized hand images and image documentation (if it is available). Based on image quality related decisions made by means of the QAP, appending a new standard to the existing DHA set is possible.

3.2. Quality assurance protocol

Clinical implementation of a CAD workstation requires some functions preventing the failure of the image analysis due to unpredictable events and image artifacts to be implemented. While the CAD was developed it turned out that both the DHA and the CAD may improve in terms of: higher reliability of the data collection and better performance and robustness of the CAD if a quality control will be applied. The QAP is such a control tool built on the top of the CAD and DHA. It had been designed during extensive testing of CAD on images from DHA set. Generally the QAP encompasses quality checking of the image and the evaluation of its suitability for the automatic CAD processing. The workflow of the QAP is presented in (Fig.2).

The QAP consists of four steps (Step1 can be completed by the operator, whereas Steps 2-4 are non-interactively performed by the CAD software):

- **Step1**: the image standardization is verified by the operator utilizing the GUI of the CAD. If the hand image is not aligned properly with respect to the image plane or the image quality is not acceptable, then such image is immediately rejected.
- **Step2**: a comparison between the radiologist readings and the chronological age is performed. The image is rejected if the difference between the chronological age and the radiologist bone age reading is larger than a certain threshold *trh*. In this protocol the *trh* was derived from statistical discrepancy of growth in normal children's population and discrepancy between radiologist readings. Its value has been set to three years.

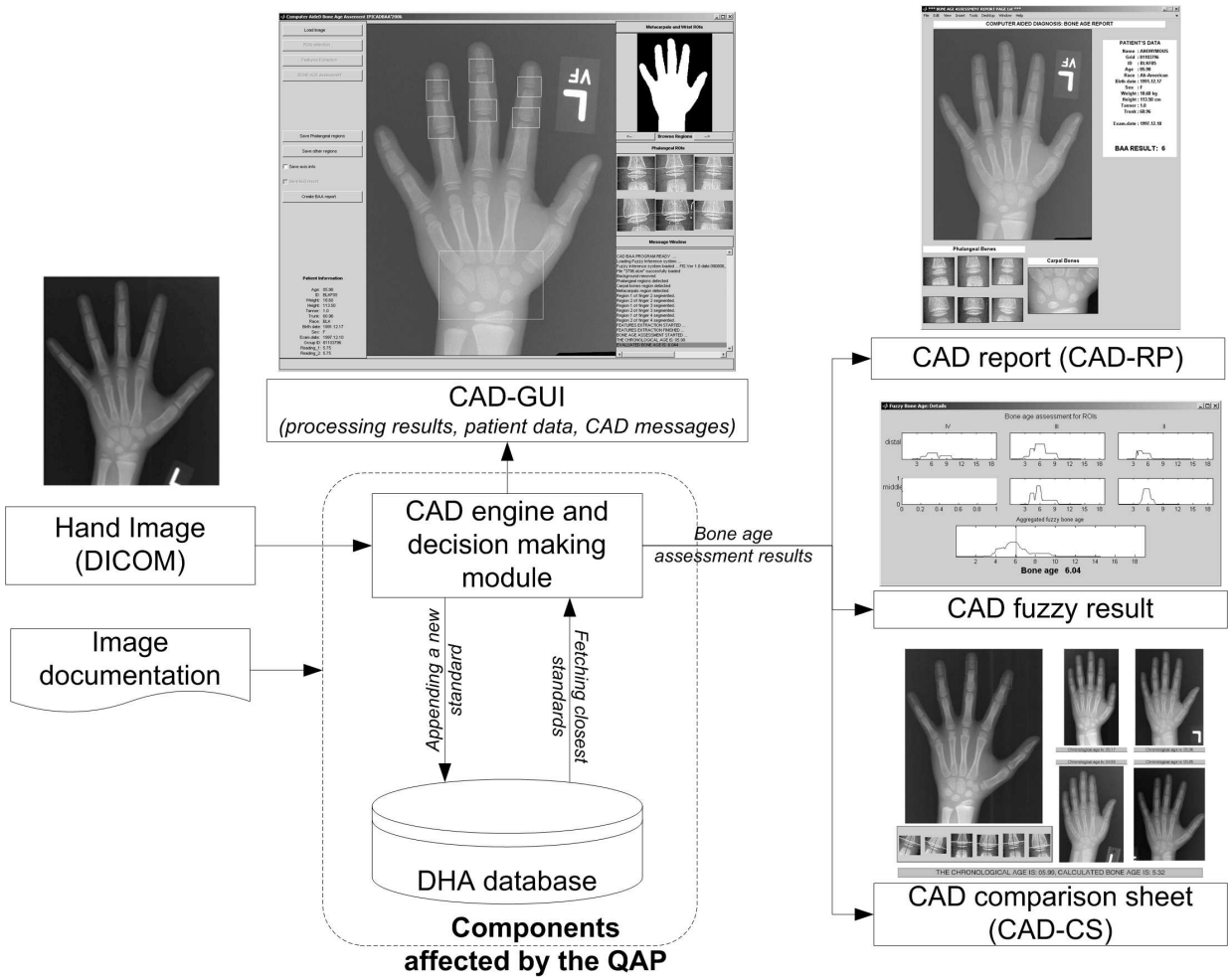

Figure 1. The CAD work-flow. A DICOM hand image is processed by the CAD engine. Bone age assessment results can be displayed in the form of CAD report (CAD-RP), CAD comparison sheet (CAD-CS) and CAD fuzzy result. Details of the QAP content are explained in Fig. 2.

- **Step3**: the content of the DICOM image header containing the subject's demographic data is compared with the original patient documentation. Any inconsistencies in the DICOM header require corrections.
- **Step4**: image preprocessing procedures may reveal artifacts caused by nonuniform background, underexposed film borders, scratches and radiological markers that may cause difficulties in automatic image processing. Automatic error detection routines verify the segmentation results and range of extracted features. Finally CAD results like: regions of interests and bone age value are evaluated. In Step 4 the CBBA result is also compared with subject's chronological age. If the discrepancy is smaller than the predefined threshold *trh*; the same as used in Step 2, then this image is subjected to the acceptance procedure and appended to the existing data collection. Otherwise it requires a CAD verification step to be taken. In such cases, the image will be subjected to bone age recalculation after a modification of the CAD. Modification of the CAD can be preformed in two ways: first, more reliable error detection technique can be incorporated to all image analysis steps, second if new images are appended to DHA it may require to retrain the decision making module (fuzzy classifier).

The ultimate image acceptance decision is made by the CAD operator. At this stage all requirements in

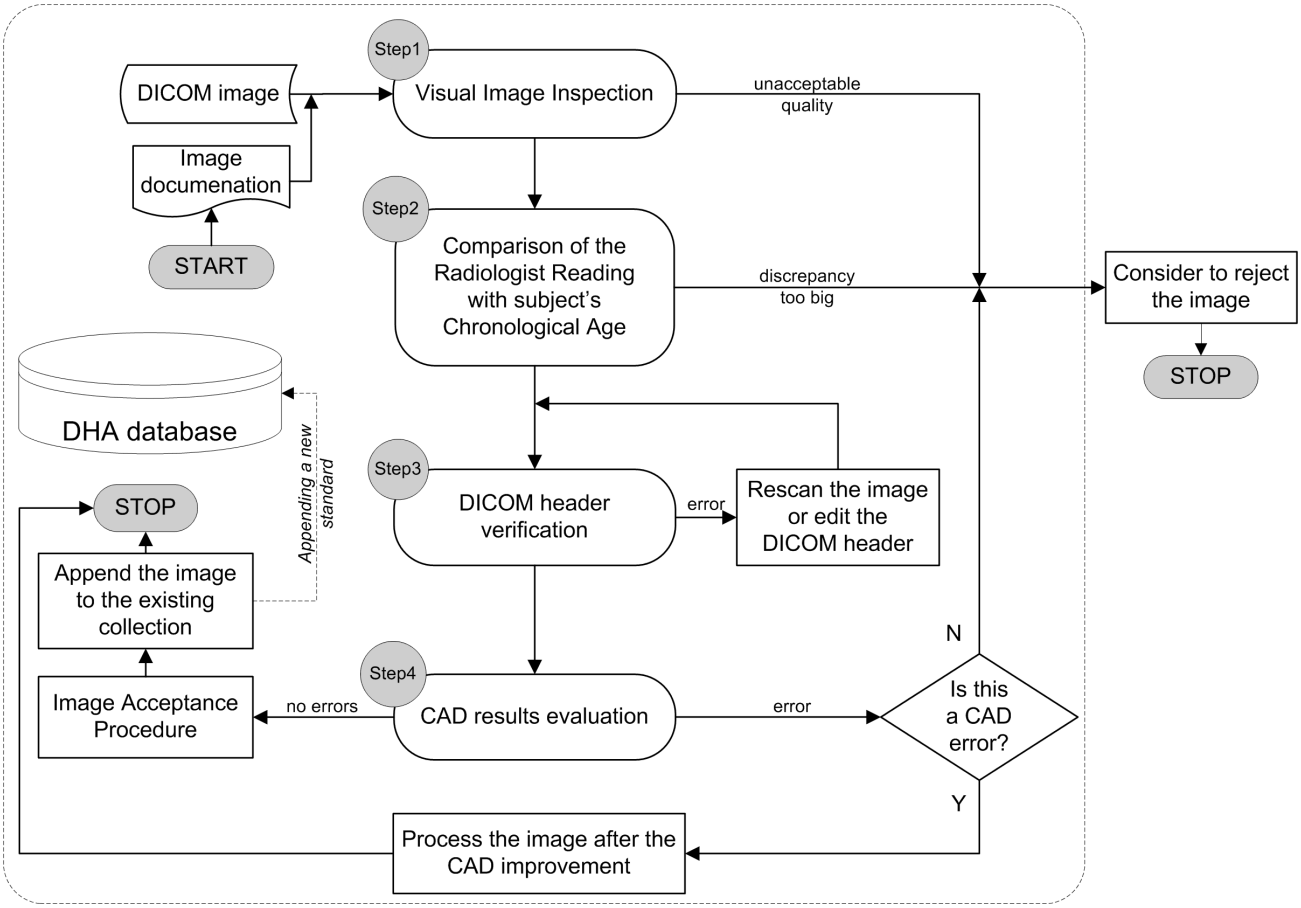

Figure 2. The quality assurance protocol work flow with the CAD in the loop. Acceptance of the CAD results allows appending the image to the existing collection.

terms of image quality, correct subject's demographic data, feasibility and correctness of the CAD result are met and the image can be appended to existing database unless it is not necessary to collect additional cases for a particular age group.

The application of the QAP has also another aspect. By gathering knowledge from rejected and retained images there is a possibility to modify or even improve the hand image clinical acquisition protocol (Fig.3). Let us assume that 300 images have already been acquired in clinical environment and they can be used to test and eventually improve the performance of the existing CAD-DHA system. In clinical scenario the patient's hand is first set-up and the X-ray image is acquired. The hand set-up is very key not only for the entire CAD-DHA workflow. It may also hamper visual assessment performed by the radiologist. According to the Data Acquisition Protocol the image together with patient's demographical data is converted to a DICOM format and can be stored in the PACS. In the next step a PACS workstation with the CAD installed may query-retrieve (Q/R) the DICOM image. In this case the CAD software can accept DICOM images. It may directly access it and process on the workstation.[12] Once the image is loaded via CAD-GUI, its quality can be assessed using QAP steps. If the image satisfies all QAP requirements it can be retained in the DHA, otherwise the rejection of the image is considered. At this point it is assumed that a further effort to improve the CAD to solve image analysis related problems may be time consuming or not profitable. The rejected and retained images together with messages generated by the CAD contain a knowledge describing *good* and *bad* quality images. This knowledge can be mined from such data and an improved acquisition protocol can be worked-out. The new protocol can be used to adjust existing set-up of a patient before future examinations. Such procedure may be simple to perform;

for example a radiology technician may better prepare and instruct patient. If necessary modality acquisition parameters may also require some adjustment to achieve i.e. better image contrast and protect the image from artifacts. A number of images rejected by the QAP-CAD-DHA system could be measured as a factor of the overall QAP-CAD-DHA system improvement. This factor will reflect the number of errors detected by the QAP and errors yielded by the CAD. By minimizing this factor both better CAD performance and reliability of DHA can be achieved.

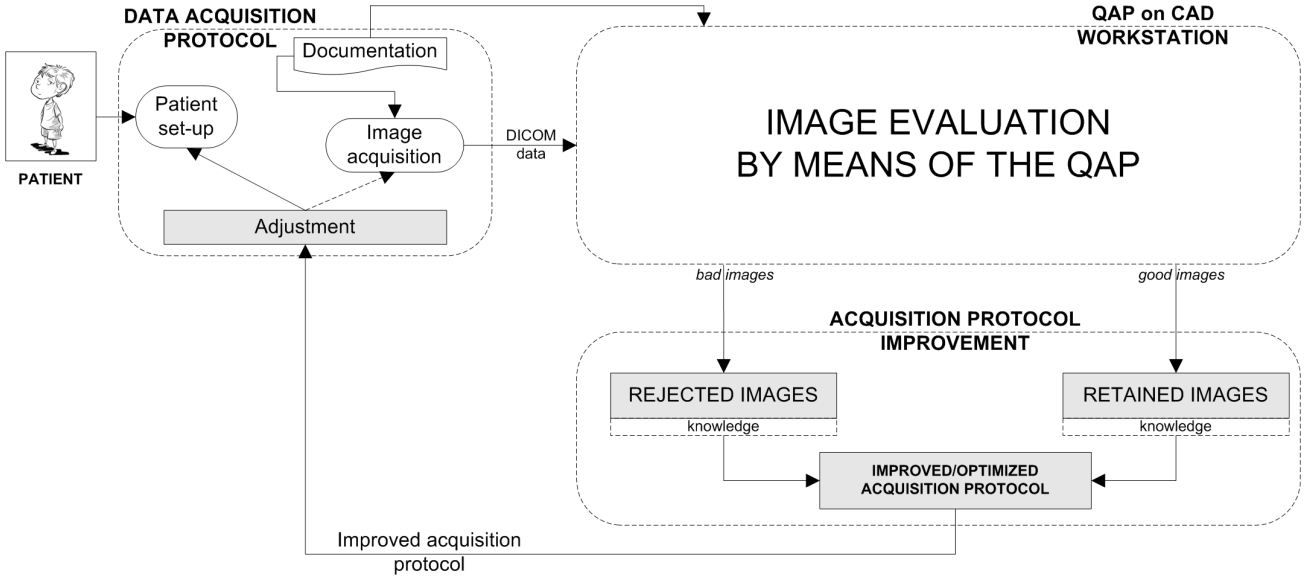

Figure 3. General overview of the QAP work-flow with the CAD in the loop. Mining knowledge from rejected and retained images allows adjusting acquisition protocol and minimize the number of rejected images.

4. RESULTS

Since data collection for the DHA spanned for more than ten years, the quality control is important to assure consistence and reliability of the DHA. By incorporating the QAP, in about 5% of DHA cases misspelled dates and other numeric data in the DICOM study description field were detected and corrected. Forty six images failed to pass the Step 1 of the QAP work-flow and were replaced by others. Main reasons were: the hand placement was not aligned properly during the X-rays exam and/or numerous artifacts on the image. Application of the Step 4 of the QAP greatly improved the passage of all 1,390 images through the CAD in terms of smooth CAD running. All cases that caused errors were investigated and more robust CAD errors detection was implemented to prevent from providing wrong BAA outcomes. It also means that some of the steps of the QAP have been permanently biult-in the CAD.

All images were used for CAD accuracy evaluation after all QAP tasks were done. Accuracy of phalangeal regions of interest location was not worse than 93% in the entire atlas data, whereas the accuracy of regions segmentation verified by experts reached level about 89%. Reasons of the CAD failure were still images of not good quality that could not be replaced by the QAP and images in very young children from 0 to 3 years when phalangeal analysis failed due to lack of detected regions or features. In this scenario the CAD yielded no BAA value, but this problem can be potentially solved by full implementation of the analysis of regions less sensitive to the hand placement ie. carpal bones, radius and ulna bones. The decision making module was also subjected to the modification induced by the QAP. It is capable to process incomplete and uncertain information by implementing feature range checking and excluding of regions that may potentially contribute with erroneous bone age value. In such cases only regions evaluated as correct may contribute to the final CAD outcome. In the last stage the CAD classification result were evaluated. For this purpose 50% of images were

randomly selected from the DHA. Since the hand images were derived from a normal population the bone age corresponds to the chronological age. By comparing these two values the accuracy of the overall CAD method can be assessed. Similarly to Pietka et al.[8] the classification accuracy of the CAD was evaluated by utilizing the city-block metrics. Results are presented in Table1.

Table 1. Accuracy of the CBAA vs chronological age (CA) using the city-block metric.

CBAA, CA distance [*years*]	$\delta \leq 0.5y$	$0.5y < \delta \leq 1y$	1.0y $< \delta \leq$ 1.5y	$1.5y < \delta \leq 2.5y$	$\delta > 2.5y$
ρ [% of cases]	30.1%	25.4%	17.2%	20.1%	7.2%

The difference in assessed bone age by the CAD and chronological age is lower than 1.5 year in 72.7% of cases, whereas in 7.2% the difference exceeds 2.5 years. The latter discrepancy, however relatively high may reflect the distribution of developmental stage in normal population. It could also be influenced by the thresholding value *trh* applied in QAP work-flow. The average bone age delivery time for a single hand image by the CAD does not exceed one minute regardless the image size.

5. CONCLUSIONS

The digital atlas together with CAD removes the disadvantages of the currently used Greulich-Pyle atlas and allows the bone age assessment to be computerized. The CAD software can be used to load a DICOM clinical hand image from a local repository or retrieve it from a PCAS server. The CAD and data collection benefited from incorporating the QAP into CAD development and image collection process loop. The digital atlas method together with the CAD provides an alternative to supplement the traditional BAA method for a quantitative, accurate and cost-effective assessment of the bone age. The CAD has built in error detection routines, is able to recognize certain image content and report these events in the GUI message window. In clinical practice the standardization of image causes many problems. An X-ray or CR image may be rotated at any angle and/or flipped. Artifacts, scratches, markers or transparent borders caused by blocking of the collimator that touch or overlap the anatomical structures may lead to a failure of the automatic image analysis. Such artifacts may also influence diagnosis performed by humans. Most of the non-standard images were rejected by applying QAP. Another group of errors detected as results of image processing procedures prevent from providing wrong BAA value. In such cases the CAD yields no BAA result.

In summary, the QAP applied to the Digital Hand Atlas encompasses checking the image features and patient data at various levels. Image quality is assessed in terms of correct hand placement, presence of image artifacts and capability of radiological findings extraction performed by the CAD. Verification of subject's demographic data can be performed in the QAP by the CAD operator and the CAD. The presence of the operator in QAP can be further reduced by implementing more advanced error detection routines. Using the QAP, the reliability of the data collected for the Digital Hand Atlas has been improved. The CAD-RP,-CS also enhance the CAD capabilities. Development of the QAP allowed increasing robustness of the CAD by incorporating QAP steps into the CAD. The results of the CAD classification may be improved by adjustment of data acquisition protocol and better selection of cases. The latter could be probably achieved by lowering the thresholding *trh* value. One may anticipate that the entire CAD-DHA system may gain further benefit in terms of better classifier training and more close CAD results to the chronological age, however the question how much the *trh* can be lowered is not easy to answer. By applying the QAP the following benefits were achieved: faster and more flawless CAD operation, more robust and reliable second BAA opinion, improvement of the database containing reference images possibly to be used for diagnosis, teaching and research. General methodology presented in this paper can be possibly expanded to other CAD and quality control related areas for example: measurements of carotid wall thickness using ultrasound technique, reduction of bias field in MR studies, detection of lung nodules reduction in CT studies and others.

ACKNOWLEDGMENTS

This work has been sponsored by grant no. NIH R01 EB 00298.

REFERENCES

1. W. Greulich and S. I. Pyle, *Radiographic Atlas of Skeletal Development of Hand Wrist*, Stanford University Press, Stanford, CA, 1971 (second edition).
2. J. Tanner, M. Healy, and H. G. ans N. Cameron, *Assessment of Skeletal Maturity and Prediction of Adult Hight (TW3 Method)*, W. B. Saunders, London, 2001 (third edition).
3. F.Cao, H.K.Huang, E.Piętka, and V.Gilsanz, "Digital hand atlas for web-based bone age assessment: System design and implementation," *Computerized Medical Imaging and Graphics* **24**(5), pp. 297–307, 2000.
4. S. Mora, M. Boechat, E. Piętka, H. Huang, and V. Gilsanz, "Skeletal age determinations in children of european and african descent: Applicability of the greulich an pyle standards," *Pediatric Research* **50**(5), pp. 624–628, 2001.
5. E. Piętka, A. Gertych, S. Pośpiech, F. Cao, and H. Huang, "Integration of computer assisted bone age assessment with clinical pacs," *IEEE Trans. Med. Img.* **20**(8), pp. 715–719, 2001.
6. E. Piętka, S. Pośpiech-Kurkowska, A. Gertych, F. Cao, H. Huang, and V. Gilsanz, "Computer automated extraction of the epiphyseal regions in hand radiographs," *Journal of Digital Imaging* **14**(4), pp. 165–172, 2001.
7. E. Piętka, S. Pośpiech, A. Gertych, and F. Cao, "Integration of computer assisted bone age assessment with clinical pacs," *Comp. Med. Img. Graph* **27**(2-3), pp. 217–228, 2003.
8. E. Piętka, A. Gertych, and K. Witko, "Informatic infrastructure of CAD system," *Comp. Med. Img. Graph* **29**(2-3), pp. 157–169, 2005.
9. A. Gertych, E. Piętka, and B. Liu, "Segmentation of regions of interest and post-segmentation edge location improvement in computer-aided bone age assessment," *Pattern Analysis and Applications* , 2007. (in press).
10. A. Gertych, A. Zhang, J. Sayre, S. Pośpiech-Kurkowska, and H. Huang, "Bone age assessment of children using a digital hand atlas," *Journal of Comp. Med. Img. Graph* , 2007. (in press).
11. A. Zhang, A. Gertych, and B. Liu, "Bone age assessment for young children from newborn to 7-year-old using carpal bones," *Journal of Comp. Med. Img. Graph* , 2007. (in press).
12. H. Huang, *PACS imaging and informatics basic principles and applications*, Wiley-Liss, Hoboken, New Jersey, 2004.

A CAD system for assessment of MRI findings to track the progression of multiple sclerosis

Alexis Wong[1,2], Arkadiusz Gertych[1], Chi-Shing Zee[2], Bing Guo[1], Brent J.Liu[1]

[1] Image Processing and Informatics Laboratory, Department of Radiology, University of Southern California, 4676 Admiralty Way, Suite 601, Marina Del Rey, California 90292
[2] Keck School of Medicine, Department of Radiology, University of Southern California Los Angeles, CA 90033, phone (323) 442-8572

ABSTRACT

Multiple sclerosis (MS) is a progressive neurological disease affecting myelin pathways. MRI has become the medical imaging study of choice both for the diagnosis and for the follow-up and monitoring of multiple sclerosis. The progression of the disease is variable, and requires routine follow-up to document disease exacerbation, improvement, or stability of the characteristic MS lesions or plaques. The difficulties with using MRI as a monitoring tool are the significant quantities of time needed by the radiologist to actually measure the size of the lesions, and the poor reproducibility of these manual measurements. A CAD system for automatic image analysis improves clinical efficiency and standardizes the lesion measurements. Multiple sclerosis is a disease well suited for automated analysis. The segmentation algorithm devised classifies normal and abnormal brain structures and measures the volume of multiple sclerosis lesions using fuzzy c-means clustering with incorporated spatial (sFCM) information. First intracranial structures mask in T1 image data is localized and then superimposed in FLAIR image data. Next, MS lesions are identified by sFCM and quantified within a predefined volume. The initial validation process confirms a satisfactory comparison of automatic segmentation to manual outline by a neuroradiologist and the results will presented.

Keywords: quantitative image analysis, magnetic resonance, detection

1. INTRODUCTION

Multiple sclerosis is a frequently encountered neurological disease with a progressive but variable course affecting the central nervous system. It is characterized by damage, likely autoimmune in etiology, to the layer of myelin surrounding the axons of neurons within the brain and spinal cord. The damaged myelin sheath degenerates and forms scar tissue (sclerosis). Focal areas of scar tissue large enough to visualize on an MRI scan are termed "plaques". The sclerotic myelin can no longer properly aid in conduction of electrical impulses along the axon, and this is the basis of neurological dysfunction in multiple sclerosis (MS). Patients often present with sudden and sporadic blurry or deteriorated vision as their initial clinical symptom. Depending on the regions of the brain affected, multiple sclerosis may result in a variety of organ system and neurological dysfunctions, including balance and gait, cognitive dysfunction, fatigue, and bladder and bowel incontinence.[1–3]

Accurate and expeditious measurement of multiple sclerosis lesion load is a clinically important goal because it is a quantifiable and readily obtainable measure of multiple sclerosis progression. Traditionally, the radiologist has manually measured each individual lesion. Manual lesion measurement is a particularly tedious and time consuming task. Automated CAD measurement of lesion load can be both consistent and efficient and will help the radiologist by providing useful information regarding the patient's disease status. Quantification of MS plaques preceded by plaque segmentation is a crucial step in the assessment of lesions load.[4] Once the pathology has been diagnosed, a longitudinal monitoring of the disease is clinically essential.

The task of tracing multiple sclerosis plaque changes becomes more difficult if several MR studies of the same patient (follow-up studies) require quantitative comparison. Manual outlining is a tedious, time consuming, and difficult to reproduce process. Both overall global plaque volume and small, subtle local changes may be of particular interest to the neuroradiologist. Quantifying plaque volume, number, and changes in lesion load

Corresponding author: A.Wong; alexiswong@gmail.com; phone: (310) 448 9442, fax: (310) 448 9440

between consecutive studies is clinically useful. Detection of subtle changes is often followed by a registration and alignment step and requires thin slices and high resolution of the images.[5] In the assessment of global changes, less computational burden is required, and images of lower resolution with larger slices thickness may be used.[6] Numerous methods have been devoted to the segmentation and quantification of MS plaques; both semi-automated,[7,8] and fully automated approaches[6,9–11] have been presented, however the automatic segmentation of plaques still remains a challenging task due to the difficulty in outlining low intensity and obscure plaques. In most of the previous approaches, the plaques are segmented from brain parenchyma via global brain segmentation. First, images are subjected to a preprocessing including artifacts removal. Then, intensity normalization is performed followed by the segmentation of plaques identified as spots of abnormal intensity within the brain parenchyma white matter. Recent studies show that MS plaques location can be defined with a certain probability of occurrence within the deep white matter and periventricular area.[9] The periventricular area refers to the brain parenchyma surrounding the brain ventricles. It reflects the locus of points where multiple sclerosis plaques most likely occur. The exact size and location of the 3D map within the periventricular area has not been quantitatively defined. However, the high probability of plaques occurrence within the deep and periventricular area may become a useful reference point in an automated approach of MS plaques quantification and segmentation guided by prior location of the brain CSF structures. In this approach the automatic quantification of MS plaques within the intracranial structures will require prior localization of the cerebrospinal fluid (CSF) spaces. In our study, an automated approach to the quantification of MS plaques designed to perform comparison of consecutive MR studies is presented. Brain mask and CSF spaces segmentation are results of the analysis of T1 images. The 3D brain and CSF spaces masks are superimposed on FLAIR images to perform the MS lesions detection. Then a geometrically guided fuzzy c-means (GGFCM) algorithm is proposed to segment out the MS lesions in the remaining area. Quantified MRI findings include plaque numbers and volumes. A follow-up study can be processed in the same way and the results can be displayed for comparison. 3D view is also available. This method was developed and tested based on clinical image data of MS patients.

2. MATERIALS

Currently, 31 cases of adult patients aged 25 to 55 years with clinically definite multiple sclerosis (CDMS) have been collected. Eight of these patients have one follow up study. All studies contain T1/FLAIR weighted axial MR sequences with acquisition matrices varying form 256x224 to 512x456 regarding available sequences. All sequences were acquired by a 1.5T MR Scanner with gray scale resolution of 12 bits/pixel. The space between cross-section thicknesses is 6.5mm which includes 1.5mm gap between cross-sections. Pixel size of acquired images varies from 0.89mm x 0.89mm to 0.449mm x 0.449mm respectively. The image data was acquired at the USC Health Consultation Center in Los Angeles.

3. METHODS

An overview of the methodology of volume image data analysis is depicted in Figure 1. At the very beginning the differences in resolution between T1, FLAIR sequences are standardized. Usually FLAIR images are largest so all studies are adjusted to fit the size of FLAIR images. The analysis begins with T1 images that are subjected to the background removal procedure yielding a binary head mask. Then structures under this mask undergo brain mask location procedure. 3D mask of brain structures with removed CSF spaces is superimposed on FLIAR image data. MS plaques are identified and segmented from the masked FLAIR volume images by GGFCM method. Finally MS plaques are quantified.

3.1. Preprocessing

Image analysis starts with a background removal procedure which is performed by histogram thresholding of the entire T1 volume data Fig. 2a.[12] A line connecting the last gray level value and the maximum of the histogram is constructed, and then a distance function between the line and histogram points is derived. A maximal value of the distance function marks the thresholding value. This procedure yields a binary 3D head mask. The mask is then shrunk by a morphological erosion procedure to partially remove skin objects. Next, volume data of the T1 sequence delimited by the refined head mask is subjected to suppression of bone structures. In order to model the histogram of the intracranial structures in the T1 MR head sequence the expectation-maximization

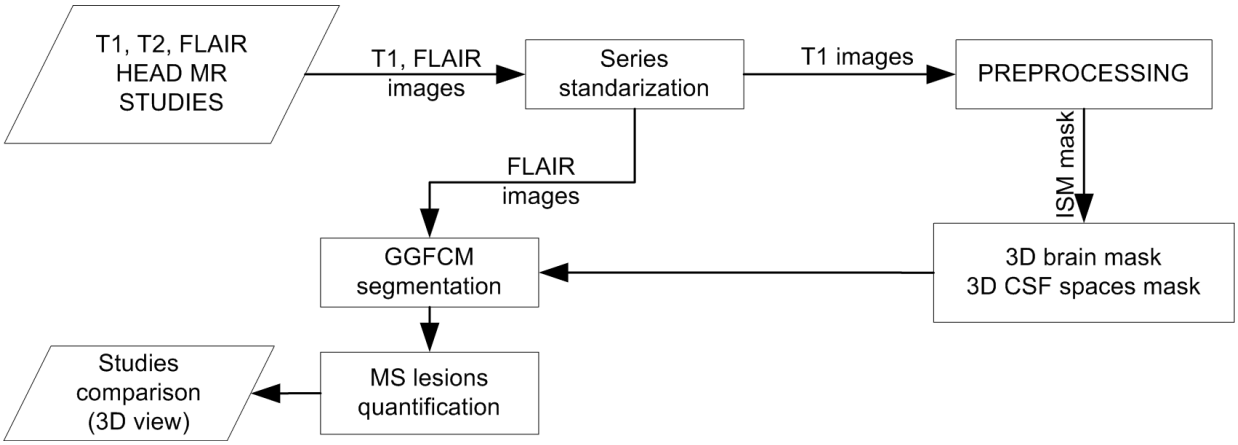

Figure 1: The image analysis work-flow. T1/T2/FLAIR sequences are standardized and preprocessed to get quantification of MS lesions. Volume data in FLAIR images delimited by 3D mask Quantified results of MS plaques are displayed.

method[13] is used. Such approach allows modeling a data histogram containing multiple modes assuming that data consist of mixed Gaussian distributions. A typical histogram is shown in the Fig. 2b. Four components can be distinguished: cerebrospinal fluid (CSF), white matter (WM), gray matter (GM) and bone structure (BS) objects respectively. All four modes are modeled by their standard deviation and mean value (μ,σ). In order to suppress the bony and CSF structures two thresholding values were derived from this histogram: trh_1 and trh_2. They were set experimentally to $trh_1 = \mu_{BS} - 1.75\sigma_{BS}$ and $trh_2 = \mu_{CSF} + 1.5\sigma_{CSF}$. All pixels larger than the trh_1 yield binary bony structure mask. This mask is dilated and closed by means of morphological operators and then subtracted from the head mask yielding instracranial structure mask (ISM).

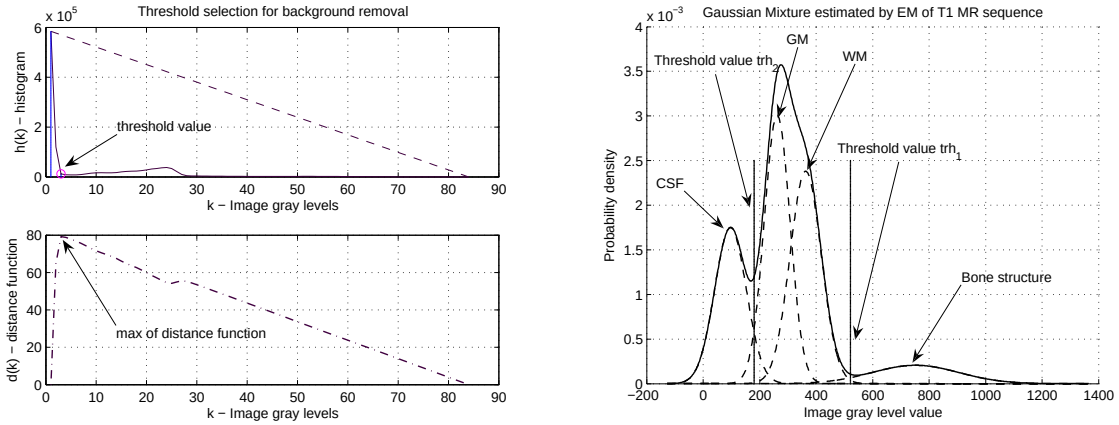

(a) (b)

Figure 2: Histograms of T1 volume data: a) the 3D background thresholding technique, b) the histogram of the T1 data under a head mask modeled by expectation-maximization method.

3.2. 3D brain mask

Segmentation of brain mask follows the idea described in[14] with few modifications. Voxels delimited by the ISM which intensities are bigger than trh_2 mostly represent gray and white matter structures. The are subjected to 3D morphological opening and a procedure preserving largest 3D binary object. An axial slice with largest 2D object is located within this 3D object and splits it into two sub-volumes. The sub-volumes are analyzed separately in axial direction using morphological erosion and reconstruction to disconnect and suppress structures of fat, dura and muscles remaining inside this object. Afterwords they are combined back and yield 3D brain mask (BM). Voxels inside the BM and smaller than the threshold trh_2 represent location of CSF spaces within the ventricular system. This mask is also subjected to morphological analysis yielding largest 3D connected component of CSF structures. It is refereed to CSF structures mask (CSFs) containing ventricular system. The periventricular area consists of both white matter and grey matter, MS lesions only develop within white matter. In a normal patient MRI, there are thin areas of normally increased FLAIR signal intensity immediately surrounding the ventricles. In order to prevent this normally hyperintense voxels from being included as an MS lesion, the CSFs undergoes morphological dilatation so that this normal area will not be included in the BM.

3.3. Segmentation of MS plaques

Segmentation of MS plaques is performed by modified version of well known fuzzy c-means algorithm[15] with incorporated spatial information.[16] Its main advantage is that the spatial information about neighborhood clusters can be incorporated into the clustering process, in other words membership function of a pixel depends on membership value of surrounding pixels. The GGFCM method in general outperforms original fuzzy c-mens approach because it is less sensitive to various types of noise. In our approach the entire 3D FLAIR image data delimited by BM is subjected to segmentation into 4 classes. The last class defines the plaques location whereas other classes define remaining brain tissues. After plaques segmentation a quantification step was performed. Area, volume and number of segmented plaques in every sub-volume cross-section are calculated.

4. RESULTS

Quantification of MS lesions comes out as a straightforward result of the segmentation procedure performed on FLAIR image data. The following findings: areas, volumes and number of segmented plaques in single cross-sections are calculated. Areas and volumes are expressed as pixel quantities but can be easily converted to volume units based on the voxel size. Findings calculated in single cross-sections are presented in Table 4. In the Figure 3 results of plaques segmentation performed by GGFCM in two consecutive studies in a 44 years old male subject are presented. Slices numbered as 1,2,3 (Table 4) presented in figure 3 correspond to sub-figures a), b) and c) respectively. Certain lesions detected in this manner can now be presented in 2D and 3D space. In 2D

Table 1: Example of plaques quantification in original and follow-up study of a 44 year old male subject (single slice plaques).

Study	Follow-up		Original	
Finding	Area	Number	Area	Number
Slice 1	9	481	8	495
Slice 2	7	524	9	591
Slice 3	10	704	12	557
Total	26	1709	29	1643

case they can be highlighted in one of the following ways: lesions which total volume is bigger than a predefined threshold, or lesions that occupy predefined number of neighboring cross-sections. Our focus is on the latter case. In other words a single large plaque penetrating the white matter can be emphasized if it is "thicker" than a cross-section. A plaque is treated as a multi-slice one if areas of two detected lesions lying on neighbouring slices overlap. Tracking changes may be in some way difficult just by knowing total plaques volume, numbers in single cross-sections. More information can be provided by visualization and quantification of multi-slice plaques while

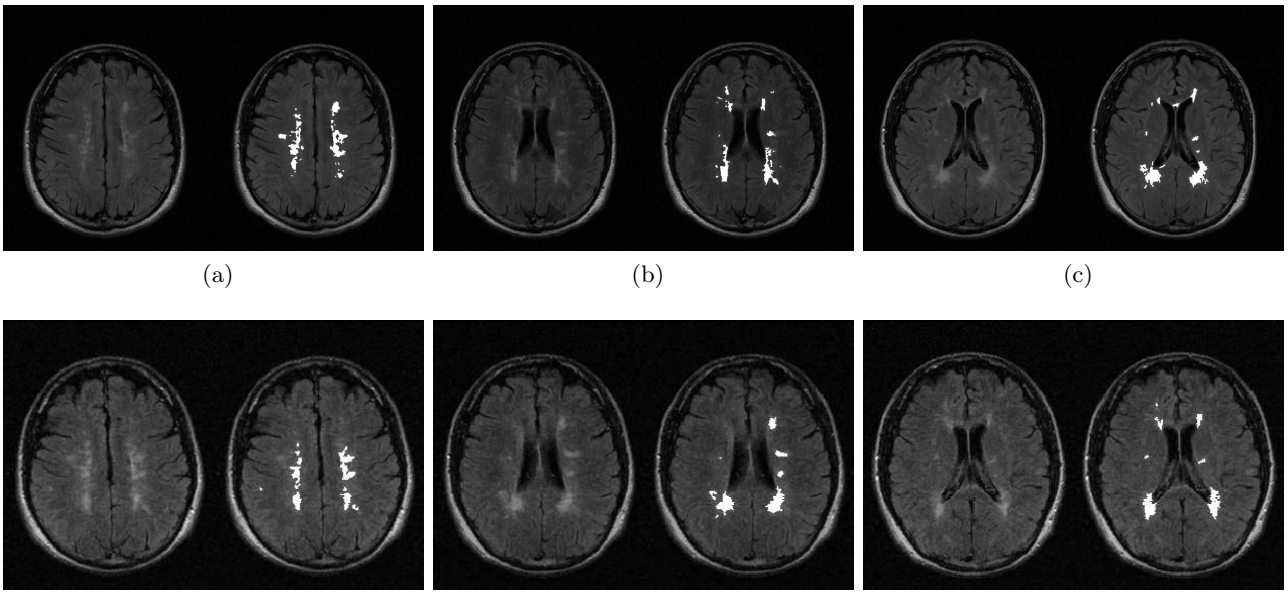

(a) (b) (c)

(d) (e) (f)

Figure 3: An example of 2D plaques presentation in three consecutive cross-sections a)-f) of the 44 year old male subject MR study with slice plaques detection (images on the right sides): a)-c) original study, d)-f) follow-up study. Quantified results from this images are presented in Table 4.

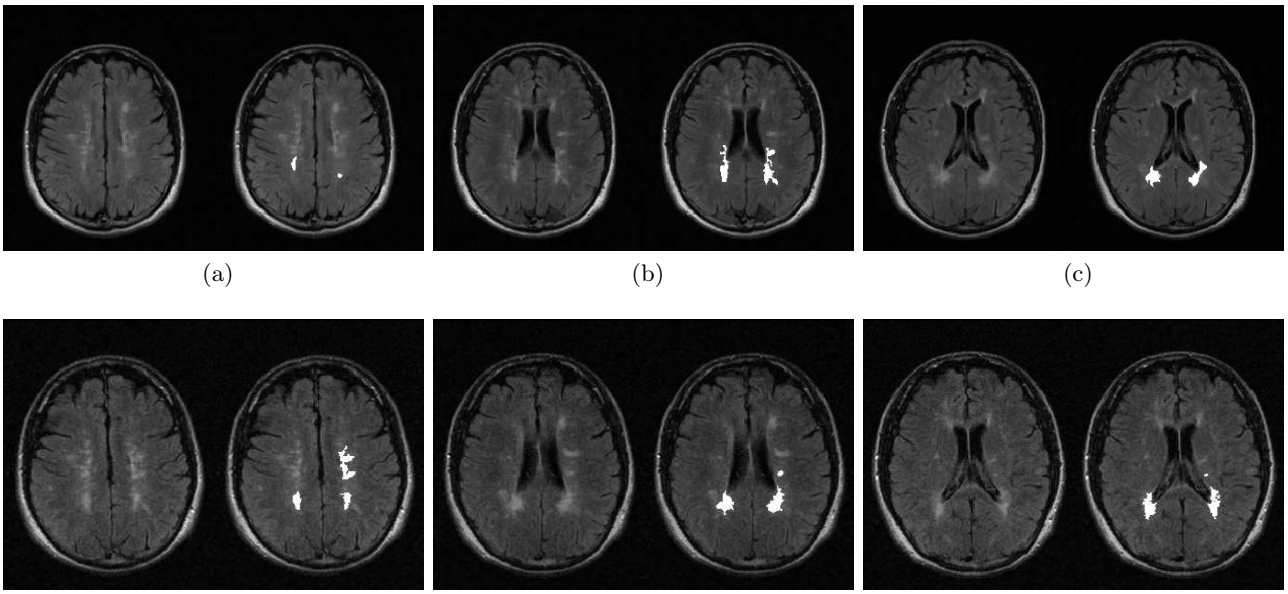

(a) (b) (c)

(d) (e) (f)

Figure 4: An example of 2D plaques presentation in three consecutive cross-sections from Fig 3. a)-c) original study, d)-f) follow-up study.)

comparing the original study with the follow-up one. Examples of 3-slice plaques fragments visible in particular

cross-sections are presented in the figure 4. Quantification results of multi-slice plaques are presented in table 4. A natural extension of such 2D presentation approach is 3D rendering of all detected plaques within previously segmented intracranial structure area. Results are presented in Figure 5. Automated lesions segmentation by

Table 2: Example of plaques quantification in original and follow-up study of a 44 year old male subject (multi-slice plaques).

Study	Original		Follow-up	
Finding	Number	Area	Number	Area
	2	437+417=854	3	442+473+232=1147

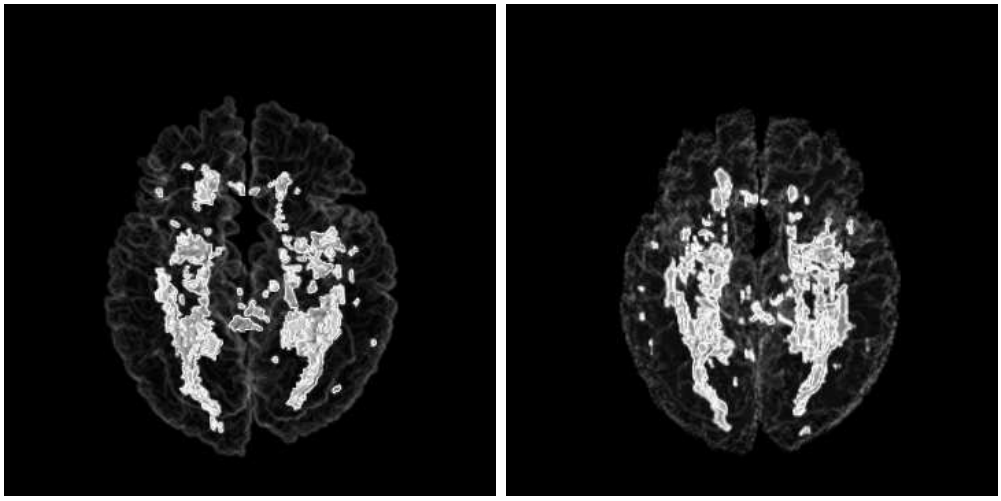

(a) (b)

Figure 5: An example of 3D plaques rendering in 44 year male subject MR studies presented within segmented brain masks: a) original study, b) follow-up study.

this approach was compared to manual segmentation performed by the neuroradiologiest in 3 studies. In terms of lesions number the system, the CAD generates 5% of false positive detection rate and 7.5% false negative detection rate of true MS lesions. In terms of plaques area these errors oscillate around 8.5% respectively. There was a 15% difference between total lesions load noted between original study and the follow-up study.

5. CONCLUSIONS AND FUTURE WORKS

Automatic processing of MR exams provides volumetric measurements of multiple sclerosis lesions. Within the same patient, a change in lesion load between two or more temporally separated MR exams is a quantifiable indicator of disease progression. False positive detection mostly occurs in the area adjacent to the lateral ventricles were physiologic increased signal intensity is within normal limits. This will still require improvement and more precise analysis to suppress CSF spaces. Additionally false positive errors in lesions segmentation were also observed when image data was highly corrupted by RF field inhomogeneity. In such cases false lesions were detected in the gray matter area. The preliminary steps of the methodology including location of brain mask, and CSF spaces were in general acceptably performed by this CAD approach in 25 cases. Other 6 cases failed to detect brain mask due to either large amount of noise or MR signal artifacts other than RF field inhomogeneity. In future works application of intensity inhomogeneity correction and improvement of brain mask segmentation will be planned. This method copes with clinical data of low spatial resolution but due to

relatively large spacing between cross-section sensitivity and specificity of the method in detection of quantitative changes of lesions load must be assessed by comparison with experts verdict. Development of a CAD graphical user interface is an ongoing process. Validation of method using larger clinical data set with ground truth plaques outline performed by clinical expert is also considered. Generally this CAD system is well suited to making objective comparisons between two MR studies from the same patient. The combined single slice, multi-slice and 3D rendering superimposed into 3D brain mask improves lesions presentation and provides the general comparison. Progression of a patient's MS lesions can be readily documented by comparing the quantitative changes in lesion size or number between original and follow-up studies when information about plaque size and relative thickness may be also helpful in visual plaque identification and comparison. This automated approach to MS quantification may be helpful in assisting the neuroradiologist in assessing the progression, stability or improvement of MS lesions over time.

REFERENCES

1. C. Confavreux, S. Vukusic, J. Grimaud, and T. Moreau, "Clinical progression and decision making process in multiple sclerosis," *Multiple Sclerosis Journal* **5**(4), pp. 212–215, 1999.
2. C. Pachai, Y. Zhu, J. Grimaud, M. Hermier, A. Dromigny-badin, A. Boudraa, G. Gimenez, C. Confavreux, and J. Froment, "A pyramidal approach for automatic segmentation of multiple sclerosis lesions in brain mri," *Comput. Med. Imag. Grap.* **22**(5), pp. 399–408, 1998.
3. Y. Ge, O. Gonen, M. Inglese, J. Babb, and C. Markowitz, "Neuronal cell injury precedes brain atrophy in multiple sclerosis," *Neurology* **62**, pp. 624–627, 2004.
4. C. Guttmann, R. Kikinis, M. Anderson, M. Jakab, S. Warfield, R. Killiany, H.Weiner, and F. Jolesz, "Quantitative follow-up of patients with multiple sclerosis using mri: Reproducibility," *Journal of Magnetic Resonance Imaging* **9**(4), pp. 509–518, 1999.
5. M.Bosc, F.Heitz, J.-P. Armaspach, I. Namer, D. Gounot, and L. Rumbach, "Automatic change detection, in multimodal serial mri: application to multiple sclerosis lesion evolution," *M. S. Journal* **20**(2), pp. 642–656, 2003.
6. R. Kikinis, C. Guttmann, D. Metcalf, W. Wells, G. Ettinger, and F. J. H. Weiner, "Quantitative follow-up of patients with multiple sclerosis using mri: Technical aspects," *Journal of Magnetic Resonance Imaging* **9**(4), pp. 519–530, 1999.
7. J. Mitchell, S.Karlik, D. Lee, M. Eliasziw, G. Rice, and A.Fenster, "The variability of manual and computer assisted of computer assisted quantification of multiple sclerosis lesion volumes," *Med. Phys.* **23**(1), pp. 85–97, 1996.
8. M.Kohn, N.Tanna, and G. Herman, "Analysis of brain and celebrospinal fluid volumes with mr imaging, methods reliability and validation," *Radiology* **178**(1), pp. 115–122, 1991.
9. A. Zijdenbos, R. Forghani, and A. Evans, "Automatic pipeline analysis of 3-d mri data for clinical trials: application to multiple sclerosis," *IEEE Transactions on Medical Imaging* **21**(10), pp. 1280–1291, 2002.
10. B. Alfano, A. Brunetti, M. Larobina, M. Quarantelli, E. Tedeschi, A. Ciarmiello, E. Coveli, and M. Salvatore, "Automated segmentation and measurement of global white matter lesion volume in patients with multiple sclerosis," *Journal of Magnetic Resonance Imaging* **12**(6), pp. 799–807, 2000.
11. K. V. Leemput, F. Maes, D. Vandermeulden, A. Colchester, and P. Sueletens, "Automated segmentation of multiple sclerosis lesions by model outlier detection," *IEEE Trans Med Imag* **20**(8), pp. 667–6885, 2001.
12. L. S. Zack G.W, Rogers W.E, "Automatic measurement of sister chromatid exchange frequency," *J Histochem Cytochem* **25**(7), pp. 741–753, 1977.
13. D. R. A. Dempster, N. Laird, "Maximum likelihood from incomplete data via the em algorithm.," *Journal of the Royal Statistical Society* **39**(1), pp. 1–38, 1977.
14. Z. Shan, G. Yue, and J. Liu, "Automated histogram-based brain segmentation in t1-weighted three-dimensional magnetic resonance head images," *Neuroimage* **17**(3), pp. 1587–1598, 2002.
15. J. Bezdek, L. O. Hall, and L. Clark, "Review of mr, image segmentation techniques using pattern recognition," *Medical Physics* **20**(4), pp. 1033–1048, 1993.
16. J. Noordam, W. van den Broek, and L. Buydens, "Geometrically guided fuzzy c-means clustering for multivariate image segmentation," *Proceedings. 15th International Conference on Pattern Recognition, IEEE* **1**, pp. 462–465, 2000.

A Data Grid for Imaging-based Clinical Trials

Zheng Zhou, Sander SD Chao, Jasper Lee, Brent Liu, Jorge Documet, H.K Huang

Department of Radiology, USC, Marina del Rey, CA 90292, 310-448-9437

ABSTRACT

Clinical trials play a crucial role in testing new drugs or devices in modern medicine. Medical imaging has also become an important tool in clinical trials because images provide a unique and fast diagnosis with visual observation and quantitative assessment. A typical imaging-based clinical trial consists of: 1) A well-defined rigorous clinical trial protocol, 2) a radiology core that has a quality control mechanism, a biostatistics component, and a server for storing and distributing data and analysis results; and 3) many field sites that generate and send image studies to the radiology core. As the number of clinical trials increases, it becomes a challenge for a radiology core servicing multiple trials to have a server robust enough to administrate and quickly distribute information to participating radiologists/clinicians worldwide.

The Data Grid can satisfy the aforementioned requirements of imaging based clinical trials. In this paper, we present a Data Grid architecture for imaging-based clinical trials. A Data Grid prototype has been implemented in the Image Processing and Informatics (IPI) Laboratory at the University of Southern California to test and evaluate performance in storing trial images and analysis results for a clinical trial. The implementation methodology and evaluation protocol of the Data Grid are presented.

Keywords: Data Grid, Archive, Fault-Tolerance, Clinical Trials, Medical Image

INTRODUCTION

Medical imaging in clinical trials plays a crucial role in developing new treatments and devices for use in modern medicine. However, the massive amount of information being collected in today's large and complex clinical trials make it increasingly important to develop new tools for managing and disseminating the information. Imaging based clinical trials typically have field sites to recruit patients and acquire images, a radiology core responsible for controlling quality and distributing images, and expert sites to perform analysis of acquired images [3]. A general diagram of the organization of an imaging-based clinical trial and the responsibilities of each component is shown in Figure 1.

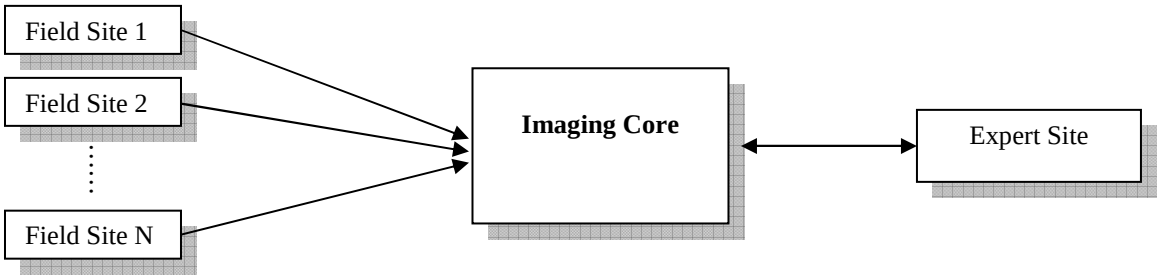

Field Site Responsibilities:

1. Recruit Patients
2. Collect Images

Core Responsibilities:

1. Perform Quality Control of Images Sent by Field Sites
2. Store Images Acquired by Field Sites
3. Distributes Acquired Images for Analysis by Experts

Expert Site Responsibilities:

1. Analyze Images Sent by Core
2. Sends Analysis Back to Core for Storage

Figure 1: General Clinical Trial Organizational Layout and Responsibilities

The technical and administrative challenges involved in managing a clinical trial increases exponentially with each additional trial or field site added to a radiology core's workload, specifically in terms of managing the increase in the number of large image data sets [4]. Coordination and distribution also becomes substantially more costly and difficult once a trial starts increasing in geographic size or extends globally to international locations. The administrative difficulty can be put into perspective when one considers that burning and mailing CDs is a common method used for transporting large amounts of information between different sites.
This paper presents an easily implemented Data Grid solution merging both the globus toolkit 4.xx and the DICOM standard for imaging that can efficiently store and share the images and results of a large multi-site clinical trial. The setup and testing of a Data Grid for use will be discussed in addition to the system performance and capabilities.

MATERIALS

The proposed Data Grid solution is developed using grid computing technology and is based upon the integration of the defacto imaging standard of DICOM and the Globus Toolkit 4.xx[11]. The components of the Data Grid run on either a desktop PC or a server. Although, a high speed connection between components of the Data Grid is not required, it is highly recommended. The five-layer architecture of the Data Grid is shown below in Figure 2, with the services developed by IPI shown in dark grey.

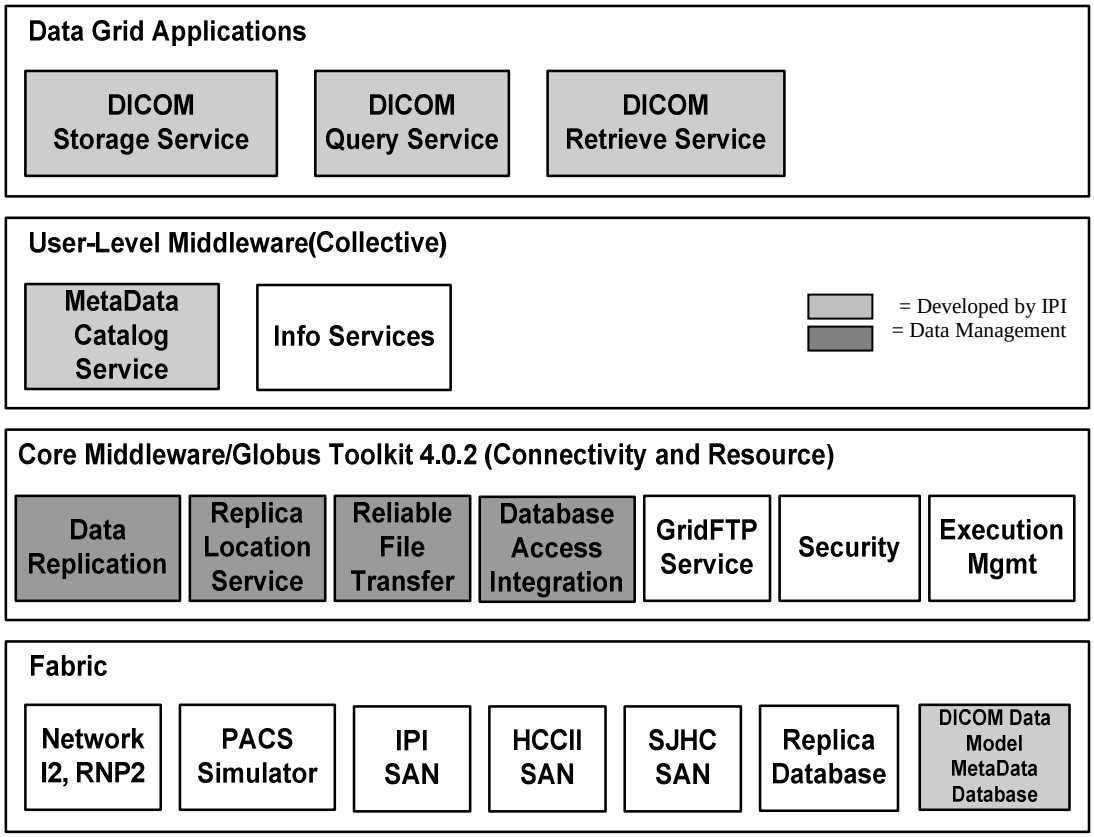

Figure 2: Five-layer architecture and the contents of the Data Grid for clinical image backup: The combination of 2nd and 3rd layers of connectivity and resource, respectively, are sometimes referred to as the Core Middleware. Gray-shaded boxes represent components developed or modified at the IPI Lab. The three services in Data Grid Applications layer are not the standard Grid Services defined in the Globus Toolkit 4.0, but are Grid Service users which use standard Grid Services plus the DICOM services [1].

There are three primary components to the Data Grid (illustrated below in Figure 3):

a. **Storage Node:** Computer(s) and storage devices providing storage resources for the Data Grid.

b. **Database:** Service that keeps track of meta data as well as file locations on the different storage nodes within the Data Grid. Dynamic and robust access to data is provided by a Data Access Interface (DAI) integrated with the database [2].

c. **Grid Access Point (GAP):** Service provides DICOM compliant storage and Query/Retrieve capabilities for accessing data within the Data Grid.

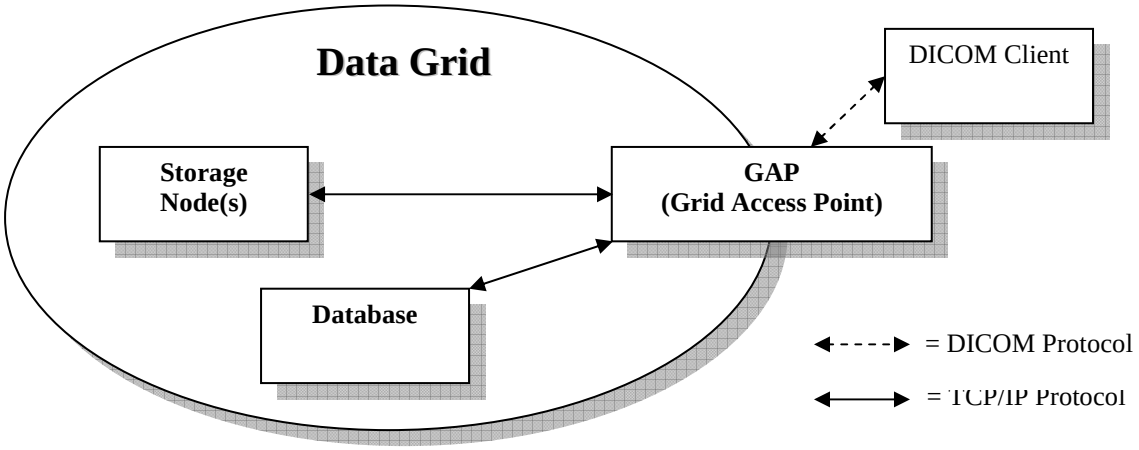

Figure 3: Conceptual illustration of Data Grid components

A clinical trial Data Grid test bed has been setup with two onsite and one offsite storage node at the Image Processing and Informatics (IPI) Laboratory of the University of Southern California (Figure 4). The GAP provides access to the test bed Data Grid and has been configured to forward information to both storage nodes, thus the Data Grid provides fault tolerant archiving as well as access to all trial data sent to it[13]. Workstations can then access the trial images and analysis results stored in the Data Grid by connecting to the GAP using the internet. A detailed description of the Query/Retrieve workflow implemented in the Data Grid can be found in "The Role of a Data Grid in Worldwide Imaging-Based Clinical Trials"[1].

Fault Tolerance

Fault tolerance is built into the architecture of the test bed Data Grid shown in Figure 4. Images sent to the GAP by outside computers are replicated when the GAP distributes that information to the storage nodes within the Data Grid. If there are two storage nodes within the Data Grid, and the GAP is configured to forward incoming data to both storage nodes, then there will be two copies made of the original data. Thus, the fault tolerance capabilities of the Data Grid for clinical trials depend upon the number of storage nodes available and the user configuration[12]. High availability access to the Data Grid can also be assured by having multiple GAPs provide access instead of a single entry point.

Data Distribution

Efficient data distribution is a difficulty for administrators of clinical trials with multiple locations. The IPI test bed Data Grid solves the problem by adding DICOM Query/Retrieve capability to that of a standard Data Grid. Thus, researchers and administrators can use the header information contained in a DICOM image file to search for data of interest in a manner similar to that of a PACS workstation. One of the most significant advantages of a DICOM Data Grid solution is the ease of integration with existing DICOM modalities, display workstations and other equipment currently in use by imaging trials. Connecting to a DICOM Data Grid for storage needs is then greatly simplified by only requiring the configuration of IP address, port number and AE title.

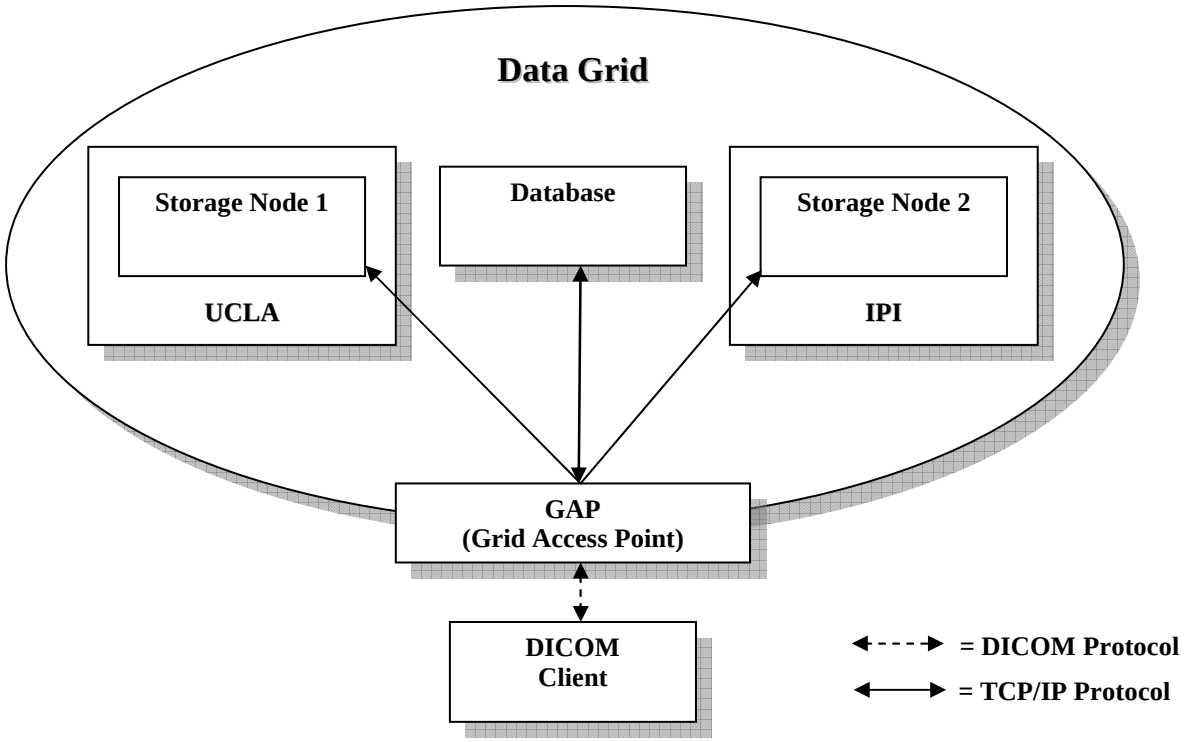

Figure 4: Illustration of the test bed Data Grid setup at IPI and UCLA

METHODOLOGY

The file transfer performance as well as fault tolerant archiving capabilities of the prototype Data Grid has been evaluated to determine feasibility for use in clinical trials. Installation and setup of the core grid components took approximately two weeks and each additional site to be added required an additional week for testing and configuration. The procedures used to setup the Data Grid and the methodologies used to evaluate the different functionalities as well as performance are described below.

1. Data Grid Setup

There are six steps to setting up the Data Grid for use:

1. *Installation of Prerequisite Software:* The Data Grid software requires a Linux or UNIX based operating system because the globus toolkit was developed in and performs best on those platforms. Thus, the first step is to install the appropriate operating system on machines and then the Data Grid software itself. This step is fairly straight forward, unfortunately working through the occasional incompatibilities between some Linux/Unix operating systems and the required software proved to be very time consuming. Approximate time for completion of this step was two days.

2. *Installation of Data Grid Software (Globus Toolkit):* The primary objective of this step is to install the general Globus Toolkit Data Grid software on the machines that will be a part of the Data Grid. The open source Data Grid package provides the services for communication, security, and file transport that tie the different components of the Data Grid together. The full Data Grid package was installed on every machine that is a part of the grid, but only the services for each machine's designated role were activated. (i.e.: Computer designated as storage node only had the storage and file transport functions activated). Completion of installation and configuration of all user accounts necessary took two days.

3. *Installation of IPI Data Grid Software:* This step installs the software developed by the IPI lab to add DICOM Query/Retrieve functionality to the standard Data Grid installation. Installation of the package was straight forward and error free on all machines. The time required for the installation was less than an hour.

4. *Establishing Connectivity:* Establishing a connection between all the different components of the Data Grid was probably the most time consuming step in setting up the test bed. Connecting machines within the same network was simple. However, establishing communication with components located offsite under another organization's jurisdiction took additional time due to the need to reconfigure firewall settings to allow communication through specific ports and to create a system architecture that satisfies the security requirements of both parties. This step of the installation took two weeks with the bulk of the time devoted to determining the best connection policies between two separate institutions.

5. *Configuring Data Grid Services:* This step consists of configuring the databases used for storing the metadata information of all images being stored within the grid, generating security certificates to authenticate the identities of all machines on the grid and setting up the Data Grid services to run with the desired options. This is the step that differentiates the machines into the different components of the Data Grid such as storage node or GAP. An example of some of the specifications that need to be set are location for images to be stored in, port for services to run on, number of storage nodes to be used for storing received information. Typical configuration time required is one to two days.

6. *Testing the Data Grid:* Connections between components are first tested by using ping and telnet to get a response from the different components of the Data Grid. Next file transfer is tested by initiating a manual file transfer command between different components. DICOM functionality is then activated and file transfer to all storage nodes is tested by using an external workstation to send DICOM images to the Data Grid. Lastly, DICOM Query/Retrieve functionality is tested by using an external DICOM workstation to query the Data Grid and retrieving studies of interest. Redundancy and failover testing is achieved by deleting one storage node's copy of a file and making sure that the Data Grid will search and transfer from other storage nodes containing the requested file. Total time required for testing is one week.

1.1. Connecting Field Sites

There are two different system architectures for connecting field sites to the Data Grid. The first uses a GAP located offsite to a field site while the second provides each field site with a local GAP. The performance difference between the two architectures is due to a compilation/compression function of the GAP. When a GAP receives studies containing multiple images it will compile/compress them into a single file and use ftp to transfer the file to the storage nodes instead of sending individual images using DICOM. The two architectures are illustrated below in Figure 5.

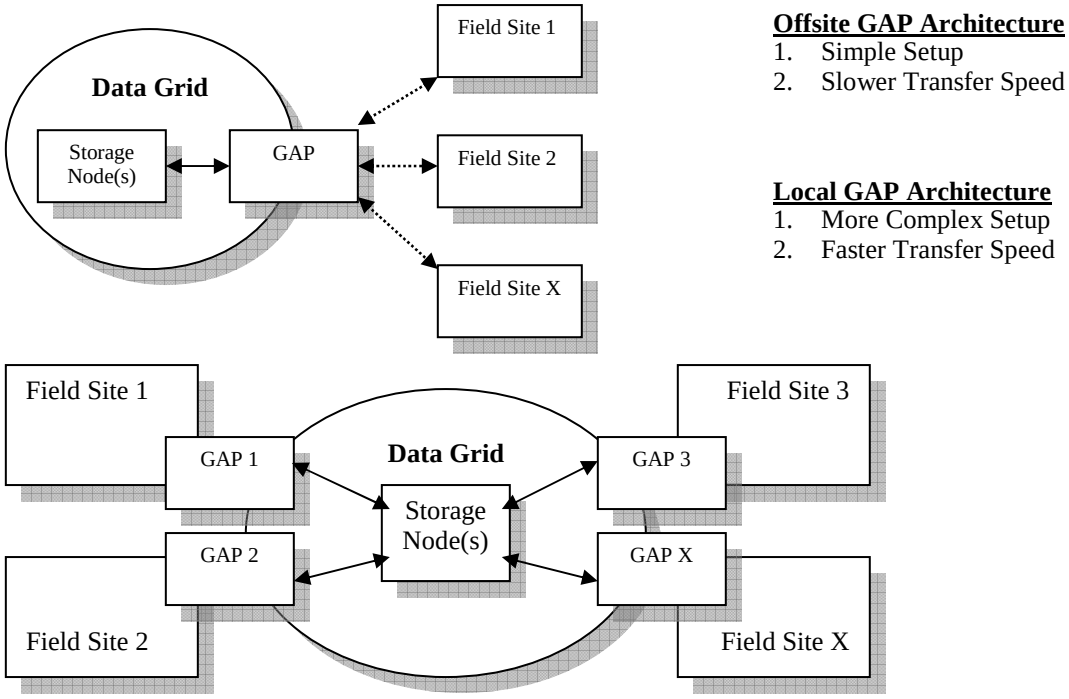

Figure 5: Comparison of two GAP architectures

1. *Offsite GAP:* This method requires field sites to direct all Data Grid access requests to a GAP that is located off site. Configuration and setup is greatly simplified for this method because a field site only has to direct its DICOM modalities and workstations to an existing GAP to connect to the Data Grid. However, transfer speeds will suffer due to the fact that multiple images will be transferred using DICOM over a slower WAN connection between a GAP and field site. (Note: There can be more than one GAP for this architecture, one shown for illustrative purposes only)

2. *Local GAP:* This architecture provides each field site with its own local GAP. File transfer performance is improved because the individual DICOM images of a study will be sent to the GAP using a LAN connection and then only a single file will be transferred via ftp to the storage nodes using a WAN connection. The drawback to this architecture is the increase in administrative complexity of having multiple GAPs to configure and maintain. This drawback can be easily resolved by shipping a pre-packaged tested and evaluated GAP installed with hardware to the field site.

1.2. Performance Testing

File transfer performance was measured between workstations setup in the IPI lab and the UCLA storage node. A local GAP architecture was used and the UCLA storage node chosen because it is located the farthest away on a network separate from the workstation involved in the test. A DICOM display client with Query/Retrieve capabilities was used to initiate file transfers and view received images. All images used were from the National Cancer Institutes Lung Image Database Consortiums (LIDC) public database[7].

The three steps for the file transfer test are listed below and are shown graphically in Figure 6:

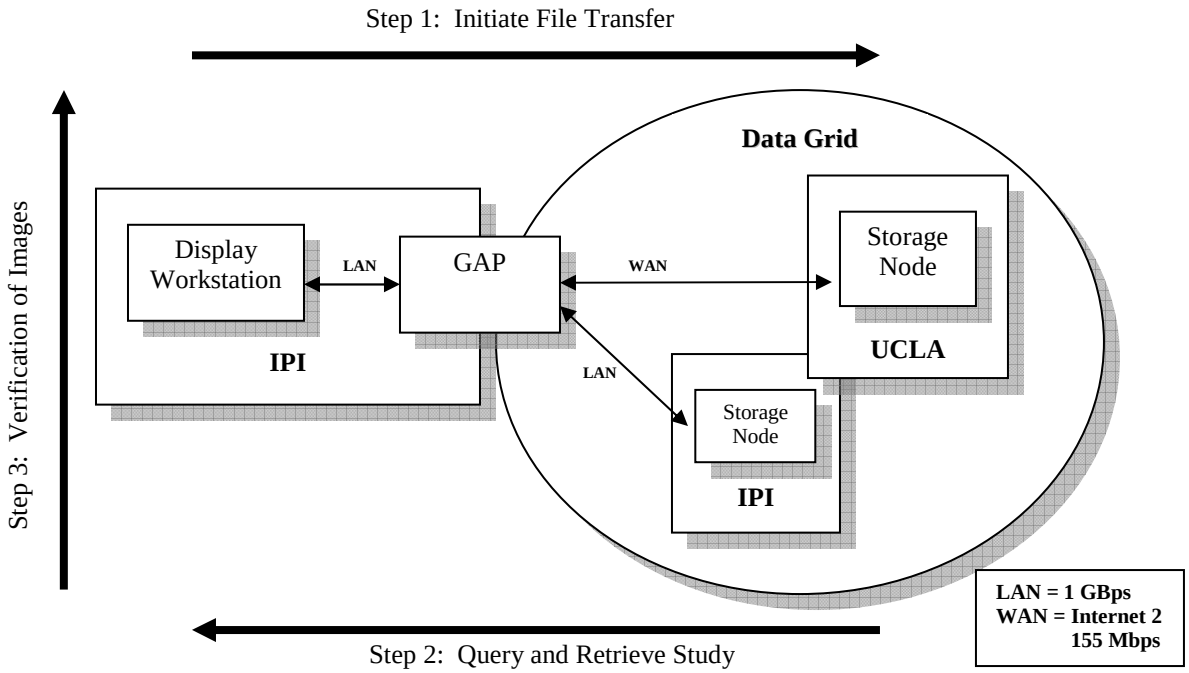

Figure 6: Performance testing

1) Initiate file transfer: Send DICOM studies from a display workstation to the local GAP. The GAP automatically compresses all studies into one file before sending to storage nodes. File transfer status is monitored by terminal windows logged into the storage node and GAP involved in the transfer.

2) Query and Retrieve Study: The study sent in step one is retrieved by sending a query to the GAP. Queries can contain information specific to a study such as patient name, ID number, or a general query that returns a list of all studies stored in the Data Grid. A study of interest is selected by the user and a transfer request sent by the workstation to the GAP. The GAP receives the transfer request and automatically retrieves/forwards the relevant study to the workstation requesting the information.

3) *Verification of Images:* The received images appear on a queue within the display workstation and the total transfer time from the initiation of transfer is recorded by the display software. The received studies are then opened to verify correct retrieval and completeness of the study.

RESULTS

The results of the file transfer testing described in section 3.3 are given in Table 1 below.

Transfer Set	1	2	3	4	5
# Images (CT)	124	268	104	525	181
File Size (MB)	46.8	134	18.6	163.3	91
Transfer Time*	0:32	0:40	0:22	1:44	0:28
Transfer Speed (Megabits)	11.7	26.8	6.8	12.6	26.0
Average File Size	0.38	0.50	0.18	0.31	0.50

Table 1: Preliminary file transfer results

*All transfer times listed are from the initiation of the transfer by the workstation at IPI to the complete reception of all images in a study from UCLA.

Transfer speeds attained ranged from a low of 6.8 Megabits per second to a high of 26.8 Megabits per second. Average transfer time for image studies containing between 100-130 images was under 45 seconds. Studies containing over 500

images were generally transferred in under 2 minutes. The inefficiency of transferring numerous small files versus small numbers of large files is demonstrated in our results when comparing transfer speeds to average file sizes. Studies 1, 3 and 4 with the slowest transfer times had the smallest average file size as well. Opportunities for improving the data transfer between Data Grid components as well as the performance of the services are now being investigated.

CONCLUSIONS

A Data Grid for clinical imaging trials has been developed using grid computing technology. The test bed setup consists of distributed storage nodes at two different sites, a database and grid access points developed using the Globus Toolkit. Software developed by USC IPI adds DICOM functionality to the Data Grid and transforms the technology into a powerful tool for storing and distributing image data for large multi-site clinical trials. Fault tolerance is also built into the framework of the Data Grid, thus protecting valuable knowledge assets from catastrophic loss.

Different setups of the Data Grid offer a mix of performance and administrative benefits. However, one of the primary limiting factors is the bandwidth available between various components of the Data grid. The flexible nature of the Data Grid can easily integrate additional field sites into an existing trial, thus providing administrators with a hassle free expansion of resources.
More work remains to be done on the Data Grid, but Clinical trial administrators will soon have an easy way to share information with all participants of a trial, and rest easy knowing that their data is not vulnerable to sudden catastrophic loss.

REFERENCES

1. Z. Zhou, M.G., J. Documet, L. Chan, H.K. Huang, B. Liu, *The Role of a Data Grid in Worldwide Imaging-Based Clinical Trials*. 2006, USC IPI: Marina del Rey.
2. J. Lee, J.D., B. Liu, Z. Zhou, *Design and Implementation of a Fault Tolerant and Dynamic Metadata Database for Clinical Trials*, in *SPIE*. 2007: San Diego.
3. C.L. Meinert, Clinical Trials: Design, Conduct, and Analysis, Oxford U.Press, Oxford, 1986.
4. S. Piantadosi, Clinical Trials: A Methodologic Perspective, John Wiley & Sons, 1997.
5. S.C. Chow and J.P. Liu, Design and Analysis of Clinical Trials: Concepts and Methodologies, John Wiley & Sons, NY, 2004.
6. M.S. Brown, S.K. Shah, R.C. Pais, Y. Lee, M.F. McNitt-Gray, J.G. Goldin, A.F. Cardenas and D.R. Aberle, Database Design and Implementation for Quantitative Image Analysis Research, IEEE Trans. Information Technology in Biomedicine 9 (2005), 99-108.
7. M.F. McNitt-Gray, S.G. Aramato, L.P. Clarke, G. McLennan, C.R. Meyer and D.F. Yankelevitz, The lung imaging database consortium: creating a resource for the image processing research community, Radiology 225 (2002), 739-748.
8. Digital Imaging and Communications in Medicine (DICOM) 2004, http://medical.nema.org/dicom/2004.html, accessed on March 14, 2006.
11. A. Chervenak, I. Foster, C. Kesselman, C. Salisbury and S. Tuecke, The Data Grid: Towards an Architecture for the Distributed Management and Analysis of Large Scientific Datasets, Journal of Network and Computer Applications 23 (2001), 187-200.
12. W. Allcock, J. Bresnahan, R. Kettimuthu, M. Link, C. Dumitrescu, I. Raicu and I. Foster, The Globus Striped GridFTP Framework and Server, Proceedings of Super Computing 2005 (SC05).
13. B.J. Liu, M.Z. Zhou and J. Documet, Utilizing data grid architecture for the backup and recovery of clinical image data, Computerized Medical Imaging and Graphics 29 (2005), 95-102.
14. H.K. Huang, A. Zhang, B. Liu, Z. Zhou and etc, Data Grid for Large-Scale Medical Image Archive and Analysis, Proc. the 13th ACM International Conference on Multimedia 2005, 1005-1013.

Design and Implementation of a Web-based Data Grid Management System for Enterprise PACS Backup and Disaster Recovery

Zheng Zhou, PhD; Kevin Ma*; Elisa Talini, MS**; Jorge Documet, MS; Brent Liu, PhD

Image Processing & Informatics Laboratory, University of Southern California, Marina del Rey 90292, CA
*Department of Biomedical Engineering, UT Austin, TX
**Department of Diagnostic and Interventional Radiology, University of Pisa, Italy

ABSTRACT

A cross-continental Data Grid infrastructure has been developed at the Image Processing and Informatics (IPI) research laboratory as a fault-tolerant image data backup and disaster recovery solution for Enterprise PACS. The Data Grid stores multiple copies of the imaging studies as well as the metadata, such as patient and study information, in geographically distributed computers and storage devices involving three different continents: America, Asia and Europe. This effectively prevents loss of image data and accelerates data recovery in the case of disaster. However, lack of centralized management system makes the administration of the current Data Grid difficult. Three major challenges exist in current Data Grid management: 1. No single user interface to access and administrate each geographically separate component; 2. No graphical user interface available, resulting in command-line-based administration; 3. No single sign-on access to the Data Grid; administrators have to log into every Grid component with different corresponding user names/passwords.
In this paper we are presenting a prototype of a unique web-based access interface for both Data Grid administrators and users. The interface has been designed to be user-friendly; it provides necessary instruments to constantly monitor the current status of the Data Grid components and their contents from any locations, contributing to longer system up-time.

Keywords: Data grid, management system, graphical user interface, single sign-on, web

INTRODUCTION

We have developed a Data Grid infrastructure for fault-tolerant image archiving and disaster recovery of Enterprise PACS. The Data Grid stores multiple copies of imaging studies as well as patient information in geographically distributed computers and storage devices. This effectively prevents loss of image data and speeds up data recovery in the case of a disaster. Even though the Data Grid provides a promising solution for fault-tolerance of image data archive and fast disaster recovery, the Data Grid management has three major challenges. First, each component in the Grid has to be accessed and managed individually. Second, every user command is command-line-based; users must manually input commands to access the grid. Third, each user must log into each component with his or her password, which can result in many username/password management complications. In this paper we propose a web-based Data Grid management system that addresses these issues to ease the administration of the Data Grid.

THE DATA GRID ARCHITECTURE

Data Grids are becoming increasingly important for sharing large data collections and for archiving and disseminating them in a digital library framework. This technology is spreading even outside scientific communities: many companies are looking at Data Grid as current solutions for enterprise PACS architecture and integration between heterogeneous systems. [1, 2]

Data Grid concepts permit data storage from different PACS systems without interfering with their architectures. They incorporate Enterprise PACS systems in successive steps and thus provide a scalable solution. Scalability is a key concept for developing an Enterprise PACS because of the continuously healthcare center migration to digital radiology systems and the enormous amount of produced data and images involved.
Currently, our Data Grid project aims to allow storing and sharing PACS metadata and images between 4 sites located in geographically separated countries and continents. The healthcare institutions involved in the project are located in:

- Image Processing and Informatics (IPI) Laboratory at University of Southern California, USA – North America
- Polytechnic University, Hong Kong, HK – Asia
- InCor (Heart Institute), São Paulo, BR – South America
- Diagnostic and Interventional Radiology Department, University of Pisa, IT – Europe

The chosen sites, or components in the Data Grid, are connected with high speed international networks, including the US Internet2 (Abilene), the Hong Kong Academic and Research Network (HARNET), the Brazilian National Research and Education Network (RNP2) and the Pan-European Research and Education Network (GEANT2). [5]

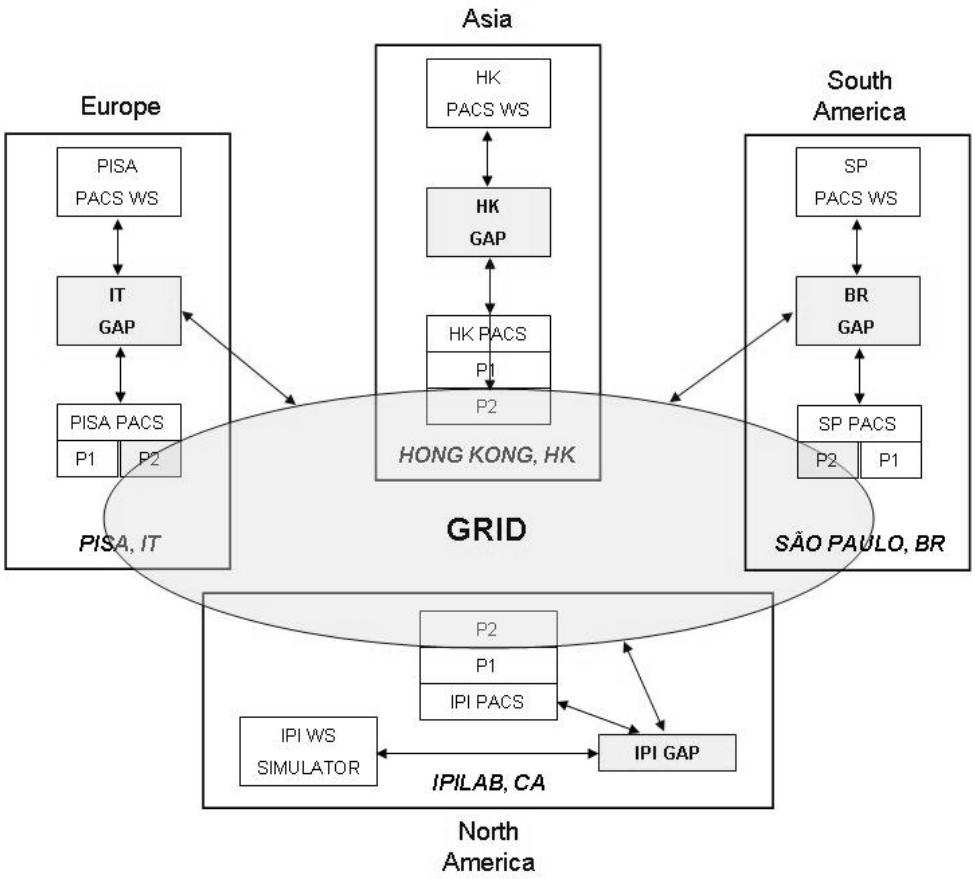

Figure 1. Four-sites Data Grid testbed.

Figure 1 shows the architecture of the testbed Data Grid with the four sites mentioned above. Each site has been provided with a Grid Access Point (GAP), which is opportunely configured to be a member of the four-site testbed.
Together with the Grid Storage Resource (shared storage partitions P2), the GAP is the key Grid component that manages storage and access to data and images at each site.
The Data Grid architecture can be considered a data backup and recovery solution as well as an instrument for quick and easy access to remote data and images resulting from examinations and clinical trials. In order to integrate with PACS, the Data Grid architecture is applied to a DICOM (Digital Imaging and Communications in Medicine) environment since DICOM has become the standard for clinical image data and PACS utilizes this standard. In particular, some PACS/DICOM resources include Storage services, Query services and Retrieve services, which are integrated with the DICOM standard protocols in addition to the use of other Data Grid Services.

After an examination is completed at one site, the modality sends out the image data to the PACS server, as opportunely configured in its usual workflow. PACS server, provided with auto-routing function, is then configured to send a second copy of the same examination data to the Data Grid for backup. Therefore, two archiving systems are achieved: the short-term archive is the PACS local archive (P1), and the long-term archive is provided by the shared storage belonging to the Data Grid architecture (P2). The GAP receives the second copy of the images and automatically sends them to a Data Grid storage area provided by shared partition (P2) of other sites. The Replica Location Table keeps track of the physical location of the images in the storage area to simplify and speed up query/retrieve operation from any workstation outside the Data Grid.
When radiologists want to retrieve a study from the Data Grid, they can simply select the study they want to view; the GAP retrieves the study from the local storage or other storage areas if it belongs to other sites. This action is completely transparent to the users, who receive images in their workstation even if they belong to other sites.

The aim of the Data Grid is indeed to distribute data and images across the sites:
- Robustly: Each file must be replicated at least in two sites;
- Efficiently: Where possible, files should be stored close to where they are needed most often;
- Transparently: End users should not need to be concerned with how the data grid is implemented.

The data and images transfers between the different sites are realized through GridFTP protocol, which is a high-performance, secure, reliable data transfer service optimized for high-bandwidth wide-area networks.

DATA GRID MANAGEMENT SYSTEM

Our goal is to provide a centralized management system, allowing geographically diverse Data Grid Nodes to be managed from a central location. This location doesn't have to be in a fixed position; therefore our system is built to provide a remote access with full status and control. The web-based graphical user interface (GUI) is used to provide summary views of the Grid elements, providing instant access to any individual service from any of the four Nodes. The diagram view includes icons for each site sharing the Grid and highlights the active Node. This view provides a particular service in the network, allowing instant notification if certain Grid Node services failed. When such case occurs, the Grid Management System makes it possible for administrators to immediately take notice of the occurred problem, fix the problem, and restore the Node system.

In an enterprise environment consisting of many systems, as the Data Grid is designed to provide, it is not optimal for each system to possess its own different set of administrators and users. A separate and centralized system has to be created and dedicated to manage all of the Data Grid Nodes, as well as all of the administrators and users. The system should be able to assign each administrator and user with specific tasks and privileges concerning data access from the Grid.
Lack of centralized management system makes the administration of current Data Grid difficult. A new Data Grid management system needs to be able to answer the three following major challenges:

1. To realize a single user interface to access and administrate each geographically separate component;
2. To provide a graphical user interface, replacing the command-line-based administration;
3. To realize a single sign-on access to the Data Grid; administrators no longer have to log into every Grid component with different corresponding user names/passwords.

A web-based management system for the Data Grid is presented to address these challenges.
First, Grid portal and user interface tools are able to support the construction of graphical user interfaces for invoking, monitoring, and/or managing activities involving Grid resources.
The proposed management system aims to solve technical difficulties in accessing geographically distributed components securely by enabling access to Grid systems from Web browsers. Therefore, it should be able to access each component of the Data Grid from a remote workstation, replacing command lines with easy-to-navigate functions and providing a centralized single sign-on access to every component, instead of logging in multiple components individually.
The Web browser-oriented management system includes a three-layer infrastructure, which consists of three major components: a web server, an agent in each component of the Data Grid, and Grid services (Figure 2).

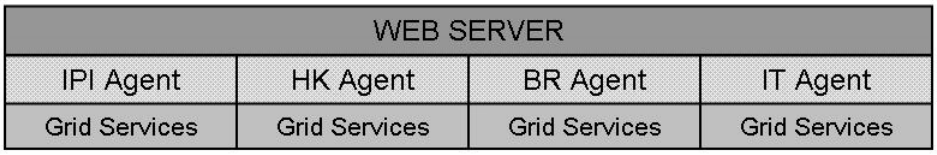

Figure 2. The three-layer infrastructure

In the presentation we use Apache2 as the web sever. The web container hosts the application that both generates the various elements of the first-layer Web user interface and interacts with third-layer Grid resources and services. Data presentation and exchange between the web server and Grid resources are implemented using JAVA and web technology, such as PHP and its extensions.
The agent, installed in every Grid component, acts as the bridge between the web server and the Grid service: it aggregates information from the Grid services and displays the information in the web server, based on user commands and queries. Administrators can send operational commands to the Grid services through the web server and through the agent. The agent plays the key role of matching user and administrator commands from the user interface to commands that are understood by the Grid service. The agent is also responsible for retrieving the correct information from the Grid service to the web server. The successful implementation of the management system will greatly improve the management of the Data Grid and facilitate its usage for the Enterprise PACS backup and disaster recovery.
Grid Services are profiled in Globus Toolkit 4.0, the software toolkit used for building Grid system and applications.
Its Core Middleware provides a set of services, such as Grid Security (GSI), remote job submission and control using the Grid Resource Data Allocation and Management (GRAM), high performance secure data transfer (GridFTP), Replica Location Service (RLS) and other core tools for building the Connectivity and Resource Layer.

Figure 3 shows the system architecture where the web interface provides access to the Data Grid system for both users and administrators. The web server addresses them respectively to the browsing page and the management page. Every request coming from the node administrator is processed by the agent of that node, which communicates with Globus services and performs the requested action.
Every query request coming from the user is also processed by the agent which through OGSA-DAI (Open Grid Services Architecture Data Access and Integration) lets the user access and browse the resources. Through OGSA-DAI, a Globus project that produces a pure Java data service framework for accessing and integrating data resources on to Grids, we are able to access data in a consistent, data resource-independent way and provide a way of querying and delivering data via web services [6]. In addition, the agent manages requests for uploading and downloading of images, packaging or un-packaging of files and file insertions in the database.

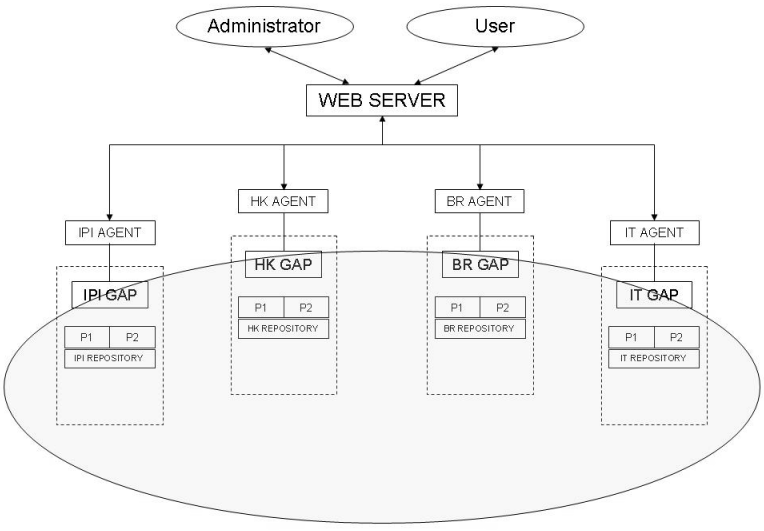

Figure 3. Administrator and User Web Interface Architecture

1. System features

The web-based interface of the Data Grid management system provides a suite of functionalities that can be used to implement data and information management systems.
It is a single sign-on system in which all applications that use the separate user management component would have one single login and password. This feature avoids the user to use or remember a set of passwords to access different services in the same system or different systems.
User management and security authentication would be cleanly and modularly decoupled from the application itself.
There are mainly two administration levels: the node administrator and the global Grid administrator. The former has restricted power: the node administrator can execute commands only on his or her node GAP; however the local administration status doesn't prevent the user from monitoring other GRID Nodes, including their current status. The second level, the global Grid administrator, can monitor Grid node status, modify node configurations and restart services of every node in the Grid.
The local administrator is able to discover faults in the Data Grid due to problems occurred in the local Node as well as other Nodes. If the Grid fault happens in the local Node, the administrator can act locally in order to fix the problem, otherwise one can warn the global Administrator to fix the problem occurred in another Node.

2. Administrator functionalities

- Login

Each Data Grid node administrator is provided with a username and a corresponding password to access to the system. Figure 4 shows the Login Page, which is the same for both administrators and users. In the future we can implement a secure system authentication, such as the fingerprint verification to access the system.

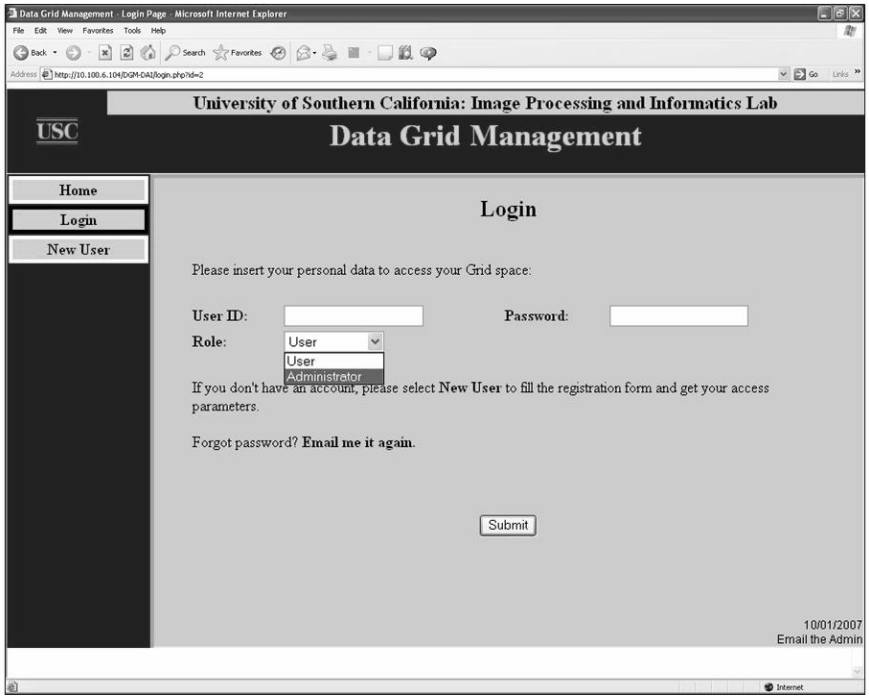

Figure 4. Access Interface

Currently we do not provide a registration form for administrators; rather, we provide a registration form for general users. The request of an administrator account must be processed and approved by the global Grid administrator.

- Monitoring systems status

Administrators of both levels can view and verify the current status of the Grid services displayed on the user interface. When a Grid error occurs, the administrators can fix the problem if they have permission to do so, or they can notify the global administrator. Because the error can be detected and notified to administrators immediately, this feature is able to speed up the recovery process when the node fails.
For every Grid Nodes, its local node administrator (and the global administrator for all nodes) can perform the following operations:

- Restarting the database
- Restarting Globus GT4 services
- Restarting GridFTP
- Restarting the Replica Location Service (RLS)
- Generate a proxy for the GAP
- Modify Grid Store (gstore) configuration and restart the service
- Modify Grid Query/Retrieve (gqr) configuration and restart the service

The global administrator has the power to perform these actions on every Grid Node, thus the global administrator is able to manage the entire Data Grid system freely at any time.

3. User functionalities

The same web interface is also an instrument for accessing the data and metadata more conveniently for the users. The system allows simple users, including radiologists or referring physicians, to share their scientific data collections with their colleagues in a secure fashion. It provides a system where users can organize their files independent of the physical location and formats of the files through a common web browser. Users can upload images on the Data Grid directly from their PC, without the need of a DICOM server on their machine.
The Data Grid management system provides the following three primary functionalities for the users: a registration form, a login page, and an image query and display page, with the option to download and upload images.

- Registration Form

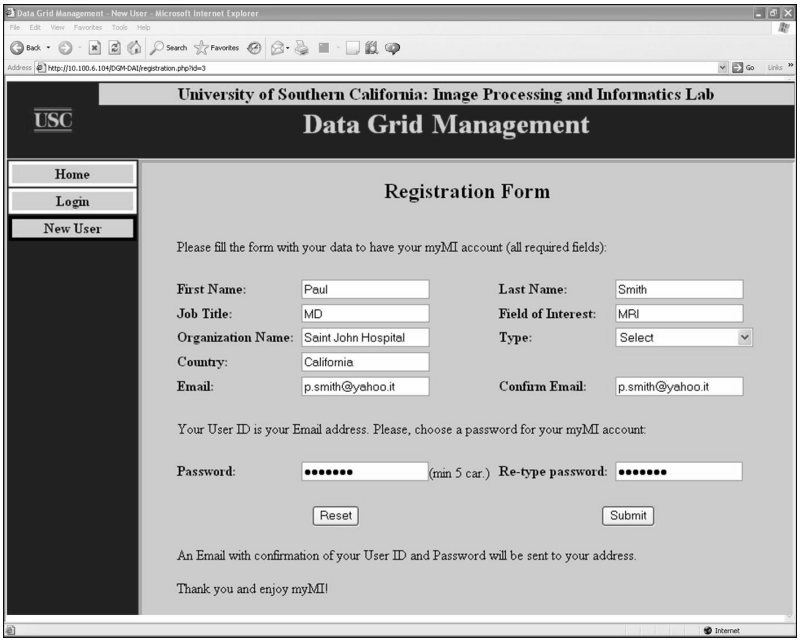

Figure 5. User Registration Form

The registration form is shown in Figure 5. It provides a secure Web-based registration of users and the subsequent generation and management of their credentials. The registration process allows large user communities an easy access to Grid resources. When the user accesses the system for the first time, he is asked to register by entering his or her personal data. The required personal data includes First Name, Last Name, Job Title, Field of Interest, Organization Name, Organization Type, and Country. The Email will become the user ID and the password is chosen by the user. All fields are mandatory, and the system checks if they are correctly filled in. Registration is completed only if data are correctly inserted.

- Login Page

This page is the same page of Administrator access (Figure 4): the system recognizes the role by entering username and password.
Once logged in, users are directed in the image/data search page (Figure 6).
Each login session is given a unique session key (stored as an in-memory cookie at the browser). These session keys have a maximum time limit set on them (currently 60 minutes). The system also performs security checks on the session keys when validating a user request.

- Access, display and download of metadata and images

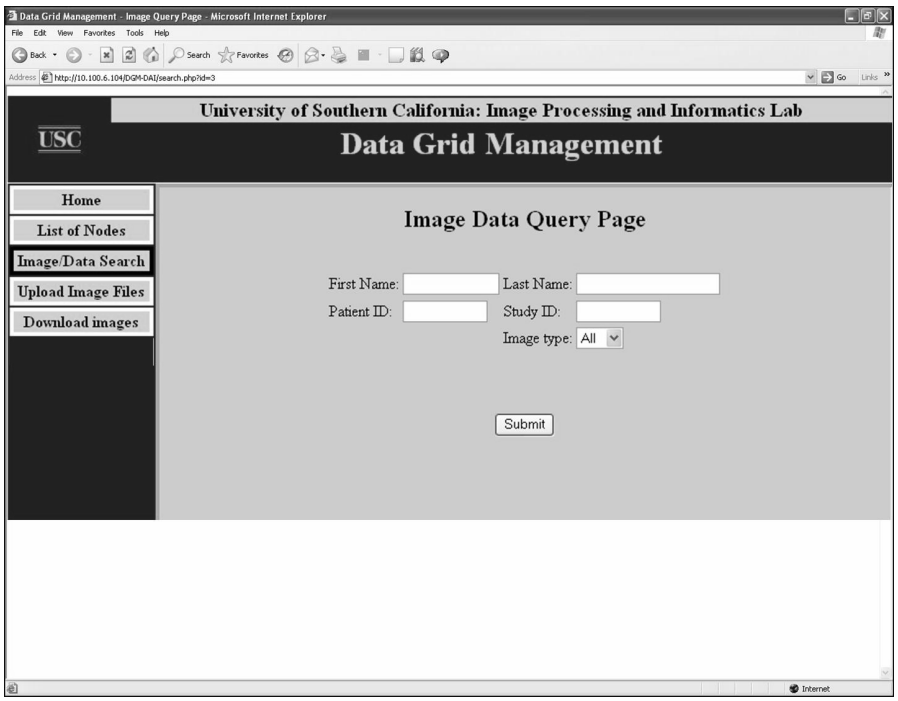

Figure 6. Image/Data Search Form

Users can search images by filtering the content of the Data Grid. The browser page then shows the query result and allows to expand the study in series and images, and to download them both as DICOM files and as a zip file.

- Upload images to remote resources

Users can upload images in the Grid simply by browsing in their file system and selecting both native DICOM images and zip package file. The system uploads images on the server and the Agent unpacks (if in zip format) and extracts metadata from DICOM header and sends them to the GAP.

CONCLUSION

The proposed management system provides a solution to Data Grid management for enterprise PACS backup and disaster recovery. The graphical user interface of the management system allows easy-to-use data management and searching and viewing of images. The secure connections allow users to access the components in the Grid freely without lengthy login processes at each Grid component. Overall, an efficient and user-friendly Data Grid Management System is a more practical solution for managing the enterprise PACS backup and disaster recovery.

REFERENCES

1. "Kodak Demos Enhanced CARESTREAM Radiology Solutions", GRID Today, Dec 2006.
(http://www.gridtoday.com/grid/1129930.html)
2. "IBM introduces Grid Medical Archive Solution to manage healthcare storage growth", Jun 2005.
(http://www-03.ibm.com/industries/healthcare/doc/content/news/pressrelease/1322952105.html?g_type=rhc)
3. H.K. Huang, A. Zhang, B. Liu, Z Zhou, J Documet, N. King, L.W.C. Chan, "Data Grid for Large-Scale Medical Image Archive and Analysis", 2005.
4. Huang, HK, *PACS and Image Informatics: Basic Principles and Applications*, 2004.
5. B. J. Liu, Z. Zhou, M.A. Gutierrez, J. Documet, L. Chan, HK Huang, "International Internet2 Connectivity and Performance in Medical Imaging Applications: Bridging the Americas to Asia", 2006.
6. J. Lee, Z. Zhou, J. Documet, B.J. Liu, "Design and Implementation of a Fault-Tolerant and Dynamic Metadata Database for Clinical Trials", 2007.

Is Greulich and Pyle Atlas still a Good Reference for Bone Age Assessment?

Aifeng Zhang [a], Sinchai Tsao [a], James W. Sayre[b], Arkadiusz Gertych [a], Brent J. Liu [a], H.K. Huang [a]

[a]Image Processing and Informatics Lab, Department of Radiology, ISI/USC,
Marina Del Rey, CA USA 90292
[b]Department of Biostatistics and Radiological Sciences, UCLA School of Public Health,
Los Angeles, CA USA 90095-1772

ABSTRACT

The most commonly used method for bone age assessment in clinical practice is the book atlas matching method developed by Greulich and Pyle in the 1950s. Due to changes in both population diversity and nutrition in the United States, this atlas may no longer be a good reference. An updated data set becomes crucial to improve the bone age assessment process. Therefore, a digital hand atlas was built with 1,100 children hand images, along with patient information and radiologists' readings, of normal Caucasian (CAU), African American (BLK), Hispanic (HIS), and Asian (ASI) males (M) and females (F) with ages ranging from 0 – 18 years. This data was collected from Childrens' Hospital Los Angeles. A computer-aided-diagnosis (CAD) method has been developed based on features extracted from phalangeal regions of interest (ROIs) and carpal bone ROIs from this digital hand atlas. Using the data collected along with the Greulich and Pyle Atlas-based readings and CAD results, this paper addresses this question: "Do different ethnicities and gender have different bone growth patterns?" To help with data analysis, a novel web-based visualization tool was developed to demonstrate bone growth diversity amongst differing gender and ethnic groups using data collected from the Digital Atlas. The application effectively demonstrates a discrepancy of bone growth pattern amongst different populations based on race and gender. It also has the capability of helping a radiologist determine the normality of skeletal development of a particular patient by visualizing his or her chronological age, radiologist reading, and CAD assessed bone age relative to the accuracy of the P&G method.

Keyword: Bone Age Assessment, Digital Hand Atlas, Web-based application, Computer-aided-diagnosis

1. INTRODUCTION

Pediatric bone age assessment is an important procedure that allows a physician to judge the degree of a patient's skeletal bone development relative to the patient's chronological age. Discrepancies between bone age and chronological can occur due to growth disorders that can stem from endocrine disorders or malnutrition. Accurate diagnosis is required to help determine proper treatment.

The most commonly used method for bone age assessment in clinical practice is the book atlas matching method developed by Greulich and Pyle [1-2]. This method is based on visual comparison of the patient's hand x-ray with images collected in the atlas. The closest match is subjectively selected by the radiologist and yields the bone age of the patient (Figure 1).

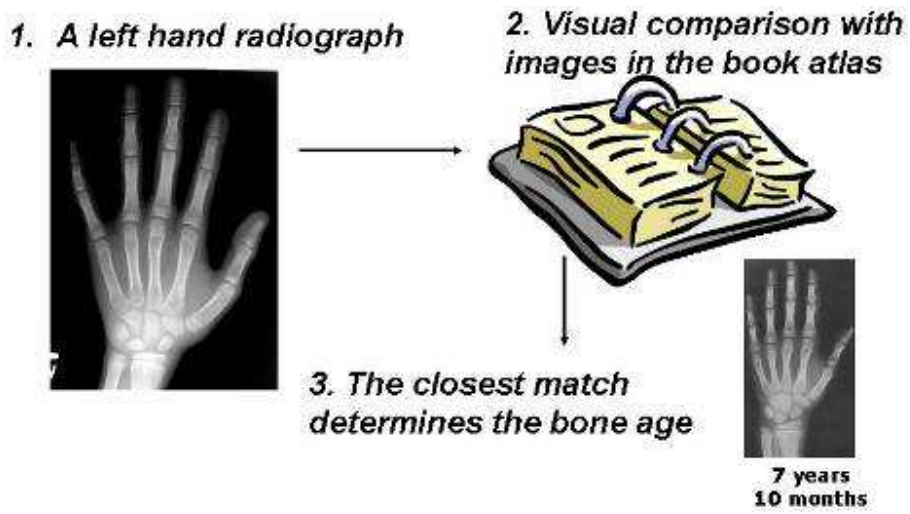

Figure 1. Bone age assessment procedure in clinical practice.

However the book atlas has not been updated since its initial publication in the early 1950s. The data collected in the original atlas was derived solely from upper middle class Caucasian populations residing in the midwest of the United States. Due to changes in both population diversity and nutrition in the United States, this atlas may no longer be a good reference. An updated data set has become crucial to improve the bone age assessment process. For this purpose, left hand X-ray films of normal children along with pertinent data related to patient growth factors were acquired at Children's Hospital Los Angeles. [3-5] The data was divided into eight categories by race and gender. A computer-aided diagnosis (CAD) method was developed based on features extracted from phalangeal regions of interest (ROI) and carpal bone ROI. [6-10] For data analysis, a web-based statistical visualization application was developed to help address the following issues: 1) Does each race have distinct bone growth patterns? and 2) More importantly, is the G & P atlas still a good reference for bone age assessment of today's children?

2. MATERIALS & METHODS

2.1 Data Collection - Building of the Digital Hand Atlas

A digital hand atlas was developed with data from eleven hundreds children. This consisted of hand images collected from Children's Hospital Los Angeles accompanied by patient information and radiologists' readings. The data consisted of normal Caucasian (CAU), African American (BLK), Hispanic (HIS), and Asian (ASI) males (M) and females (F), with ages ranging from 0 – 18 years. [3-5] Each hand image and the subject's demographic data, along with two radiologists' readings and CAD-based bone age were populated into a mysql database. The database was integrated with a web server at the Image Processing and Informatics Laboratory, USC. To simplify statistical testing as well as data visualization, the two radiologists' readings were averaged to get one reading-based age per subject. Figure 2 is a sample hand image with phalangeal and carpal ROIs outlined.

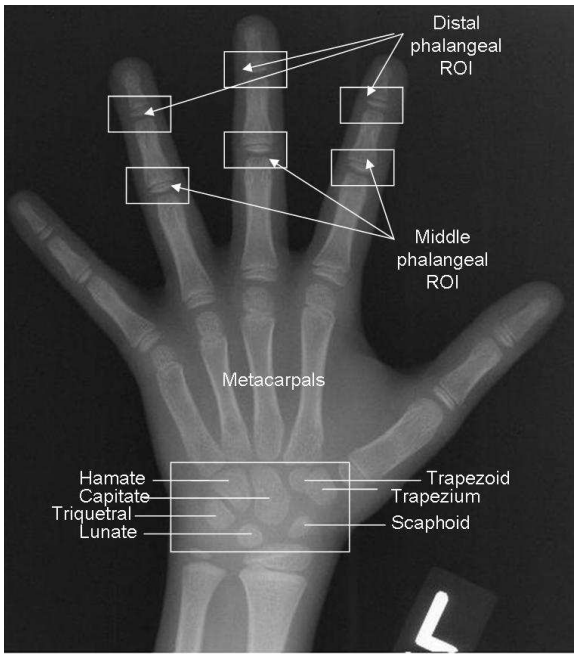

Figure 1 - Sample Hand Image from the CHLA data collection process. All pertinent bones that were used as ROIs in the CAD program are labeled.

Table 1 - Total of 1,103 cases from.first Cycle Data Collection.

Age group /Category	ASIF	ASIM	BLKF	BLKM	CAUF	CAUM	HISF	HISM
00	1	2	4	5	3	3	1	4
01	5	5	5	5	5	5	5	5
02	5	5	5	5	5	5	5	5
03	5	5	5	5	5	5	5	5
04	5	5	5	5	5	5	5	5
05	5	5	5	5	5	5	5	5
06	5	5	5	5	5	5	5	5
07	5	5	5	5	5	5	5	5
08	5	5	5	5	5	5	5	5
09	5	5	5	5	5	5	5	5
10	10	10	10	10	10	10	10	10
11	10	10	10	10	10	10	10	10
12	10	10	10	10	10	10	10	10
13	10	10	10	10	10	10	10	10
14	10	10	10	10	10	10	10	10
15	10	10	10	10	10	10	10	10
16	10	10	10	10	10	10	10	10
17	10	10	10	10	10	10	10	10
18	10	10	10	10	10	10	10	10
Total	136	137	139	140	138	138	136	139

**This table is divided into 9 columns: the first column represents the age group, the rest eight columns are categorized by race and gender. The first 3 characters in each column header represents the race; ASI: Asian, BLK: African American, CAU: Caucasian, and HIS: Hispanic. The last character stands for gender: F: female and M: male. Each row depicts an age group in ascending order from 0 to 18 years old.

2.2 Data Visualization - Web GUI (Graphical User Interface) Development

A separate JAVA applet-based platform-independent software was developed to assess relevant data in the Digital Hand Atlas database and to plot results. The GUI programs were developed to compare Pediatric Radiologist Readings, CAD results with Chronological Age amongst different racial and gender groups. The first GUI program (see figure 2) was used as a tool to plot graphs with the user's choice of Radiologist's Readings, CAD-based result or Chronological age as the X or Y axis.

The JAVA applet runs on a web server of choice and connects to a mysql database on the same machine for its input data. [11-12] A php script that connected to the mysql database was used as an intermediary data source for the JAVA applet. The JAVA applet passes the necessary inputs to the php script, which then retrieves the relevant information from the database without compromising data integrity. One feature of this design is that as the data is updated in the database, the graphing output will change accordingly.

In this study, four comparison studies based on the specific population combinations were conducted using this GUI: 1) All eight categories are individually compared, 2) Male and Female are combined to form four ethnic groups for comparison, 3) All male and all female are combined to form two gender groups for comparison, and 4) All eight categories were combined to form one group.

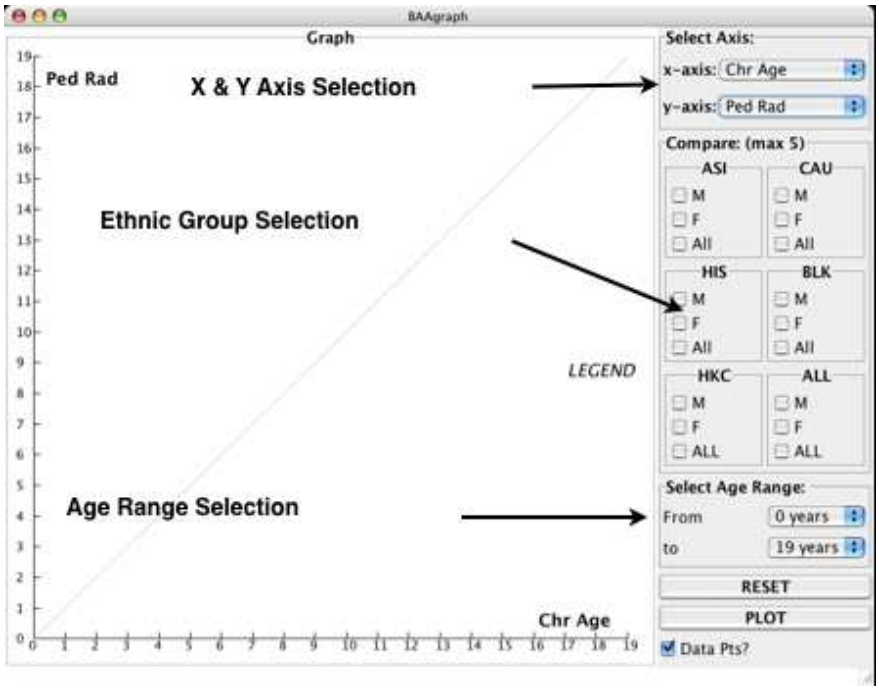

Figure 2 – Simple GUI to visualize differences between the different Study Groups

2.3 Prototype of a Clinically Applicable GUI

To demonstrate the clinical viability of the CAD methodology, a second GUI was developed to allow the user to visualize the current patient's data against information in the database. The mean and standard deviation of the

radiologist's readings of the normal cases in the database for that particular chronological age is shown along with the current patient's results. If the CAD assessed bone age or the Pediatric Radiologist Readings falls outside of the range of error, the patient could have a case of suspected abnormal bone development. (see figure 3)

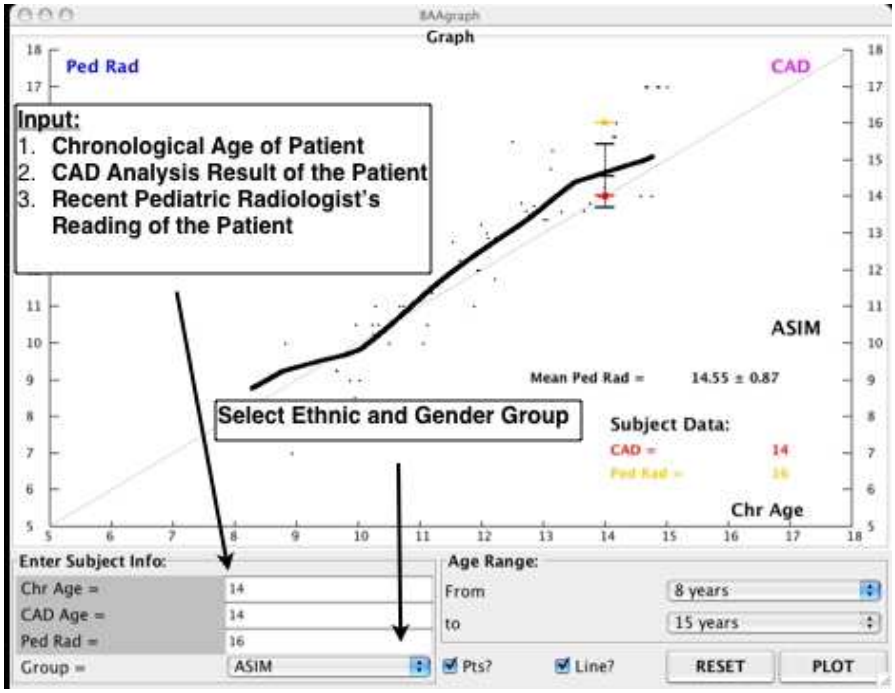

Figure 3 – Clinical GUI to compare a patient's CAD and Radiologist's Readings relative to the accuracy of the Radiologist's Readings from the Digital Hand Atlas Database. The three black horizontal lines bisected by the vertical line marks the mean as well as the upper and lower standard deviation of the pediatric radiologist's G&P-based readings of normal cases with that specific chronological age. The yellow marker represents the radiologist reading of the current case. The red marker represents the CAD output of the current case. The GUI allows the user to assess the CAD and Pediatric Radiologist's readings against the accuracy of the gold standard - the accuracy of G&P readings of the normal cases in the database. Any reading variation away from the chronological age that is greater than the accuracy as set by the gold standard indicates a possible growth disorder.

3. RESULTS

3.1 Plots

The plotting application allows users to visualize the normal data from the digital hand atlas, by race, gender or combination among race and gender. Figures 4-5 shows the output of the web applet when using CAD and Readings against Chronological Age. However, the user can compare a particular patient using any three inputs: Chronological age, Radiologist's readings and CAD assessed bone age. In this section, general trends shown from the graphical plots will be outlined. Statistical studies will be outlined in the following section.

Comparing radiologists' readings and CAD results versus chronological age, the graphs show that ethnicity and gender does have influence on the growth pattern as shown by the variability of both CAD results as well as radiologists' reading in figure 4. Variation in both the radiologists' reading and the CAD results between the different gender (figure 6) and different ethnic groups (figure 5) show that both ethnicity and gender have an independent effect on bone age assessment. With gender, it is well documented that females bone structure variations end earlier, making it more difficult to differentiate between the later age groups. However, the use of different ethnic groups / populations is novel.

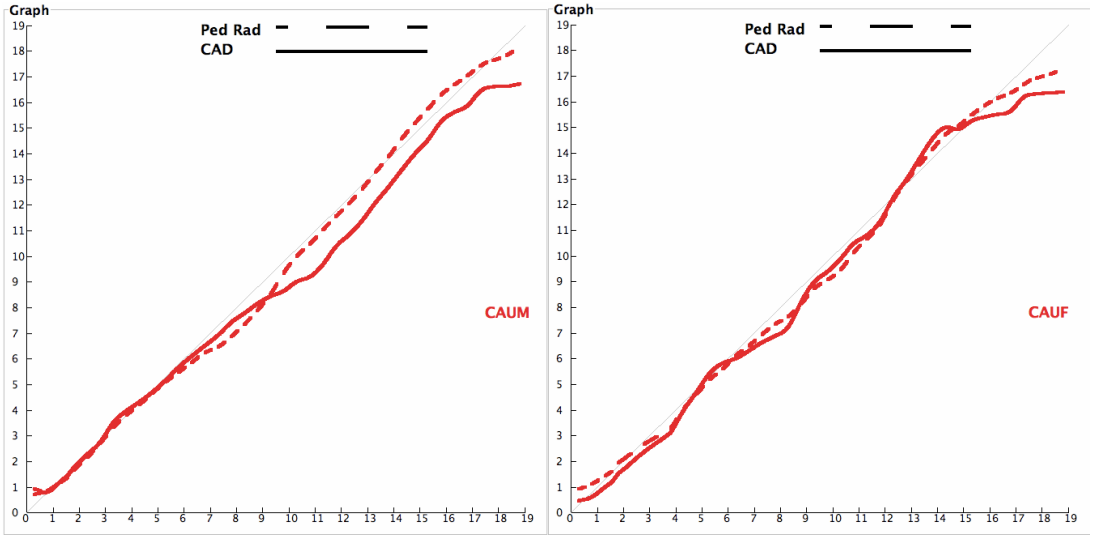

(a) (b)

Figure 4. The figure illustrates that gender effects bone age assessment with both reading and CAD methods. (a) Caucasian male; (b) Caucasian female. The x-axis is chronological age and the y-axis is either radiologist's reading or CAD result.

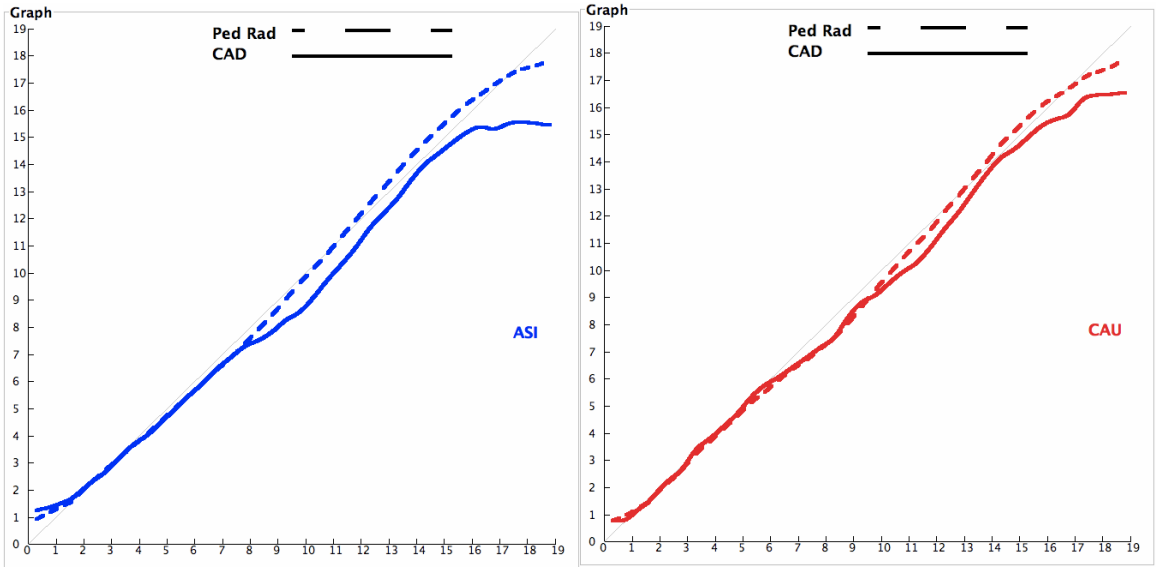

Figure 5. The figure illustrates that ethnic or racial origin effects bone age assessment with both the reading and CAD methods. (a) Asian; (b) Caucasian. The x-axis is chronological age and the y-axis is either radiologist's reading or CAD result. The x-axis is chronological age and the y-axis is radiologist's reading.

Assessing the G&P-based Radiologists' readings, it can be seen that it correlates well with chronological age (see figure 7), except at later ages. This can be primarily attributed to the lack of variation in older females (see figure 6). The CAD method sensitivity decreases at age 15+ (see figure 7). This is attributed to the lack of variation in the current ROIs. At the time of writing of this paper an addition ROI, the Radius, with known variation from 15-19 years is being added to remedy this problem.

3.2 Statistical analysis between races

To study the discrepancy between races, paired-samples t-test was performed between the chronological age and the average of two readings. Table 2 shows the mean difference between average reading and chronological age for eight categories by race and gender. The numbers with an asterisk represents a difference with a significant p-value of $< .05$.

Table 2. CAD evaluation for eight categories by race and gender. Values in the table represent the mean difference between chronological age and the average reading in year. Significant mean difference is indicated by an asterisk.

Mean Difference with Chr. Age	**ASI**		**BLK**		**CAU**		**HIS**	
	F	**M**	**F**	**M**	**F**	**M**	**F**	**M**
Average Reading	-.20*	-.45*	-.02	.01	.16*	-.03	-.22*	-.37*
No. of Cases	129	132	127	124	134	130	128	126

* p-value < .05, significant difference

As we can see from Table 2, radiologists' using the G&P atlas are able to assess bone age very accurately for the African American sample population and the Caucasian male sample population. However, significant discrepancies were observed in Asian and Hispanic groups. To study this in greater detail, the entire age range was divided into four age groups. The Males and Females were divided in differently according to Figure 6.

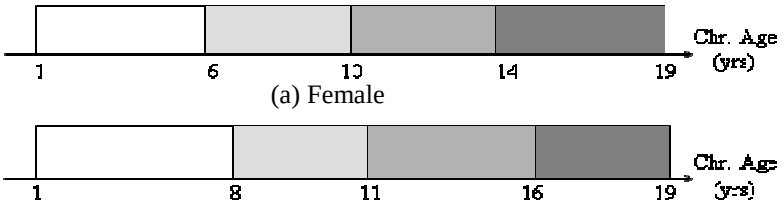

(a) Female

(b) Male

Figure 6. The divided age sets in evaluation. (a) for female and (b) for male

Comparisons of the difference between radiologists' average reading and chronological age for two races was conducted by analysis of variance (ANOVA). The results for the four age sets are presented in Table 3 for female and Table 4 for male.

Table 3. Cross racial comparison of chronological age vs. reading for female. Each block was divided into four sub-blocks, each of which encompasses one age set. (unit: year, "-": over read)

	ASIF	BLKF	CAUF	HISF
ASIF		-.79*	-.83*	
BLKF				.59*
CAUF				

* p-value < 0.05

As the data in Table 3 shows, significant mean differences of readings between races are observed at age group from 10-14 years old. Radiologist over-read Asian cases by approximately 0.80 years compared with their African American and Caucasian peers. In the same fashion, over-reading was observed between the Hispanic and African American groups. Figure 6 shows the plots of readings between the Asian female population and the Caucasian female population as well as the Hispanic female and African American female populations.

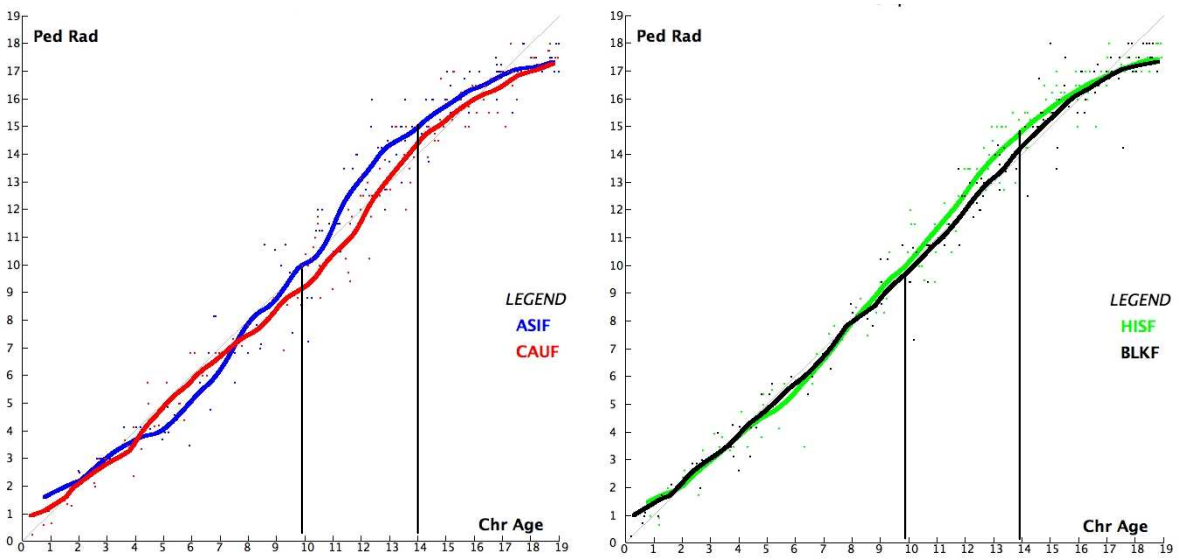

Figure 6. Plots of readings between race pairs (a) Asian female and Caucasian female; (b) Hispanic female and African American female. The x-axis is chronological age and the y-axis is radiologist's reading.

Table 4. Cross racial comparison of chronological age vs. reading for male. Each block was divided into four sub-blocks, each of which encompasses one age set. (unit: year, "-": over read)

	ASIM	BLKM	CAUM	HISM
ASIM		-1.17* -.65*	-.71*	
BLKM			-.74*	1.02*
CAUM				

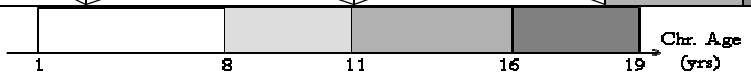

* p-value < 0.05

For the male populations from the digital atlas, significant differences were the groups ranging from 11 to 16 years of age. In comparison with the African American population, Radiologists tends to over-read Asian and Hispanic cases about a year. (Figure 7)

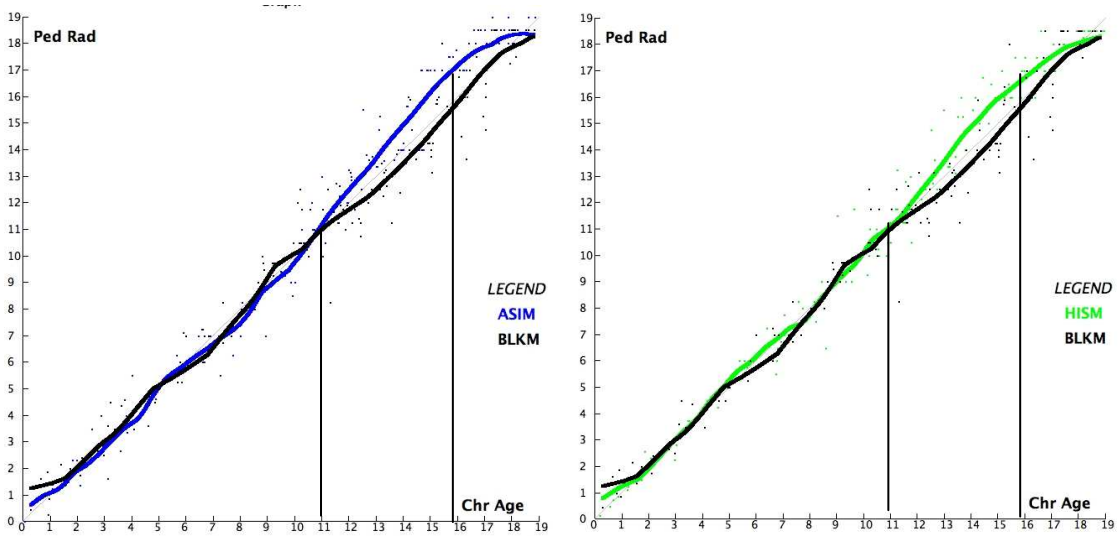

Figure 7. Plots of readings between race pairs (a) Asian male and African American male; (b) Hispanic male and African American female.

From Table 3 and 4 discrepancies were observed in the Asian and Hispanic populations in both genders when compared with the African American and Caucasian populations.

4. CONCLUSIONS

The aforementioned study represents a novel statistical analysis of bone age assessment for differing gender and ethnic populations. Through the study we attempted to answer the following questions: 1) Does each race have distinct bone growth patterns? and 2) Is the G & P atlas still a good reference for bone age assessment of today's children?

Addressing the first question, the hypothesis is that genetic differences with influences from diet and nutrition may cause variation in growth patterns, thereby influencing the bone age assessment process. The statistical analysis (Section 3.2) discovered significant differences for Asian and Hispanic ethnic populations, which to a certain extent nullifies the null hypothesis. This therefore illustrates that the accuracy of the Greulich and Pyle atlas can indeed be improved by taking ethnic population and gender into account. This potential can be captured by a CAD trained to adapt to reading images of different genders and populations as previously outlined. The answer to the latter question is that until this CAD methodology is complete and compared against the Greulich and Pyle method, the extent of which patient demographic background can be exploited to give a more accurate bone age assessment cannot be fully determined.

ACKNOWLEDGMENT

This work has been supported by NIH R01 EB 00298.

REFERENCES

[1] W. Grelich, S. Pyle, Radiographic Atlas of Skeletal Development of Hand Wrist, Stanford, CA: Stanford University Press, 1959.

[2] A. Albanese, C. Hall, and R. Stanhope, "The use of a computerized method of bone age assessment in clinical practice," Horm Res, vol. 44 Suppl 3, pp. 2-7, 1995.

[3] A. Gertych, A. Zhang, J. Sayre, S. Pospiech-Kurkowska, H.K Huang, Bone Age Assessment of Children using a Digital Hand Atlas, to appear in J Comp Med Imag & Graphic, 31(4-5), May, 2007.

[4] H.K. Huang, A. Zhang, Brent Liu, Zheng Zhou, Jorge Documet, Nelson King, L.W.C. Chan, Data Grid for Large-Scale Medical Image Archive and Analysis. Proceedings of the 13th ACM International Conference on Multimedia, pp. 1005-1013, 2005.

[5] E. Pietka, A. Gertych, and K. Witko, "Informatics infrastructure of CAD system," Comput Med Imaging Graph, vol. 29, pp. 157-69, 2005.

[6] E. Pietka, A. Gertych, S. Pospiecha Euro Kurkowska, F. Cao, H. K. Huang, and V. Gilzanz, "Computer-assisted bone age assessment: graphical user interface for image processing and comparison," J Digit Imaging, vol. 17, pp. 175-88, 2004.

[7] Zhang, A. Gertych, B. J. Liu, Automatic Bone Age Assessment for Young Children from Newborn to 7-Year-Old Using Carpal Bones, to appear in J Comp Med Imag & Graphic, 31(4-5), May, 2007.

[8] E. Pietka, S. Pospiech-Kurkowska, A. Gertych, and F. Cao, "Integration of computer assisted bone age assessment with clinical PACS," Comput Med Imaging Graph, vol. 27, pp. 217-28, 2003.

[9] E. Pietka, A. Gertych, S. Pospiech, F. Cao, H. K. Huang, and V. Gilsanz, "Computer-assisted bone age assessment: image preprocessing and epiphyseal/metaphyseal ROI extraction," IEEE Trans Med Imaging, vol. 20, pp. 715-29, 2001.

[10] F. Cao, H. K. Huang, E. Pietka, and V. Gilsanz, "Digital hand atlas and web-based bone age assessment: system design and implementation," Comput Med Imaging Graph, vol. 24, pp. 297-307, 2000.

[11] Paul DuBois, MySQL: the definitive guide to using, programming, and administering MySQL 4. Pearson Education, 3rd Edition, 2003

[12] Hugh E. Williams, David Lane Web Database Applications with PHP & MySQL, 2nd Edition, O'Reilly, 1 edition (March, 2002)

A Method for Assurance of Image Integrity in CAD-PACS Integration

Zheng Zhou

Image Processing & Informatics (IPI) Laboratory, Radiology Department, University of Southern California, Marina del Rey, CA, 90292, USA

ABSTRACT

Computer Aided Detection/Diagnosis (CAD) can greatly assist in the clinical decision making process, and therefore, has drawn tremendous research efforts. However, integrating independent CAD workstation results with the clinical diagnostic workflow still remains challenging. We have presented a CAD-PACS integration toolkit that complies with DICOM standard and IHE profiles. One major issue in CAD-PACS integration is the security of the images used in CAD post-processing and the corresponding CAD result images. In this paper, we present a method for assuring the integrity of both DICOM images used in CAD post-processing and the CAD image results that are in BMP or JPEG format. The method is evaluated in a PACS simulator that simulates clinical PACS workflow. It can also be applied to multiple CAD applications that are integrated with the PACS simulator. The successful development and evaluation of this method will provide a useful approach for assuring image integrity of the CAD-PACS integration in clinical diagnosis.

Keywords: PACS, CAD, Security, System Integration

1. INTRODUCTION

CAD applications in mammography [1-3], chest [4] and 3-D CT lung imaging [5] have been commercialized and used for clinical decision support over the last 5-6 years. In order to share CAD results among most physicians, CAD applications must be integrated with a PACS where physicians can access CAD results easily. However, image integrity issues are crucial to the success of the integration of CAD with a PACS. Assurance of image integrity not just guarantees the objectivity of CAD results for clinical decision support, but more importantly, it enhances physician's confidence to use CAD in clinical service.

A typical CAD application consists of three types of data: 1. original DICOM medical images used in the CAD applications, 2. image results generated from CAD application, such as segmented or annotated images that are in JPEG/BMP/TIFF format, and 3. CAD textual results that contains report and numeric measurements. When a CAD application is integrated with a PACS, data types from items 2 and 3 described above must be converted into DICOM format so that they can be archived and retrieved in the PACS along with data type item 1. We have developed a CAD-PACS integration toolkit [6] that provides two integration methods (Figure 1): DICOM-SC (secondary capture) and DICOM-IHE. The former converts the screen capture of CAD results, including images and textual results, into a DICOM image, while the latter converts images generated in CAD to DICOM images and CAD textual results to DICOM structured report (SR) data.

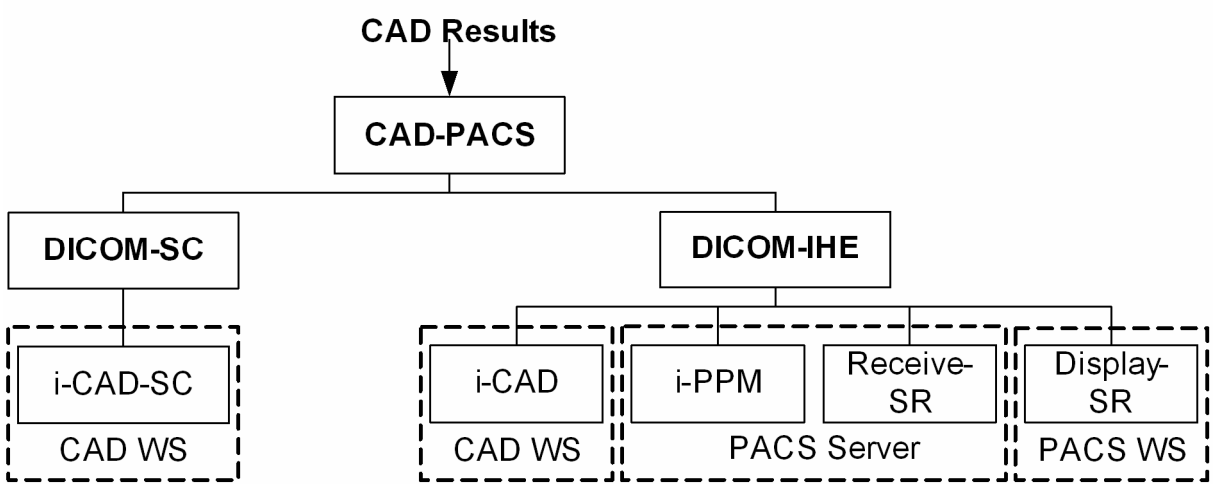

Figure 1 The CAD-PACS toolkit has two versions, Left: DICOM-SC (Secondary Capture), and Right: DICOM-IHE. The major software package in DICOM-SC is the i-CAD-SC which resides in the CAD WS and uses the DICOM secondary capture function. The DICOM-IHE has four modules, i-CAD; and i-PPM (Post-Processing Manager), Receive-SR, and Display-SR. The former resides in the CAD WS, and the latter three reside in the PACS Server and PACS WS as shown, respectively.

Generally, data security can be characterized by three major issues: privacy (or confidentiality), authenticity, and integrity [7]. Privacy seeks to protect medical data from being accessible or disclosed to unauthorized individuals. Authenticity verifies that the source of medical data is what it claims to be. Integrity assures that medical data is not altered, destroyed, or deleted by unauthorized personnel.

In this paper, we focus on the integrity issue of data from types 1 and 2, original DICOM images and DICOM CAD images, since traditional methods, such as encryption and access control by user password, are able to protect their privacy and authenticity. The integrity of the type 3 data, the textual results, can be assured through the traditional one-dimensional digital signature method.

We have developed a novel lossless digital signature embedding (LDSE) method [8, 9] that can automatically detect the alteration of even a single pixel in a DICOM image and can completely restore the original image data due to data embedding process. In this paper, the LDSE method is applied to assure the integrity of CAD result, especially the DICOM CAD images. The CAD-PACS toolkit is used as an example to illustrate the LDSE method, which is applicable to other CAD-PACS integration methods as well.

2. METHODS

2.1 Lossless Digital Signature Embedding (LDSE) Method

The LDSE method consists of two processes: Sign & Embed and Extract & Verify [8, 9]. The Sign & Embed processes are to generate the digital signature (DS) of the image pixels and embed the DS into image pixels using lossless embedding method, while the Extract & Verify processes are the reverse operations of the Sign & Embed. As shown in Figure 2, the embedding starts with the scanning of image pixels to find R and S groups. Every R or S groups can be converted to an “R” (R group) or “S” (S group) symbol. As a result, an “R” and “S” sequence of the image is formed. One bit is assigned to every “R” or “S” symbol in this sequence and the value in this bit would be “1” for “R” and “0” for “S”. In this case, the “R” and “S” sequence is converted to a bit stream of 1s and 0s, which is called an “RS bit stream”. The RS bit stream is further compressed using a lossless compression method. The extraction and compression progress ends when sufficient space in the RS bit stream is available for embedding the DS. Afterward, the bit stream of DS is appended to the compressed RS bit stream to form a new bit stream. This new bit stream then replaces the original bit stream to complete the embedding process and the result is a signature embedded image.

Since the forming of R and S groups as well as the embedding are all reversible processes, the original image can be completely recovered after the DS is extracted. The extracting process starts with the same scanning to find R and S groups from the signature embedded image. As a result, the embedded bit stream is reconstructed from the R and S groups. The bit stream is then broken down into the compressed RS bit stream and the DS. The compressed RS bit stream is decompressed to recover the original R and S groups. The original R and S groups is used to recover the original image pixels. The recovered DS is verified with the restored image. If verification result is true, there is no alteration of the image and the image integrity is assured.

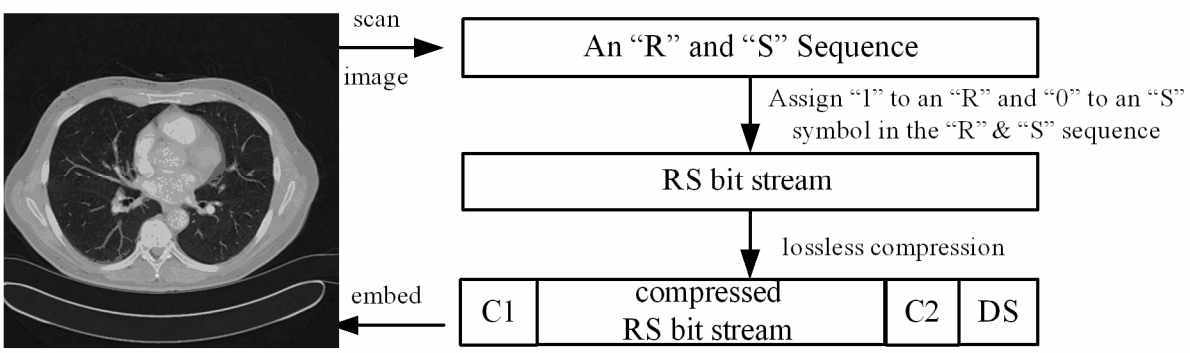

Figure 2 Embed the DS in a CT lung image using LDSERS. The U groups are not used. C1: counter 1 to record the length of the compressed RS bit stream. C2: counter 2 to record the length of the DS.

2.2 Integrate LDSE with CAD-PACS

The CAD-PACS toolkit is used to test the use of LDSE for assuring the integrity of images in CAD-PACS integration. The CAD-PACS toolkit (Figure 1) includes two approaches, DICOM-SC and DICOM-IHE. The former converts the screen capture of CAD results, including images and textual results, to a DICOM image, while the latter converts images generated in CAD to DICOM images and CAD textual results to DICOM structured report (SR) data. The integration of LDSE with DICOM-SC is to assure the integrity of the DICOM image of the screen capture of the CAD result, while the integration of LDSE with DICOM-IHE is to assure the integrity of DICOM CAD images.

Integrate LDSE with CAD-PACS DICOM-SC

Figure 3 shows the integration of the LDSE method with the CAD-PACS DICOM-SC:

1) The LDSE Sign & Embed component is added to the DICOM-SC i-CAD-SC software at the CAD workstation. The LDSE Sign & Embed component generates the digital signature of the DICOM SC CAD result image created by the i-CAD-SC software and embeds the digital signature in the image pixels. As a result, a signature embedded DICOM SC CAD result image is generated and sent to the PACS server.

2) The LDSE Extract & Verify component is added to the PACS server. The server extracts the digital signature from the signature embedded DICOM SC CAD result image and verifies the signature. If verify succeed, the CAD result image is archived. Otherwise, the CAD result image is rejected.

3) The LDSE Extract & Verify component is also added to the PACS viewing workstation. When the signature embedded DICOM SC CAD result image is retrieved to the workstation for review, the signature is extracted and verified.

With the LDSE being integrated with the CAD workstation, the PACS server and the PACS viewing workstation, the integrity of the DICOM SC CAD result is completely assured within the PACS environment.

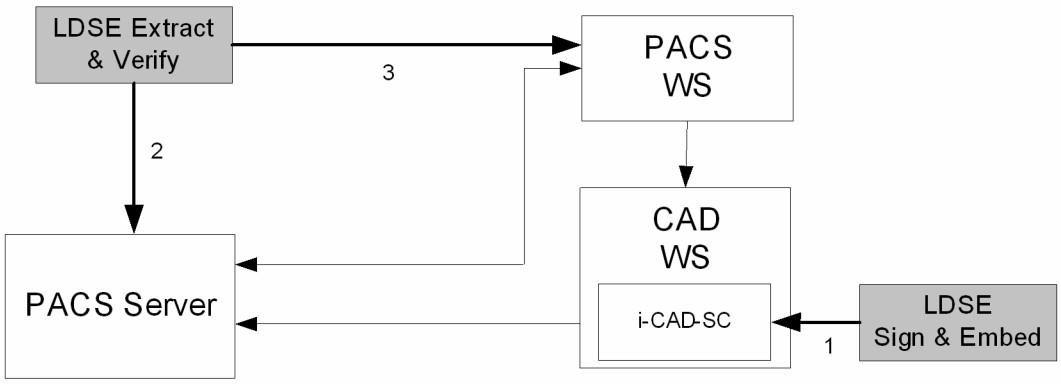

Figure 3 Integrate the LDSE with the CAD-PACS DICOM-SC.

Integrate the LDSE with the CAD-PACS DICOM-IHE

Fig. 6 shows the integration of the LDSE and DICOM SR digital signature with the CAD-PACS DICOM-IHE:
1) The LDSE Sign & Embed component is added to the i-CAD software at the CAD workstation. The CAD images, such as segmented images, are converted to DICOM SC images, which are processed by the LDSE Sign & Embed component to generate the signature embedded DICOM SC images. The signature embedded DICOM SC images are sent to the PACS server for archive.
2) The LDSE Extract & Verify component is added to the PACS server to verify the signature embedded DICOM SC images.
3) The LDSE Extract & Verify component is added to the PACS workstation to verify the signature embedded DICOM SC images before they are reviewed.

The integrity of the DICOM SR can be assured by integrating the DICOM SR RSA Digital Signature with the CAD-PACS DICOM-IHE approach [10].

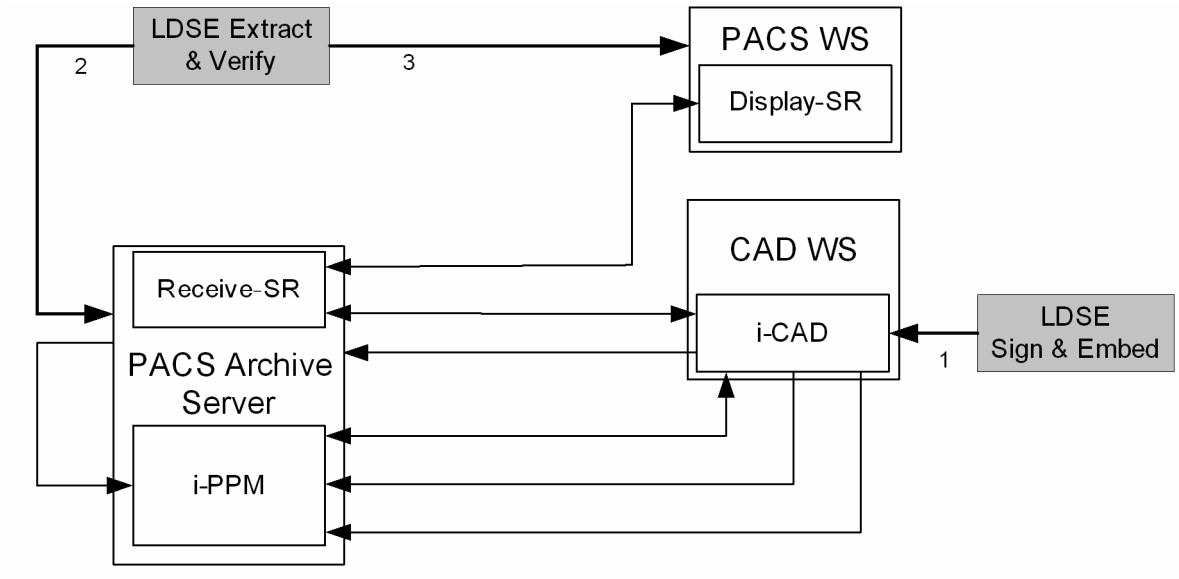

Figure 4 Integration of LDSE and the DICOM SR Digital Signature with the CAD-PACS DICOM-IHE.

With LDSE, the integrity of DICOM SC CAD images is assured within the PACS environment. The integrity of original DICOM images used in the CAD application can also be assured by integrating the LDSE method with the PACS [8, 9].

3. RESULTS

Two CAD results from computer aided detection of small acute intracranial hemorrhage on CT of brain [11] and computer aided detection of emphysema [12] were used for evaluation of the LDSE method.

3.1 Examples

Two examples are shown (Figures 5 and 6). Figure 5(a) shows an example of the DICOM SC image file that contains a screen-captured chest emphysema CAD result with the digital signature embedded in the RGB color image pixels, while Figure 5(b) shows an example of the subtracted image between the signature embedded image and the original DICOM SC image. Figure 6(a) shows the DICOM SC annotated image with its signature embedded and Figure 6(b) the subtracted images between the signature embedded DICOM SC image and the original DICOM SC image. The signatures in both signature embedded images (Figure 5(a) and Figure 6(a)) have been extracted and verified successfully.
These results demonstrate that the LDSE method is effective for assuring the integrity of the CAD results when the CAD is integrated with a PACS using the CAD-PACS integration toolkit.

4. DISCUSSION

The aforementioned LDSE method can effectively assure the integrity of a 2-D DICOM image, including the modality generated original image and the CAD generated image converted to a DICOM file. However, a new challenge arises in three dimensional (3-D) CAD results. For example, a 3-D tumor volume is segmented from a 3-D CT lung study. Intuitive thoughts are to apply the 2-D LDSE method to each slide of the 3-D tumor segmented images. But this is not time-efficient, because the same LDSE process, which requires about 0.06 seconds for one CT image, will be repeated 30 or 40 times for the tumor volume. The total process time will cause a significant delay in clinical diagnostic workflow. An even more crucial problem is that the 2-D LDSE method is not able to detect any deletion or loss of images in the 3-D tumor volume. The same problem can happen to the original 3-D CT lung study used for the CAD application.
We have developed a novel 3-D LDSE method [8] for assuring the 3D volume image integrity. This method has demonstrated to be applicable and more efficient than the 2-D LDSE method for 3-D volume image integrity.

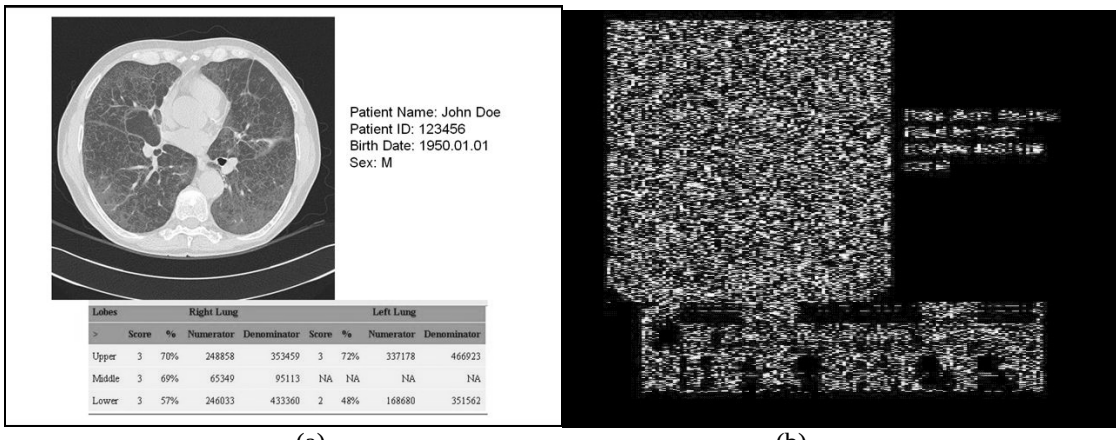

(a) (b)

Figure 5 An example of the DICOM SC CAD result image with signature embedded. (a) the DICOM SC image file that contains a screen-captured chest emphysema CAD result with the digital signature embedded, (b) the subtracted image between the signature embedded image and the original DICOM SC image. The white dots in (b) show the bits of the embedded digital signature. (Courtesy of Dr. Matthew Brown.)

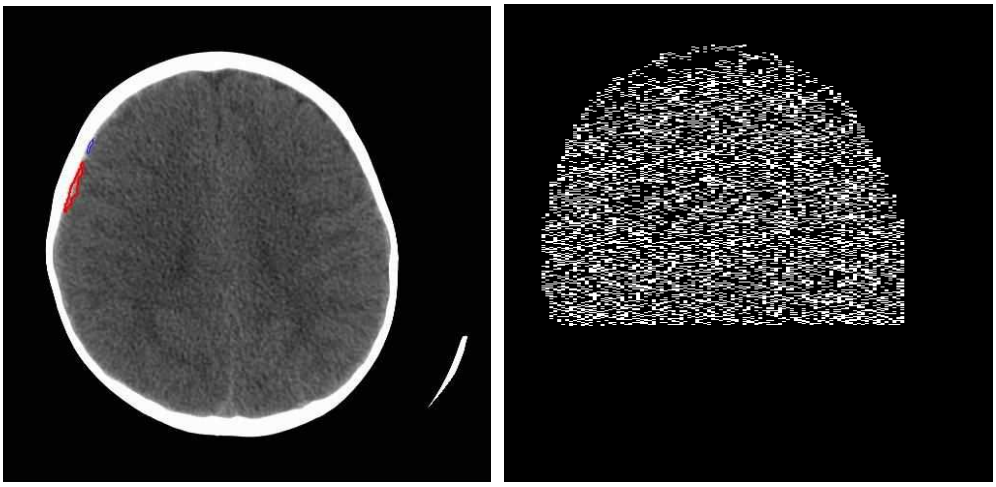

(a) (b)

Figure 6 An example of the DICOM SC CAD image with signature embedded. (a) the DICOM SC CAD annotated image with its signature embedded, (b) the subtracted images between the signature embedded DICOM SC image and the original DICOM SC image. The white dots in (b) show the bits of the embedded digital signature.

5. CONCLUSION

A 2-D LDSE method has been developed for assuring the integrity of CAD images and results when the CAD software is integrated with a PACS. Our experimental results demonstrate that the LDSE method is effective for assuring CAD image integrity. The LDSE method can be combined with the DICOM SR RSA digital signature method to provide a complete integrity assurance solution for CAD results.

REFERENCES

[1] L.W. Burhenne, et al., Potential contribution of computer-aided detection to the sensitivity of screening mammography, Radiology 215 (2000) 554 – 562.
[2] J.A. Baker, et al., Computer aided detection (CAD) in screening mammography: sensitivity of commercial system in detecting architecture distortion, AJR 181 (2003) 1083-1088.
[3] H.P. Chan, et al., Image feature analysis and computer-aided diagnosis in digital radiography: 1. Automated detection of microcalcifications in mammography, Med. Phys. 14 (1987) 538-548.
[4] M.T. Freedman, et al., A computer aid for radiologists: improved detection of small volume lung cancer on chest radiographs, RSNA (2003) 523.
[5] S.A. Wood, et al., CAD of actionable lung nodules on multislice CT scans of the lung: sensitivity and false positive marker rates, RSNA (2002) 477.
[6] Z. Zhou**,** B. Liu, A, Le**,** CAD-PACS Integration Tool Kit Based on DICOM Secondary Capture, Structured Report and IHE Workflow Profiles, Computerized Medical Imaging and Graphics, accepted for publication.
[7] Information processing systems, Open systems Interconnection, Basic Reference Model-Part 2: Security Architecture, ISO 7498-2, 1989.
[8] Z. Zhou, Lossless digital signature embedding for medical image integrity assurance, Ph.D. dissertation, Univ. of Southern California, Los Angeles, CA, 2005.
[9] Z. Zhou, H.K. Huang, B.J. Liu, Digital signature embedding for medical image integrity in a data grid off-site backup archive, Proc. SPIE Medical Imaging, vol. 6, pp. 306-317, 2005.
[10] Z. Zhou, Assuring the Security of Images and Results in CAD-PACS Integration, Computerized Medical Imaging and Graphics, accepted for publication.
[11] T. Chan, H.K. Huang, Computer Aided Diagnosis of Acute Intracranial Hemorrhage on CT, RSNA Annual Meeting InfoRAD Exhibits, 2006.
[12] K.L. Boedeker, M.F. McNitt-Gray, S.R. Rogers, D.A. Truong, M.S. Brown, D.W. Gjertson, J.G. Goldin, Emphysema: Effect of Reconstruction Algorithm on CT Imaging Measures, Radiology, 232, 295-301, 2004.

Comparison of fingerprint and facial biometric verification technologies for user access and patient identification in a clinical environment

Bing Guo, MD, Yu Zhang[2], BS., Jorge Documet[1], MS., Brent Liu[1], PhD., Jasper Lee[1], BS., Rasu Shrestha[1], MD., Kevin Wang[1], BS., H.K. Huang[1], D.Sc.,

[1]Image Processing and Informatics Laboratory (IPI), Department of Radiology, University of Southern California (USC), USA,
[2] Georgia Institute of Technology, Atlanta GA, USA

ABSTRACT

As clinical imaging and informatics systems continue to integrate the healthcare enterprise, the need to prevent patient mis-identification and unauthorized access to clinical data becomes more apparent especially under the Health Insurance Portability and Accountability Act (HIPAA) mandate. Last year, we presented a system to track and verify patients and staff within a clinical environment. This year, we further address the biometric verification component in order to determine which Biometric system is the optimal solution for given applications in the complex clinical environment. We install two biometric identification systems including fingerprint and facial recognition systems at an outpatient imaging facility, Healthcare Consultation Center II (HCCII). We evaluated each solution and documented the advantages and pitfalls of each biometric technology in this clinical environment.

Keywords: LTVS, Location Tracking and Verification System, HIS, RIS, PACS, HIPAA Security

1. PURPOSE

The issue of patient misidentification has attracted public interest and scrutiny over the past two decades, as the increased incidence of adverse events in hospitals has led to mounting malpractice costs and incited concern over patient safety. Studies report that as much as 3.7% of hospital admissions experience some sort of adverse event, often involving patient misidentification [1]. Although the vast majority of these adverse events are non-permanent, it is estimated that every year in the United States between 44,000 and 98,000 deaths result from medical errors [2]. The Joint Commission on Accreditation of Healthcare Organizations (JCAHO) processed root cause analysis information on 126 cases of wrong site surgery between 1998 and 2001. Seventy-six percent of cases involved surgery on the wrong body part or site, 13% surgery on the wrong patient, and 11% the wrong surgical procedure. JCAHO has identified the factor that human error such as misuse of addressograph labels, mishearing, misspelling and misfiling may lead to mis-identification [3]. Applying biometric verification systems in these clinical environments can significantly reduce instances of patient misidentification, and in turn reduce medical errors. This paper presents the evaluation results of implementing a Location Tracking and Verification System (LTVS) with various biometric verification components. Two different ID verification Biometrics technologies are evaluated: 1) Facial Biometrics; and 2) Fingerprint Biometrics systems. Pitfalls and advantages for each of the two biometrics systems integrated within a clinical environment are presented and discussed.

2. METHODS AND MATERIALS

2.1 Biometric verification systems

Biometric verification systems work by analyzing certain characteristics, such as irises or fingerprints, which are considered unique to an individual. The biggest advantage of biometrics over traditional knowledge-based or token-based verification systems is that it relies on an inherent attribute of a person, as opposed to passwords which can be forgotten, or keycards which can be lost or stolen [4][5]. Many

different types of biometric verification systems are currently available. For example, face recognition, fingerprint scanning, voice recognition and iris scanning biometric system. The technical merits of two popular systems – face recognition and fingerprint scanning – are presented in this paper, followed by a discussion of the applicability of these systems in a clinical environment.

2.2 Face Recognition

In recent years automated face recognition as a method of biometric identification has gained popularity with such notable applications as the surveillance of the London Borough of Newham (1998) and Superbowl XXXV (2000), both of which used regular closed-circuit video cameras integrated with sophisticated facial recognition algorithms. Many of these algorithms rely on the special relationship between "nodal points" on the face such as eyes, nose, mouth, chin, and others [6]. One major advantages of using a facial recognition system is its unobtrusive nature. Detection and identification of faces can be done from several meters away and without the subject's active participation. It is one of the few biometric verification systems that work well in dynamic setting such as a large crowd. The facial biometrics recognition module uses an advanced software that calculates and analyzes landmark positions and features on a face to verify a person's identity (Figure 1). By using a prepared database, the facial biometrics recognition system can identify the person named "Bing" which is detected in the video camera.

Figure 1 – The figure shows how the facial recognition biometric system can identify a person in an image.

2.3 Fingerprint Recognition

Of all the types of biometric verification, fingerprint recognition perhaps has the longest history, dating back over one hundred years. Though rudimentary, traditional fingerprinting methods allowed for identification with a high degree of accuracy. They were performed by manually examining the pattern of ridges and valleys on fingers, which are thought to be unique to each individual. Modern fingerprint sensors are able to automatically capture, analyze, and match a person's fingerprint against a database of known identities. The technologies behind these sensors are quite varied, ranging from solid-state capacitive to optical, but most are smaller than the size of a postage stamp and are quite economical [7]. Fingerprint scanning has become so ubiquitous that many laptops now have integrated scanners to supplement traditional password protection. Also, police departments are able to match fingerprints against

large databases in real time. The fingerprint biometric recognition module we choose is using a unique semiconductor-based fingerprint reader that uses small RF signals to detect the fingerprint ridge and valley pattern. The RF electronic imaging mechanism called "TruePrint technology" works by reading the fingerprint pattern from the live, highly-conductive layer of skin that lies just beneath the skin's dry outer surface layer. The sensors are less affected by common skin surface conditions -- including dry, worn, calloused, dirty or oily skin -- that can impair the ability of other sensors to acquire accurate fingerprint images [8] (Figure 2).

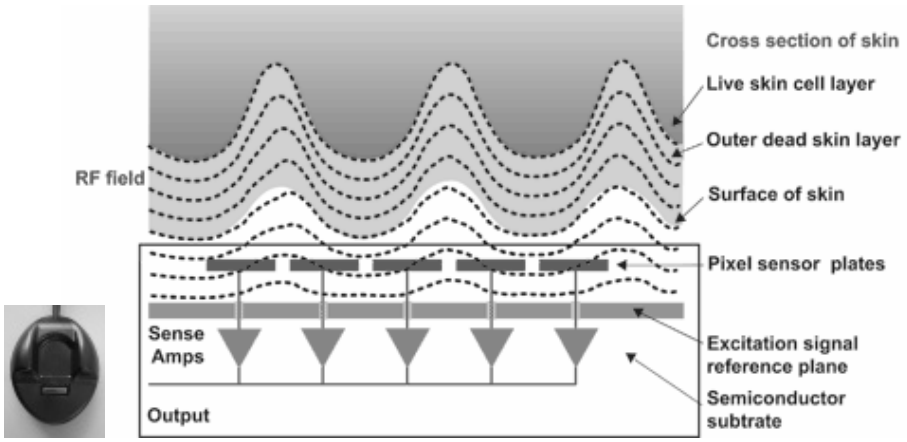

Figure 2- The fingerprint biometric recognition module we choose is using a unique semiconductor-based fingerprint reader that uses small RF signals to detect the fingerprint ridge and valley pattern.

2.4 Location Tracking and Verification System

The Location Tracking and Verification System (LTVS) integrates wireless technology and biometrics verification system to monitor and automatically identify staff and patients. The purpose to develop this system is to provide a simple yet systematic solution to monitor and automatically identify staff and patients in order to streamline the patient workflow, protect against erroneous examinations and create a security zone to prevent and audit unauthorized access to patient healthcare data for partial compliance of the HIPAA mandate. The application is robust and flexible and can be used on a standard PC workstation with a web browser application with add-on features where the application can be accessed from a Personal Digital Assistant (PDA). The methodology for design and implementation of the LTVS within a clinical environment at the Healthcare Consultation Center II (HCCII) was presented at SPIE Medical Imaging Conference last year. We integrated a facial recognition biometric system as the biometric verification module last year. This year we have integrated another biometric verification component, which is a fingerprint recognition biometric system in order to determine which biometric system is the optimal solution for given applications in the complex clinical environment.

An outpatient radiology facility is considered for the purposes of this discussion, because there exists a crucial need for medical staff to be certain of patients' identities. This is not a reason for why an outpatient is a good choice. It's more because an outpatient is a good first clinical test bed since it is a controlled environment. For example, incidences of erroneous exams in radiology departments could lead to misdiagnosis and improper treatments, which could have severe legal and financial ramifications. Implementation of the appropriate biometric verification system could remedy the issue of patient misidentification.

HCCII is an outpatient imaging facility with a fully digital environment with integrated HIS/RIS/PACS/VR (Voice Recognition) located in the University of Southern California (USC) Health Science Campus. The facility has one Computed Tomography (CT) Scanner, one Magnetic Resonance Imaging (MRI) Scanner, one Ultrasound Scanner (US), two Computed Radiography (CR) units, and one Special Procedure Room (Fluoroscopy/Angiography). There are a total of thirty-one clinical personnel including eight technologists, seven support staff and sixteen rotating radiologists. A clinical workflow study of the day-to-day operations was performed to observe the physical locations of patients and clinical staff in procedure rooms, reading

room area, and waiting room area of HCCII. There are unsecured exit doors and a reading room at HCCII. There is always a risk that unauthorized person can easily access patient information on the workstation of the reading area without permission, and a potential mis-identification of a patient at the working area before the patient enters the procedure room. Based on this workflow study as well as user needs, the LTVS system was designed with an application integrating both real-time locating system and biometrics identification which allows users to extract precise real-time location and identity verification information. The system was implemented in key areas of HCCII where identity verification was necessary according to the workflow analysis in order to determine which Biometric system is the optimal solution for given applications in the complex clinical environment.

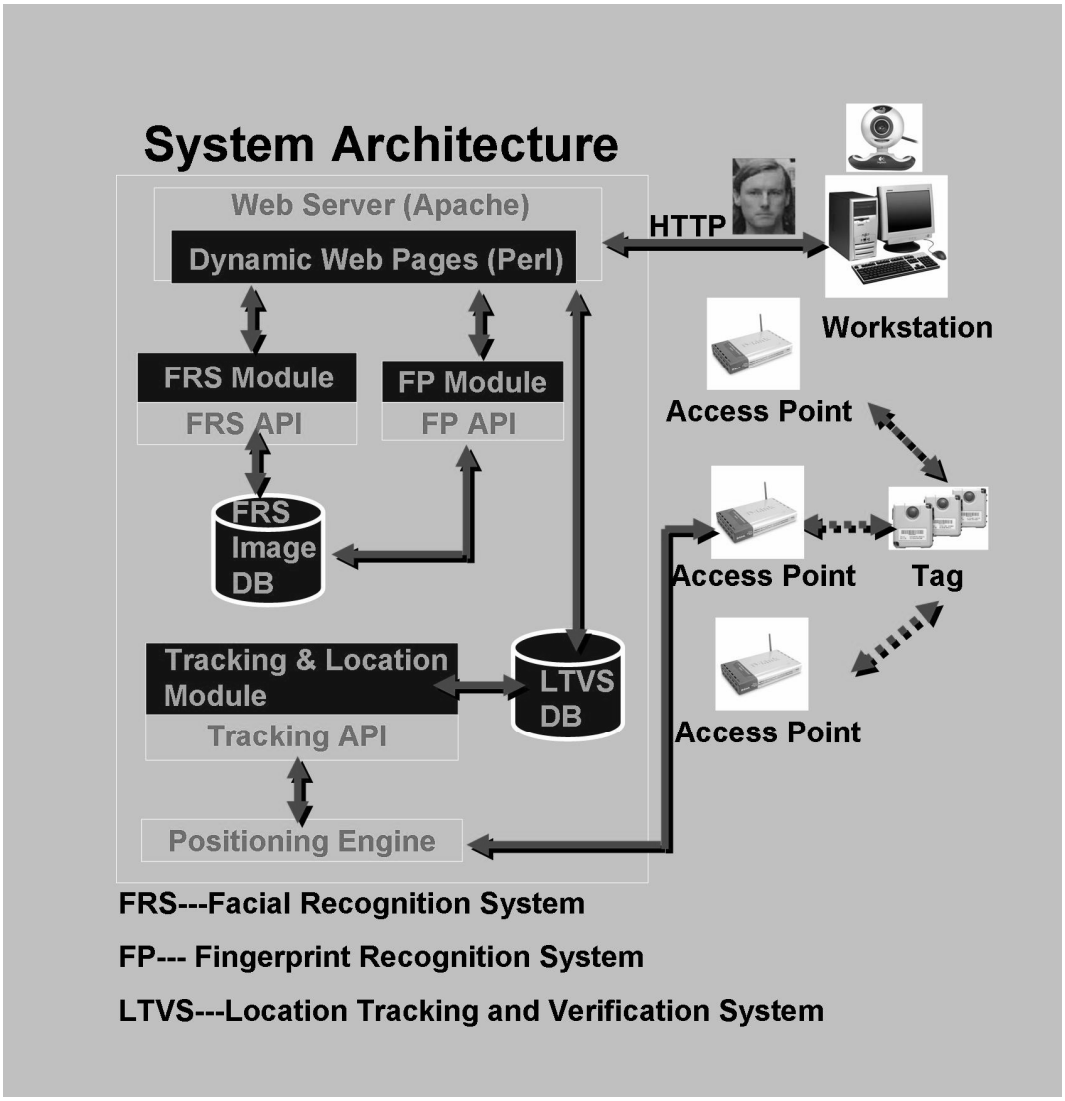

Figure 3- System architecture shows the Location Tracking and Verification System (LTVS) Server which consists of a web server application that runs the LTVS web-based Graphical User Interface (GUI). The system design and implementation were developed in-house.

The components for the LTVS consists of a facial biometric recognition module, a fingerprint biometric recognition module, a Wi-Fi (‘wireless fidelity) based tracking module integrated into a web-based application as shown in Figure 3. “Wi-Fi” stands for certain types of wireless local area networks (WLAN) that use specifications conforming to IEEE 802.11 network. The facial biometrics recognition module uses

an advanced software that calculates and analyzes landmark positions and features on a face to verify a person's identity which is discussed above in the paper. High resolution USB video cameras are used for identity verification purpose. The facial biometrics recognition module and the fingerprint biometrics recognition module share the same database for image storage. The tracking module consists of a wireless radio frequency solution that utilizes IEEE 802.11 b/g access points and Wi-Fi tags to track the location of patient and staff. The LTVS database stores the location information of the patient and staff. The integrated web-based application stores data inputs into the LTVS database from both the facial and fingerprint biometric recognition modules as well as other data from the tracking module.

The LTVS application can be used with any standard PC workstation with a web browser. The system integration design and the Graphical User Interface (GUI) were developed by the Image Processing and Informatics (IPI) laboratory. Based on the workflow, the GUI was developed which allows healthcare providers to extract real-time location information and verify the identity of the patient. The tracking and biometrics module runs independently and synchronously using the Windows 2000 Professional operating system. The LTVS is modular in design to facilitate any improvements and replacements to either the biometric module or the tracking module in the future. Finally, the LTVS was implemented within the clinical environment of HCCII and initial results and experiences will be discussed in the paper.

3. RESULTS AND DISCUSSION

The prototype Location Tracking and Verification system for a clinical environment was designed and developed within the Image Processing and Informatics laboratory (IPI), USC. The LTVS was then evaluated at an out patient imaging center Healthcare Consultation Center II (HCCII) with 13,000 square feet. A total three-week testing period was performed at HCCII. Major key technical features and system workflows of the LTVS were developed to address these clinical needs to prevent patient mis-identification based on the clinical workflow shown below:

Facial Image and Fingerprint Image Registration

First, a patient photo was captured at the registration desk by the video camera, correlated with patient information from RIS/HIS or input manually by front desk staff, such as the patient name and patient birth date, and stored in the database of the LTVS. It is important to include a biometric ID because tracking devices can be easily stolen and used to impersonate in order to gain access or perform sabotage. After patient photo was registered, the fingerprint enrollment step started by a system message says "Place finger on sensor" as shown in figure 4. The fingerprint biometric module requires an initial five-time enrollment action in order to complete the registration step and obtain enough fingerprint data samples for verification. The system shows a message "Enroll complete" to notify the user that enrollment process is complete as shown in figure 5.

Figure 4- Patient registration page shows how to register a new patient into the LTVS system. First, a patient photo was captured by the video camera, correlated with patient information. After patient photo registration, the fingerprint enrollment step started by a system message says "Place finger on sensor".

Figure 5- The system shows a message "Enroll complete" to notify the user that enrollment process is complete.

Facial Recognition and Fingerprint Recognition

In order to prevent patient mis-identification, before the patient enters the procedure room for an exam, the technologist could verify the identity of the patient by capturing the patient's facial image, and the facial recognition software would verify and confirm the patient information including the patient ID, name, and original photos. Figure 6 shows how to verify the identity of a patient by using facial recognition module. After the camera captures the photo of the patient, the system sends the photo to compare with the image stored in the database and sends back the verification result which is displayed on the GUI.

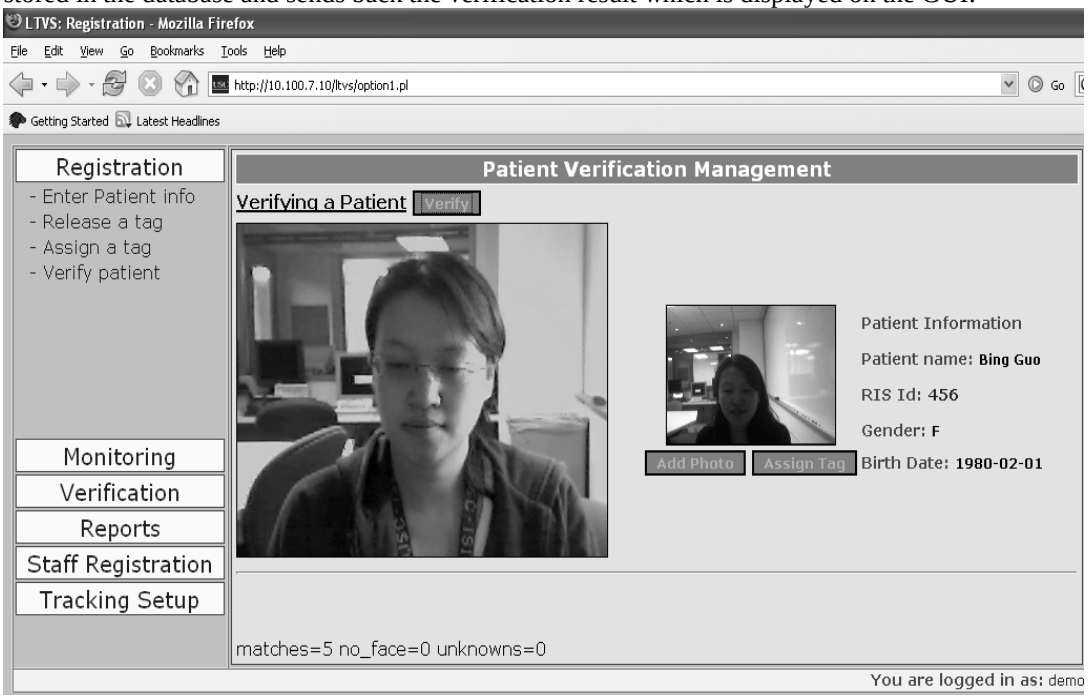

Figure 6- shows how to verify the identity of a patient by using facial recognition module.

In addition, the system provides the ability to use a fingerprint recognition biometric system to verify the identity of the patient. Since the patient photo is attached with patient information, the system is able to

display patient's identification information with the photo of the patient. Figure 7 and Figure 8 depicts the LTVS "Fingerprint Verification page" menu and the steps how to verify a patient by using the fingerprint verification module. In Figure 7, a message "Place finger on sensor" notifies the user that the verification process has started. In Figure 8, the system matches the fingerprint placed on the sensor with the patient ID "123" in the database. As a result, patient information including photo image is displayed on the verification page.

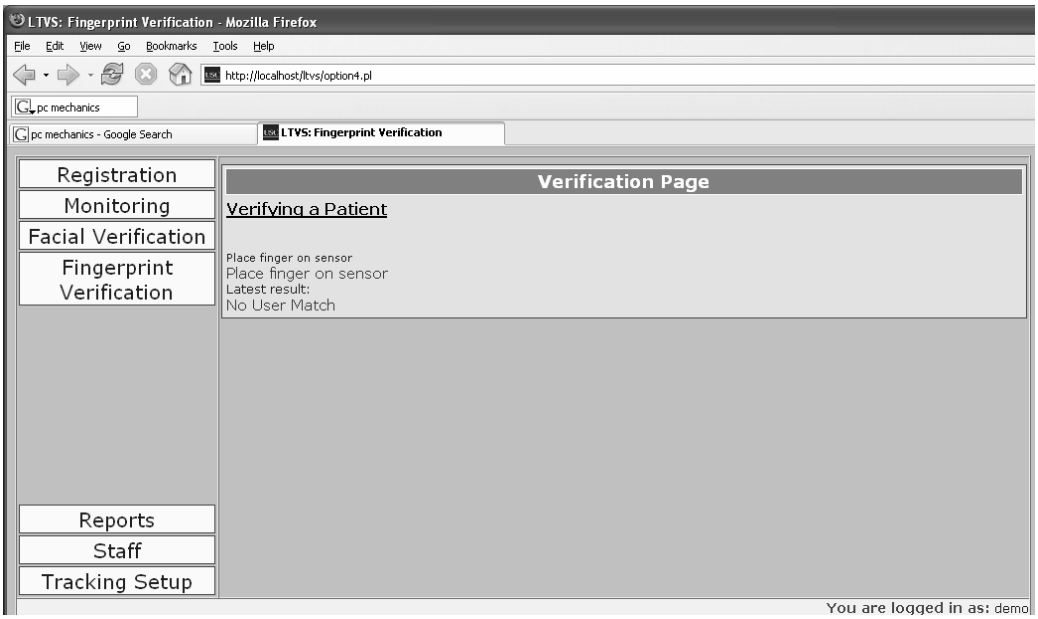

Figure 7- A message "Place finger on sensor" notifies the user that the verification process starts.

Figure 8- The system matched the fingerprint placed on the sensor with the patient ID "123" in the database. As a result, patient information including photo image is displayed on the verification page.

Cost Analysis

The cost of facial biometric system including hardware and software installed at HCCII is nearly six thousand dollars. The potential additional cost of facial recognition biometric system includes five thousand dollars of annual license fees. With the fingerprint identification device, the cost of the LTVS is relatively cheaper than the facial biometrics system because it does not require annual license fees. The cost of the fingerprint recognition biometric system is nearly three thousand dollars.

Performance and accuracy

The accuracy of face recognition, and many biometric verification systems, varies depending on the degree and type of error allowed by the particular environment/client. Although humans have little trouble recognizing thousands of faces, algorithms that perform the same function are much more sensitive to factors such as illumination, camera view/orientation, facial expressions, aging, and accoutrements. We found that the facial biometric recognition system worked best in well-lit rooms using web cams with a minimum resolution of 640x480 or higher. Also, the patients or staff having their facial biometric image taken had to be sitting within a certain distance of the web cam to yield sufficient biometric values. Although attaining web cams with the 640x480 resolution was feasible, it was difficult to achieve proper lighting and seating in certain rooms such as the radiology reading room and hallways where the workstation required the user to be standing.

Fingerprint recognition systems are the oldest and most widely used as a biometric system, it is also most susceptible to counterfeit possibilities. The disadvantage of fingerprint biometric system is that silicon duplicates can be easily made, either with co-operation of its owner or by lifting fingerprints left behind on surfaces. Some of the more advanced fingerprint scanners attempt to reconcile this by testing for additional factors such as temperature, conductivity, heartbeat, relative dielectric constant, and blood pressure.

Privacy concern

The patients were agreed to the surveillance because we explained to them about the purpose of this project before we enrolled their photos and fingerprint images with personal information into the system. In addition, all the information in the database will be deleted after the testing period. At this point, the photographs and fingerprint images of the patients in the LTVS system were provided on a voluntary basis since LTVS is a system prototype.

4. CONCLUSION

No one form of biometric identification is universally superior to another; the specific environment or application ultimately defines which system is most effective. An outpatient radiology facility has several requirements upon which the systems presented in this paper can be evaluated. First of all, hospital patients would not need to be identified en masse; the purpose here is to use biometrics to verify a single individual's identity rather than locate him or her in a crowd. Thus facial recognition's exclusive attribute of scanning a large group of people is not applicable here. As mentioned earlier, face recognition systems are sensitive to factors such as aging, illumination, accoutrements, and camera orientation. The error rate for using face recognition on the diverse population expected in a clinical setting would be so high that the system might prove to be more of a hindrance than an asset. Therefore fingerprint scanning would be more appropriate than face recognition. In addition, the cost of the fingerprint recognition biometric system is much cheaper than the facial recognition biometric system.

With regards to the technical requirements of the two systems, none demand cumbersome hardware and both the systems can be easily integrated into existing computer setups common in a clinical setting. However, to be effective in a clinical setting, the biometric verification equipment must easily accommodate patients regardless of age, height, or state of consciousness. Facial recognition requires a great deal of user participation because imaging must be done at close range. This may present obstacles to patients who are unconscious, confined to wheelchairs, or for some other reason cannot physically access the camera. Because fingerprint scanners are so portable and versatile, physical access to the equipment would not be an issue. Also, because of its history and ubiquity, fingerprint scanning would most likely be viewed by the public as a less invasive procedure than facial recognition system.

While both of the systems possess their unique strengths and weaknesses, fingerprint scanning is the most appropriate biometric verification system for clinical settings. Also, fingerprinting is more user-friendly

and has a proven track record. Therefore, based on these criteria, fingerprint recognition is the recommended solution for a clinical environment.

REFERENCES

[1] T.A. Brennan, et al, "Incidence of adverse events and negligence in hospitalized patients: results of the Harvard Medical Practice Study," Qual Saf Health Care, vol. 13, pp. 145-152, 2004.
[2] M.F. Murphy, and J.D.S. Kay, "Patient identification: problems and potential solutions," Vox Sanguinis, vol. 87, suppl. 2, pp 197-202, 2004.
[3] Joint Commission on Accreditation of Healthcare Organizations (JCAHO), http://www.jointcommission.org/, accessed in January, 2007
[4] History of Biometrics http://ntrg.cs.tcd.ie/undergrad/4ba2.02/biometrics/history.html , accessed in January, 2007
[5] A. Jain, L. Hong, and S. Pankanti, "Biometric identification," Communications of the ACM, vol. 43, no. 2, pp. 91-98
[6] P.J. Phillips, A. Martin, C.L. Wilson, and M. Przybocki, "An introduction to evaluating biometric systems," Computer, vol. 33, no. 2, pp. 56-63, 2000.
[7] T. van der Putte, and J. Keuning, "Biometrical fingerprint recognition: don't get your fingers burned," Fourth Working Conference on Smart Card Research and Advanced Applications, Kluwer Academic Publishers, pp. 289-303, 2000.
[8] Authentec, Inc. http://www.authentec.com/getpage.cfm?sectionID=3, accessed in January, 2007

Design and Implementation of a Fault-Tolerant and Dynamic Metadata Database for Clinical Trials

J. Lee, Z. Zhou, E. Talini*, J. Documet, B. Liu

Image Processing & Informatics Laboratory, USC 90292, CA
*Department of Diagnostic and Interventional Radiology, University of Pisa, Italy

ABSTRACT

In recent imaging-based clinical trials, quantitative image analysis (QIA) and computer-aided diagnosis (CAD) methods are increasing in productivity due to higher resolution imaging capabilities. A radiology core doing clinical trials have been analyzing more treatment methods and there is a growing quantity of metadata that need to be stored and managed. These radiology centers are also collaborating with many off-site imaging field sites and need a way to communicate metadata between one another in a secure infrastructure. Our solution is to implement a data storage grid with a fault-tolerant and dynamic metadata database design to unify metadata from different clinical trial experiments and field sites. Although metadata from images follow the DICOM standard, clinical trials also produce metadata specific to regions-of-interest and quantitative image analysis. We have implemented a data access and integration (DAI) server layer where multiple field sites can access multiple metadata databases in the data grid through a single web-based grid service. The centralization of metadata database management simplifies the task of adding new databases into the grid and also decreases the risk of configuration errors seen in peer-to-peer grids. In this paper, we address the design and implementation of a data grid metadata storage that has fault-tolerance and dynamic integration for imaging-based clinical trials.

Keywords: Clinical Trials, Metadata, Fault-Tolerance, Data Grid, Globus, OGSA-DAI, quantitative image analysis, CAD

INTRODUCTION

Imaging-based clinical trials are the assessment of new medical treatment procedures by comparing pre- and post-treatment imaging results. Such trials are usually done in a collaboration of multiple imaging centers and radiology expert sites, also known as a radiology core. A single radiology core can perform multiple clinical trials that has different database requirements specific to different experimental variable.[1] With the sensitivity of clinical trial data, the usage of a robustly designed storage data grid serves purposes including fault-tolerant backup, secure sharing of images and data results, and streamlining of dataflow between databases and physically separate storage.

Our data storage grid design is implemented using the Globus Toolkit as seen in figure 1 below. The architecture of our design has a client interface layer, that is connected to a user-level middleware, then down to the core Globus middleware, and finally to the storage hardware at the bottom-most layer.[2] All the listed services in the grid framework run simultaneously for the data grid to work. The grey components in the figure are components not provided by the Globus Toolkit, and thus have required development tailored for clinical trials purpose. In this paper, the focus will be on a fault-tolerant and dynamic Metadata Catalog Service that manages imaging-based clinical trials metadata.

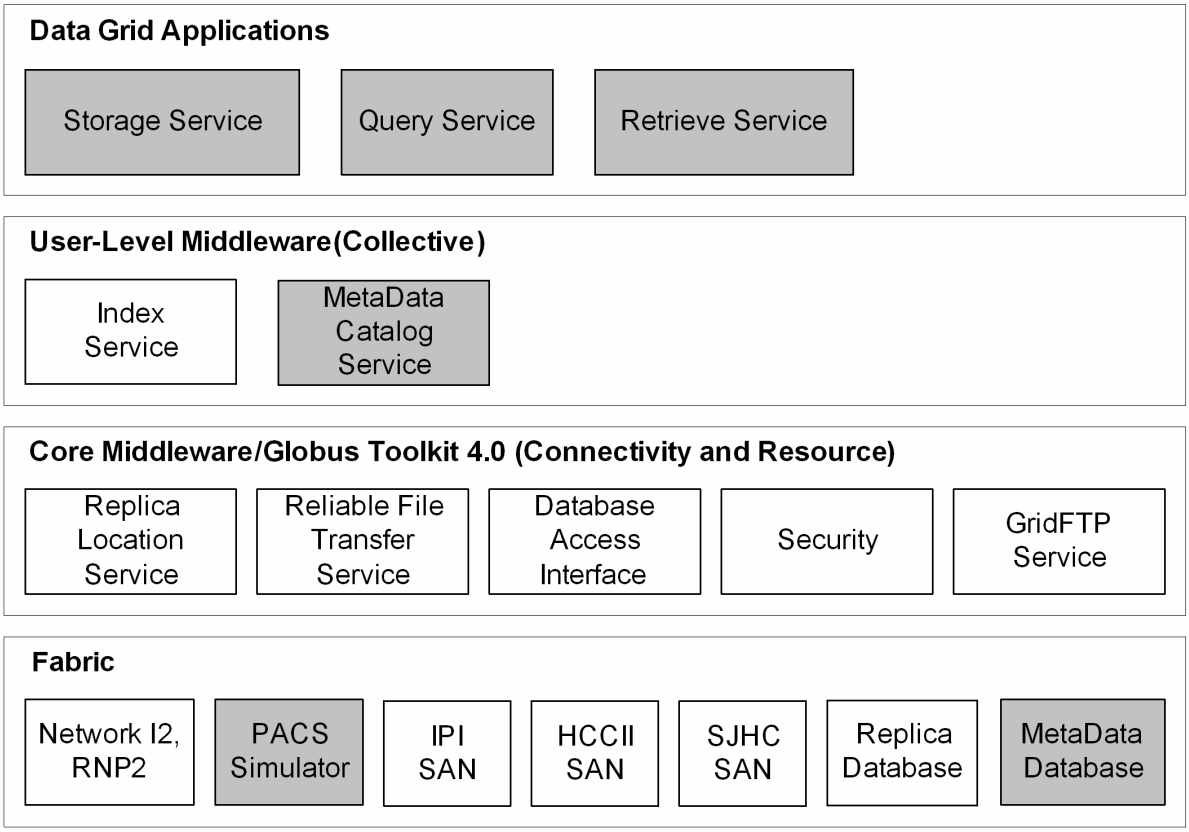

Figure 1. Overall data storage grid architecture for imaging -based clinical trials .

Considering the importance and sensitivity of metadata in clinical trials, the previous data grid design was insufficient in fault-tolerance and access management because the metadata databases were not replicated to other storage nodes in the grid, nor was there a master index of all metadata available within the grid.[3,4] Thus each clinical trial site had to pull metadata separately from other storage sites if they wanted to query metadata from outside their local storage. This project utilizes a Globus integration toolkit called OGSA-DAI in our metadata management layer to provide fault-tolerance of the metadata database and to allow multiple GAP nodes to access all metadata in the data grid.

METHODS AND MATERIALS

The data grid requires a metadata database system that can store, distribute, retrieve and modify DICOM metadata as well as CAD and quantitative image analysis results produced during clinical trials. The main challenge is the different metadata parameters involved in clinical trials. Handling different quantitative image analysis values and CAD results outside of the DICOM standard have previously required separate non-compatible databases for each clinical trial experiment. Our design merges these databases into a single dynamic metadata database within a grid environment so that DICOM-metadata, quantitative image analysis values, and CAD metadata can all be queried from all authorized nodes in the grid.

2.1. Imaging-based Clinical Trials Workflow

When the radiology core wants to perform a clinical trial study on a specific group of images, they query the metadata fields of relevant treatment images specific to their field of interest. These images are stored onto the data grid from collaborating imaging centers where the medical images are being taken. But in addition to storage and query functionality, another requirement of a clinical trials metadata catalog service is to allow modification of metadata database tables so that quantitative image analysis results and CAD tools can be added back into the database after they

are performed. Thus, there are three fundamental tasks of the metadata catalog service: storage, querying, and modification.

2.2. Overview of the Imaging-based Clinical Trials Data Grid

The term data grid is a peer-to-peer network that has multiple nodes, called grid access points (GAP) that communicate data securely between one another. For our purposes, we are managing medical DICOM images and clinical trials data.[5] Since all nodes in the data grid run basically the same services, figure 2 below should suffice for a general overview of the data grid architecture. To describe it, we go through the query/retrieve workflow as a use-case scenario.

Step 1: Radiologist or medical expert performs a parameterized query of metadata database.
Step 2: The local GAP's metadata catalog service queries the metadata database.
Step 3: The user chooses from the result list of metadata which images to retrieve.
Step 4: The Replica Location Service finds out where DICOM images are stored in the grid.
Step 5: The File Transfer Manager utilizes GridFTP to pull the DICOM images back to the GAP either from a storage node in the Data Grid.
Step 6: The GAP gives DICOM images back to the workstation to be viewed and analyzed.

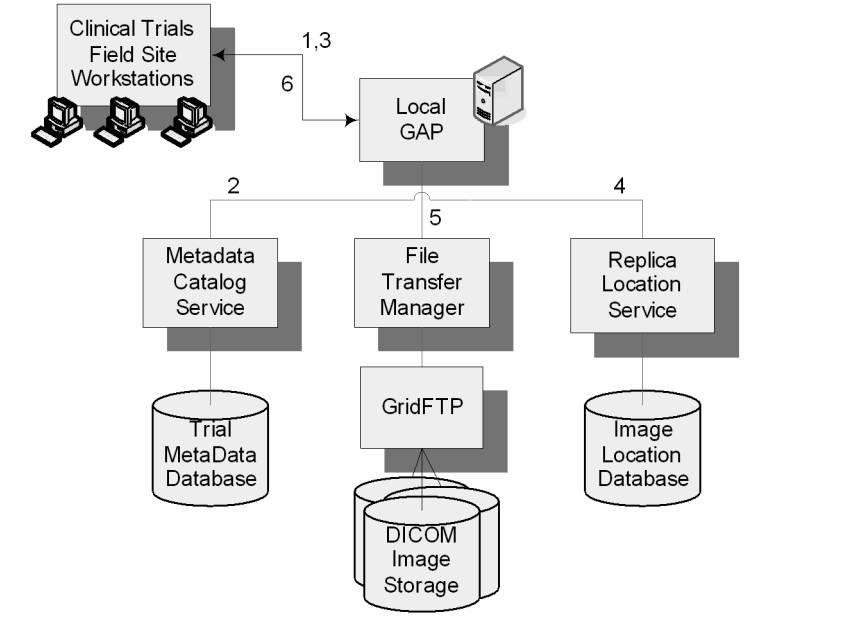

Figure 2. General Workflow and Architecture of Data Storage Grid (DSG)

2.3. Metadata Architecture Utilizing OGSA-DAI

To provide centralization and fault-tolerant replication, our metadata database architecture is shown in figure 3 below with an added middle layer called the DAI server. Each field site has clinical trial workstations that connect to their local grid-access-point (GAP). These sites may be medical imaging center, expert field sites, or even hospitals. All the GAP's access a DAI server that performs reading and writing of metadata information to the various metadata databases within the grid. Note that there can be multiple GAP's and multiple metadata storage nodes connected to a DAI server and are not limited to only four. The three main roles of the DAI server are: centralization of metadata access, replication of metadata into multiple storage nodes, and handling metadata for different clinical trials.

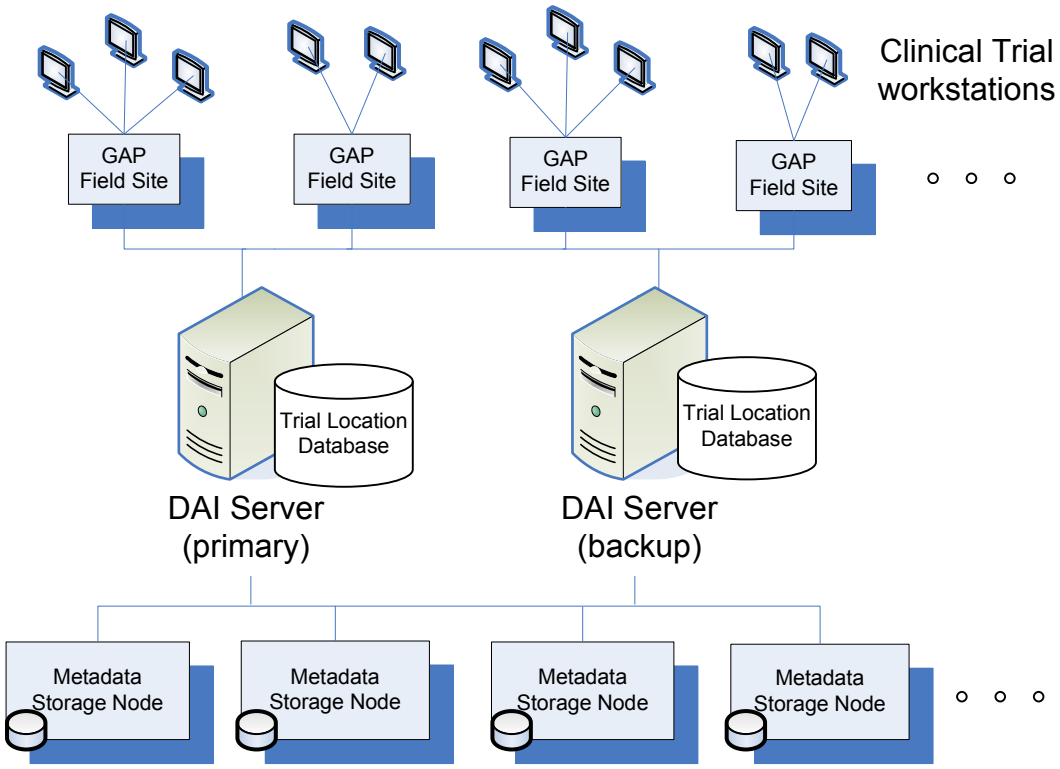

Figure 3. General Architecture of the Metadata System for Clinical Trials Data Grid.
Note that there can be multiple workstations per single GAP, multiple GAP field sites, and multiple metadata storage nodes.

As seen in figure 3 above, the DAI server actually becomes the portal to metadata in the grid because all metadata goes through the DAI server. This layer of convergence below the GAP layer is necessary because there are a large number of field sites participating in a clinical trial and configuring each and every GAP to know where a replicated copy of their metadata is would be extremely labor-intensive and prone to error during configurations. But more importantly, this design allows for fault-tolerance of metadata in clinical trials. If the metadata database at one site is not accessible due to network, hardware, or software failure, the DAI server will be able to automatically query or store metadata from another site until the first site is back up. And when the failed site comes back alive, it can be recovered and updated by a DAI server administrator.

Connectivity between GAP's and the DAI Server

The GAP machines connect to the DAI server via a unique URL using the OGSA-DAI (Open Grid Services Architecture Data Access and Integration) toolkit [6] which deploys onto a web container such as Apache Tomcat. After an OGSA-DAI data service is set up at a DAI server, a unique URL is available. This URL is then entered into each GAP's configuration file where existing management software on the GAP can access the URL string. This data service is secure because each GAP node must have existing grid authenticated certificates to have access to it

As seen in figure 3 above, there is also a backup DAI server. We have designed the system to have a secondary backup DAI server so that GAP's can automatically redirect to it in case the primary DAI server goes down or even if there is heavy network traffic. In the event a GAP cannot connect to the primary DAI server, there is a secondary URL for the backup DAI server to which the GAP's can connect to. Software on the GAP nodes are automatically programmed to handle loss of connectivity exceptions by switching to the backup DAI Server. And since all data sent to the primary DAI server is also replicated to the backup DAI server, the metadata and configuration databases will be exactly the same on the backup server.

Connectivity Between the DAI Server and Metadata Databases

After the data service is deployed on the DAI server and a data service URL is generated, the next step is to connect the metadata databases to the DAI server. Since the purpose of the DAI server is to aggregate metadata from multiple

clinical trial experiments into one dynamic database, each metadata database is defined on the DAI server by a configuration file that describes the type, location, database driver, and name of the specific metadata database. Note that a single metadata storage node can have multiple metadata databases, one for each clinical trial experiment.

Although all metadata databases in the grid are deployed onto a single DAI server, the metadata catalog service still needs a way to organize metadata databases so that metadata is only replicated to participating field sites and not every single metadata storage node in the grid. Thus the DAI server maintains a Trial Location Database, as seen in figure 3 above, that keeps track of which clinical trial experiments a field site is participating in and what the database names are for those experiments. The Trial Location Database enables the metadata database service to replicate metadata to only the nodes participating in a specific clinical trial, as opposed to every single field site in the data grid.

2.4. Metadata Workflow Scenarios

Storage of Metadata

When an image study is taken at a medical imaging center, or when a clinical trials expert site performs quantitative image analysis, or when a CAD performs its image processing analysis, metadata is generated in the form or text and needs to be stored into the grid for later access. Below in figure 4 diagrams this workflow for our metadata database design.

Step 1: The GAP at imaging center 'A', for example, has extracted DICOM metadata from its images and is sending it to the DAI server.
Step 2: The metadata catalog service accesses the Trial Location Database to find out which imaging center has a metadata database for clinical trials #2.
Step 3: Metadata is entered and cataloged into the metadata database at the originating imaging center 'A' as well as the participating imaging center 'C'.

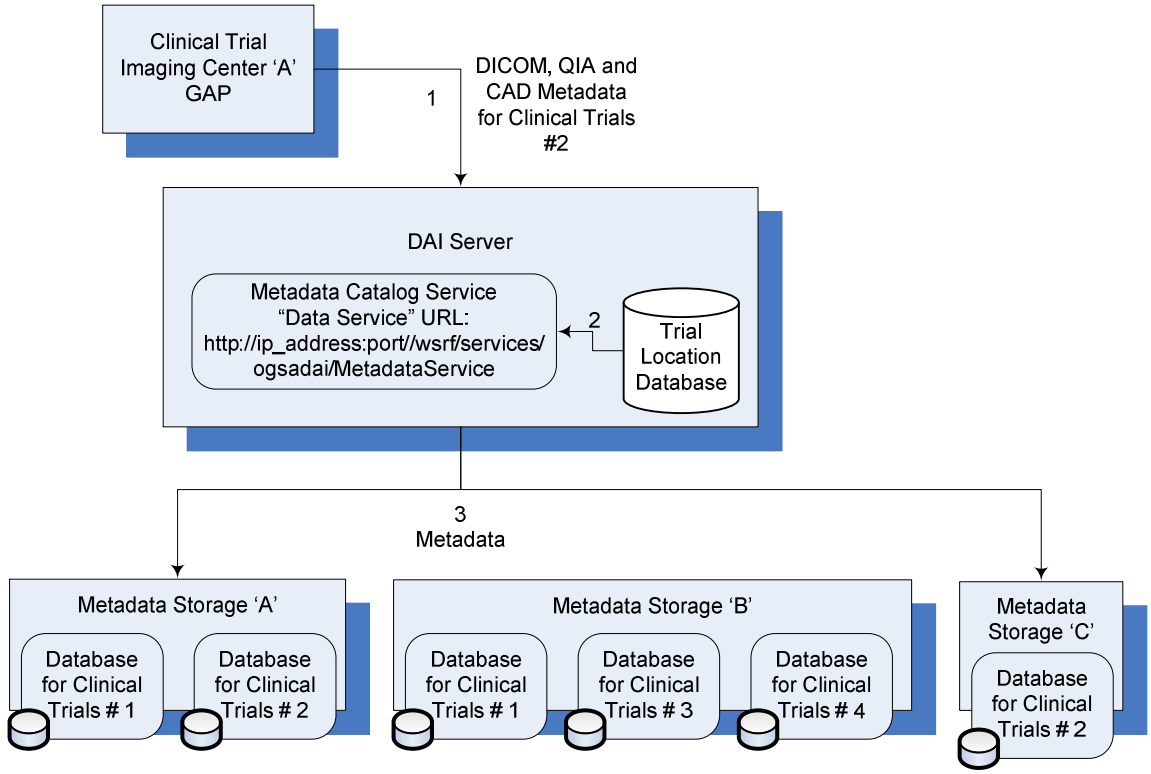

Figure 4. Sample Metadata Storage Workflow Scenario.

Querying Metadata

To query metadata with specific data fields and values, a clinical trials workstation would send a database query request to the local GAP node. Then the GAP software would connect and contact the DAI server so that all the metadata storage sites will be queried. If, however, the user provides a specific clinical trials metadata database to query from, then the DAI server would contact its Trials Location Database and perform the query statement only on the involved metadata storage sites.

Configuring a Metadata Database into the Data Grid for a New Clinical Trial

For the metadata database system to host a new clinical trial, field sites must create a new metadata database with the appropriate data fields. Then the DAI server just needs to be exposed and configured for the database. Since GAP nodes already have the URL of the metadata data service in configuration files, most of the configurations involved are done on the DAI server.

Step 1: Create new metadata database at involved field sites by executing a pre-defined script.
Step 2: Deploy the new database as a data service resource on the DAI server.
Step 3: Expose the new data service resource to the new data service on the DAI server.[7]
Step 4: Add the data service resource to the Trials Location Database so the metadata data service can categorize which data service resource is involved in which clinical trial experiment.

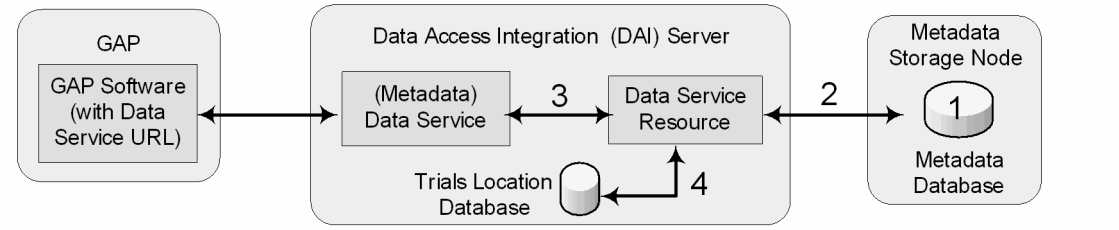

Figure 5. Adding a new metadata database into the data grid: OGSA-DAI connectivity & Trials Location Database

RESULTS AND DISCUSSION

The fault-tolerant and dynamic metadata database architecture has been developed for imaging based clinical trial data grid, but the laboratory evaluation is still ongoing now. Using the OGSA-DAI client toolkit, we were able to centralize all metadata database requests for multiple clinical trial sites and experiments. Although configurations are still required of the DAI server and grid access points, they are kept to a minimum because of the centralized and multi-tier infrastructure. A benefit of our metadata database design is it creates a dynamic workflow in which imaging centers can communicate metadata with the central DAI server via a secure web-based service. Another benefit is all participating clinical trial sites have fault-tolerant access to their metadata database because the DAI server replicates metadata to every participating node in the grid.

CONCLUSION

In a grid-based environment of distributing metadata information, there requires a sharing of physical storage space between imaging centers for clinical trials. This paper discusses how multiple clinical trial experiments can be centralized into a configurable DAI server. The users of the clinical trials grid can have the security that is provided by a fault-tolerant metadata database, with the comfort of knowing their pertinent metadata is being stored locally as well as being replicated at other physical sites within the grid. Furthermore, the multi-level design of OGSA-DAI allows databases with different fields to be integrated into one dynamic database. With the metadata catalog service, DICOM-compliant metadata, quantitative image analysis and CAD results can be sent to a single DAI server that does all the integration, replication and retrieval internally. There are many components involved in this fault-tolerant and dynamic metadata database system, but the benefits of collaborating data and resources with authenticated security are significant in today's growing image-based clinical trials.

REFERENCES

1. M. Brown, S. Shah, R. Pais, Y.Z. Lee, M. McNitt-Gray, J. Goldin, A. Cardenas, D. Aberle. Database Design and Implementation for Quantitative Image Analysis Research. IEEE Transactions on Information Technology in Biomedicine, Vol.9, No.1, Mar. 2005
2. B. Liu, Z. Zhou, J. Document. Utilizing Data Grid Architecture for the Backup and Recovery of Clinical Image Data. JCMIG 2005
3. J. Documet, Z. Zhou, B. Liu, N. King, H.K. Huang. A Design Methodology for Fault-Tolerance in a DICOM-Compliant Data Storage Grid. Proceedings of the SPIE, Medical Imaging 2006
4. H.K. Huang, A. Zhang, B. Liu, Z. Zhou, J. Documet, N. King, L.W. Chan. Data Grid for Large-Scale Medical Image Archive and Analysis. Proceedings of the 13th ACM International Conference on Multimedia, November 6-11, 2005 Singapore pp: 1005-1013
5. Z. Zhou, B. Liu, H.K. Huang, J. Lee, J. Documet. A Data Grid for Imaging-based Clinical Trials. Proceedings of the SPIE, Medical Imaging 2007
6. The Globus Toolkit. GT 4.2 Tech Preview: OGSA-DAI. http://www.globus.org/toolkit/docs/development/4.2-drafts/data/ogsadai/, accessed Sept 20, 2006
7. The OGSA-DAI Project. http://www.ogsadai.org.uk/, accessed Sept. 20, 2006

Bone Age Assessment for Young Children from Newborn to 7-Year-Old Using Carpal Bones

Aifeng Zhang, Arkadiusz Gertych, Brent J. Liu, H.K. Huang

Image Processing & Informatics Lab, Department of Radiology, ISI/USC
Marina del Rey, CA 90292

ABSTRACT

A computer-aided-diagnosis (CAD) method has been previously developed based on features extracted from phalangeal regions of interest (ROI) in a digital hand atlas, which can assess bone age of children from ages 7 to 18 accurately. Therefore, in order to assess the bone age of children in younger ages, the inclusion of carpal bones is necessary. In this paper, we developed and implemented a knowledge-based method for fully automatic carpal bone segmentation and morphological feature analysis. Fuzzy classification was then used to assess the bone age based on the selected features. Last year, we presented carpal bone segmentation algorithm. This year, research works on procedures after carpal bone segmentation including carpal bone identification, feature analysis and fuzzy system for bone age assessment is presented. This method has been successfully applied on all cases in which carpal bones have not overlapped. CAD results of total about 205 cases from the digital hand atlas were evaluated against subject chronological age as well as readings of two radiologists. It was found that the carpal ROI provides reliable information in determining the bone age for young children from newborn to 7-year-old.

Keywords: Bone Age Assessment, Computer-aided-diagnosis, Carpal Region of Interest, Carpal Bone Segmentation, Anisotropic Diffusion, Canny Edge Detection, Feature Extraction, Fuzzy Classification

1. INTRODUCTION

Bone age assessment (BAA) is a clinical procedure performed in pediatric radiology to quickly and non-invasively evaluate the stage of skeletal maturation. The most commonly used method in clinical practice is the book atlas matching assessment developed by Greulich and Pyle[1]. This method is based on visual comparison of the patient's hand image with images collected in the atlas. The closest match is subjectively selected by the radiologist and yields the bone age of the patient (Figure 1).

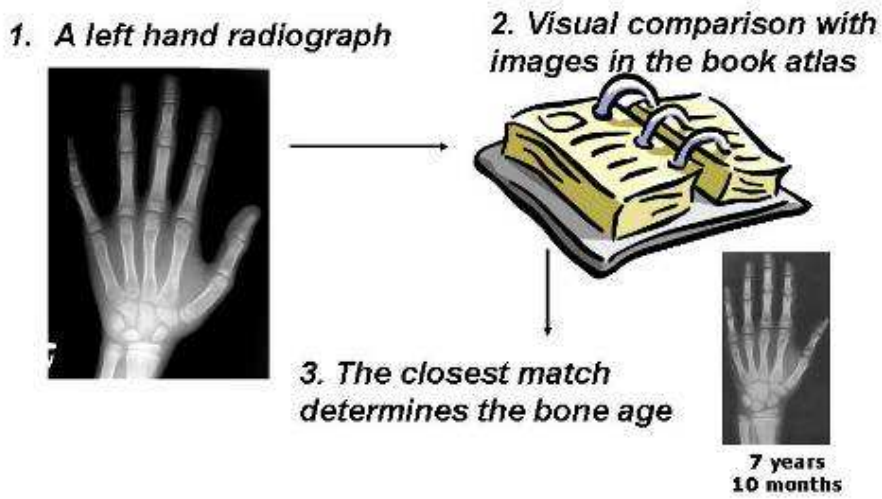

Figure 1 Bone age assessment procedure in clinical practice

However the book atlas remains unchanged from its initial publication in the early 1950s with data collected entirely from upper middle class Caucasian populations in the midwest of the United States. Due to changes both in population diversity and nutrition, an updated data collection becomes crucial to improve the bone age assessment process. In addition, our study found that two radiologists' readings on the 137 African American girls from newborn to 13 years old

have the mean difference at 0.53 years and it could be up to 2.50, which confirm results achieved by other researches[2]. Double reading of hand images (consecutive reading by two radiologists) may increase the accuracy, but at high costs. So, an automatic bone age assessment tool is highly desirable in assisting the radiologists to achieve high efficiency and effectiveness.

2. MOTIVATION OF CARPAL BONE ANALYSIS

The classical bone age assessment of children is based on bone growth of three areas: phalanges, carpal bones, and the wrist joints (Figure 2). A computer-aided-diagnosis (CAD) method has been previously developed based on features extracted from phalangeal regions of interest (ROI) in a digital hand atlas[4, 5, 9]. The images in our collection have been subjected to fully automatic procedure of image processing yielding a vector of features for each successfully processed region of interest [6, 7]. To perform objective evaluation of the bone age based on extracted features, a fuzzy logic classifier has been applied [4].

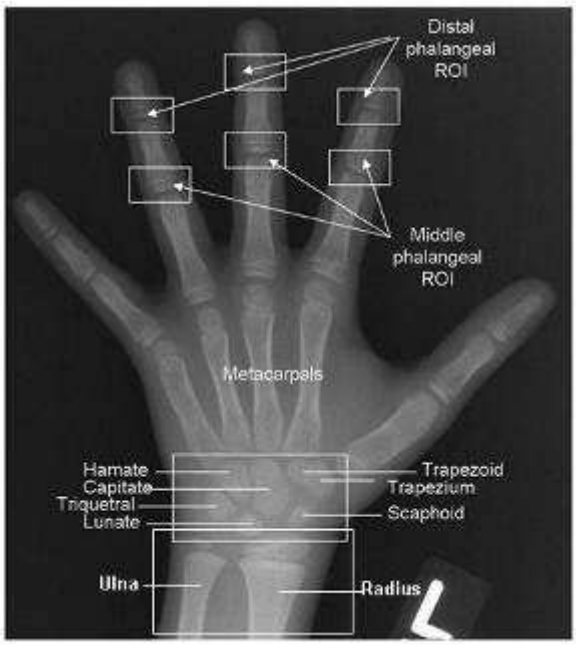

Figure 2 A hand and wrist radiograph with phalanges, carpal bones, and the wrist joints ROIs.

For cases of children 12 to18 years of age, phalangeal ROI features were successfully extracted by wavelet transformation; for cases of children 5 ~ 7 to18 of ages, phalangeal ROI features were successfully extracted by size and shape analysis. Very accurate bone age assessment was ensured for both age groups. However, for ages below 5 ~ 7, the ROI segmentation methods failed in some cases, particularly in very young children. Due to inaccuracies of hand position in the radiographs almost 10% of cases remain unprocessed. This value mainly includes X-rays performed in newborns and children below 3 years of age, where the up-right hand position is difficult to achieve. The number of unprocessed images is also increased by an additional 10% of cases where the image processing methodology was unsuccessful due to poor image quality. Hence, the bone age could not be calculated for a total of 20% of the cases. Figure 3 demonstrates the number of images for each age group in African American girls at the age ranging from newborn to 12 years old. Black bars represent the number of images per age group and white bars represent the number of images which are successfully processed by phalangeal analysis.

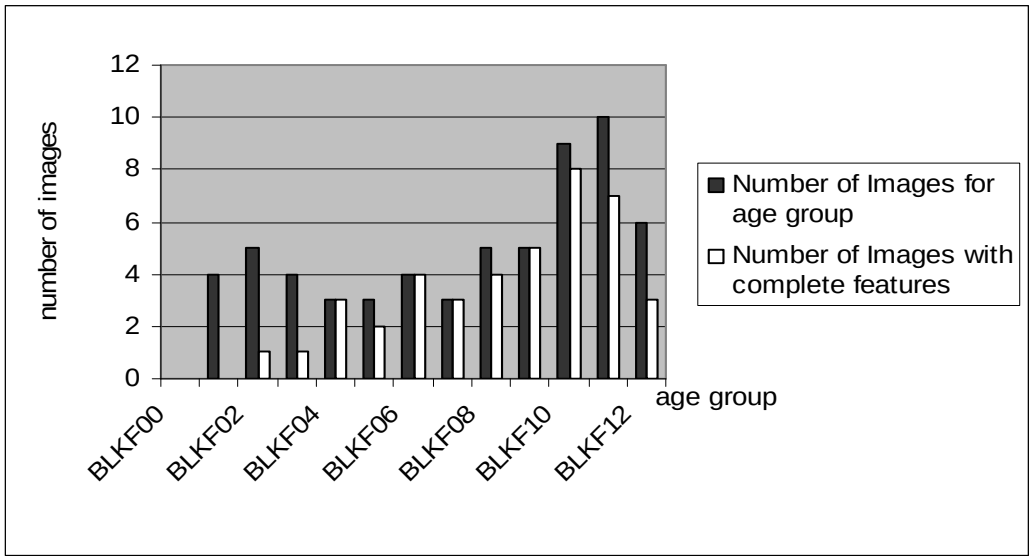

Figure 3: Images collected for African American girls by age group

Therefore in order to achieve similar degree of accuracy in bone age assessment for children of all ages, we hypothesize that the CAD method may benefit from the augmentation of features extracted from the carpal bone ROI. Table 1 shows the reliability of ROI analysis for different age groups in CAD method. This paper proposes to augment the bone age assessment method by using a novel carpal bone ROI analysis with the existing phalanges ROI analysis to improve the accuracy of computerized bone age assessment and adding the features of carpal bones ROI to the phalangeal ROI feature space. Before the carpal bones start to overlap, the carpal bone segmentation and feature extraction could be very reliable.

Table 1. Reliability of ROI analysis for different age groups in CAD method.

ROI / Age group (years)	Phalangeal ROI Analysis	Carpal ROI Analysis
0 – 5 (female) 0 – 7 (male)	Size & shape analysis of epi-metaphysis - Feature extraction is not reliable	Size & shape analysis of carpal bones - Feature extraction is reliable
6 – 12 (female) 8 – 12 (male)	Size & shape analysis of epi-metaphysis - Feature extraction is reliable	Degree of overlapping of carpal bones - Feature extraction is not reliable
13 – 18 (female & male)	Degree of fusion of epi-metaphysis - Feature extraction is highly reliable	

This paper described a knowledge-based carpal ROI analysis for fully automatic carpal bone segmentation and feature analysis for bone age assessment by fuzzy classification.

3. DATA COLLECTION

We have acquired a total of 1,103 digitized hand images of normally developed children, 5 images for each group of pre-pubertal children and 10 images for children during puberty from the Childrens Hospital Los Angeles (CHLA) [19]. The cases were grouped accordingly to sex and age. Thus there are 19 clusters (newborn, 1 – 18) in eight categories (i.e. Caucasian, African-American, Hispanic, and Asian). In order to evaluate and compare other findings, two readings were performed by radiologists for all images collected in the database. All the films were digitized using laser scanner and stored in DICOM (Digital Imaging and Communications in Medicine) format.

A normal image collection is a key issue in the hand atlas. Two radiologist experts were asked for independent readings of our collected image data. The image was accepted only when both readings fall within the standard deviation of the corresponding image in the book atlas.

4. CARPAL BONE SEGMENTATION METHODOLOGY

The workflow of carpal ROI analysis procedure which includes seven steps is shown in Figure 4. The carpal bone region of interest was first extracted from the entire hand image (Figure 1, 1). Due to the non-uniform background and noise, the carpal bone ROI was subjected to an anisotropic diffusion filter (2) which smoothed out the noise and preserves the edges at the same time. Then, the object contours were extracted by the Canny edge detector (3). A series of knowledge-based operations based on morphological properties of segmented objects were implemented in order to single out the carpal bones by eliminating the non-carpal bones (4). The carpal bones contours went through feature extraction phase which yields the inputs into the fuzzy classifiers to assess the bone age (5, 6, 7). This section discusses the procedure in the following order: carpal bone segmentation, carpal bone identification, feature analysis and bone age assessment using fuzzy logic.

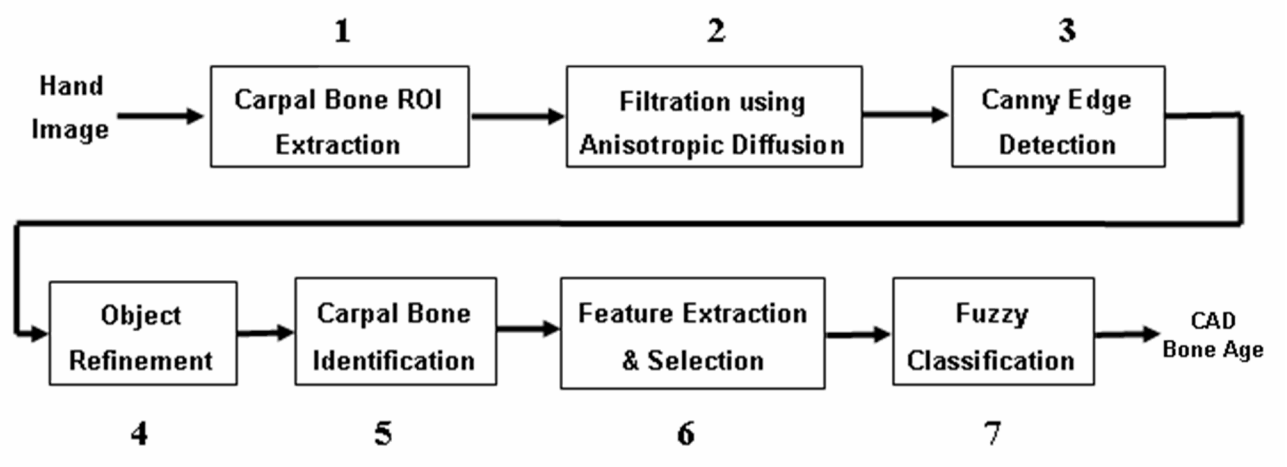

Figure 4 Carpal ROI analysis workflow with 7 steps

4.1 Carpal Bone ROI Extraction

The carpal bone ROI was located and extracted before the segmentation procedure. Robust image preprocessing needs to be developed to handle the difficulty in positioning the hand of the subject adhering to the image acquisition protocol. The entire hand image is divided into four quarters, and the background is estimated based on the histogram of each quarter. The corrected image after background subtraction undergoes adaptive thresholding which yields the binary image. Various labels, markers or clips might be placed within the radiation field. Therefore, the objects in the binary image are labeled and the small objects are removed based on the size and shape of the objects. The outcome image is the hand silhouette. Analyzing the hand silhouette, the carpal bone region of interest (CROI) is located. The upper edge of the CROI is found by scanning a horizontal line and searching for the junction between the second and third metacarpal bone. Perpendicular to the upper edge of the image, starting from its middle, two lines are scanned one pixel at a time toward the left and right borders of the image. The first line on both sides that does not intersect the wrist, fixes the left and right border, respectively. The lower edge of the CROI is the line that intersects the forearm with the minimal width. It is determined by scanning the forearm, one line at a time, from the proximal end of the hand and moving toward the distal end. The CROI image is defined within these four edges.

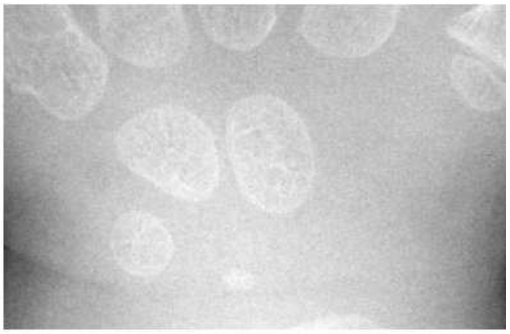

Figure 5 Carpal bone region of interest image

4.2 Anisotropic Diffusion

Carpal bones in the image are generally poor in contrast. Furthermore, the bone edges are often degraded by noise and artifacts. In order to better differentiate carpal bones from the background, an anisotropic diffusion filter proposed by Perona and Malik [12] was applied to the carpal ROI image. (Second step in Figure 4)
This filter was able to greatly reduce noise in homogeneous areas of carpal ROI images while preserving the edges and contrast associated with bony structures. Figure 6(a) and Figure 6(b) show the original carpal ROI image and the result after anisotropic diffusion filtration respectively. The comparison of profiles along one horizontal line (same position in both images) which runs across the capitate and hamate is given in Figure 6c) and 6(d). It demonstrates that noise is greatly suppressed by the diffusion process while the sharp edges are well preserved.

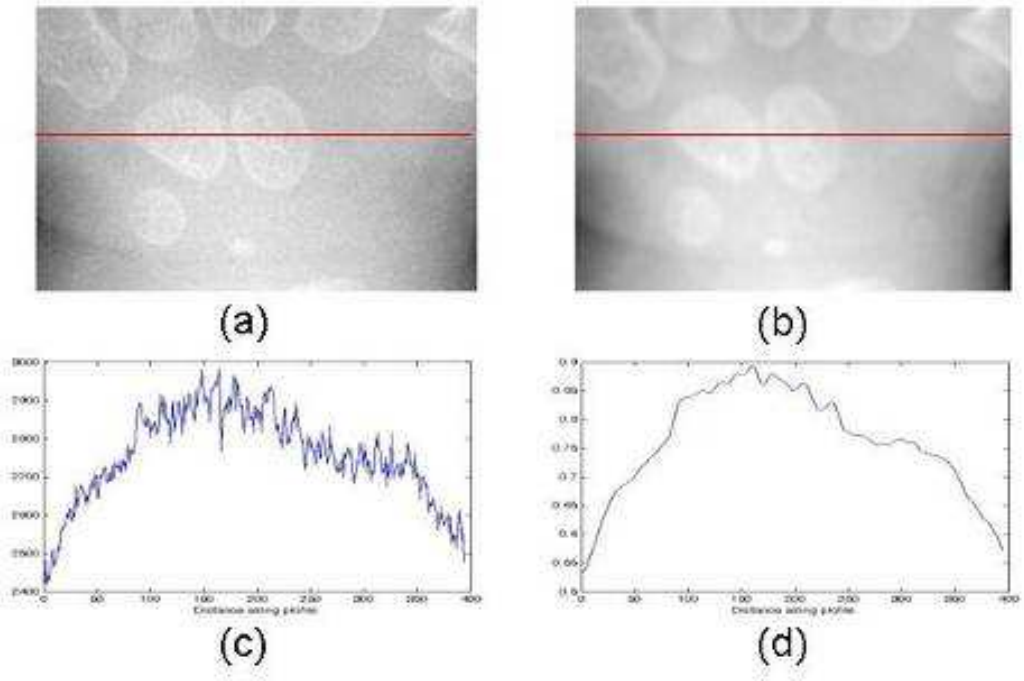

Figure 6 (a) original carpal bone ROI image (b) the result after anisotropic diffusion filtration (c) profile of the original image along the horizontal line (d) profile of the filtered image along the horizontal line

4.3 Canny Edge Detection

Edge detection by Canny method was performed on the smoothed ROI image. The Canny edge detector finds linear, continuous edges and is known as the optimal edge detector[17,18]. The Canny method differs from other edge-detection methods in that it uses two different thresholds, and includes the weak edges in the output only if they are connected to strong edges. Figure 7 shows an example of a filtered image by using the anisotropic diffusion (shown in Figure 7(b)) and the edges detected by Canny method. This method is less likely than the others to be confused by noise and the carpal bones were detected as closed-contours.

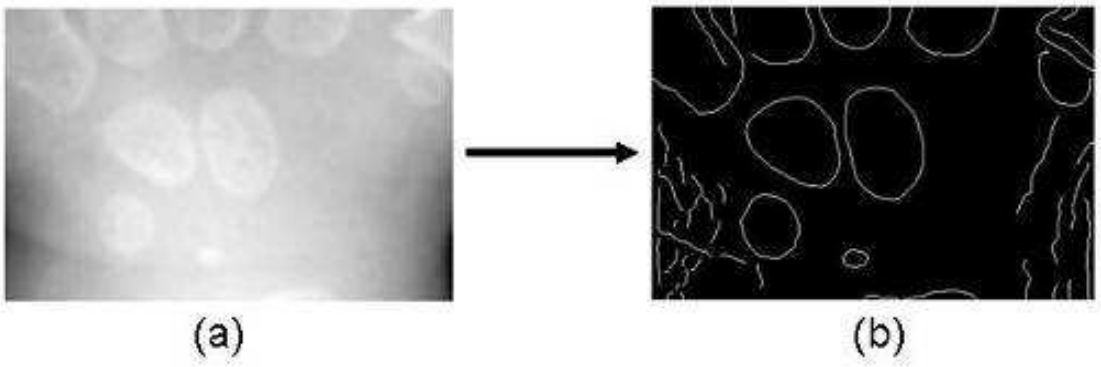

Figure 7 (a) Original smoothed image and (b) Result image after Canny edge detection

4.4 Objects Clean-up by Morphological Operations

The CROI includes carpal bones and parts of the radius, ulna, and metacarpals. Before the features that describe the carpal bones are extracted, the carpal bones themselves need to be identified from the result of Canny edge detection. In order to extract the contours of carpal bones, the contours of metacarpal bones and wrist and short lines and spots need to be removed. Knowledge-based morphological operations were used to clean-up the objects. An original image and the final result after clean-up are shown in Figure 8 (a) and (b) respectively.

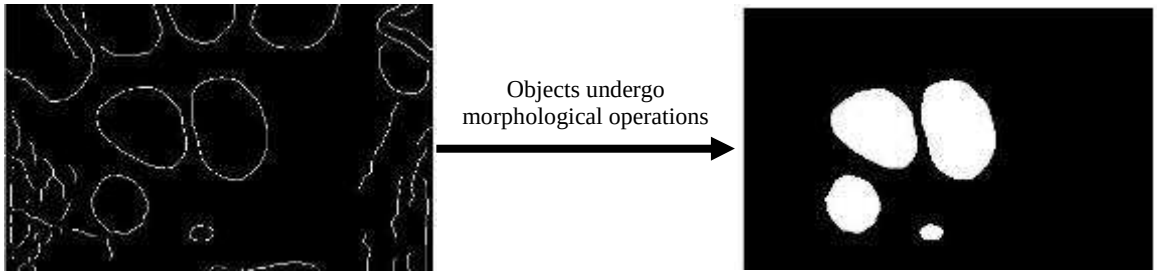

Figure 8 The goal of clean-up procedure shows four carpal bones

4.5 Model-based carpal bone identification

From the carpal bone contours, the post-processing procedure utilizing a prior knowledge was developed to identify the bones. The Capitate is the first bone to appear in chronological order and the biggest one among all the carpal bones. It is also the most reliable bone to segment out. A polar coordinate system with the origin at the center of gravity of the Capitate, which was identified as the largest object, was built. The major axis was set as the original normal axis of the polar system. The carpal ROI was then divided into five empirical regions shown in Figure 9. The positions of regions define the prior knowledge about where a carpal bone should be located in the carpal ROI.

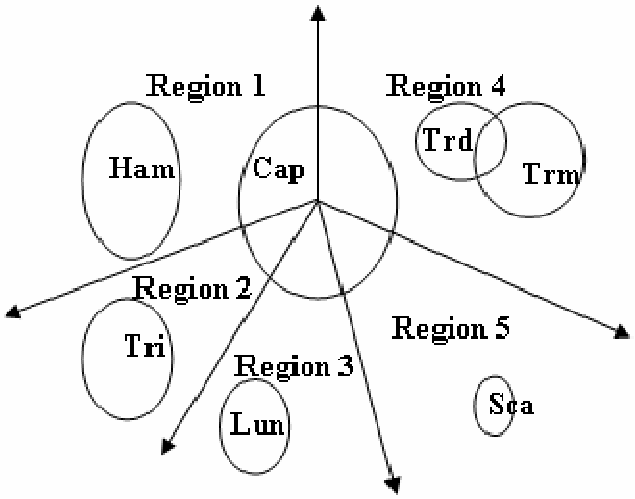

Figure 9. Carpal bone identification model. The polar coordinate system with the centroid of the capitate as the origin is divided into five regions. Based on a priori anatomical knowledge, each of which houses a carpal bone(s): Capitate, Hamate, Triquetral, Lunate, Scaphoid, Trapezium and Trapezoid

The center of gravity of each object was then computed based on polar coordinates. Each object was assigned to the region it belongs to, based on the polar angle and radius of each object. The first two bones which appear in chronological order, Capitate and Hamate, were selected for further analysis.

4.6 Feature analysis

From the identified carpal bones, features related to the bony growth were extracted for bone age assessment. To describe the size and shape of the carpal bones identified, four morphological features were extracted from Capitate and Hamate. Feature 1 measures equivalent diameter, which specifies the size of the object. An ellipse that has the same normalized second central moments as the region was found for each bone. Feature 2 is eccentricity, which value is between 0 and 1. Feature 3 is solidity. Feature 4, triangularity measures the ratio of equivalent diameter and the product of major axis length and minor axis length.

To evaluate the performance of each feature in assessing the bone age, correlation with the chronological age was analyzed. Among all the features, sizes of Capitate and Hamate have the most significant correlations with age, which are over 0.90. To simplify the feature space, all features which have the correlation above 0.60 were selected and form the feature space for bone age assessment. Table 2 shows the correlation coefficients for selected features from an example category of one race and one gender.

Table 2. Correlation coefficients for selected features. High correlation is marked with double asterisks.

	Capitate			**Hamate**		
	size	eccentricity	triangularity	size	eccentricity	triangularity
Correlation Coeff.	.94 (**)	.74(**)	-.65(**)	.92 (**)	.70(**)	-.62(**)

** p-value < 0.01, highly correlated

4.7 Bone age assessment using fuzzy logic

The last step in carpal ROI analysis is to assess the bone age using fuzzy classification based on the features extracted and selected from the Capitate and Hamate. The three features, size, eccentricity and triangularity extracted from

Capitate and Hamate each were taken as an input into the fuzzy classifier. The system was broken into smaller sub-classifiers based on Capitate and Hamate respectively. Figure 10 shows the workflow of the fuzzy classification for bone age assessment.

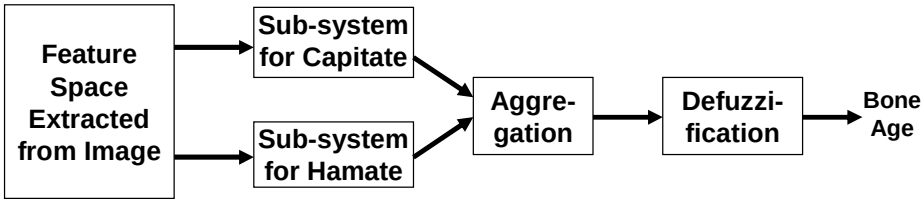

Figure 10. Fuzzy classification workflow for bone age assessment.

A final output (CAD bone age) needs to be aggregated from the sub-systems based on the Capitate and the Hamate, respectively. It was determined by finding the logic mean of the two outputs. The defuzzification process used center of gravity method to obtain a final CAD bone age.

5. RESULTS

Hand images for females of age groups from 0 to 5 and males from 0 to 7 from the entire data collection of 205 images went through the carpal ROI analysis, including carpal bone segmentation, feature extraction and fuzzy classification for bone age assessment.

Three types of tests were conducted to evaluate the performance of using the fuzzy logic for bone age assessment. Test 1 separated the data into eight categories of four races and two genders. Classifiers were trained and tested on each case from each category. Test 2 had two categories for female and male with four races combined together. Test 3 combined the entire data collection into one universal category.

For the above three tests, CAD bone age assessed by fuzzy classification was evaluated against chronological age which was taken as the gold standard as the normality of each case was ensured. The same evaluation was performed on readings. The CAD bone age results were plotted with the average reading of two radiologists against chronological age. The mean difference of each of the two readings versus chronological age or CAD bone age versus chronological age was computed by paired t-test.

The CAD results based on carpal ROI were compared with the average reading of two radiologists. Figure 11 shows the results set for eight categories from test 1. Figure 12 is the results set for two categories from test 2. Figure 13 is for the universal category from test 3. The CAD results generally follow the average reading of two radiologists comparing with the chronological age.

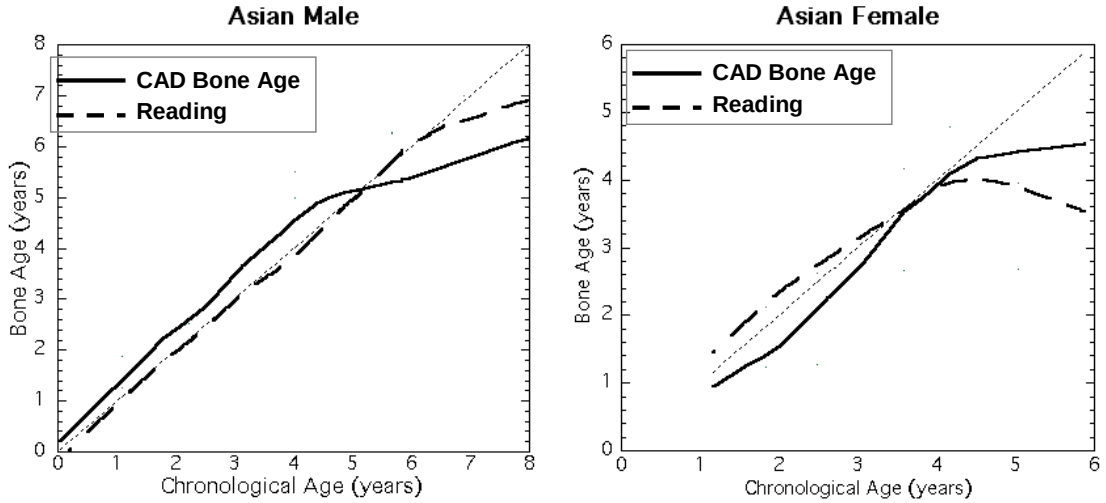

(a) (b)

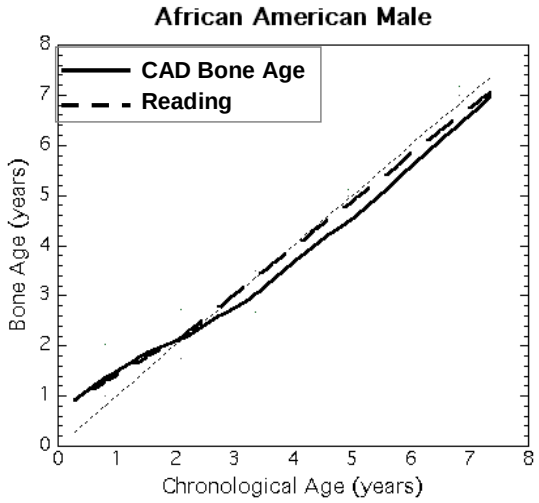
African American Male
CAD Bone Age
Reading
Bone Age (years)
Chronological Age (years)

(c)

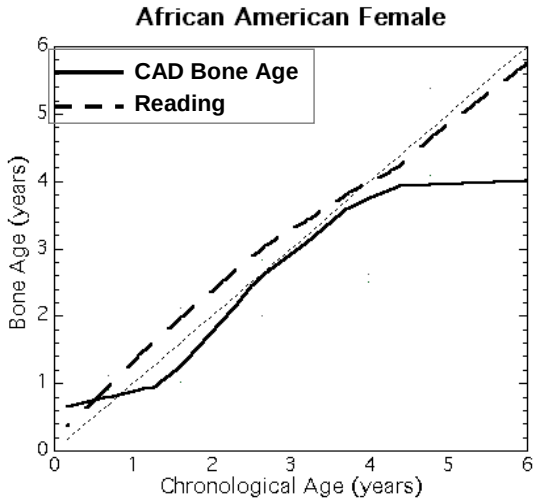
African American Female
CAD Bone Age
Reading
Bone Age (years)
Chronological Age (years)

(d)

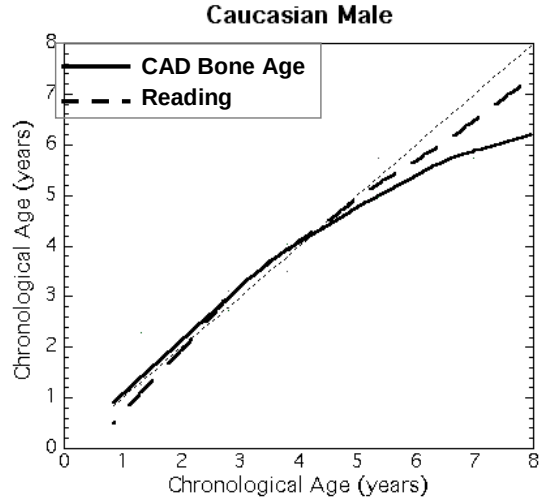
Caucasian Male
CAD Bone Age
Reading
Chronological Age (years)
Chronological Age (years)

(e)

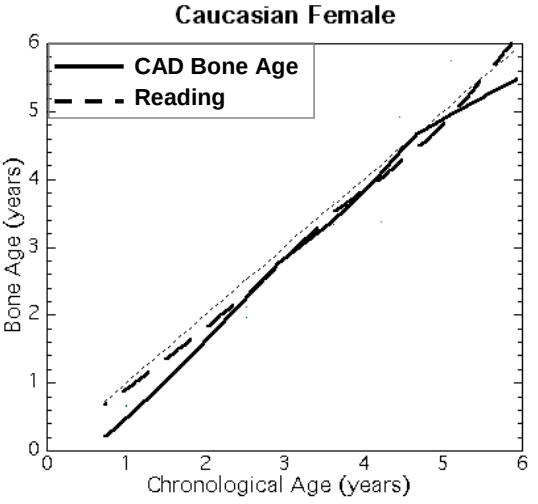
Caucasian Female
CAD Bone Age
Reading
Bone Age (years)
Chronological Age (years)

(f)

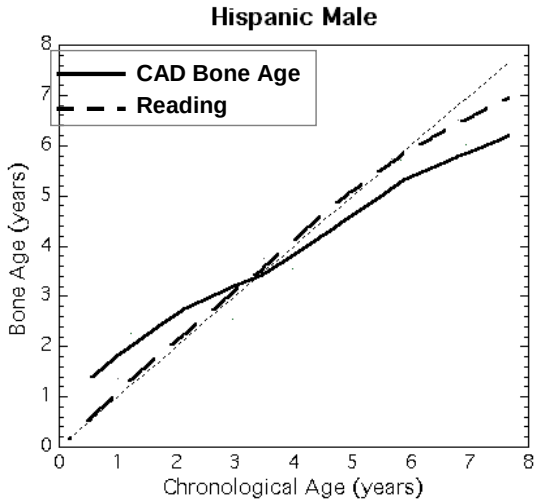
Hispanic Male
CAD Bone Age
Reading
Bone Age (years)
Chronological Age (years)

(g)

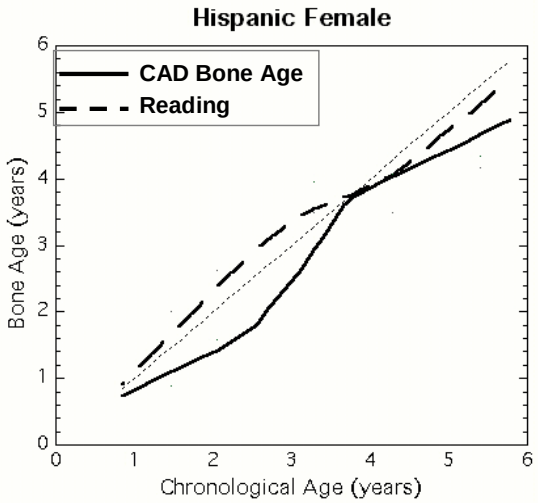
Hispanic Female
CAD Bone Age
Reading
Bone Age (years)
Chronological Age (years)

(h)

Figure 11. Results from the test with race and gender separated. In each plot, the solid line represents the CAD results and dashed line represents the average reading of two radiologists. The results show that CAD result generally follows average reading of two radiologists comparing with chronological age.

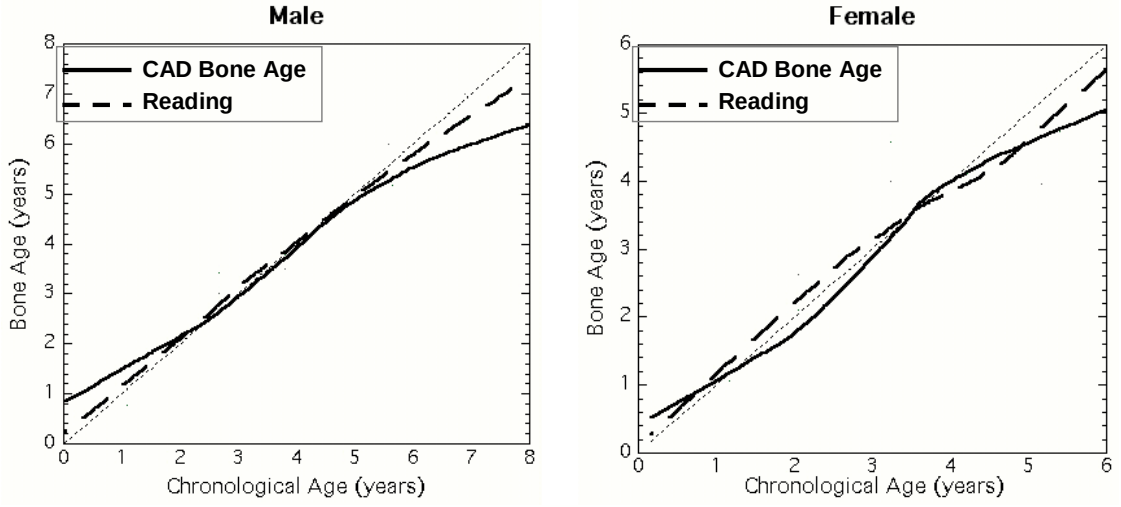

(a) (b)

Figure 12. Results from the test for two genders with four races combined. In each plot, the solid line represents the CAD results and dashed line represents the average reading of two radiologists. The results show that CAD result generally follows average reading of two radiologists comparing with chronological age.

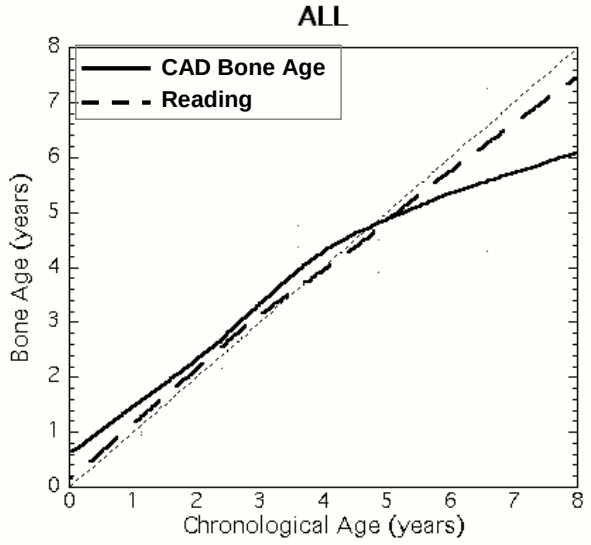

Figure 13. Results from the test for one universal category with both races and genders combined. In this plot, the solid line represents the CAD results and dashed line represents the average reading of two radiologists. The results show that CAD result generally follows average reading of two radiologists comparing with chronological age.

6. DISCUSSIONS AND CONCLUSIONS

A method of carpal ROI determination, carpal bones segmentation, feature extraction and fuzzy classification for bone age assessment was developed and tested on the 205 young children from the data collection in the digital hand atlas. The percentage of successfully processed cases was improved significantly over the one with phalangeal ROI analysis only. This demonstrates that the feature extraction of carpal ROI is reliable for young children.

The CAD results by fuzzy classification were evaluated by comparison with readings and chronological age. The CAD results based on carpal ROI features follow the readings comparing with chronological age. The results verified the value of carpal ROI in assessment of skeletal development for young children.

ACKNOWLEDGMENT

This work has been supported by NIH R01 EB 00298.

REFERENCES

1. W. Grelich, S. Pyle, *Radiographic Atlas of Skeletal Development of Hand Wrist*, Stanford, CA: Stanford University Press, 1959.
2. D. Kirks, *Practical Pediatric Imaging*, Diagnostic Radiology of Infants and Children, (Little, Brown & Company, Boston/Toronto), 1st ed., 1984, chap. 6, pp. 198-201.
3. J.M. Tanner, R.H Whitehouse, *Assessment of Skeletal Maturity and Prediction of Adult Height (TW2 Method)*, Academic Press, London, 1975.
4. E. Pietka, S. Pospiech, A. Gertych, F. Cao, *Integration of Computer Assisted Bone Age Assessment with Clinical PACS*, Computerized Medical Imaging and Graphics, 1-12, 2002.
5. F. Cao, HK. Huang, E. Pietka, V. Gilsanz, *Digital Hand Atlas and Web-based Bone Age Assessment: System* Design and Implementation, Computerized Medical Imaging and Graphics, 297-307, 2000.
6. H.K. Huang, *Picture Archiving and Communication Systems: Principle and Applications*, Wiley & Sons, NY, p. 521, 1999.
7. A. Zhang, et al. *Data Mining for Average Images in a Digital Hand Atlas.* Proceedings of SPIE Medical Imaging, Vol. 5371, pp. 251-258, February 2004.
8. E. Pietka, A. Gertych, S. Pospiech, F. Cao, HK. Huang, V. Gilsanz, *Computer Assisted Bone Age Assessment: Image Processing and Epiphyseal/Metaphyseal ROI Extraction*, IEEE Trans. Medical Imaging, 20, 715-729, 2001.
9. E. Pietka, S. Pospiech, A.Gertych, F. Cao, H.K. Huang, V. Gilsanz, *Computer Automated Approach to the extraction of epiphyseal regions in hand radiographs*, Journal of Digital Imaging, 14, 165-172, 2002.
10. F. Cao, HK. Huang, E. Pietka, V. Gilsanz, P. Dey, A. Gertych, S. Pospiech, *An Image Database for Digital Hand Atlas*, SPIE Medical Imaging, vol 5033, 461-470, 2003.
11. S. Pospiech-Kurkowska, E. Pietka, F. Cao, H.K. Huang, *Fuzzy System for the Estimation of the Bone Age from Wavelet Features*, Proc. BIOSIGNAL 2002, Brno, 441-443, 2002.
12. E. Pietka, A. Gertych, Witko K, *Remotely Accessible Computer Assisted Skeletal Maturity Assessment*, Proc. RSNA Chicago, p.807, 2004.
13. E. Pietka, A. Gertych, S. Pospiech-Kurkowska, F. Cao, HK. Huang, V Gilsanz, *Computer Assisted Bone Age Assessment: Graphical User Interface for Image Processing and Comparison*, Journal of Digital Imaging, 17(3), 175-188, 2004
14. A. Gertych, E.Piętka, *An automated segmentation and features extraction from hand radiographs*, Archive of Applied and Theoretical Informatics, vol. 15, Book 3, pp 315-326, 2003, ISSN 0867-2121.
15. K. Simmons, *Brush Foundation Study of Child Growth and Development II: Physical Growth and Development*, Periodicals Service Co, 1972.
16. P. Perona, J. Malik, "Scale-space and edge detection using anisotropic diffusion", PAMI 12(7), pp. 629-639, 1990.
17. J. F. Canny, Finding edges and lines in images, Master thesis, Massachusetts Institute of Technology, 1983.
18. J. F. Canny, A computational approach to edge detection, IEEE transaction PAMI, Vol. 8(6), p. 679, 1986.
19. A. Zhang, Arkadiusz Gertych, Brent J. Liu, H.K. Huang, Sylwia Kurkowska-Pospiech, Carpal Bone Segmentation and Features Analysis in Bone Age Assessment of Children. Proceedings of RSNA Conference, Chicago, pp. 688, 2005.
20. Ross TJ, Fuzzy Logic with Engineering Applications, 2nd edition, John Wiley & Sons Ltd, England, 2004
21. Zadeh LA, Fuzzy sets, Information and Control, Vol. 8, pp. 338-353, 1965
22. Zadeh LA, Fuzzy Logic, Computer, Vol. 1, No. 4, pp. 83-93, 1988.

Utilization of a Global Data Grid Repository in CAD Assessment of Carotid Wall Thickness

Marco A. Gutierrez[a*], Jasper Lee[b] , Zheng Zhou[b] , Paulo E. Pilon[a] ,Silvia G. Lage[a]

[a]Heart Institute (InCor), University of Sao Paulo Medical School, Sao Paulo, Brazil
[b]Image Processing & Informatics (IPI) Laboratory, Department of Radiology, University of Southern California, California, USA

ABSTRACT

A CAD method of calculating wall thickness of carotid vessels addresses the time-consuming issue of using B-mode ultrasound as well as inter- and intra-observer variability in results. Upon selection of a region-of-interest and filtering of a series of ultrasound carotid images, the CAD is able to measure the geometry of the lumen and plaque surfaces using a least-square fitting of the active contours during systole and diastole. To evaluate the approach, ultrasound image sequences from 30 patients were submitted to the procedure. The images were stored on an international data grid repository that consists of three international sites: Image Processing and Informatics (IPI) Laboratory at University of Southern California, USA; InCor (Heart Institute) at Sao Paulo, Brazil, and Hong Kong Polytechnic University, Hong Kong. The three chosen sites are connected with high speed international networks including the Internet2, and the Brazilian National Research and Education Network (RNP2). The Data Grid was used to store, backup, and share the ultrasound images and analysis results, which provided a large-scale and a virtual data system. In order to study the variability between the automatic and manual definition of artery boundaries, the pooled mean and the standard deviation for the difference between measurements of lumen diameter were computed. The coefficient of variation and correlation were also calculated. For the studied population the difference between manual and automatic measurement of the lumen diameter (LD) and intima-media-thickness (IMT) were 0.12 +/-0.10 and 0.09+/- 0.06, respectively.

Keywords: CAD, Carotid Wall Thickness, Global Data Grid, inter-, intra-observer variability

1. INTRODUCTION

The use of digital imaging technology has become a key component in both basic research and clinical practice. Although advances in data acquisition technology have improved the resolution and speed at which we can collect image data, most researchers have access to a limited image repository mainly due to lack of efficient software for managing, manipulating, and sharing large volumes of data [1-4]. In general, the image collection in research and clinical studies intrinsically creates a distributed database, as it involves many hospitals and/or centers in different locations. In addition, the amount of data generated by some imaging procedures can be so large that it is not efficient to concentrate them in a single computing center. As an example, a single study to evaluate ultrasound images of the carotid for the assessment of the degree of atherosclerotic disease has an average size of 64 Mbytes (250 images, 16 sec of acquisition time). This quantity linearly increases with time and a full transfer over the network from the acquisition site to a central repository would be large enough to saturate the available commodity connections.

Despite of the problems involving the manipulation and sharing of large medical image volumes, current image acquisition equipments do not have the software or computational power for the state-of-the-art data post-processing, typically available at Computer-Aided Diagnostic systems (CAD). Typically, on-line computation is oriented towards image acquisition and reconstruction. As a result, computationally demanding tasks are performed off-line, on desktop workstations after the completion of an exam. This has the adverse consequence of delaying the interpretation and communication of radiological results and makes adoption of advanced imaging techniques inefficient for radiologists.

On the other hand, making the whole image database available to authorized users, regardless of the data distribution, would provide several advantages. For example, a CAD system could be tested and trained on a much larger data set,

* Correspondence: marco.gutierrez@incor.usp.br; phone +551130695385; fax +551130695311; Heart Institute (InCor), University of São Paulo Medical School, Av. Dr. Eneas de Carvalho Aguiar, 44, CEP-05403-000, São Paulo, BRAZIL

with an improvement of its performance in terms of both sensitivity and specificity. The CAD system could be used as a real time selector of images, with a remarkable reduction of the delay between image acquisition and diagnosis. Moreover, data associated to the images, or metadata, would be available to select the proper input for epidemiology studies or for the training of new radiologists.

In this work, we present a CAD system method to segment carotid vessels in a large scale data grid repository. The operator selects a region-of-interest (ROI) in a series of carotid images obtained from B-mode ultrasound. This set of images is convolved with the corresponding partial derivatives of the Gaussian filter. The filter response is used to compute a 2D gradient magnitude image in order to refine the vessel's boundaries. Using an active contour technique the geometry of the lumen and the plaque surface are determined automatically. The near wall media-adventitia (NWMA), far wall media-adventitia (FWMA) and far wall lumen-intima (FWLI) borders are obtained by a least-square fitting of the active contours result. The distance between NWMA and FWLI (vessel diameter) and between FWLI and FWMA (far wall intima-media thickness) are obtained for all images and the mean value is computed during systole and diastole. To evaluate the approach, ultrasound image sequences from 30 patients were submitted to the procedure. The images were stored on an international data grid repository that consists of three international sites: Image Processing and Informatics (IPI) Laboratory at University of Southern California, USA; InCor (Heart Institute) at Sao Paulo, Brazil, and Hong Kong Polytechnic University, Hong Kong. The three chosen sites are connected with high speed international networks including the Internet2, and the Brazilian National Research and Education Network (RNP2). The Data Grid enables the three sites to share the image data and to analyze the results to improve the clinical research outcome.

2. METHODS

2.1 Grid technologies

Grid technologies provide mechanisms for sharing and coordinating the use of diverse resources and thus enable the creation, from geographically and organizationally distributed components, of virtual computing systems that are sufficiently integrated to deliver desired quality of service. These technologies include a high-performance hardware and software infrastructure to provide: a) security solutions that support management of credentials and policies when computations span multiple institutions; b) resource management protocols and services that support secure remote access to computing and data resources and the co-allocation of multiple resources; c) information query protocols and services that provide configuration and status information about resources, organizations, and services; d) data management services that locate and transport datasets between storage systems and applications.

The above characteristics and requirements lead to the definition of grid protocol architecture as shown in Figure 1.

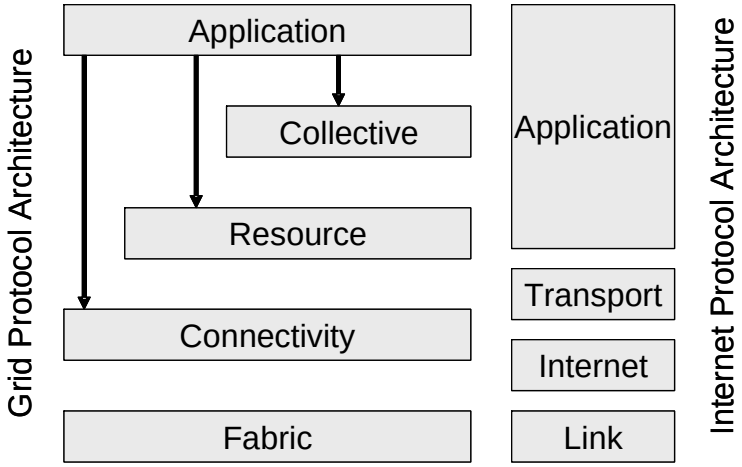

Figure 1. The layered Grid architecture and its relationship to the Internet protocol architecture

This protocol architecture defines common mechanisms, interfaces, schema, and protocols at each layer, by which users and resources can negotiate, establish, manage, and share resources. Figure 1 shows the component layers of the grid architecture and the capabilities of each layer. Each layer shares the behavior of the underlying component layers. The following describes the core features of each of these component layers:

- **Fabric layer** – defines the interface to local resources, which may be shared. This includes computational resources, data storage, networks, catalogs, software modules, and other system resources.
- **Connectivity layer** – defines the basic communication and authentication protocols required for Grid specific networking-service transactions.
- **Resource layer** – this layer uses the communication and security protocols to control secure negotiation, initiation, monitoring, accounting, and payment for the sharing of functions of individual resources.
- **Collective layer** – this layer is responsible for all global resource management and interaction with collections of resources.
- **Application layer** – enables the use of resources in a Grid environment through various collaboration and resource access protocols.

Several large-scale Data Grids, such as TeraGrid [5] and Data Replication for LIGO [6], have been established for fast movement of large amount of data among multiple research institutes. A Data Grid [7] specifically for clinical image backup and disaster recovery has been developed previously at IPI (Image Processing & Informatics Laboratory) using the Globus Toolkit 4 (GT4) [8]. This Data Grid was designed to utilize the strengths of grid technology along with PACS (Picture Archiving and Communication Systems)/DICOM (Digital Imaging and Communications in Medicine) technology for storing and distributing clinical images [9,10]. In particular, some PACS/DICOM resources are embedded within the five layer grid architecture. These include Storage services, Query services, Retrieve services, which are integrated with the DICOM standard protocols in addition to the use of other Data Grid Services. The five layer architecture of the Data Grid embedded with DICOM technology is shown in Figure 2, which illustrates some of the basic components already developed at IPI, such as the Metadata Catalog Service. The experience and knowledge learned from the Data Grid for clinical image recovery has been utilized to design the Data Grid architecture for CAD assessment of carotid wall thickness.

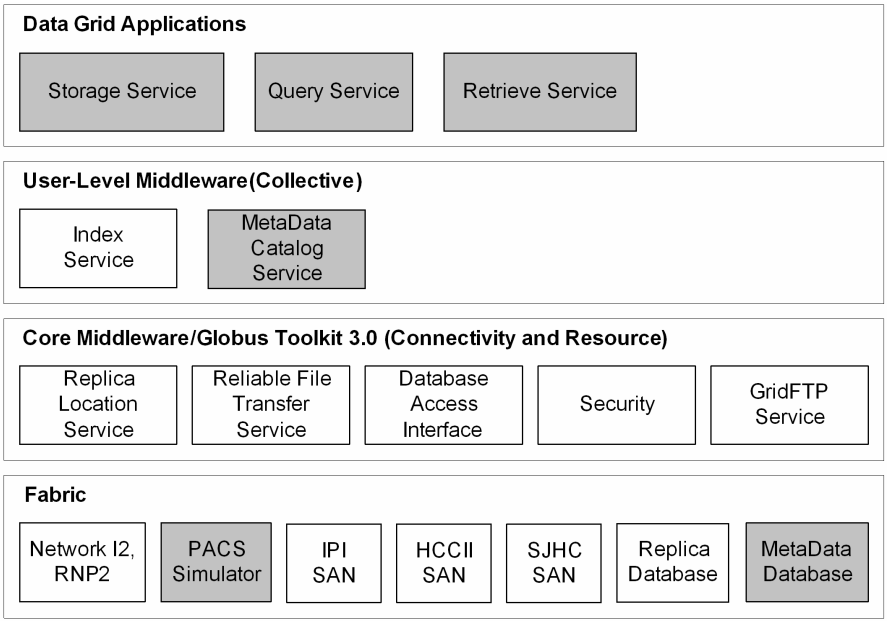

Figure 2. Five-layer architecture and the contents of the Data Grid for clinical image backup: The combination of 2nd and 3rd layers of connectivity and resource, respectively, are sometimes referred to as the Core Middleware. Gray-shaded boxes represent components developed or modified at the IPI Lab. The three services in Data Grid Applications layer are not the standard Grid Services defined in the Globus Toolkit 4.0, but are Grid Service users which use standard Grid Services plus the DICOM services.

2.2 Assessment of carotid wall thickness in ultrasound images

Non-invasive ultrasonic B-mode imaging is an increasingly important method for studying progress and regress of atherosclerotic lesions in the carotid artery. Figure 3 shows a representative B-mode ultrasound image of the carotid artery and a schematic illustration of the relevant leading edges of echo responses. Previous studies [11-13] have shown that the leading edges can be mapped to the following interfaces: near-wall intima-lumen, far-wall lumen-intima and far-wall media-adventitia. The lumen diameter (LD) is defined as the distance between the media-adventitia interface of the near-wall and the lumen-intima interface of the far-wall. The far-wall intima-media thickness (IMT) is defined as the distance between the far-wall lumen-intima and the far-wall media-adventitia interfaces.

The complete geometry of the carotid vessels can be manually determined using B-mode ultrasound. However, this approach is a time consuming procedure and based on subjective operator assessment that inevitably results in inter and intra-observer variability. Efforts have been made to make the measurement less operator dependent by introducing automated image analysis procedures.

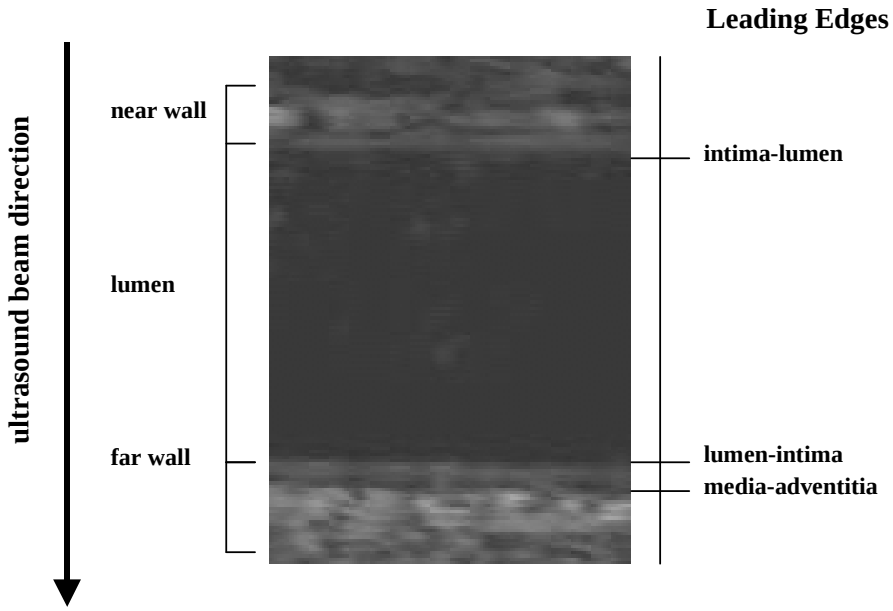

Figure 3 – Interfaces between carotid tissue layers obtained from B-mode ultrasound

2.3 Artery boundary enhancement

To enhance border detection accuracy, a multiscale border identification was implemented using filters in the form of scaled convolution operators [14,15]. The scale space of an image is constructed through convolution of the image with a two-dimensional (2D) Gaussian density kernel with zero mean and standard deviation:

$$G(\vec{x},\sigma)=\frac{1}{\sqrt{2\pi\sigma^2}^{D}}e^{-\frac{\|\vec{x}\|^2}{2\sigma^2}} \quad (1)$$

where D denotes the dimension of the input domain. A blurred replica of the original image is obtained by convolution with $G(\vec{x};\sigma)$ for a specific σ. The stack of images as a function of increasing scale parameter σ is coined a linear scale space. Hence, as σ increases the detailed object structures vanish, while gross structures persist. Figure 4 shows the 2D gradient magnitude calculated for a carotid vessel image (B-mode ultrasound) in three different scales.

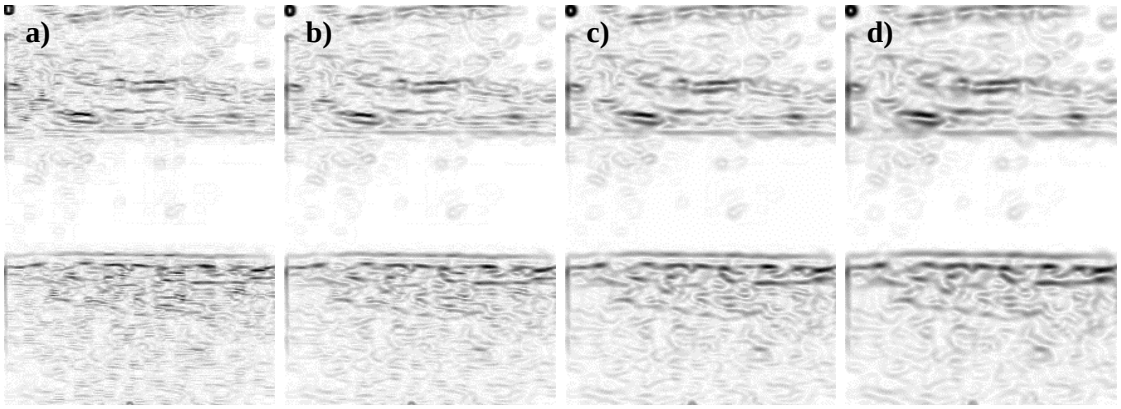

Figure 4 - 2D gradient magnitude calculated for a carotid vessel image (B-mode ultrasound) in three different scales: a) $\sigma = 0.5$; b) $\sigma = 1.0$; c) $\sigma = 1.5$; d) $\sigma = 2.0$

Based on these features a scaled artery image is used to identify the approximated position of the near and far walls. Two complementary images, based on the gradient value in y-direction are obtained: one that enhances pixel values transitions from high to low echoes, such as edges encountered in near wall tissue interfaces, and other that enhances pixel values transitions from low to high echoes (such as edges encountered in far wall tissue interfaces). Figure 5 shows the boundary enhancement of the near and far wall.

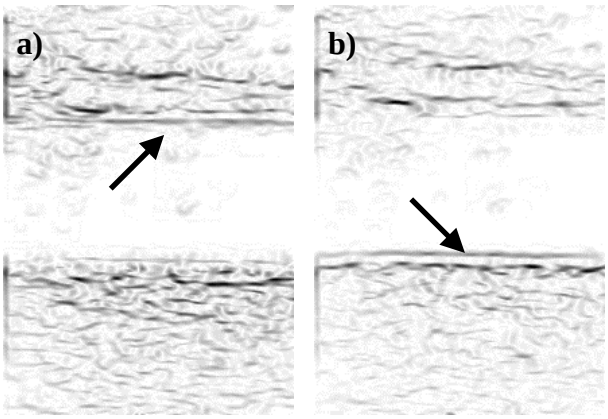

Figure 5 – Boundary enhancement of the near wall a) and far wall b)

2.4 Contour modeling

The contour of each wall is modeled following the Geometrically Deformed Model proposed by Lobregt and Viergever [9].In this model, a set of vertices which are connected by straight line segments or edges forms the basic contour structure (Figure 6). The position of a vertex V_i is represented by a vector p_i, and the edge between V_i and V_{i+1} by a vector d_i. The contour deformation is caused by a combination of forces which act on the vertices. The resulting acceleration in vertex V_i is denoted by a vector a_i.

The contour local curvature at a vertex V_i is defined as the difference between the directions of the two edge segments that join at that location:

$$\hat{c}_i = \hat{d}_i - \hat{d}_{i-1} \tag{2}$$

The local tangential unit vector $\hat{t}_i$ is defined as the normalized sum of the unit vectors of two joining edge segments:

$$\hat{t}_i = \frac{\hat{d}_i + \hat{d}_{i-1}}{\left\| \hat{d}_i + \hat{d}_{i-1} \right\|} \tag{3}$$

The local radial direction at a vertex V_i is obtained from $\hat{t}_i$ by a rotation over $\pi/2$ radians:

$$\hat{r}_i = \begin{bmatrix} 0 & 1 \\ -1 & 0 \end{bmatrix} \hat{t}_i \tag{4}$$

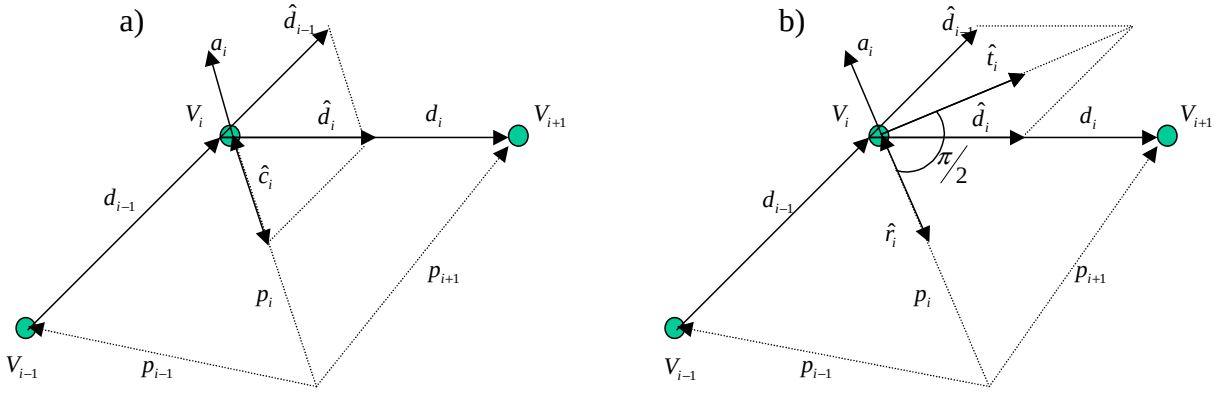

Figure 6 – Contour model consisting of a set of vertices V_i which are connected by segments or edges. The difference between the unit vectors $\hat{d}_{i-1}$ and $\hat{d}_i$ is defined as the local curvature $\hat{c}_i$ at the position of a vertex V_i. The normalized sum of the unit vectors $\hat{d}_{i-1}$ and $\hat{d}_i$ is defined as the local tangential direction $\hat{t}_i$ at the position of a vertex V_i. The local radial direction $\hat{r}_i$ is defined as a $\pi/2$ rotation of $\hat{t}_i$.

2.5 Dynamic force formulation

In the model definition, the dynamic in each vertex V_i must satisfy the Newton´s second law,

$$\begin{aligned} F_i &= F_{\text{int},i} + F_{ext,i} + F_{damp,i} \\ F_i &= \mu_i a_i \end{aligned} \tag{5}$$

where μ_i is a coefficient that has a mass unit, $F_{damp,i}$, $F_{\text{int},i}$ and $F_{ext,i}$ are the damping (or viscous), the internal and the external forces, respectively.

The internal force can be estimated from the local contour curvature along the local r-axis (Figure 6):

$$F_{\text{int},i} = \left(c_i \cdot \hat{r}_i \right) \tag{6}$$

The external force acting in each vertex can be approximated by some image feature. In this paper we used the information obtained from the local image gradient as the external force.

The damping force is proportional to the velocity of the vertex and points in opposite direction:

$$F_{damp,i} \approx -k.v_i \tag{7}$$

The total force F_i acting on a vertex is a weighted combination of damping, internal and external

$$F_i = w_{\text{int}} F_{\text{int},i} + w_{ext} F_{ext,i} + w_{damp} F_{damp,i} \tag{8}$$

where w_{int}, w_{ext} and w_{damp} are the weighting factors.

The deformation process over the contour is implemented as a numerical time integration process in which the complete state of the contour is calculated at a sequence of discrete positions in time [16,17]. A set of state equations controls the deformation process in terms of position, velocity and acceleration of each vertex on the contour:

$$\begin{cases} p_i(t+\Delta t) = p_i(t) + v_i(t) \\ v_i(t+\Delta t) = v_i(t) + a_i(t).\Delta t \\ a_i(t+\Delta t) = \dfrac{1}{m_i} F_i(t+\Delta t) \end{cases} \tag{9}$$

where $p_i(t+\Delta t)$, $v_i(t+\Delta t)$ and $a_i(t+\Delta t)$ define the position, velocity and acceleration, respectively, of the vertex in a incremental time Δt. The vertex mass, m_i, is setting constant for all vertices and the resulting force, F_i, is calculated using equation (8).

3. RESULTS

3.1 Data Collection

A sequence of B-mode ultrasound images of the carotid artery was acquired with spatial resolution of 456 x 576 pixels, 8 bits/pixel, 15 frames /sec and acquisition time of 16 sec. This setup gives an average data size of 64 Mbytes/exam (250 images). The Data Grid was used to store, backup, and to share the ultrasound images and to analyze the results, which provided a large-scale and a virtual data system. The exams were stored on an international data grid repository that consists of three international sites: Image Processing and Informatics (IPI) Laboratory at University of Southern California, USA; InCor (Heart Institute) at Sao Paulo, Brazil, and Hong Kong Polytechnic University, Hong Kong. The three chosen sites are connected with high speed international networks including the Internet2, and the Brazilian National Research and Education Network (RNP2). The Data Grid enables the three sites to share the image data and to analyze the results to improve the clinical research outcome (Figure 7).

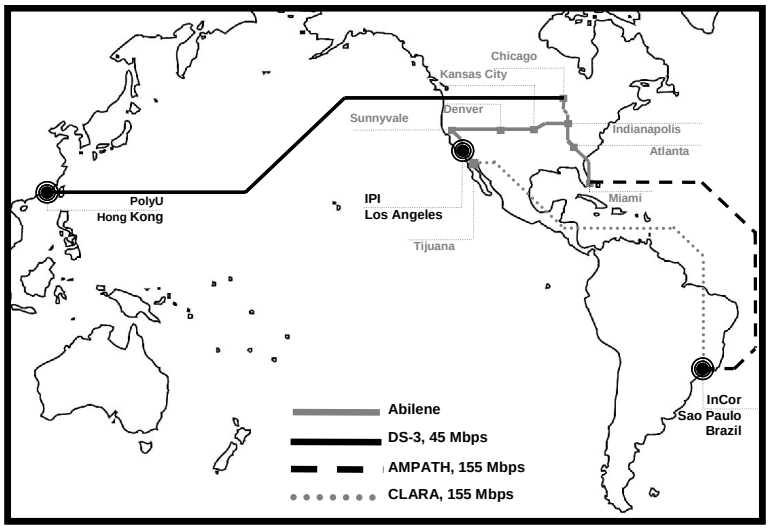

Figure 7 - Topology of the International Internet-2 Connectivity Between the Three Sites Linking IPI/USC in North America, InCor in South America, and PolyU in Asia. Note that the Routing Path from InCor to PolyU utilizes AMPATH instead of CLARA which is the routing path between IPI and InCor.

3.2 Evaluation procedure

After the retrieval of an exam previously stored in the Data Grid, the operator selects a region-of-interest (ROI) in a series of carotid images. This set of images is convolved with the corresponding partial derivatives of the Gaussian filter. The filter response is used to compute a 2D gradient magnitude image in order to refine the vessel's boundaries. Using an active contour technique the geometry of the lumen and the plaque surface are determined automatically. The near wall media-adventitia (NWMA), far wall media-adventitia (FWMA) and far wall lumen-intima (FWLI) borders are obtained by a least-square fitting of the active contours result. The distance between NWMA and FWLI (vessel diameter) and between FWLI and FWMA (far wall intima-media thickness) are obtained for all images and the mean value is computed during systole and diastole.

In this evaluation a total of 180 images from 30 patients (3 images in diastole and 3 images in systole for each patient) were analyzed, all of which included manually defined interfaces for reference. The minimum and maximum artery diameters were measured for each patient using the manual and the automatic procedure. However, for clinical purposes, some interactive tools for manual tracing were incorporated to the model to correct remaining detection errors in regions with poor image quality. In order to study the variability between the automatic and manual definition of artery boundaries, the pooled mean, $\overline{\mu}$, and the standard deviation, σ, for the difference between automated and manual measurements of lumen diameter were computed. The coefficient of variation, CV, was calculated according to:

$$CV = \left(\frac{\sigma}{\overline{\mu}\sqrt{2}} \times 100 \right)\% \tag{11}$$

The strength of the relationship between automated and manual methods is indicated by the correlation, $R_{a,m}$, between the two measurements:

$$R_{a,m} = \frac{Cov_{a,m}}{\sigma_a . \sigma_m} \tag{12}$$

where $Cov_{a,m}$ is the covariance between the automated and manual and σ_a and σ_m are the standard deviation of automated and manual measurements, respectively.

The means ($\mu_{a,m}$) and standard deviations ($\sigma_{a,m}$) for the differences between the automatic and manual methods were calculated for the population (n=30). The coefficients of variability ($CV_{a,m}$) and the correlation ($Corr_{a,m}$) between both methods were also obtained.

The results obtained for the parameters $\mu_{a,m}$, $\sigma_{a,m}$, $CV_{a,m}$ and $Corr_{a,m}$ are summarized in Table 1.

Table 1. Lumen diameter (LD) and Intima-Media Thickness (IMT) measured using automatic and manual methods (n=30). The difference, Δ, the coefficient of variability, CV and the correlation, $Corr_{a,m}$, between both measurements are also presented

	Automatic $\mu_a \pm \sigma_a$ (mm)	**Manual** $\mu_m \pm \sigma_m$ (mm)	**Difference** Δ $\mu_{a,m} \pm \sigma_{a,m}$ (mm)	Variability CV (%)	Correlation $Corr_{a,m}$
Lumen Diameter (diastole)	7.85 ± 1.01	7.78 ± 1.01	0.13 ± 0.09	0.83	0.99
Lumen Diameter (systole)	6.81 ± 1.06	6.77 ± 1.05	0.12 ± 0.10	1.00	0.99
Intima-Media Thicknes	0.72 ± 0.14	0.63 ± 0.12	0.09 ± 0.06	6.16	0.90

4. DISCUSSION

Measurements of lumen diameter (LD) and intima-media thickness (IMT) of carotid and femoral arteries from B-mode ultrasound are defined as the average distance of interfaces between vessel tissue layers. In order to determine the interface location a manual tracing is commonly used. However, this approach is a time consuming procedure and based on subjective operator assessment. This procedure, inevitably results in inter and intra-observer variability. This is due to the complex nature of the echogenic zones, mainly at the lumen-intima interface, which frequently present weak echoes, echo dropouts and irregularities caused by scattering.

We have proposed a method that uses the active contour technique where the external forces are proportional to the local image gradient obtained from a multiscale analysis. The automated measurements, when compared to those obtained by manual tracing, are equally accurate and the coefficients of variability between both methods are below 1.0% for Lumen Diameter and 6.5% for Intima-Media thickness measurements. However, for clinical purposes, some interactive tools for manual tracing may still be need in order to correct remaining detection errors due to poor image quality.

In this paper, we present a Data Grid testbed with three international sites for store, query and retrieve medical images. The laboratory prototype of this DICOM compliance Data Grid has been completed. Currently, the three International sites have been connected, and we are implementing the Data Grid at the Hong Kong Polytechnic University, and the Heart Institute at Sao Paulo, Brazil.

Once the Data Grid testbed for research and clinical study is established, we can incorporate the multiple trials databases into the Data Grid in the future. The multiple trials databases are equally important as the image data. Such a Data Grid can provide three benefits to the trials databases: 1) fault-tolerance, 2) data and result sharing using for instance the DICOM Structured Reporting, and 3) dynamic creation and modification of data model to support any new trial or change of trials.

ACKNOWLEDGEMENTS

This work has been supported by Grant #2436 of the National Network for Education and Research (RNP), the National Council for Scientific and Technological Development (CNPq), Grant No. 300499/2005-1 and the Zerbini Foundation.

REFERENCES

1. R. Bellotti, P. Cerello, S. Tangaro, V. Bevilacqua, M. Castellano. Distributed medical image analysis on a Grid infrastructure. Future Generation Computer Systems, 23:475-484, 2007.
2. J.C. Crane, F.W. Crawford, S.J. Nelson. Grid enabled magnetic resonance scanners for near real-time medical image processing. Journal of Parallel and Distributed Computing, 66:1524-1533, 2006.
3. B. Marovie, Z. Jovanovie. Web-based grid-enabled interaction with 3D medical data. Future Generation Computer Systems, 22:385-392, 2006.
4. S. Hastings, S. Oster, S. Lancella, T.M. Kurc, T. Pan, U.V. Catalyurek, J.H. Saltz. A Grid-based image archival and analysis system. Journal of the American Medical Informatics Association, 12(3):287-295, 2005.
5. TeraGrid, http://www.teragrid.org/, accessed on March 14, 2006.
6. Large-scale Data Replication for LIGO, http://www.globus.org/solutions/data_replication/, accessed on March 14, 2006.
7. B.J. Liu, M.Z. Zhou and J. Documet, Utilizing data grid architecture for the backup and recovery of clinical image data, Computerized Medical Imaging and Graphics 29 (2005), 95-102.
8. I. Foster, Globus Toolkit Version 4: Software for Service-Oriented Systems, IFIP International Conference on Network and Parallel Computing, Springer-Verlag LNCS 3779, 2005, 2-13.
9. H.K. Huang, PACS and Imaging Informatics: Basic Principles and Applications, Wiley & Sons, NJ, 2004.
10. B.J. Liu, F. Cao, M.Z. Zhou, G. Mogel and L. Documet, Trends in PACS Image Storage and Archive, Computerized Medical Imaging and Graphics 27 (2003), 165-174.
11. C.P. Loizou, C.S. Pattichis, M. Pantziaris, T. Tyllis, A. Nicolaides. Quality evaluation of ultrasound imaging in the carotid artery based on normalization and speckle reduction filtering. Med. Bio. Eng. Comput., 44:414-426, 2006.
12. C. Liguori, A. Paolillo, A. Pietrosanto. An automatic measurement system for the evaluation of carotid intima-media thickness. IEEE Transaction on Instrumentation and Measurement, 50(6):1684-1685, 2001.
13. A. Zahalka, A. Fenster. An automated segmentation method for three-dimensional carotid ultrasound images. Physics in Medicine and Biology, 46:1321-1342, 2001.
14. J.J. Koenderink. The structure of images. Biological Cybernetics 1984;50:363-370.
15. T. Lindeberg. Discrete derivation approximations with scale-space properties: a basics for low-level feature extractions. Journal of Mathematical Imaging and Vision, 1993;3:349-376.
16. S. Lobregt, M. Viergever. A discrete dynamic contour model. IEEE Trans. Medical Imaging, Vol.14, No. 1, pp.12-24, 1995.
17. D.Terzopoulos, M. Vasilescu. Adaptive surface reconstruction. SPIE, vol. 1383, pp. 257-264, 1990.

A Knowledge-Based Imaging Informatics Approach to Managing Patients Treated with Proton Beam Therapy

B. J. Liu[1], H.K. Huang[1], M. Law[2], Anh Le[1], Jorge Documet[1], Arek Gertych[1]
[1]Image Processing & Informatics Laboratory, Dept. of Radiology, Keck School of Medicine, USC, Marina del Rey, 90292
[2]Hong Kong Polytechnic University, Hong Kong, China

ABSTRACT

Last year we presented work on an imaging informatics approach towards developing quantitative knowledge and tools based on standardized DICOM-RT objects for Image-Guided Radiation Therapy. In this paper, we have extended this methodology to perform knowledge-based medical imaging informatics research on specific clinical scenarios where brain tumor patients are treated with Proton Beam Therapy (PT). PT utilizes energized charged particles, protons, to deliver dose to the target region. Protons are energized to specific velocities which determine where they will deposit maximum energy within the body to destroy cancerous cells. Treatment Planning is similar in workflow to traditional Radiation Therapy methods such as Intensity-Modulated Radiation Therapy (IMRT) which utilizes *a priori* knowledge to drive the treatment plan in an inverse manner. In March 2006, two new RT Objects were drafted in a DICOM-RT Supplement 102 specifically for Ion Therapy which includes Proton Therapy. The standardization of DICOM-RT-ION objects and the development of a knowledge base as well as decision-support tools that can be add-on features to the ePR DICOM-RT system were researched. We have developed a methodology to perform knowledge-based medical imaging informatics research on specific clinical scenarios. This methodology can be used to extend to Proton Therapy and the development of future clinical decision-making scenarios during the course of the patient's treatment that utilize "inverse treatment planning". In this paper, we present the initial steps toward extending this methodology for PT and lay the foundation for development of future decision-support tools tailored to cancer patients treated with PT. By integrating decision-support knowledge and tools designed to assist in the decision-making process, a new and improved "*knowledge-enhanced* treatment planning" approach can be realized.

Keywords: DICOM, DICOM-RT, DICOM-RT-ION, ePR, Decision-Support, Image-Guided Proton Therapy

1. INTRODUCTION

Proton Beam Therapy (PT) is a particular treatment that utilizes energized charged particles, protons, to deliver dose to the target region. Protons are energized to specific velocities which determine where they will deposit maximum energy within the body to destroy cancerous cells, allowing for maximum dose to the target region while minimizing dose to surrounding tissues. This is due to the fact that the Proton Depth Dose (Bragg Peak) is inversely proportional to the square of the particle velocity. In comparison, Photon Depth Dose is proportional to an exponential function. [1,2] Figure 1 shows a comparison between 6MV Photons from a Linear Accelerator utilized in traditional radiation therapy and different energy Protons. Each of the different energy protons have minimal dose in water but deposit their maximum dose at a target depth. This translates to less dose to normal healthy tissue in the body while depositing most of the energy within the target tumor located at a certain depth within the body. In addition, proton beams have no exit dose which also minimizes damage to health tissue beyond the target tumor. Proton Therapy is especially effective for types of cancer that require controlled high concentration dose and tumors that are close to sensitive tissue. Some examples of the types of cancer treated include: Prostate, Brain, Spinal Cord, Head and Neck, Base of Skull, Eye, Lung, and tumors in children.

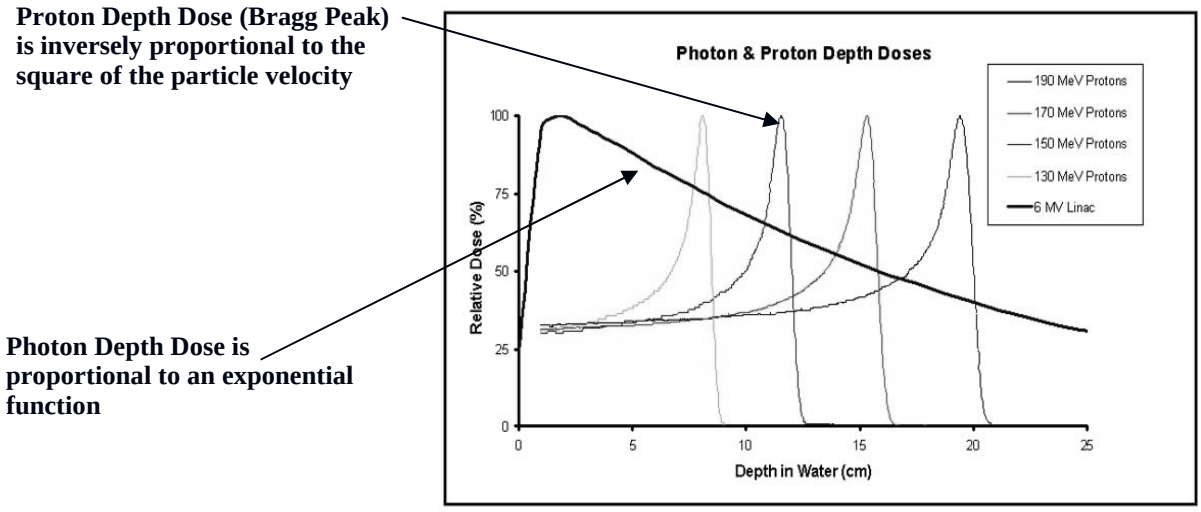

Figure 1: Graph showing a comparison between Photon Depth Dose (6MV) and Proton Depth Dose (130, 150, 170, 190 MeV) percentages as measured in water. The maximum dose from the proton can be deposited at a certain depth. This can be utilized to treat cancer tumors at a certain depth while minimizing dose to surrounding normal health tissue.

Similar to traditional Radiation Therapy (RT), complex clinical imaging and informatics data are generated during the treatment process that guide the planning and the success of the treatment. In addition, there are few PT sites across the country due to the complex and expensive system requirements which include a synchrotron, linear accelerator, and large rotating gantry and require a very large square area footprint. Loma Linda University Medical Center (LLUMC) was the first to open a clinical PT treatment center and began treating patients starting October 1990. There are now facilities in Bloomington, IN; Boston, MA; with emerging sites in Houston, TX and the East coast, as well as established international sites [2]. The need for a standardized and centralized clinical data repository and integrated system with proper data distribution to manage cancer patients becomes crucial. Distances between PT sites and the proprietary nature of vender-of-choice between PT sites will undoubtedly lead to a similar fate as the fractured industry market in RT. Therefore, initiating this integrated system for PT is not only timely, but urgent in order to prevent this. In addition, as new PT facilities come online, global distribution of standardized data for information sharing of best practice can impact a greater adoption of this type of treatment for cancer patients. An integrated system of standardized data can serve as the mandate for future PT sites and drive the industry, ultimately reducing costs, improving clinical efficiency, and patient outcomes.

In this paper, we present the initial steps towards extending the medical imaging informatics methodology to develop decision-support knowledge for managing cancer patients treated with PT. We have established a research collaboration with LLUMC to develop the first prototype system. To date, over 45,000 patients have been treated with PT, of which 11,562 patients were treated at LLUMC. Of the types of cancer treated, 65% were male patients with prostate cancer, which represents the largest population of patients treated with PT anywhere in the world [3,4]. Figure 2, shows the floor plan of the Proton Treatment Center located at LLUMC. Currently, LLUMC is treating approximately 50 to 170 patients per day and up to 64 total hours of beam time making the center one of the most efficient PT facilities nationwide. By extending our knowledge-based imaging informatics methodology for cancer patients treated with PT, we can develop a knowledge base as well as decision-support tools that can be add-on features to an ePR DICOM-RT system for sharing of best practice data. This methodology can be used for future clinical decision-making scenarios during the course of the patient's treatment that utilize inverse treatment planning and an example of decision-support tools developed for IMRT presented in this paper can similarly be developed for PT. Various generic RT information/management systems feature the availability of necessary clinical data within the RT department. However, the most complete clinical data model is from the proposed DICOM-RT based ePR system of this research. Furthermore, the DICOM-RT based ePR system features open system integration based on the DICOM standard instead of proprietary like other RT information/management systems. In summary, the DICOM-RT based ePR system has the following superior features:

1) Complies with DICOM-RT Object definitions.
2) Global data distribution.
3) Global Treatment Updates.

4) Open System Integration.

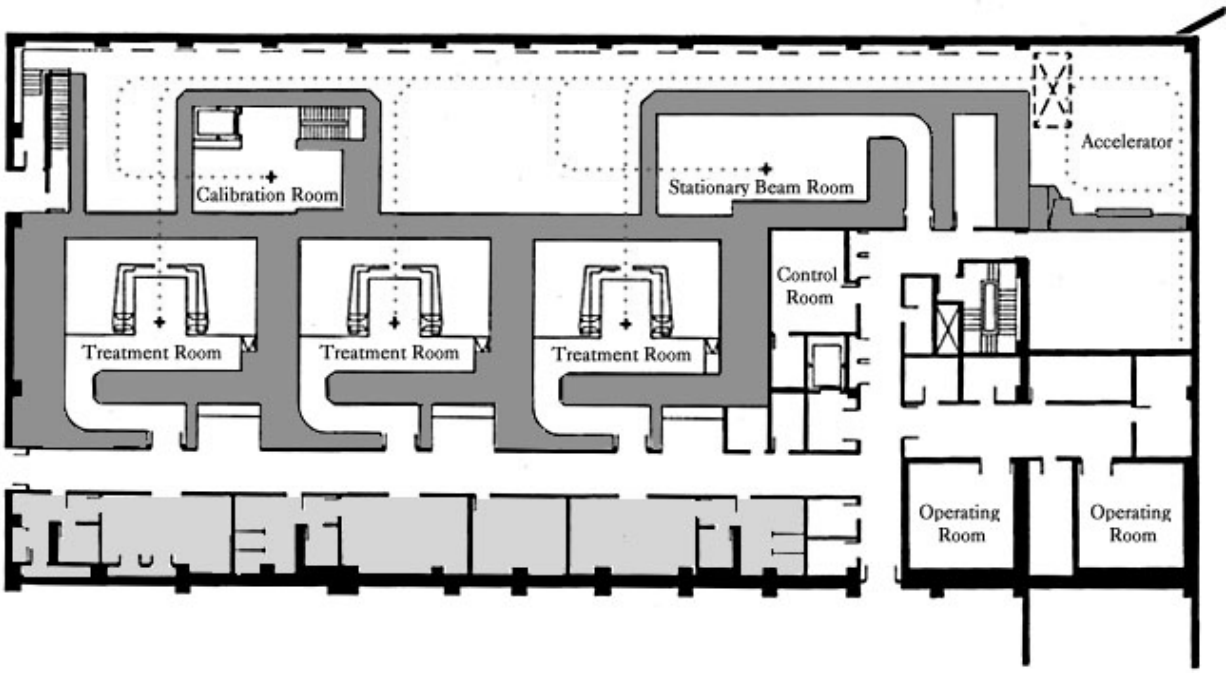

Figure 2: Floor Plan of the Loma Linda Proton Treatment Center.

2. METHODS AND MATERIALS

2.1 Medical Imaging Informatics Methodology

Figure 3 shows a summary of the methodology for standardizing PT data objects and performing Medical Imaging and Informatics research to develop the knowledge base, the data mining, and quantification and visualization tools which ultimately become add-on features to the DICOM-RT based ePR system [5]. With these decision-support tools, the end result is that clinicians can be assisted in their decision-making process for new cancer patient cases. This methodology can be applied to different lesion types as well as treatment types to quickly research and develop new decision-support tools.

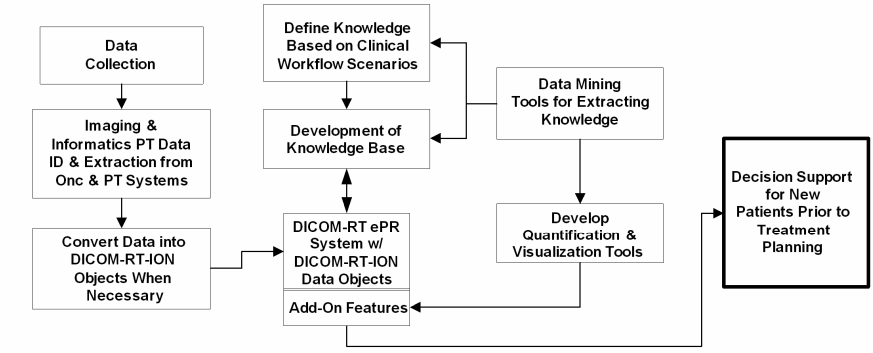

Figure 3: A Medical Imaging Informatics approach towards development of decision-support tools for the DICOM-RT based ePR system. The final results are add-on features for the ePR system to provide decision-support for new patient cases. This methodology can be applied to different lesion types as well as treatment types to quickly research and develop new decision-support tools.

2.2 Workflow Model for Proton Therapy (PT) of Cancer Patients

One of the most important first steps for system integration of clinical image and information systems is to research the workflow model of the clinical operations. Since the focus of this research will be on patients treated with PT, the workflow related to these particular treatment cases will be studied. A general clinical workflow model for PT was developed for LLUMC as shown in Figure 4.

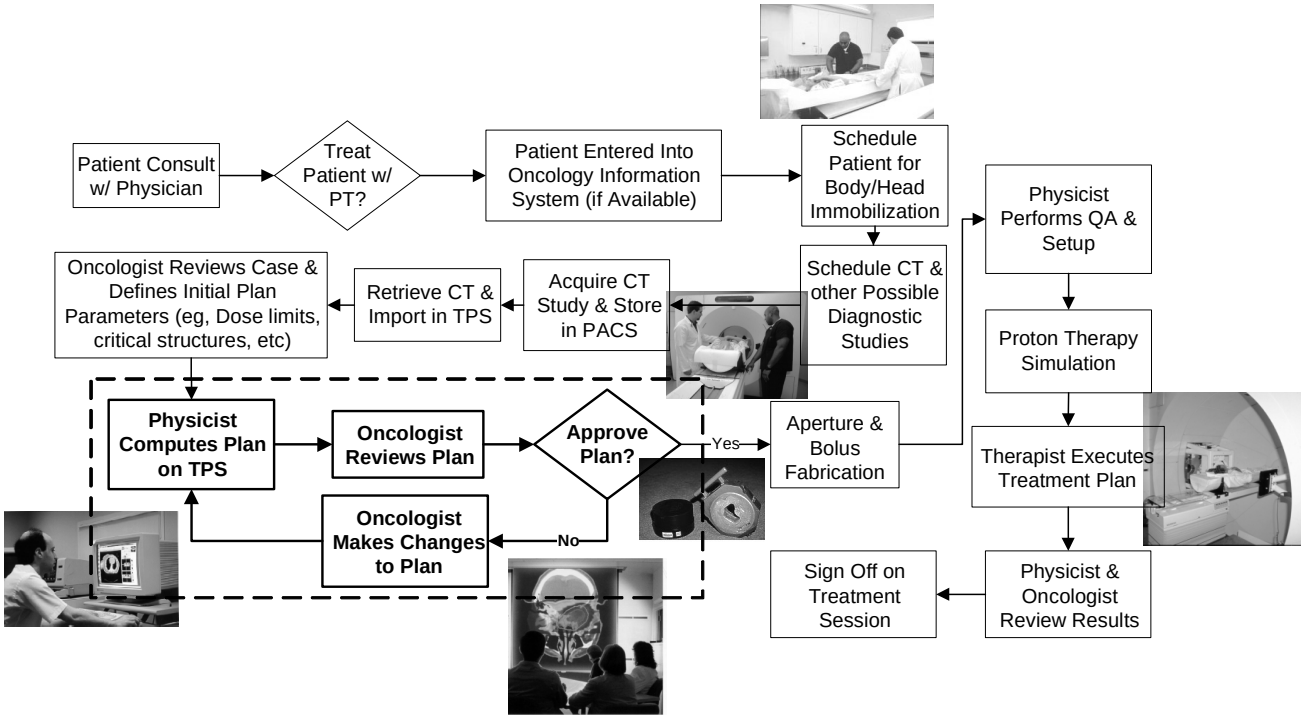

Figure 4: General Clinical Workflow for PT of Cancer Patients.

The treatment begins with the patient diagnosed with cancer lesion or multiple lesions. The patient consults with the physician(s) and determines whether to treat the tumor(s) and whether PT will be performed. The patient is entered in an oncology information system and is scheduled for treatment if the system is available, otherwise the scheduling is performed on a paper-based system. Next, the patient is scheduled for body immobilization or head immobilization. If the treatment is to be performed for the brain or head and neck, a head cage made of lightweight plastic is cast to immobilize the head during the CT scan and the actual treatment. If the body is to be immobilized, then a plastic cradle is utilized with injected foam cushioning to immobilize the body for imaging, planning, and treatment. A diagnostic CT will be acquired to plan the treatment based on the patient being immobilized. In addition, other imaging may be acquired, such as PET or MRI to help better define the cancer to be treated. Most of the time, a CT study is adequate for treatment planning. The Radiologist and Radiation Oncologist review the patient's case and then the Radiation Oncologist defines the initial plan parameters such as dose limits and constraints, critical structures, and tumor volume to be treated. The physics team then computes the plan based on these dose constraints on the corresponding TPS. Once the initial plan is computed, the Oncologist reviews the results and makes any necessary changes. This process can be iterative and the feedback loop is defined in Figure 4 by a dashed line region similar to traditional Intensity-Modulated Radiation Therapy (IMRT). Once the treatment plan has been approved, the data is used to build a 3D computer assisted bolus made of high-grade wax and apertures made from an alloy called cerrobend that will shape the proton beam for treatment of the target tumor(s). QA and setup is performed and a simulated treatment plan will be executed in order to make any fine-tuned adjustments to the overall plan. The PT session is then executed by the Radiation Therapist within the gantry and the corresponding PT plan data are stored in the treatment planning systems and some results are also inputted into the oncology information system or a Record and Verify system. Since there are a variety of tumor types, the treatment paths can differ. Therefore, it is important to research and develop a more robust workflow model that can accommodate the various treatment paths and identify points within the workflow that can be improved. Not only would this enhance the design of the DICOM-based ePR System, but also serve as the foundation for a methodology to build

quantification and visualization tools for decision-support. In this case, the iterative feedback loop is identified as a potential area of improvement. The feedback loop represents the inverse treatment planning process and can be quite tedious if much iteration is necessary. This becomes the area of focus where decision-support tools may benefit during the decision-making. If more *a priori* knowledge and robust quantification and visualization tools can be included during the decision-making process of the initial plan parameters, then it is possible to reduce the iterative process.

2.3 DICOM-RT-ION Data Model Development and Data Collection

The DICOM (Digital Communication in Medicine) standard has been well established and widely successful for clinical imaging systems in Radiology, in particular PACS (Picture Archiving and Communication System). Image data acquired from equipment from different vendors can readily communicate with each other and integrate into a system through the DICOM standard. In 1997, the DICOM standard was extended to include radiotherapy information and further updated in the latest version released in 2003. [6] Seven DICOM radiotherapy (DICOM-RT) objects have been included by the DICOM standards committee for transmission and storage of radiotherapy images and related information. These DICOM-RT objects are: 1) RT Image, 2) RT Plan, 3) RT Structure Set, 4) RT Dose, 5) RT Treatment Record, 6) RT Brachy Treatment Record, and 7) RT Summary Record. [7, 8] In March 2006, supplement 102 was finalized to include two additional RT objects for Ion Therapy applications which include PT. These two objects include RT ION Plan and RT ION Treatment Record. These two additional objects refer to the same RT Objects: RT Image, RT Dose, and RT Structure Set. Figure 5 shows the DICOM model of the real world showing where the Radiotherapy Objects reside. Figure 6 shows in greater detail how the DICOM-RT-ION objects are added to the overall set of Radiotherapy Objects. Generally, the sources for these data come from a treatment planning systems (TPS), an oncology information systems, and PT systems. The DICOM-RT-ION object information models can be utilized to develop the data structure for the electronic patient record. To develop a conceptual data model, the PT workflow must be reviewed to define the data required. Additionally, clinical user input is needed as well. With these input sources, a conceptual model can be developed for a PT electronic patient record.

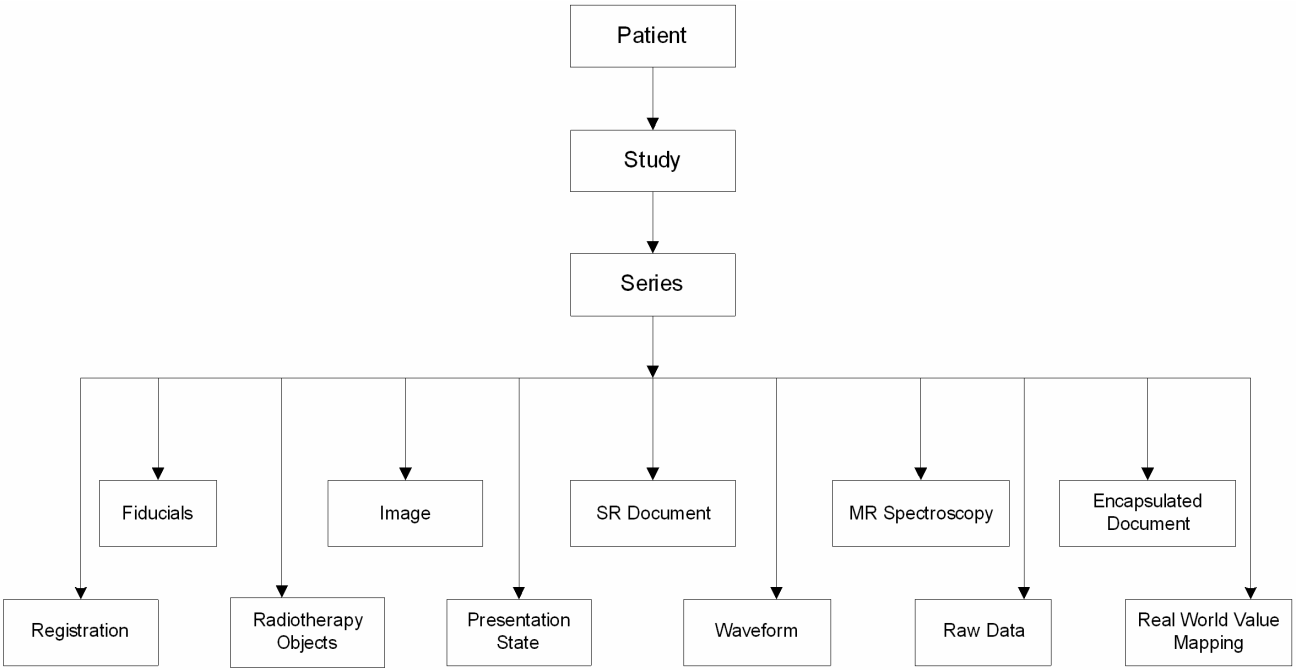

Figure 5: Portion of the DICOM Model of the Real World showing where the Radiotherapy Objects reside.

An initial data survey was performed to track patient cases utilizing the clinical information systems at LLUMC. Two types of patient cases of brain and prostate tumors were tracked to determine the treatment path and outcome. The two cancer types were chosen since they represent complex treatment planning cases with surrounding critical structures that require controlled dose to the target tumor while limiting dose to normal and healthy tissue. These results were implemented into the clinical workflow model. From these cases, a total of 5 cases of each tumor type treated by PT will

be extracted for a specific workflow model and later conversion into the DICOM-RT-ION data model. The preliminary data collection survey was performed to determine the feasibility of data collection at LLUMC. The brief survey was performed using clinical information systems to track historical patients and their record and was performed under the HIPAA Regulations and Compliance Guidelines set forth by LLUMC.

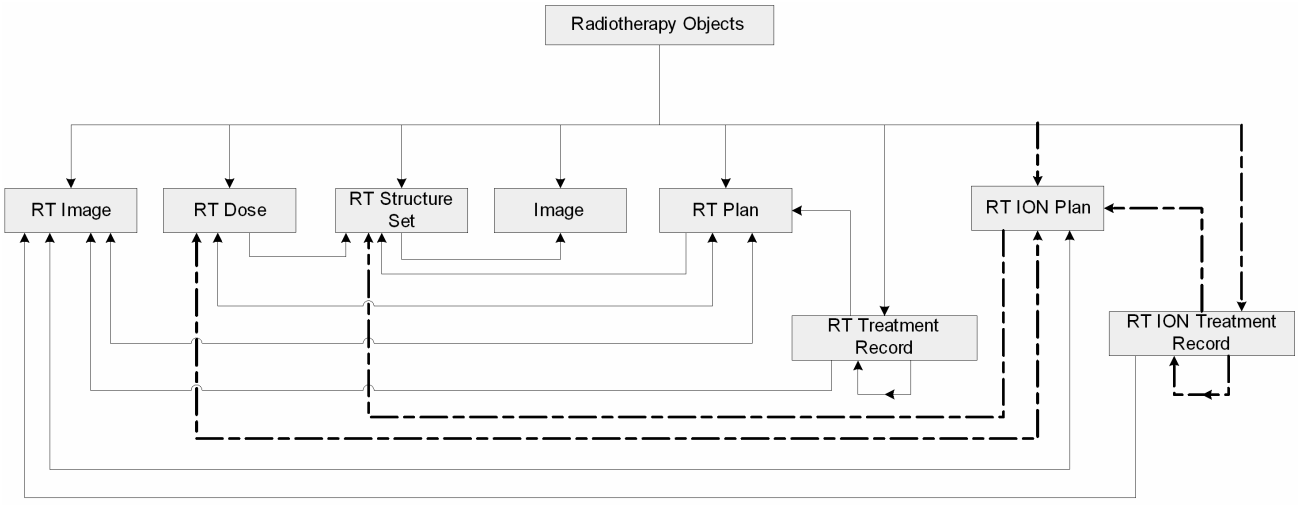

Figure 6: Portion of the DICOM model of the Real World showing the extension of the two RT-ION objects. Note: The two ION objects, RT-ION Plan and RT-ION Treatment Record, refer to the same RT objects as the two RT Objects, RT Plan and RT Treatment Record.

2.4 System Integration

For the DICOM RT ePR system, a three-tier architecture was developed [10]: 1) The RT archive server manages, archives and distributes DICOM images and DICOM-RT objects, 2) The RT web-based application server processes patient planning and treatment data, and 3) the RT web-based client application presents the RT data. The database schema reflects this three-tiered system by physically representing the data as well as providing data structures, file organizations and mechanisms for system operation as well as data storage. In the design of the workflow, there are two database schemas developed; one for the RT archive server and the second for the RT web-based ePR application server. Because there is more RT data presentation at the web-based application server level, the latter database schema is much more complex as compared to the RT archive server.

Data from the Oncology Information System, TPS, and PT systems will be converted into DICOM-RT-ION objects and sent to the DICOM-RT Gateway. The diagnostic images will be sent from a PACS Server into the DICOM-RT Gateway as well. Once the DICOM-RT-ION objects have been received by the DICOM-RT gateway, they will be sent to the Archive server. A database schema will be developed for the archive server so that the DICOM-RT-ION objects can be archived and distributed to the web-based application server. This archive server is a Continuous Available (CA) server design with 99.999% uptime that has been utilized for a variety of clinical applications. [11, 12]

2.5 Knowledge Base Development

Knowledge is defined and quantified based on the expert's ability, in this case, either the oncologist or physicist, to utilize data and other criteria in evaluating, grouping, and defining certain clinical characteristics that are extracted from the standardized DICOM-RT-ION objects stored within the ePR system. The knowledge base is designed in an object-oriented and modular fashion so that additional knowledge and new object classes defined in the future can be easily integrated without affecting the overall design. One example of quantified knowledge modeling is the relationship between the Dose Volume Histogram (DVH) curves and the isodose curve lines on each of the image slices which can be loosely defined as:

$$DVH_i = \sum_{j=1}^{M} isodose_j$$

where a particular tumor or critical structure's DVH curve *i* is a summation of all the 1 to *M* isodose curves within the diagnostic image slices of the treatment plan. The two models above will depend on rudimentary quantified knowledge data elements. These data elements can be derived from the knowledge base schema which can be defined into class objects. A few are shown in Figure 7 along with their attributes: Class Object 1) DVH; Class Object 2) Isodose curve; Class Object 3) Critical Structure; and Class Object 4) CT image. Then, for each of these classes, attributes can be defined as shown. For example, for the CT Image class object, there are the primary key (PK) identifier and five attributes: Critical Structure Curve; Isodose Curve; Spatial Coordinates of the image including x, y, and z-directions; Pointer to the image data; and DICOM header data. The relationships between each of the class objects are through the Foreign Keys (FK). For example, in Figure 7, Isodose Curve FK1, and Critical Structure FK2 are related to CT Image object. This is because a CT image would contain multiple isodose curves and multiple critical structures. Once the knowledge has been defined and knowledge base schema developed, the knowledge can be extracted and stored within the knowledge base. A search engine can be built to perform queries on the quantified knowledge for automatic extraction of particular knowledge.

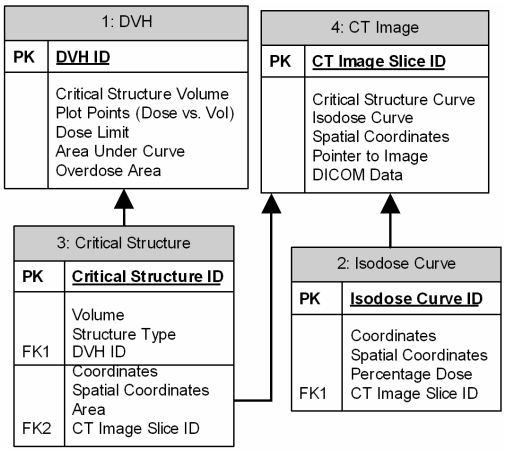

Figure 7: Entity-Relationship Example of a Sample Knowledge Base for a Clinical Scenario to perform treatment plan assessment for IMRT. The classes defined have attributes that are extracted from the standardized DICOM-RT data integrated in the ePR system. Each class carries a Primary Key (PK) Identifier, and can contain Foreign Keys (FK) which link it to another class object.

2.6 Data Mining for Knowledge and the Development of Quantification and Visualization Tools

Referring again to the clinical scenario described in section 2.2, a quantification and visualization tool is developed to automatically mine the knowledge base for the information needed to assess a treatment. The tool design and user interface is developed through the guidance of the expert, which are the oncologist and physicist. The design shows how quantified knowledge can be mined for and then visually presented as an example for further development of decision-support tools. One example of a specific tool eliminates the tedious manual procedure of first analyzing the DVH curves, which is a 2-D plot graph, and then having to toggle through a 3-D volume of CT image slices overlaid with multiple isodose curves to identify locations and characteristics of regions within critical structures that are receiving radiation overdose called "hot spots". The exact diagnostic CT image slice together with the exact critical structure and tumor contours and isodose curves representing hot spots can be automatically displayed as a warning and red flag to the oncologist during the review of the treatment plan. In addition, important quantified knowledge measurements can also be displayed. The results from a treatment plan utilizing IMRT and based on the above design and quantified knowledge measurements further emphasize the potential of extending this method to develop quantified knowledge and decision-support tools for PT and are further discussed in the Results Section. Other potential development of what quantified knowledge to present and how it will be presented are closely guided by the oncologist and physicist. In the long term, as more knowledge data is collected from additional patients treated with PT, the knowledge base will be enriched accordingly.

Figure 8 shows the *knowledge-enhanced* inverse treatment planning workflow with the ePR system integrated with dashed lines. This knowledge-enhanced inverse treatment planning approach may eliminate the feedback loop and subsequent iterative steps of re-computing of a treatment plan since the first attempt was acceptable based on the prior knowledge. Because each plan is computationally complex and time-consuming, a best practice first computed plan aided by previous knowledge would greatly enhance the decision-making process and ultimately shorten the length of time before the patient is exactly treated as well as better preserve normal tissue and quality of care.

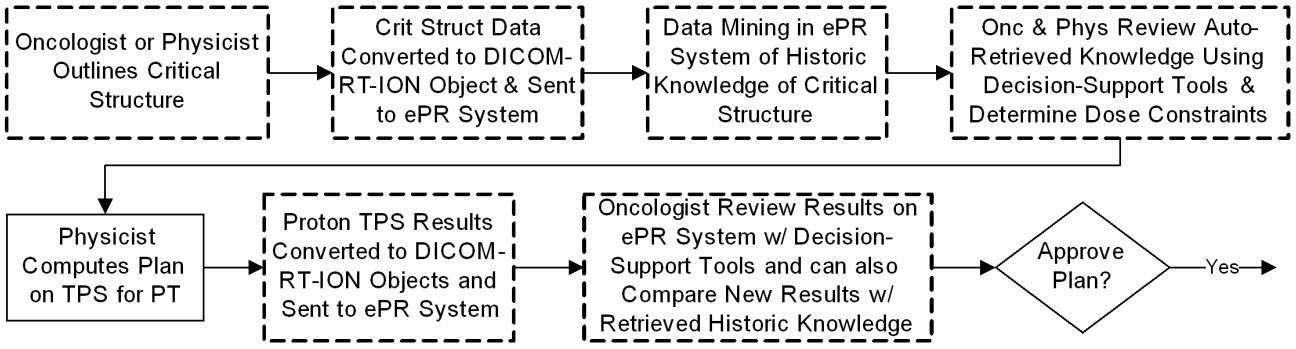

Figure 8: Knowledge-enhanced Inverse Treatment Planning. Dashed lines show where workflow steps would be performed in the ePR System as compared to the current feedback loop workflow shown in Figure 4.

3. RESULTS AND DISCUSSION

The clinical scenario where an oncologist needs to assess the isodose plan of critical structures from a treatment plan for a patient is utilized to develop decision-support tools. During treatment planning, the treatment plan developed, usually by the physicist, must be approved by the oncologist as shown earlier in the workflow in Figure 4. Part of the clinical decision-making process for the physician is to analyze the DVH curves of critical structure areas to evaluate whether the critical structures are receiving an overdose of radiation that is clinically unacceptable. These curves only show dose values in relation to the critical structure volume. The physician must then evaluate the various isodose plans to first locate areas of overdose within the critical structures called “hot spots”, and then to determine whether the plan is acceptable or whether it must be modified and recalculated. Navigation of this knowledge, while crucial, is also extremely tedious and complex since there is no tool to quantify and visualize the direct relationship between the DVH curves to the diagnostic images and the corresponding dose and critical structure curves. The tool designed in this example automatically displays the DVH curve of a critical structure linked with the diagnostic image slice(s) that contain corresponding isodose curves and critical structure regions.

Figure 9 shows a screenshot of an overview of a particular IMRT Treatment Plan (TP) as an example to show the potential impact of developing decision-support tools for PT. Although IMRT utilizes photons for treatment of cancer instead of protons, both IMRT and Proton Therapy utilize the inverse treatment planning approach and share similar RT objects. As the Proton Therapy data is collected and integrated with the DICOM-RT based ePR system, we will be able to verify and evaluate the impact of extending more fully the methodology presented in this paper from IMRT to Proton Therapy. Referring back to Figure 9, the Letter A indicates tabs that display different page views. The first view is the TP Overview which shows the general overview of the DVH curves and the DICOM CT Images with isodose curves overlaid. The TP Evaluation page allows the User to quickly assess a treatment plan for hot spots. The TP Knowledge Base Search page allows users to query for specific knowledge. The TP Comparison page shows quantified knowledge for two different TP iterations in a comparison mode. The Letter B indicates a timeline display showing all TP’s, both current and historical, of a particular patient. The letter C indicates a drop-down window which allows the user to view different iterations within a current plan. The Letter D indicates the DVH Curve of a particular plan with the overdose area shaded for the Optic Chiasm. The letter E indicates DICOM Images with isodose curves overlaid from the TPS. All data is in DICOM-RT Format and standardized. The User can further view each of the DICOM images with isodose curves by selecting one of the images. A pop-up window is generated with a larger image view window. Tools such as Zoom, Pan, and Window/Level are included as well as the ability to toggle on and/or off particular isodose curves or critical structure curves to allow the User to properly review the plan.

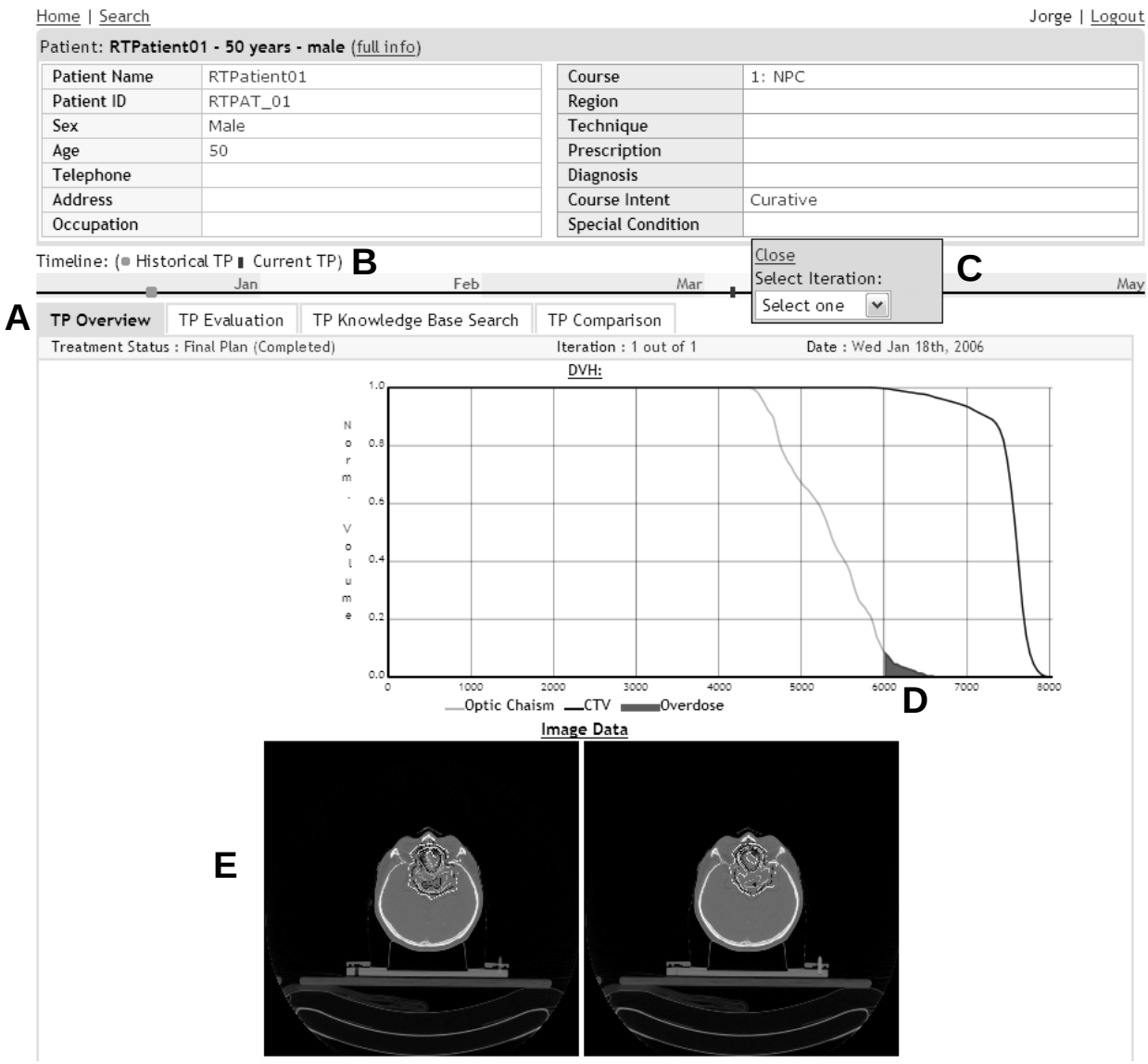

Figure 9: Screenshot Showing an Overview of a Treatment Plan. A: Tabs that Display Different Page Views. B: Timeline Display Showing all Treatment Plans, both Current and Historical of a Particular Patient. C: Drop-Down Window Allowing the User to View Different iterations Within a Current Plan. D: Dose Volume Histogram (DVH) Curve of a Particular Plan with Overdose Region Shaded for the Particular Critical Structure, in this case, the Optic Chiasm. E: DICOM Images with Isodose Curves Overlaid from the TPS.

Figure 10 shows the TP Evaluation Page with the DVH curves of a specific critical structure, the Optic Chiasm with the overdose area shaded under the Optic Chiasm curve, and the Tumor depicted in the leftmost column. In the middle column, only the image slices with overdose regions are extracted from the entire CT study and displayed with the regions highlighted. In addition, quantified knowledge such as percent area overdosed are displayed as well. The rightmost column shows only the image slices where the tumor is not receiving the full clinically prescribed radiation dose. In this manner, the User can quickly assess the treatment plan to determine whether the critical structures are being overdosed while at the same time the tumor is being prescribed as much dose as possible without having to review the entire CT Image Study.

These tools help to eliminate the tedious manual procedure of first analyzing the DVH curves and then having to toggle through a volume of CT image slices with multiple isodose curves to review and assess the plan. Since data is already mined, the exact diagnostic CT image slice together with the exact structure and isodose curves can be automatically displayed the moment the oncologist opens the case within the ePR system. The oncologist would then have the ability

to continue to navigate the presented data or view a different DVH curve if desired to make a quicker assessment of the treatment plan for approval. If the oncologist decides that changes are needed in the treatment plan, the decision-support tools can be used to perform a real-time consult with the physicist either at different locations or at the same location or even directly on the treatment planning system, since the ePR is web-based and portable. In the future, if there are historical patients stored within the ePR system, the tools can display all the similar critical structures (eg, in the above case, the Optic Chiasm) of similar treatment plans with the corresponding dose configurations that have been approved. This extracted *a priori* knowledge would help the clinician to decide on an initial plan for a new brain tumor patient planning to be treated with PT and perhaps shorten the iterative process of the inverse treatment planning workflow.

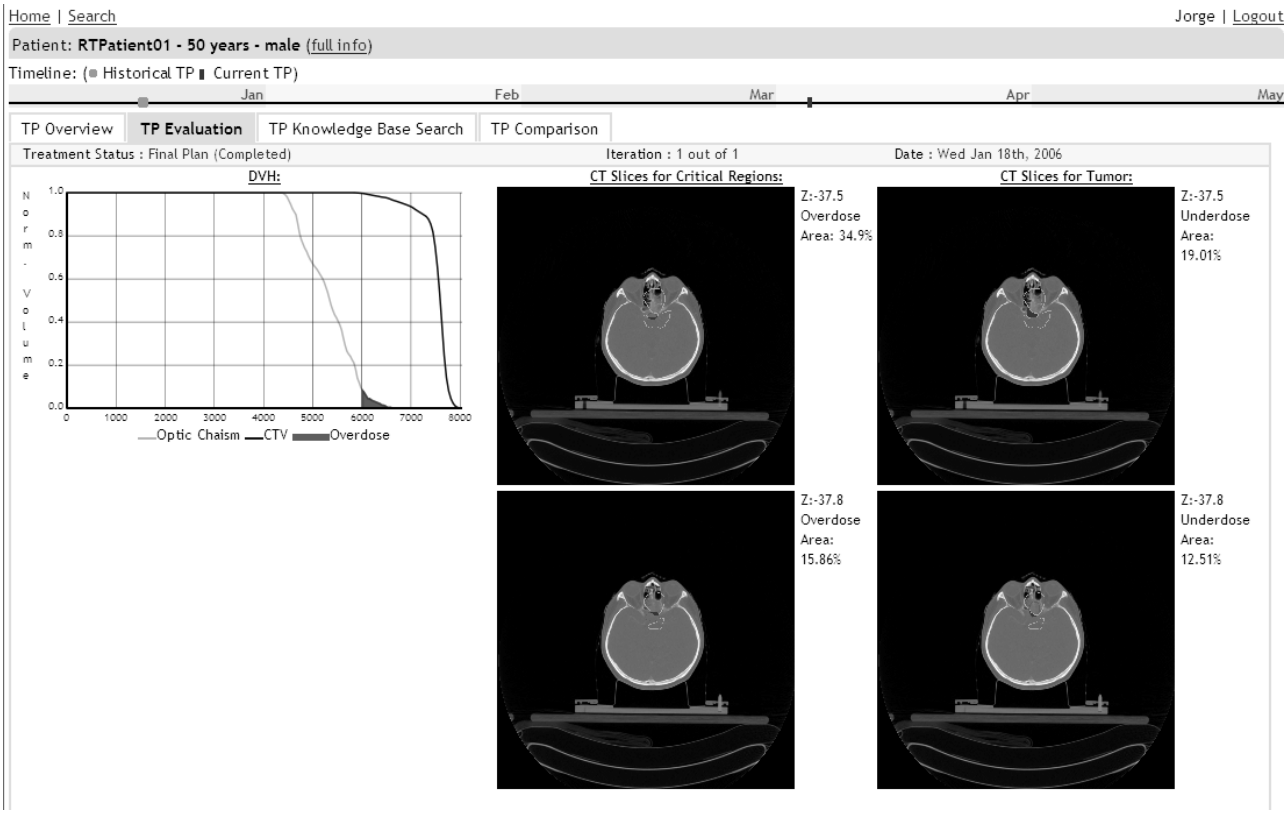

Figure 10: TP Evaluation Page Showing the DVH Curves of a Specific Critical Structure and the Tumor. Only image slices with overdose regions extracted from the entire CT Study are displayed in the middle column with the regions highlighted including quantified knowledge (eg, Percent Area Overdose). The rightmost column shows only image slices where the tumor is not receiving the full clinically prescribed Radiation Dose. In this manner, the User can quickly assess the Treatment Plan to determine whether the critical structures are being overdosed while at the same time the Tumor is being prescribed as much Dose as possible without having to review the entire CT Image Study.

4. CONCLUSION

A medical imaging informatics approach towards the development of quantified knowledge and decision-support tools was extended to include Proton Therapy for treatment of cancer patients. Currently, data collection at LLUMC is ongoing in order to collect PT data and standardize them into DICOM-RT-ION objects. The methodology was introduced for the development of decision-support tools based on the standardized DICOM-RT-ION data within the ePR system. As a first step, initial data models and clinical workflow models for Proton Therapy were investigated to determine the impact of integrating these new RT objects into the ePR system so that quantified knowledge and decision-support tools can be developed and evaluated. Current decision-support tools developed for IMRT show the great potential of extending this methodology to PT. The following are benefits obtained from this approach and development of this standardized DICOM-RT based ePR system with quantified knowledge and decision-support:

A PDA Study Management Tool (SMT) Utilizing Wireless Broadband and Full DICOM Viewing Capability

Jorge Documet[a], Brent Liu[a], Zheng Zhou[a], HK Huang[a], Luis Documet[b]

[a]Image Processing and Informatics Laboratory, Department of Radiology, University of Southern California, Marina Del Rey, California
[b]Department of Radiology, Saint John's Health Center, Santa Monica, California

ABSTRACT

During the last 4 years IPI (Image Processing and Informatics) Laboratory has been developing a web-based Study Management Tool (SMT) application that allows Radiologists, Film librarians and PACS-related (Picture Archiving and Communication System) users to dynamically and remotely perform Query/Retrieve operations in a PACS network. The users utilizing a regular PDA (Personal Digital Assistant) can remotely query a PACS archive to distribute any study to an existing DICOM (Digital Imaging and Communications in Medicine) node. This application which has proven to be convenient to manage the Study Workflow [1, 2] has been extended to include a DICOM viewing capability in the PDA. With this new feature, users can take a quick view of DICOM images providing them mobility and convenience at the same time. In addition, we are extending this application to Metropolitan-Area Wireless Broadband Networks. This feature requires Smart Phones that are capable of working as a PDA and have access to Broadband Wireless Services. With the extended application to wireless broadband technology and the preview of DICOM images, the Study Management Tool becomes an even more powerful tool for clinical workflow management.

Keywords: Study Management Tool, PDA, PACS, WiFi, Wireless Broadband, DICOM viewer

1. INTRODUCTION

PDAs are becoming more accessible and Wireless Network speeds are increasing considerably. Therefore, it is important to provide users with the required tools to enhance the Radiology Clinical Workflow. In this paper we will describe the cache mechanisms that help improve the performance for previewing DICOM images on PDAs. The general workflow for distributing medical examinations is described by Documet et al [1]. Also we will describe the DICOM viewer itself; and finally present the wireless configurations from where this application can be utilized. Because the tool is a web-based application, the users can access it from either a Personal Computer (PC) or a PDA as long as a connection can be established with the SMT server. Understanding the differences between PCs and PDAs allow us to provide specific contents according to the type of device that is accessing the application. Giving the Radiologists a remote DICOM study preview capability where there is no access to a regular and more powerful PC and limited to just cellphone coverage increases the availability and accessibility for cases that require a critical and timely review. When the users access the application thru a PDA they can take advantage of a DICOM viewer that has the basic features to preview images in such a device. This tool allows the user to Zoom In, Zoom Out, Window/Level, Pan, and browsing thru the images of a given study.

2. METHODS AND MATERIALS

During the last 4 years we have developed a Web-based application that provides mobility, flexibility and convenience to the users allowing them to perform Query and Retrieve operations to manage the distribution of DICOM examinations in a clinical environment. To enhance the features provided by this tool, last year we started the development of a DICOM Viewer for Pocket PC.

This section describes the overall SMT architecture at SJHC, the cache mechanism used for delivering the DICOM images to the handheld devices, the functionality of the DICOM Viewer and the wireless and broadband connectivity configurations.

2.1. SMT Architecture

Figure 1 shows the current System Architecture of the SMT at SJHC. The SMT Server acts as a gateway between the web users and the main PACS Archive. The users connect wirelessly to the SMT server either internally via the WiFi network, discussed in Section 2.4.1, or thru Wireless Broadband connections, discussed in Section 2.4.2. The SMT server transforms all the requests from the users to proper DICOM command, such as DICOM Query/Retrieve. The output generated from the DICOM nodes is then interpreted by the SMT and properly transformed to html code. Section 2.3 describes the SMT workflow in more detail.

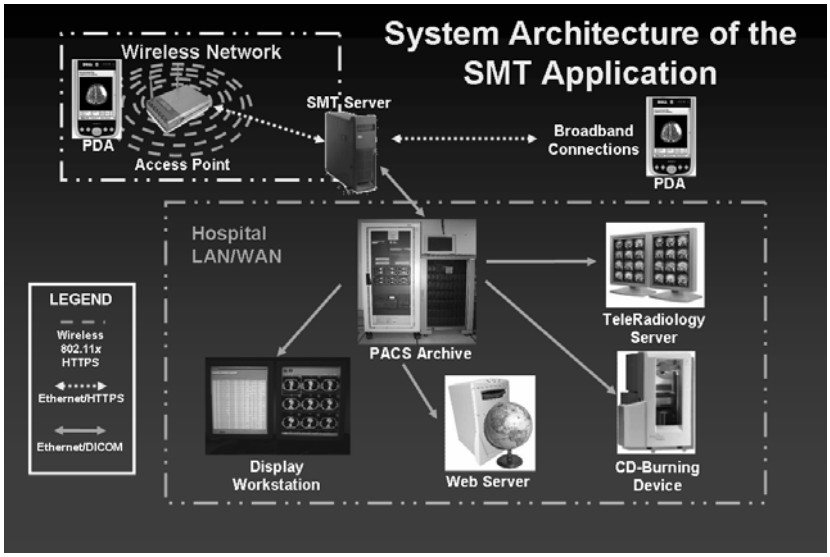

Figure 1 - SMT Sytem Architecture at SJHC

2.2. Cache mechanism

The Study Management Tool has been implemented with 2 layers of cache; the first at the SMT server and the second at the client. Both levels take place every time a DICOM study is shown to the user. The technical assumptions that we have considered are based on the constraints imposed by the limited hardware on the PDAs and the transfer speed rates while using wireless connections.

2.2.1. Cache at the PDA

PDAs are handy tools that provide excellent mobility and flexibility but at the expense of other desirable features. For example, the ROM memory on these devices, which is equivalent to the hard drives on regular PCs, comes with only 256MB for a Dell Axim x51v Handheld. Also, if we consider that other applications will be installed on the same device, then there is only very limited capacity for our tool in order to store DICOM images. Thus, storage space becomes key as well as the mechanism to maintain the storage used under certain limits. The storage space for the cache at the client is negotiated according to the size of the DICOM images, the smaller the images the more images that are kept temporarily in the client. By default the number of concurrent images stored locally at the client side is set to seven, where one image is the currently displayed image and the other ones are from three of the next images in the study and three of the previous images in the study. Once the user finishes reading the images are removed to avoid any confidential patient information disclosure. The images are transferred using the https (secure hypertext transfer protocol) and are stored as DICOM files on the client. Another factor that plays a key role in the accessibility of the application is the transfer speed of the wireless networks, which is discussed in greater detail in section 2.4. Figure 2 shows the components that interact at the client side. The connection marked as “A” refers to the interaction the users need to perform prior to previewing the DICOM study. Once the user is viewing the DICOM images, all the communication takes place directly within the SMT server and the DICOM viewer. This communication is marked as “B” on Figure 2. The internal architecture of the SMT server is shown in Figure 3 in the next section.

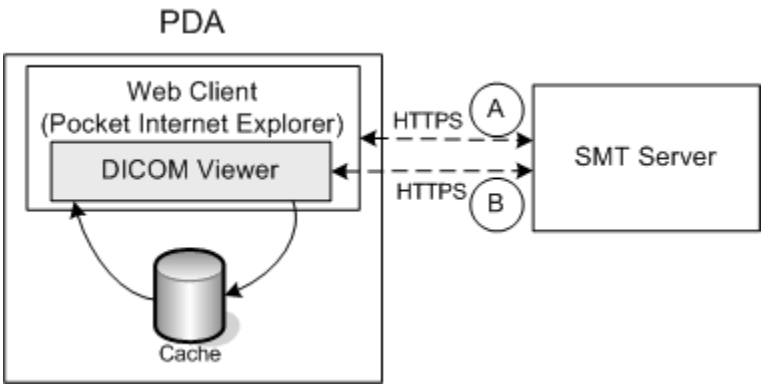

Figure 2 – Client internal Architecture

2.2.2. Cache at the SMT Server

The SMT Server is the key component of this application. It is a web server with an installed DICOM library that allows the users to perform Query and Retrieves via a Web interface. Fortunately, the SMT Server does not face the limitations for hardware resources as the PDAs do; especially at the storage capacity. In our configuration, the SMT server was implemented on a Linux family server SuSe 10 (Dell PowerEdge 840 with Dual Core Intel® Pentium®D 915, 2.8GHz, 2GB of Memory and 160GB hard drive [3]). The SMT Server runs Apache 2.0 as web server and Perl 5.8 as scripting language for dynamic contents.

The SMT server handles all requests from the users via the https protocol; which are interpreted by the Perl web pages, and then passed to the DICOM Library to perform the necessary DICOM commands. The internal architecture of the SMT server is shown in Figure 3.

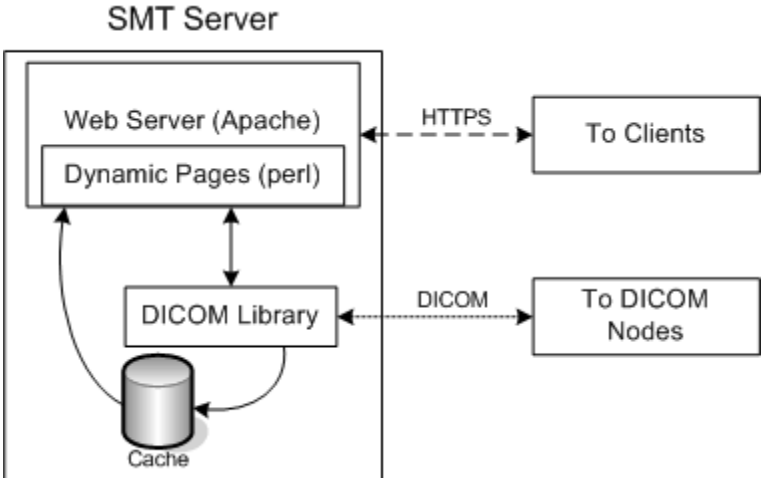

Figure 3 - SMT Server Internal Architecture. Cache by default set to a limit of 80% of available space

Once a user requests to preview an examination the SMT server retrieves the DICOM images from the PACS Archive. Those images are stored locally at the SMT server and then transfer to the PDA. If a subsequent request to the same study is perform later, the SMT does not need to retrieve those images from the PACS Archive, instead they are provided directly from the local cache. The number of studies that are maintained on cache can be configured by the administrator; the default value is to keep the cache under 80% of the available storage. Once the upper limit is met, a cleaning process deletes the older studies.

2.3. DICOM Viewer for PDA

This year we have extended the capability of the SMT to display real DICOM images on the PDA. For this purpose we have developed at IPI an ActiveX control component that serves as a DICOM viewer. The DICOM Viewer component takes care of downloading the DICOM images from the SMT server and displaying them on the web interface. This component is compatible with Windows Mobile 2003 Second Edition version or newer. The development of this component came from the need to handle all the image manipulation needs as responsive as possible at the client side because the client-server model is not best suitable yet for wireless networks due to the inherent latency.

The necessary steps for previewing DICOM images on the PDA are as follow:

1. The user searches a specific patient by the last name.
2. From the output generated in step 1 the user selects an examination.
3. Once the study information is shown, the user clicks on the study description to preview the study.
4. The DICOM images are displayed utilizing a DICOM Viewer pre-installed on the PDA. The user can perform basic image manipulation such as Zooming In, Zooming Out, Window/Level, Pan and browsing thru the Study Images.

The first three steps (Figures 4-6) from the workflow above are performed by the connection marked as "A" in Figure 2. The step 4 is performed by the connection marked as "B" in Figure 2. Once the user is at the step 4, the browser, called Pocket Internet Explorer, performs the downloading of the DICOM images of the selected study. If the same study has been requested previously, then those images from the cache at the SMT server will be available for download immediately; in the case the study has not been previously reviewed, then the SMT retrieves it from the PACS archive prior to sending the images to the PDA. At the PDA, the expected delay the user experiences is the time that takes to download the first image, once this happens, the rest of the images are downloaded in the background by the browser without being noticed by the user.

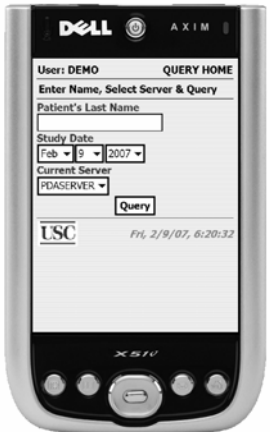

Figure 4 - SMT Workflow, step 1

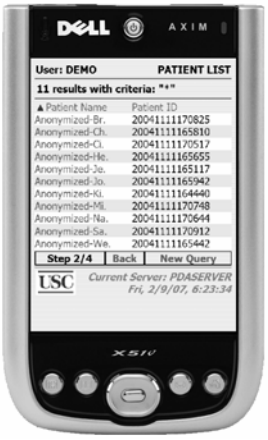

Figure 5 - SMT Workflow, step 2

Figure 6 - SMT Workflow, step 3

Figures 7 thru 9 show the DICOM viewer at the PDA client. In those images at the top it is shown basic patient information; at the center the DICOM previewing itself and at the bottom the navigation tool for the Viewer. Figure 7 shows a DICOM image of a brain with no image manipulation. Figure 8 shows the same DICOM image showed in previous on but with a zooming in and window/level adjustment. The image shown in Figure 9 corresponds to the previous image of the study; once a new image is requested then the window/level adjustments are maintained and the new image is centered.

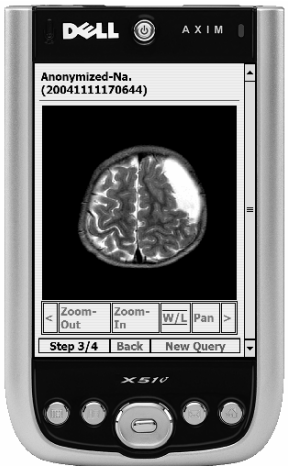

Figure 7 - DICOM preview

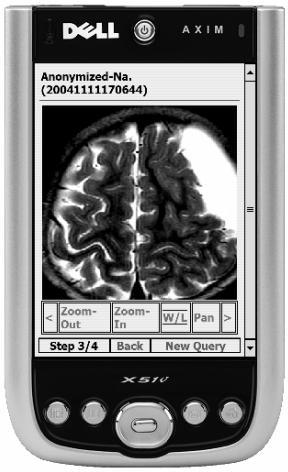

Figure 8 - Zoom in and Window Level change

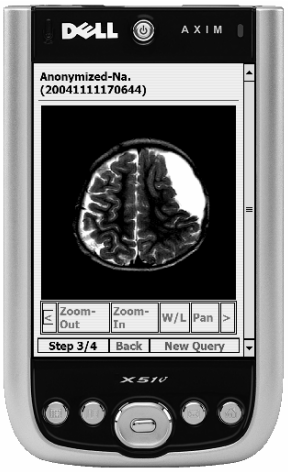

Figure 9 - Browsing next image

2.4. Wireless and Broadband connectivity

The application can be accessed from a PDA thru WiFi (Wireless Fidelity) or from a Smart Phone utilizing a broadband connection from a Cell Phone carrier. The Study Management Tool has been tested with a Dell Axim x51v PDA in a local wireless network; for the broadband connection we have used the Sprint PCS VisionSM Smart Device PPC-6700. In this section we provide information related to the wireless connectivity configuration for PDAs and Smart Phones; in Section 3 we will discuss the technical differences when accessing the Study Management Tool from those devices tested in the laboratory environment, we still need to test the application in the clinical environment.

2.4.1. Wireless Connectivity (WiFi)

The users while inside the hospital utilized the internal WiFi connectivity in order to access the SMT. Even though we have seen new wireless standards with faster transfer speeds that have recently arrived to the market for PCs and laptops, PDAs in the other hand have still limited support. The Dell Axim x51v PDA, which came out in the year 2005, comes with built-in support for IEEE 802.11b. The maximum transfer rate for this standard is 11mbps, but for real scenarios where walls and other frequencies are present, the resulting transfer speeds are affected considerable.

In our clinical testbed scenario at Saint John's Health Center (SJHC) we have utilized a single access point for the Radiology Department [1] utilizing a D-Link DI-624. Greater wireless range can be provided with the configuration of Roaming capability for WiFi networks.

2.4.2. Broadband Connectivity

Due to the very limited access range that a WiFi connection can provide to the users, we have tested a broadband wireless connection to increase the accessibility of the application, and to allow the users to a greater flexibility and mobility. The requirements that need to be met prior running the Study Management Tool using a broadband connection is to have a Smart Phone with Windows Mobile 5 Operating System installed and an account that has the broadband access enabled, which is provided by a cell phone carrier. The average download speeds range from 400 to 700 Kbps with peak rates up to 2 Mbps [4].

There exist two different approaches to connect to the SMT server, one of them is by making the SMT server publicly accessible via the Internet, the other approach is to first establish a VPN connection to the hospital network and then connect to the SMT server. In the first approach there is a risk of being more vulnerable to attacks over the Internet because the server can be accessed by any computer that is also connected to the Internet. The latter approach offers a more secure solution because the SMT server is hidden from outside networks and the user is required to authenticate

first to the VPN server and then to the SMT server. However, the VPN connection can incur in extra processing and bandwidth requirements due to the applied encryption to the transmitted data [5].

3. RESULTS

3.1. Lab Evaluation

Table 1 shows the data collected at the lab evaluation phase.

Table 1- Studies sent using the SMT server at the lab evaluation stage

Modality	# of Images	Size (MB)
CT	30	15
MRI	50	6.5
CR	2	16

As explained in Section 2.3, the delay the user experiences when previewing a DICOM study is the time that it takes to load the first DICOM image from the selected study. Even if the study is big in size (eg. CR), the key factor for the speed of the transmission is the size of each individual image. The results shown above were gathered in a lab environment using a WiFi connection, with a home-grown PACS Archive with minimal concurrent load installed on the same Local Area Network (LAN) as the SMT Server This configuration is very unlikely to occur in a real clinical environment, but still places a great testing environment for any further enhancements to be done.

3.2. Clinical Evaluation

The SMT system has been successfully integrated in a clinical environment at Saint John's Health Center, a small community hospital located at Santa Monica, California; and at Healthcare Consultation Center II, an outpatient facility at USC (University of Southern California). The application can retrieve and display DICOM images within the PDA from the local WiFi network as well as utilizing Broadband networks. However, we are still in the process of collecting performance data from the clinical sites.

The SMT application with support for DICOM viewing and Wireless Broadband access has been implemented at SJHC and HCCII for the last month. A formal user satisfaction survey will be performed after 6 months of operation at the clinical sites; the focus of the survey will be to obtain feedback regarding the DICOM viewer functionality as well as the users' perception about performance and responsiveness of the application.

Even though the survey has not been performed yet, some preliminary comments obtained at demonstration done at RSNA last year and at the IPI Laboratory include:

- Include Preset values of Window/Level for known type of images and body structures.
- Send the Key images marked by radiologists at the beginning of the transmission. This will reduce the time needed to preview a study and by consequence improve the clinical workflow management.
- Include a worklist of patients for Referring Physicians. Once they login to the application they will have access to the images from their patients; which can lead to more efficient process by showing the most relevant information to accommodate the different types of users.
- Include text reports of the studies. By adding the report information of the study, the application will be more complete and useful, serving as great complement to the DICOM display.

4. DISCUSSION

The utilization of Mobile Wireless infrastructure in conjunction with a DICOM viewer capability provide users a more complete and powerful tool for Study Management with the use of mobile technology such as PDA's and Smart Phones [6]. The SMT application has been successfully installed (still testing phase) at 2 clinical sites: SJHC and HCCII. Further data collection is needed to provide the basic ground about the performance and usefulness of the application in real clinical environments.

ACKNOWLEDGMENTS

This research is supported by MI[2]

REFERENCES

1. J. Documet , B. Liu, L. Documet., H.K. Huang , "Wireless Remote Control of Clinical Image Workflow: Using a PDA for Off-Site Distribution and Disaster Recovery", Journal of the American College of Radiology, **Volume 3**, Issue 7, pp 520-527
2. B. Liu, L. Documet, J. Documet , H.K. Huang , J. Muldoon, "Clinical Experiences Utilizing Wireless Remote Control and an ASP Model Backup Archive for a Disaster Recovery Event", *Proceedings of SPIE Medical Imaging*, 5371:288-296, 2004.
3. Dell, http://www.dell.com, accessed in February 2007
4. Sprint PCS, http://www.sprint.com, accessed in February 2007
5. R. Hunt, C. Rodgers Virtual Private Networks: Strong Security at What Cost? University of Canterbury, New Zealand (http://www.cosc.canterbury.ac.nz/research/reports/HonsReps/2001/hons_0109.pdf)
6. R. Andrade, A. Wangenheim, M.K. Bortoluzzi, "Wireless and PDA: a novel strategy to access DICOM-compliant medical data on mobile devices". Int J Med Informatics 2003; **71**:157-63

Managing Healthcare Information Using Short Message Service (SMS) in Wireless Broadband Networks

Jorge Documet[a], Sinchai Tsao[a], Luis Documet[b], Brent J. Liu[a], Zheng Zhou[a]
[a] Image Processing and Informatics Lab, Department of Radiology, ISI/USC,
Marina Del Rey, CA USA 90292;
[b] Saint Johns Health Center, 1328 Twenty-Second Street,
Santa Monica, CA USA 90404-2091;

ABSTRACT

Due to the ubiquity of cell phones, SMS (Short Message Service) has become an ideal means to wirelessly manage a Healthcare environment and in particular PACS (Picture Archival and Communications System) data. SMS is a flexible and mobile method for real-time access and control of Healthcare information systems such as HIS (Hospital Information System) or PACS. Unlike conventional wireless access methods, SMS' mobility is not limited by the presence of a WiFi network or any other localized signal. It provides a simple, reliable yet flexible method to communicate with an information system. In addition, SMS services are widely available for low costs from cellular phone service providers and allows for more mobility than other services such as wireless internet. This paper aims to describe a use case of SMS as a means of remotely communicating with a PACS server. Remote access to a PACS server and its Query-Retrieve services allows for a more convenient, flexible and streamlined radiology workflow. Wireless access methods such as SMS will increase dedicated PACS workstation availability for more specialized DICOM (Digital Imaging and Communications in Medicine) workflow management. This implementation will address potential security, performance and cost issues of applying SMS as part of a healthcare information management system. This is in an effort to design a wireless communication system with optimal mobility and flexibility at minimum material and time costs.

Keywords: DICOM, PACS, PDA, SMS, Study Management Tool, Query-Retrieve

1. INTRODUCTION

The paradigm of remotely accessing and controlling Healthcare information via cell phone-based SMS has yet to be explored. To illustrate the utility of this paradigm, a system has been designed to perform DICOM Query-Retrieve on a standalone model PACS. Traditionally, the distribution of PACS images in a standalone model PACS would require a user performing DICOM Query-Retrieve operations on a free workstation and waiting for the retrieve operation to complete before being able to view the images. Wireless devices such as PDAs (Personal Digital Assistant) and cell phone-based SMSs have the potential to streamline this process by allowing the user to wirelessly command the PACS to transmit the images to a specified workstation beforehand. [1] These tools are particularly useful when viewing cases that are not normally pre-fetched automatically. In order to elicit key features vis-a-vis security, performance and costs, the design of the aforementioned system has been outlined.

2. METHODS AND MATERIALS

2.1 System Components

The system can reside on either two separate machines or a single machine. The software components are distributed on both the Web Server as well as the Gateway Server (see Table 1). Both single machine and dual machine configurations were tested. In an attempt to provide a clear distinction between the Gateway and Web server, the systems will be treated as two separate entities connected by an https (hypertext transfer protocol - secure) web link as shown in Figure 1.

This design utilizes Kannel Open Source SMS Gateway as the Gateway Server software. The Gateway Server is serially connected to the SMS modem (MultiModem GPRS Wireless Modem from MultiTech Systems, Mounds View, Minnesota, USA) and communicates via AT commands[1]. The SMS modem is associated with a GSM (Groupe Spécial Mobile or Global System for Mobile Communications) cell phone account via a SIM (Subscriber Identity Module) card. The phone number of the cell phone account is used as the server access number.

On the Web Server machine, a Perl capable web server such as Apache is required. The Perl scripts allow the web server to dynamically create web pages by calling a C++ program that performs the DICOM communications with the PACS archive.

Table 1. System Components

Gateway Server

Hardware	Software
• Server with Linux OS • Network Connection with Web Server (Optional if on the same Physical Machine)	• Kannel Open Source SMS Gateway

SMS Modem

Hardware	Software
• GPRS Wireless Modem** • Serial Interface to Gateway Server	• Not Applicable

** The author used MultiModem® GPRS Wirless Modem from MultiTech Systems, Mounds View, Minnesota, USA

[1] AT commands or Hayes commands (AT is short for attention) - a commonly used modem command code set.

Web Server

Hardware	Software
• Server with Linux OS • Network Connection with Gateway Server (Optional if on the same Physical Machine) and PACS archive	• Apache Server with Perl Capabilities • C++ Program to interface with PACS archive

2.2 Standard Workflow

2.2.1 Component Perspective

The standard workflow illustrated in Figure 1 shows how the different components interact with each other. The following steps describe the workflow: In step 1, a standard query will start with the cell phone sending a SMS to the SMS gateway. Steps 2 and 3 shows the gateway accessing a dynamic Perl-based web page from the Web Server via a build-in web client, thus passing-on the query parameters indicated by the user to the perform a DICOM operation. In order to respond back with dynamic data, the Web Server calls a C++ program to perform a DICOM query with the PACS archive in step 4 and 5. The data is then passed back to the user through the web page and SMS gateway. Once the user has found the study of interest, the user can then tell the SMS Gateway to issue a command down the system (steps 2 to 4) to the C++ program, which can then issue a DICOM send command with the desired parameters as indicated in step 6.

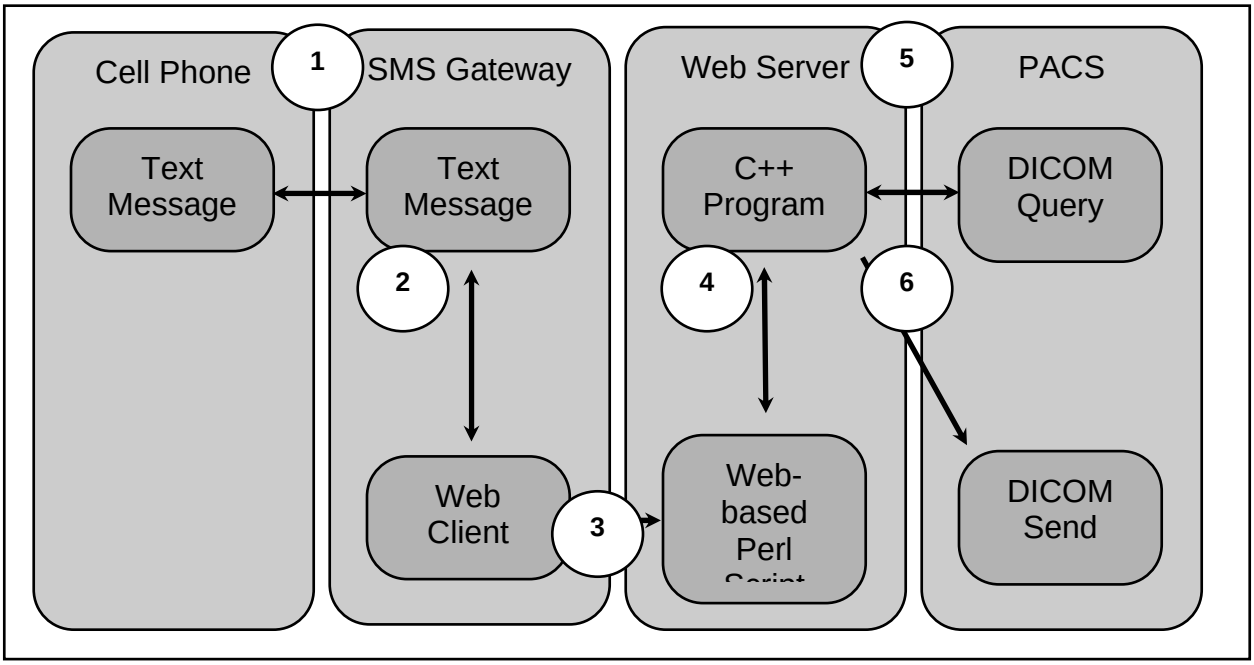

Fig. 1. Component Interaction Diagram

Table 2. Sample User - Server Interaction: Send Patient Doe, Joe (Patient ID: X8787224)'s Chest CT from February 1998 to EFILM workstation in Exam Room 1.

User's Cell Phone -> SMS Gateway	SMS Gateway -> User's Cell Phone
(1) Send Patient Name Query: Doe	(2) Select Patient: 1) Doe, John (X123456) 2) Doe, Jane (X227645) 3) Doe, David (X229884) 4) Doe, Mary (X8787834) n) next
(3) Get Next Page of Results: n	(4) Select Patient (continued): 5) Doe, Jacob (X123226) 6) Doe, Chelsea (X222245) 7) Doe, James (X222284) 8) Doe, Joe (X8787224) n) next b) back
(5) Select Patient of Interest: 8	(6) Select Study: Doe, Joe (X8787224): 1) Thorax CT (01.02.96) 2) Thorax CT (02.02.98)
(7) Select Study of Interest: 2	(8) Select Destination: Doe, Joe (X8787224): 1) EFILM - WS1 (ExamRoom1) 2) Cedara - WS2 (ExamRoom4) 3) CD Burner -WS5 (ExamRoom2)
(9) Select Destination: 1	(10) Confirmation Data: Doe, Joe (X8787224): E-00787981 (06.26.04) -> EFILM : Sent

2.2.2 User's Perspective

Consider table 2, in a standard workflow the user (1) sends an SMS to the Gateway with a potential patient name. The system then takes the query from the user and performs a query based on the criteria sent, generating output (2) in the form of an SMS reply to the user. To browse the potential matches to the initial query, the user can send two commands "n" for next page, which sends a request to the gateway to send an SMS with the next set of possible matches, or "b" to send a query to the gateway to resend the previous choices. In the example, the user does not see the desired patient in the first 4 results and sends "n" to get the next set of results (see step 3). In (4) , the server returns the next group of

results. When the user finds the desired patient "Doe, Joe ID number X8787224", the user then sends "8" to select the desired patient (step 5). The server returns the studies associated with patient Doe, Joe together with the examination date. In this case, the server returns two Thorax CTs with its respective date of examination in brackets. Since the user is looking for the examination performed in 1998 and therefore it is appropriate to send the associated index number 2 (step 7). The user is then presented with a list of destinations and as in the previous menu, chooses the desired destination by sending the number "1" for the EFILM workstation 1 in examination room 1 (step 9). The system has recorded all of the user's choices in its cache and sends the appropriate DICOM send command to the PACS archive (see number 5 in figure 1 or section 2.2.1). To confirm that the command has been sent successfully, the SMS gateway responds with a confirmation SMS in step 10. The system is now ready to accept a new query and has cleared the user's cache of the previous data.

2.2.3 Background Processes

To be able to perform a full DICOM-query and direct a specified study to a destination via DICOM send, the state of the user must be tracked. In other words, the server must be able to track the input associated with user so as to give the user the appropriate options to choose from. This process is necessary because no session is kept on the user. The user's choices and data is stored in the user's cache which is associated with the user's cell phone number as detected by caller ID. The user's state is indicated by the state diagram (see figure 2), the cache is updated every time the user state changes. Each row of table 2 is associated with a single state indicated by a number in figure 2. The arrows shows how the user moves from one state to another. For example, to move from state 1 to state 2, the user has to send a patient name. From state 2 to 3, the user sends a number that associated the desired patient. The user is also able to send another "Name" or patient name while in the patient state, which will elicit another list of possible patient matches as seen in output 2 in table 2.

2.2.4 Other Features

To allow the user to return to the new query menu at anytime, there is a special command "0" that resets the system back to its initial state should the user make any mistakes and wishes to start over. Other feathers include prefixing the initial query with "ID:" allowing the user to query by patient ID (see figure 2).

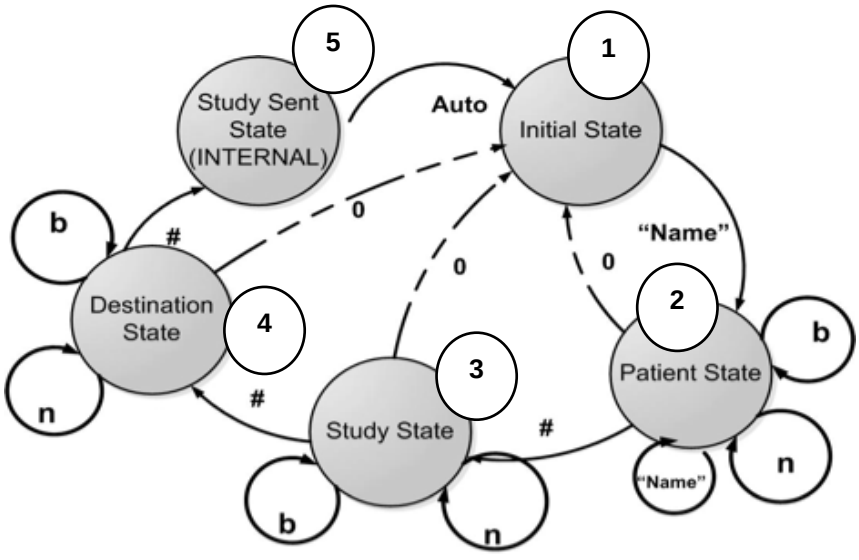

Fig. 2. The System State diagram shows how the system keeps track of the user's selections. This state tracking system allows the user to use the simplistic SMS text-based interface to select the study of interest from the patient of interest to be sent to a designated DICOM node.

3. RESULTS AND DISCUSSION

3.1 SMS System Architecture vis-a-vis PDA System Architecture

The SMS system adds the advantage of being able to direct DICOM studies in the PACS archive without being requiring internet or local area network access. The only limitation is a cellular phone carrier signal. It works off the same web server architecture as the PDA system. [1] Therefore, the Web Server for the SMS is identical to the PDA server except that the generated output is now modified for the SMS, with added functionality to read from a users' state tracking mechanism that allows for navigation between the different states (see Figure 2). The limitation of the SMS is that it lacks the previewing capability on the web browser as on the PDA system.

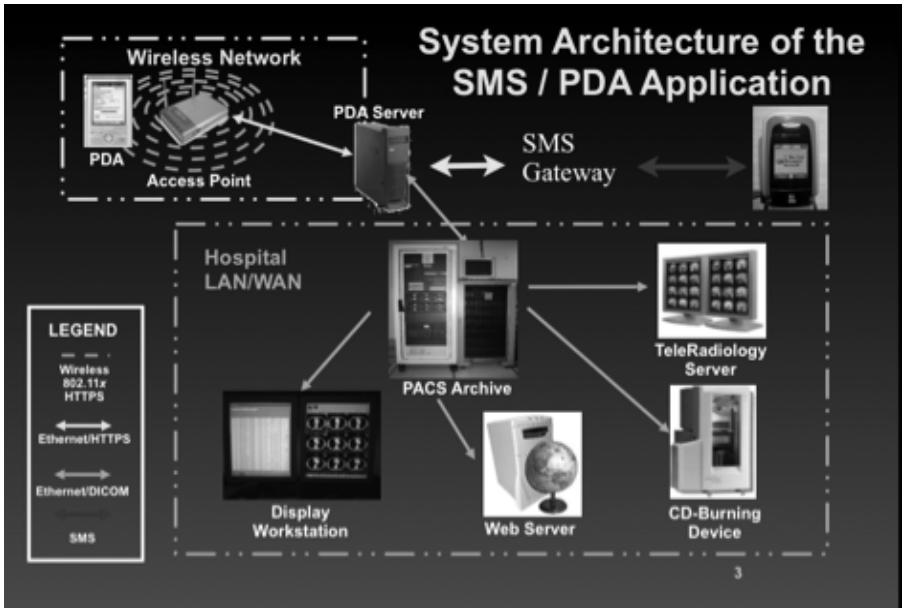

Fig. 3. The SMS System Architecture is a powerful extension of the existing PDA System Architecture, allowing any authorized user with a cellular phone to direct DICOM images within the Hospital network.

3.2 System Performance

The average turn around time for a SMS command and a reply from the gateway was measured to be 15-20 seconds. However, users noted that turn-around time depended on cellular network congestion. Therefore, the navigation through the three states is on the order of 2-3 minutes provided that the query does not yield too many possible matches. The system was tested with the PDA server and SMS gateway server on the same machine.

3.3 System Security

If the SMS gateway needs to be in a separate machine its communication with the PDA server is via https, a secure protocol. The SMS gateway only allows queries of 3 types of information: Patient Name, Patient ID and Study Information. This ensures that minimal patient demographic information can be extracted from the PACS archive. Moreover, the SMS gateway does not allow transfer of images outside of the pre-designated list of access-protected destinations. The system can also allow or disallow user-access based on the user's phone number.

3.4 User Preferences

Since the user's states are tracked internally, the system allows the administrator to set user preferences such as authorized destinations. Other possible user-based preferences could include user customized filters during searches, or a preference to search only by Patient ID.

3.5 Interface Usability

Referring to Table 2 above, it shows the complete workflow to perform a retrieve on a study. The user only has to enter a number at each step following the initial query by patient name. The only latency in the system is waiting for the server reply, which is about 15 seconds depending on cellular phone network congestion. For a large PACS archive, the screen size and limited number of characters of the SMS protocol becomes a severe limitation when querying with common last or first names only. One way to overcome this problem is to use query by patient ID. Otherwise, the system is user friendly and requires simple inputs of numbers to make necessary choices.

3.5 System Component and Operation Costs

The system runs autonomously after setup and therefore should require minimal maintenance. Since the system can be run from a single machine, the hardware costs are relatively low. Moreover, the scripts and web server does not put a heavy load on the CPU or RAM, therefore the minimum hardware requirements are sufficient. The cost of the modem is also relatively low at about USD $300. Thus, the main burden lies in the cellular phone subscription plans. Most normal cellular phone plans can be used and usually gives 3000 SMS and 5 cents for each additional SMS received and transmitted a month for about USD $60.00. However, large hospitals may consider a fixed rate plan with a cellular provider due to their high volume.

4. CONCLUSIONS AND FUTURE WORK

4.1 Future Work

4.1.1 User Authentication

An additional authentication step is required to ensure proper access protection to the SMS system. This can be easily implemented as extra user authentication state (see figure 2). The user will send an SMS with a password that will be authenticated against the origin (user) phone number.

4.1.2 Hospital Information System (HIS) / Laboratory Information System Applications (LIS)

Potential other use cases of such a system could include retrieving patient data from HIS and LIS, provided ways of circumventing HIPAA requirements are found.

4.1.2 Multimedia Capabilities

With the advent of 3G (Third Generation) cellular technologies such as video streaming and higher bandwidth data connections with cellular networks, it is possible that DICOM images can also be relayed in the same manner as the SMS messages through the use of MMS or Multimedia Messaging Service. One of the destinations in our system could be to the user's cellular phone. This would enable the user to see images on the cellular phone display. Possibilities of features such as Window / Level and Zoom / Pan are possible but may be limited by the processing power of the cellular phone. Display resolution is another concern that needs to be addressed.

4.2 Conclusions

The SMS protocol provides an easy and simple way to deploy an application that can manage the DICOM workflow without being constrained by networking requirements. It complements the PDA technology by providing the user with a simpler interface with less network and bandwidth requirements. This paper shows that although SMS is a text-only communication tool, it can allow a user to perform tasks on a PACS network wirelessly. What remains is to see how receptive physicians and technologists are to such a method of streamlining their workflow. However, certain tasks and workflow scenarios will lend itself more to SMS-based wireless control. Tasks such as CD burning of studies through a CD burning DICOM node would lend itself well to SMS control.

We also consider that there is a potential for a variety of use cases for SMS in healthcare information management. Certainly, text-based laboratory information could easily be transmitted over SMS. Application of MMS to transmit images may open up greater possibilities in the realm of image-based information.

REFERENCES

1. Documet, J., et al., Wireless Remote Control of Clinical Image Workflow: Using a PDA for Off-Site Distribution and Disaster Recovery. Journal of the American College of Radiology, 2006. 3(7): p. 520-527.
2. Tellis, W.M. and K.P. Andriole, Integrating multiple clinical information systems using the Java message service framework to enable the delivery of urgent exam results at the point of care. J Digit Imaging, 2005. 18(4): p. 316-25.
3. Kim, D.K., S.K. Yoo, and S.H. Kim, Instant wireless transmission of radiological images using a personal digital assistant phone for emergency teleconsultation. J Telemed Telecare, 2005. 11 Suppl 2: p. S58-61.
4. Raman, B., et al., Radiology on handheld devices: image display, manipulation, and PACS integration issues. Radiographics, 2004. 24(1): p. 299-310.
5. Liu, B.J., et al., Wireless remote control clinical image workflow: utilizing a PDA for offsite distribution [5371-29]. Proceedings - SPIE (The International Society for Optical Engineering), 2004. 5371: p. 178-184.
6. Yaghmai, V., et al., Evaluation of personal digital assistants as an interpretation medium for computed tomography of patients with intracranial injury. Emerg Radiol, 2003. 10(2): p. 87-9.
7. Tachinardi, U., et al., Real time information from bedside monitors as part of a web-based patient record. Proc AMIA Symp, 2001: p. 691-5.
8. Kannel Open-Source SMS Gateway, http://www.kannel.org/
9. Apache Software Foundation, http://www.apache.org/
10. Perl Dynamic Programming Language, http://www.perl.org/
11. MultiTech Systems, Mounds View, Minnesota, USA, http://www.multitech.com/

SPIE Medical Imaging 2007 - (6516-1)

Specification and Design of a Therapy Imaging and Model Management System (TIMMS)

Heinz U. Lemke, PhD, University of Southern California, Los Angeles, CA
Leonard Berliner, MD, New York Methodist Hospital, NY

Abstract
Appropriate use of Information and Communication Technology (ICT) and Mechatronic (MT) systems is considered by many experts as a significant contribution to improve workflow and quality of care in the Operating Room (OR). This will require a suitable IT infrastructure as well as communication and interface standards, such as DICOM and suitable extensions, to allow data interchange between surgical system components in the OR. A conceptual design of such an infrastructure, i.e. a Therapy Imaging and Model Management System (TIMMS) will be introduced in this paper.

A TIMMS should support the essential functions that enable and advance image, and in particular, patient model guided therapy. Within this concept, the image centric world view of the classical PACS technology is complemented by an IT model-centric world view. Such a view is founded in the special modelling needs of an increasing number of modern surgical interventions as compared to the imaging intensive working mode of diagnostic radiology, for which PACS was originally conceptualised and developed.

A proper design of a TIMMS, taking into account modern software engineering principles, such as service oriented architecture, will clarify the right position of interfaces and relevant standards for a Surgical Assist System (SAS) in general and their components specifically. Such a system needs to be designed to provide a highly modular structure. Modules may be defined on different granulation levels. A first list of components (e.g. high and low level modules) comprising engines and repositories of an SAS, which should be integrated by a TIMMS, will be introduced in this paper.

1. Introduction

Since the OR and image-based interventional suites are the most cost-intensive sector in the hospital, the optimization of workflow processes has become of particular concern for healthcare providers, managers, and administrators. The understanding and management of workflows should become an integral part in the planning and implementation of complex digital infrastructures supporting diagnostic and interventional procedures (i.e. interventional radiology, minimal interventional surgery, computer assisted surgical procedures and Image Guided Therapy (IGT)).

Examples of workflow and OR infrastructure related issues are [1]:

a) Inefficient, ineffective and redundant processes
b) Inflexible "systems" of operation
c) Ergonomic deficiencies which hinder the workflow

d) Data (text, 1D, 2D, 3D, 4D) presentations not adequate, e.g. intraoperative and perioperative
e) Soft knowledge (info+action strategy) presentation not available
f) Scheduling (and tracking/RFIDing) of patients, personnel, operating rooms, equipment etc. not facilitated or coordinated (often the seeds of "busted" schedules)
g) Too long set up times for image-guided and robotic surgery
h) Lack of consistent working practices/guidelines or workflows (the hospital as a high risk and high velocity "production" environment is not scripted enough, there is too much diversity of behaviour)
i) No standardised integration of surgical devices and systems
j) Lack of quantified information on workflow and error handling
k) Communication across disciplines not adequate, e.g. between radiology and surgery

Possible solutions are:

a) improve situational awareness
b) ensure availability of real-time information regarding (peri)operative processes to respond to best practices and variances in actual patient care
c) develop standard interfaces to integrate seamlessly ICT and MT systems into the OR by taking account of the special needs of imaging and modelling tools within the surgical workflow

This leads to the concept of an ICT supported OR which may be named surgical PACS (S-PACS) or more specifically a “Therapy Imaging and Model Management System” (TIMMS). A TIMMS [2] should support the essential functions that enable and advance image, and in particular, patient model guided therapy. Within this concept, the image centric world view of the classical PACS technology is complemented by an IT model-centric world view. Such a view is founded in the special modelling needs of a number of modern surgical interventions as compared to the imaging intensive working mode of diagnostic radiology, for which PACS was originally conceptualised and developed.

A TIMMS provides the ICT based infrastructure necessary for surgical/interventional workflow management of the modern Digital Operation Room (DOR). The concept and design of a TIMMS is based on the assumption that significant improvement in the quality of patient care, as well as ergonomic and health-economic progress in the OR can only be achieved by means of an ICT infrastructure (based for example on a suitable DICOM extension) for data, image, information, model and tool communication. A proper design of a TIMMS, taking into account modern software engineering principles, such as service oriented architecture, will clarify the right position of interfaces and relevant standards for a Surgical Assist System (SAS) in general and their components specifically.

2. TIMMS and its interfaces

Engineering of ICT systems for the assistance of surgical interventional activities implies the specification, design, implementation and testing of Computer Assisted Surgery (CAS) or IGT

systems. A number of components for such systems have been developed in academic and industrial settings and are applied in various surgical disciplines. In most cases, however, they are stand alone systems with specific ad hoc propriety or vendor interfaces. They can be considered as islands of IT engines and repositories with varying degrees of modularization and interconnection.

Figure 1 shows an abstraction of seven engines with associated repositories, which may form part of an SAS. Ideally they should be integrated by a suitable TIMMS infrastructure.

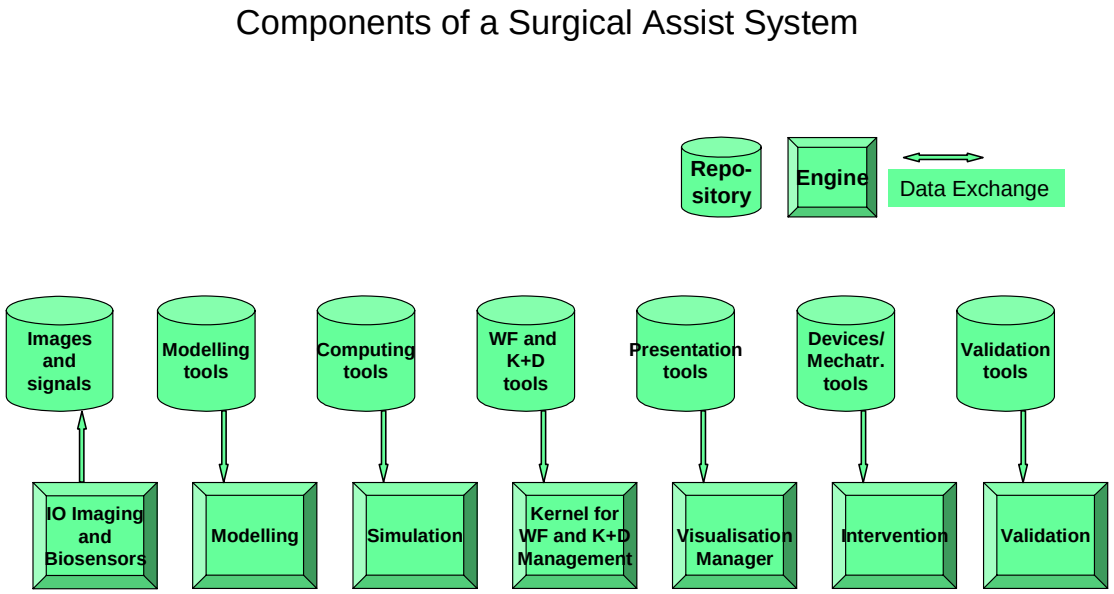

Fig. 1: Components of a Surgical Assist System

Considering software engineering principles, such a system needs to be designed to provide a highly modular structure. Modules may be defined on different granulation levels. A first list of components (e.g. high and low level modules) comprising engines and repositories of an SAS, which should be integrated by a TIMMS, is currently being compiled in a number of R&D institutions and also within the DICOM Working Group 24 (WG24) “DICOM in Surgery”.

Figure 2 shows a concept (meta architecture) of a high level generic modular structure of a surgical assist system. The high level modules are abstracted from many specific CAS/IGT systems which have been developed in recent years. In general, a combination of these can be found in most R&D as well as commercial SAS systems. A central position in Fig. 2 is occupied by the “Kernel for workflow and knowledge and decision management”. It provides the strategic intelligence for preoperative planning and intraoperative execution. Often this module (or parts thereof) is integrated into some of the other engines, as the need may have demanded.

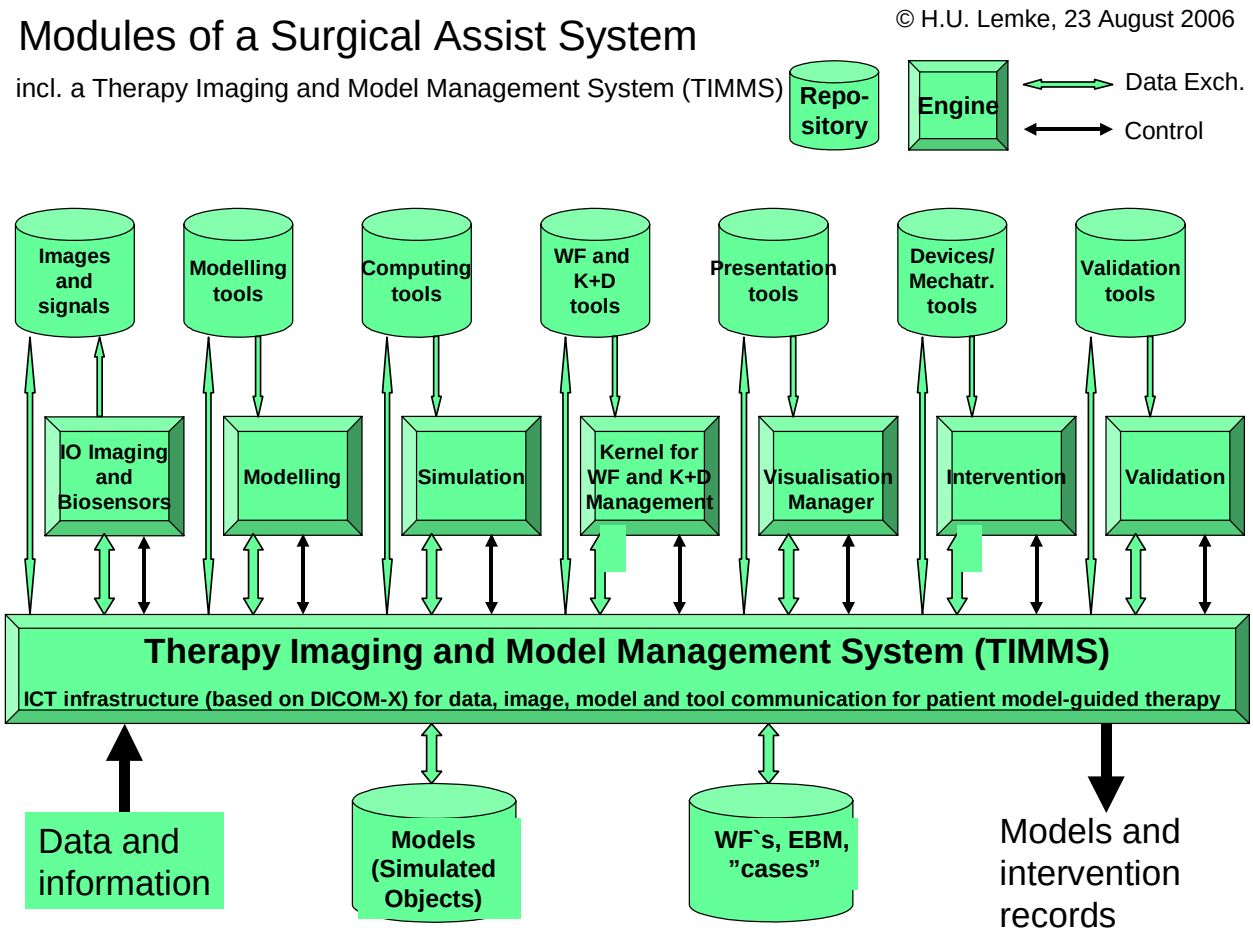

Fig. 2: Therapy Imaging and Model Management System (TIMMS)

Low level modules (LLM's) responsible for interfacing and communication are embedded in each of the engines and repositories given in Fig. 2. LLM`s should be derived from a single or from a combination of several distinct surgical workflows. In the latter case, therethese are sometimes referred to as surgical integration profiles (SIP's). An LLM may be a surgical function or related activity using information objects, which ideally, may be part of different types of interventions. In order to identify LLM`s which satisfy the above requirements, it is of critical importance to select a representative set of surgical/interventional workflows which cover the domain of interest for standardisation of image and model-guided interventions. This selection should not only focus on the present state of the art of surgery, but also take into account future potential developments of patient image- and model-guided interventions.

3. Components of TIMMS and functionalities

3.1. Engines and repositories

The components of TIMMS, which are modular, scalable and may be distributed in location, act synergistically to provide functionality and utility that exceeds the sum of its individual parts. The components include:

1. Seven “Engines” which work independently and dependently, and account for all facets of complex medical and surgical procedures. (Engine may be defined as a software module which can be executed on an appropriate computing machine.)

The seven engines are:

1. Intraoperative Imaging and Biosensors Engine
2. ModelingModelling Engine
3. Simulation Engine
4. Kernel for Workflow and Knowledge and Decision Management Engine
5. Visualization Representation Manager Engine
6. Intervention Engine
7. Validation Engine

2. Associated Repositories linked to each of the seven engines. (A repository may be defined as an integrated hardware and software structure which stores, and makes available, data and/or data processing tools)

1. Images and signals Repository for the Intraoperative Imaging and Biosensors engine
2. ModelingModelling tools Repository for the ModelingModelling engine
3. Computing tools Repository for the Simulation engine
4. Workflow and Knowledge and Decision tools Repository for the Kernel for Workflow and Knowledge and Decision Management engine
5. Representation tools Repository for the Visualization Representation Manager engine
6. Devices and Mechatronic tools Repository for the Intervention engine (Mechatronics is defined as the synergistic combination of mechanical engineering, electronic engineering, and software engineering.)
7. Validation tools Repository for the Validation engine and for the Kernel for Workflow and Knowledge and Decision Management engine

3. Additional Repositories which are provided for:

1. Models (Models are defined as Simulated Objects)
2. References such as Workflow Models, Evidence-Based Medical Data, Case-Based Medical Data

The system provides for real-time data mining from these repositories during the performance of the surgical procedure. The Kernel for Workflow and Knowledge and Decision Management Engine is the central computing kernel (or “brain”) of the system. It may use different forms of logic, different database structuring, intelligent agents and other forms of artificial intelligence, depending on the specific applications of the procedure or procedures being performed. Intelligent agents may be defined as software modules, containing some form of artificial intelligence, which, with some degree of autonomy and adaptability, carry out functions or tasks.

Intelligent agents may be called by the workflow engine when executing a given activity component/element of a given workflow. In general, intelligent agents are part of the Kernel for workflow and knowledge and decision management, but theyre may bey may also be part of and/or be accessible by to the other engines of TIMMS. An Information and Communication Technology Infrastructure allows for intercommunication and interactivity between all components of TIMMS.

All of the engines, tools, repositories, ICT infrastructure, data sources, including the operative team are linked, through a distributed network, providing for the full functionality of TIMMS, including planning, guidance, learning, and data mining and processing.

The ICT infrastructure used by TIMMS includes structures, objects, processes and interfaces from well established sources, to ensure compatibility. This includes, but is not limited to,:

- IHE
- HIS
- RIS
- PACS
- DICOM
- HL7

Interfaces are provided for the input of data and information from the outside world which are then processed and utilized by the functional components of TIMMS and stored within the repositories. A possible realization of interfaces required between major functional groups within and outside TIMMS is shown in Figure 3.

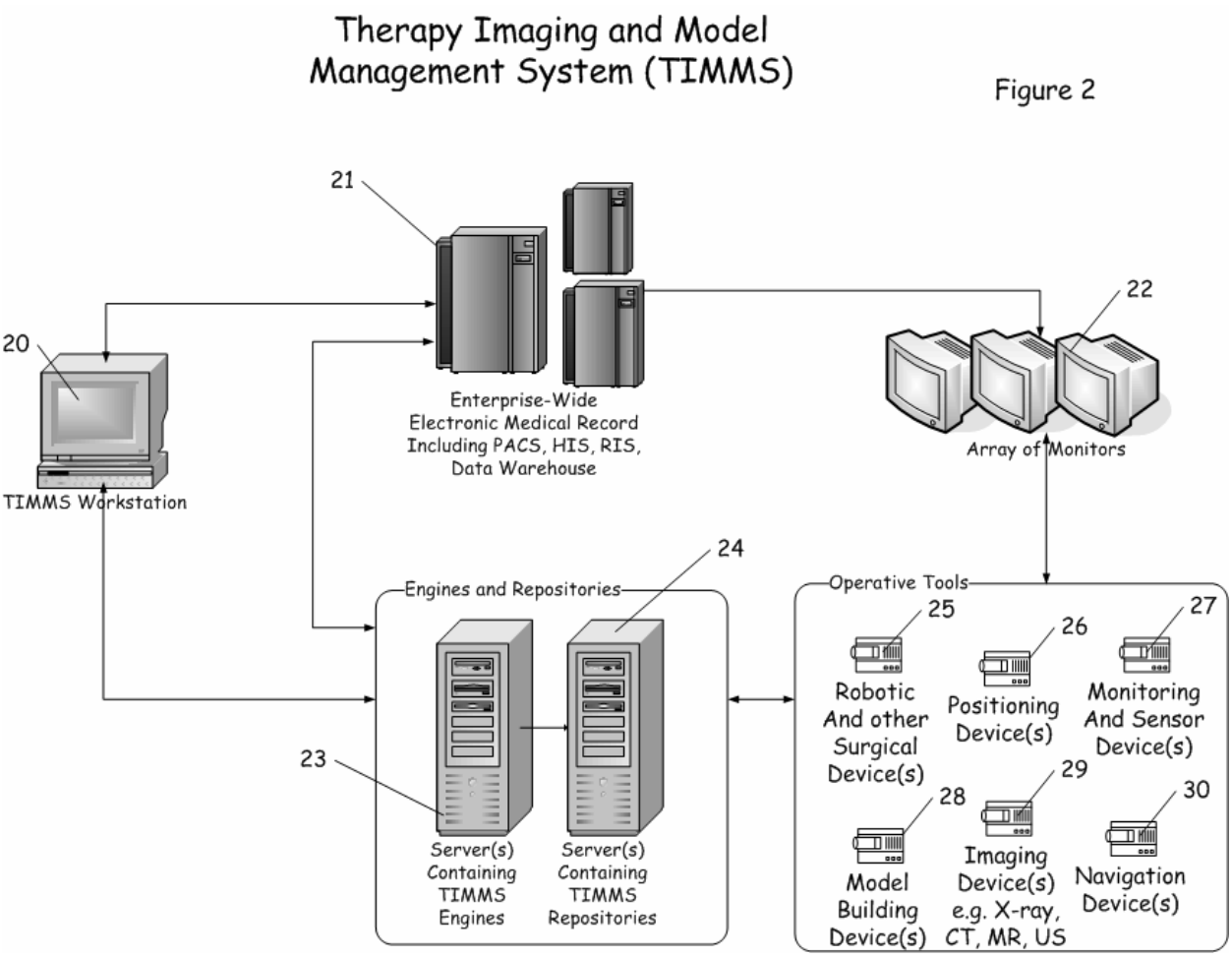

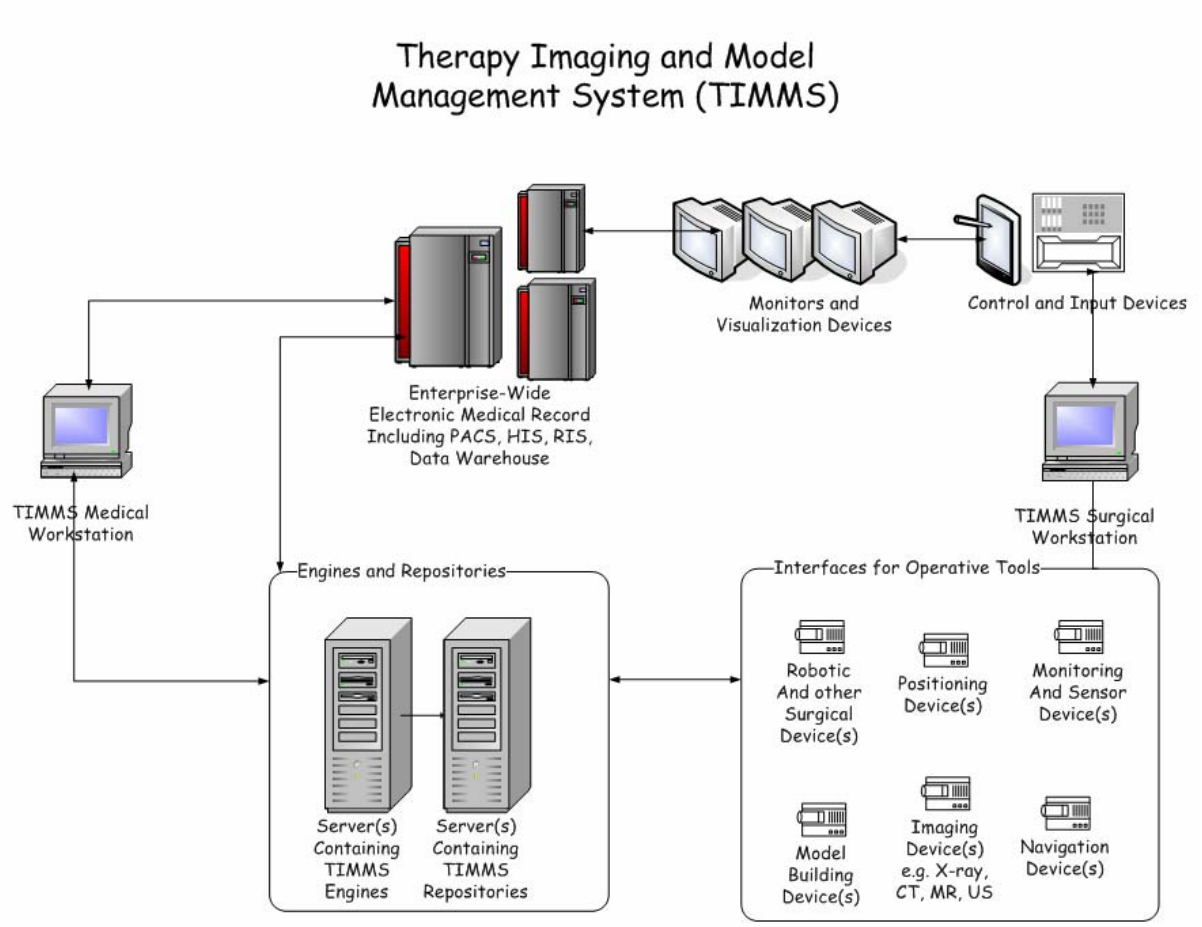

Fig. 3: Data interfaces of TIMMS

Interfaces are also provided for the output of various models, intervention records, data and information that have been synthesized within the TIMMS structure.

3.2. Major functionalities

Patient specific modelling

TIMMS is based on an underlying construct or approach to patient management entitled a Model-Centric World View. Traditionally, the approach to medical imaging when applied to clinical aspects of patient care has been limited to the realm of the images themselves. This has been called the Image-Centric World View.

However, the approach to medical imaging employed by TIMMS is extended far beyond the realm of the images. In the Model-Centric World View a wide variety of information, relating to the patient, can be integrated with the images, providing a more comprehensive and robust view of the patient. TIMMS employs the Model-Centric World View, providing and utilizing all available data for surgical interventions.

Adaptive Workflow Engines

The incorporation and utilization of workflow processes, within the Kernel for Workflow and Knowledge and Decision Management is central to the functioning of TIMMS.

TIMMS employs an adaptive workflow engine that is flexible and capable of learning and providing guidance throughout the procedure. A reference workflow engine, which provides the basic framework for a surgical procedure, evolves into an executing workflow engine, which is patient specific and is based on the model-centric view of the patient that also evolves throughout the entire patient encounter. For example, modifications to the executing workflow engine may be based on feedback from physiologic monitoring of the patient, from the surgeon, from operative robots, from operative haptic devices, from stored data within repositories.

Modifications to the executing workflow engine are in synchronization with updates to the Patient Model by the modelingmodelling engine. The selected reference Surgical Workflow is extracted from the appropriate repository during the planning stage of the surgical procedure.

Validation Processes

Data collection is automated for all aspects of the pre-surgical evaluation, intra-operative procedures, and post-operative evaluation. Methodology is provided for the application of statistical processes to the accumulated data.

The methodology for error handling and validation is built into the system so that variations in human performance, as well as machine performance, and patient response are factored in, and learned from, at any given step of the surgical procedure.

The system contains the functionality to achieve refinements in medical and surgical ‘best practices” and to facilitate quality improvement programs. Prospective medical research projects will be more easily achieved through the automated collection, monitoring and measuring of large volumes of data, with numerous variables.

Key aspects for the validation engine:

- Assess the surgical workflow activities, in particular the imaging, model and representations accuracy of the surgical intervention;
- Assess specific surgical domain data, information, knowledge and decision presentations, intervention protocols;
- Ascertain that the specific surgical workflow selected fulfils the purpose for which it is intended and is properly executed;
- Ascertain that selected critical activities, which imply given accuracy, precision, real-time response, etc. are properly carried out;
- Ascertain that the appropriate tool sets selected from the repositories will provide the capabilities required
- Secure that completeness and consistency checks produce the correct results;
- Ascertain that appropriate documentation and reporting for the intervention is carried out
- Ascertain that the appropriate hardware and software devices required are on-line and functioning

4. Modelling tools of TIMMS and steps towards standards

Standards relating to medical imaging and communication for non-real time diagnostic and related activities are well defined by DICOM and are an integral part of TIMMS. Most of the Image and Presentation States IOD's, which are defined in DICOM, etc. are also relevant to surgery.

Models and their associated management have not been considered in DICOM intensively, except through some work done in DICOM WG 07, WG 17 and WG 22. Modelling and simulation in surgery however, are key functions for SAS's pre- and intraoperatively. Interfacing of tools which support these functions comprises a relatively new scope for DICOM.

To define model and simulation, a definition by O. Balci [3] may be used "A model is a representation or abstraction of something such as an entity, a system or an idea. Simulation is the act of experimenting with or exercising a model or a number of models under diverse objectives including acquisition, analysis and training." As indicated in Fig. 2, both modelling and simulation are critical components of an SAS, particularly for planning and intervention activities.

It will be a significant extension of current DICOM efforts to complement the image centric view with a model centric view for developing DICOM objects and services. Some IOD's which make use of the concept of a model are listed in DICOM PS 3.3 as part of annex C 8.8. "radiotherapy modules". Currently, approximately 40 modules have been specified for radiation therapy. They imply a limited spectrum of data types and data structures with different degrees of complexity, e.g. simple lists or tree structures. In the context of a TIMMS, a more comprehensive view on modelling than for example in Rradiation Ttherapy, will be necessary. Not only as regards the modelling tools for generating different types of data structures, but also with respect to the modelling engine which carries out the modelling task. This engine will occupy a central position in the design of a SAS and the TIMMS infrastructure.

By default, the broader the spectrum of different types of interventional/surgical workflows which have to be considered for standard interfacing support, the more effort has to be given for designing appropriate IOD modules and services. The following list contains some examples of modelling tools and aspects, derived from different types of surgical workflows, which may have to be considered for future standard activities such as DICOM:

- Geometric modelling incl. volume and surface representations
- Properties of cells and tissue
- Segmentation and reconstruction
- Biomechanics and damage
- Tissue growth
- Tissue shift
- Prosthesis modelling
- Fabrication model for custom prosthesis
- Properties of biomaterials
- Atlas-based anatomic modelling
- Template modelling

- FEM of medical devices and anatomic tissue
- Collision response strategies for constraint deformable objects
- Variety of virtual human models
- Lifelike physiology and anatomy
- Modelling of the biologic continuum
- Animated models
- Multi-scale modelling
- Fusion/integration of data/images
- Registration between different models incl. patient, equipment and OR
- Modelling of workflows
- ...

Real-time aspects identified for imaging during intervention are equally applicable for the generation and management of these models. In addition to define defining mechanisms to enable real-time communication, it will also be one of the first tasks of standardization to agree on a list of relevant models to be considered for DICOM IOD's etc.

5. Conclusion

In summary, TIMMS provides a process and system for a comprehensive surgical assist system, which combines and integrates all of the necessary information and communication technology; workflow analysis, data processing and data synthesis; interactive interfaces between surgeon and mechatronic devices; and, intelligent agents; to provide comprehensive assistance and guidance throughout complex medical and surgical therapies, such as image and model guided surgery. The components of TIMMS, which are modular, scalable and may be distributed in location, act synergistically to provide functionality and utility that exceeds the sum of its individual parts.

References

[1] Pentacost M.: Review of the operating room of the future, OR-2020, UCLA Seminar on Imaging and Informatics, October 4-6, 2004.

[2] Lemke HU, Vannier MW. The operating room and the need for an IT infrastructue and standards, International Journal of CARS, Springer, Vol. 1 No. 3, Nov. 2006.

[3] Balci, O.: Verification, validation and certification of modeling and simulation applications. Proceedings of the 2003 Winter Simulation Conference, 2003.

SPIE Medical Imaging 2007
(6516-2)

Summary of the White Paper of DICOM WG24 'DICOM in Surgery'

Heinz U. Lemke, PhD, University of Southern California, Los Angeles, CA

Abstract

Standards for creating and integrating information about patients, equipment, and procedures are vitally needed when planning for an efficient Operating Room (OR). The DICOM Working Group 24 (WG24) has been established to develop DICOM objects and services related to Image Guided Surgery (IGS). To determine these standards, it is important to define day-to-day, step-by-step surgical workflow practices and create surgery workflow models per procedures or per variable cases.

A well-defined workflow and a high fidelity patient model will be the base of activities for both, radiation therapy and surgery. Considering the present and future requirements for surgical planning and intervention, such a patient model must be n-dimensional, were n may include the spatial and temporal dimensions as well as a number of functional variables.

As the boundaries between radiation therapy, surgery and interventional radiology are becoming less well-defined, precise patient models will become the greatest common denominator for all therapeutic disciplines. In addition to imaging, the focus of WG24 should, therefore, also be to serve the therapeutic disciplines by enabling modelling technology to be based on standards.

1. Introduction

Standards in health care are justified on the basis of medical, technical, legal, and economic consideration. In a wider context they should improve health care delivery and enable "healthy" business developments. These considerations motivate companies and standard organizations, in close cooperation with academic institutions and government agencies to work towards developing standards. The development of DICOM for radiological applications resulted from such an initiative.

The call for and the historic development of "DICOM in Surgery" can be traced to a number of special workshops/seminars which addressed the topic of the OR, Image Guided Therapy (IGT), workflow and interoperability. More recently, as part of the situational awareness, also workshops on systems architecture and engineering design of IGT systems have been arranged. Representatives from many institutions provided valuable insight into why and how standards in the OR should be developed.

This paper summarizes the result of these activities and provides the background for the need of designing a “Therapy Imaging and Model Management System” (TIMMS) for the digital operating room (DOR) and specifying appropriate standards based on medical, technical, and business reasons.

2. General motivation for standards in surgery

A number of special workshops and seminars which have addressed the medical, technical, economic and related problems of the OR have taken place in recent years in Europe and in the USA. The most notable recent meetings with a focus on IGT, surgical workflow and standards in the OR were:

1. UCLA Seminars on Imaging and Informatics, September 22-25, 2003, Lake Arrowhead, CA, USA [1]
2. Leipzig University Forum, ICCAS, October 2003. [5]
3. Workshop on "OR2020: Operating Room of the Future", March 18-20, 2004, Ellicott City, MA, USA [2].
4. CARS/SPIE “Joint meeting on Surgical Workflow, PACS and the OR of the Future”, June 26, 2004, Chicago, IL, USA [3].
5. UCLA Seminars on Imaging and Informatics, October 4-6, 2004, Lake Arrowhead, CA, USA [4].
6. NCIGT and NA-MIC Workshop on Image Guided Therapy, Rockville, MD, October 19-20, 2006 [6].

Standards and interoperability of devices were a common theme of almost all of these meetings. Exemplary for this effort are the insight and results given by two working groups established for the OR 2020 Workshop [2]. It is worth noting that approximately one third of the participants of the OR 2020 Workshop were MD’s, R&D PhD’s and representatives from industry and government institutions respectively. The problems which were identified before and then elaborated during the workshop by the two working groups, are summarized as follows:

Working Group 1: Operational Efficiency and Workflow

This group focused on examining requirements for achieving increased efficiencies in the OR. These requirements focused on needed mechanisms for accessing and obtaining correct and current patient-related information and scheduling, and accessing use of correct surgical tools. The group also discussed developing surgical practice standards that define day-to-day, step-by-step surgical workflows. Four of the most critical technical needs which were identified for improving OR efficiencies and workflow are as follows:

1) creating accessible “patient-centric” medical records,
2) developing readable equipment locator/tracking mechanisms,
3) resolving OR teamwork/personnel issues, and
4) developing and following technical standards in the OR.

Working Group 2: Systems Integration and Technical Standards

This group focused on the need for interoperability among a broad range of devices that are used in the OR. To achieve seamless integration among devices, it was recommended, that a standard interface for interoperability among these technologies should be developed using a plug and play platform. This group also discussed the need for device standards that will enable configurability and easy use of these tools in the OR.

Recommendations

Many details have been listed by the two working groups as potential solutions to the above problems, here included as a summary recommendation [2]:

1. Standards, standards, standards. If there was an overarching theme of the workshop, this was it. Standards are needed in all areas, and must be developed through a concerted effort involving companies, government agencies, academic institutions, and perhaps standards organizations. Research studies of surgical workflow and efficiencies are required to develop practice standardization and thus realize improvements.

2. Progress on the first recommendation will also enable progress on device interoperability. It is recommended that research be devoted to developing common user interfaces among medical devices, and that the device industry take the lead in performing this research with input for academic institutions and government agencies. A "plug and play" architecture for medical devices is also needed.

Of particular interest is here the statement that standards are needed in all areas and must be developed through a concerted effort involving companies, government agencies, academic institutions, and perhaps standards organizations. Motivating these players to work in a concerted effort towards standards can only be achieved, of course, if it is in their business interest. One of the critical questions which needs to be addressed is:

"Is the OR of the Future (ORF) a viable economic reality?" [7].

3. The business case for DICOM in Surgery

Considering the high number of OR's and surgical interventions carried out on a worldwide basis, it is surprising how little ICT support is actually applied to patient treatment on a daily basis. The number of academic and industrial institutions engaged in R&D of SAS's is impressive, their total impact, however, disappointing. As indicated in [1], there are problems in the OR, particularly relating to workflow issues and appropriate use of digital data. This is certainly a contributing factor why approximately only one percent of expenditure for equipments and supplies used in connection with surgery, is directed towards CAS and surgical robotics.

In 2001 the amount of this expenditure for the USA was approximately 245 M$ and it is expected to raise by 2007 to 673 M$ in the USA and globally to 1.1 B$ [8]. Considering that there are more than 50 industrial vendors in the market, the share of revenue each of these can expect, is limited.

Organizational Aspects for enabling Standards

A closer observation of SAS's in the OR clearly shows, that the current situation of SAS development is characterized by stand alone prototypes and products as well as isolated systems solutions with relatively closed systems architectures. SAS's are difficult to introduce, (inter)connect and maintain in an OR environment. The number of these stand-alone components/systems continues to grow, specifically as these systems can demonstrate in an exemplary way, that selected parts of a surgical workflow can be optimized through their use.

Other areas of human endeavour to optimize the working environment, e.g. factory automation or modern pilot systems (cockpits), have shown that a much higher degree of process optimization is possible, particularly if the stand-alone systems can be equipped with more intelligence and interaction/communication capabilities to other systems. Introducing more intelligence into systems components will continue to take place through natural market forces driving the individual system producers and vendors.

The interaction/communication ability between these systems, however, is a fundamental problem and needs to be addressed at its roots, i.e. by developing communication standards and interfaces through an overarching organizational structure (e.g. DICOM and NEMA). It is equally important to make these standards speedily available to a large section of the academic and industrial institutions engaged in R&D and distribution of SAS's.

These institutions will be encouraged to participate in the development and in the use of the standard(s), if at the same time hospital management as well as buyers and vendors of OR equipment will be made aware of the new business potentials made possible by standards. By using the standard(s), their business situation will improve not least by more streamlined workflows, but also by a safer and higher quality patient care.

Standards as a Market Driver

It is recognized and accepted also in the surgical community, that in addition to demographic and epidemiological trends, the development of new technologies and in particular standards, can be an important market driver. However, these technologies such as ICT enabled systems and devices have to simplify the tasks of surgeons and OR personnel alike. Even though it does not yet exist in practice, a TIMMS infrastructure and a controlling module such as a "Kernel for workflow and knowledge and decision management" with appropriate ergonomic and standard interfaces is a step in the right direction [9].

This type of new (intelligent) DOR, if made available and supported at reasonable cost, will impact the OR market substantially. Any DICOM standard effort should therefore address the R&D community as well as buyers, vendors and users of SAS's to promote the potential of standards within the domain of the DOR.

4. Surgical informatics

Informatics generally and ICT specifically, are destined to play a major role not only in the OR but also in surgery as a discipline. A significant part of the OR 2020 Workshop was therefore dedicated towards surgical informatics, with the following main observations [2]:

Overview

Surgical informatics is in a nascent phase as a discipline today. By definition, surgical informatics is the collection, storage/organization, retrieval, sharing, and rendering of biomedical information that is relevant to the care of the surgical patient. Its purpose is to seamlessly use computer-based informatics programs to provide comprehensive and decision making support to the health care team. As a result of applying surgical informatics to both usual and problematic surgical cases, improved decision making and problem solving in surgery are possible.

Clinical Needs

Significant clinical issues that are currently limiting the development of surgical informatics include disparate information systems, and few checks and balances in available informatics systems to guide surgeons in their tasks and decisions. Clearer requirements for information and its presentation to surgeons and other professionals have to be developed and made available during surgeries via text, voice, and video images. Particular attention must be devoted to building informatics systems that integrate preoperative, operative, and postoperative information and making it available where and when needed. Errors in the OR related to incomplete information can then be avoided.

Technical Requirements

Standards for procedures and use of surgical informatics must be defined and implemented. These standards should encompass uniform language/terminology as well as uniform and seamless electronic medical records that will include patient and surgical information, billing, and patient safety issues. Surgical informatics technology for the OR of the Future needs to encompass processing, storing, and indexing details on biomedical/kinetic markers, tissue/pathologic recognition, and other information for instant retrieval by surgeons.

Research Priorities

Three key research priorities that were identified by the Working Group of the OR2020 Workshop are:
1) Standards development in surgical informatics;
2) Precisely defined uses of surgical informatics systems (e.g., for optimizing the skills of surgeons, and for teaching students differently and helping them to perform better); and
3) Intelligent agents that can become virtual experts/consultants which will work with surgeons in the OR.

Specifically with respect to the development of standards it is noticed, that there is a need for arranging a multi-level conference among representatives from government, equipment and information technology vendors, the hospital industry, and the surgical community, to set surgical informatics standards, like the DICOM standard that was developed for the imaging arena. The federal government should take the lead in this effort.

Surgical informatics systems and their standards ought to develop from the perspective of a surgeon and aim to optimize his or her skills. This development can also help to teach students in a different way; that is, using surgical informatics may allow them to practice procedures in more specific detail and so perform better.

5. Surgical Workflows (WF) for Medical Imaging (MI) in surgery

Standards for creating and integrating information about patients, equipment, and procedures are vitally needed at the outset in planning for an efficient ORF. To determine these standards, research is needed to define day-to-day, step-by-step surgical workflow practices and create surgery workflow models per procedures or per variable cases.

An example that might be used to better understand (and eventually improve on) OR workflows and efficiencies is the recent work carried out by the Integrating the Healthcare Enterprise (IHE) initiative and its definitions of work profiles and efficiencies in healthcare outside of the surgical room. This body of experts develops recommendations for the healthcare industry on how to implement standards. (Note: IHE's members do not develop the standards themselves.)

Furthermore, the IHE initiative has developed "integration profiles" that enable consistent access to images and reports for certain medical specialties (such as radiology). Surgical profiles have not been developed yet, but they are needed (a widespread opinion expressed at the OR 2020 Workshop), as is a "surgical DICOM." Today's DICOM standard is not suitable for many imaging types and working modes that are needed in the OR (e.g., it does not cover real-time, and 3D and higher dimensional issues, nor does it address interactivity).

Standards for creating and integrating information about patients, equipment, and procedures are vitally needed when planning for an efficient OR. The DICOM Working Group 24 (WG24) has been established to develop DICOM objects and services related to Image Guided Surgery (IGS). To determine these standards, it is important to define day-to-day, step-by-step surgical workflow practices and create surgery workflow models per procedures or per variable cases.

Recording of Workflows

With these objectives in focus, a detailed workflow-analysis [10] has been carried out by the Technical University Berlin (TUB) and the Innovation Center for Computer Assisted Surgery (ICCAS) in Leipzig. The aim is to model and visualize surgical procedures in order

- to allow a correlation between workflows of different types of surgical procedures, e.g. to obtain a measure of similarity between workflows,

- to assist in identifying (e.g. through simulation, see Figure 1), those parts of the same and between different workflows (Surgical Integration Profiles - SIP's) where a process redesign with automated activities may prove to be of a clinical and economic advantage,

- to provide concepts and data to assist in the specification, design, implementation and in-vivo usage of new information and communication technology and mechatronic systems.

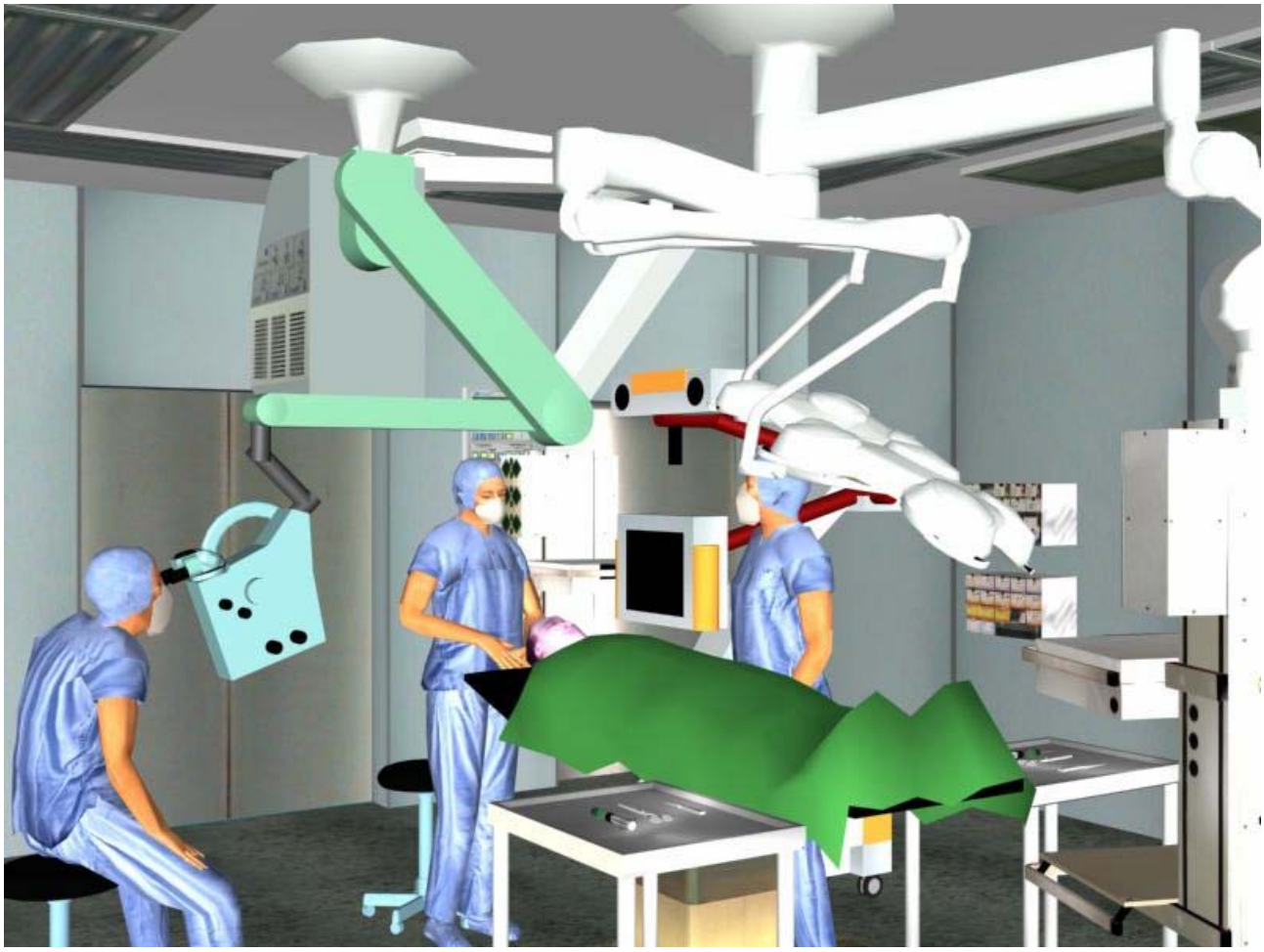

Figure 1: Simulation of surgical workflow.

An important aspect when recording workflows is their modelling and representation technology. Amongst many possibilities and derived from the above work, the workflow management coalition standard is being recommended for workflow recording within WG24. Figure 2 shows an example of a surgical workflow in orthopaedic surgery.

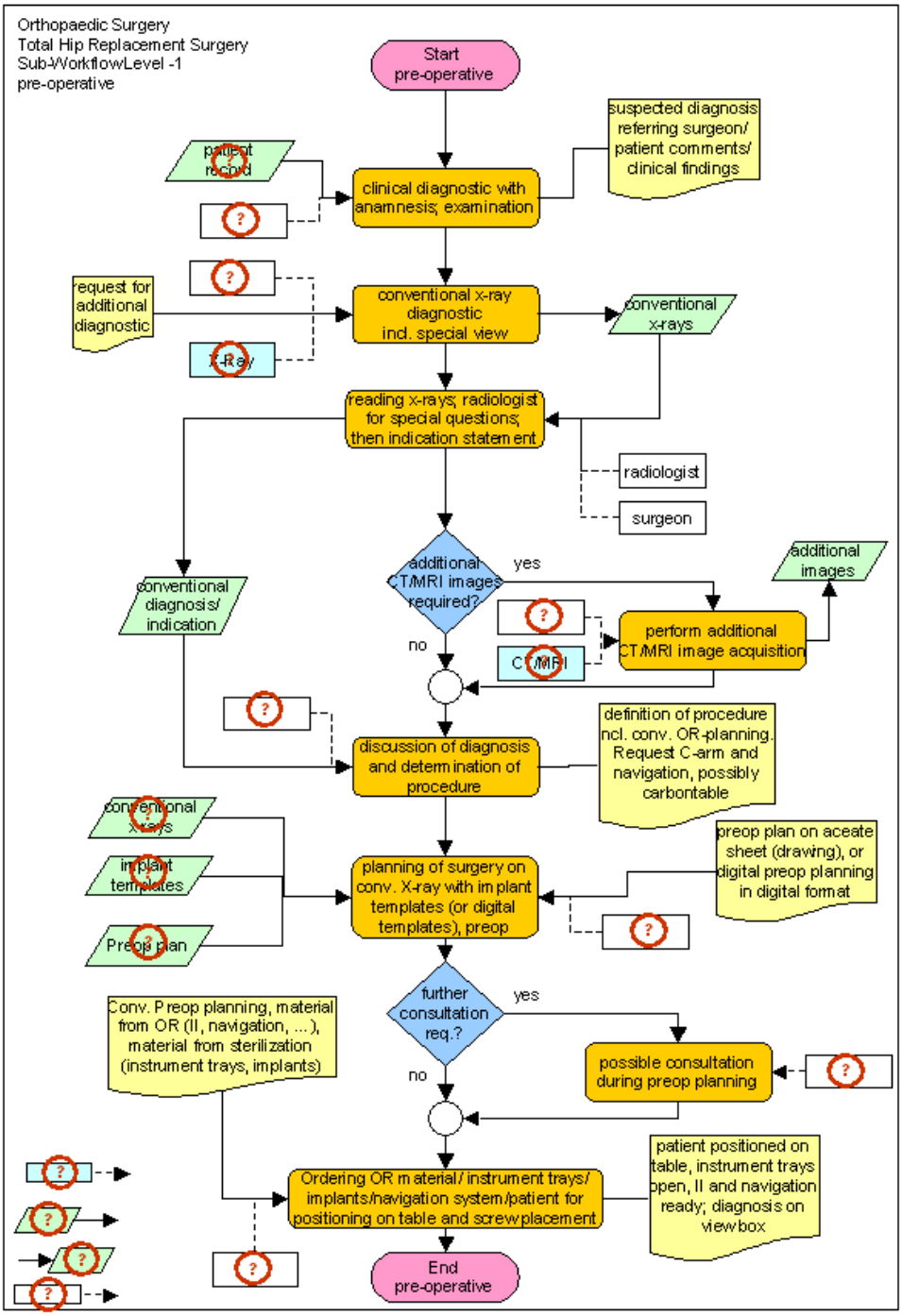

Figure 2: Workflow example from orthopaedic surgery

Dynamics of Workflows and the Model of the Patient

It is important to consider workflows to be dynamic entities. For WG24 they serve as reference (not best practiced!) workflows and are updated at regular intervals to detect within the workflows possible changes in imaging and patient modelling requirements. For example, it can be expected,

that molecular imaging modalities will impact workflow for oncologic patients substantially [11]. Radiation resistant parts of a tumour may be defined with molecular imaging to a higher precision giving rise to include surgical/interventional ablation procedures combined with radiation therapy as a possible regimen.

A well-defined workflow and a high fidelity patient model will be the base of activities for both, radiation therapy and surgery. Considering the present and future requirements for surgical planning and intervention, such a patient model must be n-dimensional, were n may include the spatial and temporal dimensions as well as a number of functional variables. 2D imaging and 2½D or 3D reconstructions are, by definition as subset of an n-dimensional patient model and its representation in the Electronic Medical Record (EMR).

As the boundaries between radiation therapy, surgery and interventional radiology are becoming less well-defined [12], precise patient models will become the greatest common denominator for all therapeutic disciplines. In addition to imaging, the focus of WG24 should, therefore, also be to serve the therapeutic disciplines by enabling modelling technology to be based on standards. A more detailed discussion which emphasises a model-centric world view of therapeutic disciplines as a compliment to the traditional image-centric world view of diagnostic radiology is be presented in [13].

6. WG24 roadmap including project groups

Following the inauguration of WG24 on June 25, 2005 during CARS 2005 in Berlin, the following strategic direction has been agreed on by the members of WG24:

Scope of WG24

“To develop DICOM objects and services related to image guided surgery (IGS)”.

Roadmap

1. Identify and build up a user community of IGS disciplines in WG24. Initially five surgical disciplines (Neuro, ENT, cardiac, orthopaedics, thoracoabdominal and interventional radiology) are selected. Anaesthesia is included as long as surgery is affected.
2. Encourage experts from vendor and academic institutions to join WG24. Vendors of endoscopic and microscopic devices as well as implants (templates) should be included in addition to the classic vendors of medical imaging and PACS.
3. Compile a representative set of surgical workflows (with a suitable high level of granularity and appropriate workflow modeling standards and surgical ontologies) as a work reference for the scope of WG24. Initially, 3-5 workflows, characteristic for each discipline, should be recorded with sufficient level of detail. Workflow tools can be provided by the Innovation Center Computer Assisted Surgery, Leipzig, Germany.
4. Derive potential DICOM services from these surgical workflows.
5. Design an information/knowledge model based on electronic medical record (EMR) related work and identify IOD extensions to DICOM. Because of similarities to the IHE activities, a close relationship to IHE should be established.

6. Take account of the special image communication (1D - 5D) requirements for surgery and mechatronic devices. A close cooperation with WG 2 and 17 should be established.
7. Work in close cooperation with DICOM experts from radiology, cardiology, radiotherapy and related fields which are represented in WG1 - WG23.
8. Encourage close cooperation with working groups in the International Society for Computer Aided Surgery (ISCAS), Japan Institute of CARS (JICARS), German Society for Computer- and Robot-Assisted Surgery (CURAC), European Federation for Medical Informatics (EFMI), European Association for Endoscopic Surgery, American College of Surgery, International Society for Surgery, etc.
9. Disseminate knowledge gained following the roadmap through workshops, conferences and special seminars. Special presentations should be planned each year for CARS, SPIE, RSNA, DICOM-Meeting, and at a minimum for one surgical conference.
10. Connect to integration profiles specified for surgery by IHE activities.

Short Term Goals

1. Specify the scope of WG24 relating to peri-operative workflows.
2. Consolidate the relatively large number of interested individuals of WG24 into effective project groups.
3. Produce a White Paper which identifies the current problems with IGS, possible solutions and derive from this a more detailed roadmap for WG24.
4. The following project groups (PG) have been established (project group chairs and co-chairs in brackets):
   PG1 WF/MI Neurosurgery (N. Hata, R. Fahlbusch, G. Ogrezeanu, R. Bucholz)
   PG2 WF/MI ENT and CMF Surgery (J. Raczkowsky, G. Strauss, G. Eggers, A. Federspil, S. Hassfeld)
   PG3 WF/MI Orthopaedic Surgery (A. Loepfe, U. Stoeckle, L. Joskowicz)
   PG4 WF/MI Cardiovascular Surgery (K. Verstreken, V. Falk)
   PG5 WF/MI Thoraco-abdominal Surgery (A. Pietrabissa, K. Vosburgh)
   PG6 WF/MI Interventional Radiology (L. Berliner, K. Cleary, R. Kikinis)
   PG7 WF/MI Anaesthesia (W. Sandberg)
   PG8 S-PACS Functions (W. Korb, R. Chau, R. Hoecker, Y. Bao)
   PG9 WFMS Tools (O. Burgert, P. Jannin)
   PG10 IPD (J. Sabczynski, R. Shahidi, J. Thiem)
   PG11 Ultrasound in Surgery (S. Horii, T. Layden)
   PG12 White Paper (H. Lemke, O. Ratib, S. Horii)
5. Each PG shall be included in the White Paper. There may be two or three PG leaders coming from the technical and medical disciplines respectively. They are responsible for providing the content of the White Paper.
6. PG 10 and PG 11 are planned to achieve some short (12-18 months) and/or middle term (18-36 months) results. For example, they could select some image acquisition, image processing and display functionalities, specific to IGS, and relate them to DICOM objects and services.
7. Establish a working relationship to professionals in anesthesia.
8. During the starting phase it is planned to have four WG24 meetings per year.
9. Meetings of WG24 for 2006 are scheduled for SPIE, CARS, World Congress of Endoscopic Surgery and RSNA.

Current Status:

- The inaugural meeting of WG24 took place at CARS 2005 in Berlin on 25th June, 2005, which was attended by more than 50 participants.
- Consolidation of the many opinions expressed during the Berlin meeting as regards scope, roadmap and short term goals, etc. has been carried out in WG24 meetings in Budapest, 28th September 2005, Chicago, 29th November 2005 and during four meetings in 2006.

Current Work Items

- Preparation and editing/updating of a strategic summary for WG24.
- Preparation of a White Paper for WG24.

Risks:

- The complexity of surgical workflows (absence of good/best practice surgical procedures) may render the implementation of a surgical PACS and the definition of DICOM objects and services a difficult task. To establish a balanced "voice of surgeons" in different surgical disciplines may require risky compromises and may not be achievable.

Challenges and Opportunities:

Challenges

- IGS takes on very different forms between the surgical disciplines. It is important to include the right spectrum of users from different fields of surgery into WG24. In order to reduce image communication and management functions from the different IGS disciplines to a canonical set suitable for DICOM supported services, it requires not only analytical but also innovative work. It is therefore also important to include the right spectrum of experts from vendor and academic institutions into WG24. An additional challenge is to achieve the above on an international level.
- Workflows for surgical procedures need to be integrated within the overall workflow of patient care, with the aim to integrate the ICT (Information and Communication Technology) island of the OR with the rest of the hospital. Contrary to many other health care activities, a generally accepted surgical ontology and good/best surgical workflow practices are not available to serve as a basis for the activities of WG24. Links to appropriate R&D activities need to be established.

Opportunities

- The digital Operating Room (DOR) is becoming a reality. The market potential for those institutions which bring into the OR digital systems (e.g. a surgical PACS) which conform to standards, such as a suitable DICOM extension, is extremely high.
- Last but not least, patients will benefit from every step taken towards an EMR (Electronic Medical Record) which is embedded in a standard DOR infrastructure.

Relationship to other Standards and Standard Bodies

1. Geometric models (stl, vtk, …)
2. X-ray-dose
3. anaesthesia protocols / measurements

4. Electronic patient record (IEEE/ISO 11073 part 5&6)
5. DICOM WG2
6. DICOM WG17 (Standards for high definition displays)
7. IHE

Election of WG24 Co-Chairs

- In addition to the general chair, WG24 decided to have two co-chairs: one medical (user) and one industry/vendor co-chair.
- The medical co-chair has been elected and will ascertain that clinical considerations are reflected in the standard.
- The industry co-chair will be established after the participating vendors in WG24 have compiled a list of potential candidates. Industry co-chair candidates should give a short summary about their intent to serve as a co-chair to fschweikert@cars-int.org.

References

[1] http://www.radnet.ucla.edu/Arrowhead2004/Seminar2003.html

[2] Cleary K, Kinsella A: “OR 2020: the operating room of the future”. J Laproendosc Adv Surg Tech A, Vol. 15, No. 5, 2005, 497-573.

[3] Lemke HU, Trantakis C, Kochy K et al.: Workflow Analysis for Mechatronic and Imaging Assistance in Head Surgery. In: Lemke HU, Vannier MW, Inamura K et al. eds. Computer Assisted Radiology and Surgery. Chicago, IL: Elsevier, 2004, 830-835.

[4] http://www.radnet.ucla.edu/Arrowhead2004/

[5] Leipzig University Forum 2003 (Technical Report)

[6] Image Guided Therapy Workshop, Rockville, MD, October 19-20, 2006, Technical Report (to be published).

[7] Dritz R: Is the operating room of the future a viable economic reality? In: Anesthesiology, Vol. 104, No. 6, June 2006.

[8] www.bccresearch.com

[9] Lemke, H.U. “Specification and Design of a Therapy Imaging and Model Management System (TIMMS)” SPIE Proceedings on PACS and Imaging Informatics, 2007

[10] Lemke HU: Surgical Workflow and Surgical PACS, UCLA Seminar on Imaging and Informatics, October 4-6, 2004.

[11] Niederlag W, Lemke HU et al. Molecular Imaging, Health Academy 2006.

[12] Onik G. Prostate imaging goals shift as therapeutic options expand, Diagnostic Imaging, November 2005, pp 55-64.

[13] Stahl JE et al: Reorganizing patient care and workflow in the operating room: a cost-effectiveness study. In: Journal of Surgery, Mosby, 2005.

SELECTED PEER REVIEWED REPRINTS AND PREPRINTS

DICOM Image Secure Communications with Internet Protocols IPv6 and IPv4

Jianguo Zhang, Fenghai Yu, Jianyong Sun, Yuanyuan Yang, and Chenwen Liang

Abstract—Image data transmission from one site to another through public network is usually characterized in term of privacy, authenticity, and integrity. In this paper, we first describe a general scenario about how image delivered from one site to another through a WAN with security features of data privacy, integrity and authenticity. Secondly, we give the common implementation method of the DICOM image communication software library with IPv6/IPv4 for high speed broadband Internet by using open source software. Thirdly, we discuss two major security transmission methods, the IP Security (IPSec) and the Secure Socket Layer (SSL) or Transport Layer Security (TLS), being used currently in medical image data communication with privacy supported. Fourth, we describe a test schema of multiple modality DICOM image communications through TCP/IPv4 and TCP/IPv6 with different security methods, different security algorithms and operating systems, and evaluate the test results.

We found that there are trade-off factors between choosing the IPsec and the SSL/TLS based security implementation of IPv6/IPv4 protocols. If the WAN networks only use IPv6 such as in high speed broadband Internet, the choice is IPsec-based security. If the networks are IPv4 or the combination of IPv6 and IPv4, it is better to use SSL/TLS security. The Linux platform has more security algorithms implemented than the Windows (XP) platform, and can achieve better performance in most experiments of IPv6 and IPv4 based DICOM image communications. In teleradiology or enterprise PACS applications, the Linux operating system may be the better choice as peer security gateways for both the IPsec and the SSL/TLS based secure DICOM communications cross public networks.

Index Terms—DICOM Communications, data security, Internet IPv6 andIPv4 protocols, PACS

Manuscript received on September 29, 2005. This work was supported in part by the National Nature Science Foundation of China (Grant No. 39925009 and No. 30570512), China High Tech. Plan (Contract No. 2003AA0010), and Shanghai Sci.&Tech. Plan (Contract No. 03DZ19709 and 05DZ19510), and Chinese Academy of Sciences. The authors would like to thank the colleagues of Shanghai Huadong Hospital for image data acquisition, transmission, and system testing. *Asterisk indicates corresponding author.*

*Jianguo Zhang, corresponding author, is with the Shanghai Institute of Technical Physics, Chinese Academy of Sciences, Shanghai, 200083, China. Tel: +86-21-55510087; fax: +86-21-63248028; e-mail: jzhang@mail.sitp.ac.cn.

Fenghai Yu is with the Shanghai Institute of Technical Physics, Chinese Academy of Sciences, Shanghai, 200083, China (e-mail: .herryyufh@x263.net)

Jianyong Sun is with the Shanghai Institute of Technical Physics, Chinese Academy of Sciences, Shanghai, 200083, China (e-mail: nobm@vip.sina.com)

Yuanyuan Yang is with the Shanghai Institute of Technical Physics, Chinese Academy of Sciences, Shanghai, 200083, China (e-mail: whyyy78@163.com)

Chenwen Liang is with the Shanghai Institute of Technical Physics, Chinese Academy of Sciences, Shanghai, 200083, China (e-mail: cwliang@hotmail.com)

Nomenclature

AES	Advanced Encryption Standard
AH	Authentication Header
API	Application Programming Interface
Blowfish448	448 bit Blowfish Encryption Algorithm
CA	Certificate Authority
CBC	Cipher-Block Chaining
CTN	Central Test Node
DES	Data Encryption Standard
DICOM	Digital Imaging and Communication in Medicine
3DES	Triple DES
DES-CBC	DES in CBC mode
DHCP	Dynamic Host Configuration Protocol
DIMSE	DICOM Message Service Element
ESP	Encapsulating Security Payload
HIPAA	Health Insurance Portability and Accountability Act of 1996
HMAC	Keyed-Hash Message Authentication Code
ICMPv6	Internet Control Message Protocol for the Internet Protocol Version 6
IDEA	International Data Encryption Algorithm
IDEA-CBC	IDEA algorithm in CBC mode
IPv4	Internet Protocol Version 4
IPv6	Internet Protocol Version 6
IPSec	Internet Protocol Security
ISAKMP	Internet Security Association and Key Management Protocol
ISO	International Standards Organization
MD5	Message Digest-5
Null_enc ESP	Null encryption
OSI	Open Systems Interconnect
PDU	Protocol Data Unit
QoS	Quality of Service
RC4	Rivest Cipher 4
RFC	Requests for Comments
SA	Security Association
SCU	Service Class User
SCP	Service Class Provider

SHA	Secure Hash Algorithm
SSL	Secure Socket Layer
TSL	Transport Layer Security
UDP	User Datagram Protocol
VPN	Virtual Private Network
WAN	Wide Area Network

I. Introduction

PACS (picture archiving and communication system) requires high-speed networks to transmit large image files between components. In case of intranet, that is, PACS within a healthcare campus, Gbits/s switches with Mbits/s connections to workstations are mostly adequate and is a standard in most hospital and university network infrastructures. Their transmission rates, even for large image files, are acceptable for clinical operation. However, in case of using the Internet for teleradiology applications or enterprise PACS, image data must be transmitted between hospitals and campuses. There are two important issues needed to be addressed when medical image transmissions are over public Internet: the first issue is cost-effective, and the second is data security. Current low-cost commercial WAN (wide area network) is too slow for medical imaging application, whereas high-speed WAN is too expensive for cost-effective use. To solve the first problem, the broadband high speed Internet technology with new communication protocol IPv6 emerges as a potential solution with high-speed networks and acceptable cost for image data transmission [1]. For security issue, there are certain critical features needed to be addressed in image data exchanging through WAN between application entities, that is, data privacy, authentication, and integrity. There are three organizations issued guidelines, mandates, and standards for image/data security. First, the ACR (American College of Radiology) Standard for Teleradiology, adopted in 1994, defines guidelines for qualifications of both physician and non-physician personal, equipment specifications, quality improvement, licensure, staff credentialing, and liability [2-5]. Second, HIPPA of 1996, Public Law 104-191, which amends the Internal Revenue Service Code of 1986, requires certain patient privacy and data security [6-7]. And third, Part 15 of the DICOM Standard specifies security profiles and technical means for application entities involved in exchanging information to implement security policies (PS 3.15-2001) [8].

Despite these initiatives, to our knowledge, there have not been active systematic research and development efforts in the medical imaging community to seriously tackle the secure DICOM image communication over the Internet protocols IPv6/IPv4 and evaluate their performance with different secure methods and various algorithms used to encrypt the image data for privacy and authentication.

In this paper, first, we describe a general scenario about how image delivered from one site to another through a WAN with security features of data privacy, integrity and authenticity. Second, we describe the implementation method of the DICOM image communication software library with IPv6/IPv4 with open source software. Third, we discuss two major security transmission methods, the IP Security (IPSec) and the Secure Socket Layers (SSL) or Transport Layer Security (TLS), used in medical image data communication with privacy supported. Third, we design a test schema of DICOM image communications through TCP/IPv4 and TCP/IPv6 with different security channels, different security algorithms and operating systems, and evaluate the test results. Finally, we discuss the outcome of our research results to clinical applications.

II. Secured Image Communication Through Wide Area Network

Secure transmission of image data from one site to another through public networks is usually characterized in terms of privacy, authenticity, and integrity. Privacy refers to denial of access to information by unauthorized individuals. Authenticity refers to validating the source of a message, that it was transmitted by a properly identified sender. Integrity refers to the assurance that the data was not modified accidentally or deliberately in transit, by replacement, insertion, or deletion. Figure 1 shows a data flow of image secure delivering from one site to another through WAN. There are two processing steps to provide secure measures on the delivered images: First, for the data integrity and authenticity, the digest (or hash computing on data) and digital signature, as well as decoding signature and comparing digest, on the images before and after transferring are performed in both the sending and the receiving site [9]; Second, for data privacy, the secured communication channels are provided to transmit the image through networks.

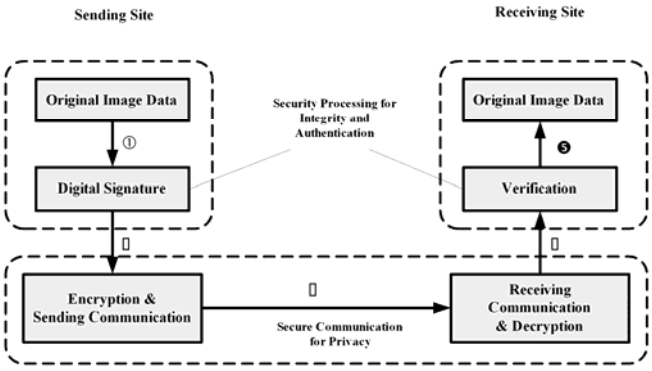

Figure 1. Data flow of medical image secure communication from one site to another through public Internet.

For the first secure measure, there are already many papers and books discussing the technical methods and algorithms [10-11]. In the following sections, we will focus on the second secure measure, which is data privacy, with evaluation results. Currently, there are two methods to provide secure communication channels with TCP/IP protocols: IPSec and SSL/TLS. In the next section, we will discuss the implementation of the TCP/IPv6/IPv4 enabled DICOM communication library and application software.

III. IPv6/IPv4 Communication Protocols and DICOM Communication Software

A. Basic Architecture of TCP/IP

Most of today's Internet uses IPv4, which is now nearly twenty years old. IPv4 has been remarkably resilient in spite of its age, but it is beginning to have problems. Most importantly, there is a growing shortage of IPv4 addresses, which are needed by all new machines added to the Internet. Most network applications and protocols (Client/Server, Web, http, DICOM, …) used in the Internet or intranet are developed based on TCP/IPv4, which is partitioned into three layers according to the ISO (International Standards Organization Open Systems Interconnection, ISO-OSI) definition [12], i.e. the application layer, the transport layer, and the IP layer. Due to the over subscription of Internet addresses and the availability of higher networks bandwidth, TCP/IPv4 starts to show certain strains, such as: (a) Address shortage; (b) Security is not integrated and the IPSec is an add-on; (c) Problems of multicasting; (d) Complicated header; (e) Fragmentation/ retransmission problems; (f) Poor QoS (Quality of Service); (h) Inability to handle large frames; and (i) Limited auto- configuration support (needed by DHCP).

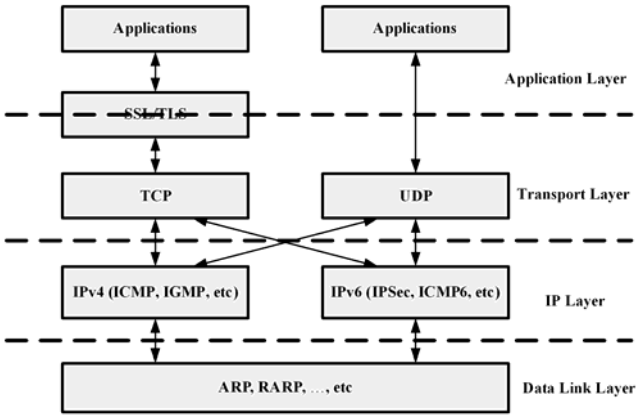

Figure 2. TCP/IPv4/IPv6 protocols family architecture.

IPv6 is a new version of IP which is designed to be an evolutionary step of IPv4 [13]. IPv6 is designed to run well on high performance networks (e.g. Gigabit Ethernet, OC-12, ATM, etc.) and at the same time still be efficient for low bandwidth networks (e.g. wireless). In addition, it provides a platform for higher speed internet functionality that will be required in the near future. IPv6 were designed to solve many of the problems of the current version of IPv4 with regard to address depletion, security, autoconfiguration, extensibility, and other more. IPv6 includes many associated protocols, such as IPSec, ICMPv6, etc. IPv6 has some special features as follows: (a) Larger Address Space; (b) Aggregation-based address hierarchy and efficient backbone routing; (c) Efficient and Extensible IP datagram, such as no fragmentation by routers, 64 bits field alignment, and simpler basic header; (d) Auto configuration; (e) Security; (f) IP Renumbering as part of the protocol. Figure 2 shows the architecture of TCP/IPv4 and TCP//IPv6, from which we see that the major difference of TCP/IPv4 and TCP/IPv6 is in the IP layer. Also, the IPSec is integrated into IPv6 as default security protocol, whereas SSL was adopted to provide security channel in the application layer in the IPv4 network environment, although IPSec was added-on to IPv4 later on.

B. DICOM Communication Software over TCP/IPv6

Most medical image communication uses DICOM communication services to transfer the image data or objects between imaging modalities, PACS archiving server, workstations, and other components; as well as between teleadiology systems, and in enterprise PACS environment with WAN interconnection. In DICOM, the OSI (open System Interconnection) Basic Reference Model is used to model the interconnection of medical imaging equipments, as shown in Figure 3. DICOM uses the OSI Upper Layer Service to separate the exchange of DICOM Messages or objects at the Application Layer from the communication support provided by the lower layers. This OSI Upper Layer Service boundary allows peer Application Entities to establish Associations, transfer Messages and terminate Associations. As indicated in Figure 3, the Upper Layer protocol augmenting TCP/IP is now adopted by most DICOM communication applications to implement DICOM communication services to transfer or deliver DICOM Messages or image objects between equipments or devices. As such, the major tasks to implement DICOM communication software are to develop APIs (Application Program Interface) to implement DICOM Upper layer protocol for TCP/IP in different computer platforms.

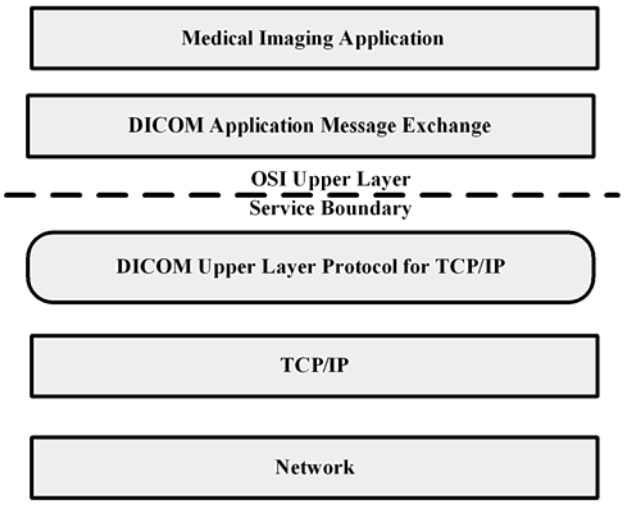

Figure 3. DICOM network communication protocols architecture.

In order to enable medical image transmission through high speed broadband networks with IPv6, it needs to develop the DICOM Upper layer for TCP/IPv6 and also make it compatible with IPv4. There are some of open source reference implementation of DICOM standard, such as CTN

(Central Test Node) DICOM toolkit which was developed by the Mallinckrodt Institute of Radiology (MIR) in St. Louis (USA) [14], and the OFFIS DICOM Toolkit DCMTK which was developed in Oldenburg (Germany) [15], and these open source software implemented most APIs of DICOM Upper Layer protocol for TCP/IPv4 on different operating systems (Unix/Windows/Linux). In this study, we chose CTN DICOM toolkit as a base to implement the DICOM Upper layer for TCP/IPv6, since it served as a test bed for cross-vendor testing of DICOM communication services [14]. The implementation was straight forward: For software, it only needs to replace the original TCP/IPv4 socket functions with RFC (Requests for Comments) standard TCP/IPv6/v4 compatible socket functions, provided by each operating system, re-compile the software, and link it to DICOM applications services. For operating environment, it needs to install the IPv6 stack software and perform some re-configurations, such as assigning IP address, configure the tunnel in the specific operation system, such as Windows XP, Linux (e.g., Red Hat version 3.0 or up) and Solaris (version 7 or up) which have already supported the IPv6. As a result, we come up with four basic IPv6/IPv4 enable DICOM communication services and applications:

1) DICOM C-Store SCU (Service Class User) and SCP (Service Class Provider);
2) DICOM C-Find SCU and SCP;
3) DICOM C-Move SCU and SCP;
4) DICOM QUERY/RETRIEVE SCU and SCP;

IV. Implementation of DICOM Secure Communication Protocols

DICOM Standard Part 15 (PS 3.15-2004) provides a standardized method for ensuring secure communication and digital signature verification. It specifies technical means (selection of security standards, algorithms and parameters) for application entities involved in exchanging information to implement security policies. The implementation of the DICOM Part 15 Secure Transport Connection Profiles for DICOM image security transmission utilizes the framework and negotiation mechanism specified by the TLS (Transport Layer Security) version 1.0 protocol, which is derived from SSL (Secure Socket Layer) version 3.0. The secure communication of IPv6 enabled DICOM image transmission utilizes IPsec protocol, which is now mostly used in VPN (virtual private network) applications, and will be widely used in high speed broadband netwroks. In this section, we first give the software implementations of IPv6/IPv4 secure DICOM communication with IPsec supported, and then discuss the SSL/TLS-based DICOM secure communication. In the next section, we describe tested experiments and compare the efficiencies of both secure DICOM communication methods, namely, IPSec-based and SSL/TLS-based with different modality DICOM images, secure algorithms, and computer platforms.

A. DICOM Communication with IPSec-Based Security Supported

From the right hand side of Figure 2, we can see that IPSec is a member of the IPv6 protocol family. It provides security to the IP and the upper-layer protocols. IPSec is composed of two protocols: AH (Authentication Header) protocol and ESP (Encapsulating Security Payload) protocol. AH is used to ensure the authentication and integrity of message, while ESP is used to ensure confidentiality. The AH protocol uses HMAC (hash message authentication codes) to protect integrity. Many algorithms can be used in AH, such as SHA (Secure Hash Algorithm), MD5 (Message Digest-5), etc [16]. The ESP protocol uses the standard symmetric encryption algorithms to protect confidentiality, such as 3DES (Triple DES), AES (Advanced Encryption Standard) and Blowfish448 (448 bit Blowfish Encryption Algorithm), etc. [16].

Figure 4 shows the data flow of the service pairs of the IPv6/IPv4 DICOM Storage SCU and SCP with IPsec supported. The DICOM SCU and SCP have its own certificate which is created by the same Certificate Authority (CA). There are three steps in IPsec communications. The first is IKE (internet key exchange) protocol association. In this step, the ISAKMP (Internet Security Association and Key Management Protocol) daemons running in both SCU and SCP sites negotiate the IKE parameters and exchange certificate, which is used for IPSec association. In the second step, the SCU and SCP entities establish DICOM association which includes the IPSec association. In this step, both sites negotiate IPSec parameters and create session key, which is used for secure communication of DICOM data. The third is transferring the DICOM data on the secure channel.

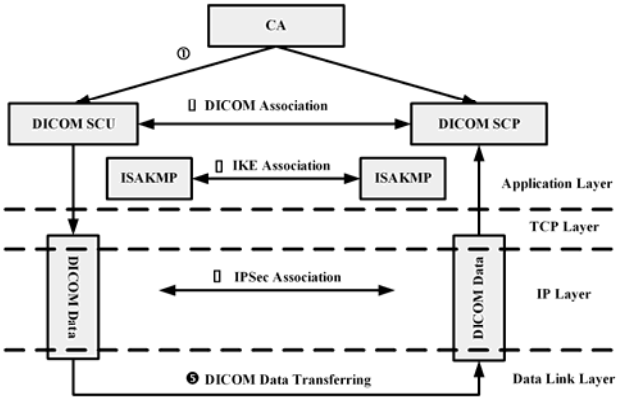

Figure 4. The data flow of TCP/IPv6-based DICOM C-Store communication with IPSec security supported: First, CA assigns the X.509 certificates to SCU and SCP sites respectively prior the testing, and the ISAKMP daemons running in both SCU and SCP sites create the IKE association, negotiate the IKE parameters and exchange certificate which is used for IPSec association; Secondly, the SCU and SCP entities establish DICOM association including IPSec association, and both sites negotiate IPSec parameters and create session key; Third, the SCU transfers the DICOM data

to SCP through IPSec-based secure channel.

The IPSec works in two modes: tunnel mode and transport mode. In tunnel mode, the entire IP datagram is encapsulated by a new datagram which includes outer IP header, IP header and IP payload; while in transport mode, it only handles the payload (upper layer data) by inserting AH header, ESP header, or both. Since the tunnel mode needs to configure routing in network communications and the transmission performance, it would be affected by the network hardware selected and it does not truly represent the IPsec performance. For this reason we only evaluated the transport mode.

Since the secure operation is in the IP layer, the IPSec has no effect on DICOM communication entities, which works in the application layer. To test the performance of DICOM communication with IPSec supported, we need to setup SA (Security Association) for peer entities to establish the secure channel. During the set up process, we create certificates for both peers and set SA associated parameters.

B. DICOM Image Communication with SSL/TLS-Based Security Supported

The SSL was originally developed by Netscape Communications to allow secured access of a browser to a Web server, SSL has become the accepted standard for Web security [17]. It provides secure communication channel between client and server by allowing mutual authentication, which uses digital signatures for integrity, and encryption for privacy. The protocol was designed to support multiple choices of specific algorithms used for cryptography, digests, and signatures. SSL 3.0 is the basis for the TLS protocol, which is still being developed by the Internet Engineering Task Force (IETF) [18]. The SSL protocol uses both public-key and symmetric key encryption. Symmetric key encryption is much faster than public-key encryption, but public-key encryption provides better authentication techniques.

SSL consists of two protocols: the handshake protocol and the SSL record protocol. The handshake protocol defines how the peer entities exchange associated information, such as, SSL version, ciphers and authenticates certificate. The SSL record protocol defines the format of SSL record or message, in which all of the SSL associated messages or application data should be transferred. The SSL connection is executed in two phases: the first is handshake, and the second is data transfer.

The data flow of the DICOM Storage SCU and SCP entities with SSL/TLS supported is shown in Figure 5. The SSL/TLS works between the TCP layer and the application layer. Most implementations of SSL(v.3.0)/TLS communication library simulate the style of the Berkeley Socket APIs [19]. In our implementation of DICOM secure image communication with the SSL/TLS supported, we replaced TCP APIs with that by using the OpenSSL toolkit of the SSL(v.3.0)/TLS communication library in the DICOM CTN library software, recompiled the CTN library, and linked the application with SSL/TLS-based DICOM secure communication library.

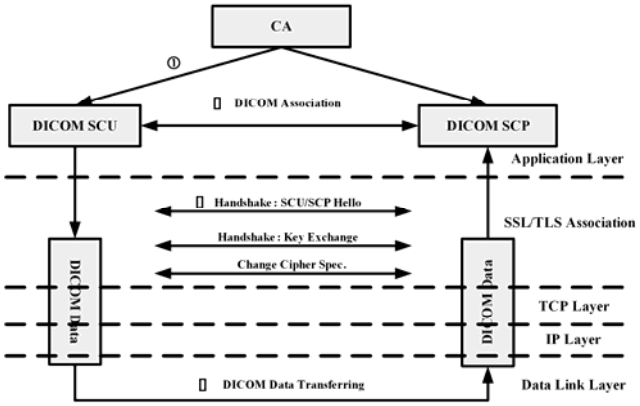

Figure 5. The data flow of DICOM C-Store communication through SSL/TLS secure channel: The first, CA assigns the X.509 certificates to SCU and SCP sites respectively prior the testing; Secondly, SCU and SCP establish DICOM association, which executes SSL handshakes; Third, the DICOM SCU transforms the DICOM data into SSL record format and send it to SCP through SSL secure channel, the DICOM SCP does the reverse process and gets the original DICOM data.

V. Test Environment and Conditions of Using DICOM Image Secure Communication Protocols

The transmission performance of using TCP/IP for medical image communications with IPsec or SSL/TLS security supported depends on various parameters including transmission protocol, PDU (Protocol Data Unit) size, security algorithm, and computer operating system. It also depends on the types of images being transmitted. We designed a set of image transmission experiments by permuting these parameters in order to evaluate the DICOM image communication performance under various conditions. We also compared the measured results.

We used the DICOM C-STORE DIMSE (DICOM Message Service Element) as an example to evaluate the transmission performance of DICOM images under different security environments. We used two computers, one works as the DICOM C-STORE SCU (Service Class User) for sending images, and the other serves as the DICOM C-STORE SCP (Service Class Provider) for receiving images.

The data flow of the entity SCU consists of the following steps: open DICOM image files and read the header and pixel data, then send the DICOM objects including the header and pixel data to the peer entity. The entity SCP receives the DICOM objects and writes them as individual DICOM files respectively. Since the overhead of reading and writing operations of the software from and to the computer hard disks of the same DICOM image was the same in all experiments, the transmission performance measurements reflect the differences due to IPv4 and IPv6 protocols, secure algorithms, and security methods used, PDU sizes, and operating systems, respectively.

In order to avoid bias in measurements arisen from network equipments such as network switches and routers, we connected the two computers directly with the reticle connection. The two computer hardware and software used are with almost identical configurations, except one has SCU application and the other has SCP application as follows:

1) C-Store SCU: Dell Dimension personal computer with Intel P4 CPU:2.8G, RAM:512M, NCI:100Mb/s, and Hard Driver: 80GB IDE;
2) C-Store SCP: Dell Dimension personal computer with Intel P4 CPU:2.8G, RAM:512M, NCI:100Mb/s, and Hard Driver: 80GB IDE;
3) Operating systems (OS): Red Hat Enterprise Linux V3.0, and Microsoft Windows XP Professional Edition.

All operating systems are installed in both computers. During each experiment, we boot the selected OS as we decided. The four sets of DICOM images used for the experiments are:

1) CT : one series with 100 DICOM images (512x512x2byte), and the total size is 53,016,540bytes;
2) MRI: one series with 200 DICOM images (256x256x2byte), and the total size is 35,219,944 bytes;
3) CR: 10 DICOM images (2048x2495x2byte), and the total size is 89,150,896 bytes;
4) US: one single multiframe DICOM images (one DICOM file contains multiple frames of images with the frame size of 768x576xRGB (8bitsx3)), and the total file size is 135,322,856 bytes.

For IPSec and SSL/TLS based security communications, we created X509 certificates for both sites of DICOM C-Store SCU and DICOM C-Store SCP from the same CA attached in OpenSSL tool kit.

In order to measure the transmission speed, we need to measure the transmission times of the images, since we already knew the total sizes of image data to be transmitted. So, we embedded the APIs (application program interface) about the Date/Time of the operating system (Linux/Windows XP) in the start and end points of the testing program of DICOM secure communication to get the times of starting transmission and ending transmission, and then calculated the transmission speed.

VI. Experimental Results and Discussion

We evaluated the DICOM image communications with three sets of different parameters, and

1) TCP/IP protocols (IPv6 and IPv4),
2) Security configurations (IPSec and SSL/TLS) and algorithms, and
3) PDU sizes.

Three scenarios:

1) Measured the performance of IPv6 DICOM communications of different modality images with different PDU sizes on Linux and Windows XP computer platforms, and compared the results with that of IPv4 without security setting;
2) Measured the performance of IPv6 IPsec-based secure DICOM communications of different modality images with different PDU sizes on Linux and Windows XP computer platforms with different secure algorithms in the IPsec secure setting and
3) Measured the performance of IPv4 SSL/TLS-based secure DICOM communications of different modality images with different PDU sizes on Linux and Windows XP computer platform with different security algorithms.

In following three sub sections, we give the experimental results in tables. In the tables, CT (IPv4) represents the experiment used CT images with the IPv4 protocol, the 4096(Linux/3DES) means that the maximum PDU size is 4096, the operating system is Linux, and the security algorithm is 3DES. The unit of measured speed of DICOM communication is Kbytes/sec. All the data listed in the tables is an average of three repeated measurements on same testing.

A. The Performance of IPv6 DICOM Image Communications and Its Comparison with IPv4 without IPsec-based Security

The evaluation of the IPv6 and IPv4 DICOM communications of different modality images was performed on Linux platform with the following steps:

1) We set up computer network communications using TCP/IPv6 without IPsec enabled, and ran the DICOM SCU on one computer and SCP on the other respectively;
2) We used DICOM C-Store SCU to send one series of modality image, e.g., CT, MR, CR, or US from one computer, and used the SCP to receive the series in the other computer, and measured the transmission times; and
3) We first changed the PDU sizes of TCP/IP configuration in SCU/SCP from 4096, 16384, to 65536 Bytes, respectively. Second, we rebooted both computers by changing SCU and SCP from IPv6 Linux O.S. to IPv6 Windows XP, and repeated the same measurements as on the Linux. Third, we switched one of the two computers from Windows XP to Linux, such that SCU ran on Windows and SCP ran on Linux, and repeated the measurements.

After IPv6 DICOM image communication testing, we did the same testing steps with TCP/IPv4 based DICOM C-Store communication without IPsec-based security applied on the transmitted DICOM image data sets as we did with IPv6.

Table I gives experimental results of IPv6 and IPv4 DICOM C-Store communications with different modality image sets, PDU sizes, and operating systems without IPsec-based security. From Table I, we can conclude:

1) The DICOM C-Store communications on Linux platform is faster than that of on Windows XP for the same image set;
2) The DICOM communications based on IPv4 is in general faster than that of on IPv6. This is because the header size of IPv4 packet is smaller than that of IPv6.
3) As the PDU size increases, the speeds of C-Store DICOM image communication on Windows platform

slow down in both IPv4 and IPv6 protocols. This phenomenon was not observed obviously on Linux platform.

Table I. Experimental results of IPv4 and IPv6 DICOM C-Store communications on CT, MR, CR and US image data sets with different PDU sizes and operating systems without IPSec-based security (unit: Kbytes/sec).

PDU Size (Operating System.)	Speed CT(IPv4)	Speed CT(IPv6)	Speed MR(IPv4)	Speed MR(IPv6)	Speed CR(IPv4)	Speed CR(IPv6)	Speed US(IPv4)	Speed US(IPv6)
4096(Lin.)	2715	2699	1046	1037	9926	9763	10100	9996
16384(Lin.)	2732	2726	1063	1056	9893	9875	10131	10137
65536(Lin.)	2762	2740	1066	1093	9888	9759	10186	10044
4096(Win.)	2543	2414	843	811	9203	8962	7783	7097
16384(Win.)	1219	1212	530	422	8995	8324	7151	6840
65536(Win.)	1192	1212	558	509	8878	8421	6651	5999
4096(Win./Lin)	1654	1598	551	537	8158	8206	7024	6917
16384(Win./Lin)	1643	1584	540	536	7338	7377	6309	6363
65536(Win./Lin)	1643	1577	552	543	7372	7418	6555	6874

Table II. Experimental results of IPSec-based IPv4 and IPv6 DICOM C-Store secure communications on CT, MR, CR, and US image data sets with different PDU sizes, security algorithms, and operating systems (unit: Kbytes/sec).

PDU Size (O.S./Security Algorithm)	Speed CT(IPv4)	Speed CT(IPv6)	Speed MR(IPv4)	Speed MR(IPv6)	Speed CR(IPv4)	Speed CR(IPv6)	Speed US(IPv4)	Speed US(IPv6)
4096(Win./DES)	2435	Null	841	Null	7347	Null	6082	Null
4096(Win./3DES)	1886	Null	761	Null	5305	Null	4902	Null
16384(Win./DES)	1251	Null	535	Null	6045	Null	4931	Null
16384(Win./3DES)	967	Null	418	Null	4791	Null	3978	Null
65536(Win./DES)	1013	Null	493	Null	4876	Null	4713	Null
65536(Win./3DES))	973	Null	400	Null	4501	Null	3732	Null
4096(Lin./DES)	2670	2694	995	1004	9696	9512	9923	9622
4096(Lin./3DES)	2273	2145	957	938	5789	4948	5869	4958
4096(Lin./AES256)	2678	2617	1032	1030	9513	9478	9772	9575
4096(Lin./Blowfish448)	2698	2683	1009	992	9601	9497	9607	9706
4096(Lin./Null_enc)	2172	2185	955	903	5677	5512	5745	5625
16384(Lin./DES)	2511	2666	994	1008	9691	9537	9621	9604
16384 (Lin./3DES)	2212	2272	968	963	5849	5747	5828	5836
16384 (Lin./AES256)	2703	2696	1024	1035	9522	9429	9643	9597
16384 (Lin./Blowfish448)	2687	2684	1028	1036	9563	9523	9729	9747
16384 (Lin./Null_enc)	2172	2188	924	954	5721	5547	5792	5669
65536(Lin./DES)	2427	2633	1012	1009	9617	9379	9767	9494
65536 (Lin./3DES)	2279	2226	1001	988	5819	5674	5843	5684
65536 (Lin./AES256)	2649	2628	1037	1049	9451	9249	9142	8845
65536 (Lin./Blowfish448)	2629	2622	1051	1078	9499	9437	9725	9843
65536 (Lin./Null_enc)	2160	2234	988	996	5706	5554	5744	5634

Table III. Experimental results of DICOM C-Store communications passing through SSL/TLS secure channels using different modality images, security algorithms, PDU sizes and operating systems (unite: Kbytes/sec).

PDU Size (O.S./Security Algorithm)	Speed CT(IPv4)	Speed CT(IPv6)	Speed MR(IPv4)	Speed MR(IPv6)	Speed CR(IPv4)	Speed CR(IPv6)	Speed US(IPv4)	Speed US(IPv6)
4096(Lin./DES-CBC)	2442	2349	952	939	9362	8880	9286	8193
4096(Lin./AES256)	2446	2410	946	943	9360	9246	9593	9318
4096 (Lin./RC4)	2488	2474	960	955	9613	9330	9789	9576
16384(Lin./DES-CBC)	2450	2416	946	940	9686	9456	9631	8154

16384(Lin./AES256)	2456	2459	950	937	9653	9548	10102	9678
16384 (Lin./RC4)	2557	2502	982	984	9776	9622	9855	9856
65536(Lin./DES-CBC)	2385	2354	941	930	9573	9322	10132	8147
65536 (Lin./AES256)	2454	2413	944	937	9613	9455	9883	9862
65536 (Lin./RC4)	2587	2554	995	991	9594	9616	10309	9516
4096(Lin.-Win./DES-CBC)	1477	1439	539	508	6514	5760	6027	5854
4096(Lin.-Win./AES256)	1462	1465	546	518	6645	6732	5899	6008
4096 (Lin.-Win./RC4)	1572	1486	548	531	7174	7182	6405	6193
16384(Lin.-Win./DES-CBC)	1209	1196	518	511	5287	5185	4850	4706
16384 (Lin.-Win./AES256)	1208	1202	516	512	5645	5300	5215	4980
16384 (Lin.-Win./RC4)	1222	1191	526	509	6106	6139	5485	5677
65536(Lin.-Win./DES-CBC)	1204	1209	518	512	5351	5218	5040	4887
65536 (Lin.-Win./AES256)	1212	1212	525	511	5571	5535	5301	5116
65536 (Lin.-Win./RC4)	1227	1203	531	514	6333	6196	5683	5692
4096(Win./DES-CBC)	2314	2214	826	778	7505	7619	6379	6716
4096(Win./AES256)	2163	2210	814	794	7901	7981	6726	6255
4096 (Win./RC4)	2329	2200	817	799	8508	8725	7040	7059
4096 (Win./IDEA-CBC)	2093	1950	800	783	7067	6784	6220	5807
16384(Win./DES-CBC)	1215	1088	530	458	6728	4974	5742	4592
16384 (Win./AES256)	1101	1074	501	376	6653	5747	5506	4955
16384 (Win./RC4)	1210	988	486	382	7564	6352	5998	5278
65536(Win./IDEA-CBC)	1107	907	524	398	5723	4918	4966	4734
65536(Win./DES-CBC)	1166	1093	444	383	7153	5216	5689	4727
65536 (Win./AES256)	1147	1105	438	389	7209	5976	5796	5021
65536 (Win./RC4)	1212	991	509	420	6928	6211	6298	5234
65536(Win./IDEA-CBC)	1177	1104	538	411	5942	4843	5139	4235

Table IV. The comparison of DICOM C-Store communications passing through secure channels of SSL/TLS or IPSec using modality images, security algorithms, PDU sizes in Linux platform (unite: Kbytes/sec).

PDU Size (SSL/IPSec, O.S., Algorithm)	Speed CT(IPv4)	Speed CT(IPv6)	Speed MR(IPv4)	Speed MR(IPv6)	Speed CR(IPv4)	Speed CR(IPv6)	Speed US(IPv4)	Speed US(IPv6)
4096(SSL LINUX DES-CBC)	2442	2349	952	939	9362	8880	9286	8193
4096(IPSec LINUX DES-CBC)	2670	2694	995	1004	9696	9512	9923	9622
4096(SSL LINUX AES256)	2446	2410	946	943	9360	9246	9593	9318
4096(IPSec LINUX AES256)	2678	2617	1032	1030	9513	9478	9772	9575
16384(SSL LINUX DES-CBC)	2450	2416	946	940	9686	9456	9631	8154
16384 (IPSec LINUX DES-CBC)	2511	2666	994	1008	9691	9537	9621	9604
16384 (SSL LINUX AES256)	2456	2459	950	937	9653	9548	10102	9678
16384 (IPSec LINUX AES256)	2703	2696	1024	1035	9522	9429	9643	9597
65536(SSL LINUX DES-CBC)	2385	2354	941	930	9573	9322	10132	8147
65536 (IPSec LINUX DES-CBC)	2427	2633	1012	1009	9617	9379	9767	9494
65536 (SSL LINUX AES256)	2454	2413	944	937	9613	9455	9883	9862
65536 (IPSec LINUX AES256)	2649	2628	1037	1049	9451	9249	9142	8845

B. The Performance of IPv6 and IPv4 DICOM Image Communications with IPsec-based Security

We performed similar IPv4 and IPv6 DICOM C-Store image communications experiments as described in Section 6.1, but with IPsec security enabled. Since the data encryption of
IPsec in IPv6 is not supported in Windows XP, the IPsec security enabled DICOM communications was only performed using Windows XP with IPv4, and Linux with IPv4 and IPv6 with different security algorithms.

Table II shows the experimental results of IPsec enabled IPv4/ and IPv6 DICOM C-Store communications. Table II demonstrate:

1) All encryption algorithms slow down DICOM image transmissions. This is reasonable because it would take times to perform the security processing on image before and after the transmission. CR and US images are worse than CT and MR images. It is properly due to two reasons. First, it would take more times for DICOM C-Store SCU and SCP to establish association to transmit CT or MR images than that for CR or US images for the amount of image data if IPsec-based security was not enabled. Second, after data encryption and decryption using IPsec-based security on the transmitted image data, the transmission time would be more because security processing takes longer on larger data set (e.g., CR, or US with multi-frame DICOM file) than that on smaller ones (MR and CT).
2) In Linux platform, of 3DES and Null_enc (ESP Null encryption) algorithms require longer time for DICOM image transmissions than that of DES, AES and Blowfish448. In Window platform, the 3DES requires longer times for the DICOM image transmissions than that of DES. The implementation of IPSec-based security is not good on Windows platform, since it only supports DES and 3DES algorithms in IPsec-based security of IPv4, and it does not support IPv6.
3) General speaking, the performance of DICOM image transmissions over TCP/IPv4 is faster than that over TCP/IPv6 if IPsec-based security was not enabled. But it is not always true when the IPsec-based security was enabled. From Table II, we see that the performance of DICOM image transmissions over TCP/IPv6 is faster than that over TCP/IPv4 in some cases when IPsec-based security is enabled. The reason for this is that the integration of IPv6 and IPSec may be smoother than that of IPv4 and IPSec.

C. The Performance of DICOM Image Communications Through SSL/TLS Security Channels over TCP/IPv4/IPv6 in Different Operating Systems

The security processing on the transmitted data is executed in IP layer if IPsec-based security was enabled, but, the similar security processing is performed in application/TCP layer if SSL/TLS is used. In order to compare the performance of these two security processing methods on transmitted image data, we measured the transmission speeds of the same DICOM image data sets passing through SSL/TLS secure channels with different security algorithms over TCP/IPv4 and TCP/IPv6 and in different operating systems. Table III gives the measured data of DICOM C-Store communication passing through SSL/TLS secure channels by using different modality image data sets, security algorithms, PDU sizes, and operating systems.

From Table III, we observe that:

1) Transmission speeds of DICOM images through SSL/TLS secure channels over TCP/IPv4/IPv6 on Linux and Windows platforms are faster than that of cross-platforms such as SCU (Linux) to SCP (Windows) with same security setting.
2) All encryption algorithms contribute to slower transmission speeds on CR and US images than that of CT and MR images. The explanation is the same as stated in Section 6.2.
3) The DES-CBC (DES in CBC mode) and IDEA-CBC (IDEA algorithm in CBC mode) security algorithms require longer time to execute and therefore contribute to slower image transmission speeds than that of AES and RC4 (Rivest Cipher 4).

D. Comparison of DICOM Image Transmissions Using IPsec and SSL/TLS

Since the numbers of security algorithms implemented in both IPSec and SSL/TLS based security in the Windows platform are few compared to the Linux platform, we only chose Linux platform to compare the transmission performance of DICOM image data secured by using IPsec and SSL/TLS with different security algorithms and PDU sizes. Table IV gives results of different data image sets using DICOM C-Store communications passing through secure channels of SSL/TLS and IPSec using various security algorithms, PDU sizes in the Linux platform.

Table IV show that:

1) The transmission speeds of all DICOM images through IPSec security channel are faster than that through SSL/TLS channel if the image data secured with security algorithms of DES-CBC in Linux operating system for all PDU sizes;
2) The transmission speeds of CT and MR DICOM images through IPSec security channel are faster than that through SSL/TLS channel with all security algorithms and PDU sizes in Linux operating system;
3) While, for the CR and US images, the speeds of DICOM image communication through SSL/TLS security channels are faster than that through IPSec channels when the PDU sizes are 16384 and 65536 and the security algorithm is AES.

VII. CONCLUSIONS

We have performed exhaustive experiments to evaluate secured DICOM communication protocols under various

conditions. We confirm that it is straight forward to use open source DICOM software and libraries to develop both IPv6 and IPv4 supported DICOM communications protocols.

The evaluation results show that:

1) There are some overheads in using IPv6 DICOM image communication compared to IPv4 since more advanced features are achieved in IPv6.
2) All encryption algorithms used in IPsec and SSL/TLS based securities slow down transmission performance on CR and multi-frame US (or DSA) images than that on CT and MR images in TCP/IPv6/IPv4 networking.
3) The performance of DICOM image transmissions is faster over TCP/IPv4 than that over TCP/IPv6 if IPsec-based security was not enabled, but it is not always true when the IPsec-based security was enabled, and the integration of IPv6 and IPSec may be better than that of IPv4 and IPSec.
4) Transmission speeds of DICOM images with different SSL/TLS security algorithms over TCP/IPv4 in Linux and Windows are faster than that with same security setting but cross-platforms such as SCU (Linux) to SCP (Windows).

There is trade-off in choosing security solution between IPsec and SSL/TLS based security implementation of IPv6/IPv4 protocols. If WAN networks only use IPv6 such as in high performance broadband networks, the choice is IPsec-based security, since IPv6 and IPsec are implemented in IP layer, no change in application software is needed. But, the operating systems have to be re-configured to enable the IPv6 protocols with IPsec security integrated. If the networks are IPv4 or the combination of IPv6 and IPv4, it is better to use SSL/TLS security by modifying the TCP/IP APIs of the application software, since the integration of IPv4 with IPsec is not so good as IPv6 with IPsec; or to find a VPN product. However, in the latter, there are certain limitations in network deployment.

The Linux platform achieves better performance and has more security algorithms implemented than the Windows (XP) platform in most experiments of IPv6 and IPv4 based DICOM image communications. In the teleradiology or enterprise PACS applications, the Linux operating system may be better choice as the peer security gateways for both IPsec and SSL/TLS based secure DICOM communications cross public networks. Otherwise, the Windows platform could be the other choice if the communication speeds are considered as one of most important factors, since the combination of Linux and Windows platforms, such as Linux with SCU and Windows with SCP in secured DICOM communications had the worst transmission performance than pure Linux platform or Windows. Since most Linux operating systems were derived from the Unix operating systems, the most conclusions achieved from the research presented in this paper may suit to Unix platforms if the hardware of the computers were same.

REFERENCES

[1]. Huang HK, Ed., Chapter 9: Communications and Networking, Book: PACS and Imaging Informatics, Wiley-Liss Press, New Jersey, 2004.
[2]. James Jr. AE, James III E, Johnson B, James J. Legal considerations of medical of medical imaging, Leg Md 1993; 87-113.
[3]. Berger SB, Cepelewicz BB, Medical-legal issues in teleradiology. Am J Roentgenolo 1996; 166:505-2.
[4]. Berlin L. Malpractice issue in radiology-teleradiology. Am J Roentgenolo 1998; 170:1417-22.
[5]. Kamp GH. Medica-legal issues in teleradiology: a commentary. Am J Roentgenolo 1996; 166:511-2.
[6]. HIPAA, http://aspe.os.dhhs.gov/admnsimp, US Department of Health and Human Services.
[7]. HIPAA, http://www.rx2000.org/KnowledgeCenter/hipaa/hipfaq.htm.
[8]. Digital Imaging and Communications in Medicine (DICOM). National Electrical Manufactures Association (NEMA). Rosslyn, VA, http://medical.nema.org/dicom/ 2004.html, Part 15: Security Profiles, PS 3.15-2004; 2004.
[9]. Zhou X Huang HK, Lou SL. Authenticity and integrity of digital mammography image. IEEE Trans Med Imaging 2001; 20(8): 784-91.
[10]. Wong STC, Abundo M, Huang HK. Authenticity techniques for PACS images and records, SPIE Med Imaging 1995;2435:68-79.
[11]. Rives R, Shamir A, Adleman L. A method for obtaining digital signatures and public-key cryptosystems. Commun ACM 1978; 21(2):120-6.
[12]. International Organization for Standardizations, http://www.iso.org.
[13]. Christian Huitema, Book: IPV6 the new Internet protocol, Prentice Hall, Nov. 1999. ISBN 7-302-03547-4.
[14]. Radiological Society of North America (RSNA) & Mallinckrodt Institute of Radiology, Overview of 1997 RSNA DICOM Demonstration, file:/wuerlb/documentation/dicom/dicom.97/ overview.doc.
[15]. http://dicom.offis.de/dcmtk.php.en
[16]. http://www.ipsec-howto.org/
[17]. Eric Rescorla, SSL and TLS: Designing and Building Secure Systems, Addison-Wesley Press, 2001.
[18]. http://www.ietf.org/
[19]. http://www.openssl.org/

Jianguo Zhang, received his B. S. and M. S. degrees in 1984 and 1987 from optical department, Shandong University, China, and Ph.D. in 1991 from Chinese Academy of Science.

From 1992 to 1994, he was Associate Professor in Changchun Institute of Optics, Chinese Academy of Sciences; From 1994 to 1998, He was a research fellow in the Laboratory for Radiological Informatics, Department of Radiology, University of California at San Francisco; From 1998 to date, he is the Director and Professor of Laboratory for Medical Imaging Informatics in Shanghai Institute of Technical Physics, Chinese Academy of Science. Also, from 2004 to date, he has appointed as a Visiting Professor at the Department of Radiology, University of Southern California.

His major interests include PACS technologies, medical image processing and visualization, imaging informatics, security technologies in healthcare, and electronic patient record. Currently, he serves as an associate editor of Chinese Journal of Computerized Medical Imaging, and the reviewer of National Nature Science Foundation of China on Biomedical Electronics.

Fenghai Yu, received his BS degree from Shanghai MS degree from Shanghai Institute of Technical Physics in 2002, and now is PhD candidate of Chinese Academy of Sciences. His research topics include secure DICOM image communications with IPv6 and IPv4, and performance evaluation of PACS image communications.

Jianyong Sun, received his BS degree from Electronic Engineering department of Shandong University, and MS and PhD degrees in 2001 and 2004 from Shanghai Institute of Technical Physics, Chinese Academy of Sciences. Currently, he is assistant professor in the Laboratory for Medical Imaging Informatics of Shanghai Institute of Technical Physics. His interests include teleradiology and image display and visualization.

Yuanyuan Yang, received her BS and MS from Computer Science department and Biomedical Engineering department in 1999 and 2002. She joined the Laboratory for Medical Imaging Informatics of Shanghai Institute

of Technical Physics in 2002. Currently, she is PhD candidate in the graduate school of Chinese Academy of Sciences. Her interests include telemedicine and grid computing.

Chenwen Liang, received his BS and MS from Biomedical Engineering department of Xi'an Jiaotong University in 2001 and 2004. He joined the Laboratory for Medical Imaging Informatics of Shanghai Institute of Technical Physics in 2004. Currently, he is research associate in the Laboratory for Medical Imaging Informatics. His interests include PACS image acquisition technology and servers clustering.

Journal of High Speed Networks 00 (2006) 1–13
IOS Press

The role of a Data Grid in worldwide imaging-based clinical trials

Z. Zhou [a], M. Gutierrez [b], J. Documet [a], L. Chan [c], H.K. Huang [a] and B. Liu [a]

[a] *Image Processing & Informatics (IPI) Laboratory, Department of Radiology, University of Southern California, California, USA*
[b] *InCor, University of Sao Paulo, Sao Paulo, Brazil*
[c] *Hong Kong Polytechnic University, Hong Kong*

Abstract. Clinical trials play a crucial role in testing new drugs or devices in modern clinical practice. Medical imaging has become an important tool in clinical trials because images provide a unique and fast diagnosis with visual observance and quantitative assessment. A typical imaging-based clinical trial consists of: (1) A well-defined rigorous clinical trial protocol, (2) a radiology core that has a quality control mechanism, a biostatistics component, and a server for storing and distributing data and analysis results; and (3) many field sites that generate and send clinical trial image studies to the radiology core. With ever-increasing number of clinical trials, it becomes a great challenge for a radiology core which handles multiple clinical trials to have a robust server to administrate multiple trials as well as satisfy the requirements to quickly distribute information to participating radiologists/clinicians worldwide to assess trials' results.

Data Grid in the grid computing technology can satisfy the aforementioned requirements of imaging-based clinical trials. In this paper, we present a Data Grid architecture for worldwide imaging-based clinical trials. The Data Grid testbed has been set up in three international sites: Image Processing and Informatics (IPI) Laboratory at University of Southern California, USA; the Hong Kong Polytechnic University; and InCor (Heart Institute) at Sao Paulo, Brazil. The three chosen sites are connected with high speed international networks including the Internet2, the HARNET (Hong Kong Academic and Research Network), and the Brazilian National Research and Education Network (RNP2). The concept, design and implementation of the Data Grid are presented. Grid computing technology open source software Globus Toolkit 4.0 and DICOM technology were used to implement the DICOM compliance Data Grid. This paper also describes results of using Data Grid in imaging-based clinical trails for fault tolerance image data backup.

The successful implementation and evaluation of the Data Grid for imaging-based clinical trials provide three major benefits: (1) an understanding of the methodology for using data grid technology and high speed networks in clinical trails; (2) an establishment of the performance benchmarks of Data Grid over high speed networks; and (3) a Data Grid test bed for performing worldwide imaging based clinical trials.

Keywords: Data Grid, Internet-2, clinical trial, medical imaging, DICOM

1. Introduction

1.1. Imaging-based clinical trials

Medical imaging is taking on more prominent role in early detection and quantization of new disease or change in disease. Multiple imaging-based clinical trials provide the require number of cases examined by using images from unbiased populations required to test new diagnostic, therapeutic techniques or agents. Through the years, although the methodology and protocols of clinical trails have changed gradually [1–3], Fig. 1 remains a good representation of a general organization chart of an imaging-based clinical trial. The radiology core in this figure has the responsibilities of collecting imaging data from multiple field sites with quality control, and a server for storing and distributing trial results to field sites. The field sites [4,5] recruit patients and generate images and send to the radiology core. The workflow of an imaging-based clinical trial (Fig. 1) is shown in Fig. 2:

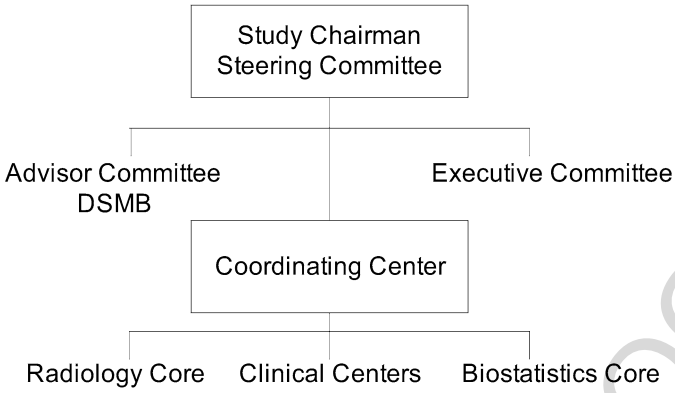

Fig. 1. Organization chart of an imaging-based clinical trial.

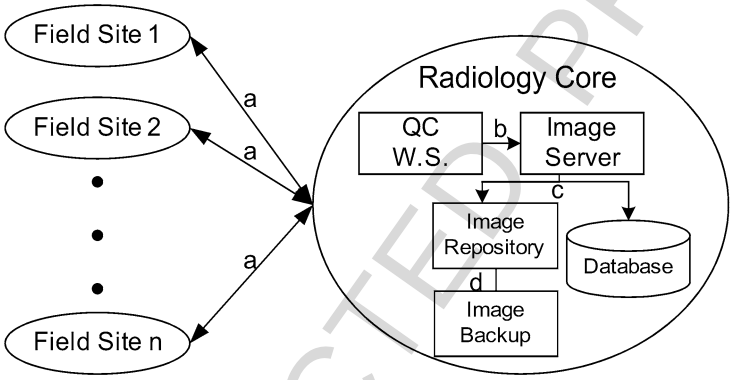

Fig. 2. A typical workflow of imaging-based clinical trial.

(a) Field Sites $(1 - n)$ generate DICOM [6] format image data related to the patients enrolled in a specific clinical trial and transmit the image data to the Radiology Core through various digital networks or storage media (e.g., a CD). The image data are de-identified before they are sent out.
(b) The images received by the Radiology core go through a QC (Quality Control) W.S. (workstation) [4] to assure the quality of the image, such as patient positioning, equipment calibration, space localization, acquisition parameters and patient demographic information. Once the quality of the images is approved, the images are sent to a centralized image server.
(c) The image server extracts the metadata from the DICOM header of the image and stores the metadata and related patient information in the database of a data repository, such as RAID (Redundant Array of Independent Disks) [7,8]. The images are distributed to assigned radiologists of field sites worldwide to make diagnosis. The diagnosis results, usually quantity numbers, are returned and stored in the metadata database.
(d) The images stored in the repository are also backed up in an offline storage device.

This workflow and setup at the radiology core can satisfy a small number of clinical trials. With ever-increasing number of clinical trials, it becomes a great challenge for a radiology core which handles multiple clinical trials to have a robust server to administrate multiple trials as well as satisfy the requirements to quickly distribute information to participating radiologists/clinicians worldwide to assess trials' results. In addition, different clinical trials usually vary in the parameters of results. A dynamic database model is necessary for the image server in the radiology core to accommodate new clinical trials. All these issues presented underline the need for a new

infrastructure that can satisfy these requirements of imaging-based clinical trials. Data Grid [9–12], an emerging image storage and distribution computing technology, is an ideal solution to this new demand.

1.2. General Data Grid

Data Grid is a service of the Grid Computing technology [9,13,14]. Several large-scale Data Grids, such as TeraGrid [15] and Data Replication for LIGO [16], have been established for fast movement of large amount of data among multiple research institutes. A Data Grid [11] specifically for clinical image backup and disaster recovery has been developed previously at IPI (Image Processing & Informatics Laboratory) using the Globus Toolkit 4 (GT4) [17]. This Data Grid was designed to utilize the strengths of grid technology along with PACS (Picture Archiving and Communication Systems)/DICOM (Digital Imaging and Communications in Medicine) technology for storing and distributing clinical images [18,19]. In particular, some PACS/DICOM resources are embedded within the five layer grid architecture. These include Storage services, Query services, Retrieve services, which are integrated with the DICOM standard protocols in addition to the use of other Data Grid Services. The five layer architecture of the Data Grid embedded with DICOM technology is shown in Fig. 3, which illustrates some of the basic components already developed at IPI, such as the Metadata Catalog Service. The experience and knowledge learned from the Data Grid for clinical image recovery has been utilized to design the Data Grid architecture for imaging-based clinical trials.

1.3. Three international sites chosen for test bed

Three international sites are chosen to set up a Data Grid test bed for imaging- based clinical trials. These three sites are described in order as follows.

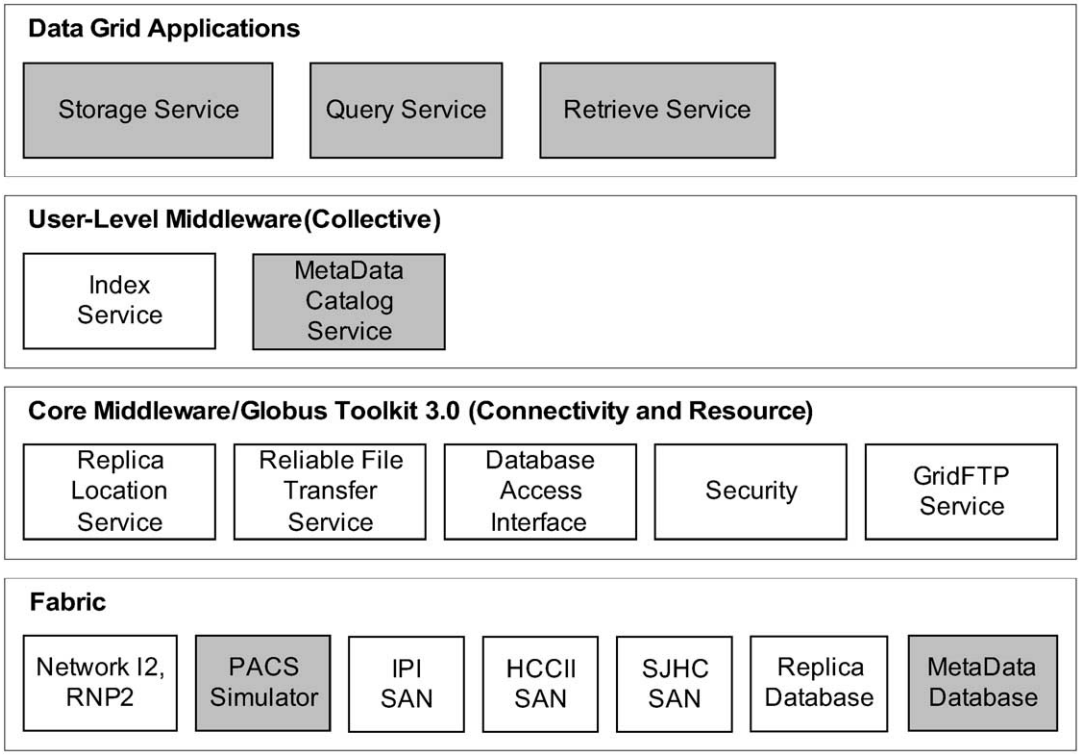

Fig. 3. Five-layer architecture and the contents of the Data Grid for clinical image backup.

1.3.1. Image Processing & Informatics Laboratory (IPI), Marina del Rey, CA, USA

The IPI Laboratory performs pioneering research and development and participates in clinical R & D services related to medical imaging and informatics. Currently, IPI provides clinical image data backup service for two clinical sites, St. John's Health Care at Santa Monica, California and Healthcare Consultation Center II at USC. The Internet2 [20,21] connection has been established between IPI and USC, through which IPI is connected to CalRen [22], the Internet2 backbone in California.

1.3.2. Hong Kong Polytechnic University, Hong Kong, China

The Hong Kong Polytechnic University (PolyU) is one of the eight tertiary institutions in Hong Kong connected together by the HARNET (Hong Kong Academic and Research Network) [23], which is linked to the Internet2 through an Internet Service Provider (ISP). PolyU has been carrying out collaborative research on its applications with other collaborating institutions in the US since October 2002. For instance, this international Internet2 connection has been used for teleconferencing and daily medical image exchange between IPI and PolyU [24].

1.3.3. Heart Institute (InCor) at University of Sao Paulo, Sao Paulo, Brazil

The Heart Institute (InCor), part of the Clinical Hospital Complex of the Faculty of Medicine of the University of Sao Paulo, is the most important Brazilian tertiary hospital devoted on the treatment of patients with cardiac diseases, education and research in cardiology. Approximately, 80% of InCor's services are devoted to patients whose treatment is funded by the National Health System.

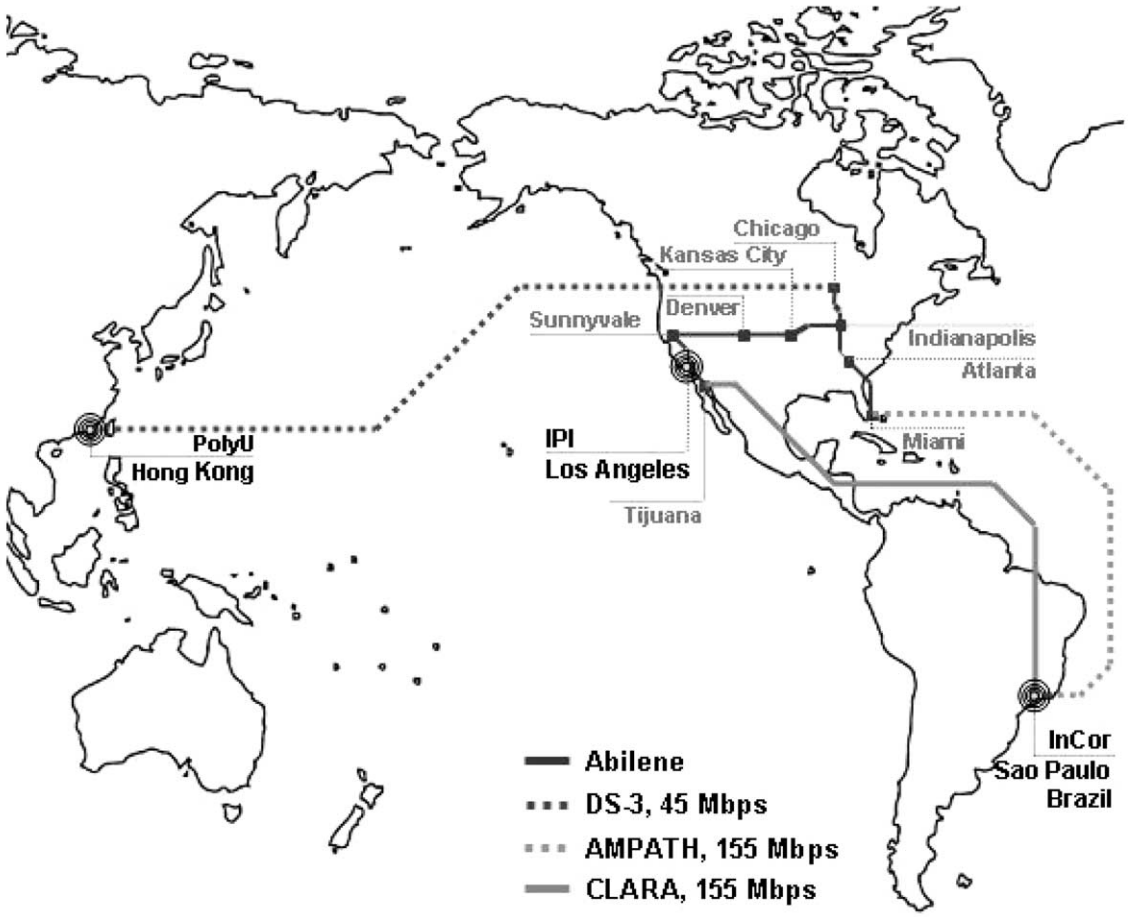

Fig. 4. The three sites of the Data Grid test bed are connected by international high speed networks.

InCor is connected to the Brazilian National Research and Education Network (RNP2) [25] since 1999, a high performance network infrastructure for communication and collaboration among educational and research institutions and a test bed for the development of advanced network applications and technology. RNP2 is connected to RedCLARA since 2003, the advanced Latin American network. Through RedCLARA, RNP2 is connected to other advanced networks worldwide, such as Géant, the European network, and the North American Internet2.

The details of the network connection of these three sites are shown in Fig. 4, and network capabilities and performance are given in another paper of this Special Issue [28].

2. Method

A Data Grid is designed for multiple radiology cores in a multiple clinical trials environment. The data Grid is to store, backup, and share their trials images and analysis results, which will provide a large-scale, virtual data system for future data mining to improve clinical outcomes from clinical trials results. The transition from the current radiology core using a standard storage system with a disk backup to this Data Grid will take several phases of implementation, because the current radiology core must be continuously functioning. In this section, we will first focus on the data Grid design concept, followed by DICOM storage, and query/retrieve operations, and backup and disaster recovery procedures. Section 3 will discuss the set up of three International cores and three phases of implementation.

2.1. Data Grid for clinical trials image storage and backup

In order to form the Data Grid, participated radiology cores have to join a Data Grid confederation. Three radiology cores are modeled to illustrate the Data Grid concept using DICOM store for data backup and recovery, and DICOM query/retrieve for work flow analysis. The premises are that during the implementation phase, the Data Grid can not affect the current radiology core data storage backup operation, and that once the Data Grid is in operation, the current radiology core storage backup can be abolished and replaced by the Data Grid. The Data Grid concept can be extended to support more than three radiology cores.

Figure 5 shows the system design of the three-core Data Grid for clinical trials image backup. Each core has the same setup (Fig. 2) described previously. The image backup storage (e.g., Storage Area Network (SAN)) in every radiology core is separated into partitions 1 (P1) and 2 (P2), P1 is for local backup, while P2 is contributed to the Data Grid to form a virtual large backup storage for other radiology cores participated in the Data Grid. The image server in each core sends a second copy of the image to the Data Grid, which automatically replicate it into two additional copies stored in the other two cores. In this case, images from Core A will be stored in P2 at Cores B and C. This will insure Fault-Tolerance (FT) within the Data Grid in case one of the storage resources is unavailable. Notice that in the current operating radiology core, the backup uses standard hard disks as shown in Fig. 2.

The Data Grid design needs to utilize the capabilities of Grid Computing technology along with DICOM technology for storing clinical trials images. In particular, some DICOM resources are embedded within the five layer grid architecture. These include Storage service, Query service, and Retrieve service (Fig. 3), which are integrated with the DICOM standard protocols.

2.1.1. DICOM storage for image backup in the Data Grid

The Data Grid backup procedure starts from the image server at Core A (Fig. 6 left) which sends DICOM images to its image backup P1, and an additional copy (a very minor change in the image server) to the Data Grid using the DICOM Storage Class operation [6]. The images are then replicated in the Data Grid using Grid Services. Figure 6 illustrates the workflow of the storage procedure from Core A to the Data Grid:

(1) A DICOM image is sent from the Image Server at Core A to a GAP (Grid Access Point) at the Data Grid (Left). If the primary GAP is unavailable, the DICOM image can be sent to a secondary GAP for Fault-

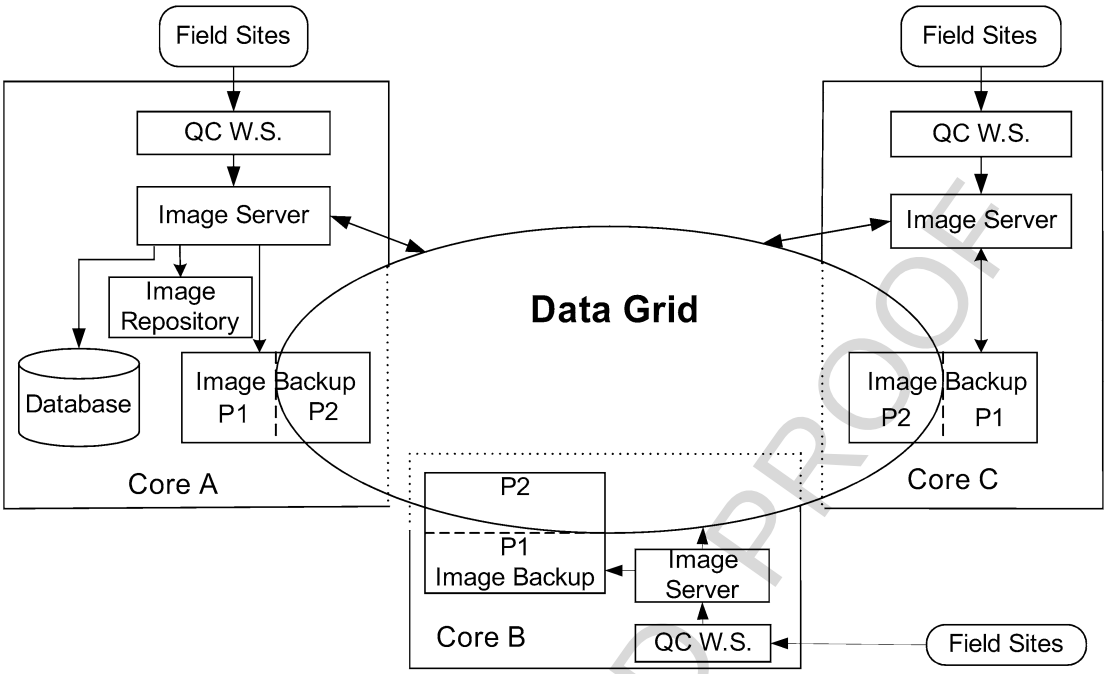

Fig. 5. A three-core Data Grid architecture for clinical trials image backup.

Tolerance. A DICOM Receive component within the GAP receives the image file and adds this image to a queue.

(2) A Storage Service component at the GAP moves the image out of the queue.
(3) The Storage Service calls a Metadata Catalog Service to extract the clinical image metadata from the DICOM header.
(4) The Metadata Catalog Service stores the extracted metadata into the Metadata database.
(5) Once the Metadata Catalog Service notifies the Storage Service that storing the metadata is complete, the Storage Service calls a RFT (reliable file transfer) Service to move the image file from the GAP to the storage destinations, in this case, a SAN (P2) at Core B and the storage device P2 at Core C.
(6) The RFT Service activates and monitors the image file transmission from the GAP to the SAN at Core B.
(7) The RFT Service activates and monitors the image file transmission from the GAP to the storage device at Core C.
(8) Once the RFT Service notifies the Storage Service that the image file transmission is complete, the Storage Service calls a RLS (Replica Location Service) to update the file locations.
(9) The RLS updates the file location information within the Replica database, which consists of a Master database and three distributed subset databases for Fault-Tolerance. The three distributed databases contain only information regarding files stored at one of the three storage resources. This will accommodate the Data Recovery Process should one of the storage resources encounter downtime and loss of data.

2.1.2. Query/retrieve for clinical trial images from the Data Grid during downtime for disaster recovery

Figures 7 and 8 illustrate a detailed example of the recovery procedure during a downtime/disaster scenario at Core A. The scenario is that Core A's local image storage and backup went down during a disaster and a physician at a Trial Site of Core A can query/retrieve trials image data from the Data Grid immediately. Figure 7 shows the

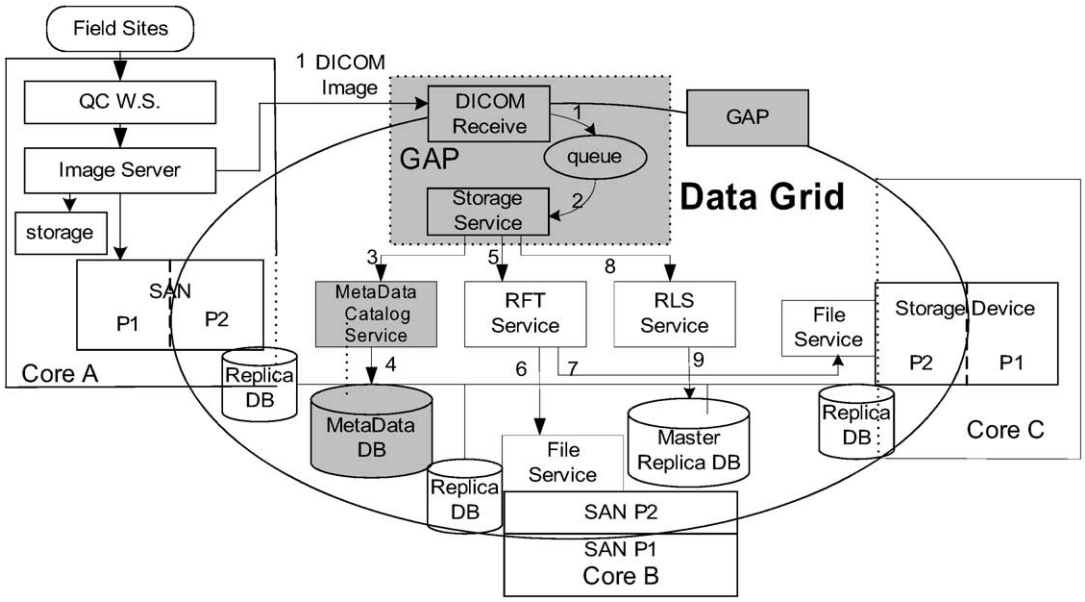

Fig. 6. The Data Flow for DICOM Storage of a clinical image for backup in the Data Grid.

Query process while Fig. 8 shows the Retrieve process, including the grid services involved and the data flow in a step-by-step fashion:

Query

Query Patient Information from the Data Grid (Fig. 7)

(1) A workstation in a Site at Core A sends a DICOM query request to a DICOM query component at the GAP. The DICOM query component passes the searching request to a Query Service at the GAP. If the primary GAP is unavailable, the DICOM query request can be sent to a secondary GAP for Fault-Tolerance.
(2) The Query Service calls the Metadata Catalog Service to search the Metadata database based on the given keys.
(3) The Metadata Catalog Service searches the database and returns the searching result back to the Query Service, which in turn forwards the result back to the DICOM Query component. The DICOM Query component formats the result into a DICOM query response object and sends it back to the workstation in the Site of Core A.

Retrieve

Retrieve Image Data from the Data Grid (Fig. 8)

(1) After the workstation at the Site of Core A receives the DIOCM query work list from the GAP, the physician selects pertinent items from the work list and issues a DICOM retrieve request. Assuming the workstation requests to retrieve the clinical trials results back to it, a DICOM retrieve component in the Gap of the Data Grid receives the request and passes the retrieve request to a Retrieve Service within the GAP. If the primary GAP is unavailable, the DICOM retrieve request can be sent to a secondary GAP for Fault-Tolerance.
(2) The Retrieve Service calls the Metadata Catalog Service to find the logical file name based on the given searching keys.
(3) The Metadata Catalog Service searches the Metadata database and returns the logical file name back to the Retrieve Service if the file exists within the database.

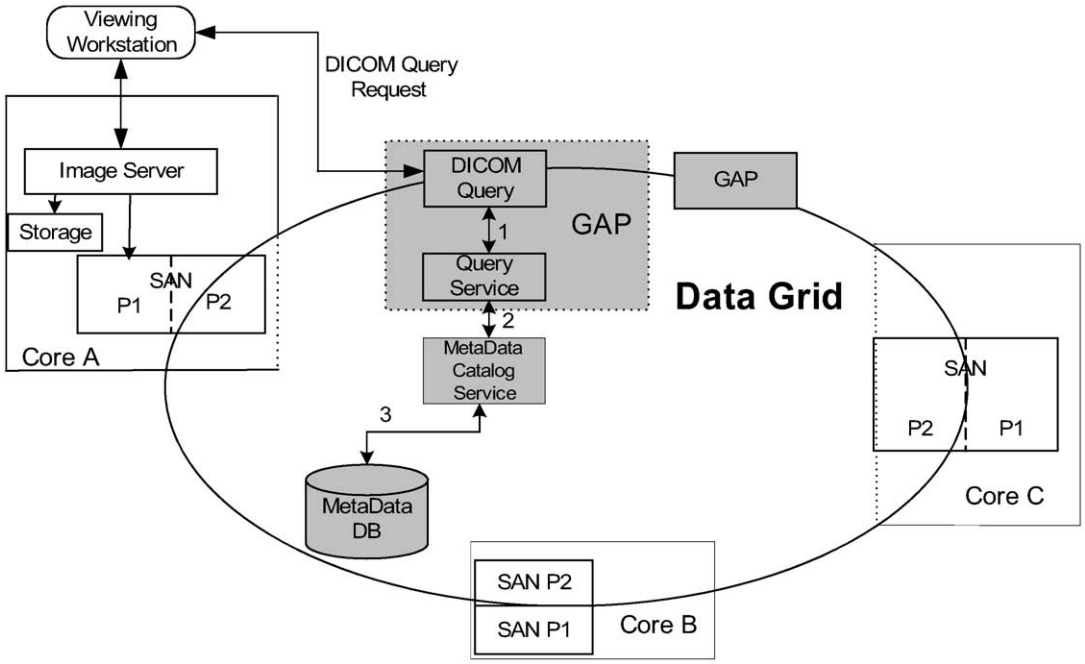

Fig. 7. The Data Flow for a DICOM query request to the Data Grid.

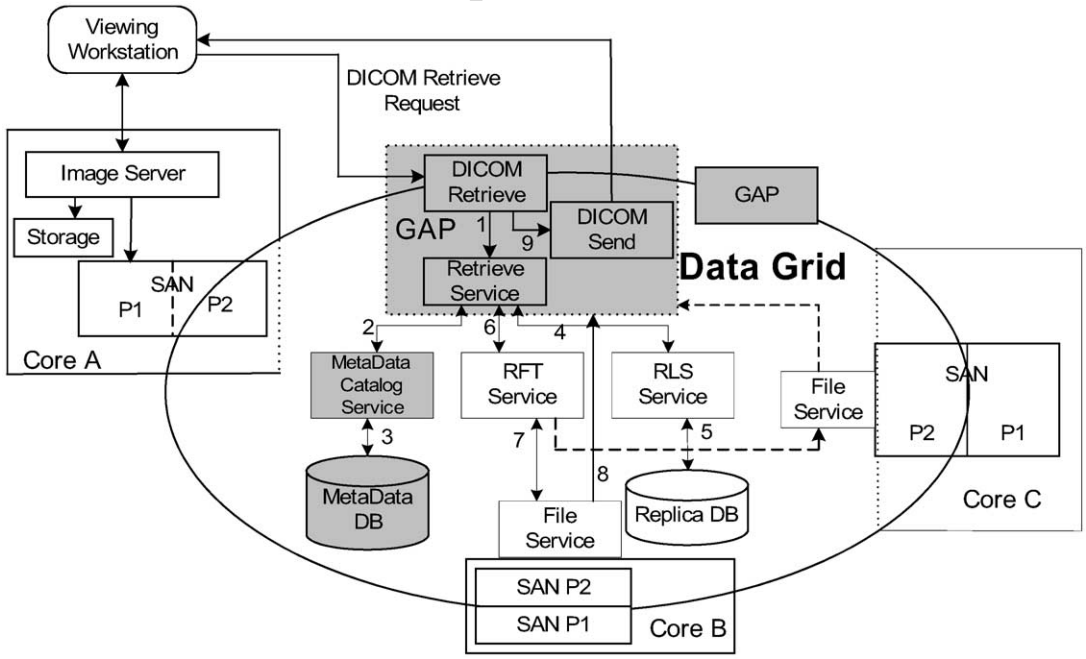

Fig. 8. The Data Flow for a DICOM retrieve request (upper left) to the Data Grid.

(4) The Retrieve Service calls the RLS service to find the physical locations of the file based on the logical file name.
(5) The RLS searches the Replica database and returns the physical file locations to the Retrieve Service.
(6) The Retrieve Service calls the RFT service to move the file from the most optimized location, in this case, either from the SAN at Core B and P2 storage component Core C. The optimization can be made based on certain criteria, such as the network bandwidth, physical distance, or load balance of current file transmissions. In this case, it is assumed that the optimized location is P2 SAN of Core B.
(7) The RFT service activates and monitors the file transmission between the File Service at the IPI SAN (P2).
(8) The File Service at the IPI SAN (P2) sends the image file to the GAP.
(9) The DICOM Retrieve starts a DICOM Send component sending the clinical trials results back to the requesting workstation at the Site of Core A.

3. Three International Sites Test Bed Setup

3.1. Sites connectivity

Based on the Data Grid concept described in Section 2, a testbed for imaging-based clinical trials using Data Grid is designed. The testbed consists of three International sites, IPI, PolyU, and InCor. These three sites are chosen because they are geographically located in two Continents and are connected to each other through high speed international networks (see Fig. 4).

3.2. Three phases system implementation

The system implementation of this Data Grid is staged in three phases.

3.2.1. Phase One

Phase One is to implement a prototype of the Data Grid for clinical trials image backup in the laboratory environment. This is the major Data Grid software development and initial test stage. IPI is chosen for the laboratory prototype development. The goal of Phase One is to validate that any two of the three storage devices can be used as the backup storage of the third one.

The Data Grid consists of three Radiology Cores simulated by three Linux servers, each of which has a storage device as follows:

- Core A: A Linux Server with P1 of a SAN as the storage device.
- Core B: A Linux Server with hard disk 1 as the storage device.
- Core C: A Linux Server with P2 of a SAN as the storage device.

The Globus Toolkit 4.0 and the Grid software developed at IPI were installed in the three servers connected by a LAN (local area network). The PACS Modality Simulator [26,27] is connected to the Linux Server of Core A. The former emulates the real-life Image Server of the Radiology Core, and the latter emulates the GAP of the Data Grid, respectively. During the experiment, clinical trial images are sent from the Modality Simulator to the Linux Server. This scenario emulates the Image Server (Modality Simulator) sends a backup copy of images to the GAP (Linux Server) which replicates two backup copies to two Data Grid storage devices (see Fig. 6 Data Flow of DICOM storage). In this case, P2 of SAN and D1 receive the images, no images are sent to P1. The Modality Simulator is then connected to Linux Server of Core B and the experiment is repeated, and so forth. Figure 9 depicts the connectivity of the emulation. Phase One validation has been completed.

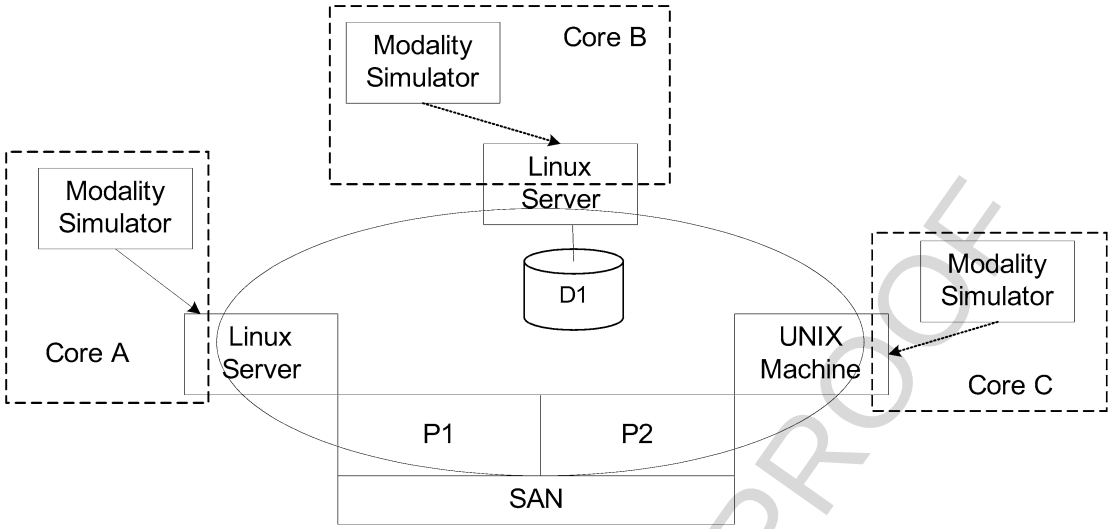

Fig. 9. Data Grid test: Phase One at the laboratory environment with simulated clinical trial images.

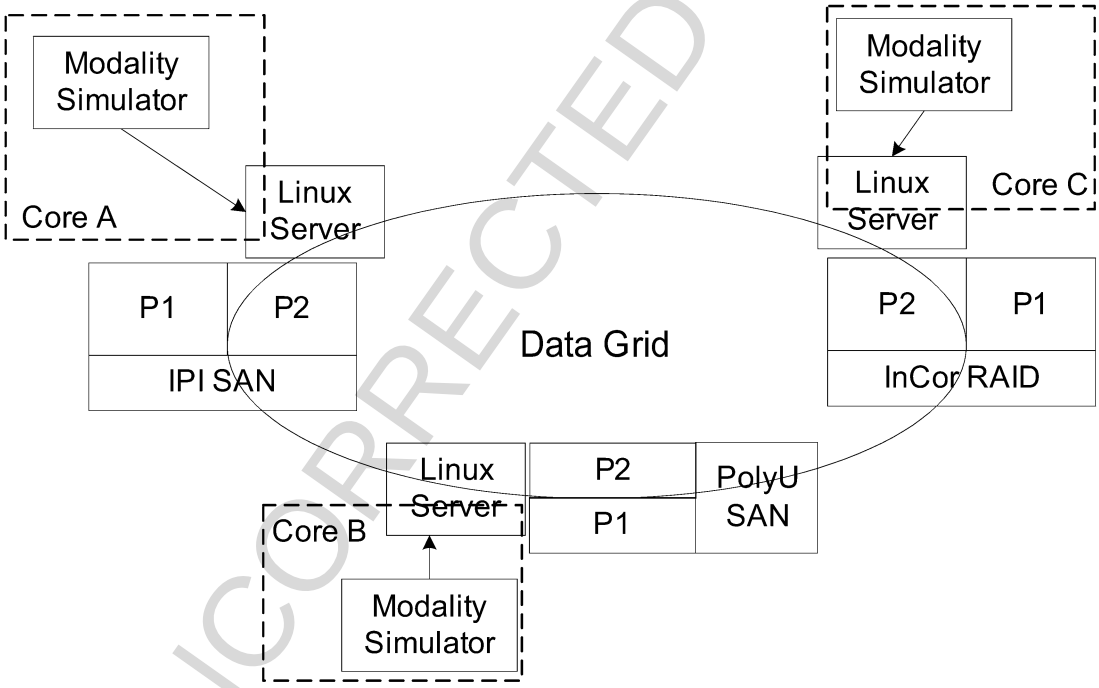

Fig. 10. Data Grid test: Phase Two with three international emulated radiology cores A, B, and C.

3.2.2. *Phase Two*

Phase Two is to implement the Data Grid as the backup storage of three emulated International Radiology Cores at IPI, PolyU, and InCor, respectively. Figure 10 shows the equipment allocations and their connectivity.

The Data Grid consists of three International Radiology Cores emulated by three Linux servers, each of which has a storage device as follows:

- Core A : A Modality simulator is connected to a Linux Server with P2 of the SAN at IPI.
- Core B: A Modality simulator is connected to a Linux Server with P2 of the SAN at PolyU.
- Core C: A Modality simulator is connected to a Linux Server with P2 of the RAID at InCor.

The experimental procedures are the same as in the Phase One test except that all three Modality Simulators emulating the Image Servers at each Image Server of a Radiology Core can send clinical trials images at any time. Therefore, all three storage devices in the Data Grid may not be idle at a given time. The goals of this test are: (1) to validate the International Internet 2 connectivity, performance and reliability; and (2) to assure the quality of the Data Grid storage performance under simultaneous loading conditions.

3.2.3. Phase Three

Phase Three is to use images from two real clinical trials to validate and evaluate the performance of the International Data Grid for clinical trails images backup. The experimental set up would be similar to that in Phase Two.

Initially, a small clinical trial 1 (T1) with limited number of patients will be tested at the Core IPI. Once the test is stable, a second clinical trial (T2) will be added while the first trial continues. Since the images from both trials must be physically and logically separated in the storage, the SAN and RAID at three cores will be partitioned into smaller components for this experiment. Figure 11 depicts the data flow of the test. In this test, the IPI Radiology Core also sends the Core images to its own backup storage in P1 SAN. Therefore, three copies of the trails images are available, one at P1 and two at P2 of other sites. The goal of this test is validate that the Data Grid can actually replace the current backup storage of the Core to be described in Section 4.

4. Backup data storage migration

One major goal of using Data Grid concept for clinical trials is to replace its current storage backup system. This section discusses the data storage migration steps to replace the current local backup at the radiology core by the Data Grid. Following the Data Grid configuration discussed in Section 3.2.3 and Fig. 11, Fig. 12 shows how to migrate images at the local backup to the Data Grid. IPI SAN is used as a Data Grid confederation for illustration purpose.

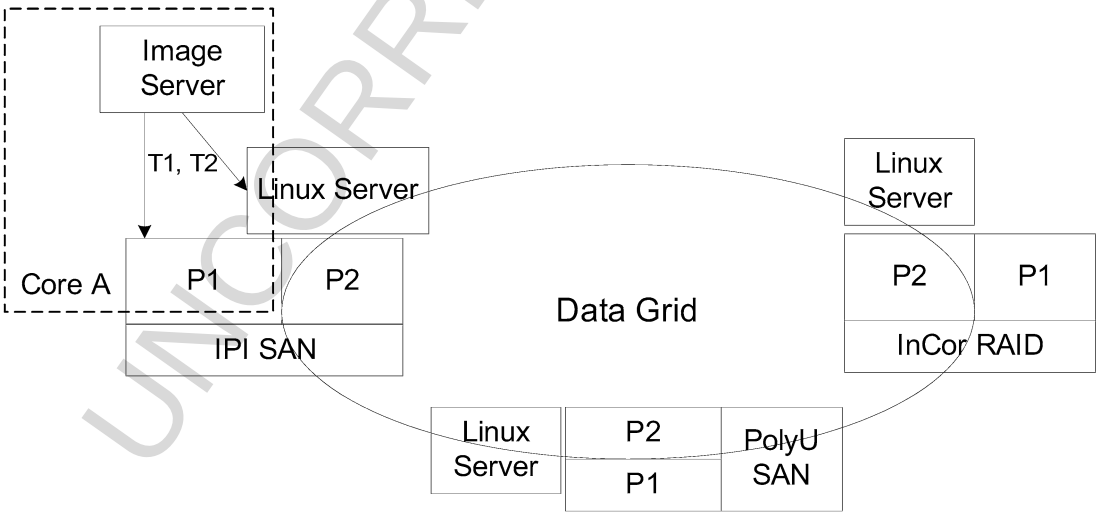

Fig. 11. Data Grid test: Phase Three at three international sites with real clinical trials images (T1 and T2).

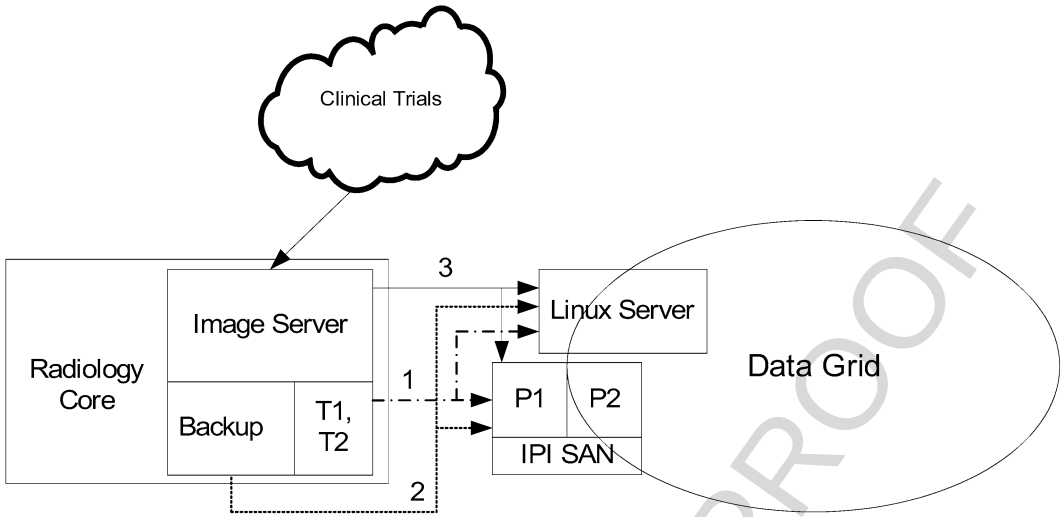

Fig. 12. Migrate images in the local backup of the radiology core to P1 of the IPI SAN and the Data Grid through a three-step procedure.

(1) Start with two clinical trials (T1 and T2) with small number of patients. For a ***new*** image received by the image server sent by a clinical trial site (see Fig. 2), one copy of the image is stored within the radiology core local backup storage. The local backup sends a copy to P1 of the IPI SAN as the backup in the core, which migrates new images from the local backup to the SAN, one image at a time. Meanwhile, the local backup also sends a copy to the Linux Server (GAP) at the Data Grid for backup. The Data Grid will maintain two copies of the image in two remote storages (see Fig. 11, two P2s).
(2) Once all testing and evaluation of Step 1 are satisfactory, the next step is to send one copy of all ***historical backup images*** of T1 and T2 in the local backup to the P1 of the IPI SAN, and send another copy to the Linux Server at the Data Grid, which replicates it to two more copies stored at two remote cores. Step 1 continues if more ***new*** images are coming in during Step 2.
(3) Once Step 2 is completed, P1 has all backup images of Trials T1 and T2, ***new and historical***. The image server will stop sending images to the local backup. Instead, the image server will begin to send any ***new*** images of trials T1 and T2 to P1 of the SAN for local backup, and also send a copy to the Data Grid for backup which replicates two copies in two P2s of other cores. The data migration procedure for trials T1 and T2 is completed, and traditional local backup at the core can be dismounted.

5. Discussion

With the use of digital mammography, multi-slice CT, MRI and US imaging in clinical trials and the ever-increasing number of clinical trials, current information system infrastructure of the radiology core that handles multiple trials can no longer satisfy the requirements of fault-tolerance of image data and analysis results and the quick distribution of images and results to worldwide experts involved in the trials. In this paper, we present a Data Grid testbed with three international sites for backup of clinical trial images from multiple imaging cores. The laboratory prototype of this DICOM compliance Data Grid has been completed. Currently, the three International sites have been connected, and we are implementing the Data Grid at the Hong Kong Polytechnic University, and the Heart Institute at Sao Paulo, Brazil.

Once the Data Grid testbed for clinical trial image backup is established, we can incorporate the multiple trials databases into the Data Grid in the future. The multiple trials databases are equally important as the image data. Such a Data Grid can provide three benefits to the trials databases: (1) fault-tolerance, (2) data and result sharing, and (3) dynamic creation and modification of data model to support any new trial or change of trials.

A further advance of using the Data Grid in clinical trials is to embed radiology/imaging cores inside the Data Grid so that the computer process or analysis software from multiple cores can be shared and fault-tolerant. The ultimate goal of the Data Grid is to provide a large virtual distributed fault-tolerant data system for variety of clinical trials to store, backup, and share images and results. Such a Data Grid infrastructure would allow trials images and results to be pooled and mined for hidden knowledge which could eventually improve clinical trials outcomes.

References

[1] C.L. Meinert, *Clinical Trials: Design, Conduct, and Analysis*, Oxford U. Press, Oxford, 1986.
[2] S. Piantadosi, *Clinical Trials: A Methodologic Perspective*, Wiley, 1997.
[3] S.C. Chow and J.P. Liu, *Design and Analysis of Clinical Trials: Concepts and Methodologies*, Wiley, NY, 2004.
[4] M.S. Brown, S.K. Shah, R.C. Pais, Y. Lee, M.F. McNitt-Gray, J.G. Goldin, A.F. Cardenas and D.R. Aberle, Database design and implementation for quantitative image analysis research, *IEEE Trans. Information Technology in Biomedicine* **9** (2005), 99–108.
[5] M.F. McNitt-Gray, S.G. Aramato, L.P. Clarke, G. McLennan, C.R. Meyer and D.F. Yankelevitz, The lung imaging database consortium: creating a resource for the image processing research community, *Radiology* **225** (2002), 739–748.
[6] Digital Imaging and Communications in Medicine (DICOM) 2004, http://medical.nema.org/dicom/2004.html, accessed on March 14, 2006.
[7] Redundant Array of Independent Disks (RAID), http://en.wikipedia.org/wiki/Redundant_array_of_independent_disks, accessed on March 14, 2006.
[8] N.K. Ouchi, System for recovering data stored in failed memory unit, US Patent 714/5, 714/6, 714/807, 1977.
[9] A. Chervenak, I. Foster, C. Kesselman, C. Salisbury and S. Tuecke, The Data Grid: towards an architecture for the distributed management and analysis of large scientific datasets, *Journal of Network and Computer Applications* **23** (2001), 187–200.
[10] W. Allcock, J. Bresnahan, R. Kettimuthu, M. Link, C. Dumitrescu, I. Raicu and I. Foster, The globus striped GridFTP framework and server, in: *Proceedings of Super Computing*, 2005 (SC05).
[11] B.J. Liu, M.Z. Zhou and J. Documet, Utilizing data grid architecture for the backup and recovery of clinical image data, *Computerized Medical Imaging and Graphics* **29** (2005), 95–102.
[12] H.K. Huang, A. Zhang, B. Liu, Z. Zhou, et al., Data Grid for Large-Scale Medical Image Archive and Analysis, in: *Proc. the 13th ACM International Conference on Multimedia*, 2005, pp. 1005–1013.
[13] I. Foster, The Grid: a new infrastructure for 21st century science, *Physics Today* **55** (2002), 42–47.
[14] J.M. Schopf and B. Nitzberg, Grids: top ten questions, *Scientific Programming, Special Issue on Grid Computing* **10** (2002), 103–111.
[15] TeraGrid, http://www.teragrid.org/, accessed on March 14, 2006.
[16] Large-scale Data Replication for LIGO, http://www.globus.org/solutions/data_replication/, accessed on March 14, 2006.
[17] I. Foster, Globus Toolkit Version 4: software for service-oriented systems, in: *IFIP International Conference on Network and Parallel Computing*, Springer, LNCS 3779, 2005, pp. 2–13.
[18] H.K. Huang, *PACS and Imaging Informatics: Basic Principles and Applications*, Wiley, NJ, 2004.
[19] B.J. Liu, F. Cao, M.Z. Zhou, G. Mogel and L. Documet, Trends in PACS image storage and archive, *Computerized Medical Imaging and Graphics* **27** (2003), 165–174.
[20] G. Mogel, H.K. Huang, F. Cao, Z. Zhou, P. Dev, M. Gill and B.J. Liu, NGI performance in teleradiology applications, *Proc. SPIE, Medical Imaging* **3** (2002), 25–30.
[21] Internet2, http://www.internet2.edu/, accessed on March 14, 2006.
[22] CalRen, http://www.cenic.org/calren/index.htm, accessed on March 14, 2006.
[23] HARNET, http://www.jucc.edu.hk/jucc/content_harnet.html, accessed on March 14, 2006.
[24] L.W. Chan, M.Z. Zhou, S.K. Hau, M.Y. Law, F.H. Tang and J. Documet, International Internet-2 performance and automatic tuning protocol for medical imaging applications, *Computerized Medical Imaging and Graphics* **29** (2005), 103–114.
[25] RNP2, http://www.rnp.br/en/, accessed on March 14, 2006.
[26] M.Y.Y. Law and Z. Zhou, New direction in PACS education and training, *Computerized Medical Imaging and Graphics* **27** (2003), 147–156.
[27] Z. Zhou, B.J. Liu, H.K. Huang and J. Zhang, Educational RIS/PACS simulator integrated with the HIPAA compliant auditing (HCA) toolkit, *Proc. SPIE Medical Imaging* **6** (2005), 491–500.
[28] B.J. Liu, Z. Zhou, M.A. Gutierrez, J. Documet, L. Chan and H.K. Huang, International Internet2 connectivity and performance in medical imaging applications: Bridging Americas to Asia, *J. High Speed Networks* (submitted.)

CAD-PACS Integration Tool Kit Based on DICOM Secondary Capture, Structured Report and IHE Workflow Profiles*

Zheng Zhou[1], Brent J. Liu[1], Anh H. Le[1]

[1]Image Processing & Informatics (IPI) Laboratory, Radiology Department, University of Southern California, Marina del Rey, CA, 90292, USA

** Paper accepted to be published in Journal of Computerized Medical Imaging and Graphics*

ABSTRACT

Computer Aided Diagnosis/Detection (CAD) goes beyond subjective visual assessment of clinical images providing quantitative computer analysis of the image content, and can greatly improve clinical diagnostic outcome. Many CAD applications, including commercial and research CAD, have been developed with no ability to integrate the CAD results with a clinical picture archiving and communication system (PACS). This has hindered the extensive use of CAD for maximum benefit within a clinical environment. In this paper, we present a CAD-PACS integration toolkit that integrates CAD results with a clinical PACS.
The toolkit is a software package with two versions: DICOM (digital imaging and communications in medicine)-SC (secondary capture) and DICOM-IHE (Integrating the Healthcare Enterprise). The former uses the DICOM secondary capture object model to convert the screen shot of the CAD results to a DICOM image file for PACS workstations to display, while the latter converts the CAD results to a DICOM structured report (SR) based on IHE Workflow Profiles. The DICOM-SC method is simple and easy to be implemented without ability for further data mining of CAD results, while the DICOM-IHE can be used for data mining of CAD results in the future but more complicated to implement than the DICOM-SC method.

Keywords: *CAD, PACS, System Integration, DICOM, IHE*

1. INTRODUCTION

Computer aided detection/diagnosis (CAD) can improve the efficiency and accuracy of clinical diagnosis by automatically detecting abnormalities and/or pathologies in medical imaging and performing quantitative analysis. Many CAD applications have been conducted in the imaging community during the last twenty years [1-3]. Among them, CAD applications in mammography [4-6], chest [7] and three dimensional (3-D) CT lung imaging [8] have emerged as commercial products over the last 5-6 years. While these commercial CAD companies have devoted most of their time to CAD algorithm development and robustness, little effort has been performed on the system integration of CAD results with a picture archiving and communication system (PACS) [9, 10] where CAD is used. Current clinical practice and workflow usually have CAD results limited to a standalone CAD workstation or a CAD server without integrating the CAD results with a PACS. Fig. 1 shows a typical CAD process flow in current clinical practice. Generally, the RIS (radiology information system) orders the CAD process for an exam when the exam is scheduled. The technician or the radiologist pushes the original image exam from the

PACS server or the PACS workstation (WS) to the CAD WS for process. The CAD result is reviewed in the CAD WS. Any physician who wants to review the CAD results has to access the CAD WS, which is usually only available in the radiology department. In order to benefit most clinical physicians, CAD results must be integrated with a PACS where physicians can easily query and retrieve CAD results and the original clinical images to their viewing WS for reviewing.

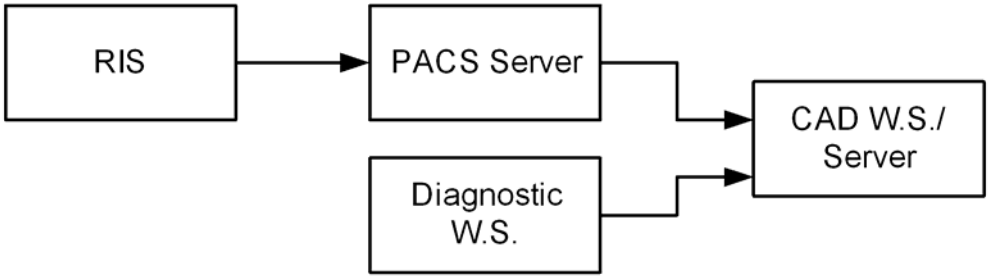

Fig. 1 Current CAD work flow. The CAD results are limited to the CAD workstation or the CAD server for reviewing.

Digital imaging and communications in medicine (DICOM) [11] standard has defined two structured report (SR) templates for mammography and chest CAD results. The Integrating the Healthcare Enterprise (IHE) [12] has also published a Post-processing workflow profile for integrating CAD applications with clinical PACS workflow. Under the guidance of these initiatives, some commercial vendors [13, 14] are developing the software to integrate their CAD application results with a PACS. However, the system integration software is tightly coupled to their CAD applications and is difficult to be used to integrate third party CAD applications with a PACS.

The ever-increasing field of CAD research and development has produced many applications developed by academic institutions or small companies. Unfortunately, these applications still remain in a standalone CAD workstation, CAD server, or diagnostic workstation. Thus, a toolkit that can facilitate the integration of CAD results of these standalone CAD applications has become an urgent requirement for clinical CAD use.

In this paper, we present a CAD-PACS integration toolkit for this purpose. The remainder of this paper explains the system integration approach of the toolkit and shows some examples of applying the toolkit for CAD-PACS integration.

2. METHODS

The goal of the CAD-PACS toolkit is to store the CAD results in the PACS server and integrate the CAD process flow with a PACS seamlessly. The CAD-PACS toolkit is developed under the premise that the CAD software can be either in a standalone CAD workstation, a CAD server, or integrated within the PACS workstation (WS). The CAD-PACS toolkit is a software package with two versions, the DICOM-SC (Secondary Capture) version, and the DICOM-IHE version (Fig. 2). The major software package in DICOM-SC is the i-CAD-SC which resides in the CAD WS and uses the DICOM secondary capture function to convert CAD results to a DICOM image file. The DICOM-IHE has four modules, i-CAD; and i-PPM (Post-Processing Manager), Receive-SR, and Display-SR. The former resides in the CAD WS to convert CAD results, including textual data and segmented images, to DICOM SR data and DICOM SC images, and the latter three reside in the PACS Server and PACS WS as shown, respectively.

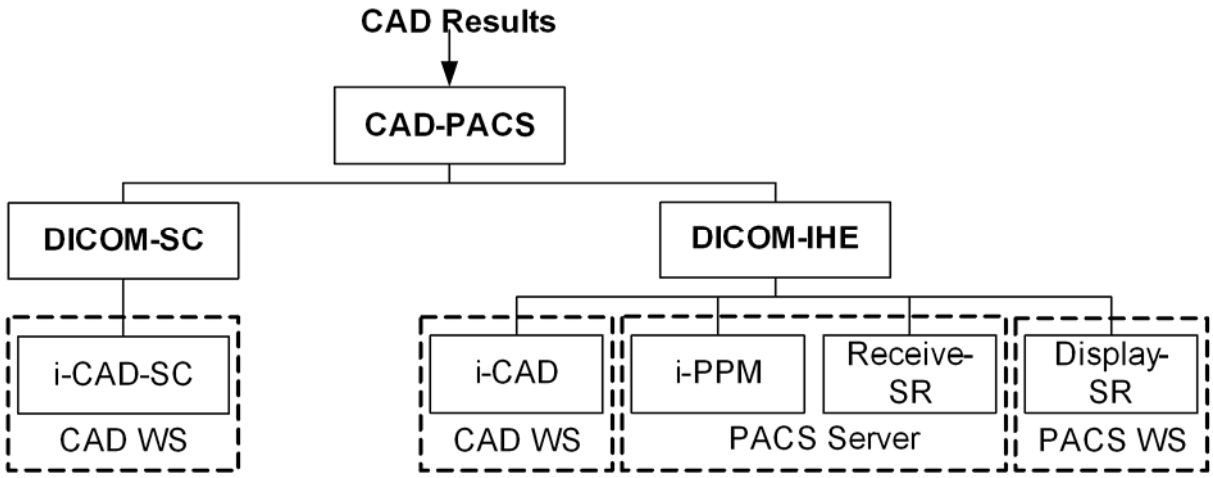

Fig. 2 CAD-PACS has two versions, Left: DICOM-SC (Secondary Capture), and Right: DICOM-IHE. The major software package in DICOM-SC is the i-CAD-SC which resides in the CAD WS and uses the DICOM secondary capture function. The DICOM-IHE has four modules, i-CAD; and i-PPM (Post-Processing Manager), Receive-SR, and Display-SR. The former resides in the CAD WS, and the latter three reside in the PACS Server and PACS WS as shown, respectively.

2.1 The CAD-PACS DICOM-SC version

The CAD-PACS DICOM-SC does not need to change the existing PACS server software. The advantage of using the DICOM-SC version is an immediate and low cost solution to review CAD results and reports at a PACS WS (Fig. 3).

The DICOM-SC version converts the screen shot of the CAD results to a DICOM image file at the CAD WS. The DICOM image file is then transmitted to the PACS server so that CAD results can be stored in the PACS server and be displayed as a DICOM file in PACS WSs. To generate the DICOM CAD result image, the DICOM-SC requires patient demographic information, study information, and the screen shot of the CAD results in JPEG or TIFF format. If the CAD WS cannot provide the screen shot, the i-CAD-SC contains a module to create the screen shot.

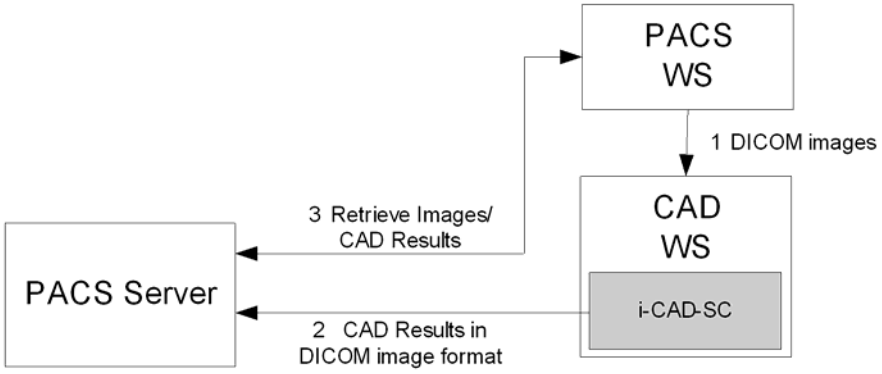

Fig. 3 Integrating the CAD results with a PACS using the i-CAD-SC.

2.1.1 The CAD-PACS DICOM-SC Workflow

Fig. 3 shows the workflow to integrate the DICOM-SC CAD result image with a PACS:

1) The PACS WS sends DICOM images to the CAD WS for CAD process.
2) The i-CAD-SC software package installed in the CAD WS converts the screen shot of the CAD results to a DICOM image file and sends it to the PACS server. The CAD result image can be stored as an additional series under the same study of the patient DICOM data model in the PACS server. This can be achieved by creating a new series for the CAD results image and adding the patient information to the DICOM header of the created CAD results image at the CAD WS.
3) When the PACS WS queries the PACS server, the new series containing the CAD results image will appear under the study of the patient in the work list. Physicians can retrieve this study for review with the CAD results shown as a DICOM image.

Due to the nature of screen-capture data, this version has two disadvantages: 1) any further data analysis and data mining of the CAD results are not possible, and 2) it does not support CAD workflow schedule and management. For these two disadvantages, we have developed the DICOM-IHE version.

2.2 THE CAD-PACS DICOM-IHE Version

The DICOM-IHE version is developed based on the DICOM Structured Report (SR) [11] standard (DICOM Working Group 15, CAD template Supplement 50), and the IHE Key Image Note (IHE Profile 6), Simple Image and Numeric Report (IHE Profile 7) and Post-Processing Workflow Profiles (IHE Profile 10) [12]. In particular, the Key Image Note (Profile 6) is used in i-CAD module, the Simple Image and Numeric Report (Profile 7) in Display-SR module and the Post-Processing Workflow (Profile 10) in i-CAD, i-PPM and Receive-SR modules. The advantage of the DICOM-IHE version is that it follows the DICOM standard and IHE Workflow Profiles. Thus, it is the correct method of approach, in the sense of its longevity, and its integration of the CAD WS with PAC systems. It supports the CAD workflow schedule and management, and allows CAD results to be archived in the PACS server in the DICOM SR format. Further data analysis and data mining of CAD results are possible since the DICOM SR data can be easily converted into structured data within a database.

In addition to the quantitative CAD results converted into the DICOM SR object, the DICOM-IHE method utilizes the previously described DICOM-SC method to convert the screen shot of CAD segmented or annotated images to DICOM images. The DICOM header of the DICOM CAD image has the same patient and study information but different series and image information. Thus, the DICOM CAD images can be stored in the PACS server as a new series under the original study of the patient. The DICOM CAD images are then linked to the DICOM SR CAD result as the reference images by adding the SOP (Service Object Pair) Instance UID of the images to the DICOM SR CAD result. Physicians can retrieve the CAD images for review when they review the CAD quantitative results.

2.2.1 Four Modules in the DCIOM-IHE Version

As shown in Fig. 2, the DICOM-IHE version has four modules. The i-CAD is used to convert the CAD results to DICOM Structured Report (SR) data and DICOM CAD images, which can be stored in the PACS server and retrieved by the PACS workstation for reviewing. The Receive-SR and Display-SR are used to store and display the DICOM SR data. They are for the PACS server and the PACS workstation not supporting DICOM SR which is required by the DICOM-

IHE for the CAD-PACS integration. The Post-Processing Manager (i-PPM) is used to manage the CAD process flow and integrate it with the RIS/PACS workflow. The CAD-PACS workflow steps are presented by numerals depicted in Fig. 5 and will be described later in greater detail.

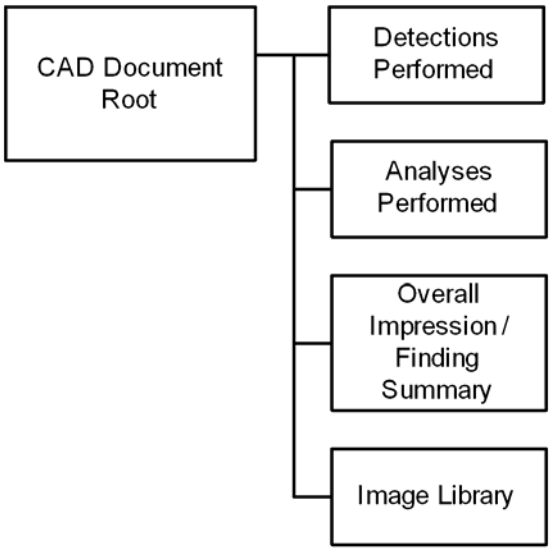

Fig. 4 The template defined for creating DICOM SR CAD result. The template is defined as two-level tree architecture based on DICOM general SR templates. The root of the tree is a CAD root document that contains four nodes: Detections Performed, Analyses Performed, Overall Impression/Finding Summary, and Image Library. The four nodes is filled by the information extracted from CAD results or be void if there is no corresponding information in CAD results

2.2.2 The i-CAD Module

The i-CAD modules, residing in the CAD WS, provides following major functions for the CAD-PACS integration:

1) Create DICOM SR objects for CAD results. The structure (Fig. 4) of the DICOM SR object is defined as two-level tree architecture based on DICOM general SR templates. The root of the tree architecture is a CAD root document that contains four nodes: Detections Performed, Analyses Performed, Overall Impression/Finding Summary, and Image Library. These four nodes will be filled by the information extracted from CAD results or be void if there is no corresponding information in CAD results. These four nodes can also be expanded to adapt to the results of different CAD applications.
2) Parse proprietary CAD results and convert them to a DICOM SR object defined in the function 1.
3) Perform DICOM SR C-Store client function to store the DICOM SR CAD results in the PACS server that acts as a DICOM SR C-Store SCP.
4) Perform DICOM C-Find client to query the CAD worklist in the Post-Processing Manager (i-PPM) module (to be described in the next section). The CAD worklist, like the DICOM worklist in the diagnostic workstation, contains a list of tasks need to be processed by the CAD workstation. The process flow of the CAD workstation is based on the CAD worklist.
5) Perform DICOM C-Move client to retrieve DICOM study/images from PACS server.

6) Exchange CAD process status message, such as Scheduled Work Item(s) Claimed, Work Item In Progress, or Work Item Complete, with the i-PPM for CAD work flow management.

The i-CAD module uses the Key Image Note (IHE Profile 6) and the Post-Processing Workflow (IHE Profile 10).

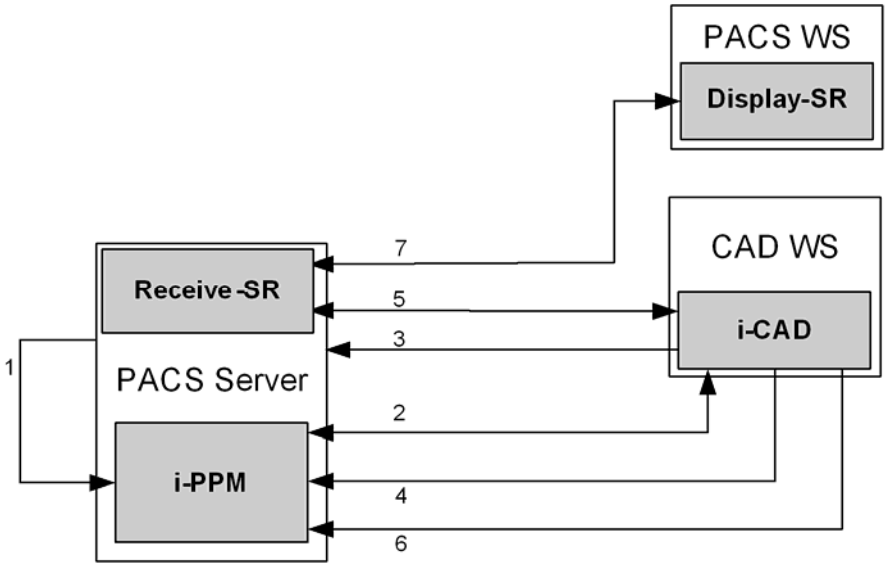

Fig. 5 Step-by-step workflow of integrating CAD results from a standalone CAD WS or a CAD server with a PACS server using the CAD-PACS DICOM-IHE. Refer to Fig. 2 for the residence of the four modules (shaded boxes); i-CAD at CAD WS; i-PPM and Receive-SR at PACS Server; and Display-SR at PACS WS

2.2.3 The Post-Processing Manager (i-PPM) Module

The i-PPM software package residing in the PACS server is used to schedule or track the status of PACS-CAD workflow steps. For those PAC systems which do not support post-processing management, i-PPM is used to supplement the PACS to be DICOM- and IHE-compliant for CAD-PACS integration.

The major functions of the i-PPM include:

1) Receive a list of available DICOM studies from the PACS server or PACS WS, or query the list from the PACS server.
2) Create the CAD worklist.
3) Perform C-Find SCP to support the worklist query from the CAD WS.
4) Exchange CAD process status message with the i-CAD.

The i-PPM module uses the Post-Processing Workflow (IHE Profile 10).

2.2.4 The Receive-SR Module

The Receive-SR Module residing in the PACS server is used to receive DICOM SR objects at the PACS server when the PACS server does not support DICOM SR and related operations, e.g., DICOM SR C-Store or C-Find. The workflow of the CAD-PACS integration involving the use of this module will be described in Section 4.The Receive-SR module uses the Post-Processing Workflow (IHE Profile 10).

2.2.5 The Display-SR Module

The Display-SR module is used when the PACS WS does not support DICOM SR C-Store, C-Find or display. The workflow of the CAD-PACS integration involving the use of this module will be described in Section 4. The Display-SR displays DICOM SR CAD results independently using the Web technology as well as acts as the DICOM SR C-Store SCP and C-Find SCU.
The Display-SR uses the Simple Image and Numeric Report (IHE Profile 7).

2.3 Steps of Integrating CAD Results with A PACS using the CAD-PACS DICOM-IHE Module

With the four modules, i-CAD, i-PPM, Receive-SR, and Display-SR in the CAD-PACS DICOM-IHE installed, Fig. 5 depicts the workflow (numerals 1 - 7) of integrating a standalone CAD WS with a PACS server. The numerals are referred to by each paragraph accordingly.
1) The PACS server pushes a DICOM worklist to the i-PPM requesting a CAD process to be included in the studies. If PACS server cannot automatically push the worklist, the i-PPM can query the PACS server for the DICOM worklist automatically.
2) The CAD WS queries the CAD worklist from i-PPM that has been grouped at the PACS server. The CAD claims work items to be performed.
3) The CAD WS queries/retrieves DICOM images from the PACS server for CAD process.
4) The CAD WS sends “work item in progress” message to the Post-Processing Manager (i-PPM).
5) The CAD Workstation performs CAD process and stores the CAD results in the Receive-SR installed in the PACS server.
6) The CAD WS reports Work Item PPS & Work Item Completed Message to the i-PPM.
7) The PACS WS retrieves the DICOM SR CAD results for physicians’ review. The web-based Display-SR can be used in the PACS WS to view the CAD results.

3. CLINICAL IMPLEMENTATION OF CAD-PACS WITH A CLINICAL PACS

Three approaches can be used for clinical implementation of CAD-PACS dependent upon where the CAD software is located, and if the PACS is DICOM- and/or IHE-compliant.

3.1 Approach 1: Integrating CAD results from a standalone CAD WS with a PACS

In this case, the i-CAD can be installed either in the CAD WS or the CAD server. The i-PPM and the Receive-SR can be installed in the PACS Server, and the Display-SR can be installed in the PACS WSs.

3.2 Approach 2: Integrating CAD results with a PACS while the CAD software package is directly installed in a PACS WS

In the case that the CAD software is already installed in the PACS WS, i-CAD and the Display-SR can be installed in the PACS WS, and i-PPM and Receive-SR can be installed in the PACS Server.

3.3 Approach 3: Integrating CAD with any Clinical PACS

In this case, assuming that i-CAD, which is DICOM- and IHE-compliant, has been installed in the CAD WS, the CAD Server, or the PACS WS. When integrating the CAD-PACS with any PACS, the method of integration is different dependent upon whether the PACS being considered is DICOM- and/or IHE-compliant. Table 1 summarizes three possible scenarios that could be encountered and how to integrate the CAD-PACS DICOM-IHE in each scenario. The CAD-PACS DICOM-IHE with the four modules, i-CAD, i-PPM, Receive-SR, and Display-SR can be used to resolve these different Scenarios.

Scenario 1: The clinical PACS server does not support DICOM SR, DICOM SR C-Store and C-Find, and does not have a Post-Processing Manager.

The Receive-SR and i-PPM software can be installed within the PACS server to support the CAD WS. The Receive-SR handles all DICOM SR and SR C-Store transactions and can be used as a standalone manager for the PACS server. The Display-SR can be installed in PACS WSs if they do not support DICOM SR store, query and display.

Once this is set up, the CAD WS can be integrated with the PACS using the i-CAD installed in the CAD WS. If the end user wants to manage the CAD worklist and process messages, the i-PPM can be installed in the PACS server. The i-CAD in the CAD WS can be configured to enable or disable the features of query CAD worklist and reporting CAD process messages.

The Receive-SR and i-PPM each can run as independent software within the PACS server until the time when the manufacturer can support DICOM SR and DICOM SR C-Store in their updated PACS. At that time, a data migration from the Receive-SR to the updated PACS server must be performed.

Scenario 2: The clinical PACS server supports DICOM SR, DICOM SR C-Store and C-Find but does not have manufacturer's Post-Processing Manager integrated.

The CAD WS with i-CAD installed can be integrated with the PACS server without tracking and managing the CAD progress. To track and manage the CAD progress can be accomplished by installing i-PPM in the PACS server and run it as an independent program. The Display-SR can be installed in PACS WSs if they do not support DICOM SR store, query and display.

Scenario 3: The clinical PACS server supports DICOM SR, DICOM SR C-Store and C-Find, and with Manufacturer's Post-Processing Manager integrated.

The CAD WS with i-CAD installed can be fully integrated with the PACS server since both of them follow the DICOM standard and the IHE Workflow Profiles. In the case that PACS WSs do not support DICOM SR store, query and display, the Display-SR can be installed in these WSs.

In the situation that some RIS/PACS integrated systems may group the Post-Processing Manager with RIS, the CAD WS with i-CAD still can be fully integrated with the RIS/PACS, but the CAD worklist and process messages would communicate directly with RIS.

Table 1 Three Scenarios to integrate CAD-PACS DICOM-IHE with a clinical PACS

	CAD-PACS DICOM-IHE Modules			
Scenarios	i-CAD installed in	i-PPM installed in	Receive-SR installed in	Display-SR installed in
1: PACS Server w/o DICOM SR and PPM*	CAD WS/ CAD Server	PACS Server	PACS Server	PACS WS
2: PACS Server w/ DICOM SR, w/o PPM*	CAD WS/ CAD Server	PACS Server	Not needed	Not needed
3: PACS Server w/ DICOM SR and PPM*	CAD WS/ CAD Server	Not needed	Not needed	Not needed

*PPM: Post-processing manager

4. RESULTS

The CAD-PACS toolkit has been integrated with a PACS simulator [15, 16] for evaluation at the IPI Laboratory. Three CAD applications, computer aided bone age assessment [17, 18], computer aided detection of small acute intracranial hemorrhage on CT of brain [19], and computer aided detection of multiple sclerosis lesions on MR of brain, have been used for evaluation of the toolkit.

4.1 An Example of a CAD Application Integrated with PACS Using the CAD-PACS Toolkit

Fig. 6 shows an example of the DICOM SC image file that contains a screen-captured computer assisted bone age assessment (BAA) result depicting the bone age 3.8-year for a Caucasian boy and seven images segmented from the left hand radiography image of the boy. The segmented images show the region of interests (ROI) in phalangeal and carpal bones where multiple features are extracted for BAA [17, 18].
Fig. 7 shows an example of the DICOM SR CAD result depicting the MR brain multiple sclerosis lesions. The left hand side of this Figure shows the DICOM SR result that contains the CAD findings of the five sclerosis lesions in the MR brain study, while the right hand side shows the original DICOM MR brain image and the DICOM SC CAD image showing the overlay of the five sclerosis lesion at the original image, which are linked as “Original Image” and “CAD Image” in DICOM SR result.

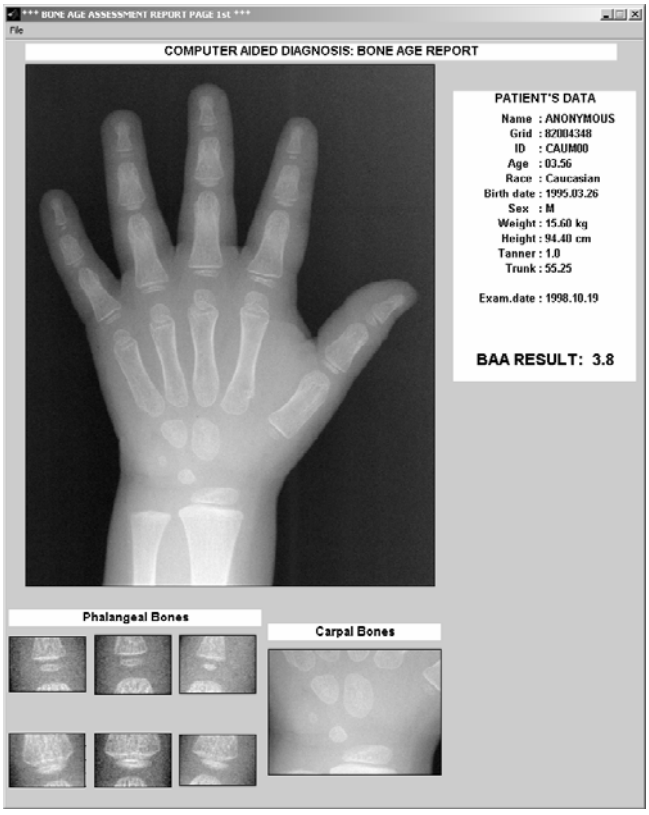

Fig. 6 An example of DICOM-SC CAD result image shows the screen capture of the CAD result that contains the original and segmented images and computer assessed bone age results. (Courtesy of Dr. Arkadiusz Gertych [17, 18].)

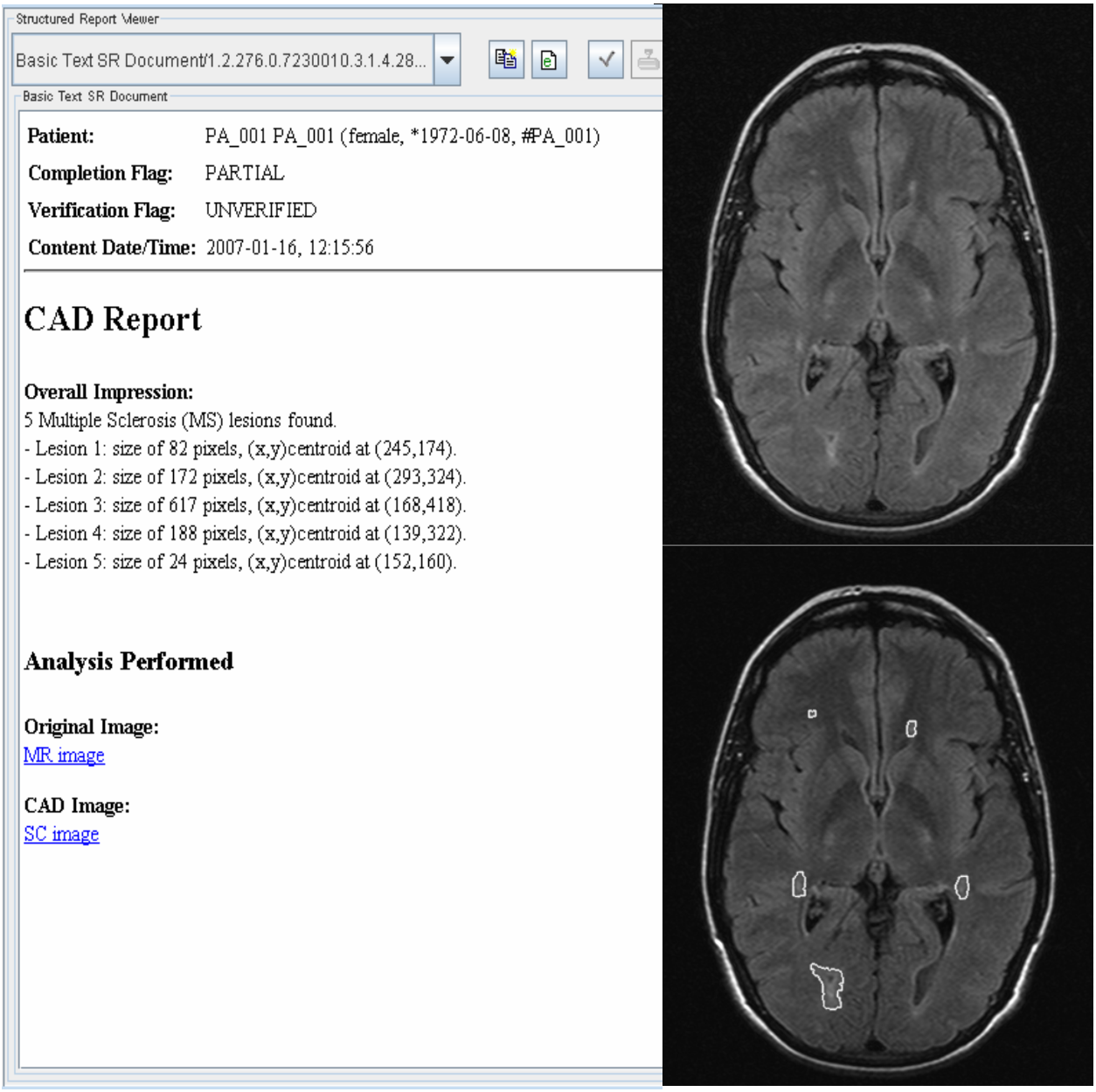

Fig. 7 DICOM Structured Report (SR) CAD results with the original and CAD images. Left: the DICOM SR result that contains the CAD findings of the multiple sclerosis lesion in an MR brain study, Right: the original DICOM MR brain image (top) and the DICOM SC CAD image showing the overlay of the five sclerosis lesions at the original image (bottom), which are linked as "Original Image" and "CAD Image" in the DICOM SR result. (Courtesy of Guardian Technologies.)

5. DISCUSSION

The integration, implementation, and evaluation of the CAD-PACS i-CAD-SC (Secondary Capture) version is simple and straight forward and does not require special methodology or additional software modules as described in Section 2.

On the other hand, the integration, implementation, and evaluation of the CAD-PACS DICOM-IHE version which uses structured report are more involved. The previous three approaches in Section 3 have been developed for the clinical implementation of CAD-PACS with a clinical PACS. In addition, the implementation of i-PPM/Receive-SR requires the cooperation of the

PACS manufacturers to open the system software of the PACS server to install the i-PPM/Receive-SR software. If this is not applicable, the i-PPM/Recevie-SR can be run in an additional computer that is connected to the PACS network until the time when the manufacturer can support IHE Post-Processing Workflow Profile and DICOM SR store in their updated PACS. At that time, a data migration from the i-PPM and the Receive-SR to the updated PACS server must be performed. The Display-SR is web-based and can be run in a PACS WS or an independent computer connected to the PACS network.

6. SUMMARY

We have developed a CAD-PACS integration toolkit to facilitate integrating results of a standalone CAD application with a PACS. The CAD-PACS toolkit contains two different integration methods, DICOM-SC and DICOM-IHE. The former is for quick deployment and the latter for long-term use with emerging DICOM and IHE compliant solutions. Our experimental results shows both methods are effective to integrate CAD results, including quantitative measurements and CAD segmented images, with a PACS seamlessly.

References

[1] M.L. Giger, K. Doi, H. MacMahon, Image feature analysis and computer-aided diagnosis in digital radiography: 3. Automated detection of nodules in peripheral lung fields, Med. Phys. 15 (1988) 158-166.
[2] K. Doi, et al., Computer-Aided Diagnosis in Medical Imaging, Elsevier, New York, 1999.
[3] M. McNitt-Gray, Lung nodules and beyond: approaches, challenges and opportunities in thoracic CAD, CARS 2004, 896-091.
[4] L.W. Burhenne, et al., Potential contribution of computer-aided detection to the sensitivity of screening mammography, Radiology 215 (2000) 554 – 562.
[5] J.A. Baker, et al., Computer aided detection (CAD) in screening mammography: sensitivity of commercial system in detecting architecture distortion, AJR 181 (2003) 1083-1088.
[6] H.P. Chan, et al., Image feature analysis and computer-aided diagnosis in digital radiography: 1. Automated detection of micro calcifications in mammography, Med. Phys. 14 (1987) 538-548.
[7] M.T. Freedman, et al., A computer aid for radiologists: improved detection of small volume lung cancer on chest radiographs, RSNA (2003) 523.
[8] S.A. Wood, et al., CAD of actionable lung nodules on multislice CT scans of the lung: sensitivity and false positive marker rates, RSNA (2002) 477.
[9] H. K. Huang, A. W. K. Wong, S. L. Lou, and T. M. Bazzil, et al, Clinical experience with a second generation PACS, J Digital Imaging, vol. 9, no. 4, pp. 151-66, 1996.
[10] Huang HK, PACS and imaging informatics. Hoboken, NJ: John Wiley & Sons, 2004.
[11] DICOM, http://medical.nema.org/, accessed on Sept. 14 2006.
[12] IHE, http://www.ihe.net/, accessed on Sept. 14 2006.
[13] P. Heffernan, H. Zhang, Software architecture for a CAD server, CARS 2004, 861-866.
[14] R2 Technology Inc., http://www.r2tech.com/main/home/index.php, accessed on Sept. 14 2006.
[15] Z. Zhou, H. K. Huang, F. Cao, B. J. Liu, J. Zhang, and G. T. Mogal, Educational RIS/PACS Simulator, SPIE Medical Imaging, vol. 4, pp. 139-147, 2003.
[16] M. Y. Y. Law, Z. Zhou, New direction in PACS education and training, J. Computerized Medical Imaging and Graphics, vol. 27, pp. 147-156. 2003.

[17] E. Pietka, A. Gertych, S. Pospiech, F. Cao, H.K. Huang, V. Gilsanz, Computer Assisted Bone Age Assessment: Image Processing and Epiphyseal/Metaphyseal ROI Extraction, IEEE Trans. Medical Imaging, 20, 715-729, 2001.
[18] E. Pietaka, S. Pospiech, A. Gertych, F. Cao, H.K. Huang, V. Gilsanz, Computer Automated Approach to the Extraction of Epiphyseal Regions in Hand Radiographs, Journal of Digital Imaging, 14, 165-172, 2002.
[19] T. Chan, H.K. Huang, Computer Aided Diagnosis of Acute Intracranial Hemorrhage on CT, RSNA Annual Meeting InfoRAD Exhibits, 2006.

Assuring the Security of Images and Results in CAD-PACS Integration*

Zheng Zhou[1]

[1]Image Processing & Informatics (IPI) Laboratory, Radiology Department,
University of Southern California, Marina del Rey, CA, 90292, USA

* *Paper accepted to be published in Journal of Computerized Medical Imaging and Graphics*

ABSTRACT

Computer aided diagnosis/detection (CAD) has been extensively used in mammography, chest, and three dimensional (3-D) CT lung imaging for clinical decision support over last 5-6 years. Recent trend is to integrate CAD applications with a PACS so that CAD results can be reviewed by most physicians for diagnosis. However, data security issue arises when a CAD application is integrated with a PACS. In this paper, we present a lossless digital signature embedding (LDSE) method for assuring the integrity of images used by the CAD and new images and results generated by the CAD application. Our experimental results show that the method is effective for assuring the integrity of CAD images. Combining this method with traditional one-dimensional digital signature technique for protecting CAD results, we provide a complete integrity assurance solution for a CAD application integrated with a PACS.

Keywords: *CAD, PACS, Security, Digital Signature, DICOM*

Definition of Terms used in this Manuscript

CAD Applications: Computer Aided Diagnosis application
CAD Images: images generated in a CAD application, such as segmented image
CAD Textual Results: textual reports and numeric measurement
CAD Results: CAD images and textual results
DICOM-SC: A method used in the CAD-PACS integration toolkit to convert CAD results to a DICOM image (see the paper "CAD-PACS integration toolkit" in this special issue)
DICOM-IHE: Another method used in the CAD-PACS integration toolkit that converts CAD results to DICOM SR and DICOM images (see the paper "CAD-PACS integration toolkit" in this special issue)

1. INTRODUCTION

CAD applications in mammography [1-3], chest [4] and 3-D CT lung imaging [5] have been commercialized and used for clinical decision support over last 5-6 years. Recent trend is to integrate CAD applications with a PACS so that CAD results can be shared among most physicians. However, data security issues arise here, such as has CAD results been altered? Or have images used in the CAD application been changed? Fig. 1 shows an example of image alteration. Fig. 1(a) shows a magnetic resonance (MR) brain image after its acquisition, and Fig.

1(b) shows the same image after it is retrieved to a CAD workstation. Without the arrow pointing toward the artificial lesion in Fig. 1(b), one would be hard pressed to identify the artificially inserted lesion even with images Fig. 1(a) and Fig. 1(b) displayed side by side. While human being is still possibly to tell that the lesion is artificially inserted, it will be difficult for the CAD to detect that the lesion is artificial in Fig. 1(b). If the CAD detects the artificial lesion and gives an impression that it is a tumor, this might lead to a false clinical decision. Such data security issues already exist in standalone CAD workstations, but will be much more crucial when a CAD is integrated to a PACS where CAD images and results can be accessed easily through PACS network. Assure the data security issues not just guarantees the objectivity of CAD results for clinical decision support, but more importantly, it enhances physician's confidence to use CAD in clinical service.

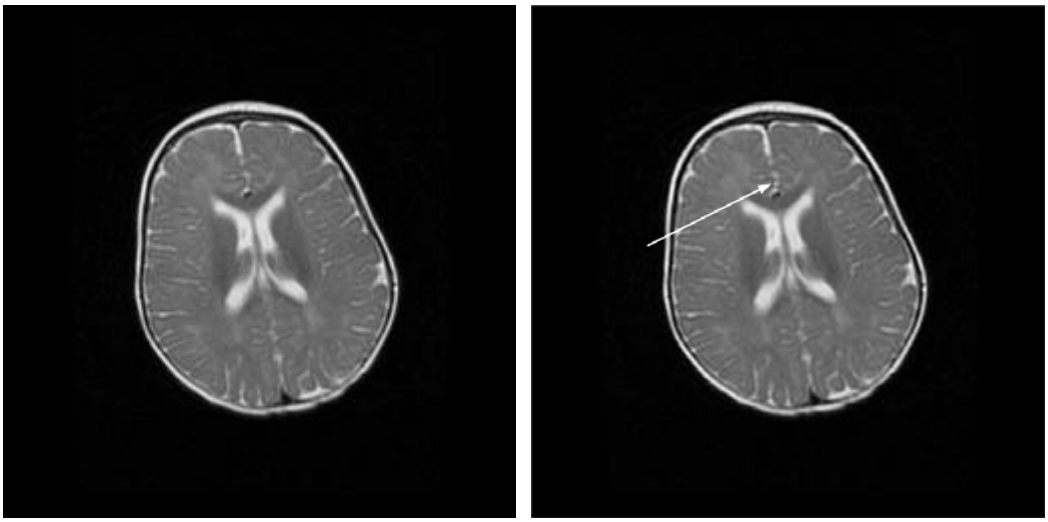

(a) (b)

Fig. 1 An example of image alteration. (a) a brain MR image; (b) the same MR image with an artificial lesion inserted.

A typical CAD application consists of three types of data: 1. original DICOM medical images used in the CAD application, 2. certain image results generated from CAD application, such as segmented or annotated images that are in JPEG/BMP/TIFF format, and 3. CAD textual results that contains report and numeric measurements. When a CAD application is integrated with a PACS, data type 2 and 3 must be converted to DICOM format so that they can be archived and retrieved in the PACS along with data type 1. We have developed a CAD-PACS integration toolkit (see the paper "CAD-PACS integration toolkit" in this special issue) that provides two integration methods (Fig. 2): DICOM-SC (secondary capture) and DICOM-IHE. The former converts the screen capture of CAD results, including images and textual results, to a DICOM image, while the latter converts images generated in CAD to DICOM images and CAD textual results to DICOM structured report (SR) data.

Generally, data security can be characterized by three major issues: privacy (or confidentiality), authenticity, and integrity [6]. Privacy seeks to protect medical data from being accessible or disclosed to unauthorized individuals. Authenticity verifies that the source of medical data is what it claims to be. Integrity assures that medical data is not altered, destroyed, or deleted by unauthorized personnel. In this paper, we focus on the integrity issue of DICOM CAD images and DICOM SR results, since traditional methods, such as encryption and access control by user password, are able to protect their privacy and authenticity. These methods are, however, not

effective for assuring their integrity.

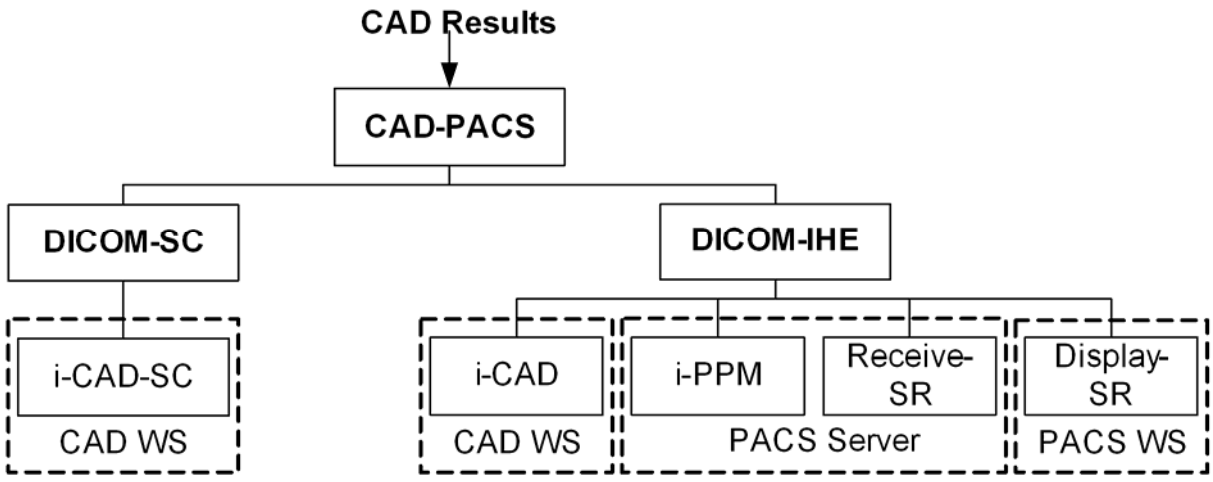

Fig. 2 The CAD-PACS toolkit has two versions, Left: DICOM-SC (Secondary Capture), and Right: DICOM-IHE. The major software package in DICOM-SC is the i-CAD-SC which resides in the CAD WS and uses the DICOM secondary capture function. The DICOM-IHE has four modules, i-CAD; and i-PPM (Post-Processing Manager), Receive-SR, and Display-SR. The former resides in the CAD WS, and the latter three reside in the PACS Server and PACS WS as shown, respectively.

We present a novel lossless digital signature embedding (LDSE) method that can automatically detect the alteration of even a single pixel in a DICOM image and can completely restore the original image data due to data embedding process. The DICOM image here can be images used in the CAD application or images generated in the CAD application, such as segmented images. A traditional digital signature method is used to assure the integrity of CAD textual results, which is a one-dimensional (1-D) data. Combining the LDSE method and the traditional digital signature method, we provide a complete solution for assuring the integrity of CAD data. The CAD-PACS toolkit is used as an example to illustrate the LDSE method, which is applicable to other CAD-PACS integration methods as well.

2. METHODS

2.1 Lossless Digital Signature Embedding (LDSE) Method

The LDSE method consists of two processes (Fig. 3) [7, 8]:

1) Sign & Embed Processes

a. Generate the DS of the image pixels with the image owner's private key

$$s = S_{k,\,priv}(I) \qquad (1)$$

where s is the digital signature (DS) of the image, S denotes the signature signing process[1], k,priv is the owner's private key, and I is the image.

b. Embed the bit stream of DS into the image pixels using lossless data embedding approaches

$$I^* = I \oplus s \qquad (2)$$

[1] Signature signing process begins by computing a hash value of all pixels of the image using cryptographic hash functions (e.g., SHA1) and follows by encrypting the hash value with public key encryption method.

where I^* is the signature embedded image, $\oplus$ denotes the lossless data embedding process, and s is the DS.

2) Extract & Verify processes

a. Extract the DS from the signature embedded image and recover the image from the embedding process

$$(s', I') = \Theta I^* \qquad (3)$$

where s' is the DS extracted from the signature embedded image, I' is the recovered image, Θ denotes the data extraction process, I^* is the signature embedded image.

b. Verify the extracted DS with the owner's public key

$$v = V_{k,\,pub}(I', s') \qquad (4)$$

where v is the verification result, V denotes the signature verification process[2], k,pub is the owner's public key, I' is the recovered image, and s' is the DS of I. If the verification result is true, which means the image has not been altered, the image integrity is assured. If the verification is false, the image has been altered.

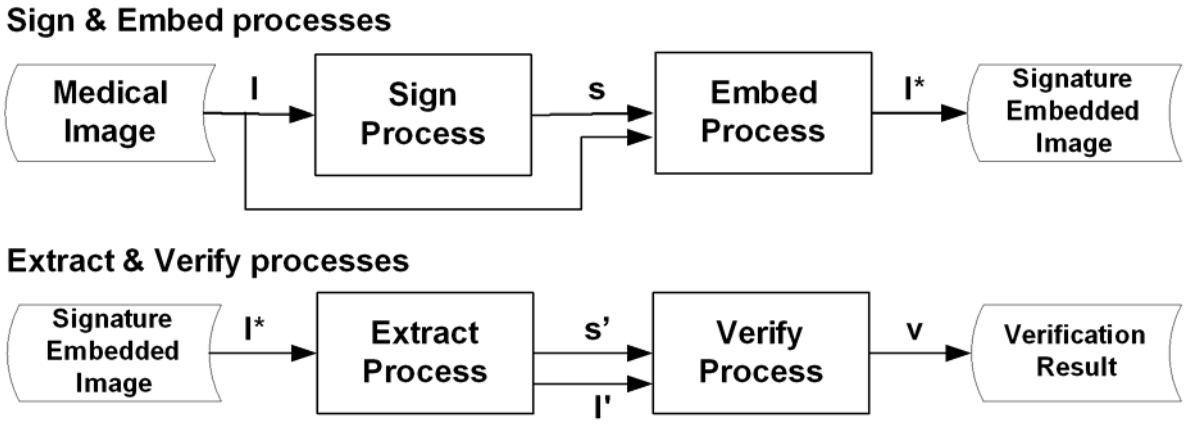

Fig. 3 Data flow of Sign & Embed, and Extract & Verify processes in the LDSE method. I: Original image, I*: Signature embedded image, I': Recovered image, s: Signature of the original image, s': Signature extracted from the signature embedded image, v: Verification result

A LDSE RS (regular/singular) method, have been developed based on a lossless data embedding approach, RS group approach [9, 10].

1) LDSE RS Algorithm Definition: Consider the original N x M medical image with pixel values in the set P = {0, …, 4095, or higher}. The algorithm starts by dividing the original image into disjoint groups of n adjacent horizontal pixels (p_1, …, p_n) (e.g., (p_1, …, p_4)), where p stands for the value of pixel and n is an integer greater than 1. A discrimination function 'f', defined in (5), computes the correlation coefficients of each pixel group G = (p_1, …, p_n). The function 'f' converts the vector G into a number f (G).

$$f(\mathrm{G}) = \sum_{1}^{n-1} | p_{i+1} - p_i | \qquad (5)$$

An invertible operation F on G called "flipping" is also defined. Flipping of a given bit in a pixel is defined as "0" → "1" or "1" → "0". The flipping would change the value of pixel and the value change would depend on the bit locations in the pixel (See more detail of the flipping operation

[2] Signature verification process begins by decrypting the DS to get the original hash value and then compares this hash value to a second hash value computed from the recovered image using the same hash function used in signing process.

in [7]). F has the property that $F(F(p)) = p$ for all p in G. Thus, there are three possibilities if $f(F(G))$ is compared with $f(G)$. These three possibilities are defined as three groups: R, S and U.

$$\text{Regular (R) group:} \quad \text{if } f(F(G)) > f(G)$$
$$\text{Singular (S) group:} \quad \text{if } f(F(G)) < f(G)$$
$$\text{Unusable (U) group:} \quad \text{if } f(F(G)) = f(G)$$

A new grouped image is formed with these three possible states in the selected bit plane.

2) *Embedding (Fig. 4):* the embedding starts with the scanning of image pixels of a CT lung image as an example to find R and S groups. The U groups are skipped during scanning. For n = 4, G = (p_1, …, p_4), our experimental results with the current medical images used in clinical practice show that $f(F(G)) > f(G)$ after the flipping operation F. This is because F makes G less correlated, where the adjacent pixels are usually correlated. The relationship of the four pixels in every found group can be converted to an "R" (R group) or "S" (S group) symbol. As a result, an "R" and "S" sequence of the image is formed. One bit is assigned to every "R" or "S" symbol in this sequence and the value in this bit would be "1" for "R" and "0" for "S". Thus, the "R" and "S" sequence is converted to a bit stream of 1s and 0s, which is called an "RS bit stream". The RS bit stream would have more 1s than 0s, because there are more "R" symbols than "S" symbols. The RS bit stream is then losslessly compressed using adaptive arithmetic coding. The extraction and compression progress ends when sufficient space in the RS bit stream is available for embedding the DS. Afterward, a two byte counter "C1" is added before the compressed bit stream to record the length of the compressed bits. Another two byte Counter "C2" is added before the DS to record the length of the DS. The bit stream of the Counter "C2" and the DS is then appended to the bit stream of the compressed bits to form a concatenated bit stream. This new bit stream is then compared with the RS bit stream bit by bit. If there is no difference in the bit value, no change is made. If there is a difference, the corresponding group of pixels (R or S group) is flipped. After all the bits are compared, the embedding process is complete and the result is a signature embedded image.

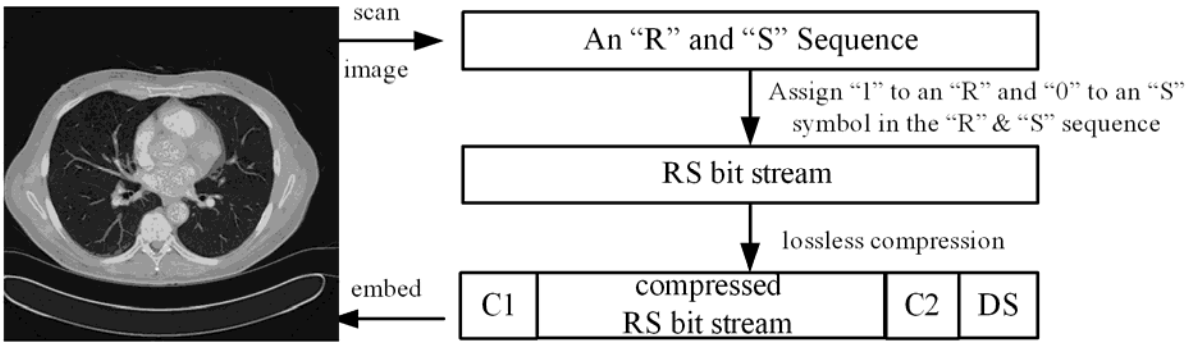

Fig. 4 Embed the DS in a CT lung image using LDSERS. The U groups are not used. C1: counter 1 to record the length of the compressed RS bit stream. C2: counter 2 to record the length of the DS

Since the forming of R and S groups as well as the embedding are all reversible processes, the original image can be completely recovered after the DS is extracted. The extracting process starts with the same scanning to find R and S groups from the signature embedded image. As a result, the embedded bit stream is reconstructed from the R and S groups. The bit stream is then broken down into the compressed RS bit stream and the DS. The compressed RS bit stream is decompressed to recover the original R and S groups. The original R and S groups are compared with the extracted groups and the corresponding group of pixels is flipped if there is any

difference. Since the flip operation is reversible, the original image pixels can be completely recovered. The recovered DS is verified with the restored image. If verification result is true, there is no alteration of the image and the image integrity is assured.

2.2 Traditional Digital Signature Method

The traditional digital signature method is based on DICOM 3.0-2006 Part 15 Structured Report (SR) RSA Digital Signature Profile [11]. A digital signature of the DICOM SR CAD textual result is appended to the DICOM SR file using an open source DICOM toolkit [12].

2.3 Integrate LDSE and DICOM SR RSA Digital Signature with CAD-PACS

The CAD-PACS toolkit is used to test the use of LDSE and DICOM SR RSA Digital Signature for assuring the integrity of images and results in CAD-PACS integration. The CAD-PACS toolkit includes two approaches, DICOM-SC and DICOM-IHE. The former converts the screen capture of CAD results, including images and textual results, to a DICOM image, while the latter converts images generated in CAD to DICOM images and CAD textual results to DICOM structured report (SR) data. The integration of LDSE with DICOM-SC is to assure the integrity of the DICOM image of the screen capture of the CAD result, while the integration of LDSE and traditional digital signature with DICOM-IHE is to assure the integrity of DICOM SR CAD textual result and DICOM CAD images.

Integrate LDSE with CAD-PACS DICOM-SC

Fig. 5 shows the integration of the LDSE method with the CAD-PACS DICOM-SC:

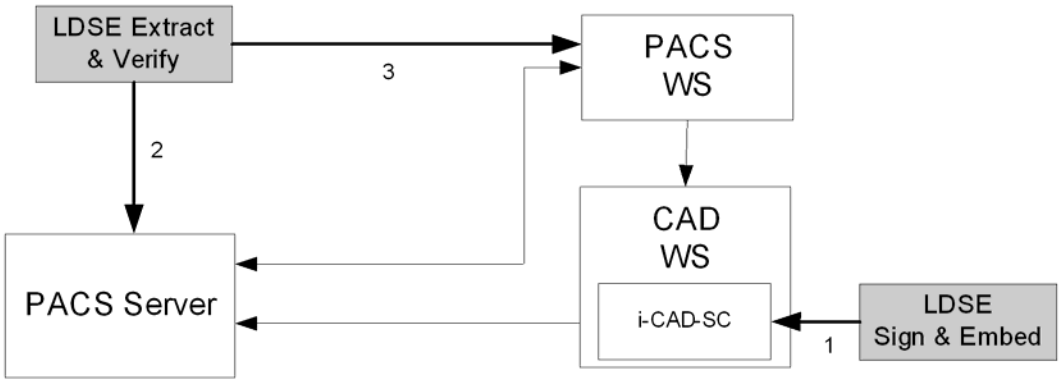

Fig. 5 Integrate the LDSE with the CAD-PACS DICOM-SC

1) The LDSE Sign & Embed component is added to the DICOM-SC i-CAD-SC software at the CAD workstation. The LDSE Sign & Embed component generates the digital signature of the DICOM SC CAD result image created by the i-CAD-SC software and embeds the digital signature in the image pixels. As a result, a signature embedded DICOM SC CAD result image is generated and sent to the PACS server.
2) The LDSE Extract & Verify component is added to the PACS server. The server extracts the digital signature from the signature embedded DICOM SC CAD result image and verifies the signature. If verify succeed, the CAD result image is archived. Otherwise, the CAD result image is rejected.
3) The LDSE Extract & Verify component is also added to the PACS viewing workstation.

When the signature embedded DICOM SC CAD result image is retrieved to the workstation for review, the signature is extracted and verified.
With the LDSE being integrated with the CAD workstation, the PACS server and the PACS viewing workstation, the integrity of the DICOM SC CAD result is completely assured within the PACS environment.

Integrate the LDSE and DICOM SR RSA Digital Signature with the CAD-PACS DICOM-IHE

Fig. 6 shows the integration of the LDSE and DICOM SR digital signature with the CAD-PACS DICOM-IHE:

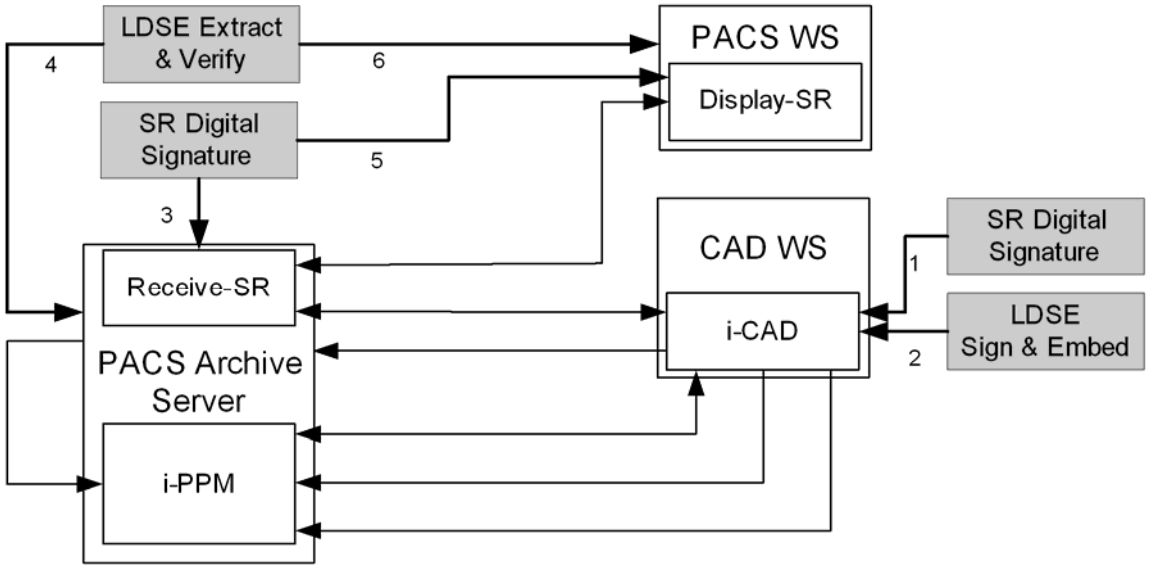

Fig. 6 Integrate the LDSE and the DICOM SR Digital Signature with the CAD-PACS DICOM-IHE

1) The DICOM SR digital signature software is added to the i-CAD software at the CAD workstation. The CAD textual result is converted to a DICOM SR, which is signed using the DICOM SR digital signature software. The signed DICOM SR CAD textual result is then sent to the PACS server for archive.
2) The LDSE Sign & Embed component is added to the i-CAD software at the CAD workstation. The segmented or annotated images are converted to DICOM SC images, which are processed by the LDSE Sign & Embed component to generate the signature embedded DICOM SC images. The signature embedded DICOM SC images are sent to the PACS server for archive.
3) The DICOM SR digital signature software is added to the Receive-SR component at the PACS server to verify the DICOM SR CAD textual result.
4) The LDSE Extract & Verify component is added to the PACS server to verify the signature embedded DICOM SC images.
5) The DICOM SR digital signature software is added to the Display-SR component at the PACS workstation to verify the DICOM SR CAD textual result received by the Display-SR.
6) The LDSE Extract & Verify component is added to the PACS workstation to verify the signature embedded DICOM SC images before they are reviewed.
With LDSE and the DICOM SR digital signature, the integrity of DICOM SR CAD textual results and DICOM SC CAD images is assured within the PACS environment. The integrity of original DICOM images used in the CAD application can also be assured by integrating the

LDSE method with the PACS [7].

3. RESULTS

Three CAD results from computer aided detection of small acute intracranial hemorrhage on CT of brain [15] and computer aided detection of emphysema [16] were used for evaluation of the LDSE method and the traditional digital signature technology.

3.1 Examples

Four examples are shown (Figures 7-10). Fig. 7(a) shows an example of the DICOM SC image file that contains a screen-captured chest emphysema CAD result with the digital signature embedded in the red color bit plane of the RGB pixels, while Fig. 7(b) shows an example of the subtracted image between the signature embedded image and the original DICOM SC image.
Fig. 8-10 depicts a set of results tested on the acute intracranial hemorrhage CAD. Fig. 8(a) shows of the original CT image with its digital signature embedded and Fig. 8(b) the subtracted image between the signature embedded CT image and the original CT image. Fig. 9(a) shows the DICOM SC annotated image with its signature embedded and Fig. 9(b) the subtracted images between the signature embedded DICOM SC image and the original DICOM SC image. Fig. 10(a) shows the DICOM SR of the acute intracranial hemorrhage CAD textual result with the digital signature appended to the DICOM SR file and Fig. 10(b) the information of the digital signature. The digital signature was appended to the end of the DICOM SR file based on the DICOM SR RSA Digital Signature Profile.
The signatures in all three signature embedded images (Fig. 7(a), Fig. 8(a) and Fig. 9(a)) have been extracted and verified successfully. The signature attached DICOM SR file has also been verified successfully.
These results demonstrate that the LDSE method combined with the DICOM SR RSA Digital Signature Profile are effective for assuring the integrity of the CAD results when the CAD is integrated with a PACS using the CAD-PACS integration toolkit.

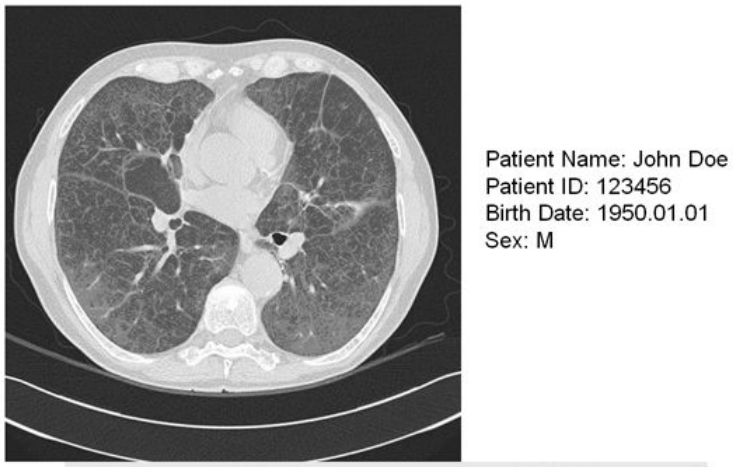

Lobes	Right Lung				Left Lung			
>	Score	%	Numerator	Denominator	Score	%	Numerator	Denominator
Upper	3	70%	248858	353459	3	72%	337178	466923
Middle	3	69%	65349	95113	NA	NA	NA	NA
Lower	3	57%	246033	433360	2	48%	168680	351562

(a)

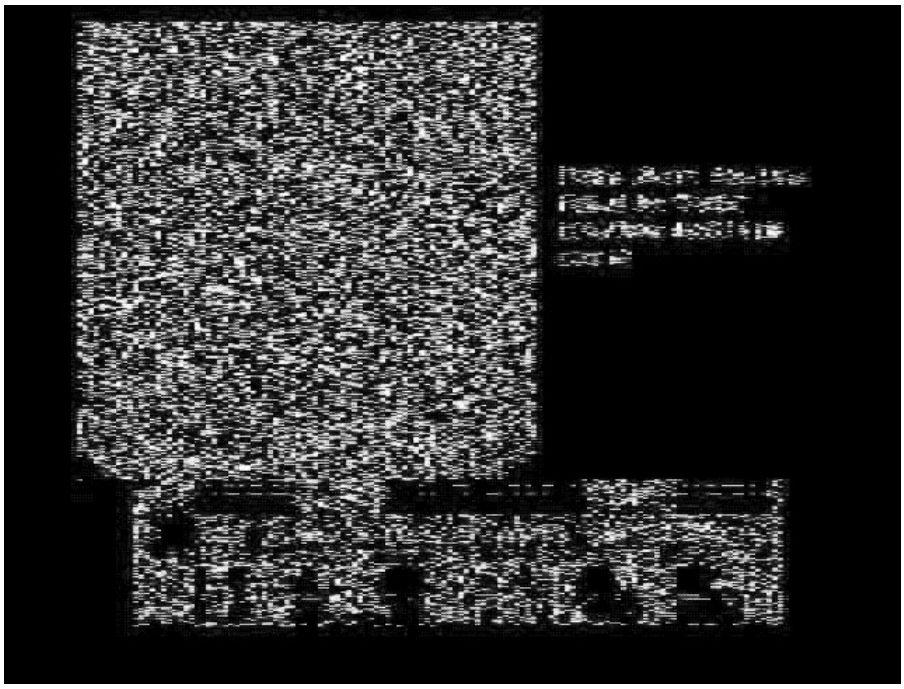

(b)

Fig. 7 An example of the DICOM SC CAD result image with signature embedded. (a) the DICOM SC image file that contains a screen-captured chest emphysema CAD result with the digital signature embedded, (b) the subtracted image between the signature embedded image and the original DICOM SC image. The white dots show the bits of the embedded digital signature

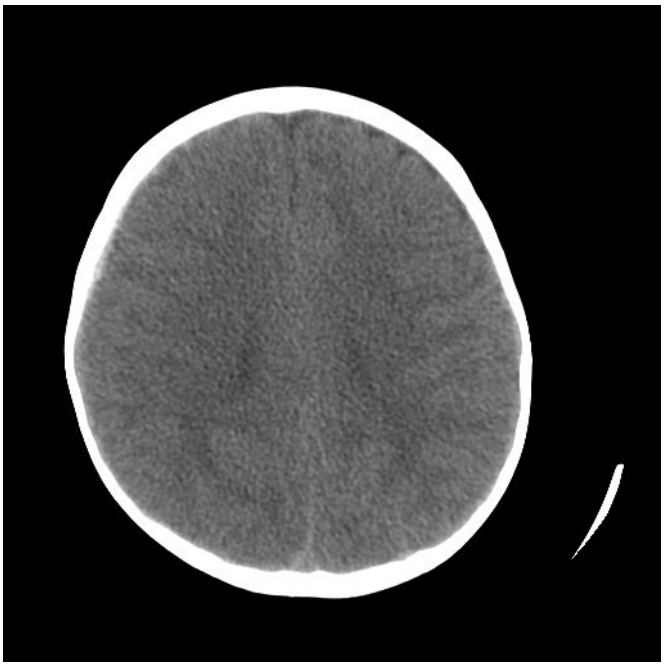

(a)

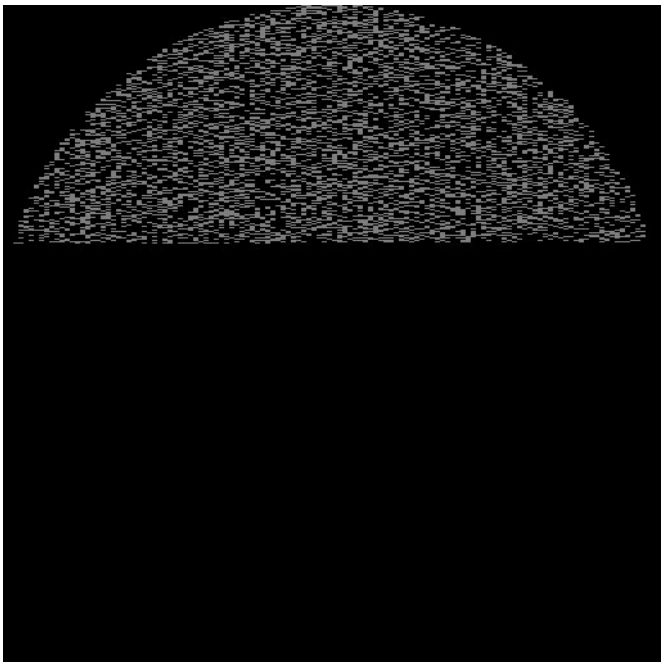

(b)

Fig. 8 An example of the DICOM CT image used in the CAD application with signature embedded. (a) the original CT image used in the acute intracranial hemorrhage CAD with its digital signature embedded, (b) the subtracted image between the signature embedded CT image and the original CT image. The white dots show the bits of the embedded digital signature

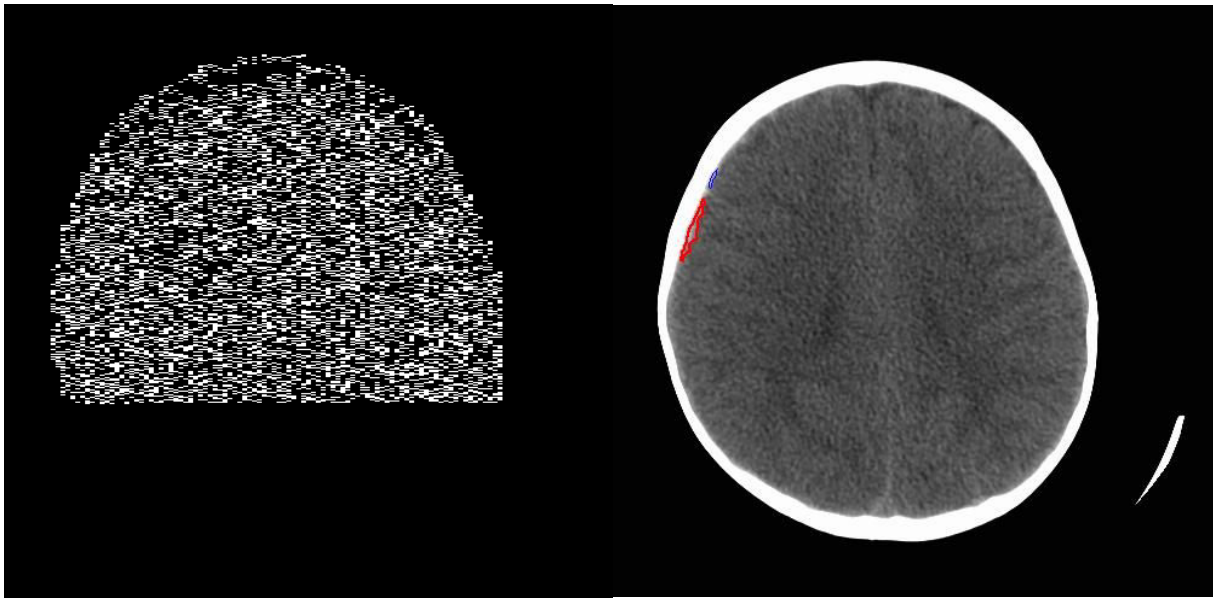

(a) **(b)**

Fig. 9 An example of the DICOM SC CAD image with signature embedded. (a) the DICOM SC CAD annotated image with its signature embedded, (b) the subtracted images between the signature embedded DICOM SC image and the original DICOM SC image. The white dots show the bits of the embedded digital signature

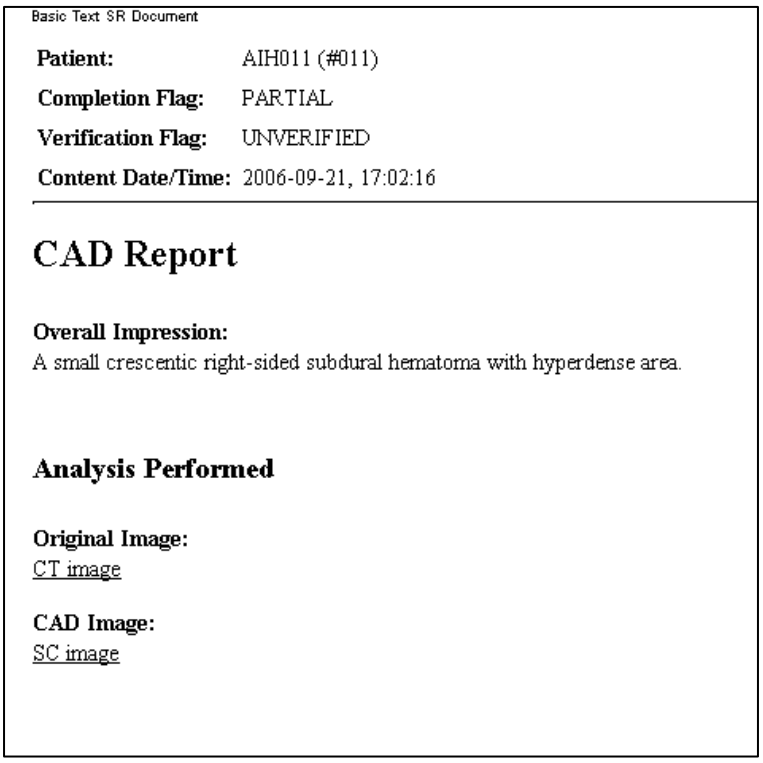

(a)

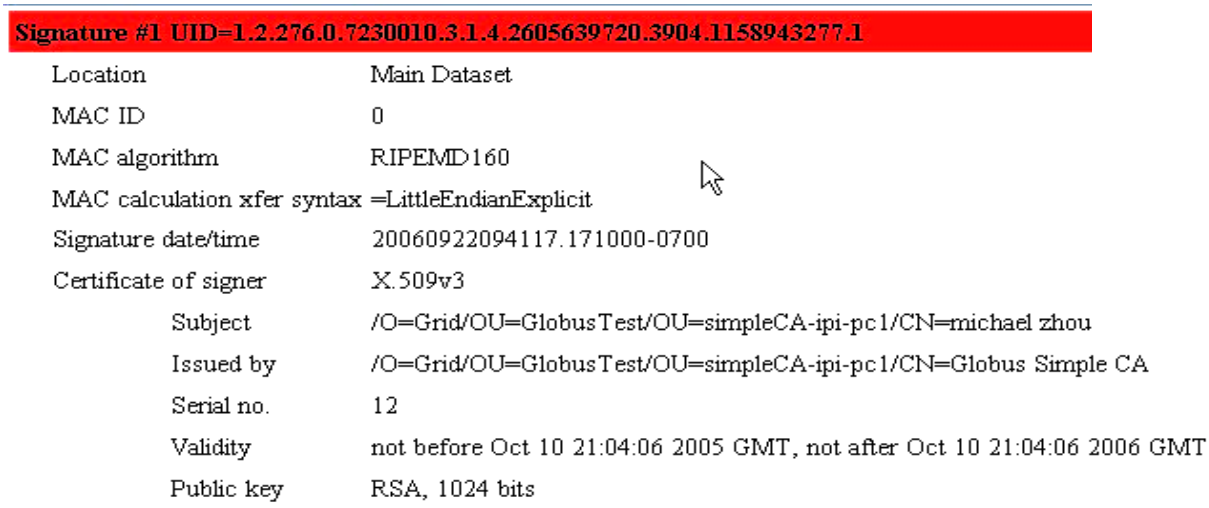

(b)

Fig. 10 An example of the DICOM SR CAD textual result signed by the DICOM SR digital signature profile. (a) DICOM SR CAD textual result, (b) the digital signature appended to the DICOM SR textual result

4. DISCUSSION

The aforementioned LDSE method can effectively assure the integrity of a 2-D DICOM image, including the modality generated original image and the CAD generated image converted to a DICOM file. However, a new challenge arises in three dimensional (3-D) CAD results. For example, a 3-D tumor volume is segmented from a 3-D CT lung study. Intuitive thoughts are to

apply the 2-D LDSE method to each slide of the 3-D tumor segmented images. But this is not time-efficient, because the same LDSE process, which requires about 0.06 seconds for one CT image, will be repeated 30 or 40 times for the tumor volume. The total process time will cause a significant delay in clinical diagnostic workflow. An even more crucial problem is that the 2-D LDSE method is not able to detect any deletion or loss of images in the 3-D tumor volume. The same problems can happen to the original 3-D CT lung study used for the CAD application.
We have developed a novel 3-D LDSE method [7] for assuring the 3D volume image integrity. This method has demonstrated to be applicable and more efficient than the 2-D LDSE method for 3-D volume image integrity.

5. SUMMARY

A 2-D LDSE method has been developed for assuring the integrity of CAD images and results when the CAD software is integrated with a PACS. Our experimental results demonstrated that the LDSE method is effective for assuring CAD image integrity. Combining the LDSE method together with the DICOM SR RSA digital signature method, we have provided a complete integrity assurance solution for CAD images and textual results.

References

[1] L.W. Burhenne, et al., Potential contribution of computer-aided detection to the sensitivity of screening mammography, Radiology 215 (2000) 554 – 562.
[2] J.A. Baker, et al., Computer aided detection (CAD) in screening mammography: sensitivity of commercial system in detecting architecture distortion, AJR 181 (2003) 1083-1088.
[3] H.P. Chan, et al., Image feature analysis and computer-aided diagnosis in digital radiography: 1. Automated detection of microcalcifications in mammography, Med. Phys. 14 (1987) 538-548.
[4] M.T. Freedman, et al., A computer aid for radiologists: improved detection of small volume lung cancer on chest radiographs, RSNA (2003) 523.
[5] S.A. Wood, et al., CAD of actionable lung nodules on multislice CT scans of the lung: sensitivity and false positive marker rates, RSNA (2002) 477.
[6] Information processing systems, Open systems Interconnection, Basic Reference Model-Part 2: Security Architecture, ISO 7498-2, 1989.
[7] Z. Zhou, Lossless digital signature embedding for medical image integrity assurance, Ph.D. dissertation, Univ. of Southern California, Los Angeles, CA, 2005.
[8] Z. Zhou, H.K. Huang, B.J. Liu, Digital signature embedding for medical image integrity in a data grid off-site backup archive, Proc. SPIE Medical Imaging, vol. 6, pp. 306-317, 2005.
[9] J. Fridrich, M. Goljan, and R. Du, Lossless Data Embedding For All Image Formats, in Proc. SPIE Photonics West, Electronic Imaging, vol. 4675, pp. 572–583, 2002.
[10] J. Fridrich, M. Goljan, and R. Du, Lossless Data Embedding – New Paradigm in Digital Watermarking, EURASIP J. Appl. Sig. Proc., vol. 2002, no. 2, pp. 185–196, 2002.
[11] DICOM Security Profiles, DICOM Standard, 2006, http://medical.nema.org/dicom/2006/06_15pu.pdf, accessed on Oct. 2, 2006.
[12] DCMTK, http://dicom.offis.de/dcmtk.php.en, accessed on Sept. 4, 2006
[13] E. Pietka, A. Gertych, S. Pospiech, F. Cao, H.K. Huang, V. Gilsanz, Computer Assisted Bone Age Assessment: Image Processing and Epiphyseal/Metaphyseal ROI Extraction, IEEE Trans. Medical Imaging, 20, 715-729, 2001.

[14] E. Pietaka, S. Pospiech, A. Gertych, F. Cao, H.K. Huang, V. Gilsanz, Computer Automated Approach to the Extraction of Epiphyseal Regions in Hand Radiographs, Journal of Digital Imaging, 14, 165-172, 2002.
[15] T. Chan, H.K. Huang, Computer Aided Diagnosis of Acute Intracranial Hemorrhage on CT, RSNA Annual Meeting InfoRAD Exhibits, 2006.
[16] K.L. Boedeker, M.F. McNitt-Gray, S.R. Rogers, D.A. Truong, M.S. Brown, D.W. Gjertson, J.G. Goldin, Emphysema: Effect of Reconstruction Algorithm on CT Imaging Measures, Radiology, 232, 295-301, 2004.

Pattern Anal Applic
DOI 10.1007/s10044-006-0056-4

THEORETICAL ADVANCES

AUTHOR PROOF

Segmentation of regions of interest and post-segmentation edge location improvement in computer-aided bone age assessment

Arkadiusz Gertych · Ewa Piętka · Brent J. Liu

Received: 28 November 2005 / Accepted: 18 September 2006

1 Introduction

Image segmentation is a procedure often performed in computer-aided diagnosis related to radiological images. Usually the procedure comes first in image analysis or is preceded by a noise reduction operation. In addition, it can be performed over the entire image, or only on a selected region of interest. In the current study two segmentation methods have been implemented sequentially in the computer-aided assessment of skeletal maturity. Bone age assessment (BAA) is a procedure frequently performed in pediatric radiology [1, 2]. Its goal is to determine the state of skeletal maturity of a patient based on detailed analysis of hand X-ray regions of interest (ROIs) (Fig. 1). Nowadays a hand radiograph of a subject is manually compared with radiological patterns. The best match yields an assessment of the bone age.

The computerized approach to BAA relies on a detailed analysis of the regions of interest of a hand (Fig. 1). The distal regions are of particular interest [3, 4]. The goal is to segment the epi-metaphyseal regions to quantitatively describe the maturation process in terms of features that are sensitive to the stage of skeletal development. Such approach allows performing the computerized bone age assessment (CBAA), however, automatic measurements require that well-defined boundaries of anatomical structures are present in the region of interest [3, 5]. To find these boundaries, the Gibbs procedure using Gibbs random fields (GRF) has been used.

In order to improve our computerized approach to the BAA, an additional segmentation stage has been employed. The GRF segmentation has been followed by a procedure based on the active contours technique. Both segmentation procedures are performed over the automatically selected [4, 5] epiphyseal regions of interest (Fig. 2). The filtration stage reduces the noise and nonuniformity of bony and soft tissue structures caused by the presence of natural tissue texture and scattered radiation.

To reduce the influence of noise, a star-shaped median filter and Lee filter are used [6]. Estimation of remaining noise and image contrast calculation routines are applied in order to keep our approach to the hand radiograph analysis fully automated. Next, the ROI is subjected to the segmentation procedure. Adaptive multigrid hierarchical GRF technique originally developed by Pappas [7] as a multi-purpose application is used. This algorithm is briefly explained in the next section. Some of the segmented contours do not reflect the correct location of a boundary between soft tissue and cartilage. Therefore, according to our proposition, the existing methodology should be improved by introducing the active contours model. In our case an initial contour i.e. the snake is provided by the previous step of image processing and does not require user interaction. Active contour parameters for

A. Gertych (✉) · B. J. Liu
Department of Radiology,
Image Processing and Informatics Laboratory,
University of Southern California, Suite 601, 4676
Admiralty Way, Marina del Rey, Los Angeles
CA 90292, USA
e-mail: gertych@usc.edu

E. Piętka
Institute of Electronics,
Department of Biomedical Engineering,
Silesian University of Technology,
Akademicka 16, 44-100 Gliwice, Poland

Journal : 10044 Dispatch : 16-11-2006 Pages : 9
Article No. : 56 LE TYPESET
MS Code : 56 CP DISK

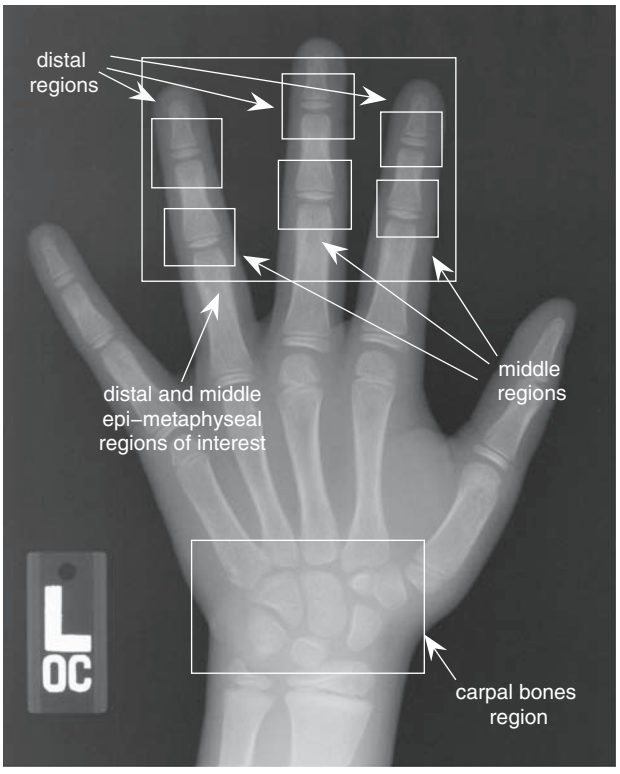

Fig. 1 Typical radiograph of the left hand with superimposed regions of interest

clinical images were adjusted based on testing of snakes over the region of interest model. As clinical data, 200 distal ROIs of a control group reflecting different stages of development ranging from 2 to 12 years of age have been randomly selected from the large-scale database of 1,100 images. These regions served as a test set for the combined methodology.

2 Adaptive image segmentation

In order to separate the image pixels into two or three clusters (bony tissue, soft tissues, or cartilage), we use the adaptive multigrid hierarchical implementation as a segmentation algorithm [7]. First, the bony structure and soft tissue are segmented, then, if necessary, the region of an additional, third type is distinguished.

Following [7], let $\boldsymbol{y}$ be an observable (filtered) image with its intensity (gray level) y_t at locations $t = \{i, g\}$, $i = (1...N_{\text{row}})$, $j = (1...N_{\text{col}})$ over an image region T of $N_{\text{row}} \times N_{\text{col}}$ Each pixel t can receive one label denoted by x_t so that $x_t = \{1,...,c\}$, where c is the number of classes. The segmentation process of the input image is described as $\mathbf{x} = (x_{11}, \ldots, x_{N_{\text{row}}N_{\text{col}}})$, where $x_t = k$, means that a pixel at site t belongs to a region type (class) k. This segmentation method, like many others of this type, provides an estimate $\hat{x}$ of the true (however, unknown) labeled scene $\boldsymbol{x}^*$, which is found based on the maximum probability given observations $\boldsymbol{y}$. Accordingly to the Bayes' theorem, estimate $\hat{x}$ maximizes the posterior probability:

$$p(\boldsymbol{x}|\boldsymbol{y}) \propto p(\boldsymbol{y}|\boldsymbol{x})p(\boldsymbol{x}) \tag{1}$$

where $p(\boldsymbol{x})$ is the prior density of the region process, and $p(\boldsymbol{y}|\boldsymbol{x})$ is the class conditional density of the observed image y given the distribution of regions. First factor in the right-hand side of (1) constrains the intensity of the region to be close to the data, the second factor imposes spatial continuity. The region process is modeled with the Markov Random Field (MRF) property:

$$p(x_t|x_q, \text{for all } q \neq t) = p(x_t|x_q, q \in N_t) \tag{2}$$

where N_t -neighborhoods of pixel t. The density of $\boldsymbol{x}$ treated as Gibbs distributions can be written as follows:

$$p(\boldsymbol{x}) = \frac{1}{Z}\exp\left(-\sum_{c \in C} V_c(\boldsymbol{x})\right) \tag{3}$$

where Z is the partition function and C is a set of all cliques. In MRF theory, a clique is a set of points that are neighbors in relation to each other. We use only single- and two-point cliques (Fig. 3), which correspond to a second order neighborhood.

Larger neighborhoods can be taken; however, this significantly elongates the computation process. The one- and two-point clique potentials are modeled by

$$V_c = \lambda(x_t), \text{ if } x_t = k \text{ and } t \in C, \forall k \tag{4}$$

and

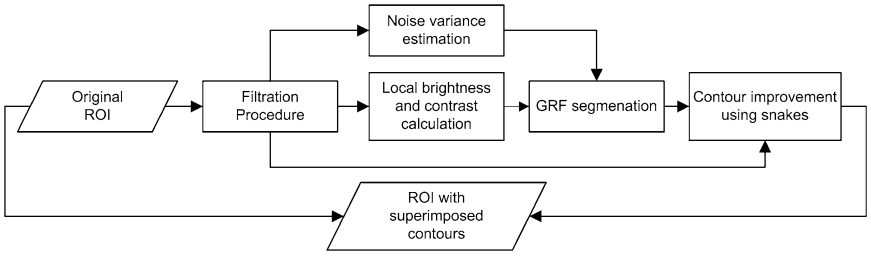

Fig. 2 The flowchart of epiphyseal ROI processing

Journal : 10044 Dispatch : 16-11-2006 Pages : 9
Article No. : 56 LE TYPESET
MS Code : 56 CP DISK

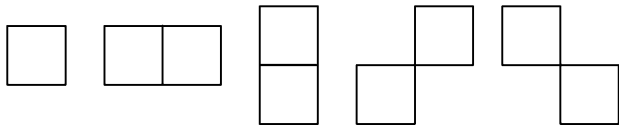

Fig. 3 Cliques in Gibbs random field model

$$V_c = \begin{cases} -\chi, & x_t = x_q \quad t,q \in C \\ +\chi, & x_t \neq x_q \quad t,q \in C \end{cases}, \tag{5}$$

respectively.

We set a parameter $\lambda(x_t) = 0,\ \forall x_t \in \{1,\ldots,c\}$, which reflects a priori knowledge of the relative likelihood of the region types and makes all regions equally likely. The $\chi = 10^K$–0.5 is kept constant and positive in order to impose spatial connectivity of a segmentation field for all iterations and for any region type. In this approach, its value depends on the global contrast $K = \hat{\mu}_{\text{bony}} - \hat{\mu}_{\text{soft}}/\hat{\mu}_{\text{bony}} + \hat{\mu}_{\text{soft}}$ related to mean values of gray levels for bony and soft tissue after the k-means clustering [14]. Due to fluctuations in tissue structures, density and radiation exposure, the contrast in ROI depends also on the patient age. Typically, in hand regions the contrast value does not exceed 0.6, which implies $\chi = \langle 0.5, 3.48\rangle$ The effect of increasing the value of χ is proportional to increasing of region boundary smoothness [7].

The conditional densities of each class are defined as follows: each image region is regarded as a slowly varying intensity functions with mean $\hat{\mu}_t(x_t)$ plus white Gaussian noise with variance $\sigma^2{}_n$. In contrast to [7], in which the noise variance is assumed to be known, we calculate the image noise estimate $\sigma^2{}_n$ directly from the ROI (Fig. 2) [8]. Thus:

$$p(\boldsymbol{y}|\boldsymbol{x}) \propto \exp\left\{-\frac{1}{2\sigma_n^2}\sum_t [y_t - \mu_t(x_t)]^2 - \sum_C V_C(x)\right\}. \tag{6}$$

Following the Markovian property (2) the combined probability (6) has the form:

$$\begin{aligned} &p(x_t|y, x_q \text{ for all } q \neq t) = \\ &p(x_t|y_t, x_q, q \in N_t) \\ &\quad \propto \exp\left\{-\frac{1}{2\sigma_n^2}\sum_t [y_t - \mu_t(x_t)]^2 - \sum_{x_t \in C} V_C(x)\right\} \end{aligned} \tag{7}$$

where σ_n^2 noise variance, t considered pixel, q clique pixel, μ_t value of intensity function for each class, x_t class number, y_t considered pixel gray level value, N_t neighborhoods of pixel t, V_C clique potential in Gibbs model.

Thus, the segmentation $\hat{\boldsymbol{x}}$ of an image $\boldsymbol{y}$ can be done by a maximization of (7) at each point t given the data y, and the current $\hat{\mu}_t(x_t)$. This approach of maximization of (6) is the well-known iterated conditional modes method (ICM) proposed by Besag [9]:

$$\hat{x}_t = \arg\max_{x_t \in \{1,c\}} \left\{ \exp\left[-\frac{1}{2\sigma_n^2}[y_t - \hat{\mu}_t(x_t)]^2 - \sum_{x_t \in C} V_C(x)\right]\right\}, \quad \forall t \in T \tag{8}$$

ICM method requires an initial estimate of $\hat{x}$. This can be found by the k-means clustering algorithm [14]. Given the initial labels of regions, the intensity functions $\hat{\mu}_t(x_t)$, which are mean values of gray levels of pixels belonging to the same class k lying within the window W centered at pixel t, are estimated. Based on the estimations of intensity functions and maximizing the conditional probability density at each point x_t according to (7), the current estimate $\hat{x}$ of a pixel's membership to one of the classes is updated (8). Thus, each iteration consists of one update of $\hat{x}$ and one update of intensity functions $\hat{\mu}_t(x_t)$. During one cycle the window size W is fixed. Then, the whole procedure is repeated with a new window size, which is a half of the previous one, until its size of (7×7) is reached. Initially, the window size is equal to the image size and thus, the intensity functions of each region are uniform. The estimation of $\hat{x}$ is assumed to converge if the number of pixels that change during a cycle is less than a threshold, typically M/10 for $N_r \times N_c$ image, where M is the smallest image dimension, $M = \min(N_r, N_c)$. A more detailed description of this segmentation algorithm can be found in [7].

The segmentation procedure yields a gray level image in which the soft tissue appears as black objects, the bony structure appears as white objects and cartilages are gray objects. The latter two areas are combined and represented by white color whereas other areas (background and soft tissue) are represented by black color. The contours of extracted structures are continuous and reflect the locations of well-outlined image details; however, in some cases when local contrast between soft tissue and cartilage is considerably low the location of structures is not accurate. Hence, our objective is to use the active contours approach to attract the borders to the locations of relatively higher gradient value or smooth them when neither edges nor lines are found in the neighborhood of contour pixels.

3 Boundary correction by active contour approach

Deformable or active contour models called "snakes" [12] as introduced by Kass et al. [10] are a special case of

Journal : 10044 Dispatch : 16-11-2006 Pages : 9
Article No. : 56 LE TYPESET
MS Code : 56 CP DISK

multidimensional deformable model theory developed by Terzopoulos [11]. Snakes are often used to determine the boundary of objects in images based on an assumption that borders are piecewise continuous or smooth. The location and movement of contour pixels depend on the values of snake energy functional which is a linear combination of two terms: the internal energy which ensures smoothness of the contour fragment and the external energy which pulls the snake toward the boundary. The total energy is written as [10]:

$$E^*_{\text{snake}} = \int_0^1 E_{\text{snake}}(\boldsymbol{v}(s))\mathrm{d}s = \int_0^1 E_{\text{int}}(\mathbf{v}(s)) + E_{\text{image}}(\mathbf{v}(s))\mathrm{d}s \tag{9}$$

where E_{int} the internal energy, E_{image} the external (image) energy.

The contour is represented by the vector $\mathbf{v}(s) = (i(s), j(s))$, having the arc length s as a parameter. The internal energy is defined as:

$$E_{\text{int}} = \frac{1}{2}\left(\alpha(s)\left|\frac{\partial}{\partial s}\boldsymbol{v}(s)\right|^2 + \beta(s)\left|\frac{\partial^2}{\partial s^2}\boldsymbol{v}(s)\right|^2\right) \tag{10}$$

where • $\alpha(s)$, $\beta(s)$ are weighting parameters that control the tension and bending, respectively. The external energy term [10] consists of the following functionals:

$$E_{\text{image}} = w_{\text{line}}E_{\text{line}} + w_{\text{edge}}E_{\text{edge}} + w_{\text{term}}E_{\text{term}} \tag{11}$$

where $E_{\text{line}} = y_{ij}$ is the line energy represented by the image intensity. For positive value of w_{line} the snake will be attracted to light lines, for the edge energy expressed as $E_{\text{edge}} = -\left|\nabla y_{ij}\right|^2$ the snake will be attracted to contour with large image gradients. The energy functional E_{term} is responsible for attracting the snake to corners and line ends in the image. In the present application the line ends are not of interest because the snakes are closed, but the sensitivity of the snake to corners should be taken into account. In this study disc-shape epiphyses at certain stage of development have corners, so placing snake points around and inside the corner is a desirable feature. Ends of line segments and corners can be found using an energy term based on the curvature of lines in an image I_{ij} which represents the image y_{ij} smoothed with a Gaussian filter with the parameter $\sigma = 1$ describing Gaussian filter mask values [12]. Let us denote the vertical and horizontal components of the gradient image as G_i and G_j, respectively. If G_{ij} is the image gradient of the smoothed image I_{ij}, then the gradient direction is defined by $\theta = \tan^{-1}(G_j/G_i)$. The unit vectors along and perpendicular to the image gradient G_{ij} are given by $\mathbf{n} = (\cos\theta,\ \sin\theta)$ and $\mathbf{n}_\perp = (-\sin\theta,\ \cos\theta)$, respectively. E_{term} is the terminal energy functional expressed as $E_{\text{term}} = \frac{\partial\theta}{\partial\mathbf{n}_\perp}$. By expanding derivatives $E_{\text{term}} = \frac{\partial^2 I/\partial\mathbf{n}^2{}_\perp}{\partial I/\partial\mathbf{n}}$ become $E_{\text{term}} = \frac{G_{j,j}G_i^2 - 2G_{i,j}G_iG_j + G_{i,i}G_j^2}{\left(G_i^2+G_j^2\right)^{3/2}}$, where for example $G_{j\,j}$ is the derivative of the gradient component G_j with respect to the coordinate j. It is then a component of the second derivative of the smoothed image I_{ij}. In (11) parameters: w_{line}, w_{edge}, w_{term}, are weights in the E_{image} term.

Internal (elasticity) forces (10) of the snake are responsible for keeping pixels of the curve close and preventing the contour from bending too much. They force the contour to be smooth and continuous. Weights • $\alpha(s)$, $\beta(s)$, control the abilities of snake to bend. If $\beta(s)$ is locally set to zero then the second-order discontinuity appears and the snake forms a local corner. The image forces (11) move the snake to a location of image features such as edges, lines or terminations of subjective contours.

In many approaches snakes require a proper initialization of the contour. An incorrect initialization may direct the contour towards an unwanted direction, or may tend to shrink it to a single point, if the image forces are not strong enough. The target contour is found by minimizing the discrete formulation of the snake energy functional [10]:

$$E^*_{\text{snake}} = \sum_{m=0}^{N-1} E_{\text{snake}}(\boldsymbol{v}_m) = \sum_{m=0}^{N-1}\left(E_{\text{int}}(\boldsymbol{v}_m) + E_{image}(\boldsymbol{v}_m)\right) \tag{12}$$

where N is the number of contour pixels. $\mathbf{v}_N = \mathbf{v}_0$ means that the contour is represented by a closed curve.

In the current study the minimization of the energy functional (Scheme 1) has been performed by the Williams and Shah (greedy) algorithm (fourth method from Table 1 in [13]):

The input image contains initial contour $p_1,\ldots,p_N$ (N is the number of contour pixels) located in the vicinity of the desired target contour.

Step-1. Search in MxM neighborhood of each pixel p_m ($m = 1,\ldots,N$) for a location that minimizes the energy functional. Move the pixel p_m towards this location.
Step-2. Estimate the curvature of the snake at each pixel p_m and look for local maxima that exceed the user-defined threshold. If any such maximum is found turn β_m to 0.
Step-3. Update the value of contour energy.

Repeat steps 1-3 until the number of iteration is exceeded or the energy E^*_{snake} does not change significantly.

Scheme 1 Scheme of the greedy algorithm [13]

Journal : 10044 Dispatch : 16-11-2006 Pages : 9
Article No. : 56 LE TYPESET
MS Code : 56 CP DISK

A normalization of every E^*_{snake} functional is required for a proper minimization of the overall snake energy. For E_{int} all components at location p_{m} are divided by a largest value found in their neighborhood of size $M \times M$. Similarly, for E_{line}, E_{edge}, E_{term} functionals of E_{image}, their local values are normalized using the expression: $\frac{E_{\text{image}(ij)} - \min(E_{\text{image}(M\times M)})}{\max(E_{\text{image}(M\times M)}) - \min(E_{\text{image}(M\times M)})}$, where $E_{\text{image}(ij)}$ is the current E_{image} component, and $E_{\text{image}(M\times M)}$ is the appropriate energy value in the neighborhood of size $M \times M$, respectively. The M is set to 3 in our study.

Before minimizing the E^*_{snake}, the input image is subjected to the filtration procedure to blur the existing edges and to enhance the gradient field. In this case, we take advantage of the preprocessing step performed before the GRF segmentation (Fig. 2). In order to calculate the E_{edge} energy of (11) a Sobel gradient operator with a 7×7 mask is implemented.

In order to implement the active contour technique to the bone age assessment process flow [5], the already located epiphysis is subjected to a detailed analysis. Usually the upper edge does not require any improvement. Yet, the presence of cartilage or bone concavities requires the edge correction of the lower epiphyseal edge. Thus, before an active contour is initialized, the lower epiphyseal region is extracted and expanded outwards by a dilation procedure using structuring element of size 5×5. The location of the lower part is found based on measurements of an epiphysis perpendicularly to an axis of ROI. This generally protects the active contour from being attracted towards stronger edges of the bony structure that were already located by the primary segmentation. Then, the initial snake pixels are evenly placed around the expanded contour.

4 Experimental results

Two types of image data have been subjected to the procedure. First, a synthetic image analysis has been performed. The synthetic image (Fig. 4) serves as a model of the epiphyseal region of interest. Three areas consisting of pixels with three different, evenly distributed gray levels: 800, 500 and 200, simulate the anatomical structures of bones, cartilage and soft tissue, respectively. To imitate the influence of the modulation transfer function the image is smoothed with a 5×5 mask Gaussian filter. In order to test the influence of various noise levels a Gaussian noise with standard deviation ranging from 20° to 70 have been added to the synthetic image after smoothing. It reflects a normally distributed random noise present in hand radiographs [15]. Blurred and noisy images are shown in Fig. 4.

The experiment has been initialized by corrupting the model of image with noise whose standard deviation σ has been set to 30. Usually the noise standard deviation in our data collection does not exceed 20 [15]. However, beyond the level of 30 the adaptive GRF segmentation starts yielding inadequate results. Then, the coefficients of the energy term have been adjusted experimentally to obtain the best boundary location. Weights adjustment process was conducted as follows: initially α and β were set to 0.5, and the remaining factors to 0.3. Next, for noise standard deviation $\sigma = 30$ added to the image, the parameters α and β were changed gradually to obtain a desired shape of the snake around the epiphyseal model. Because of random noise generation process, every weight adjustment step was conducted at least five times to obtain satisfactory and stable results. For σ higher than 30, α and β parameters were already kept constant. Influence of other weights depends more on image content than on shape of the targeted object, hence w_{edge}, w_{term}, w_{line} were changed gradually too for every new value of σ. In this way the following parameters have been finally chosen: $\alpha = 0.3$, $\beta = 0.6$, $w_{\text{edge}} = 0.18$, $w_{\text{term}} = 1$, $w_{\text{line}} = 0.05$.

Next, synthetic images with different noise level have been subjected to the GRF segmentation and active contours technique. For each noise standard deviation value, the segmentation procedure has been performed ten times to evaluate how random noise

Table 1 Number of cases with correctly located boundaries by GRF and active contour techniques

Method of contour location	Standard deviation of noise added to the synthetic image						
	10	20	30	40	50	60	70
GRF	10	7	5	3	2	0	0
GRF + snake	10	10	10	10	10	10	9

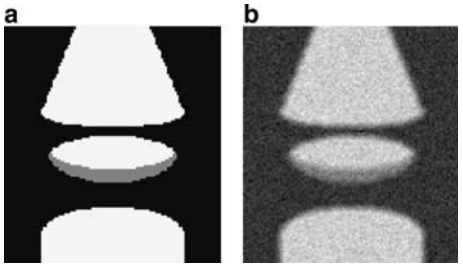

Fig. 4 Synthetic ROI image model: **a** the noise-free image model, **b** blurred and noisy image model

Springer

Journal : 10044 Dispatch : 16-11-2006 Pages : 9
Article No. : 56 LE TYPESET
MS Code : 56 CP DISK

distribution affects the accuracy of segmentation. Table 1 shows the results of the location of boundaries of the synthetic image for both GRF segmentation and GRF segmentation followed by active contours technique. A boundary after segmentation was classified as correct if all boundary pixels were located within a one-pixel range from the original boundary model. Each value in Table 1 shows the number of cases with correctly located boundaries around the epiphyseal model.

One can note that when the image noise exceeds a certain level, the adaptive GRF segmentation procedure fails and results in an incorrect outline of the cartilage tissue (Fig. 5). Two superimposed edges extracted by the GRF segmentation (black contour), combined method (white contour) and a profile line crossing the region model are shown in Fig. 5a. Gray levels of the pr1 along the profile line in a non-blurred image reflect the quantitative analysis of the difference in performing the epiphyseal segmentation by both methods (Fig. 5b). A line denoted as pr2 depicts gray level values along profile line traced through a noisy image model. The difference between lines pr3 and pr4 indicates the improvement of the segmentation achieved by implementing the active contour stage. Gray levels represented by lines pr3 and pr4 in Fig. 5b correspond to the classes to which the image pixels are assigned—bone tissue and other tissues, respectively.

The collection consisting of 1,100 cases, used in the validation of the described method, contained hand images of normally developed individuals of four races: African–American, Caucasian, Asian and Hispanic, boys and girls. This collection contains about five images per one age group for chronological age between 1 and 9 years, and about ten images per age group for 10–18 year old subjects. It approximately yields 135 cases per sex within each race.

According to [1] it can be observed that a fusion between epiphyses and metapyses in distal ROIs starts around 11 years of age (yoa) in girls and around 12 yoa in boys, respectively. Cases over 11–12 years, when epiphyses and metaphyses had already begun to fuse, were detected by the CBAA software and subjected to different type of analysis [5]. Hand images of individuals younger than 2 years were not performed by the CBAA due to its imperfections in this age range and lower quality of radiographs [4].

Distal ROIs were automatically extracted from entire collection and 200 of them were randomly selected from those radiographs of individuals older than two and younger than 12 years.

Four examples are shown in Fig. 6. Gray lines reflect the boundary found by the GRF algorithm. Contours enhanced by the snake technique are shown by the light lines.

An observable improvement in the contour location has been noticed in 62% of the processed images (Fig. 6a–f, h–l). Due to the lack of cartilage in 34.5% of cases, no difference in contour has been found. In the remaining 3.5% of cases, parts of contours have been attracted by the lower part of the metaphyses whose edges happened to be stronger (Fig. 6g) or parts of the contours have been attracted to the upper parts of the phalanx located beneath (Fig. 6c). Regions in Fig. 6d, h shows also the desirable capabilities of snakes in closing concave contours, which had emerged from imperfections of GRF approach. After the inclusion of active contours analysis into the existing computer-aided diagnosis system, an average time of processing for one region of interest is approximately 10–15% longer than in the case without active contour routines. We observed that this ratio depends on image size, which affects the number of snake points surrounding an epiphysis.

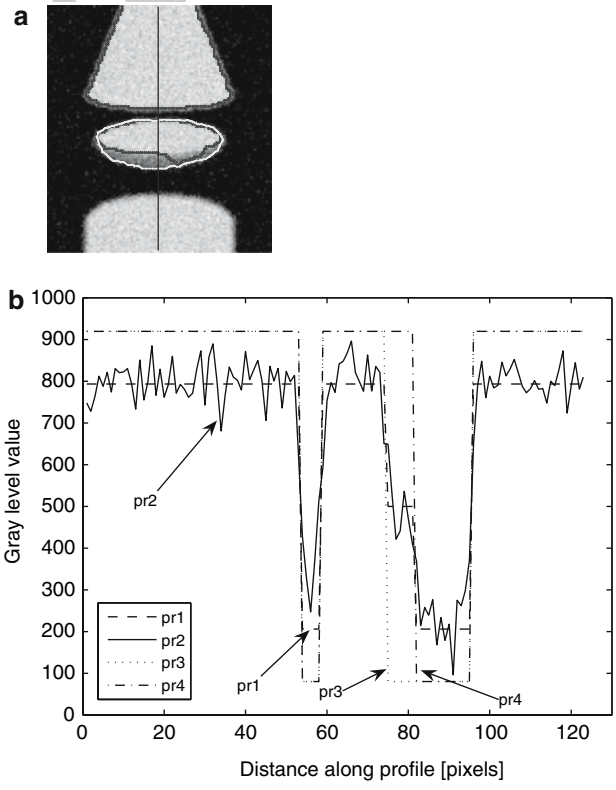

Fig. 5 The results of borders location for synthetic image: **a** synthetic ROI with edges segmented out by different techniques, **b** profiles along the black vertical line in **a** pr1—location of edges in non-blurred noise free image model, pr2—gray level values along profile in noisy image, pr3—edges detected by GRF segmentation, pr4—improved edges detection by snake technique

Journal : 10044 Dispatch : 16-11-2006 Pages : 9
Article No. : 56 LE TYPESET
MS Code : 56 CP DISK

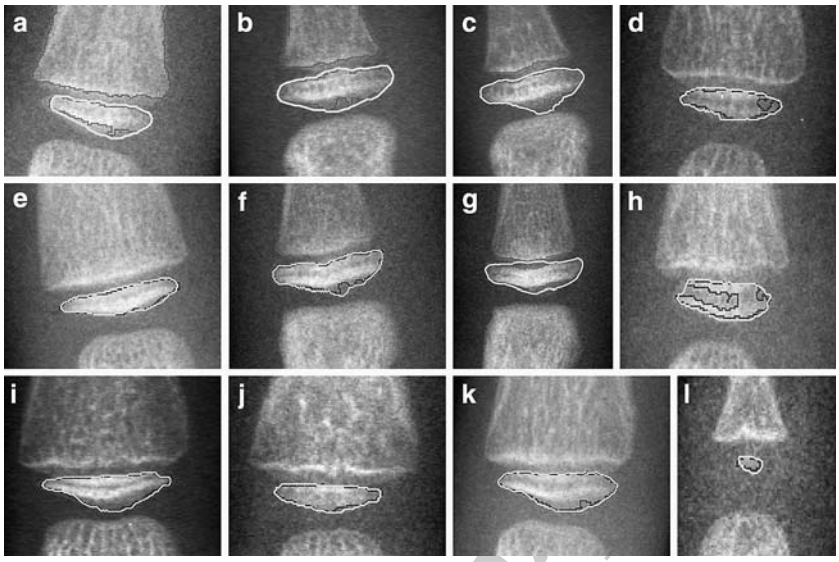

Fig. 6 Regions of interest **a–l** at different stage of development after GRF segmentation (*gray lines*), and snake improvement (*white lines*)

5 Results and discussions

The adaptive Gibbs random field image segmentation technique followed by active contour boundary enhancement applied to hand radiographs' regions of interest have been described. The results confirm an advantage of implementing the snake method as the post-segmentation contour improvement technology. The GRF segmentation serves as a reasonable solution of the initial contour setting and has overcome the main drawbacks that prevent implementing snakes in many applications. This also implies that the entire routine remains objective and automatic which is a beneficial factor important in the overall approach of an automated computer-aided skeletal maturity assessment system. Also, by incorporating noise and contrast estimation routines, an improvement of GRF segmentation algorithm [7] has been achieved. It makes the GRF approach dependent only on number of segmentation classes (k) when applied to hand radiograph analysis (Fig. 2). The time performance of our CBAA system is not drastically affected by the implementation of the snakes' methodology

The criteria of correctness of the combined approaches were based on the accuracy of model segmentation and visual inspection of real regions of interest by three non-clinical observers. The first evaluation was preformed by one observer. In this case the noise-free model of region of interest served as a validation tool. If a contour after combined segmentation outlined both the entire upper and lower part of the epiphyseal model then it was treated as a correct segmentation. Otherwise the contour was treated as a wrong one. In real ROIs, the epiphyseal contour location has been examined by all three observers and all evaluations have had to be positive in order to accept the correctness of the location. These regions were marked as good, others as bad. In order to accept the correct location of contours the following criteria were applied: (1) all structures segmented by the previous step (GRF) should be inside a new contour, (2) the outlying contour were not attracted to neighboring phalanxes, (3) the final contours should not enclose soft tissue pixels.

Unfortunately, this contour assessment has some subjective bias. Clinical evaluation of the combined methodology and the CBAA system is an ongoing process and it addresses not only the aspects of border location but also mainly the overall system accuracy, which has not been assessed at this point.

An improvement in contour location and smoothing is observed in regions with cartilage or bone convexity developed near the bottom region of the epiphysis. Nonetheless, some deterioration of contour placement after the snakes' analysis has also been observed while contours were attracted by stronger non-epiphyseal edges. So far the CBAA software has no built-in detection of such errors.

Currently, only the simplest form of snakes' methodology has been tested. Its main disadvantage in this present stage of development is the subjective choice of the set of parameters $\alpha(s)$, $\beta(s)$, • w_{edge}, t_{erm}, w_{line}. We will address this drawback while trying to apply snakes to middle regions and carpal bones segmentation targets.

In this paper the method of combined Gibbs random fields with active contours technique applied to the segmentation of phalangeal regions of interest is pre-

Journal : 10044 Dispatch : 16-11-2006 Pages : 9
Article No. : 56 LE TYPESET
MS Code : 56 CP DISK

sented. By the combined use of these two methods, a meaningful improvement in terms of more accurate outline of epiphyseal regions has been obtained, which makes a contribution and extension of our existing techniques for computerized approach to bone age assessment [3–5, 15].

Future studies will also address the following areas: analysis of quantitative features extracted by the improved CBAA system, features evaluation with radiologists' bone age readings and influence of the implementation on system accuracy.

6 Originality and contribution

The main contribution of this paper is that the two segmentation methods: the Gibbs random fields technique and the active contours have been implemented sequentially in the computer-aided approach to the assessment of skeletal maturity based on analysis of phalangeal regions interest. The first segmentation method segments out bony structure and roughly outlines the edges of cartilage and concave bones while the second segmentation method delineates edges of latter structures and improves the overall segmentation results. It is of particular importance especially when cartilage and concave bones are the target segmentation objects. A synthetic region of interest has been designed to test and adjust weights of the snake energy functional. These weights were also applied to the clinical image data. The implementation of the snakes improves results without affecting the segmentation performance and the time of analysis. This approach to the segmentation remains automatic and does not require user interaction.

References

1. Greulich WW, Pyle SI (1971) Radiographic atlas of skeletal development of hand wrist, 2nd edn. Stanford University Press, Stanford
2. Tanner JM, Whitehouse RH (1975) Assessment of skeletal maturity and prediction of adult height (TW2 method). Academic, London
3. Piętka E, Gertych A, Pośpiech S, Huang HK, Cao F (2001) Computer assisted bone age assessment: image pre-processing and ROI extraction. IEEE TransMed Imaging 20:715–729
4. Piętka E, Pośpiech S, Gertych A, Cao F, Huang HK, Gilsanz V (2001) Computer automated approach to the extraction of epiphyseal regions in hand radiographs. J Digit Imaging 14:165–172
5. Piętka E, Pośpiech-Kurkowska S, Gertych A, Cao F (2003) Integration of computer assisted bone age assessment with clinical PACS. Comput Med Imging Graph 27: 217–228
6. Lee JS (1981) Refined filtering of image noise using local statistics. Comput Vis Graph Image Process 15:380–389
7. PappasT (1992) An adaptive clustering algorithm for image segmentation. IEEE Trans Signal Process 40:901–914
8. Immerkaer I (1996) Fast noise variance estimation. Comput Vis Image Underst 64:300–302
9. Besag J (1986) On the statistical analysis of dirty pictures. J R Stat Soc B 48:259–302
10. Kass M, Witkin A, Terzopoulos D (1988) Snakes: active contour models. Int J Comput Vis 1:321–331
11. Terzopoulos D, Fleisher K (1988) Deformable models. Vis Comput 4:306–331
12. Sonka M, Hlavac V, Boyle R (1998) Image processing analysis and machine vision, 2nd edn. Thomson Learning Vocational Publishing, Florence84:374
13. Williams DJ, Shah M (1992) A fast algorithm for active contours and curvature estimation, CVGIP. Image Underst 55:14–26
14. MacQueen JB (1967) Some methods for classification and analysis of multivariate observations. In: Proceedings of 5th Berkley symposium on mathematical statistics and probability. University of California, Berkley 1:281–297
15. Piętka E, Gertych A, Witko K (2005) Informatics infrastructure of CAD system, Comput Med Imaging Graph 29:157–169

Author Biographies

Arkadiusz Gertych received the master degree in 1995 and the PhD degree in 2003 in electrical engineering from the Silesian University of Technology, Poland. In 1996 he started working for Silesian University of Technology in Department of Biomedical Electronics and from 2003 he is also an Assistant Professor at this University. From 2004 he continues post-doctoral studies at University of Southern California Department of Radiology in Image Processing and Informatics Laboratory in Los Angeles. His research activities include signal and image processing, design and development of computer-aided (CAD) medical diagnosis support systems, radiation therapy systems and medical informatics.

Ewa Piętka received the master degree in 1979, the PhD in 1987 from the Silesian University of Technology in Poland, and the D.Sc. in 1997 form the Polish Academy of Sciences. In 1979 she started working for the Silesian University of Technology. In 1989 Dr Pietka joined the staff of the University of California, Los Angeles. In 1993 she received an appointment at the University of Geneva. Currently she is a Professor at the Silesian University of

Journal : 10044 Dispatch : 16-11-2006 Pages : 9
Article No. : 56 LE TYPESET
MS Code : 56 CP DISK

Technology and a Visiting Professor at the University of Southern California. Her research activities center around image analysis, PACS, and medical information systems.

Brent J. Liu Biomedical Physics (UCLA, 1996), PD Fellow, UCLA (1996–1999). Assistant Professor in Radiology and BME, USC. From 2003–2004, he led the HIS/RIS/PACS/VR implementation at HCC2 USC and continues serving as the RIS/PACS implementation advisor to the Radiology Department. He has been Visiting Lecturer at the Hong Kong Polytechnic University. His current research interests include Imaging Informatics, Image-Guided Radiation Therapy Systems, Fault-Tolerant PACS Design; PACS model Backup Archive, Data Grid, Internet 2, PACS-based CAD and Surgery, Image Integrity. He is currently the Deputy Director of Informatics and the IPI Research Lab, Department of Radiology, Keck School of Medicine.

Journal : 10044 Dispatch : 16-11-2006 Pages : 9
Article No. : 56 ☐ LE ☐ TYPESET
MS Code : 56 ☑ CP ☑ DISK

Automatic Bone Age Assessment for Young Children from Newborn to 7-Year-Old Using Carpal Bones*

Aifeng Zhang, Arkadiusz Gertych, Brent J. Liu

Image Processing & Informatics Lab, Department of Radiology, University of Southern California, Marina Del Rey, CA 90292, USA

* *Paper accepted to be published in Journal of Computerized Medical Imaging and Graphics*

ABSTRACT

A computer-aided-diagnosis (CAD) method has been previously developed based on features extracted from phalangeal regions of interest (ROI) in a digital hand atlas, which can assess bone age of children from ages 7 to 18 accurately. Therefore, in order to assess the bone age of children in younger ages, the inclusion of carpal bones is necessary. However, due to various factors including the uncertain number of bones appearing, non-uniformity of soft tissue, low contrast between the bony structure and soft tissue, automatic segmentation and identification of carpal bone boundaries is an extremely challenging task. Past research works on carpal bone segmentation were performed utilizing dynamic thresholding. However, due to the limitation of the segmentation algorithm, carpal bones have not been taken into consideration in the bone age assessment procedure. In this paper, we developed and implemented a knowledge-based method for fully automatic carpal bone segmentation and morphological feature analysis. Fuzzy classification was then used to assess the bone age based on the selected features. This method has been successfully applied on all cases in which carpal bones have not overlapped. CAD results of total about 205 cases from the digital hand atlas were evaluated against subject chronological age as well as readings of two radiologists. It was found that the carpal ROI provides reliable information in determining the bone age for young children from newborn to 7-year-old.

Keywords: *Bone Age Assessment, Computer-aided-diagnosis, Carpal Region of Interest, Carpal Bone Segmentation, Anisotropic Diffusion, Canny Edge Detection, Feature Extraction, Fuzzy Classification*

I. INTRODUCTION

The determination of skeletal maturity (‘bone age’) plays an important role in diagnostic and therapeutic investigations of endocrinological problems and growth disorders of children [1, 2]. In clinical practice, the most commonly used bone age assessment method is atlas matching by a left hand and wrist radiograph against the Greulich & Pyle (G&P) atlas [3] which contains a reference set of normal standard images. However, besides the fact that the data in G&P atlas was collected in 1950’s, this method strongly depends on experience of the observer, leading to considerable inter and intra-observer discrepancy. Therefore, an updated data collection and an objective method are desirable.

A computer-aided-diagnosis (CAD) method [4-8] has been previously developed in our laboratory based on features extracted from regions of interest (ROI) in phalanges from a digital

hand atlas. 1,103 left hand and wrist radiographs of normal children, from newborn to 18 years old, were acquired at the Childrens Hospital Los Angeles (CHLA) and digitized at IPI (Image Processing and Informatics Lab, USC). The data was evenly distributed into four races (Asian, Caucasian, African-American and Hispanic) for both gender (Male and Female). Each case was read by two radiologists independently. Figure 1 shows an example image with phalangeal and carpal ROIs superimposed.

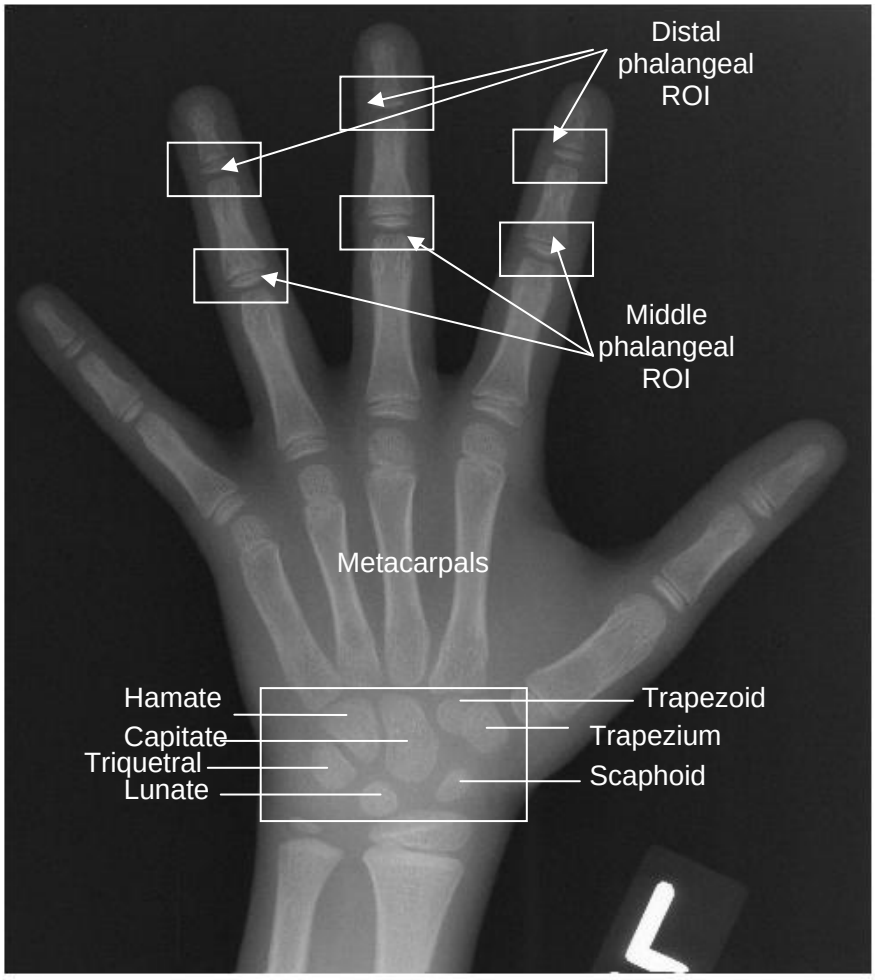

Figure 1. A left hand and wrist radiograph marked with 6 phalangeal ROIs and carpal ROI (box at the bottom)

For children above 6 of female or 8 years old of male, Phalangeal feature analysis was very reliable. Therefore, CAD method yields very accurate bone age assessment. However, for ages below 5 ~ 7, the phalangeal analysis fails to extract the features correctly in some cases, especially in very young children. This is due to the following problems: first, soft tissue deteriorates the border and makes the segmentation between epiphysis and metaphysis an extremely difficult task. Second, the developments of epiphysis of the six phalangeal ROIs are not parallel. Third, it is not reliable to locate the phalangeal ROIs correctly if the hand is rotated when the upright hand position is not achieved during acquisition. Lastly, the phalangeal ROIs analysis is sensitive to bending of fingers during acquisition.

Therefore, in order to achieve similar degree of accuracy in bone age assessment for children of all ages, we hypothesized that the CAD method may benefit from the augmentation of features extracted from the carpal ROI of young children. Medical studies [1, 2, 9] verified the value of

carpal bone in determining the bone age of young children. Past research work on carpal bone segmentation has been done by Pietka [10] utilizing dynamic thresholding. However, due to the limitation of the algorithm, carpal ROI have not been taken into consideration in the bone age assessment procedure.

This paper described a knowledge-based carpal ROI analysis for fully automatic carpal bone segmentation and feature analysis for bone age assessment by fuzzy classification. Table 1 shows the reliability of phalangeal and carpal ROIs analysis for different age groups in CAD system. The carpal bone segmentation and feature extraction were proven to be very reliable for young children before the carpal bones start to overlap. Combining with the existing phalangeal ROI, it improved the accuracy of computerized bone age assessment for young children significantly. Hence, accurate bone age assessment was ensured for the entire age range.

ROI / Age group (years)	Phalangeal ROI Analysis	Carpal ROI Analysis
0 – 5 (female) 0 – 7 (male)	Size & shape analysis of epi-metaphysis - Feature extraction is not reliable	Size & shape analysis of carpal bones - Feature extraction is reliable
6 – 12 (female) 8 – 12 (male)	Size & shape analysis of epi-metaphysis - Feature extraction is reliable	Degree of overlapping of carpal bones - Feature extraction is not reliable
13 – 18 (female & male)	Degree of fusion of epi-metaphysis - Feature extraction is highly reliable	

Table 1. Reliability of ROI analysis for different age groups in CAD method.

II. MATERIALS AND METHODS

A. Growth pattern of carpal bones

At the early stage of development, carpals appear as dense pin points on a radiograph. During development, they increase in size until reaching their optimal sizes and characteristic shapes. Figure 2 shows an ROI image with seven carpal bones appearing.

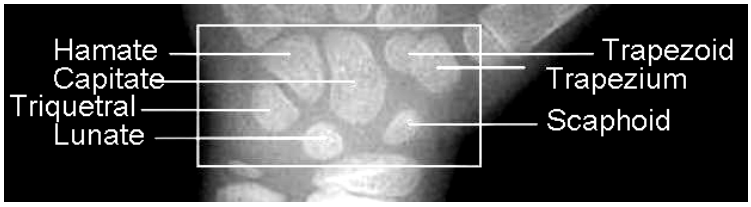

Figure 2. Description of carpal bones in a hand radiograph

Figure 3 demonstrates the growth pattern of carpal bones of Asian males from newborn to 7 years old. Carpal bones ossified in chronological order, Capitate, Hamate, Triquetral, Lunate,

followed usually by Scaphoid, then either the Trapezium or the Trapezoid. [3, 11] Female developments noticeably more advanced than male by as many as 3 years.

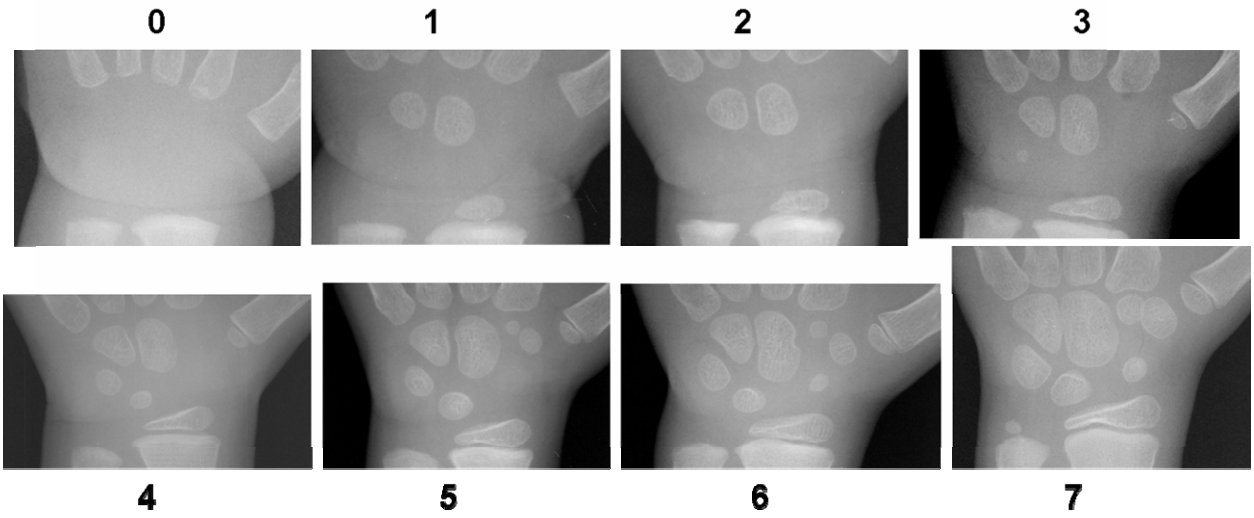

Figure 3. Growth pattern of carpal bones of Asian male from newborn to 7-year-old. The number represents the corresponding age group for each image

Medical study [9] indicated that, due to the nature of carpal bone maturity, their analysis does not provide accurate and significant information for patients older than 7-12 years of age. This is due to the fact that carpal bones start overlap at age around 7 years old in male and 5 in female. In this stage of development the phalangeal analysis yields more reliable information. Therefore, in this research, carpal bone analysis focuses on age group from 0 to 7 for male and 0 to 5 for female.

B. CAD methodology overview of carpal ROI analysis

The workflow of carpal ROI analysis procedure which includes seven steps is shown in Figure 4. The carpal bone region of interest was first extracted from the entire hand image (Figure 1, 1). Due to the non-uniform background and noise, the carpal bone ROI was subjected to an anisotropic diffusion filter (2) which smoothed out the noise and preserves the edges at the same time. Then, the object contours were extracted by the Canny edge detector (3). A series of knowledge-based operations based on morphological properties of segmented objects were implemented in order to single out the carpal bones by eliminating the non-carpal bones (4). The carpal bones contours went through feature extraction phase which yields the inputs into the fuzzy classifiers to assess the bone age (5, 6, 7). This section discusses the procedure in the following order: carpal bone segmentation, carpal bone identification, feature analysis and bone age assessment using fuzzy logic.

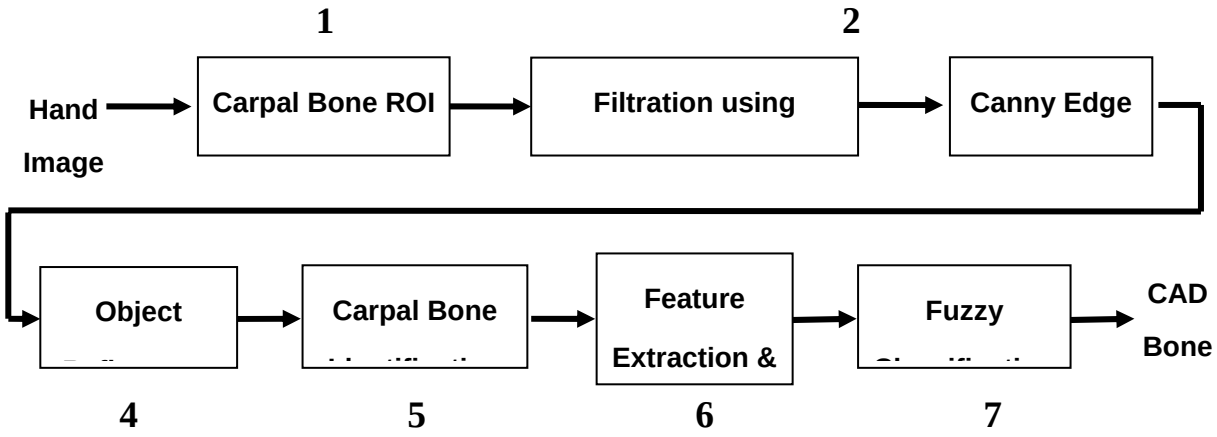

Figure 4. Carpal ROI analysis workflow with 7 steps

C. Carpal bone segmentation

1. Carpal ROI extraction from entire hand image

The first step (in Figure 4) was to locate and extract carpal ROI for further analysis. Figure 5 shows the procedure. A binary hand silhouette was obtained by adaptive thresholding of the hand image with background removed. The carpal ROI was then located in the hand silhouette after artifacts deletion. The upper edge of the carpal ROI was found by scanning a horizontal line and searching for the junction between the second and third metacarpal bone. Perpendicular to the upper edge of the image, starting from its middle, two lines were scanned one pixel at a time toward the left and right borders of the image. The first line on both sides that did not intersect the wrist, fixed the left and right border, respectively. The lower edge of the CROI was the line that intersected the forearm with the minimal width. It was determined by scanning the forearm, one line at a time, from the proximal end of the hand and moving toward the distal end. The carpal ROI was defined within these four edges.

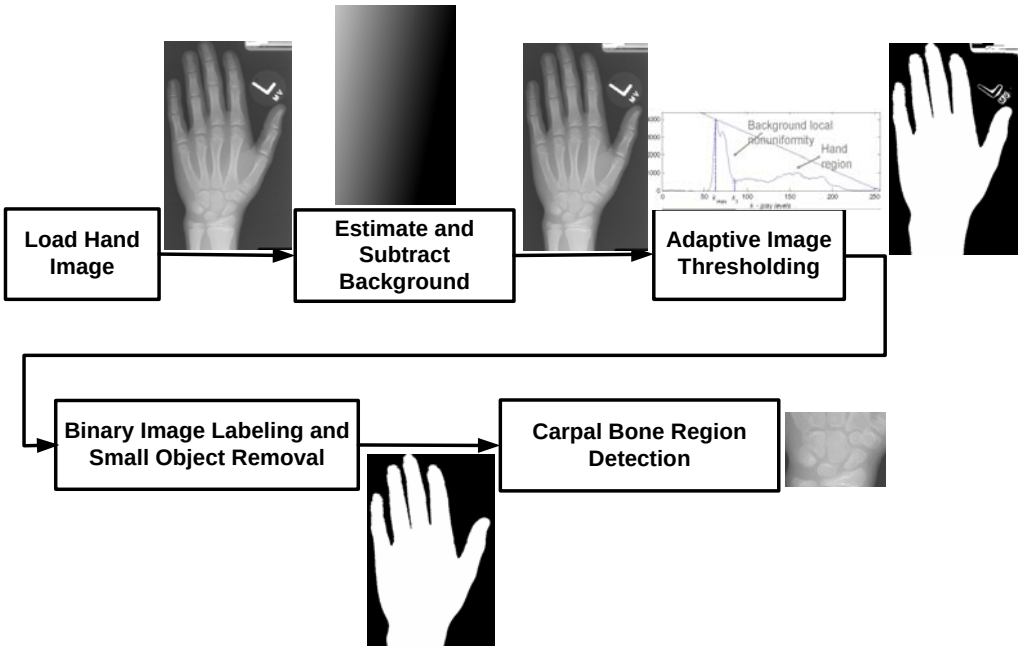

Figure 5. The procedure of carpal ROI extraction from the entire hand image

2. Image smoothing by anisotropic diffusion

Carpal bones in the image are generally poor in contrast. Furthermore, the bone edges are often degraded by noise and artifacts. In order to better differentiate carpal bones from the background, an anisotropic diffusion filter proposed by Perona and Malik [12] was applied to the carpal ROI image. (Second step in Figure 4)

This filter was able to greatly reduce noise in homogeneous areas of carpal ROI images while preserving the edges and contrast associated with bony structures. The principle is to smooth out noise locally by diffusion while at the same time preventing diffusion across object boundaries. The diffusion coefficient is chosen to vary spatially based on a measure of edge strength to encourage intra-region smoothing in preference to inter-region smoothing. The diffusion process achieves piecewise smoothing while preserving the relevant image edges.

Figure 6(a) and Figure 6(b) show the original carpal ROI image and the result after anisotropic diffusion filtration respectively. The comparison of profiles along one horizontal line (same position in both images) which runs across the capitate and hamate is given in Figure 6c) and 6(d). It demonstrates that noise is greatly suppressed by the diffusion process while the sharp edges are well preserved.

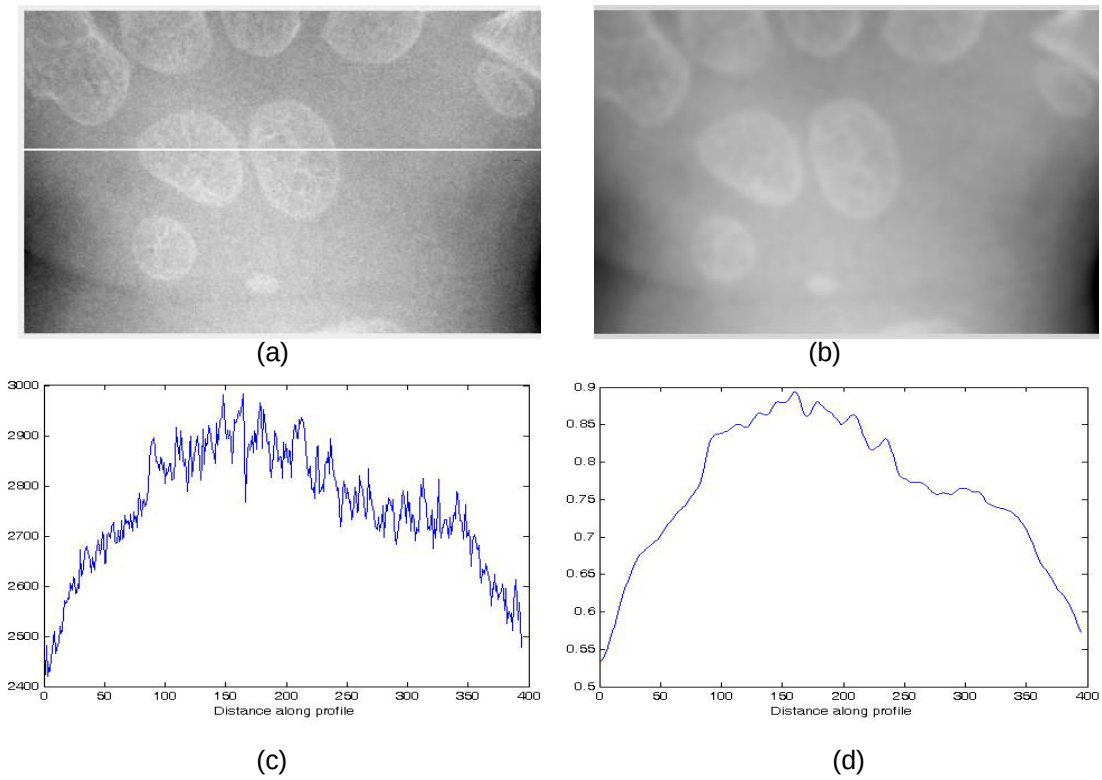

Figure 6. Illustration of anisotropic diffusion filtration (a) Original carpal bone ROI image (b) The result image after anisotropic diffusion filtration (c) profile of the original image along the horizontal line (d) profile of the filtered image along the horizontal line

Size and shape of carpal bone are the characteristics related with skeletal development. Bony texture inside the carpal bone is not the factor that radiologist investigate in assessing the bone age. The next step is to segment the carpal bones from the carpal ROI image.

3. Edge detection by Canny

Edge detection by Canny method (third step in Figure 4) was performed on the smoothed ROI image. The Canny edge detector finds linear, continuous edges and is known as the optimal edge detector. [11, 13, 14] The Canny method differs from other edge-detection methods in that it uses two different thresholds, and includes the weak edges in the output only if they are connected to strong edges. Figure 7 shows an example of a filtered image by using the anisotropic diffusion (shown in Figure 7(b)) and the edges detected by Canny method. This method is less likely than the others to be confused by noise and the carpal bones were detected as closed-contours.

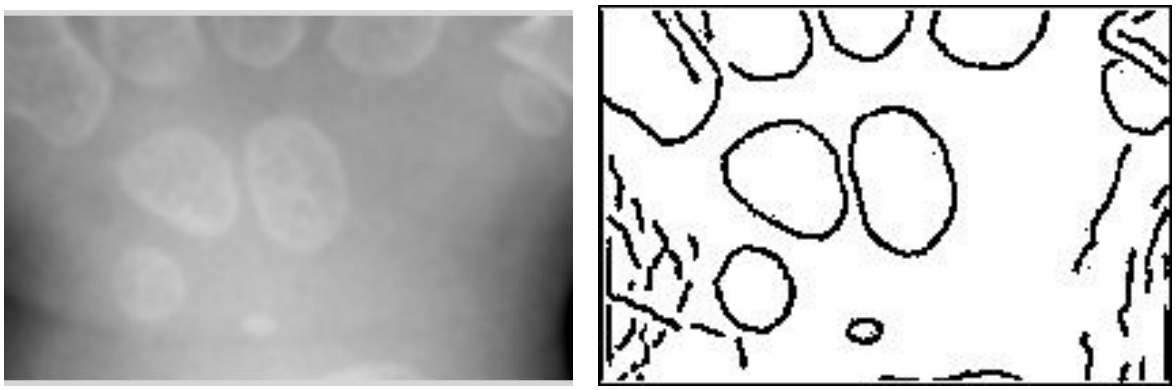

Figure 7 Canny edge detection example (a) Original image (Figure 6 b) (b) Result image after Canny edge detection

4. Objects refinement

The carpal ROI includes carpal bones and parts of the radius, ulna, and metacarpals. Before the features that describe the carpal bones were extracted, the carpal bones themselves needed to be identified from the result of Canny edge detection. An original image and the final result after object refinement (fourth step in Figure 4) are shown in Figure 8 (a) and (b) respectively.

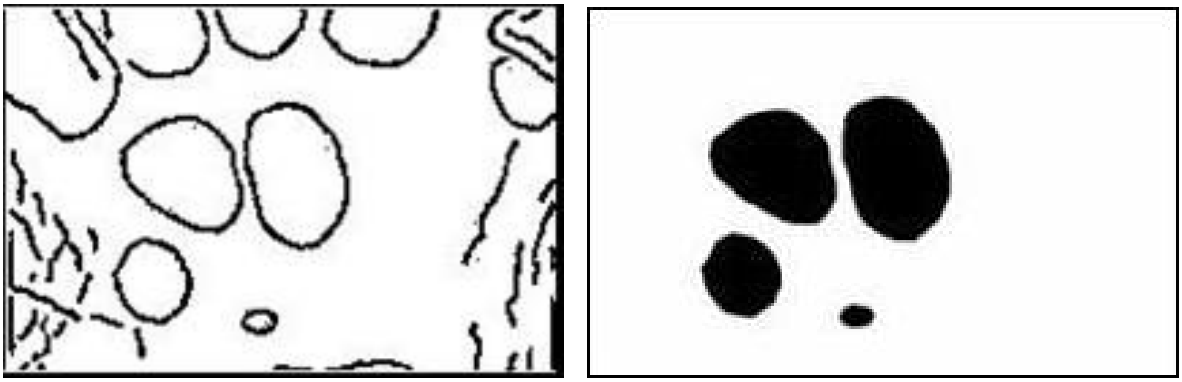

Figure 8. The goal of objects refinement procedure (a) original image (Figure 7 b) (b) image after objects refinement

Knowledge-based morphological operations were used to clean-up the objects. The removal of non-carpal bones was performed in several steps. In the first step all objects that touch the CROI borders were extracted and eliminated. These include the metacarpal bones, wrist bones including ulna and radius touching the CROI borders. In the second step straight and short lines and spots were removed. Eccentricity, a morphological property, of each object was used to

identify the carpal bones. It measures how far the object deviates from a circle. Figure 9 shows an ellipse that has the same area as the segmented carpal bone. Eccentricity is defined as the ratio of the distance between the foci (F_1 and F_2) to the major axis; i.e. $\left(\frac{\overline{F_1F_2}}{\overline{AB}}\right)$.

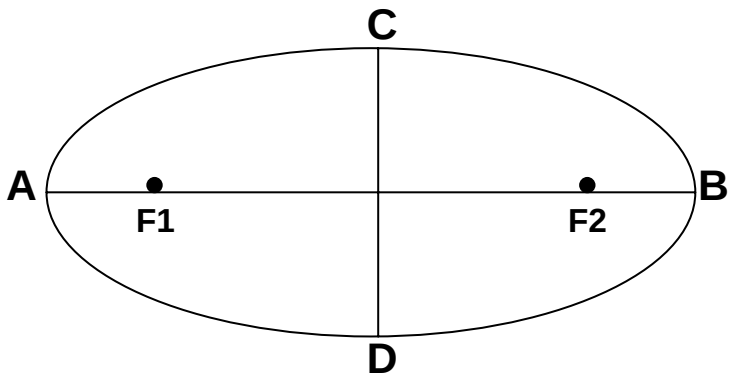

Figure 9. Illustration of an ellipse with foci (F1 and F2) and major axis (between A and B). Eccentricity is defined as the ratio of distance of F1 and F2 and major axis

Based on our experiments, the eccentricity of carpal bone falls between 0.1 and 0.9 and can be used as a prior knowledge. Therefore, objects which have eccentricities under 0.1 or above 0.9 were eliminated. In the third step objects were filled and closed-contour objects were selected based on solidity, a morpholoical property of each object. A convex hull for each filled object is first found as the smallest convex polygon that can contain the object. The proportion of pixels in its convex hull that are also in the studied object is then defined as solidity. The objects, which solidities are above 0.5, were taken as the closed-contour objects. The others were discarded. Figure 10 shows the final carpal bone contours overlapped on a carpal bone region image.

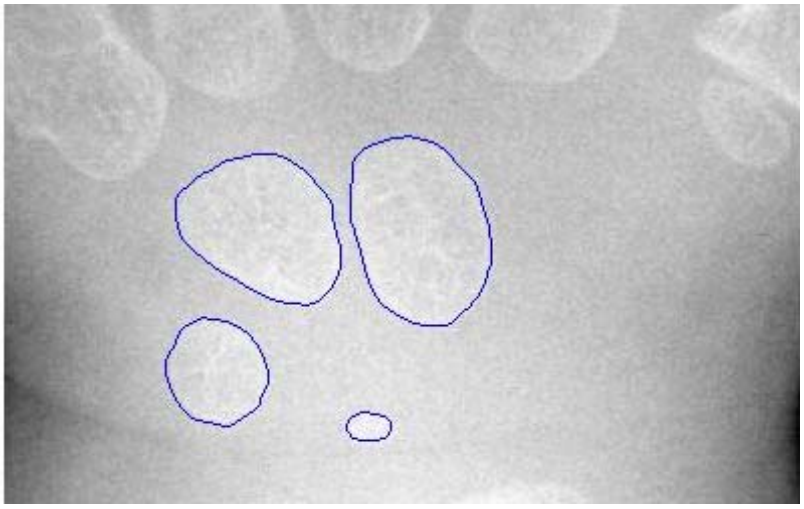

Figure 10. Final segmentation results super-imposed on the original carpal ROI shown in Figure 6 (a)

D. Model-based carpal bone identification

From the carpal bone contours, the post-processing procedure utilizing a prior knowledge was developed to identify the bones (fifth step in Figure 4). The Capitate is the first bone to appear in chronological order and the biggest one among all the carpal bones. It is also the most reliable bone to segment out. A polar coordinate system with the origin at the center of gravity of the Capitate, which was identified as the largest object, was built. The major axis was set as the original normal axis of the polar system. The carpal ROI was then divided into five empirical regions shown in Figure 11. The positions of regions define the prior knowledge about where a carpal bone should be located in the carpal ROI.

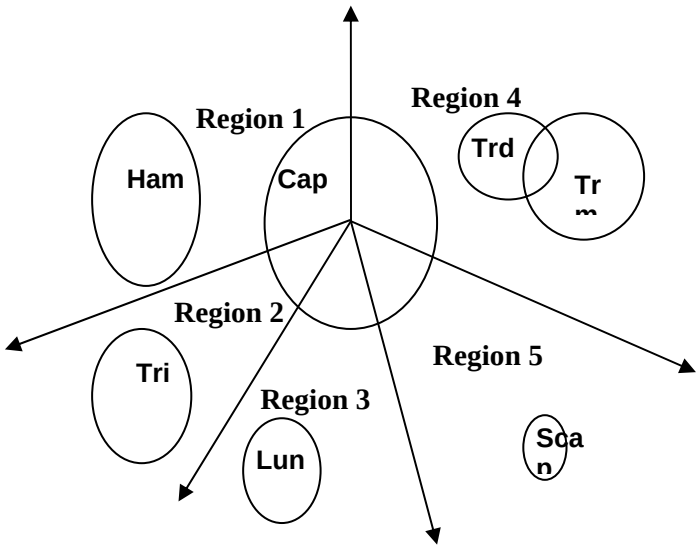

Figure 11. Carpal bone identification model. The polar coordinate system with the centroid of the capitate as the origin is divided into five regions. Based on a priori anatomical knowledge, each of which houses a carpal bone(s): Capitate, Hamate, Triquetral, Lunate, Scaphoid, Trapezium and Trapezoid

The center of gravity of each object was then computed based on polar coordinates. Each object was assigned to the region it belongs to, based on the polar angle and radius of each object. The identification model is hand rotation invariant because the major axis of Capitate follows the rotation of the hand. Figure 12 shows the one example case with identified carpal bones.

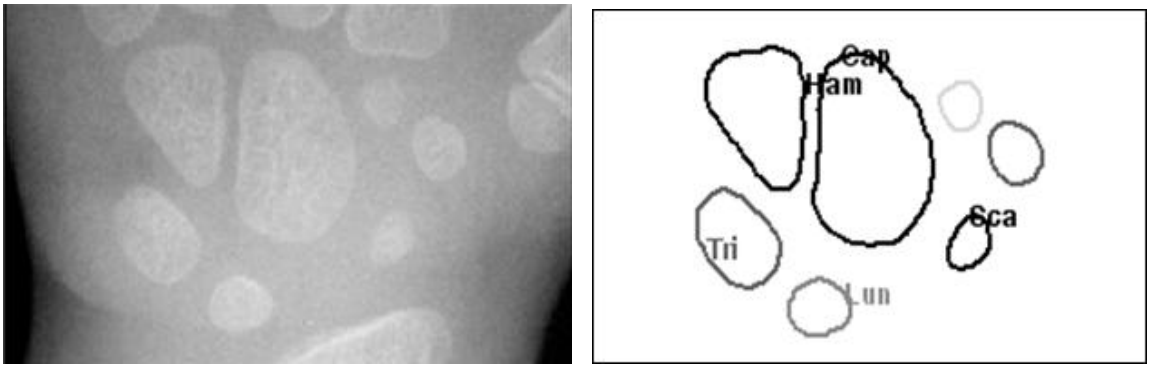

Figure 12. A Carpal bone identification example a) Original carpal ROI image, b) Identified carpal bones - Cap: Capitate, Ham: Hamate, Tri: Triquetral, Lun: Lunate and Sca: Scaphoid.

The first two bones which appear in chronological order, Capitate and Hamate, were selected for further analysis. The other identified bones which appear later will be analyzed for future refinement in case that Capitate and Hamate are failed to extract because of fusion with each other.

E. Feature analysis

From the identified carpal bones, features related to the bony growth were extracted for bone age assessment. (Sixth step in Figure 4)

1. Morphological feature extraction

To describe the size and shape of the carpal bones identified, four morphological features were extracted from Capitate and Hamate. Feature 1 measures equivalent diameter, which specifies the size of the object. An ellipse that has the same normalized second central moments as the region was found for each bone. Feature 2 is eccentricity which we defined in Section C.4. The value of eccentricity is between 0 and 1. Feature 3 is solidity (also refer to C.4). Feature 4, triangularity measures the ratio of equivalent diameter and the product of major axis length and minor axis length.

2. Feature selection

To evaluate the performance of each feature in assessing the bone age, correlation with the chronological age was analyzed. Among all the features, sizes of Capitate and Hamate have the most significant correlations with age, which are over 0.90. To simplify the feature space, all features which have the correlation above 0.60 were selected and form the feature space for bone age assessment. Table 2 shows the correlation coefficients for selected features from an example category of one race and one gender.

Table 2. Correlation coefficients for selected features. High correlation is marked with double asterisks.

	Capitate			**Hamate**		
	size	eccentricity	triangularity	size	eccentricity	triangularity
Correlation Coeff.	.94 (**)	.74(**)	-.65(**)	.92 (**)	.70(**)	-.62(**)

F. Bone age assessment using fuzzy logic

The last step in carpal ROI analysis (Seventh step in Figure 4) is to assess the bone age using fuzzy classification based on the features extracted and selected from the Capitate and Hamate. Two characteristics of carpal bone features make bone age assessment difficult. First, the growth of carpal bones does not have a linear relationship with chronological age. The imprecise nature leads to the inter- and intra-observer discrepancy. Second, some features may be missed by the segmentation and feature extraction procedure. Most of past attempts of using linear approach failed because it is insufficient to model the growth pattern. Fuzzy logic [15-18] incorporates a simple and rule-based approach and is suitable for this application because it is robust and does not require precise and noise-free inputs. As long as some features from any bone are provided, it is sufficient to activate the fuzzy system to generate the output.

The three features, size, eccentricity and triangularity extracted from Capitate and Hamate each were taken as an input into the fuzzy classifier. The system was broken into smaller sub-classifiers based on Capitate and Hamate respectively. Figure 13 shows the workflow of the fuzzy classification for bone age assessment.

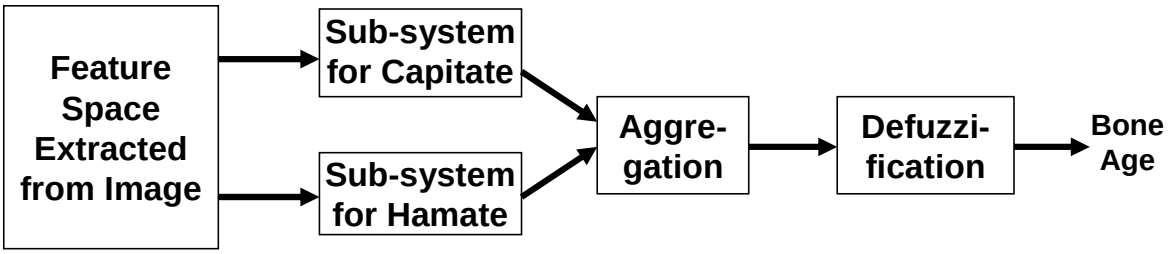

Figure 13. Fuzzy classification workflow for bone age assessment.

An automatic training algorithm with the features from our normal data collection was developed for fuzzy classifiers. The output was set as the subject chronological age since the normality of children was ensured for each case during data collection. The data of young children from newborn to age group of 7 (male) or 5 (female) was divided into age groups with an interval of one year. Therefore, total of 8 (0,1,2,…7 for male) or 6 (0,1,2,…,5 for female) initial Gaussian membership functions were generated for each input feature (size, eccentricity, and triangularity) and output (chronological age). The mean and standard deviation of each feature from each age group were calculated and taken as the Gaussian parameters for the corresponding membership functions. Merging of adjacent membership functions was then performed based on the *t*-test of the mean difference for specific feature between adjacent age groups. The same merging procedure was performed for output depending on the inputs. Fewer number of membership functions simplifies the processing logic and even improving the fuzzy logic system performance. Figure 14 use Caucasian male as an example to show the groups of membership functions for the three features (Figure 14 a, b and c) of Capitate and output (Figure 14 d) as chronological age.

A firing strength for each output membership function is computed. Then a max-min rule operation was applied to combine the inputs logically to produce output response values for all expected inputs. It took two steps. A *min* fuzzy operation was first applied to integrate the multiple inputs of features for each output class. Then the active conclusion was combined by finding the *max* from all the classes.

Take the Capitate of Caucasian male as an example, after feature extraction it yields input features (Size:89.5, Eccentricity: 0.636, Triangularity: 0.0294) shown in Fig. 15 (a), (b), and (c), an output membership function (CAD bone age based on the Capitate) was derived shown at the bottom graph of Figure 15 (d).

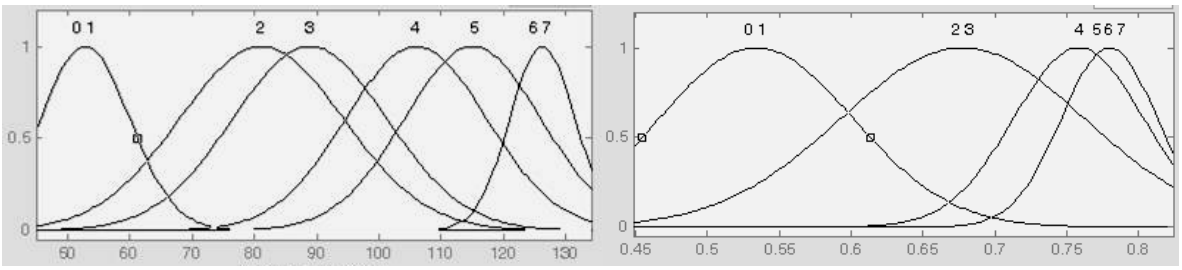

(a) Size **(b) Eccentricity**

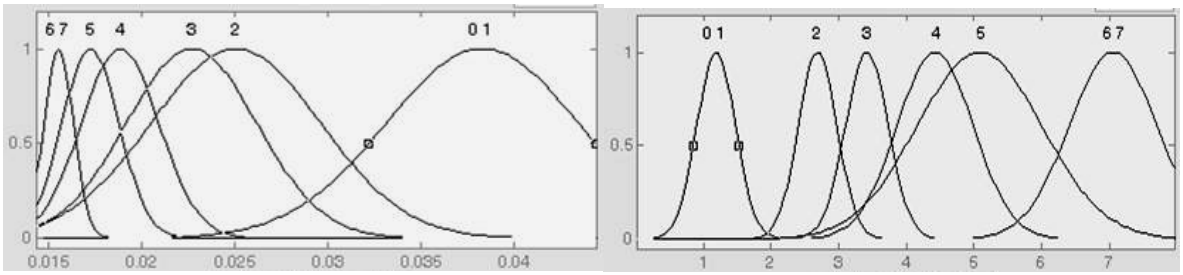

(c) Triangularity **(d) Chronological Age**

Figure 14. Four membership functions of Capitate sub-classifier for Caucasian male category. In this fuzzy logic training, a normal distribution curve is used to represent a membership function using the mean and standard deviation obtained from each feature. (a), (b), and (c) are the three input features: size, eccentricity, and triangularity, the x-axis is the value of the corresponding feature. The output membership function (d) is the chronological age represented by the x-axis. Each of the four y-axes represents degree of the membership function which has a range from 0 to 1. Number on top of each membership function represents the chronological age group. Multiple numbers appear together if membership functions for adjacent groups were merged, for instance, age group 0 and 1 in a). These membership functions were derived from the data collected from each age group

A final output (CAD bone age) needs to be aggregated from the sub-systems based on the Capitate and the Hamate, respectively. It was determined by finding the logic *mean* of the two outputs. The defuzzification process used center of gravity method to obtain a final CAD bone age.

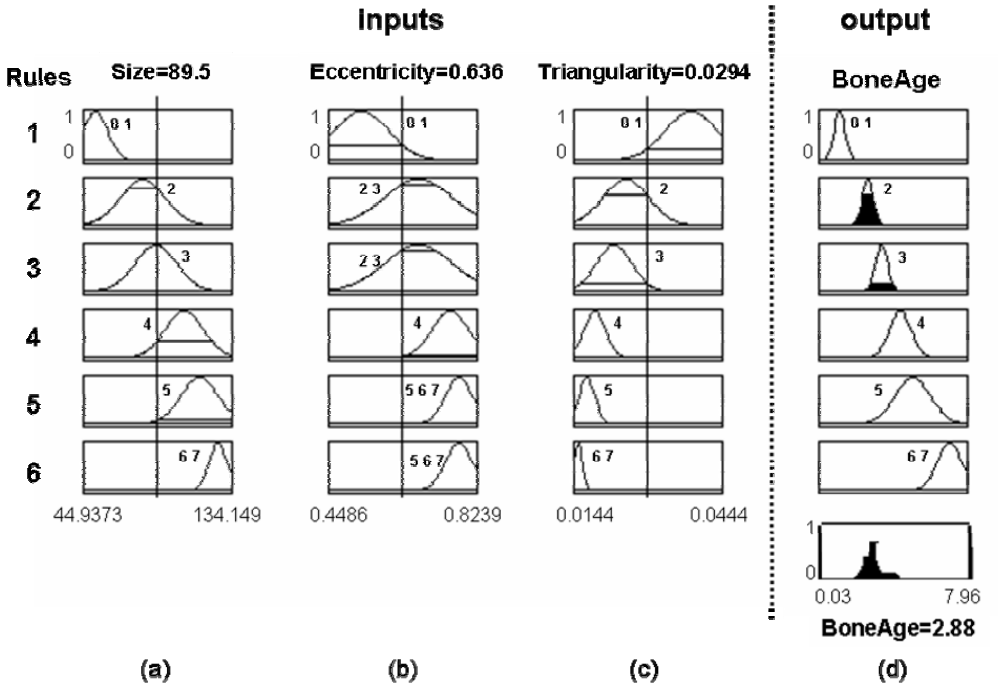

Figure 15. An example of using fuzzy classification for CAD bone age assessment of a given Caucasian male based on membership functions depicted in Fig. 14. Membership functions for each of the three input features (size, eccentricity, and triangularity; columns a, b, and c), and one output which is the chronological age, (column d) are reoriented vertically forming six rules (1, 2, …, 6) based on Fig. 14. Three extracted features from the hand image are: size: 89.5, eccentricity: 0.636, and triangularity: 0.0294, represented by three vertical lines at each of the three columns, respectively. The output is the aggregation of the solid areas under each rule, which yields a crisp CAD bone age as 2.88 year old shown in the bottom graph in column (d).

G. System evaluation

Three types of tests were conducted to evaluate the performance of using the fuzzy logic for bone age assessment. Test 1 separated the data into eight categories of four races and two genders. Classifiers were trained and tested on each case from each category. Test 2 had two categories for female and male with four races combined together. Test 3 combined the entire data collection into one universal category.
For the above three tests, CAD bone age assessed by fuzzy classification was evaluated against chronological age which was taken as the gold standard as the normality of each case was ensured. The same evaluation was performed on readings. The CAD bone age results were plotted with the average reading of two radiologists against chronological age. The mean difference of each of the two readings versus chronological age or CAD bone age versus chronological age was computed by paired t-test.

III. RESULTS

Hand images for females of age groups from 0 to 5 and males from 0 to 7 from the entire data collection of 205 images went through the carpal ROI analysis, including carpal bone segmentation, feature extraction and fuzzy classification for bone age assessment. The segmentation and CAD bone age results are presented in this section.

A. Segmentation success rate

Due to the reasons described in section 1, phalangeal ROI segmentation is not reliable for young children. The comparison of the bone age assessment results for both female and male using phalangeal versus phalangeal and carpal features together are shown in Figure 16. The striped bars show the percentage of successfully processed cases with phalangeal ROI only. However, after carpal ROI analysis was included, the percentage of successfully processed cases (gray bars in Figure 16) was improved significantly especially for age groups from newborn to 3 years. Figure 15 (a) shows the results for female and (b) for male.

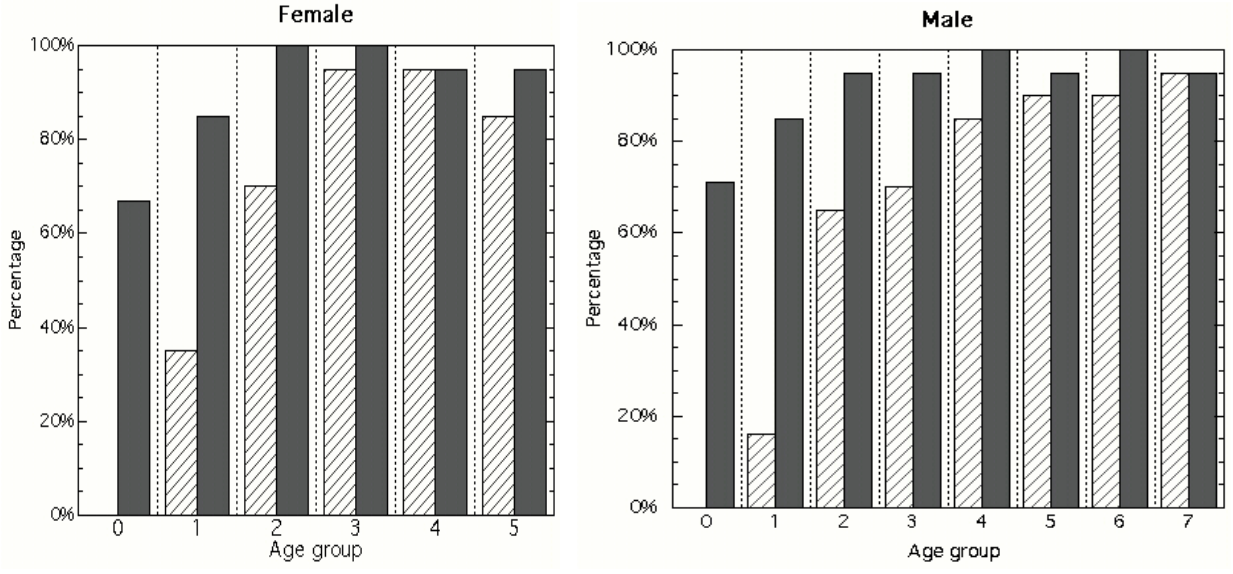

(a) **(b)**

Figure 16. Percentage of successfully processed cases of all four races. Striped bars represent the percentage for phalangeal ROI analysis only and gray bars stand for the percentage after the inclusion of carpal ROI. (a) is for female of 6 age groups from 0 to 5, (b) is for male of 8 age groups from 0 to 7.

The results show that the percentage of success rate is close to 100 percent at age above 2 years old. For case below 2 years, the success rate is about 80 percent. This is due to the general poor contrast of hand images for young children because of the low bone density and thick soft tissue. It leads to the difficulty in segmenting the carpal bones from background. This could be improved by using adaptive diffusion parameters based on the contrast of individual carpal ROI image and will be considered for future work.

B. Plots

The CAD results based on carpal ROI were compared with the average reading of two radiologists. Figure 17 shows the results set for eight categories from test 1. Figure 18 is the results set for two categories from test 2. Figure 19 is for the universal category from test 3. The CAD results generally follow the average reading of two radiologists comparing with the chronological age.

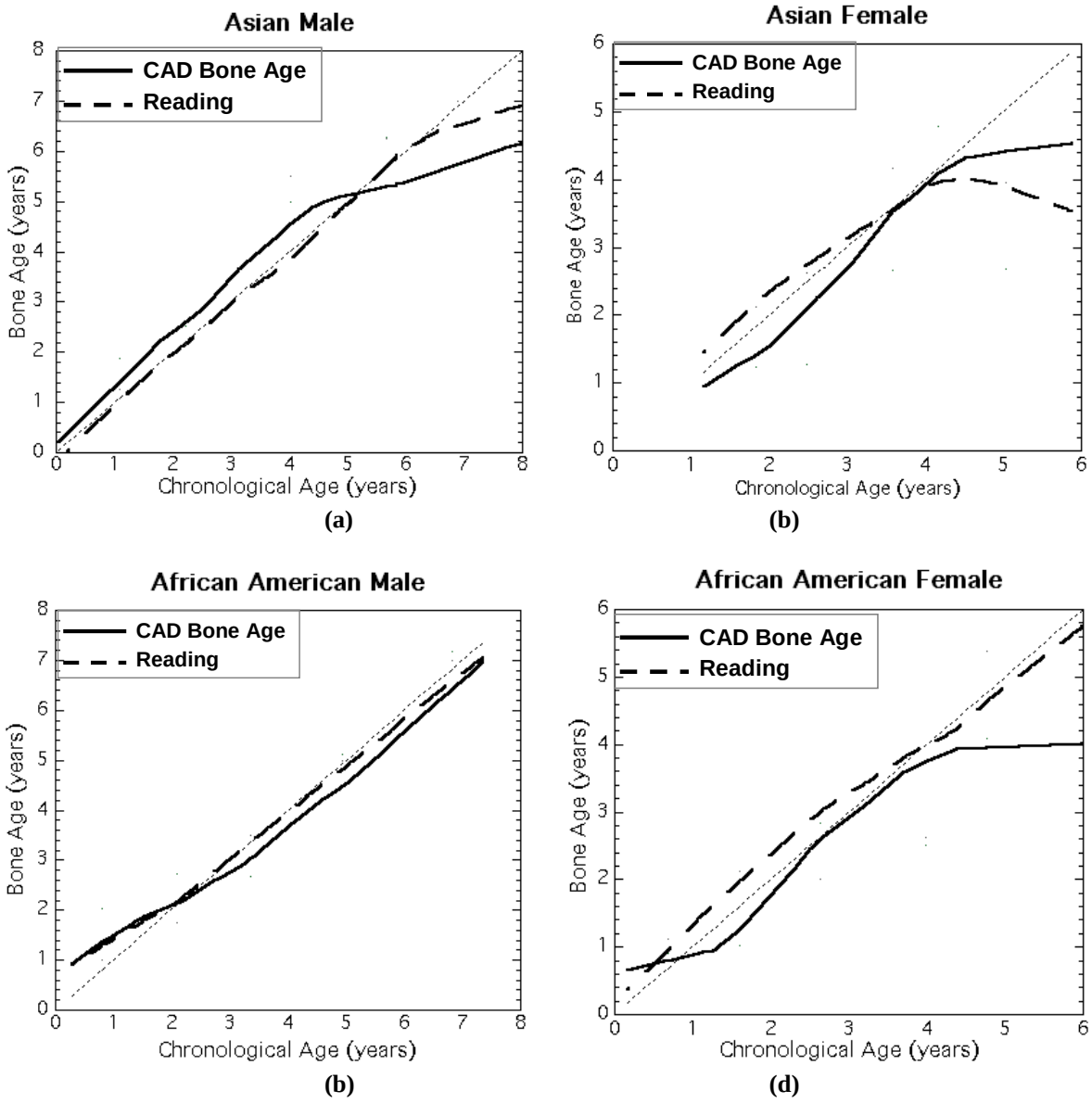

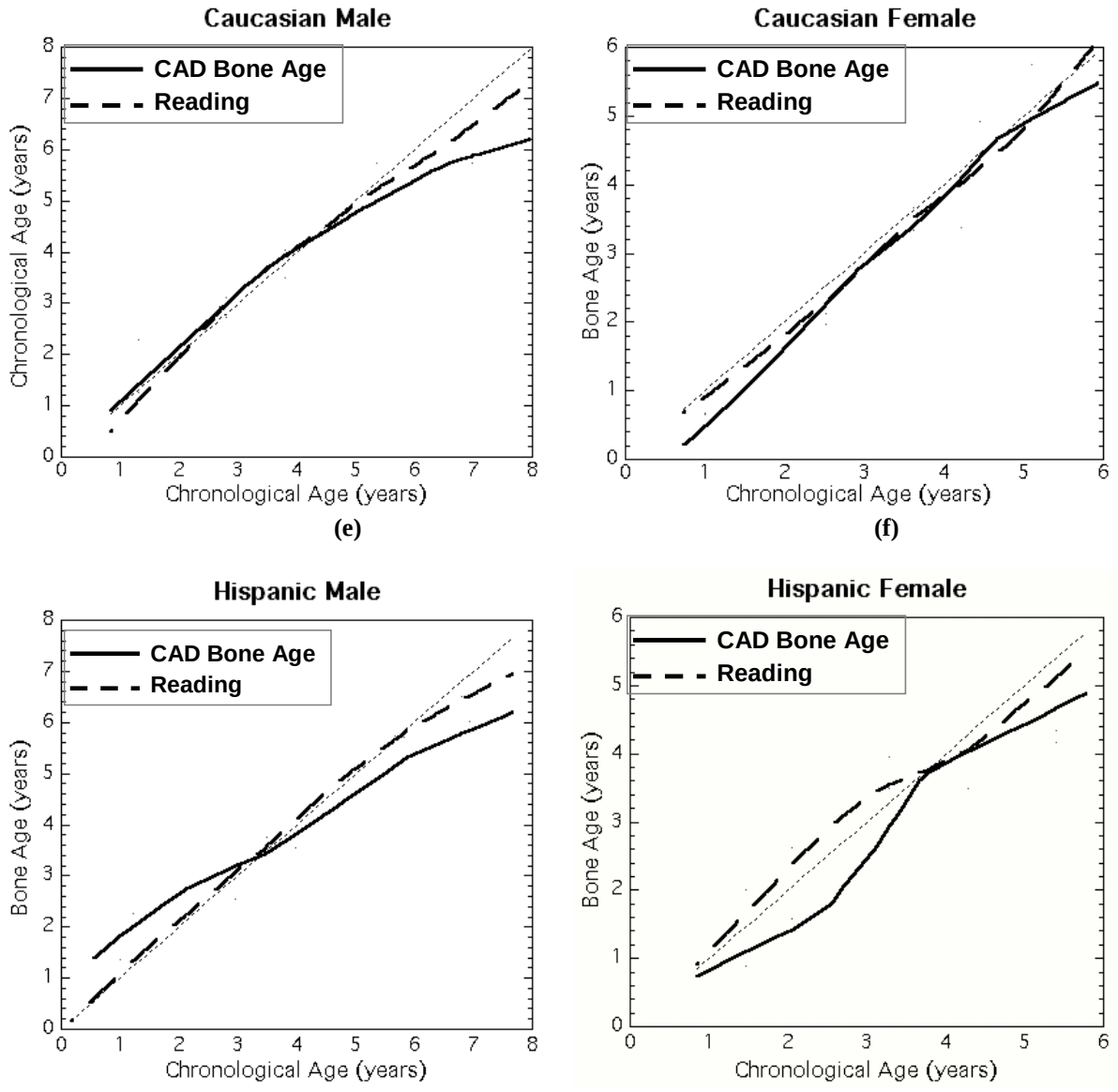

Figure 17. Results from the test with race and gender separated. In each plot, the solid line represents the CAD results and dashed line represents the average reading of two radiologists. See Section IV Discussion for discrepancies

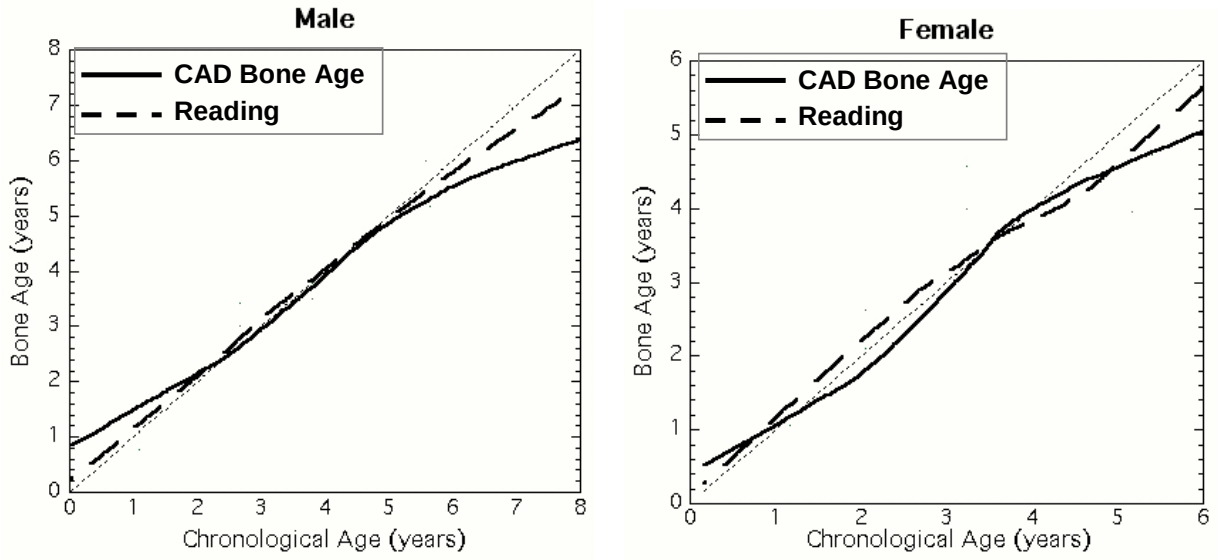

(a) **(b**

Figure 18. Results from the test for two genders with four races combined. In each plot, the solid line represents the CAD results and dashed line represents the average reading of two radiologists. See Section IV Discussion for discrepancies

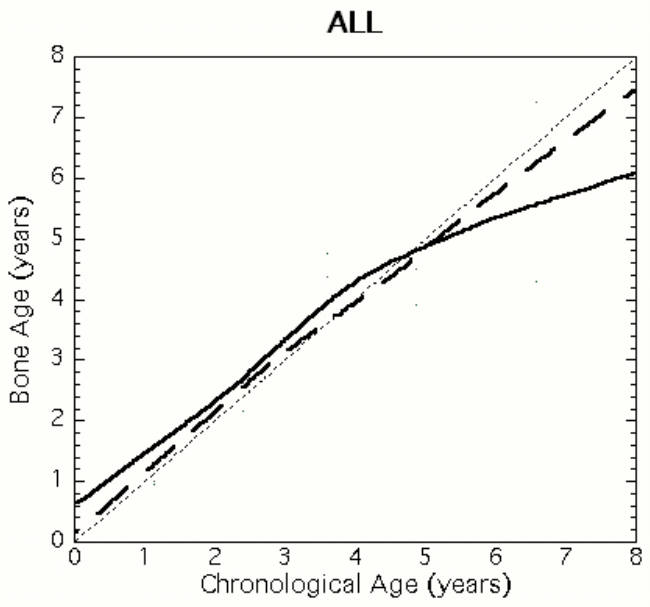

Figure 19. Results from the test for one universal category with both races and genders combined. In this plot, the solid line represents the CAD results and dashed line represents the average reading of two radiologists. See Section IV Discussion for discrepancies

C. CAD evaluation

Paired-samples *t*-test for the above three tests was performed against chronological age for two readings and CAD result. The following tables show the mean difference between reading 1, reading 2 and CAD result versus chronological age. The number with asterisk represents the difference is significant at p-value < .05.

Table 3. CAD evaluation for test 1 with races and genders separated. Significant mean difference (in year) is indicated by an asterisk.

	Asian		African American		Caucasian		Hispanic	
	Female	Male	Female	Male	Female	Male	Female	Male
Reading 1	.19	-.05	-.08	-.13	.12	.02	.07	-.04
Reading 2	.19	.23	.01	-.03	.14	.25*	-.11	.08
CAD BA	.46*	.16	.27	.12	.28*	.20	.36*	.20
No. of Cases	**21**	**28**	**21**	**30**	**22**	**34**	**22**	**27**

Table 4 CAD evaluation for test 2 with two genders, each gender is combined with four races, and test 3 has only one universal category. Significant mean difference (in year) is indicated by an asterisk

	Test 2		Test 3
	Female	Male	
Reading 1	.08	-.05	.00
Reading 1	.06	.13*	.10*
CAD BA	.25*	.20*	.01
No. of Cases	**86**	**118**	**204**

From the evaluation Tables 3 and 4, we can see that the CAD result based on carpal ROI analysis is comparable to the readings within the mean difference of half year.

IV. DISCUSSION AND CONCLUSION

A method of carpal ROI determination, carpal bones segmentation, feature extraction and fuzzy classification for bone age assessment was developed and tested on the 205 young children from the data collection in the digital hand atlas (see Introduction). The percentage of successfully processed cases was improved significantly over the one with phalangeal ROI analysis only. This demonstrates that the feature extraction of carpal ROI is reliable for young children. (Third column, first row of Table 1)

The CAD results by fuzzy classification were evaluated by comparison with readings and chronological age. The CAD results shown in Section III.B based on carpal ROI features follow the readings comparing with chronological age, with the verification from statistical analysis in III.C. The results verified the value of carpal ROI in assessment of skeletal development for young children.

Furthermore, carpal ROI has advantages over phalangeal ROI in bone age assessment for young children in that the appearance of carpal ROI in the radiograph is not influenced by finger bend

and hand rotation during acquisition. This happens frequently since straight fingers and upright position of the hand is hard to achieve in young children.
However, a general observation could be drawn from the curves of Figure 16, 17 and 18, that the CAD results have large discrepancy to the chronological age after age of 5.50 for male and 4 for female. This phenomenon appears in radiologists readings also. The possible reason is that after this point, the growth of Capitate and Hamate slow down and carpal ROI does not reflect very accurate information. The other bones which appear later than Capitate and Hamate, identified by the knowledge-based model (Figure 10) could be taken into consideration to improve the accuracy for these age groups by augmentation of feature space for bone age assessment.
The diverse growth patterns in different race and gender were observed from curves of average reading of radiologists shown in Figure 16. This justifies that it is necessary to distinguish the race in bone age assessment. Two evaluations of two readings in Table 3 and 4 show the inter-observer discrepancy between two radiologists on the same data collection.
The CAD bone age based on carpal ROI could be integrated with phalangeal ROI to provide more accurate bone age assessment. With up-to-date data collection and objective and fully automatic bone age assessment, the CAD system integrated with PACS [19] could provide the radiologists second opinion and help improve the accuracy in clinical practice.

Acknowledgements

This work has been supported by NIH R01 EB 00298.

References

1. Tanner JM, Healy MJR, Goldstein H, Cameron N, *Assessment of Skeletal Maturity and Prediction of Adult Height (TW3 Method)*, WB Saunders, London, 2001.
2. Kirks D, *Practical Pediatric Imaging, Diagnostic Radiology of Infants and Children*, (Little, Brown & Company, Boston/Toronto), 1st ed., 1984, chap. 6, pp. 198-201.
3. Greulich WW, Pyle SI, Radiographic Atlas of Skeletal Development of Hand Wrist. Stanford CA. Stanford University Press, 1959.
4. Pietka E, Gertych A, Pospiech S, Cao F, Huang HK, Gilsanz V, Computer *Assisted Bone Age Assessment: Image Processing and Epiphyseal/Metaphyseal ROI Extraction*, IEEE Trans. Medical Imaging, 20, 715-729, 2001.
5. Pietka E, Pospiech S, Gertych A, Cao F, *Integration of Computer Assisted Bone Age Assessment with Clinical PACS*, Computerized Medical Imaging and Graphics, 1-12, 2002.
6. Cao F, Huang HK, Pietka E, Gilsanz V, *Digital Hand Atlas and Web-based Bone Age Assessment: System* Design and Implementation, Computerized Medical Imaging and Graphics, 297-307, 2000.
7. Zhang A, et al. *Data Mining for Average Images in a Digital Hand Atlas*. Proceedings of SPIE Medical Imaging, Vol. 5371, pp. 251-258, February 2004.
8. Huang HK, Zhang A, Liu B, Zhou Z, Documet J, King N, Chan WC, *Data Grid for Large-Scale Medical Image Archive and Analysis*. Proceedings of the 13th ACM International Conference on Multimedia, pp. 1005-1013, 2005.
9. Johnston FE, Jahina SB: *The contribution of the carpal bones to the assessment of skeletal age*. Am. J. Phys. Anthrop., 1965, 23, 349-354.
10. Pietka E, Kaabi L, Kuo ML, Huang HK, *Feature extraction in carpal-bone analysis*, IEEE transaction on medical imaging, Vol. 12, No.1, Mar 1993.

11. Zhang A, Gertych A, Liu B, Huang HK, Pospiech S, *Carpal Bone Segmentation and Features Analysis in Bone Age Assessment of Children*. Proceedings of RSNA Conference, Chicago, pp. 688, 2005.
12. Perona P, Malik J, *Scale-space and edge detection using anisotropic diffusion*, PAMI 12(7), pp. 629-639, 1990.
13. Canny JF, *Finding edges and lines in images*, Master thesis, Massachusetts Institute of Technology, 1983.
14. Canny JF, *A computational approach to edge detection*, IEEE transaction PAMI, Vol. 8(6), p. 679, 1986.
15. Ross TJ, *Fuzzy Logic with Engineering Applications,* 2nd edition, John Wiley & Sons Ltd, England, 2004
16. Zadeh LA, *Fuzzy sets*, Information and Control, Vol. 8, pp. 338-353, 1965
17. Zadeh LA, *Fuzzy Logic*, Computer, Vol. 1, No. 4, pp. 83-93, 1988.
18. Zadeh LA, *Knowledge representation in fuzzy logic*, IEEE Transactions on Knowledge and Data Engineering, Vol. 1, pp. 89-100, 1989.
19. Huang HK, *PACS and Imaging Informatics*: Basic Principles and Applications, Wiley & Sons, NJ, 2004, p. 504-507.

Journal of High Speed Networks 00 (2006) 1–16
IOS Press

International Internet2 connectivity and performance in medical imaging applications: Bridging the Americas to Asia

Brent J. Liu [a,*], Zheng Zhou [a], Marco A. Gutierrez [b], Jorge Documet [a], Lawrence Chan [c] and H.K. Huang [a]

[a] *Image Processing and Informatics (IPI) Laboratory, Department of Radiology, University of Southern California, USA*
[b] *InCor, University of São Paulo, São Paulo, Brazil*
[c] *Hong Kong Polytechnic University, Hong Kong*

Abstract. Internet-2 is an advanced high-speed computer network, which has been widely used for medical imaging applications such as teleradiology and teleconsultation. Internet-2 can fulfill the requirements for high-speed data transmission and short turn-around time with low operation cost once installed. However, high performance may not necessarily be retained for global access from international network peers as well as commercial Internet Service Provider (ISP) solutions. This paper describes the methodology of establishing international Internet-2 connections between three different internationally linked sites: the Imaging Processing and Informatics (IPI) Laboratory, University of Southern California, Los Angeles, California; the Hong Kong Polytechnic University (PolyU), Hong Kong, and the Heart Institute (InCor) of the University of São Paulo, Brazil. Two major factors will be discussed including network looping in the US and bottleneck of the connection, raising the round-trip time and limiting the available bandwidth respectively.

In addition to the three site International Internet2 Connectivity, a consistent and repeatable tuning protocol for international Internet2 applications in the clinical environment will be presented. The experimental results of the FTP and DICOM transmission using the automatic tuning protocol at both sending and receiving sites will be presented and compared with results for the combinations where this protocol is used at either one site only or no site at all in order to demonstrate the improvement in overall network throughput by this proposed tuning method. These performance numbers will also be compared to commercially available ISP connections to further show the differences between International Internet-2 and its ability to support medical imaging applications.

Keywords: International Internet-2 connectivity, research networks, bandwidth, automatic tuning protocol, PACS, DICOM compliance

1. Introduction

1.1. Background

Internet2 is an advanced high-speed computer network technology supported by high-performance gigabit backbones and isolated from the commercial transmission loads of the public Internet. The University Corporation for Advanced Internet Development (UCAID), Internet2 consortium led by US universities in partnership with the industry and government, was established to develop, deploy, and regulate advanced network applications and technologies based on the Internet2 platform [1,3,5]. To date, over 200 research universities and laboratories in North America are connected by Internet2. Because of its high bandwidth, low latency, and low operating cost, Internet2 provides a proving ground for new technology standards and applications such as IPv6, Quality of Service

*Corresponding author.

(QoS), Multicast, and Network Security. For example, Abilene is one of the major high performance backbones of Internet2 and currently supports a bandwidth of 10 Gigabits-per-second (Gbps) with about a 50 millisecond (ms) round-trip response time across the US. Because of these examples of performance numbers and key features, Internet2 provides a solution for high-bandwidth applications such as medical imaging, which is currently not available with the public Internet in terms of data transmission, streaming, security, etc., for many academic and research disciplines.

1.2. Medical imaging

Medical imaging applications include large-volume transmission of images for tele-imaging consultation. These applications require advanced network facilities with high network throughput, short response time, low operating cost, and security assurance. Examples of medical imaging applications include teleconsultation [17,18], teleconferencing with remote medical image presentation [19] and image-assisted surgery/therapy [20] all which require a network connection with higher bandwidth and lower latency to facilitate synchronization at remote sites. A previous study showed that key features of Internet2 can fulfill all these requirements when it was demonstrated that it takes less than 80 seconds to transmit a set of 40 Computed Tomography (CT) images from Los Angeles to Washington DC as well as facilitate more than 10 cursor movements per second for synchronized image manipulation between these two remote sites [2]. Though Internet2 technology is ideal for medical imaging applications in the US, it is not easy to utilize and access Internet2 globally. This international partnership is a way for non-US research and education institutions around the world to join the Internet2 consortium.

1.3. Internet-2 Connectivity between USA and Asia

Previous work has been performed in establishing Internet2 connectivity between the Imaging Processing and Informatics (IPI) Laboratory, University of Southern California (USC) and the Hong Kong Polytechnic University (PolyU), Hong Kong to demonstrate the feasibility of medical imaging applications across the Pacific Ocean [2]. The Hong Kong Polytechnic University (PolyU) is one of eight tertiary institutions in Hong Kong which is able to utilize Internet2. PolyU has been performing collaborative research on its applications with other institutions in the US since October 2002. For instance, the international Internet2 connection has been used for daily medical image exchange between IPI and PolyU. During the *88th Annual Meeting of the Radiological Society of North America (RSNA)*, November 28 to December 3, 2002, PolyU participated as an international site in the demonstration of end-to-end performance using Internet2, yielding 1.5 Megabit-per-second (Mbps) throughput [11]. Similar performance was also demonstrated in the Internet2 Fall 2002 Member Meeting at USC. In October 2003, a multiple end-point video-teleconference connecting PolyU, Hospital Authority in Hong Kong, University of Hawaii and University of Pittsburgh was successfully held [1].

1.4. Internet-2 Connectivity between the Americas and Asia

In this paper, we present research work performed to extend the USC and PolyU Internet2 connectivity to include South America thus forming a three site international Internet2 collaboration linking the Americas with Asia. This infrastructure can ultimately support larger global medical imaging applications such as a worldwide data storage grid for storing and distributing clinical images [24]. The third site to demonstrate this three site International Internet2 collaboration is the Heart Institute of the University of São Paulo, Brazil. The Heart Institute, or Instituto do Coração (InCor), part of the Clinical Hospital Complex of the Faculty of Medicine of the University of São Paulo, is one of the world's largest hospital in cardiology care, education, and research. Each year, InCor receives approximately 260 000 outpatients, 12 000 inpatients, performs 4500 surgeries, 170 000 image diagnosis and 2 million diagnostic tests. Approximately, 80% of InCor's services are dedicated to patients whose treatment is funded by the National Health System. InCor also receives patients from others countries in Latin America and Africa. In 1999, InCor was the first Brazilian hospital to be connected to the Brazilian National Academic backbone

(RNP2), a high performance infrastructure for communication and collaboration among educational and research institutions and a test bed for the development of advanced network applications and technology. Professor Marco A. Gutierrez of University of São Paulo was a visiting Distinguished Research Fellow at IPI from January to April, 2006 when some of the experimental set up between USC and InCor, and data collection took place.

In addition to the three sites International Internet2 Connectivity, a consistent and repeatable tuning protocol for international Internet2 applications in the clinical environment will be presented. The experimental results of the non-DICOM and DICOM transmission using the automatic tuning protocol at both sending and receiving sites will be presented and compared with results for the combinations where this protocol is used at either one site only or no site at all in order to demonstrate the improvement in overall network throughput by this proposed tuning method.

2. Methods

2.1. Connectivity

2.1.1. US Internet2 connectivity and IPI, USC

In 1995, MCI/Worldcom ran the first Internet2 backbone, vBNS ($v$ery high performance Backbone Network Service) with the support of National Science Foundation (NSF). Under the development by UCAID in partnership with Qwest Communication, Nortel and Cisco Systems in 1999, Abilene became the current major backbone of Internet2 [6]. Abilene's performance bandwidth of mostly 10 Gbps and 11 fast response core router nodes interconnect all backbone links. Universities aggregate their connections to Internet2 through GigaPOPs (gigabit point-of-presence) directly through regional backbone networks. GigaPOPs are regional network aggregation points formed by Internet2 member universities to connect to a variety of high performance networks [4]. For example, CalREN-2 (California Research and Education Network) is one of the regional backbones, which is currently using regional optical network (RON) [8,10], a model of facility-based network built with owned assets supported by FiberCo. The network connection topology of CalREN-2 is illustrated in Fig. 1. The bandwidth of CalREN-2 and its uplink to Abilene are 2.4 Gbps and 622 Mbps respectively. Most of the carriers of Abilene have been upgraded to OC-192, i.e., 10 Gbps, except the OC-48 connection between Indianapolis and Atlanta. The Image Processing and Informatics (IPI) Research Laboratory at the University of Southern California is connected to Internet-2 via this calREN-2 network. In addition, IPI is also using a commercial high-speed ISP vendor for other communication applications.

2.1.2. International Internet2 connection: PolyU, Hong Kong

Non-US national research and education networks (NRENs) can peer with Internet2 through international partnership which enables collaboration between US researchers, faculty, students and their overseas counterparts. Internet2 has partnered with over 40 peer-level international organizations and networks. The Hong Kong Academic and Research Network (HARNET) is one such peer-level network. Established in 1985, HARNET has been connecting eight tertiary institutions, including the PolyU, in Hong Kong. The Joint University Computer Centre (JUCC), which is formed by these institutions, is responsible for managing and maintaining the HARNET. In September 2000, the JUCC signed a Memorandum of Understanding (MoU) with the UCAID. Based on this MoU, the tertiary institutions in Hong Kong can use Internet2 for academic and research purposes through advanced applications in a global scale. The peering between the Internet2 backbones and the NRENs is done via the international interconnection points. Figure 2 shows the international interconnection points at Abilene backbone and their corresponding NRENs. StarLight is one of the international interconnection points peering HARNET with Internet2 ("StarLight" and "HARNET": enclosed by rectangles in Fig. 2). As an optical version of StarTAP founded in 1997, StarLight is an advanced optical infrastructure at Chicago, facilitating a global proving ground for network services optimized for high-performance applications [13]. In Hong Kong, Pacific Century Cyber Works (PCCW), an Internet Service Provider (ISP), provides HARNET with routers and an international link between HARNET and StarLight starting October 2002. Due to limited funding support, the international link is a DS-3 connection with only a 45 Mbps bandwidth [2]. One of the international Internet2 connection considered in this paper is the connection between the PolyU and the IPI/USC.

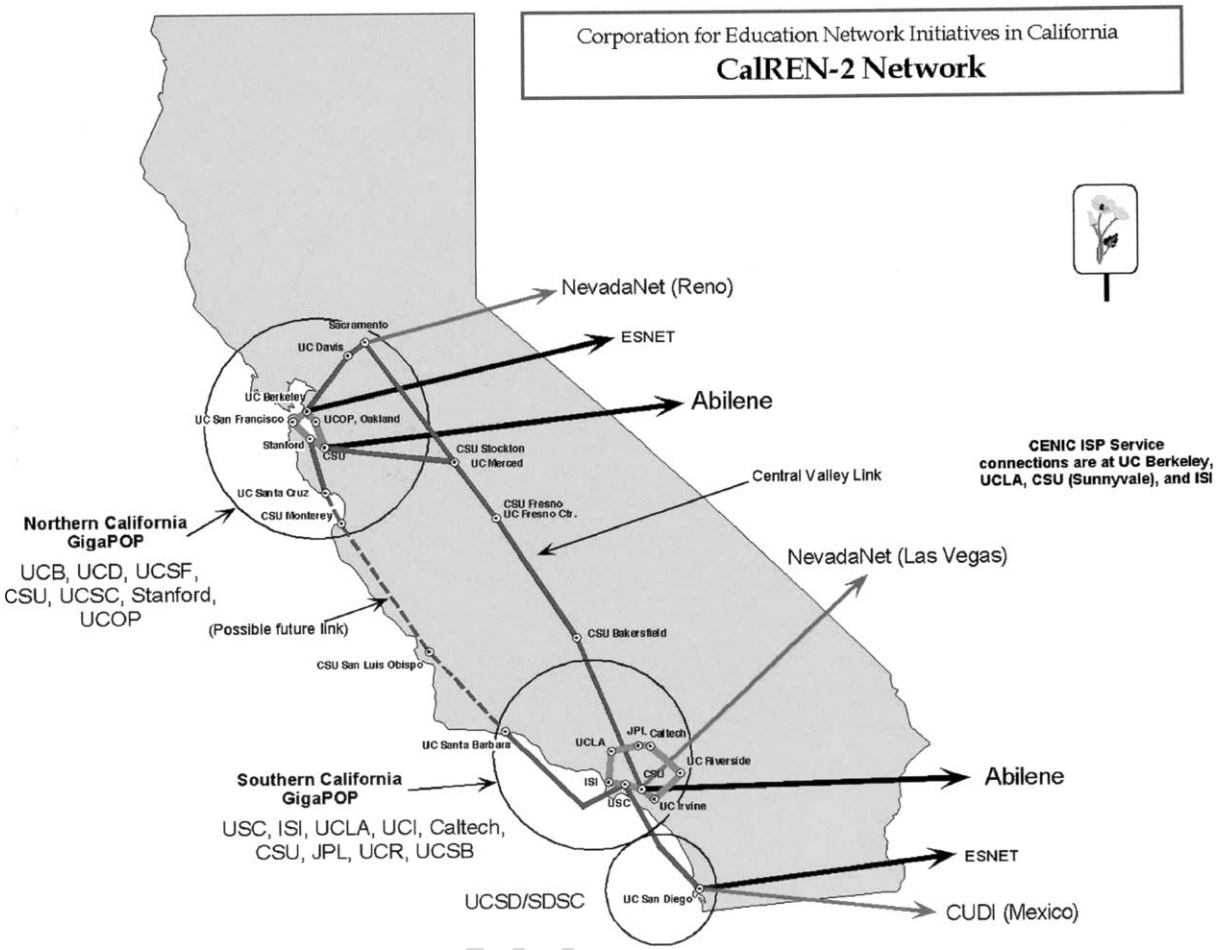

Fig. 1. Network connection topology of CalREN-2 at California. *Courtesy of California Research and Education Network, CalREN2, www.calren2.net.*

2.1.3. International Internet2 connection: InCor, São Paulo, Brazil

The National Education and Research Network, or Rede Nacional de Ensino e Pesquisa (RNP), is the Brazilian infrastructure of advanced network for collaboration and communication in the fields of education and research. Besides connecting all federal institutions of higher education and research, this infrastructure provides a testbed for the experimental development of new applications and network services for the benefit of its users. Also called RNP2 backbone, this infrastructure connects more than 400 Brazilian universities and research centers among them and with foreign institutes making it possible for people and resources to interact through advanced applications. RNP2 maintenance and updates are made by the Inter-ministerial Program of the Ministry of Education and the Ministry of Science and Technology, or Programa Interministerial dos Ministérios da Educação e da Ciência e Tecnologia (PI-MEC/MCT), through a contract signed between the RNP Association and the Ministry of Science and Technology. Besides receiving public resources, RNP, in its condition as a priority computer science program, gathers private resources by means of projects with computer science enterprises and other organizations [21]. In 1999, InCor was the first Brazilian hospital to be connected to the RNP2 backbone. The RNP2 backbone contains 27 points of presence (PoPs) installed in the main cities and capitals in the country. The speed of the connections among the PoPs is up to 10 Gbps using optical technologies (WDM) in the physical layer, ensuring the necessary

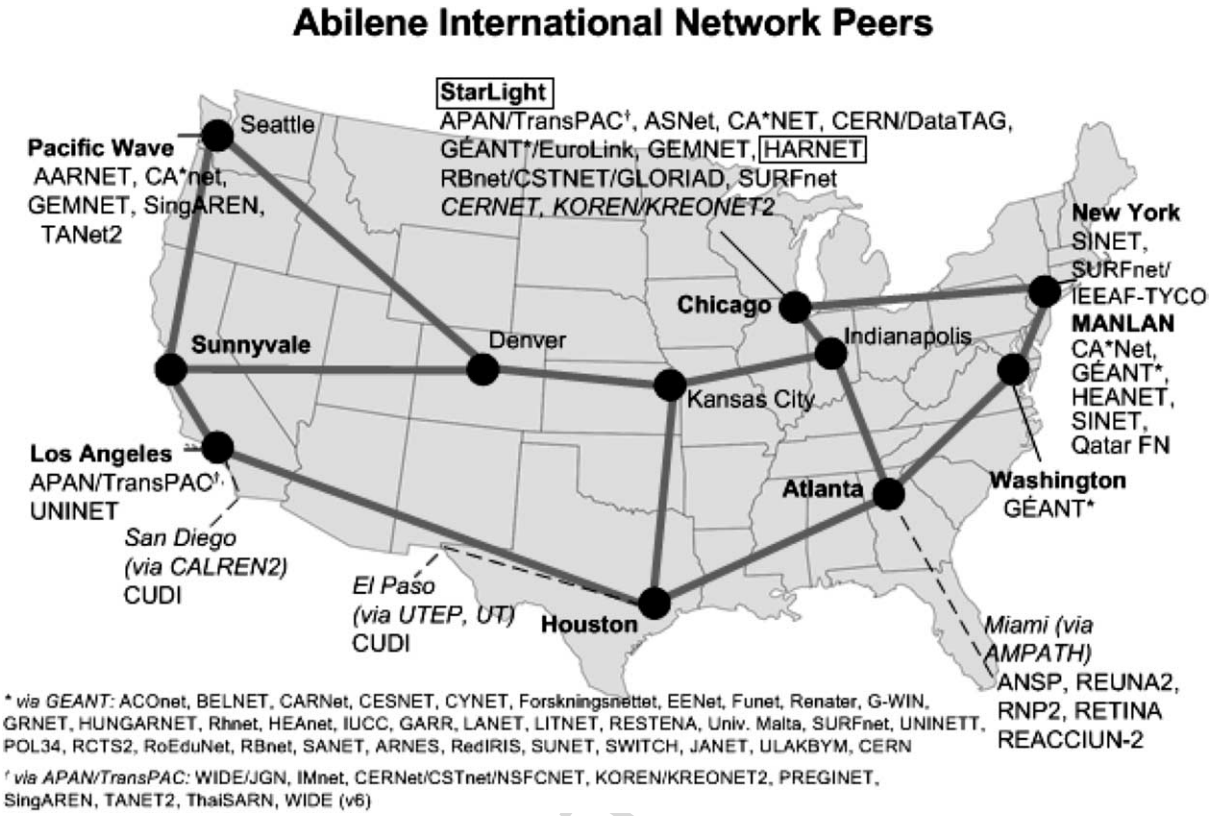

Fig. 2. Major international interconnection points of Internet-2 at Abilene backbone. *Courtesy of Abilene Network, abiline.internet2.edu.*

bandwidth for the use of advanced applications and services and for experimentation. Figure 3 shows the topology of the RNP2 backbone infrastructure.

RNP2 has two international connections of its own. One of them is used for the Internet production traffic, or Internet commodity and has performance of 155 Mbps. The other, also 155 Mbps, is connected to the Latin American Cooperation of Advanced Networks, or Cooperación Latino Americana de Redes Avanzadas (CLARA). CLARA, which was established in June 2003, is a nongovernmental nonprofit organization that can receive income which would be applied to the education, scientific, and cultural activities that constitute CLARA's objectives. In September 2004, RedCLARA began to provide direct connectivity with 155 Mbps linking the NRENs of Argentina, Brazil, Chile, Panama and Mexico, and connecting them to GÉANT, the European Network, at 622 Mbps through a connection between São Paulo, Brazil, and Madrid, Spain. RedCLARA connects more than 700 universities and research centers in Latin America. The backbone of RedCLARA is comprised of five main routing nodes connected in a ring topology. Each main node characterizes a PoP for RedCLARA and is located in a different Latin American Country. The five main IP nodes are located in São Paulo (Brazil), Buenos Aires (Argentina), Santiago (Chile), Panama (Panama), and Tijuana (Mexico). In addition to Géant, RedCLARA has established 1 Gbps connectivity to the North American Internet2 via CalREN2 in San Diego [22]. Figure 4 shows the topology of the CLARA backbone infrastructure, including PoPs, which show the 155 Mbps connection between São Paulo, Brazil and Tijuana, Mexico and then the 1 Gbps connection to Internet2 via the CalREN2 network PoP in San Diego.

2.1.4. Network topology bridging the Americas to Asia

Figure 5 shows the overall routing configuration linking each of the three sites to International Internet2 connectivity: (1) IPI, USC (IPI is a Research Lab at USC); (2) InCor, São Paulo, Brazil; and (3) PolyU, Hong Kong, China. The routing path between InCor to PolyU is slightly different than the routing path from IPI to InCor

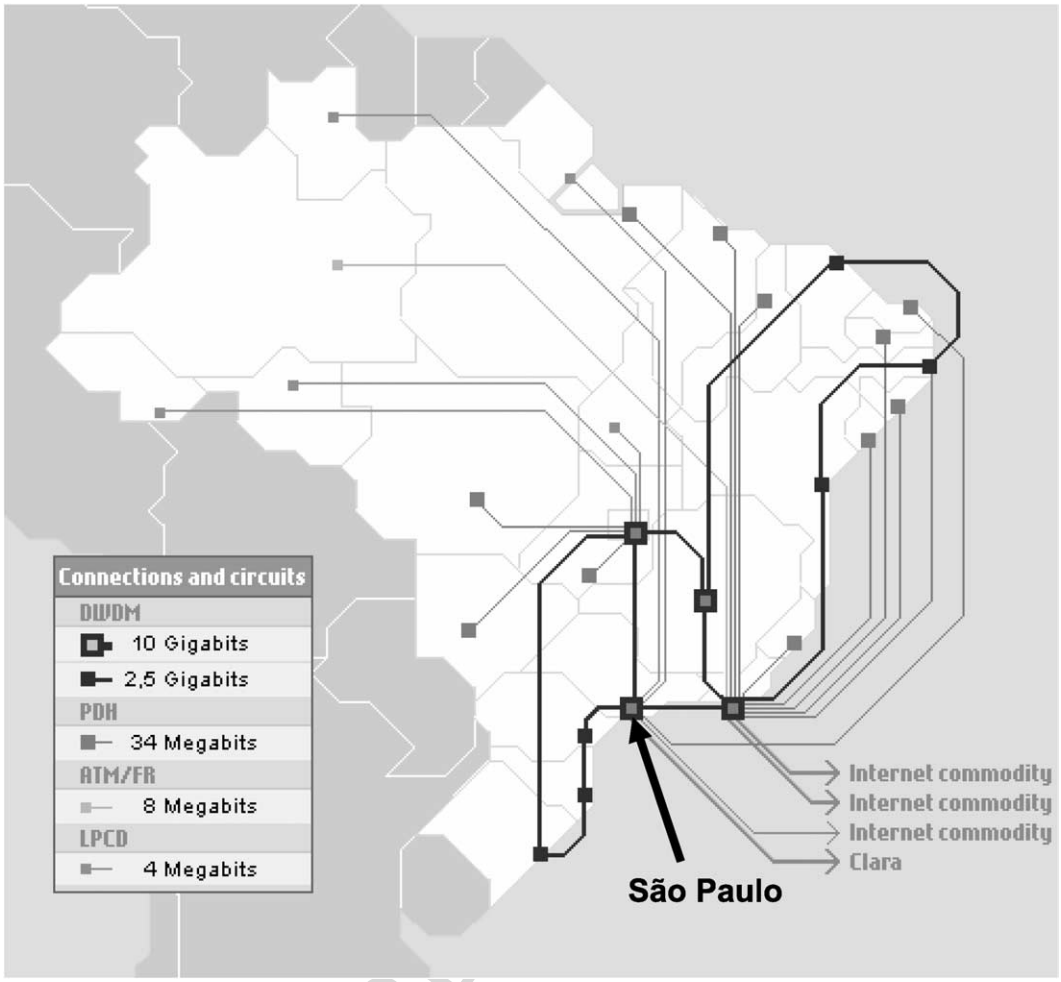

Fig. 3. Topology of the RNP2 backbone with performance bandwidths Points of Presence (PoPs), including São Paulo where InCor is connected. *Courtesy of Rede Nacional de Ensino e Pesquisa, RNP, www.rnp.br.*

which was described in the previous paragraph and utilizes AMPATH to connect to the Abilene network in Miami and onwards to Starlight in Chicago. Florida International University (FIU) has developed an international, high-performance research connection point in Miami, Florida, called AMPATH (AMericasPATH). One of AMPATH's goals is to enable wide-bandwidth digital communications between the Abilene network and ten National Research and Education Networks (NRNs) in South and Central America, the Caribbean and Mexico, as well as a variety of US research programs in the region. Since June 2001, the AMPATH project has connected four National Research and Education Networks in South America: REUNA of Chile, RNP of Brazil, CNTI of Venezuela and RETINA of Argentina; the Academic Network of São Paulo, ANSP, which is a State-funded network; the University of Puerto Rico; New World Symphony; Florida International University; the Arecibo observatory; and the Gemini-South telescope [23].

2.1.5. Commercial high speed ISP connectivity

In addition to Internet-2 Connectivity, IPI also has a high-speed commercial ISP international connectivity service that requires a monthly cost that supports the entire office building where the IPI laboratory resides. Figure 6 shows the topology for the high-speed connectivity between IPI and PolyU as well as between IPI and InCor. For

Fig. 4. Topology of CLARA Network showing performance bandwidths Points of Presence (PoPs) including the 155 Mbps connection between São Paulo, Brazil to Tijuana, Mexico and then the 1 Gbps connection to CalREN2 in San Diego. *Courtesy of Latin American Cooperation of Advanced Networks, redCLARA, www.redclara.net.*

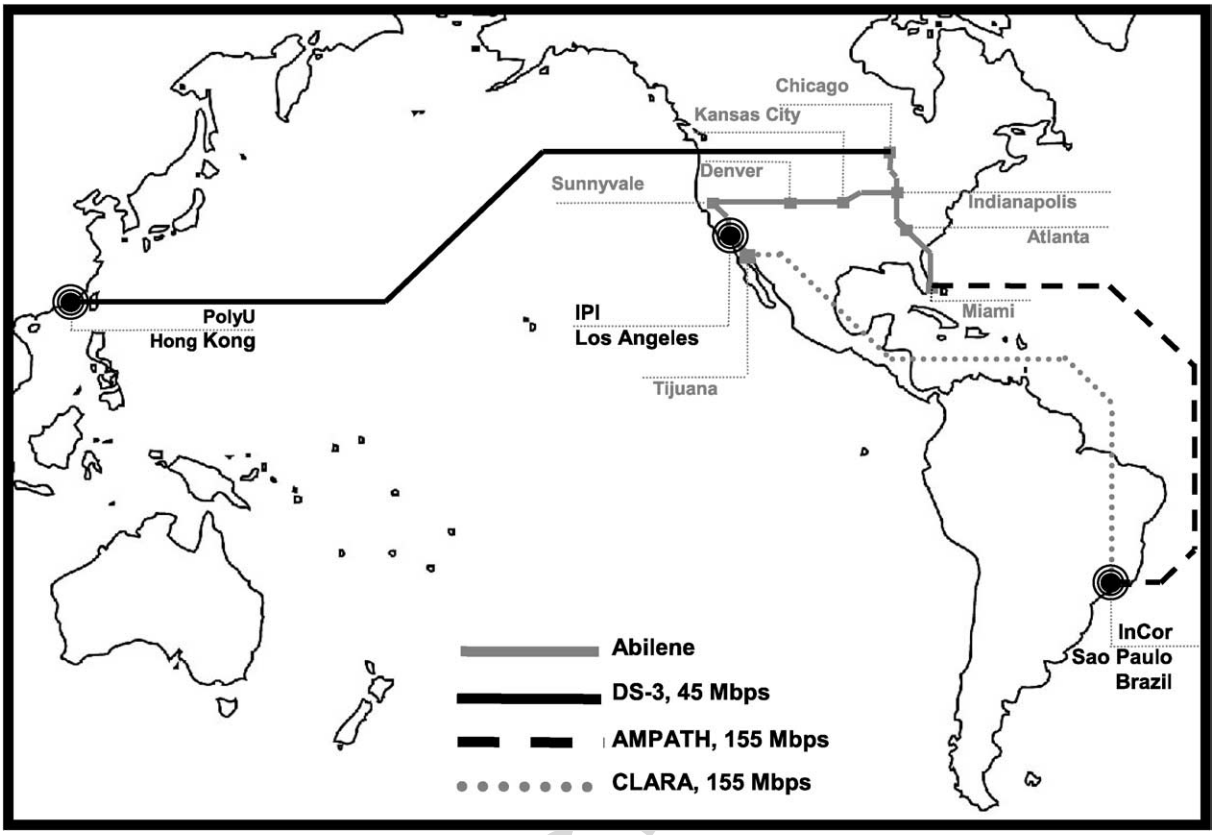

Fig. 5. Topology of the International Internet-2 Connectivity between the Three Test Sites Linking IPI/USC in North America, InCor in South America, and PolyU in Asia. Note that the Routing Path from InCor to PolyU utilizes AMPATH instead of CLARA which is the routing path between IPI and InCor.

the connection between IPI and PolyU, the service provider is Flagtelecom [25] with Points of Presence (PoPs) located in Tokyo and Hong Kong. From the Hong Kong PoP, the network connects to PolyU via the commercial Internet. For the connection between IPI and InCor, the service providers are Verio and Globalcrossing [26,27] with PoPs in Phoenix, Miami, and São Paulo. From the São Paulo PoP, the network connects to the commercial link of the RNP network and directly to InCor.

2.2. Limitations on performance of international high-speed connectivity

Global access to Internet2 does not necessarily guarantee the same level of high performance of Internet2 in North America. This is due in part with the performance of the international Internet2 connection as well as the topology of its routing path. There are three major issues regarding the degradation of network performance: (1) Network looping in the US; (2) Bottleneck of connection; and (3) Asymmetric hardware configurations. Only the first two issues exist when considering the international high-speed connection.

2.2.1. Network looping in the US

The cross-Pacific DS-3 connection, Abilene and CalREN-2 all form a physical network looping across the US continent. It is mainly caused by the StarLight global interconnection point of Internet2 located in Chicago. If alternative interconnection points were utilized it is possible that looping could be avoided. The total distance of the routing path between the PolyU and the IPI/USC is 16613 km. If the interconnection point *Los Angeles*

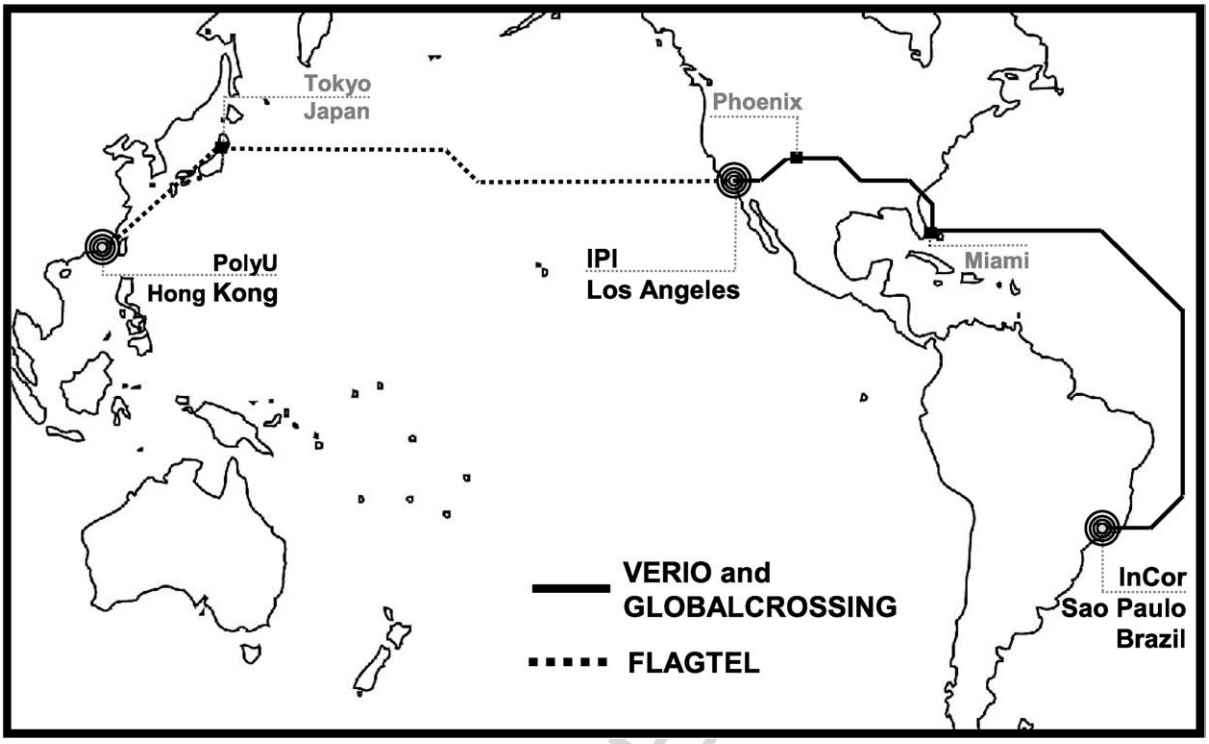

Fig. 6. Topology of the Commerical High-Speed ISP Connectivity between IPI and PolyU, and IPI and InCor. Flagtel is the ISP vendor connecting IPI to Hong Kong with Points of Presence (PoPs) in Tokyo and Hong Kong. Verio and Globalcrossing are the ISP vendors connecting IPI to InCor with POPs in Phoenix, Miami, and São Paulo, Brazil.

were chosen, the total distance would be less than 11 680 km. This implies that the network looping produces an unnecessary increase in the routing path by about 4933 km. According to the fact that the traveling speed of any signal is limited by speed of light in a vacuum, the least round-trip response time is proportional to the distance of route [2]. Thus the longer the routing path we have, the longer the round-trip response time we get. Though there exists the trade-off between cost and performance of the cross-Pacific connection, the choice of interconnection point has a distinct effect on the performance of international high-speed connectivity.

2.2.2. *Bottlenecks of international high-speed connectivity*

As an example between PolyU and IPI, the first two connection are the cross-Pacific link and the HARNET ATM network which both have only 45 Mbps bandwidth only. Therefore, the overall throughput is also bounded by this 45 Mbps throughput. The TCP/IP communication protocol provides the sending and receiving computers with a number of parameters for data transmission, in which TCP window buffer size accounts for the amount of unacknowledged data in the flight between the sender and the receiver in the computer network. Round-trip response time is defined as the weighted average time for one complete cycle of a send and acknowledgement receipt for a single data segment between the sender and the receiver in the computer network. The greatest throughput is equal to the buffer size divided by the round-trip response time [2]. The default TCP window buffer size of most operating systems is 64 kB, i.e., 512 kbits. Given the example of the round-trip response time of the connection between InCor and PolyU is 424 ms, if the default TCP/IP settings are used in both sending and receiving, the greatest throughput in this case will be 1.2 Mbps only and the utilization of available bandwidth is less than 3%. Even though there exists a bottleneck, a clinical protocol for tuning the TCP/IP parameters, such as this TCP window buffer size, will be derived in Section 3 to improve the bandwidth performance.

2.2.3. Computer performances at sending and receiving ends

In addition to latency and bandwidth of the carriers, the network throughput is also determined by the maximum memory capacity of the slowest computer amongst the sender and the receiver [15]. If the capacity of the sending or receiving computer is low, the throughput will be confined to the performance of the computer with lowest capacity. Therefore, hardware configurations of both sending and receiving computers are required to be similar and at high-end technology.

2.3. Clinical protocol for tuning high-speed network performance

Supported by the National Science Foundation (NSF), the Web100 project is a joint effort between the Pittsburgh Supercomputing Center (PSC), the National Center for Atmospheric Research (NCAR), and the National Center for Supercomputing Applications (NCSA), providing tuning software and monitoring and system diagnostic tools necessary for computer end-users to automatically and transparently achieve high bandwidth data rates over high performance research networks, such as Internet2 [12]. The installation and implementation of the Web100 software and tools requires expert attention from the network engineers which is more challenging in a clinical environment where this expertise is not readily available. The PACS team and Information Technology Services (ITS) of the PolyU and the IPI/USC have jointly developed a repeatable and consistent clinical protocol for implementing the Web100 tuning method, which will be described in the following sub-sections [2]. This method was utilized to tune all 3 internationally linked sites.

2.3.1. Web100 tuning method

The Web100 project enables ordinary network users to attain full network data rates without the frequent assistance from network experts, and to develop the software components necessary for a high performance network host software environment. Web100 software consists of a TCP Kernel Instrument set (TCP-KIS), Derived Instrument Set (DIS) and application code. TPC-KIS represents instruments coded directly in to the operating system kernel. DIS is the information collected based on the KIS parameters. The application code includes tools and applications that use the information provided by the KIS and DIS. These three components are aimed at enhancing the TCP/IP parameters with better kernel instrumentation and automatic controls.

2.3.2. Implementation into the three international sites

Web100 software optimizes automatically the network throughput by applying a patch to the operating system kernels at both the sending and receiving computers. The deployment of the patch can take some time to deploy on a new and reliable computer. The patch is installed to the kernel, which is the core of the operating system but not simply an individual application only. Moreover, the deployment and setting of the Web100 method should be the same at both connecting peers. With the added challenges of various hardware from three different sites as well as the large physical distances spanning each site, greater and tighter coordination is needed to both identify resources as well as hardware that can produce the best results. Since the Web100 method requires applying a patch to the operating system kernels, the performance numbers acquired by both tuned and untuned sending and receiving hardware had to be executed on different machines.

To alleviate some of these problems, a successfully patched and stable Linux system is completely migrated to the setup disks. The setup disks are required to be compatible to a wide range of computer hardware configurations, so that the tuning protocol embedded with Linux kernel can be easily duplicated to other computers in the network. Furthermore, the automatic tuning protocol is seamlessly embedded with the kernel of the computer and thus the end-users, such as the radiologists and the physicians, will not recognize any changes in the system. In case the operating system crashes, it is also very easy to deploy this embedded tuning protocol again. When both the connecting peers have comparably high performance hardware configurations, symmetric software and hardware configurations to optimize the capacity of the network connection can be achieved. To verify the feasibility of this protocol, an experiment was performed to obtain the network performances when this protocol is deployed at IPI/USC, PolyU, and InCor.

3. Experimental methodology

In this paper, DICOM image transmissions are considered in the experiments. Since DICOM is the de facto standard for Medical Imaging Applications, testing was performed simulating real world clinical applications by utilizing the DICOM image transmission protocol [7].

Hardware and software specifications

At IPI/USC,

Computer hardware configuration is:

Model:	Dell Optilex GX 270.
Processor:	Intel® Pentium® 4, 2.8 GHz
Memory:	512 MB RAM
Hard disk:	40 GB hardware
Network adapter:	1 Gbps network Card

At PolyU,

Computer hardware configuration is:

Model:	Dell LATITUDE C840
Processor:	Intel® Pentium® 4 Mobile CPU 1.6 GHz
Memory:	512 MB RAM
Hard disk:	Hitachi DK23FB-20, 20 GB
Network adapter:	3Com 3C920 Integrated Fast Ethernet Controller 100 Mbps

At InCor,

Computer hardware configuration is:

Model:	IBM ThinkCentre M50
Processor:	Intel Pentium IB, 2.8 GHz
Memory:	1 GB RAM
Hard disk:	Western Digital WD400BB-23FJA0, 80 GB
Network adapter:	IBM 82541EI Gigabit Ethernet

At All Three Sites,

Software configuration is:

Operating system:	Linux 2.4.24 RedHat 8 i386 (@ IPI, PolyU) and Linux 2.6.15 SuSe 9.2 (@ InCor)
Desktop Environment:	GNOME (@IPI, PolyU) and KDE (@InCor)
FTP Server:	"anonftp" and "vsftpd"
DICOM components:	DICOM "send" and "receive"
Tuning software:	Web100 release 2.3.4 for Linux 2.4.* kernels (@IPI, PolyU) and Web100 release 2.5.8 for Linux 2.6.15 (@ InCor)
GUI tools:	Web100 Userland alpha 1.3

TCP/IP tuning parameters

Due to the transaction overhead at the routers and the application layers of sender and receiver, we assume that there is 12% IP and transaction overhead for the high-speed connections. For example,

Between IPI and PolyU,

$$\text{Usable bandwidth} = 45\ \text{Mbps} * 0.88 = 39.6\ \text{Mbps} = 4.95\ \text{MB/s}$$

By the definition of bandwidth delay product (BDP) [15,16], we need data sent in window size given by,

Between IPI and PolyU,

$$\text{Maximum window size} = 4.95\ \text{MB/s} * 292\ \text{ms} = 1.4\ \text{MB}$$

to utilize the bandwidth. It is the theoretical TCP send and receive socket buffer sizes that fill up the link in any one time. If it is too small, the TCP congestion windows will never open up fully. If it is too large, the sender can overrun the receiver, and the TCP congestion window will shut down. The Web100 software will automatically tune all the TCP/IP parameters including this TCP window buffer size at all three international peers. Note the maximum window size is an indicator of the maximum size of data segment on-the-fly. If a series of CT images, each in the size of 512 KB, the DICOM image transmission will not take advantage from the 1.4 MB window size since the transmission of images is one-by-one and is limited by the size of the CT image (e.g., 512 KB).

In addition, the maximum amount of data that can be in transit in a TCP connection is the bandwidth delay product of the bottleneck link bandwidth and the Round Trip Time (RTT). It is important to define the amount of buffering that will be required at both the sender and receiver. For routes that have a large BDP, and hence require large buffers, it is necessary to have the high performance tuning enabled. In Linux Kernels 2.4 and 2.6, the maximum buffer sizes for all sockets can be set to enable large buffers. The kernel sets the actual memory limit to twice the requested value to provide sufficient memory overhead. Based on the bottleneck links bandwidth and on the RTT values found during the experiments, the BDP was estimated at 4 MBytes, and the variables were configured in all servers to reflect this condition.

Measuring Protocol

(a) FTP File Transmission

The baseline measurements were taken using standard untuned Linux for all testing sites. The FTP file transmissions are performed in the experiment utilizing a file size of 7.8 MByte. The file was sent both to and from the following two site combinations:

(1) IPI and the USC Health Science Campus (USC/HSC) located approximately 20 miles away
(2) IPI and PolyU
(3) USC/HSC and PolyU
(4) USC/HSC and InCor
(5) InCor and PolyU

(b) DICOM

In the protocol, two sets of medical images were considered to show how the difference in the DICOM image size can impact the performance results.

(i) CR examination, 2 DICOM images, 16.0 MByte
(ii) CT examination, 29 DICOM images, 15.5 MByte

All three site computers, have the DICOM "send" and "receive" components, facilitating the DICOM communication. The images were transmitted between these two computers through the DICOM communication protocol.

(c) Comparison for different experimental settings
This evaluation highlights the impact of the Web100 tuning protocol implemented for sending and receiving sites. Both FTP and DICOM transmission performance numbers were gathered in the same manner as (a) and (b) with the tuning protocol implemented.
(d) Comparison of International Internet-2 Connectivity with Commercial ISP High-Speed Networks.

In addition, the DICOM image transmission protocol mentioned in evaluation (b) was performed utilizing a commercial high-speed ISP connection described in Section 2.1 to compare against the performance measurements for International Internet-2 Connectivity. Measurements were made with both the standard Linux as well as the Web 100 tuning protocol.

4. Experimental results

Table 1 shows the results gathered for all sites utilizing the untuned international Internet-2 with the FTP protocol. From the results a few things can be observed. First, the round trip response time is nearly doubled between IPI to PolyU versus InCor to PolyU. From Fig. 5, we can see that the routing path taken between InCor to PolyU is physically double the distance in comparison to the distance between IPI to PolyU. Thus, the round trip times show that physical distance does have an effect on the network performance.

Second, the untuned performance results reflect a network performance of better than standard T1 connection (e.g., 1.5 Mbits) which is considerably much more desirable when dealing with medical imaging applications. The lowest FTP performance was from PolyU to InCor at 0.630 Mbps and the highest performance being from USC/HSC to PolyU at 2.80 Mbps. It is interesting to note that from IPI to USC/HSC, the FTP performance was extremely high (28 Mbps) and this is naturally to the close proximity between the IPI Laboratory and USC/HSC of approximately 20 miles.

In Table 2, the performance numbers show that the preliminary tuning protocol improved bandwidth performance in each case regardless of whether the data was a CR exam or a CT exam, with the highest values reaching over 9 Mbits/s. These values were almost eight times better than the standard untuned Linux performance numbers. With these types of performance numbers, even distance challenged international sites such as InCor and PolyU are able to adequately utilize the international Internet-2 connectivity for near real-time medical imaging applications in real-time utilizing the DICOM protocol as shown by the tuned performance number of 9.44 Mbps utilizing the DICOM transmission. More research will be performed to gather all the tuned and untuned performance numbers for international Internet-2 connectivity between each of the three international sites.

Table 3 shows performance numbers utilizing high-speed commercial ISP vendor as described in Section 2.1. In addition, to I2 connectivity, IPI also has commercial ISP high-speed connectivity. The same DICOM protocol evaluation methods were performed on this commercial ISP vendor to compare and contrast. This evaluation was not

Table 1

Performance numbers for the different sites connected with international Internet-2. Round trip times (RTT) in milliseconds and **FTP** performance times in Mbits per second were collected. All sites were running standard Linux. File Size used was 7.8 MBytes. Fields marked with an asterisk are previous performance values obtained [2]

To		From IPI	USC/HSC	PolyU	InCor
IPI	FTP (Mbps)	–	28.00*	1.60*	–
	RTT (ms)	–	–	292*	–
USC/HSC	FTP (Mbps)	10.00*	–	1.78	2.65
	RTT (ms)	–	–	253	171
PolyU	FTP (Mbps)	1.60*	2.80	–	1.12
	RTT (ms)	292*	254	–	425
InCor	FTP (Mbps)	–	1.50	0.63	–
	RTT (ms)	–	172	424	–

Table 2

Comparison of performance numbers between sites that utilized the Web100 tuning protocol and the same sites utilizing standard linux (STD Linux) without tuning. Performance numbers were gathered for both **FTP** file transmission as well as for **DICOM** file transmission. Fields marked with an asterisk are previous performance values obtained [2]

From	To	Protocol	STD Linux (Mbps)	Tuned (Mbps)
PolyU	InCor	FTP	0.63	4.40
		DICOM	0.62	9.44
InCor	PolyU	FTP	1.12	3.10
		DICOM	1.50	2.97
PolyU	IPI Lab	FTP	1.63*	9.79*
		DICOM	1.36*	3.06*
IPI Lab	PolyU	FTP	1.60*	9.79*
		DICOM	1.36*	3.06*

Table 3

Performance numbers for IPI connectivity to both PolyU and InCor using a commercial high-speed ISP vendor (see Fig. 6). Round trip times (RTT) were gathered between each of the sites. One CT study of 29 images total data size of 15.5 Mbytes and one CR study of 2 images total data size of 16 Mbytes were used to evaluate the **DICOM** transmission protocol performance between the sites. All performance numbers in MBits per second

From	To	RTT (ms)	CT (29 imgs, 15.5 MBytes)		CR (2 imgs, 16 MBytes)	
			Untuned (Mbps)	Tuned (Mbps)	Untuned (Mbps)	Tuned (Mbps)
IPI	PolyU	187	3.09	12.24	3.16	6.61
PolyU	IPI	187	2.3	17.9	2.23	17.67
IPI	InCor	805	0.957	10.78	0.928	13.84
InCor	IPI	831	1.36	2.6	1.7	3.04

performed between InCor and PolyU since neither site have high-speed commercial ISP connectivity and would rely on standard Internet which has already been documented as inadequate for medical imaging applications. It was observed that for the commercial RTT's, the performance varied greatly with the best performance numbers gathered during the night locally at IPI. This would indicate that the bulk of commercial traffic during the day impacts greatly network performance. However, based on Table 3, the lowest performance numbers with the Web100 tuning protocol were still acceptable for medical imaging applications at 2.6 Mbits/s. The performance numbers of the commercial ISP reach as high as 17 Mbits/s. There are two things that should be considered when comparing between International Internet-2 Connectivity and high-speed commercial ISP connectivity. First is the fluctuation of network performance due to commerce traffic during different times of the day. The RTT's collected for the commercial high-speed network reflect this variability while the International Internet-2 Connectivity was consistent regardless of time of day. Second is the high cost of a commercial high-speed connectivity in comparison to the almost no-cost utilization of International Internet-2 after installation. These two factors must be considered when weighing the performance criteria versus cost. In this case, International Internet-2 connectivity is still the most applicable for medical imaging applications and research.

5. Summary

In summary, international Internet-2 connectivity linking the Americas to Asia was investigated and researched. A three site connectivity was established between IPI, USC; PolyU, Hong Kong; and InCor, Brazil and performance numbers were gathered utilizing the FTP, and DICOM transmission protocol to measure real-world clinical

applications of medical images studies. In addition, a repeatable tuning protocol was applied to the three sites effectively improving the performance by nearly eight times in comparison to the standard configuration. Applications such as teleradiology, and medical image-based clinical trials can be globally linked to sites as far as South America to Asia to establish. The former can facilitate second opinion radiology practice, and the latter can allow a more rich collection of medical imaging data to perform medical imaging and informatics research.

Initial results gathered from the evaluation show that even without tuning, performance bandwidth numbers are comparable to that of a T1 Connection (e.g., 1.5 Mbps) linking two such geographically distant sites as Brazil and Hong Kong. In addition, these performance numbers are comparable to commercially available high-speed ISP's which require a costly monthly service fee and are subject to fluctuations of performance due to e-commerce traffic – both of which are not characteristics of International Internet-2 connectivity. This paper with results gathered from the performance evaluation has shown how three international sites can utilize the International Internet-2 connectivity as well as other non-US research networks as an adequate and acceptable solution for real-time medical imaging informatics research and related applications.

Acknowledgement

This research has been partially supported by NIH Grant R01 LM07606.

References

[1] L.W.C. Chan, F. Cao, M. Zhou and S.K. Hau, Connectivity Issues and Performance Monitoring of International Internet-2 in Tele-Imaging Consultation, Education Exhibit, RSNA, 2003.

[2] L.W.C. Chan, M.Z. Zhou, S.K. Hau, M.Y.Y. Law, F.H. Tang and J. Documet, International Internet-2 performance and automatic tuning protocol for medical imaging applications, *Computerized Medical Imaging and Graphics* **29** (2005), 103–114.

[3] F. Cao, H.K. Huang, M. Zhou, G. Mogel, L. Chan and M. Gill, Internet2 end-to-end performance for medical imaging applications, *J. High Speed Networks* (submitted).

[4] F. Yu, K. Hwang, M. Gill and H.K. Huang, Some connectivity and security issues of NGI in medical imaging applications, *J. High Speed Networks* **9** (2000), 3–13.

[5] Internet2 Consortium, UCAID, http://www.internet2.edu.

[6] Abilene Network, http://abilene.internet2.edu/.

[7] *Digital Imaging and Communications in Medicine (DICOM)*, National Electrical Manufacturers' Association, NEMA, Rosslyn, VA, 1996.

[8] http://networks.internet2.edu/rons.html.

[9] H.K. Huang, *PACS and Imaging Informatics: Basic Principles and Applications*, Wiley, NY, 2004.

[10] California Research and Education Network, CalREN2, http://www.calren2.net.

[11] G. Mogel, F. Cao, H.K. Huang, M. Zhou, et al., Internet2 performance for medical imaging applications, *RSNA 2002 Fall Meeting*, http://apps.internet2.edu/rsna2002-demos.html.

[12] Web100 project, http://www.web100.org/.

[13] StarLight, http://www.startap.net/starlight/.

[14] W. Huntoon and J. Ferguson, Internet2 Presentation – May 2002, in: *I2 Members Meeting May*, 2002, http://www.web100.org/docs/Web100_I2MM.ppt.

[15] R. Shanmugam, R. Padmini and S. Nivedita, *Special Edition Using TCP/IP*, 2nd edn, Que Pub., Indianapolis, Ind., 2002.

[16] B.L. Tierney, TCP tuning guide for distributed application on wide area networks, *Networking/Computing* (February) (2001).

[17] J. Zhang, J.N. Stahl and H.K. Huang, Real-time teleconsultation with high-resolution and large-volume medical images for collaborative healthcare, *IEEE Transactions on Information Technology in Biomedicine* **4**(2) (2000).

[18] H.K. Huang, Teleradiology Today, Telehealth, Business Briefing: Next Generation HealthCare, 1-7.

[19] J.N. Stahl, J. Zhang, C. Zellner, E.V. Pomerantsev, T.M. Chou and H.K. Huang, Teleconferencing with dynamic medical images, *IEEE Transactions on Information Technology in Biomedicine* **4**(2) (2000).

[20] Remote Treatment Planning for Radiation Therapy, Internet2/NLM infoRAD exhibit, RSNA, 2003. http://apps.internet2.edu/rsna2003-demos.html#RemoteTreatmentPlanning.
[21] Rede Nacional de Ensino e Pesquisa, RNP, http://www.rnp.br.
[22] Latina American Cooperation of Advanced Networks, redCLARA. http://www.redclara.net.
[23] International Exchange Point in Miami, Florida International University, AMPATH, http://www.ampath.fiu.edu.
[24] Z. Zhou, M. Gutierrez, J. Documet, L. Chan, H.K. Huang and B.J. Liu, The role of a data grid in worldwide imaging-based clinical trials, *J. High Speed Networks* (submitted).
[25] Flagtelecom, http://www.flagtelecom.com.
[26] Verio, http://www.verio.com.
[27] Globalcrossing, http://www.globalcrossing.com.

Image-Assisted Knowledge Discovery and Decision Support in Radiation Therapy Planning*

Brent J. Liu[1], Maria Y.Y. Law[2], Jorge Documet[1], Arkadiusz Gertych[1]

[1]Image Processing & Informatics (IPI) Laboratory, Radiology Department, University of Southern California, Marina del Rey, CA, 90292, USA

[2]Department of Health Technology and Informatics, The Hong Kong Polytechnic University, Hong Kong, China

* *Paper accepted to be published in Journal of Computerized Medical Imaging and Graphics*

ABSTRACT

The need for quantified knowledge and decision-support tools to handle complex Radiation Therapy (RT) imaging and informatics data is becoming steadily apparent. Lessons can be learned from current CAD applications in Radiology. This paper proposes a methodology to develop this quantified knowledge and decision-support tools to facilitate RT treatment planning. The methodology is applied to cancer patient cases treated by Intensity Modulated Radiation Therapy (IMRT). The use of the "inverse treatment planning" and imaging intensive nature of IMRT allows for the development of such image-assisted tools for supporting decision-making thus providing better workflow efficiency and more precise dose predictions.

Keywords: *DICOM-RT, Quantified Knowledge, Decision-Support, Inverse Treatment Planning, Intensity Modulated Radiation Therapy (IMRT), Brain Tumor*

1. Introduction

The need for comprehensive clinical imaging informatics in Radiation Therapy (RT) is steadily recognizable because of its imaging intensive nature and ever increasing demands for better diagnostic and treatment equipment and more accurate information. Traditionally, multiple information systems acquire the necessary data during the RT treatment course of a patient, however, most of the data is scattered throughout each of the varying treatment and information systems. In addition, RT utilizes some of the most technological advancements in diagnostic imaging, therapeutic radiation, and computerized treatment planning systems, which adds to the complexity of the collection and navigation of pertinent RT data. The lack of organization with standardized methods makes it difficult and time consuming to navigate through the maze of data resulting in an inefficient operation of patient treatment planning. One potential solution can be illuminated by taking radiology as precedence through adoption of the DICOM (Digital Imaging and Communication in Medicine) imaging standard and clinical workflow profiles (Integrating the Healthcare Enterprise, or IHE). This in turn led to their successful development and utilization of Picture Archiving and Communication Systems (PACS) which has become an indispensable integrated imaging system in diagnostic radiology. [1, 2] Furthermore, recently accepted concepts of Computer-Aided Diagnosis (CAD) integrated with PACS advances

radiology to the next level of excellence in clinical care. [3-6] The readily available HL7 (Health Level 7), DICOM, and IHE are basic tools in the realm of medical imaging informatics which can be utilized by RT for the next advancement of its own practice. In addition, other more advanced and powerful imaging informatics methods such as data mining for knowledge discovery, CAD, and outcomes analysis can also be adopted and invented for the benefit of more accurate and efficient patient treatment planning.

Currently in RT, the practical use of imaging informatics tools is limited. DICOM is mostly used for transmitting PACS images to an RT system; and treatment planning systems are limited to dose computations and graphical data displays. Pertinent RT data results do not have a standardized protocol. To address these shortcomings, the DICOM Standard Committee extended DICOM for the RT application by ratifying seven DICOM-RT objects [7-9]. Although some of these objects are utilized within the daily clinical operation in piece-meal fashion, they are not integrated. There are still data crucial to the decision-making process that has not utilized these standards. Therefore, a system integration infrastructure based on standards is crucial for the establishment of patient outcomes related medical informatics research. One such system integration infrastructure is the imaging-based electronic patient record (ePR), which is a patient-based digital virtual folder of clinical information obtained from various information sources. [10] The inclusion of imaging data and built-in decision support makes the ePR stand out amongst general clinical information systems, thus opening new doors to the possibility of improvement in clinical decision outcomes of the future in RT. [11] Law et al have previous developed a patient-oriented ePR system integrating DICOM-RT objects for cancer patient cases. Based on input from both Radiation Oncologists and Radiation Therapists, married with existing data and workflow models, a database schema and user interface design was developed to meet the clinical needs. This was implemented in the Web-based application server as well as the web client. [12-14]

This paper will utilize this previous work of a DICOM-Based ePR system to further apply the methodology to develop CAD for treatment planning in the form of quantified knowledge and decision-support tools that can facilitate RT in therapeutic treatment planning. As an initial first step, a specific clinical scenario from retrospective brain tumor patients treated with Intensity-Modulated Radiation Therapy (IMRT) is utilized, specifically, the "inverse treatment planning" nature of IMRT using a Treatment Planning System (TPS). Computer-assisted quantified knowledge and decision-support tools based on the expertise of Oncologists and Physicists to aid in their decision-making process are designed and developed, thus augmenting the conventional treatment planning approach into a "***knowledge-based*** treatment planning." The methodology can be extended for future clinical decision-making scenarios during the course of the patient's treatment for not only a specific RT treatment type but also a specific lesion type in any body region.

2. METHODS AND MATERIALS

Figure 1 shows the overview of the methodology for designing and developing a DICOM-RT based ePR system, standardizing RT data into DICOM-RT objects, and performing medical imaging and informatics to develop the knowledge base, the data mining, and quantification and visualization tools which ultimately become add-on features to a DICOM-RT based ePR system. In this paper, we focus on the steps of the methodology once the DICOM-based ePR system contains the necessary DICOM-RT objects. These methodology steps will be discussed further in the following paragraphs.

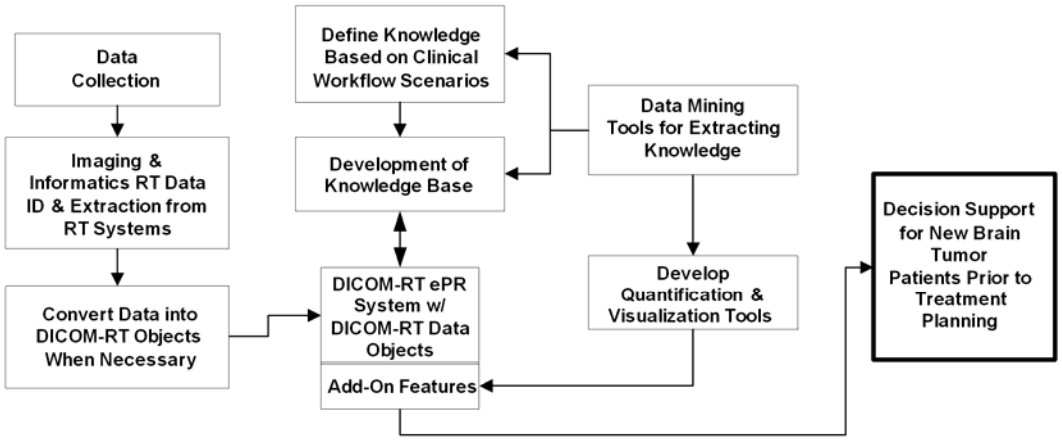

Fig. 1 A Medical Imaging Informatics approach towards development of decision-support tools for the DICOM-RT based ePR system. The final results are add-on features for the ePR system to provide decision-support for new patient cases. This methodology can be applied to different lesion types as well as treatment types to quickly develop new decision-support tools

2.1 Identifying a Decision-Making Scenario in the Clinical Workflow

A general clinical workflow model for radiation treatment of brain tumor cases was developed for the Departments of Radiology and Radiation Oncology, Saint John's Health Center (SJHC), Santa Monica as shown in Figure 2. Although this workflow may be specific to SJHC, the workflow steps can be exended to other institutions with further refinement. The treatment begins with the patient diagnosed with brain lesion or multiple brain lesions. The patient meets with the physician(s) and determines whether to treat the tumor(s) but also what type of radiotherapy will be performed. The patient is entered in an oncology information system and is scheduled for treatment. If conventional RT is prescribed, then a simulator image may be acquired. Otherwise, depending on the treatment type, a diagnostic CT will be acquired to plan the treatment. The Radiologist and Radiation Oncologist review the patient's case and then the Radiation Oncologist defines the initial plan parameters such as dose limits and constraints, critical structures, and tumor volume to be treated. The physics team then computes the plan based on these dose constraints on the corresponding TPS. Once the initial plan is computed, the Oncologist reviews the results and makes any necessary changes. This process can be iterative and the feedback loop is defined in Figure 2 by a dashed line region. Once the treatment plan has been approved, the treatment session is executed by the Radiation Therapist, the corresponding RT plan data are stored in the treatment planning systems of the RT modalities and some results are also inputted into the oncology information system or a Record and Verify system. Since there are a variety of brain tumor types, and the treatment paths can differ, it is important to develop a more robust workflow model that can accommodate the various treatment paths and identify points within the workflow that can be improved. In this case, the iterative feedback loop is identified as a potential area of improvement. The feedback loop represents the inverse treatment planning process and can be quite tedious if much iteration is necessary. This becomes the area of focus where decision-support tools may benefit during the decision-making. If more *a priori* knowledge and robust quantification and visualization tools can be included during the decision-making process of the initial plan parameters, then it is possible to reduce the iterative process.

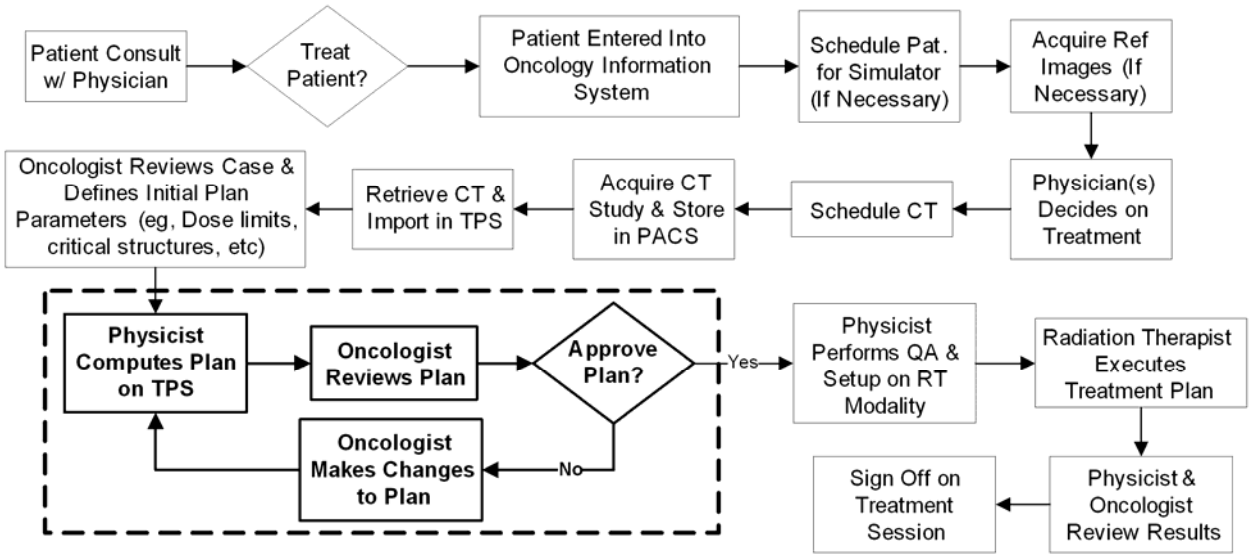

Fig. 2 General Clinical Workflow for RT of Brain Tumors

2.2 Knowledge Base Development

Knowledge is defined and quantified based on the expert's ability, in this case, either the oncologist or physicist, to utilize data and other criteria in evaluating, grouping, and defining certain clinical characteristics that are extracted from the standardized DICOM-RT objects stored within the ePR system. The knowledge base is designed in an object-oriented and modular fashion so that additional knowledge and new object classes defined in the future can be easily integrated without affecting the overall design. An example of quantified knowledge modeling is the dose constraint relationship between the weighting factor and the Dose Volume Histogram (DVH) curve of each critical structure and target tumor which can be loosely defined mathematically as:

$$w_i = f\left[DVH_1 \ldots DVH_N\right]$$

where the weighting factor wi of a particular tumor or critical structure has a value function relationship with all DVH curves from 1 to N in the treatment plan. This relationship is defined by analyzing the DVH curves and the changes to each of them when a particular weighting factor is modified between iterations. The functional form "f" can be further defined with more clinical experience and evaluation. Likewise, the relationship between the DVH curves and the isodose curve lines on each of the image slices can be loosely defined as:

$$DVH_i = \sum_{j=1}^{M} isodose_j$$

where a particular tumor or critical structure's DVH curve i is a summation of all the 1 to M isodose curves within the diagnostic image slices of the treatment plan. The two models above will depend on rudimentary quantified knowledge data elements. These data elements can be derived from the knowledge base schema which can be defined into class objects. A few are shown in Figure 3 along with their attributes: Class Object 1) DVH; Class Object 2) Isodose curve; Class Object 3) Critical Structure; and Class Object 4) CT image. Then, for each of these classes, attributes can be defined as shown. For example, for the CT Image class object, there are the primary key (PK) identifier and five attributes: Critical Structure Curve; Isodose Curve; Spatial Coordinates of the image including x, y, and z-directions; Pointer to the image data; and DICOM header data. The relationships between each of the class objects are through the Foreign Keys (FK). For example, in Figure 3, Isodose Curve FK1, and Critical Structure FK2 are related

to CT Image object. This is because a CT image would contain multiple isodose curves and multiple critical structures. Another example is that the DVH class uses the critical structure volume attribute to relate to the FK1 Volume of the Critical Structure object. Once the knowledge has been defined and knowledge base schema developed, the knowledge can be extracted and stored within the knowledge base. A search engine can be built to perform queries on the quantified knowledge for automatic extraction of particular knowledge.

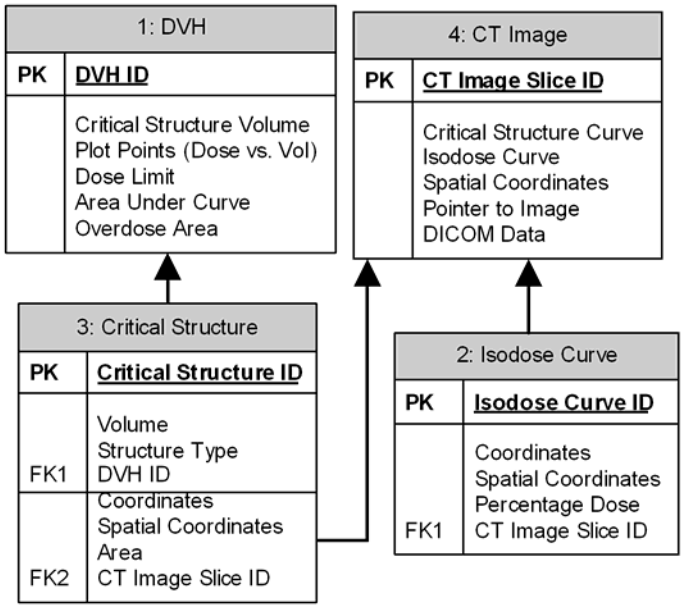

Fig. 3 Entity-Relationship Example of a Sample Knowledge Base for a Clinical Scenario to perform treatment plan assessment for IMRT. The classes defined have attributes that are extracted from the standardized DICOM-RT data integrated in the ePR system. Each class carries a Primary Key (PK) Identifier, and can contain Foreign Keys (FK) which link it to another class object. For example, the 3) critical structure class object contains FK1 and FK2 that link it to a 1) DVH Curve as well as the 4) CT Image class objects. Each DVH curve is derived from a critical structure and CT images contain critical structure contours. The knowledge base is object-oriented in design and modular to allow for additional or new knowledge to be easily integrated. This knowledge is included in the database schema of the web-based ePR application server

2.3 Data Mining for Knowledge and the Development of a Quantification and Visualization Tool

Referring again to the clinical scenario described in section 2.1, a quantification and visualization tool is developed to automatically mine the knowledge base for the information needed to assess a treatment. The tool design and user interface was developed through the guidance of the oncologist and physicist at SJHC. Figure 4 shows an illustration of a mockup for data mining utilizing quantification and visualization tools for decision-support of treatment plan assessment. This method shows how quantified knowledge can be mined for and then visually presented as an example for further development of powerful and effective decision-support tools. This specific tool example eliminates the tedious manual procedure of first analyzing the DVH curves, which is a 2-D plot graph, and then having to toggle through a 3-D volume of CT image slices overlaid with multiple isodose curves to identify locations and characteristics of regions within critical structures that are receiving radiation overdose. These areas are sometimes called “hot spots”. The exact diagnostic CT image slice together with the exact critical structure and tumor contours and isodose curves representing hot spots can be automatically displayed as a warning and red flag to the oncologist during the review of the treatment plan. In addition to the

illustration presented in Figure 4, important quantified knowledge measurements can also be displayed. The results based on this mockup design and the quantified knowledge measurements are further discussed in the Results Section. Other potential development of what quantified knowledge to present and how it will be presented are closely guided by the oncologist and physicist. In the long term, as more knowledge data is collected from additional brain tumor patients treated with IMRT, the knowledge base will be enriched accordingly.

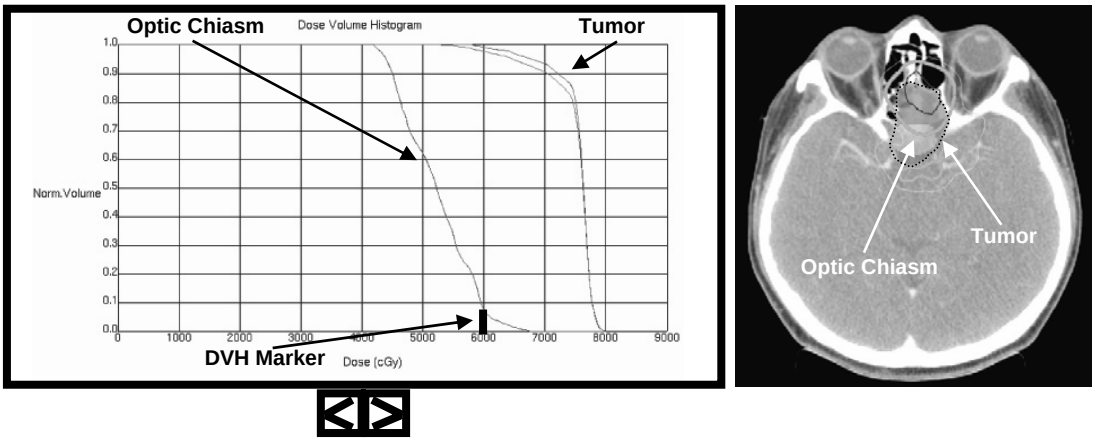

Fig. 4 Illustration of an Interactive Decision-Support Tool for clinicians. The 2-D nature of the DVH curve (Left) is automatically linked to specific image slices (Right), isodose curves, critical structure and tumor contours which all are extracted from 3-D volumes instead of the manual 2-D to 3-D data registration currently performed by the oncologist and physicist. In this example, the DVH curve for a critical structure volume, the Optic Chiasm, has been automatically displayed showing where overdose is occurring which is the region past 6,000cGY (See Left: DVH marker). In addition, the DVH curves for the Prescribed Tumor Volume (PTV) as well as the Clinical Tumor Volume (CTV) are displayed. Note that the two DVH curves for the Tumor are nearly overlapping which is a common occurrence. A CT image slice is automatically extracted and displayed superimposed with the optic chiasm region and isodose curves showing overdose. In this special case CT slice, the Optic Chiasm region (light-colored shaded region) overlaps the tumor to be treated (dashed black line contour) which can make the treatment planning complex and where the development of quantified knowledge and tools can be especially beneficial. The user can move the arrows (left, bottom) left and right adjusting the DVH Marker across the DVH curve which links and displays pertinent diagnostic images with both critical structure and superimposed isodose curves automatically. This is one example of the tools that can be developed based on quantified knowledge

3. RESULTS

3.1 Patient Cases with Brain Tumors

A data survey was performed to track patient cases utilizing the clinical information systems at the Departments of Radiology and Radiation Oncology, Saint John's Health Center (SJHC), Santa Monica, CA. Patient cases that exhibit brain tumors were tracked to determine the treatment path and outcome. The preliminary data collection survey was performed to determine the feasibility of data collection for the treatment of brain tumors. The brief survey was performed using clinical information systems to track historical patients and their records. During the past 6 months, a total of ninety-four head and neck and brain tumor cases were identified. The data survey was performed under the HIPAA Regulations and Compliance Guidelines set forth by USC and SJHC. A sample data set from the IMRT TPS was reviewed and determined to be feasible to convert non-DICOM data into DICOM-RT compliant objects. Some of this data includes: 1) Patient demographic data; 2) CT images; 3) Reference and portal images (eg, Simulator Images, Digitally Reconstructed Radiographs - DRR); 4) Critical structure

curves; 5) Isodose curves; 6) Dose limits and weighting factors; 7) Dose Volume Histogram (DVH) curves; and 8) Radiation beams records. The results of the quantified knowledge and decision-support tools are discussed below.

3.2 A Sample Brain Tumor Case in the RT ePR

This section describes some of the results obtained from a sample brain tumor case treated by IMRT utilizing the TPS for treatment planning and integrated within the DICOM-RT based ePR system. Figure 5 is a timeline overview display showing that a CT and MR diagnostic exam was acquired for a sample patient. Since this particular case is an initial survey, some of the pertinent clinical data was missing, hence an incomplete patient overview. However, it is shown that clinical data from the RT systems can be integrated within the DICOM-RT based ePR system. Referring to Figure 5 (bottom), a conventional RT management information system or record & verify system only has the DICOM RT records but no DICOM RT plan, RT images, and DICOM images. On the other hand, the DICOM-RT based ePR system is able to display information extracted from all of the DICOM-RT objects and can be expanded for more detailed views from the icons on the timeline in the User Interface (both bottom & upper sections).

Fig. 5 Timeline overview display of a patient in the DICOM-RT based ePR system. The RT ePR system has a richer database than the conventional RT information/management system. A given RT information management system has only the DICOM RT records (Bottom of figure), while the RT ePR is able to display the information extracted from all the DICOM objects including the DICOM RT plan, RT images, and DICOM images

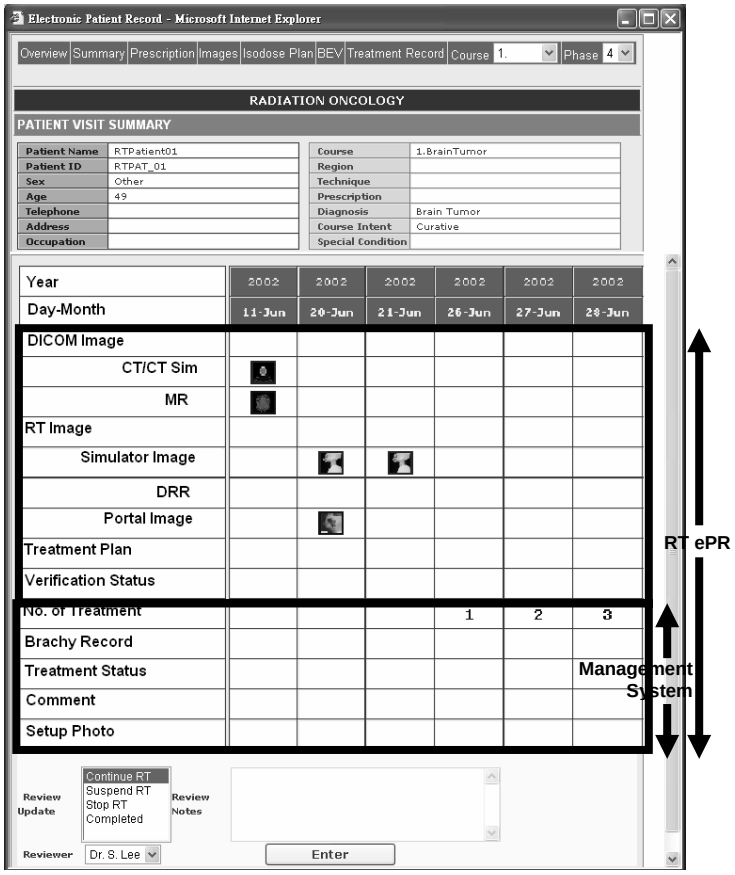

3.3 A Clinical Scenario

A clinical scenario where an oncologist needs to assess the isodose plan of critical structures from a treatment plan for a brain tumor patient is utilized to explain this methodological approach. During treatment planning for brain tumor patients, the treatment plan developed, usually by the physicist, must be approved by the oncologist as shown earlier in the workflow in Figure 2. Part of the clinical decision-making process for the physician is to analyze the DVH curves of critical structure areas to evaluate whether the critical structures are receiving an overdose of radiation that is clinically unacceptable. These curves only show dose values in relation to the critical structure volume. The physician must then evaluate the various isodose plans to first locate areas of overdose within the critical structures called "hot spots", and then to determine whether the plan is acceptable or whether it must be modified and recalculated. In order to make this clinical assessment, the oncologist must navigate through multiple image slices showing multiple isodose curve lines as well as overlapping critical structures to make the assessment. Navigation of all this knowledge, while crucial, is also extremely tedious and complex since there is no tool to quantify and visualize the direct relationship between the DVH curves to the diagnostic images and the corresponding dose and critical structure curves. A tool has been designed to automatically display the DVH curve of a critical structure linked with the diagnostic image slice(s) that contain corresponding isodose curves and critical structure regions. Figure 6 shows a screenshot of an overview of a particular IMRT Treatment Plan (TP). The Letter A indicates tabs that display different page views. The first view is the TP Overview which shows the general overview of the DVH curves and the DICOM CT Images with isodose curves overlaid. The TP Evaluation page allows the User to quickly assess a treatment plan for hot spots. The TP Knowledge Base Search page allows users to query for specific knowledge. The TP Comparison page shows quantified knowledge for two different TP iterations in a comparison mode. The Letter B indicates a timeline display showing all TP's, both current and historical, of a particular patient. The letter C indicates a drop-down window which allows the user to view different iterations within a current plan. The Letter D indicates the DVH Curve of a particular plan with the overdose area shaded for the Optic Chiasm. The letter E indicates DICOM Images with isodose curves overlaid from the TPS. All data is in DICOM-RT Format and standardized. The User can further view each of the DICOM images with isodose curves by selecting one of the images. A pop-up window is generated with a larger image view window. Tools such as Zoom, Pan, and Window/Level are included as well as the ability to toggle on and/or off particular isodose curves or critical structure curves to allow the User to properly review the plan. This is shown in Figure 7.

Figure 8 shows the TP Evaluation Page with the DVH curves of a specific critical structure, the Optic Chiasm with the overdose area shaded under the Optic Chiasm curve, and the Tumor depicted in the leftmost column. In the middle column, only the image slices with overdose regions are extracted from the entire CT study and displayed with the regions highlighted. In addition, quantified knowledge such as percent area overdosed are displayed as well. The rightmost column shows only the image slices where the tumor is not receiving the full clinically prescribed radiation dose. In this manner, the User can quickly assess the treatment plan to determine whether the critical structures are being overdosed while at the same time the tumor is being prescribed as much dose as possible without having to review the entire CT Image Study. Figure 9 and 10 show screenshots of pop-up windows to allow the User to view the images and pertinent knowledge in greater detail.

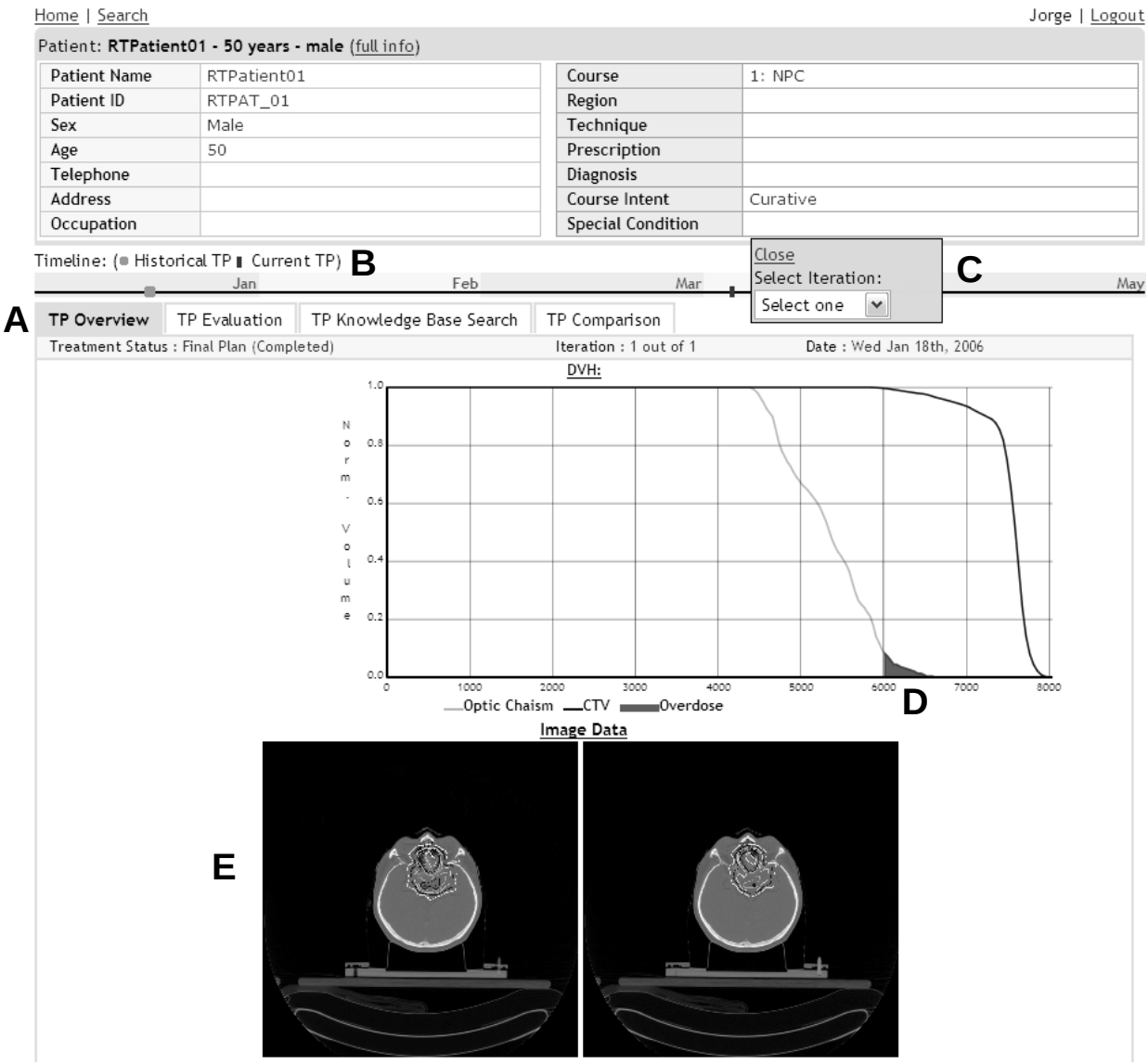

Fig. 6 Screenshot Showing an Overview of a Treatment Plan. A: Tabs that Display Different Page Views. TP Overview - Shows the General Overview showing the DVH curves and the DICOM CT Images with Isodose Curves Overlaid. TP Evaluation Page - Shows Quantified Knowledge. TP Knowledge Base Search Page - Allows Users to Query for Specific Knowledge. TP Comparison Page - Shows Quantified Knowledge for Two Different Treatment Plan iterations in Comparison Mode. B: Timeline Display Showing all Treatment Plans, both Current and Historical of a Particular Patient. C: Drop-Down Window Allowing the User to View Different iterations Within a Current Plan. D: DVH Curve of a Particular Plan with Overdose Region Shaded for the Particular Critical Structure, in this case, the Optic Chiasm. E: DICOM Images with Isodose Curves Overlaid from the TPS. All Data is in DICOM-RT Format

Finally, Figure 11 presents the TP Comparison page view which shows two iterations of a current treatment plan side by side evaluation. Only the image slices with overdosed areas to the optic chiasm are extracted and displayed with quantified knowledge. In this case, there is an improvement between iteration 1 and iteration 2 in the difference in the shaded area of the DVH Curves with less being shown in iteration 2. In addition, there are less number of image slices extracted with "hot spots" in iteration 2 as compared to iteration 1 and the quantified knowledge also confirms this with the percent areas of overdose. This comparison mode, allows the user to quickly compare between the results of one iteration and a subsequent iteration to assess any

improvements in the treatment planning process. In addition, this comparison mode can be used to review previous approved treatments within the knowledge database to help guide the oncologist and physicist in developing a new treatment plan for a new patient.

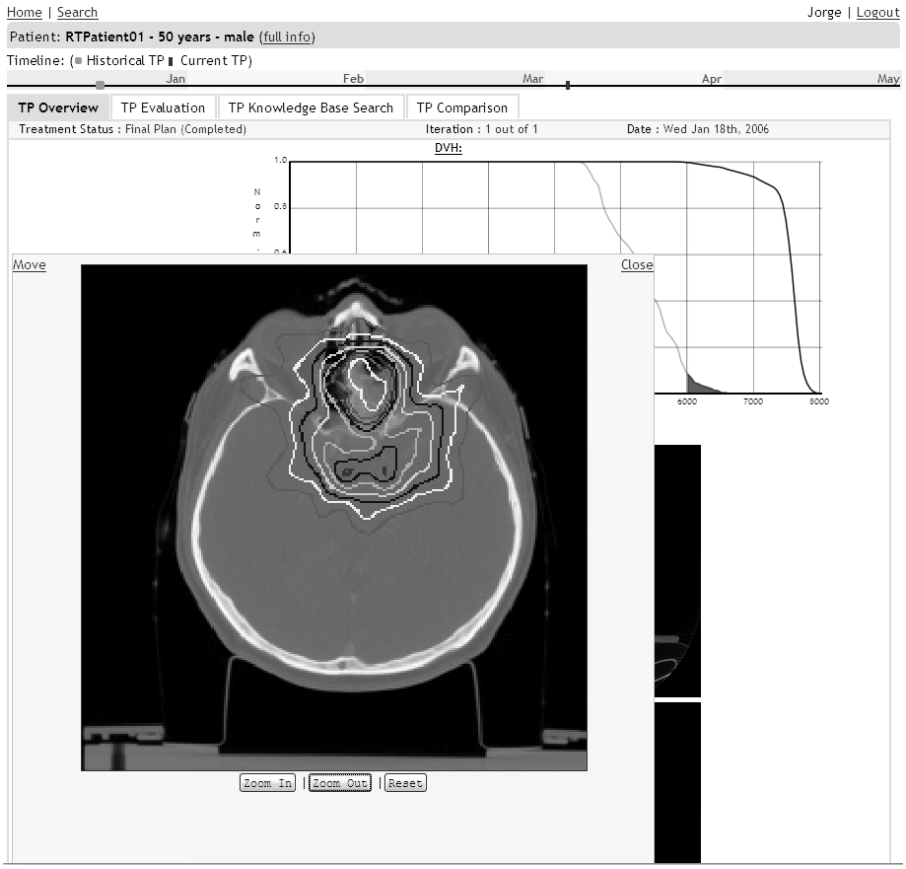

Fig. 7 TP Overview Page with Pop-Up Window to Allow User to View the DICOM Image with Overlaid Isodose Curves for Better Reviewing. The User Selects One of the Smaller Overview Images to Generate a Larger Pop-Up Viewing Window. Tools Such as Zoom, Pan, and W/L are Included as well as the Ability to Toggle Particular Isodose Curves and Critical structure Curves On or Off to Allow the User to Properly Review the Plan

These tools help to eliminate the tedious manual procedure of first analyzing the DVH curves and then having to toggle through a volume of CT image slices with multiple isodose curves to review and assess the plan. Since data is already mined, the exact diagnostic CT image slice together with the exact structure and isodose curves can be automatically displayed the moment the oncologist opens the case within the ePR system. The oncologist would then have the ability to continue to navigate the presented data or view a different DVH curve if desired to make a quicker assessment of the treatment plan for approval. If the oncologist decides that changes are needed in the treatment plan, the decision-support tools can be used to perform a real-time consult with the physicist either at different locations or at the same location or even directly on the treatment planning system, since the ePR is web-based and portable. In the future, if there are historical patients stored within the ePR system, the tools can display all the similar critical structures (eg, in the above case, the Optic Chiasm) of similar treatment plans with the corresponding dose configurations that have been approved. This extracted *a priori* knowledge would help the clinician to decide on an initial plan for a new brain tumor patient planning to be treated with IMRT and perhaps shorten the iterative process of the inverse treatment planning workflow.

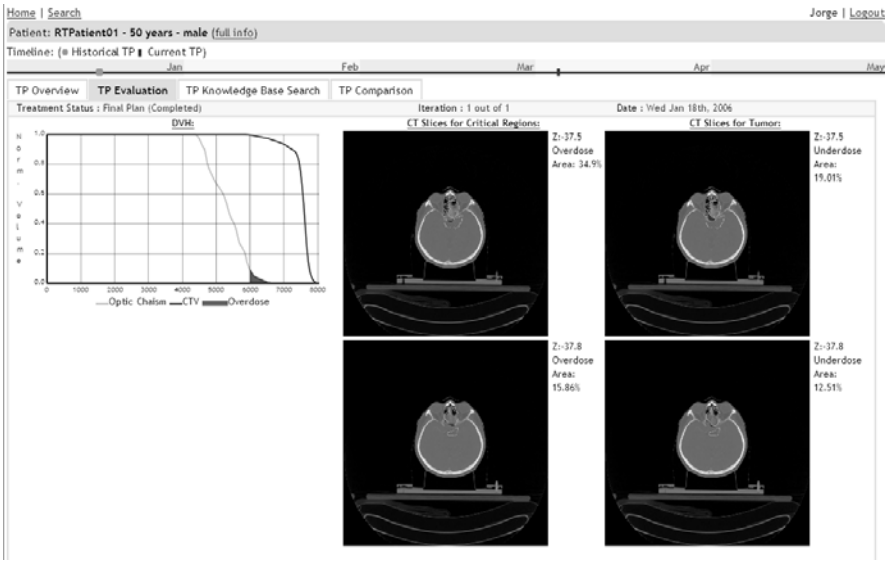

Fig. 8 TP Evaluation Page Showing the DVH Curves of a Specific Critical Structure and the Tumor (leftmost column). The middle column shows only the image slices with overdose regions extracted from the entire CT Study and displayed with the regions highlighted. In addition Quantified Knowledge such as Percent Area Overdosed is displayed as well. The rightmost column shows only the image slices where the tumor is not receiving the full clinically prescribed Radiation Dose. In this manner, the User can quickly assess the Treatment Plan to determine whether the critical structures are being Overdosed while at the same time the Tumor is being prescribed as much Dose as possible without having to review the entire CT Image Study

Fig. 9 Pop-Up Window Allowing the User to View the Area of Overdose to the Optic Chiasm in Greater Detail as Shown by the Arrow Pointing at the Shaded Region. The Optic Chiasm Region is outlined in gray while the specific percentage dose Isodose Curve that overlaps with Optic Chiasm Region producing Overdose or "Hot Spots" is outlined in White. Note that there are two separate Isodose Curves where there is a specific percentage dose, which shows that the treatment plan is attempting to avoid Radiation Dose to the Optic Chiasm Region. Even so, there is still overdose as indicated by this particular screen shot and the shaded region highlighted

Fig.10 Pop-Up Window Allowing the User to View the Area Where the Tumor is not Receiving the Fully Prescribed Radiation Dose in Greater Detail as Shown by the Arrow Pointing at the Shaded Region. The Tumor Region is Outlined in Black. The two separate Isodose Curves Representing 100% Dose are Outlined in White

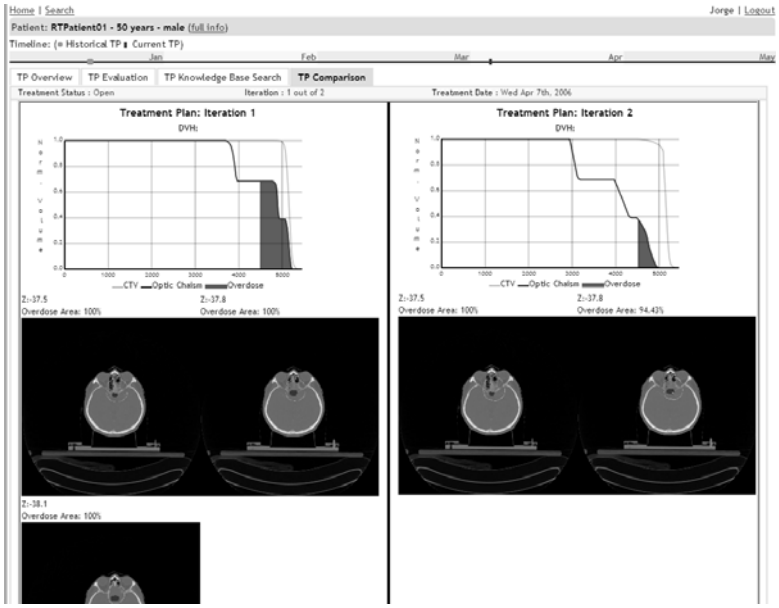

Fig. 11 TP Comparison Page View Showing Two Iterations of a Current Treatment Plan. Only the Image Slices with Overdosed Areas to the Optic Chiasm are Extracted and Displayed with Quantified Knowledge. In this Case, There is an Improvement Between Iteration 1 and Iteration 2 Both in the Difference in the Shaded Area (Less Area in Iteration 2 DVH) of the DVH Curves as well as the Number of Image Slices (Two vs. Three) Extracted with Overdose Regions and the Quantified Knowledge Showing Percent Area of Overdose. Note that the Third Image (lower left) Extracted in Iteration 1 is Cut Off Due to the Limitations of the Screen Shot Size and Can be Viewed in the Active GUI by Scrolling the Window

4. DISCUSSION

A DICOM-RT based ePR system for managing patients with brain tumor cases was utilized to design and develop quantified knowledge and decision-support tools within the Radiation Oncology Department, Saint John's Health Center, Santa Monica, CA. Data obtained from a sample brain tumor case where the treatment was planned on the IMRT TPS was collected and integrated within the ePR system. The richness of the clinical data available was shown in comparison to standard RT information management systems. With the availability of standardized DICOM-RT data, knowledge base and decision-support tools were developed to aid the clinicians in critical decision-making processes.

Figure 12 shows the new *knowledge-enhanced* inverse treatment planning workflow with the ePR system with quantified knowledge integrated in dashed lines within the clinical feedback loop described in Figure 2. This knowledge-enhanced inverse treatment planning approach may eliminate the feedback loop and subsequent iterative steps of re-computing of a treatment plan since the first attempt was acceptable based on the prior knowledge. Because each plan is computationally complex and time-consuming, a best practice first computed plan aided by previous knowledge would greatly enhance the decision-making process and ultimately shorten the length of time before the patient is exactly treated as well as better preserve normal tissue and quality of care. Future work would include the complete development and collection of the knowledge base and tools as well as a clinical evaluation of the decision-support tool development and its impact on the overall clinical workflow within the Radiation Oncology Department.

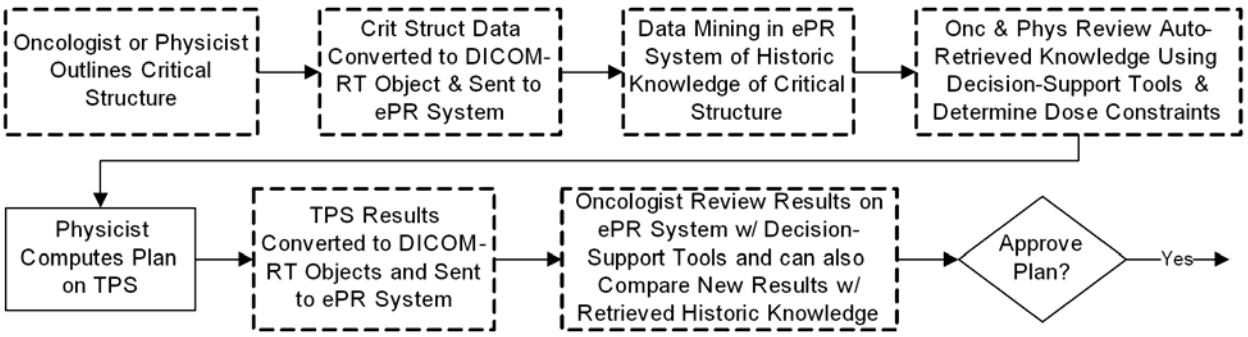

Fig. 12 Knowledge-Enhanced Inverse Treatment Planning: Dashed lines show where workflow steps would be performed in the ePR System as compared to the current feedback loop workflow shown in Figure 2

5. SUMMARY

A methodology was introduced for the development of CAD for treatment planning in the form of decision-support tools based on the standardized DICOM-RT data within the ePR system. As a first step proof of concept of how crucial standardized RT data can be, a clinical scenario was developed where knowledge base was defined and quantification and visualization tools were designed to extract the knowledge and display it for a decision-making process. By implementing this DICOM-RT based ePR system with CAD, both clinical image and related informatics data are integrated into a one-stop source of pertinent clinical information necessary for making treatment decisions within the RT department and throughout the healthcare enterprise. With the medical imaging informatics methodology introduced in this paper, the computer-assisted decision-support tools and knowledge base development can be easily extended to various lesion types as well as other treatment planning methods.

References:

[1] Liu B.J., Huang H.K., Cao F., Zhou M.Z., Zhang J.Z., Mogel G., A Complete Continuous-Availability PACS Archive Server, Radiographics 2004; 24:1203-1209.

[2] Liu B.J., Cao F., Zhou M.Z., Mogel G., Documet L. Trends in PACS Image Storage and Archive, Comput Med Imaging Graph 2003, 27:165-174.

[3] Brem R.F., Hoffmeister J.W., Rapelyea J.A., Zisman G., Mohtashemi K., Jindal G., DiSimio M.P., Rogers S.K., Impact of Breast Density on Computer-Aided Detection for Breast Cancer, Am. J. Roentgenol., Feb 2005; 184: 439 - 444.

[4] Zhou M.Z., Huang H.K., Cao F., Zhang J., Mogel G., Law M.Y.Y. A RIS/PACS Simulator with Web-Based Image Distribution and Display System for Education. Proceedings of the SPIE on CD-ROM, Medical Imaging 2004, 372-381, San Diego, CA, U.S.A.

[5] Doi K., MacMahon H., Giger M.L., and Hoffman K.R. (ed), Computer-Aided Diagnosis in Medical Imaging. Chicago: Elsevier Science Ltd, 1998.

[6] Huang HK. 1999. PACS: Basic Principles and Applications. Wiley & Sons, NY, p. 521.

[7] Digital Imaging and Communications in Medicine (DICOM), Supplement 11: Radiotherapy Objects, 1997.

[8] Digital Imaging and Communications in Medicine (DICOM), Supplement 29: Radiotherapy Treatment Records and Radiotherapy Media Extensions, 1999.

[9] DICOM Standard 2003, http://medical.nema.org/dicom/2003.html.

[10] Dayhoff R., and Siegel E., Digital Imaging Within and Among Medical Facilities, I n R Kolodner (ed): Computerized Large Integrated Health Networks – The VA Success. New York: Springer Publishing, pp. 473-490.

[11] Palta J.R., Frouhar V.A., Dempsey J.F. Web-based Submission, Archive, and Review of Radiotherapy Data for Clinical Quality Assurance: A New Paradigm. In J Radiat Oncol Biol Phys, 2003; 57(5): 1427-1436.

[12] Law M.Y.Y., Huang H.K. Concept of a PACS and Imaging Informatics-Based Server for Radiation Therapy. Comput Med Imaging Graph 27 (1): 1-9, 2003.

[13] Law M.Y.Y., Huang H.K., Chan C.W., Zhang X., Zhang J. A DICOM-Based Radiotherapy Information System. Proceedings of the SPIE on CD-ROM, Medical Imaging 2004, 309-317, San Diego, U.S.A.

[14] Law M.Y.Y. A Model of DICOM-Based Electronic Patient Record in Radiation Therapy. Comput Med Imaging Graph 29 (2-3): 91-242, 2005.

Bone Age Assessment of Children using a Digital Hand Atlas*

Arkadiusz Gertych[1], Aifeng Zhang[1], James Sayre[2,1] , Sylwia Pospiech-Kurkowska[3], H.K Huang[1]

[1] - Image Processing and Informatics Laboratory, Department of Radiology, University of Southern California, 4676 Admiralty Way, Suite 601, Marina del Rey, CA 90292

[2] - Department of Radiological Sciences, University of California, Los Angeles

[3] - Institute of Electronics, Department of Biomedical Engineering, Silesian University of Technology, Akademicka 16, 44-100, Gliwice Poland

** Paper accepted to be published in Journal of Computerized Medical Imaging and Graphics*

ABSTRACT

We have developed an automated method to assess bone age of children using a digital hand atlas. The hand Atlas consists of two components. The first component is a database which is comprised of a collection of 1,400 digitized left hand radiographs from evenly distributed normally developed children of Caucasian (CA), Asian (AS), African-American (AA) and Hispanic (HI) origin, male (M) and female (F), ranged from 1 to 18 year old; and relevant patient demographic data along with pediatric radiologists' readings of each radiograph. This data is separate into eight categories: CAM, CAF, AAM, AAF, HIM, HIF, ASM, and ASF. In addition, CAM, AAM, HIM, and ASM are combined as one male category; and CAF, AAF, HIF, and ASF are combined as one female category. The male and female are further combined as the F & M category. The second component is a computer-assisted diagnosis (CAD) module to assess a child bone age based on the collected data. The CAD method is derived from features extracted from seven regions of interest (ROIs): the carpal bone ROI, and six phanlangeal PROIs. The PROIs are six areas including the distal and middle regions of three middle fingers. These features were used to train the eleven category fuzzy classifiers: one for each race and gender, one for the female, one male, and one F & M, to assess the bone age of a child. The digital hand atlas is being integrated with a PACS for validation of clinical use.

Keywords: *bone age assessment of children, digital hand atlas, computer aided diagnosis, feature extraction, fuzzy logic*

1. INTRODUCTION

Bone age assessment (BAA) is a common radiological examination used in pediatrics to determine any discrepancy between a child's skeletal age (the developmental age of their bones) and their chronological age (in years, taken from birth date). The examination is straightforward to perform, involving a single view of the left hand which includes all relevant regions of interest within the hand and wrist (Fig. 1). A difference between chronological age and skeletal age may suggest abnormalities in skeletal development. Delayed or accelerated appearance of ossification centers caused by an illness may serve as an example. Assessment of skeletal age is helpful in the monitoring of growth hormone therapy and diagnosis of endocrine disorders. BAA is also

performed when surgery for correcting deformities of the long bones or the vertebral column is planned. Bone age determinations are also commonly used to predict individual's final height [1].

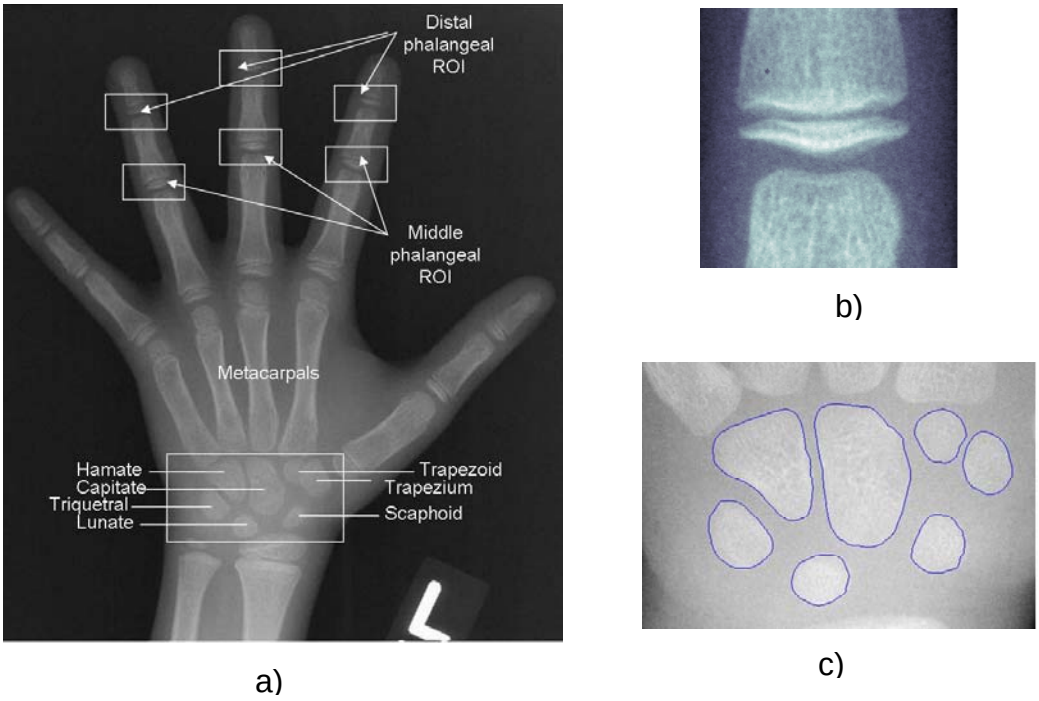

Figure 1. An example of hand image radiograph with superimposed regions of interest: a) a hand image with seven ROIs, b) the phalangeal region of interest (PROI), c) the carpal bones region.

The classical method of skeletal bone age assessment (BAA) utilizes the recognition of changes in the radiographic appearance of the maturity indicators in a hand-wrist radiograph by comparison with a reference data set which consists of series of radiographs grouped according to sex and age. The most commonly used reference standard is the atlas published by Greulich and Pyle (G&P) [1]**.** They were derived from the population of the middle socioeconomic class of Caucasian children from Midwest, USA from 1931-1942. The atlas remains unchanged from its initial publication and is commonly used in clinical practice to assess bone age of children of Caucasian, African American, Hispanic, Asian, and other descent. The examination is subjective because the radiologist analyzes each individual bone of the hand and wrist, determines an overall bone age, and finally fits the amalgamated results into a closest match to the reference radiographs in the atlas. Using the G&P atlas, inter-observer reading differences ranging from 0.37 to 0.6 years and intra-observer reading differences from 0.25 to 0.47, even up to 0.96 years have been reported [2, 6]. The average time of a single case reading depends on radiologist's clinical experience and falls within 2 - 5 minutes.

More objective methods are also available [3-5], (TW1, TW2, TW3). The radiological patterns of ossification centers were derived from the population of 3000 normal British boys and girls. An overall bone age is derived from the sum of the developmental scores from all of the individual ossification centers. Because this approach is both complicated and time consuming, it is seldom used in clinical practice, particularly in the United States.

In this paper, we describe an automated method to assess bone age of children using a digital hand atlas. The hand Atlas consists of two components: a database which is a collection of 1,400 digitized left hand radiographs from evenly distributed normally developed children of Caucasian, African-American, Hispanic and Asian origin, male and female, ranged from 1 to 18

year old. Relevant patient demographic data along with pediatric radiologists' readings of each radiograph were also included. Currently, 1,390 are included in the database. The second component is a computer-assisted diagnosis (CAD) module to assess a child bone age based on the collected data. The CAD method is derived from features extracted from seven regions of interest (ROIs), the six phanlangeal and one carpal bone ROIs.

First, the concept of the Digital Hand Atlas and the data collection is described. Next, a hand image processing work flow of the CAD is introduced. Quantitative features extraction from ROIs is followed by the preprocessing of the hand image. The final bone age assessment based on extracted quantitative features is obtained by means of an array of fuzzy classifiers. The integration of the digital hand Atlas with a PACS for validation of clinical use is presented.

2. DATA COLLECTION OF THE DIGITAL HAND ATLAS

Rationale

During past years, numerous results have demonstrated that variations in skeletal maturation in prepubertal children are greater than those reflected in the Greulich and Pyle atlas. More precisely, prepubertal American children of European (EA) descent have significantly delayed skeletal maturation when compared with those of African descent. Also, postpubertal EA males have significantly advanced skeletal maturation when compared with postpubertal African American males [7]. Therefore, it is apparent that multiethnic pediatric population normal images are needed in order to more accurately assess today's children bone age. We started to collect normal children hand images in the late 90s through the support of grants supported by the National Institutes of Health. The process of data collection was conducted at the Childrens Hospital of Los Angeles (CHLA). Candidates for this study underwent a protocol approved by the institutional review board for clinical investigations. A physical examination by a pediatric endocrinologist was performed to determine health and Tanner stage of sexual development of all subjects. According to the clinical examinations, their skeletal development had been confirmed as normal. Measurements of height, trunk height and weight were also obtained. The bone age of each normal was evaluated by at least two pediatric radiologists from the left hand radiograph according to the method of G & P atlas. Each radiograph was digitized to a 2Kx2K image using a laser film scanner (Array, Tokyo, Japan); and the patient demographic records were manually entered via the scanner GUI (graphical user interface) and saved as a DICOM file. An example of data stored in the DICOM file is presented in Table 1.

Table 1. An example of image header fields in a hand image DICOM file.

DICOM Field Name	Date of Birth	Date of Examination	Chronological Age	Patient Race	Patient Sex	Tanner Index	Trunk Height	Body Height	Body Weight	Reading R1	Reading R2
Unit	dd/mm/yy	dd/mm/yy	years	-	-	-	cm	cm	kg	years	years
Field value	26/02/89	25/06/98	9.33	CAU	M	1.0	71.12	137.8	39.1	9.0	9.5

Data Collection

The data collection was scheduled in two separate cycles. In the first cycle a total number of 1103 left hand radiographs of normally developed children of four races: Caucasian (CA), African American (AA), Hispanic (HI), and Asian (AS) for both male and female [8, 9] have been collected. The data collection protocol is given in Appendix A, with the hand positioned as presented in Fig. 1.

For each race and gender, five images per age group for children aging from one to nine years, and ten images per age group for older have been collected respectively. During an almost 10 year period of collecting the data in this cycle, groundwork of the methodology of developing the CAD for bone age assessment has also been established [10-13].

The data was evaluated as normal comparing to: (1) the body mass index (BMI) for children based on the growth chart from National Health and Nutrition Examination Survey [14], (2) Tanner maturity index, and (3) chronological age vs. skeletal age based on the 1940 Brush Foundation Study. Comparison to (1) and (2) shown that the data is normal. According to comparison with (3), bone age assessment with first cycle data was consistently lower between ages 5-14 for boys and girls in every ethnic origin. A difference of approximately ten months was observed between item (3) and data collected.

Because of the difference in item (3), in order to increase the statistical power of the first cycle data set we started a second cycle data collection with additional 287 images for the rapid maturation stage of children from ages 5 to 14 year old. A summary of first and second cycle data from the Digital Hand Atlas as of today is presented in Table 2 (a-b).

Table 2a. Digital Hand Atlas: the summary of the first cycle data collection.

First cycle of data collection: each case is with two readings								
Age group/Category	ASIF	ASIM	BLKF	BLKM	CAUF	CAUM	HISF	HISM
00	1	2	4	5	3	3	1	4
01	5	5	5	5	5	5	5	5
02	5	5	5	5	5	5	5	5
03	5	5	5	5	5	5	5	5
04	5	5	5	5	5	5	5	5
05	5	5	5	5	5	5	5	5
06	5	5	5	5	5	5	5	5
07	5	5	5	5	5	5	5	5
08	5	5	5	5	5	5	5	5
09	5	5	5	5	5	5	5	5
10	10	10	10	10	10	10	10	10
11	10	10	10	10	10	10	10	10
12	10	10	10	10	10	10	10	10
13	10	10	10	10	10	10	10	10
14	10	10	10	10	10	10	10	10
15	10	10	10	10	10	10	10	10
16	10	10	10	10	10	10	10	10
17	10	10	10	10	10	10	10	10
18	10	10	10	10	10	10	10	10
Images total / category	136	137	139	140	138	138	136	139
Images total	1,103							

Table 2b. Digital Hand Atlas: the summary of the second cycle data collection.

Second cycle of data collection: each case is with four readings								
Age group/Category	ASIF	ASIM	BLKF	BLKM	CAUF	CAUM	HISF	HISM
05	3	4	4	4	2	5	5	4
06	1	1	4	2	2	3	5	4
07	2	2	4	4	3	4	5	5
08	4	0	5	5	4	5	4	5
09	2	2	4	5	3	2	5	5
10	5	4	2	5	2	1	4	2
11	2	5	0	5	3	4	5	4
12	4	5	5	5	4	3	5	5
13	5	5	5	5	4	2	5	5
14	3	2	2	4	1	0	4	4
Images	31	30	35	44	28	29	47	43
Images total	287							

Hand Image Database

A Hand Image Database containing the image data collected along with patient demographic data and radiologist readings can be browsed using the following link: http://www.ipilab.org/BAAweb/. Fig. 2 shows a screen shot of a page retrieved from the eleven year old Asian female data.

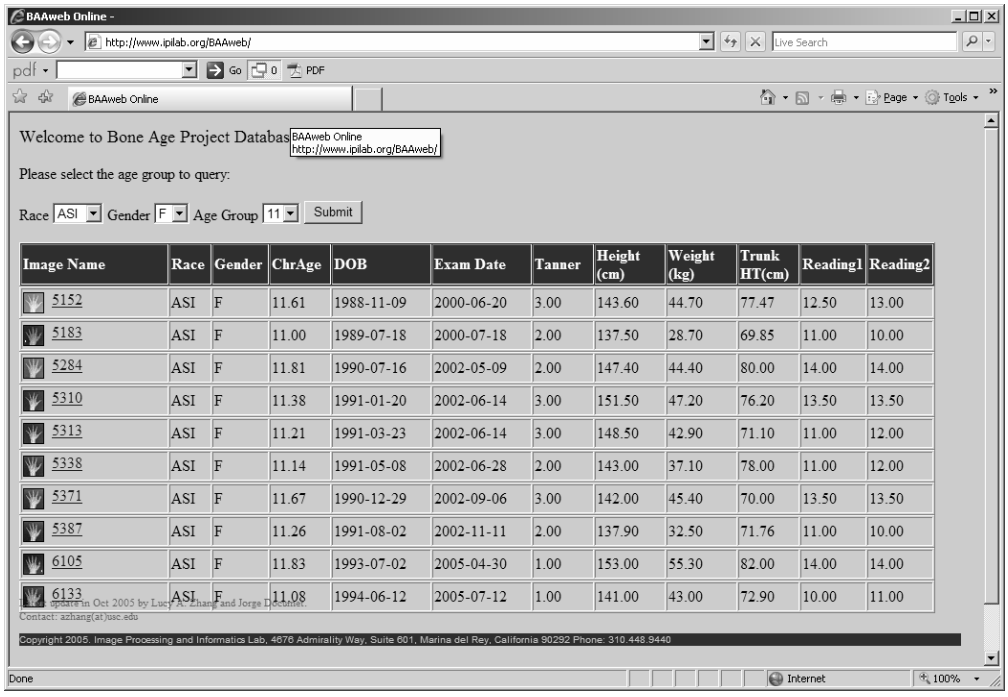

Figure 2. A GUI window of the bone age assessment web site with hand image database. The website provides hand images, information about subjects' demographic data and radiologists' readings.

3. THE CAD MODULE

CAD using the data collected described in Section 2 for the BAA has been designed and implemented to provide an objective assessment of a child's skeletal age as an aid to the pediatric radiologist's reading. The collected data together with features extracted related to skeletal development from phalangeal ROIs [15] and the Carpal bone ROI [17] were transformed into knowledge rules of fuzzy classifiers [16] for bone age assessment. The Digital Hand Atlas is a combination of the collected data and the CAD module. A work flow of the CAD is presented in Fig. 3 which consists of five steps: 1) image preprocessing, 2) ROIs determination, 3) phalangeal and carpal bones features extraction, 4) fuzzy classifiers, and 5) aggregation of fuzzy classifier results to obtain the bone age assessment.

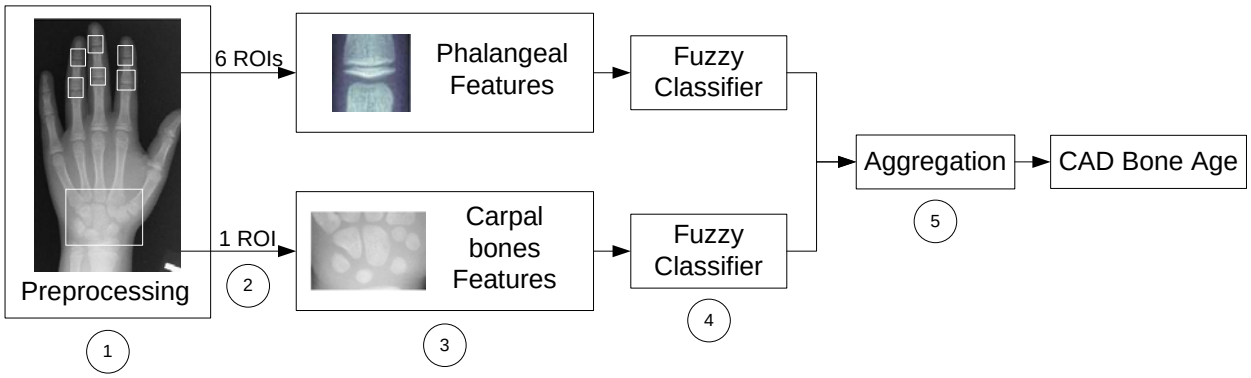

Figure 3. Five steps of the CAD workflow. Located seven regions of interest is subjected to features extraction and category classifiers provide fuzzy information about boner age derived from the regions of interest. Final bone age is calculated after the aggregation procedure

Image Pre-Processing, ROI Determination, Feature Extraction

Image preprocessing includes background suppression and radiological markers removal (see Fig. 1 stripes and background nonuniformitiy may not be well visible in this example, except for the "L" marker). [12, 13] Next, six distal and middle phalangeal ROIs (PROIs) of three middle fingers [13] and the carpal bone ROI are located [11]. Fig. 1 left shows six PROIs and the carpal bone ROI, and the right is the magnification of a PROI and the carpal bone ROI, [17]. Considering first the six PROIs, eleven features were extracted from each ROI. [16,18,19] Two feature sets, those features related to size and shape of the epiphysis, and the wavelet features derived from stage of fusion advancement of the epiphysis, describe the degree of bone development in this single PROI. Similar procedures were performed for each PROI. As a result, a total of twelve feature sets were obtained, two from each PROI. Methods of feature extraction have been discussed in details in previous publications [10-19]. These twelve feature sets were used to train twelve PROI fuzzy classifiers for bone age assessment contributed by PROIs features.

The Category Fuzzy Classifier and Aggregator

The data from 1 – 18 years shown in Table 2 was separated into eight categories (CAM, CAF, AAM, AAF, HIM, HIF, ASM, and ASF) for race and gender comparison study. In addition, CAM, AAM, HIM and ASM were combined as one male category; and CAF, AAF, HIF, and

ASF were combined as one female category. The male and female were further combined as one universal F & M category. Therefore we developed one category fuzzy classifier for each of the eleven categories.

For each category, the category fuzzy classifier using the PROIs feature sets was trained as follows. For each PROI, there were two classifiers, one was based on the shape and size features, and the other was based on wavelet features. The design and training of these two classifiers were based on Mamdani's original concept [21], and applied to phalangeal ROIs discussed in details in Ref [16]. The design and training of each category fuzzy classifier using the carpal bone ROI is given in [17]. Fifty percents of the collected images were used for training, and the other 50% for evaluation.

The design of the category fuzzy classifier is an open architecture model meaning that if fuzzy results from other ossification centers are provided they can be appended to the existing structure before the defuzzification (or aggregation) step, for example in each category classifier, the carpal bone ROI classifier could be appended to the phanlangeal ROI classifiers for bone age assessment [17].

The final BAA was derived from the aggregation of BAA results from the phalangeal ROIs and carpal ROI. In general, carpal bone ROIs determines the bone age of boys from 1 to 7, and girls from 1 to 5; phalangeal ROIs determine the bone age for both sexes above age 13. For girls from 6 – 12, and boys from 8 -12, both carpal ROI and phalangeal ROIs contribute. The final bone age value was obtained by defuzzication with the center of gravity method. Fig. 6 middle left illustrates the concept of the aggregation of 12 PROI classifiers and the carpal ROI classifier to form the combined bone age value in a category fuzzy classifier.

Graphical User Interface

A graphical user interface (GUI) was designed to visualize CAD operation steps (Window 1) and results (Window 2). After the hand image is sent to the CAD and the processes are completed, the CAD workstation Window 1 displays the patient data (Fig. 4, Left), image with superimposed ROIs (Middle) and segmentation results (Right). In addition, detailed messages about currently CAD performed step can also be visualized in the Lower Right of Fig. 4 using a scroll bar at the bottom). The CAD results are shown in Window 2 as depicted in Fig. 5.

Integration of CAD BAA with PACS

The digital atlas has been integrated with a research PACS using a CAD-PACS integration toolkit for validation study [20]. The toolkit is based on the DICOM (Digital Imaging and Communications in Medicine) Standard and IHE (Integrating the Healthcare Enterprise) workflow profiles. The toolkit has two modules, the DICOM-based SC (secondary capture) module, and the DICOM – IHE module, both modules can output the CAD BAA results as shown in Fig. 5. The former module, a fast integration method, allows the CAD GUI results shown in Figs. 5 to be directly displayed on the PACS workstations using the DICOM SC. However, PACS workstations can only display these results but can not assess the image or the textual contents directly. The DICOM – IHE module is based on the DICOM Structured Report (SR) standard and the IHE Post-Processing Workflow Profile protocol. The integration is more elaborated but the PACS workstations, in addition to displaying CAD results as shown in Figs. 5, can also access the CAD result images and data for other research, teaching, and clinical services applications. Zhou [20] in this Special Issues provides detail description of the integration methods. Fig. 6 shows the workflow of the integration of CAD BAA with PACS. Within the

dotted lines is the domain of the Digital Atlas, and PACS hardware components are the image acquisition and workstations. The CAD toolkit is integrated with the PACS software.

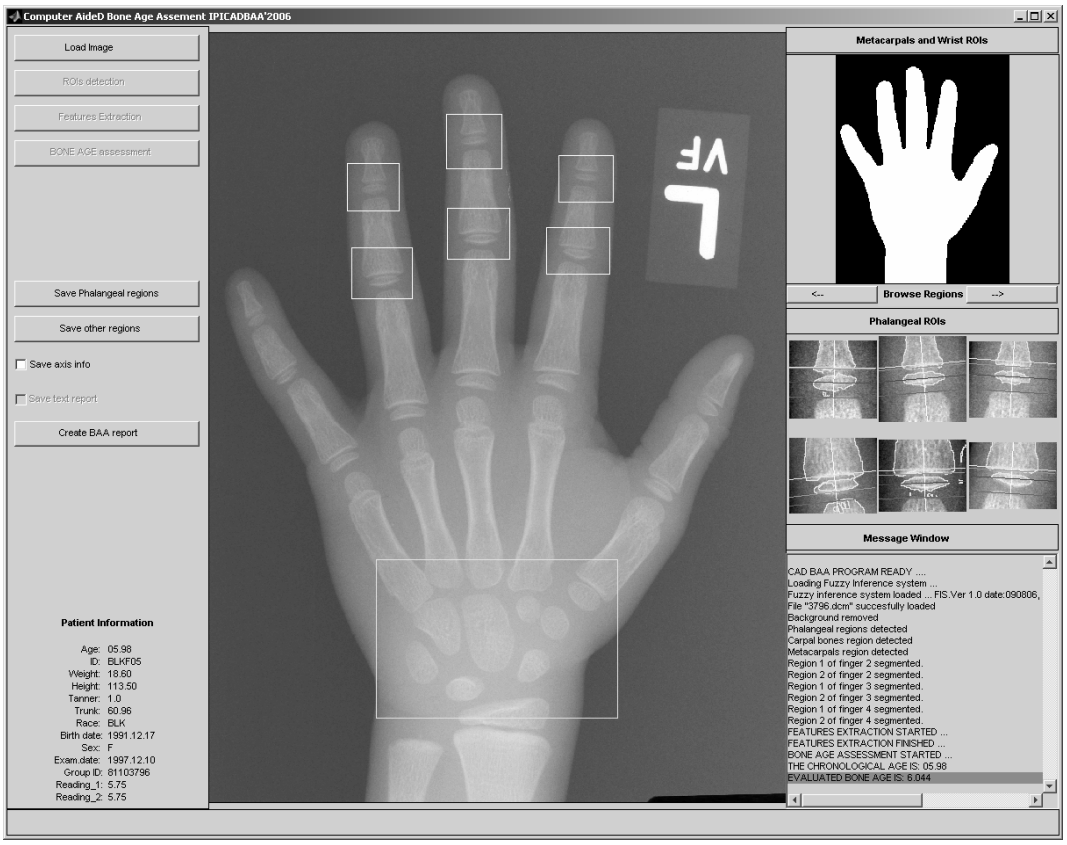

Figure 4. Graphical user interface of the CAD for BAA. The analyzed hand image with superimposed ROIs is in the GUI center. Patient data is on left side, right part of the GUI contains segmentation results and message window.

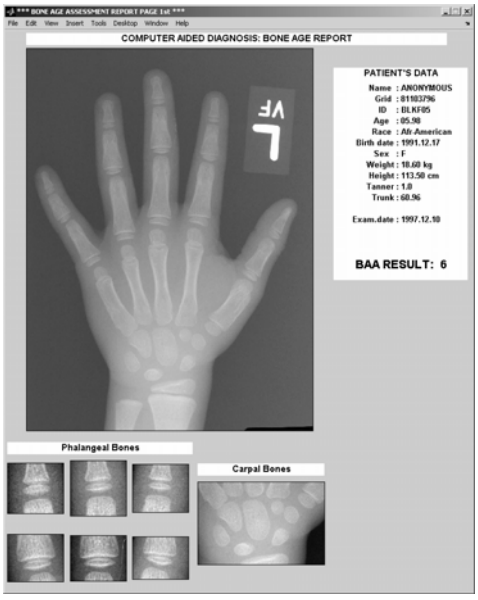

Figure 5. An example of a CAD report window with automatically extracted ROIs together with analyzed hand image. Patient data and CAD result are displayed in the upper right.

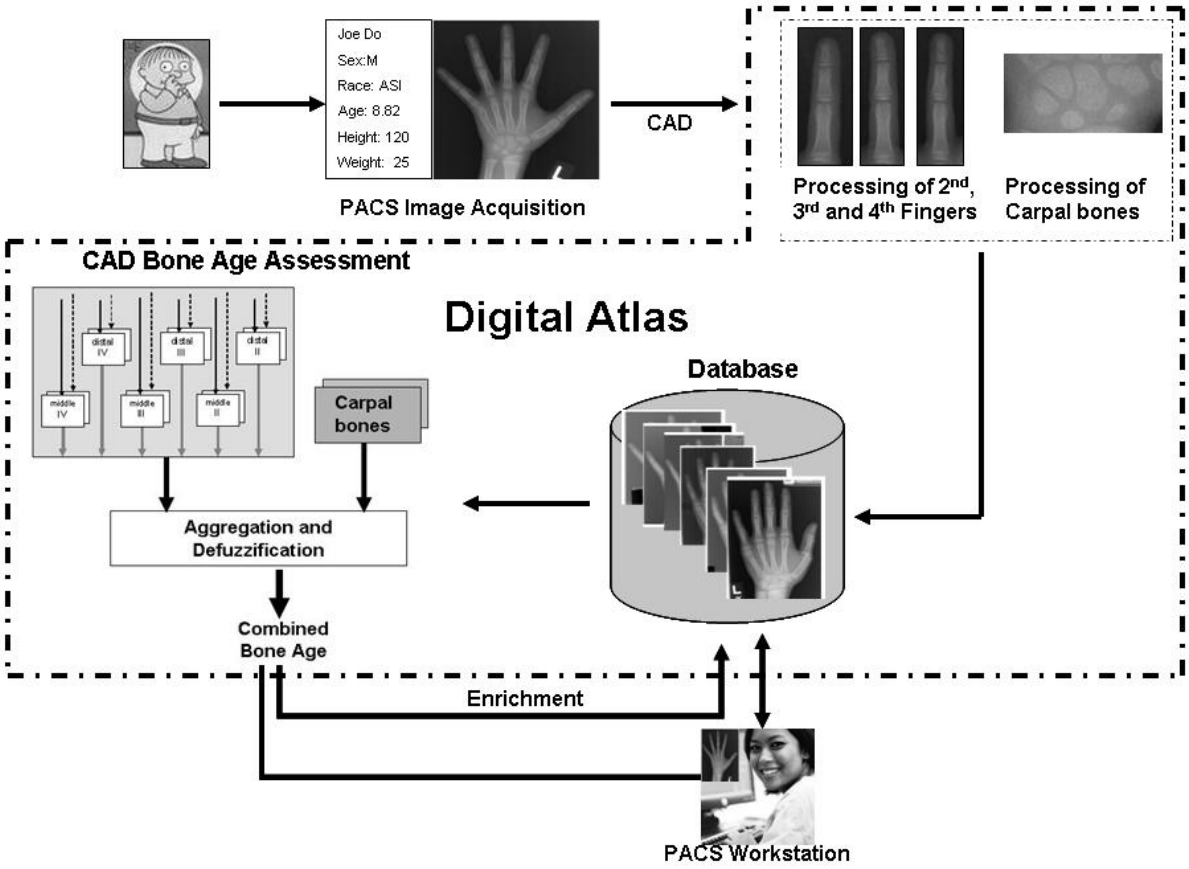

Figure 6. The workflow of CAD and PACS integration. Acquired hand image is processed by the CAD and compared with hand images in the database. The Digital Hand Atlas can be enriched by CAD bone age results.

4. RESULTS

With the large-scale data collection and elaborated design of the CAD module, many different types of meaningful clinical results could emerge. In this section, we provide results related to the evaluation of data collection methodology and its effect on the CAD bone age assessment. In particular, the effect of quality assurance protocol (QAP) to the performance of image analysis algorithm, the accuracy of image analysis algorithm in the phanlangeal ROIs (PROI), and the improvement of the CAD method in bone age assessment with the addition of second cycle data collection (See Table 2a,b) are given.

Effect of Quality Assurance Protocol (QAP) to the Performance of Segmentation Algorithm

Since data collection spanned about ten years, QAP is important to assure the consistence and quality of the data collected (See Appendix A). During the data collection process, by incorporating the QAP, about 5% of cases misspelled dates and other numeric data in the DICOM study description field were detected and corrected. Forty six images failed to pass the Step 1 of the QAP work flow (Appendix A) and were replaced by others. Main reasons were the hand placement was not aligned properly during the X-rays exam, and/or numerous artifacts on the image. Application of the Step 3 of the QAP also greatly improved the passage of all 1,400

images through the CAD in terms of smooth running of the CAD. All cases that caused errors were investigated and more robust error detection was implemented.

Evaluation of the image analysis algorithm

The evaluation of segmentation results involved 300 selected hand images from the second cycle data collection. The set covered distal and middle regions of interest with all possible stages of epiphyseal development, from those with epiphyses distinct in appearance, to epiphyses partially and completely fused with the metaphyses, otherwise. Other than these conditions, the selection process was random. The PROIs were automatically located in the hand image by the CAD software. All segmented regions with outlined cartilage and bony structure were presented to two radiologists of different clinical experience and training. Results of segmentation of each region were evaluated by these radiologists to one of three categories: *good*, *acceptable*, *unacceptable*. They were blind to the child's age, sex and race. Their subjective results are presented in Table 3. The average number of regions classified as *good* was 79.7%, and regions classified as *good* or *acceptable* was 93.7% which demonstrate that the automatic segmentation of the cartilage and bony structures is acceptable by the radiologists. For results in carpal bone ROI, see [17].

Table 3. Experts' evaluation of PROIs outlined by the CAD. The average number of regions classified as *good* is 79.7%, and regions classified as *good* or *acceptable* is 93.7%

Expert	*good*	*acceptable*	*unacceptable*
Expert 1	72.81%	19,94%	7.25%
Expert 2	86.5%	8.08%	5.24%

Improvement of the CAD method with the addition of second cycle data collection

In Section 3 we described that the CAD consists of eleven fuzzy classifiers each of which is used to assess the bone age of the eleven categories: CAM, CAF, AAM, AAF, HIM, HIF, ASM, and ASF, female only, male only, and female and male (F & M) together, respectively. These eleven classifiers were trained in two times, with data from the first cycle collection, and with data from both cycles (first and second) collection. We discuss here the improvement of the CAD method for bone age assessment of the first eight categories with the addition of second cycle data collection. Comparison between races indicated that the addition of second cycle data collection does improve the performance of the CAD based on the comparison of the CAD bone age assessment (BAA) with the chronological age. Improvement is in the sense that less discrepancy between races was observed. Table 4 depicts an example of the girl BAA, where Table 4a) is the result using the first cycle data only, and Table 4b is the results using both first and second cycle data. The girl bone age development according to the female gender was divided into four stages as a gauge of comparison shown in the bottom of both Tables 4a) and 4b).

Table 4a. Performance of the CAD Bone Age Assessment based on comparison with chronological age using first cycle data. The girl bone age development was divided into four stages as a gauge of comparison shown in the bottom. * indicates that the comparison has p-value < 0.05 which is significant.

Female: CAD BAA vs. chronological age (trained by first cycle data only) (unit: year; " - ": under-read of CAD comparing row with column)				
	ASF	AAF	CAF	HIF
ASF		-0.81*	-0.90*	-1.04*
AAF			-1.32*	
CAF				-1.18*
HIF				

* - p-value <0.05

1 6 10 14 19 Chron. age

Table 4b. Performance of the CAD Bone Age Assessment based on comparison with chronological age using both first and second cycle data. Improvement is in the sense that less discrepancy between races was observed. The girl bone age development was divided into four stages as a gauge of comparison shown in the bottom. * indicates that the comparison has p-value < 0.05 which is significant

Female: CAD BAA vs. chronological age (trained by first and second cycle data) (unit: year, " - ": under-read of CAD comparing row with column)				
	ASF	AAF	CAF	HIF
ASF				
AAF				
CAF				
HIF				

* - p-value <0.05

1 6 10 14 19 Chron. age

5. DISCUSSION AND SUMMARY

An overview of the computerized approach to bone age assessment utilizing Digital Hand atlas is presented. The Digital Hand Atlas serves as a reference data set reflecting current skeletal development of normal subjects of four descents, living in the US, in particular in the Los Angeles area. The Atlas is comprised of two components, a digital hand database with a

collection of 1,400 digitized left hand radiographs and relevant data from evenly distributed normally children of Caucasian (CA), Asian (AS), African-American (AA) and Hispanic (HI) origin, male (M) and female (F), ranged from 1 to 18 year old; and a CAD module for bone age assessment. The automatic CAD approach utilizing quantitative knowledge of the Digital Hand Atlas can provide bone age value based on radiological findings sensitive to developmental changes.

We are in the beginning of validating and evaluating the performance of the digital hand atlas. Three types of results have been obtained: the effect of quality assurance protocol (QAP) to the performance of image analysis algorithm, the accuracy of image analysis algorithm in the phanlangeal ROIs (PROI), and the improvement of the CAD method in bone age assessment with the addition of second cycle data collection. Bone age assessment for children has been assessed based on the 1950 Greulich and Pyle Atlas (G & P) from a homogeneous population. With today's diverse ethnicities in the US, the G & P atlas may no longer be a good reference. We are in the process of analyzing the Digital Atlas results to address the following questions:1. Does ethnicity and gender have different bone growth patterns? 2. Does the bone age of ethnic origins differ? 3. Is the bone growth for boys and girls different? And 4. Is the G & P atlas still a good reference for bone age assessment of today's children?

The atlas has been integrated with PACS which can directly access the hand image of a patient from the PACS and return the bone age assessment results to PACS workstations for on-line assisting clinicians to assess the bone age. The digital atlas can be expanded in bone age assessment of subjects of other ethnic origins by collecting digital hand images following the data collection protocol and the training of the fuzzy classifiers with methods discussed in this paper.

Acknowledgements

The authors would like to thank Alexis Wong, MD, and Bing Guo, MD, for their kind help in validating the segmentation results. This research work has been sponsored by NIH R01 EB 00298.

APPENDIX A

Quality Assurance Protocol of the Images collected for the Digital Hand Atlas

Testing and developing of a CAD requires the image data to be properly collected according to a standard protocol. Also, high quality of the data should be maintained if the images are intended to be used in a decision making process. A quality assurance protocol (QAP) has been developed and implemented in order to meet such needs. The QAP encompasses a manual and visual inspection of the image and the evaluation of its suitability for the automatic CAD process. The workflow of the QAP is presented in Fig. A1 which consists of four steps. Step1 can be completed by the operator whereas Steps 2-4 are non-interactively performed by the CAD.

In Step1 (Fig. A1) the quality is first visually justified by the operator utilizing the graphical user interface of the CAD. If the hand image is not aligned properly with respect to the image plane, then it is immediately rejected. In Step 2, a comparison between the radiologist readings and the chronological age is performed. The image is rejected if the difference between the chronological age and the radiologist bone age reading is larger than a certain threshold *trh*. In this protocol, *trh* value has been set to three years. In Step 3, the content of the DICOM image header containing

the subject's demographic data is compared with the data in the documentation used during the digitization procedure. Any inconsistencies between the documentation and patient record require corrections. In Step 4, image preprocessing procedures could reveal artifacts caused by nonuniform background, underexposed film borders, scratches and radiological markers that may cause difficulties in automatic image processing [12, 13]. Finally CAD results like: regions of interests and bone age value are evaluated. In Step 4 the CADBA result is also compared with subject's chronological age. If the discrepancy is smaller than the predefined threshold *trh*; the same as used in Step 2, then this image is subjected to the acceptance procedure and appended to the existing data collection. Otherwise it requires a CAD verification step to be taken. In such cases, the image will be subjected to bone age recalculation after a modification of the CAD.

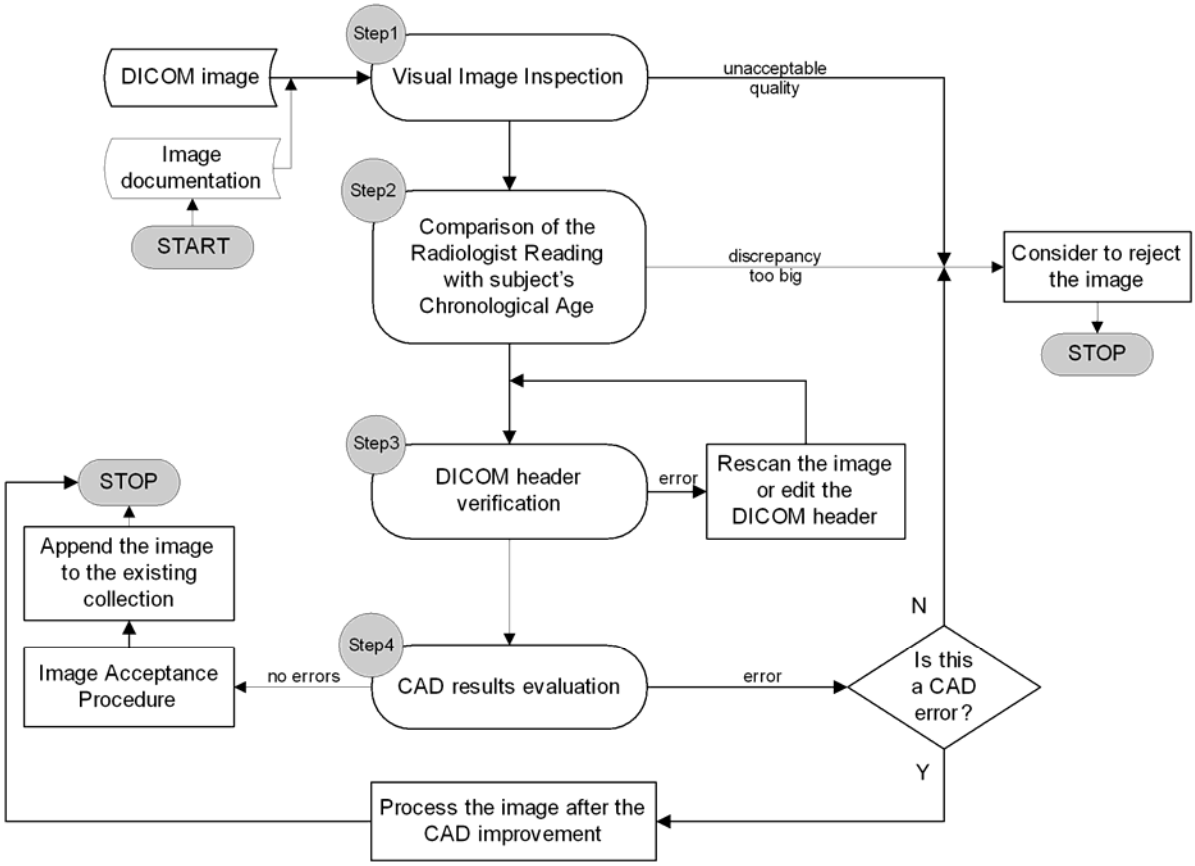

Figure A1. The quality assurance protocol work flow with the CAD in the loop. Image inspection Step 1 and DICOM header verification: Step 2, 3 are performed first. In Step 4 errors and comparison of CAD result are evaluated. Acceptance of the CAD results allows appending the image to the existing collection.

In summary, the QAP applied to the Digital Hand Atlas encompasses checking the image features and patient data at various levels. Image quality is assessed in terms of correct hand placement, presence of image artifacts and capability of radiological findings extraction performed by the CAD. Verification of subject's demographic data can be performed in the QAP by the CAD operator or the CAD; however the latter option can be modified in a more automated fashion. Images that failed to comply with the QAP protocol have been replaced by other images. Using the QAP, the reliability of the data collected for the Digital Hand Atlas has been improved.

References

[1] Greulich WW, Pyle SI, Radiographic Atlas of Skeletal Development of Hand Wrist. Stanford University Press 2nd ed, Stanford CA, 1971.
[2] Roch AF, Rochman CG, Davila GH, Effect of training of replicaability of assessment of skeletal maturity (Greulich-Pyle), Amer. Journal of Roentgenology, 1970, vol. 108, pp. 511-515
[3] Tanner JM. Growth at adolescence, 2nd ed. Oxford: Blackwell Scientific Publications, 1962.
[4] Tanner JM, Whitehouse RH, Assessment of Skeletal Maturity and Prediction of Adult Height (TW2 Method). Academic Press, London, 1975.
[5] Tanner JM, Healy MJR, H. Goldstein, N. Cameron, Assessment of Skeletal Maturity and Prediction of Adult Height (TW3 Method), Third edition, W. B. Saunders, London 2001.
[6] King DG, Steventon DM, O'Sullivan MP, Cook AM, Hornsby VP, Jefferson IG, King PR, Reproducibility of bone ages when performed by radiology registrars: an audit of Tanner and Whitehouse II versus Greulich and Pyle methods. Br J Radiol 1994;67:848–851.
[7] Mora S, Boechat MI, Pietka E, Huang HK, Gilsanz V, Skeletal Age Determinations in Children of European and African Descent: Applicability of the Greulich an Pyle Standards. Pediatric Research, 2001;50(5):624-628, 2001.
[8] Cao F, Huang HK, Pietka E, Gilsanz V, Digital hand atlas for Web-based bone age assessment: System design and implementation. Computerized Medical Imaging and Graphics, 2000;24:297-307.
[9] Cao F, Huang HK, Pietka E, Gilsanz V, Dey PS, Gertych A, Pospiech-Kurkowska S, Image database for digital hand atlas, SPIE Med. Img., Proceedings of the SPIE, 4(24):461-470, 2003.
[10] Pietka E, McNitt-Gray MF, Huang HK, Computer-assisted phalangeal analysis in skeletal age assessment. IEEE Trans. on Medical Imaging, 1991;10:616-620.
[11] Pietka E, Kaabi L, Kuo ML, Huang HK, Feature extraction in carpal-bone analysis, IEEE Trans. on Medical Imaging. 1993;12:44-49.
[12] Pietka E, Gertych A, Pospiech S, Huang HK, Cao F, Computer assisted bone age assessment: Image pre-processing and ROI extraction, IEEE Trans on Medical Imaging 2001;20:715-729.
[13] Pietka E, Pospiech S, Gertych A, Cao F, Huang HK, Gilsanz V, Computer Automated Approach to the extraction of epiphyseal regions in hand radiographs, Journal of Digital Imaging 2001;14:165-172
[14] http://www.cdc.gov/growthcharts/
[15] Pietka E, Gertych A, Pospiech-Kurkowska S, Cao F, Huang HK, Gilsanz V, Computer Assisted Bone Age Assessment: Graphical User Interface for Image Processing and Comparison, Journal of Digital Imaging, 2004;17(3):175-188.
[16] Pietka E, Pospiech-Kurkowska S, Gertych A, Cao F, Integration of Computer assisted bone age assessment with clinical PACS. Comp. Med. Img. Graph, 2003;27:217-228.
[17] Zhang A, Gertych A, Liu BJ, Bone Age Assessment for Young Children from Newborn to 7-Year-Old Using Carpal Bones, Journal of Comp. Med. Img. Graph (*in press*)
[18] Pietka E, Gertych A, Witko K, Informatic infrastructure of CAD system, Computerized Medical Imaging and Graphics, 2005;29:157-169.
[19] Gertych A, Pietka E, Liu BJ, Segmentation of Regions of Interest and Post-Segmentation Edge Location Improvement in Computer-Aided Bone Age Assessment. Pattern Analysis and Application Journal (*in press*)
[20] Zhou Z, CAD-PACS Integration Tool Kit based on DICOM Secondary Capture, Structured Report and IHE Workflow Profiles. Journal of Comp. Med. Img. Graph (*in press*)
[21] Mamdani EH. Application of fuzzy algorithms for control of simple dynamic plant. Proc IEEE 1974; 121:1585-8

Experiences with a Prototype Tracking & Verification System Implemented within an Imaging Center*

Bing Guo[1], MD., Jorge Documet[1], MS., Jasper Lee[1], BS., Brent Liu[1], PhD., Nelson King[2], PhD., Rasu Shrestha[1], MD., Kevin Wang[1], BS., H.K. Huang[1], D.Sc., Edward G. Grant[1], MD.

[1]Image Processing and Informatics Laboratory (IPI), Department of Radiology, University of Southern California (USC), USA,

[2]American University of Beirut, Lebanon

** Paper accepted to be published in Journal of Academic Radiology*

ABSTRACT

Rationale and Objectives

Most healthcare facilities currently struggle with protecting medical data privacy, mis-identification of patients, and long patient waiting times. This paper demonstrates a novel system for a clinical environment using wireless tracking and facial biometric technologies to automatically monitor and identify staff and patients to address these problems.

Materials and Methods

The design of the Location Tracking and Verification System (LTVS) was based on a workflow study which was performed to observe the physical location and movement of patient and staff at the Healthcare Consultation Center II (HCC II) running a HIS (Hospital Information Systems), RIS (Radiology Information Systems), PACS (Picture Archive and Communication Systems), and VR (Voice Recognition system). Based on the results from this workflow study, the LTVS was designed using a wireless real-time location system and a facial biometric system integrated with the RIS. The LTVS was tested for its functionality in a laboratory environment, then evaluated at HCC II.

Results

Experimental results in the laboratory and clinical environments demonstrated that patient and staff real-time location information and identity verification can be obtained from LTVS. Warning messages can immediately be sent to alert staff when patient's waiting time is over a pre-defined limit, and unauthorized access to a security area can be audited. Additionally, patient mis-identification can be prevented during their course of examinations.

Conclusion

The system enabled healthcare providers to streamline the patient workflow, protect against erroneous examinations and create a security zone to prevent and audit unauthorized access to

patient healthcare data required by the Health Insurance Portability and Accountability Act (HIPAA) mandate.

Keywords: *LTVS, Location Tracking and Verification System, HIS, RIS, PACS, HIPAA Security*

INTRODUCTION

With the explosion of digital imaging and medical records, more and more medical data are managed and stored electronically in different Medical Information Systems, for example, Hospital Information Systems (HIS), Radiology Information Systems (RIS), and Picture Archive and Communication Systems (PACS). In order to protect the privacy of personal health information, HIPAA [1] privacy rules regarding national standards were published on April 11th 2003 and mandated on April 11th 2006. Great care should be taken to protect patient confidentiality to meet partial HIPAA requirements. Moreover, in an ever-increasingly complex and dynamic clinical environment, mis-identification of patients is also a common problem in health facilities [2]. In the United States, the Joint Commission on Accreditation of Healthcare Organizations (JCAHO) processed root cause analysis information on 126 cases of wrong site surgery between 1998 and 2001. Seventy-six percent of cases involved surgery on the wrong body part or site, 13% surgery on the wrong patient, and 11% the wrong surgical procedure. JCAHO has identified the factor that human error such as misuse of addressograph labels, mishearing, misspelling and misfiling may lead to mis-identification. In addition, patient experience with long waiting time for scheduled appointment is another widespread problem within healthcare. Visitors to U.S. hospital emergency departments (ED) wait an average of 222 minutes, or 3.7 hours, before being seen by a provider, according to a new state-by-state study released by Press Ganey Associates, USA Today reports [3]. The study, which examines wait times at ED's across the nation, is based on 1.5 million patient questionnaires filled out in 2005. Most healthcare facilities nowadays struggle with protecting medical data privacy, mis-identification of patients, and long patient waiting times.

To address these issues, a Location Tracking and Verification system (LTVS) was designed and developed using wireless technology for tracking the location of patients [4] and facial biometric technology for automatically identifying staff and patients [5]. By integrating these two technologies, LTVS system provided a simple yet systematic solution to monitor and automatically identify staff and patients in order to streamline the patient workflow, protect against erroneous examinations and create a security zone to prevent and audit unauthorized access to patient healthcare data for partial compliance of the HIPAA mandate.

MATERIALS AND METHODS

Clinical Workflow Study

Performing a workflow study in a clinical environment could help to better understand the clinical issues described above [6]. A four-week observation period was performed at HCCII, an outpatient imaging facility with a fully digital environment with integrated HIS/RIS/PACS/VR (Voice Recognition) located in the University of Southern California (USC) Health Science Campus. The facility has one Computed Tomography (CT) Scanner, one Magnetic Resonance Imaging (MRI) Scanner, one Ultrasound Scanner (US), two Computed Radiography (CR) units, and one Special Procedure Room (Fluoroscopy/Angiography). There are a total of thirty-one clinical personnel including eight technologists, seven support staff and sixteen rotating radiologists.

Workflow at the modalities was observed (e.g., CT, MRI, US, CR) including any interaction with the integrated HIS/RIS/PACS/VR (Voice Recognition) systems. The workflow of the special procedure room was not observed because the room was not in clinical operation during that time. Figure 1 shows the general patient tracking location workflow which includes 7 steps, 1) Patient is scheduled at the registration desk with RIS. 2) Patient waits in the waiting room before the technologist verbally calls his/her name. 3) The patient is taken to the working area based on the modality type of examination. 4) Patient is asked to change clothes in the dressing room. 5) When the patient is ready, technologist will escort the patient into the procedure room and take the exam. 6) After the exam is completed, the patient returns to the dressing room and changes back into his/her own clothes. 7) The patient is released by the technologist and leaves the radiology department.

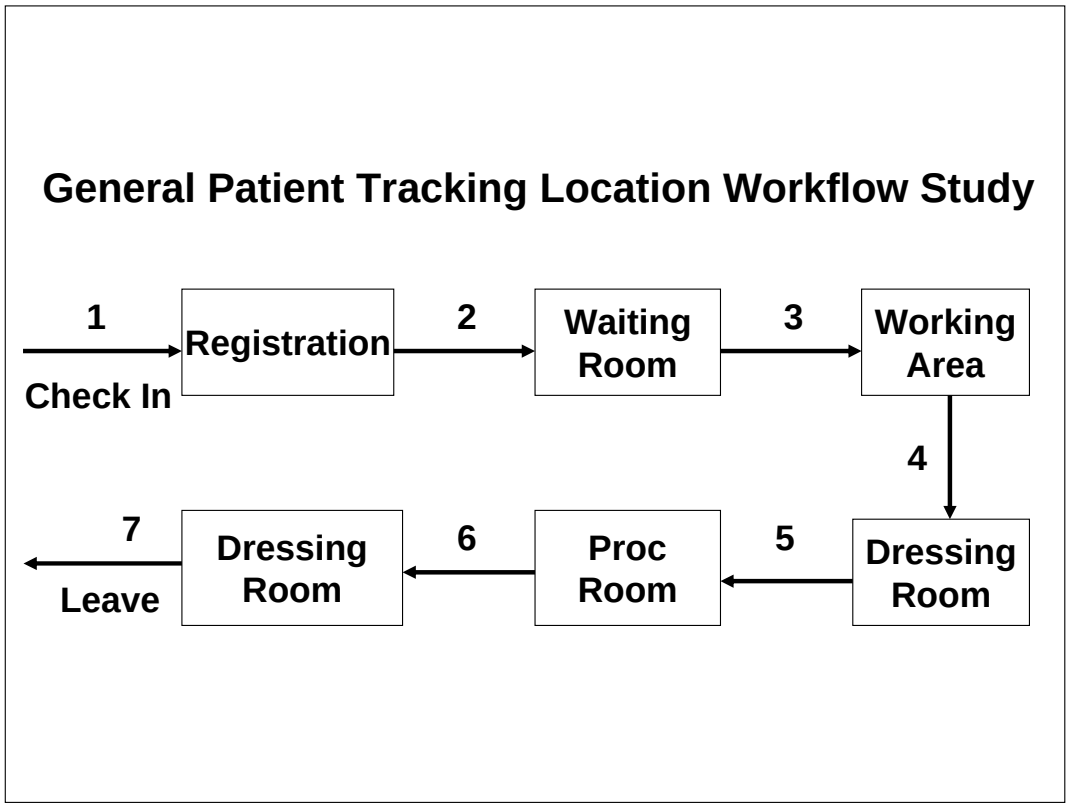

Figure 1 - The General Out-Patient Tracking Location Workflow at the Healthcare Consultant Center (HCC II), University of Southern California (USC), Los Angeles, CA

Based on the workflow study described above, we have identified that for a patient undergoing a radiological examination, the following can occur: 1) Extensive patient waiting time in the waiting room, 2) An unauthorized patient can easily access the reading area without permission, and 3) A potential mis-identification of a patient at the working area before the patient enters the procedure room. To address these problems, a Location Tracking and Verification system (LTVS) was designed and developed using wireless technology for tracking the location of patients and facial biometric technology for automatically identifying staff and patients.

LTVS Development

The components for the LTVS consists of a facial biometric recognition module (box A), a Wi-Fi (IEEE 802.11 network) based tracking module (box B) and integrated into a web-based application (box C) as shown in Figure 2.

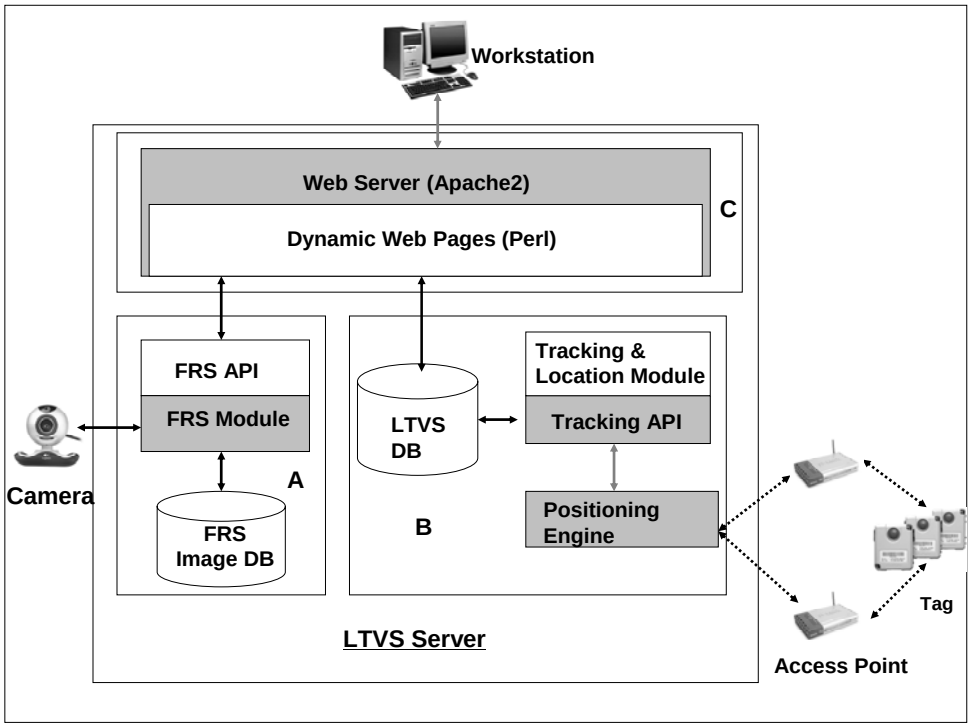

Figure 2 - System architecture shows the Location Tracking and Verification System (LTVS) Server which consists of a web server application that runs the LTVS web-based Graphical User Interface (GUI). The system design and implementation were developed in-house. Box A -- Facial biometrics verification module with cameras. Box B -- Wireless Location Tracking module with tags. Perl -- Practical Extraction and Report Language. FRS – Facial Biometric Recognition System. API -- Application Programming Interface.

The facial biometrics recognition module (box A) uses an advanced software that calculates and analyzes landmark positions and features on a face to verify a person's identity. High resolution USB video cameras are used for identity verification purpose. The facial biometrics recognition module has a database for image storage. The tracking module (box B) consists of a wireless radio frequency solution that utilize IEEE 802.11 b/g access points and Wi-Fi tags to track the location of patient and staff. The LTVS database stores the location information of the patient and staff. Any Wi-Fi network can work as the backbone and sensor network for this real-time location system so it complies with the IEEE 802.11 b/g network standard described above. In addition to location information, the integrated web-based application (box C) stores data inputs into the LTVS database from both the facial biometric recognition module as well as other data from the tracking module.

The LTVS application can be used with any standard PC workstation with a web browser. A web-based browser capable Personal Digital Assistant (PDA) can also be utilized as a mobile application for users to monitor patient and staff and verify patient and staff identities [7]. Table 1 lists all the hardware and software components of the LTVS system. The system integration design and the Graphical User Interface (GUI) were developed by the Image Processing and Informatics (IPI) laboratory. Based on the workflow, the GUI was developed which allows healthcare providers to extract real-time location information and verify the identity of the patient. The tracking and biometrics module runs independently and synchronously using the Windows 2000 Professional operating system. The design of the LTVS server is modular in design to facilitate any improvements and replacements in the future. The system was demonstrated at the InfoRAD Exhibit, 91st Scientific Assembly and Annual Meeting of the

Radiological Society of North America Conference 2005 and received Certificate of Merit Award [8].

Table 1 -- Hardware and software components of the LTVS system. System design and implementation were completed in-house

HARDWARE	SOFTWARE
Dedicated LTVS Server (PC Workstation, DELL DIMENSION 3000) Wi-Fi tracking devices: Wireless Access Points (D-Link Xtreme G Router) Ekahau Wi-Fi tags Client Workstations (PC Workstation, DELL DIMENSION 3000) Logitech USB Video cameras	LTVS GUI web application Web server (Apache) LTVS Tracking API PostGreSQL Database Ekahau Wi-Fi Positioning Engine LTVS Facial Verification API (Neven Vision) Image-Capturing software

Laboratory Testing

The performance of the LTVS was tested at our laboratory with 3,400 square feet of space. The steps for setting up the LTVS included: 1) Wi-Fi access points placement and configuration. There were three access points used to provide signal coverage for tracking purpose. 2) Configure the map of the laboratory to define the correct map scale. 3) Define tracking areas, edit tracking paths on the map and site calibration. 4) Load the map into the LTVS server. 5) Connect USB video cameras to client PC workstations for facial verification purposes.

During the calibration of the Wi-Fi tracking system at the laboratory, it was discovered that access point placement was crucial to the accuracy of the location tracking. Therefore, unknown and unwanted signals need to be blocked out during the site calibration step.

We defined the laboratory into simulated clinical logical areas including front desk, waiting room, control area, procedure room and reading room. The reading room was also considered as a security area. The pre-defined time limit for a patient stay in the Waiting room was set to 30 minutes, and patients were not allowed to enter the security area. A total three-week period of testing was performed. Based on the workflow, three volunteers were simulated as patients, given test ID number, and assigned with portable tracking tags. The first volunteer was asked to walk through each clinical area and had his identity verified before entering the Procedure Room. The system was able to track the patient's location in real time and provide the correct information for the volunteer. The second volunteer was asked to stay in the waiting room for more than 45 minutes, and a warning message was received on the GUI window. The third volunteer was asked to enter the reading room (security area), and the results were reflected with patient name, time, location and the warning message on the GUI window saying "Patient Entered Restricted Area". A total of seven volunteers were then added to evaluate the performance of the system during the testing period. The experimental results showed that the LTVS was working properly within the laboratory environment.

Clinical Testing

The LTVS were setup at HCCII with 13,000 square feet of space and a built-in wireless network infrastructure. The setup at the clinical environment differed from the laboratory test bed in the following ways:

We used six wireless access points at HCCII. The access points were properly placed within the panels of the ceiling in rooms away from each other to minimize radio interference from other access points and close to power outlets.

Performed accurate location tracking in areas around modality rooms, since random fluctuations of the signal strength was caused by large objects such as CT and MRI modality devices. The accuracy problem was overcome by placing the access points farther away from the modality rooms.

The performance of facial biometrics verification was limited by the influence of the clinical environment. For example, it was difficult to achieve proper lighting within the radiology reading room. Performance concerns arose over the use of facial biometrics verification as a reasonable biometric identification technology for the LTVS system.

As in the lab test, the pre-defined time limit of a patient waiting was configured to 30 minutes. The overall waiting time was calculated from the time the patient enters the waiting room to the time the patient enters the dressing room. A total three-week testing period was performed at HCCII. As the first step for system evaluation, patients who had CR, CT exams were selected to be tracked at HCCII and initial data from the LTVS was collected and analyzed during the testing period. Data was collected from the "Report Page" of the LTVS user interface, Figure 3. The "Report Page" provides multiple choices for querying the report from the database. In figure 3, patient John Doe, with RIS ID, device number, location, event time, event date, and system message saying "Patient waiting longer than 30 minutes" are displayed.

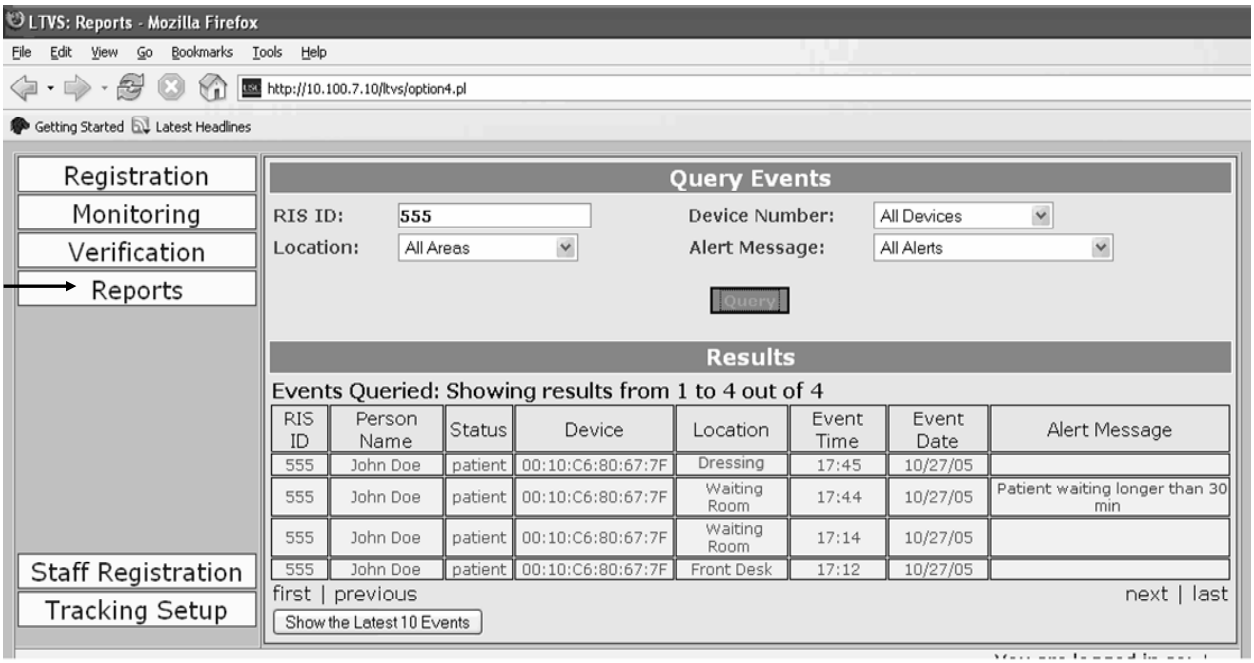

Figure 3- The "Report Page" provides multiple choices for querying the report from the database (see left column "arrow"). For example, in the figure, the GUI display a window of patients John Doe, with RIS ID, tracking device number, location, event time, event date, and system message saying "Patient waiting longer than 30 minutes".

RESULTS

Technical features of the LTVS which could meet certain clinical needs are given in Table 2. The application was shown to be robust, flexible, and could be accessed from any standard PC workstation with a web browser. In addition, the application could be accessed from a Personal Digital Assistant (PDA) with add-on features. Major key technical features and system workflows of the LTVS were developed to address these clinical needs based on the clinical workflow shown below:

Table 2 -- Fifteen sample cases in two days with tracking status including X-Ray, CT from LTVS at Healthcare Consultation Center II during the testing

Clinical issues	System Technical features
Lost patients in the department	Real-time Identification of the movement of patients
Patient waiting too long	Provide a warning to the department personnel if a particular patient has been in one location (e.g., waiting room) beyond the time limit
Patient Misidentification	Patient identity can be verified biometrically through facial recognition at the exam site
Security for Protection and Privacy of Patient information	System creates an information security zone in a given subunit. Verifies biometrically access rights to vital clinical information for authorization by the healthcare provider

Patient Registration

First, a patient photo was captured at the registration desk by the video camera, correlated with patient information from RIS/HIS, and stored in the database of the LTVS.

Tag Assignment

Then, the patient was assigned a Wi-Fi tag which links the patient information, such as the patient name and patient birth date.

Patient Tracking

Once the tags were assigned to patients or staff, the system allowed the staff to access patient location records including when, where and who. It also provides the ability to locate patients on a real-time location tracking page in the GUI window. In addition, the application provided a warning message to personnel if a particular patient had been in one location (e.g., waiting room) beyond the time limit.

Information security

The system could trigger an alert if an unauthorized person entered a pre-defined restricted area, (e.g. a reading room). These pre-defined rules were set not only for areas within the system coverage but also based on authorized and unauthorized staff. For example, a technologist

would be allowed within the Reading Room, but a patient would not. Pre-defined rules could be re-configured within the LTVS to reflect these restrictions.

Patient safety

In order to prevent patient mis-identification, before the patient entered the procedure room for an exam, the technologist could verify the identity of the patient by capturing the patient's facial image, and the software would verify and confirm the patient information including the patient ID, name, and original photos.

User Interface examples

In addition to Figure 3 which shows the real-time report, Figure 4 depicts the LTVS "Monitoring page" menu from where the real-time location of patients and staff can be located. In Figure 4, an image map of the clinical site at HCCII has been uploaded into LTVS monitoring page. Patients John Doe 1, staff 2, and staff 3 assigned with tags were tracked on the map in real-time with their names displayed next to the locations. The walking movement could be tracked on the map.

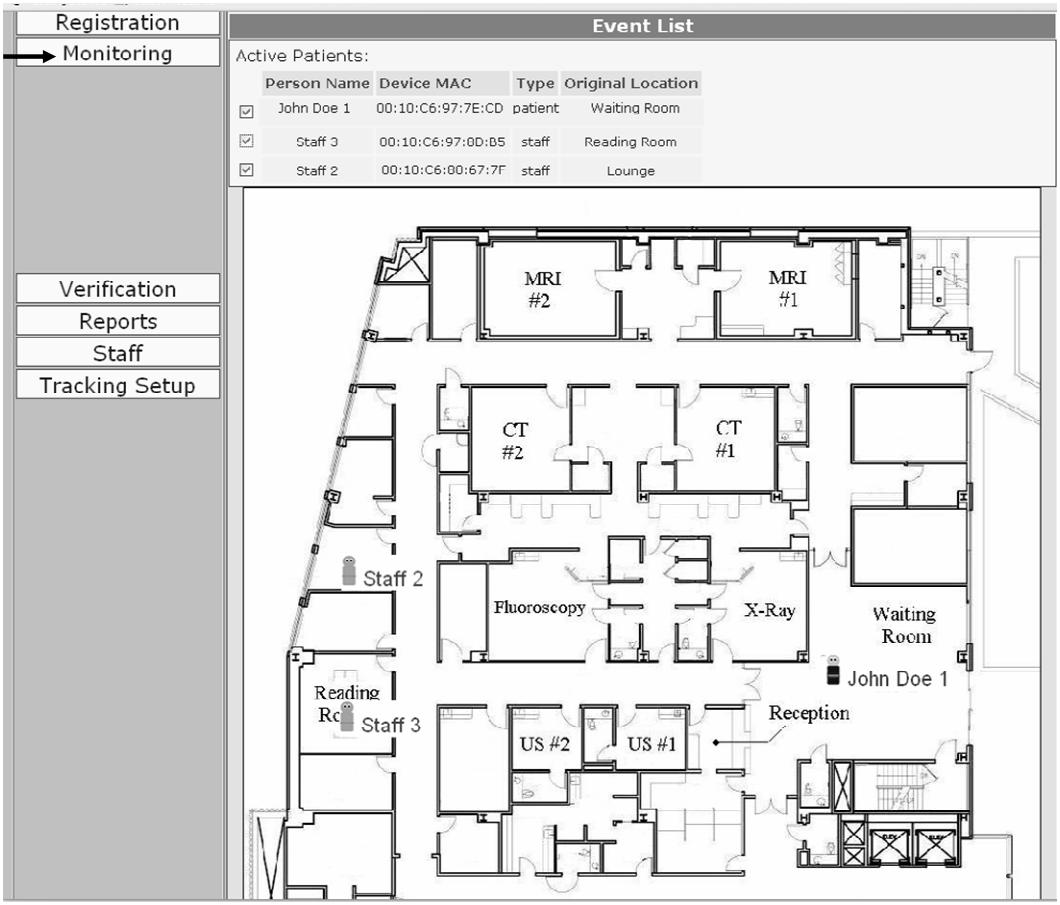

Figure 4- The GUI showing a window of the floor plan of the clinical evaluation site, USC Healthcare Consultation Center II (HCC II). This example depicts that patient John Doe 1, staff 2 and staff 3 each had been assigned a tracking tag. Their names, tag accession number, status, and physical location are shown in event list table above the floor plan

Clinical evaluation results

Table 3 shows a clinical summary of two given days. There were fifteen sample cases including different type examinations (X-Ray, CT) from HCCII collected. Clinical testing showed that there were five patients in two days who had CT exams with overall waiting time of more than 30 minutes; there were no recorded incidents of patients who had an X-ray exam waiting time of more than 30 minutes since the procedure time for X-ray was much faster than the CT modality. The identity of patient was verified from the LTVS system at HCCII during the test period. There were no unauthorized warning messages received during the test period, which seems reasonable since HCCII was a relatively controlled and secure facility.

Table 3 – Fifteen sample cases with tracking status including X-Ray, CT from LTVS at Healthcare Consultation Center II during the testing in two given days.

Case Number	Date	Enter Dept.	Start Proc.	Waiting Time (mins)
X-Ray 1	November 7th, 2005	8:38am	8:54am	16
X-Ray 2	November 7th , 2005	9:00am	9:13am	13
X-Ray 3	November 7th , 2005	9:39am	9:48am	9
X-Ray 4	November 7th , 2005	9:43am	10:03am	20
X-Ray 5	November 7th , 2005	10:05am	10:28am	23
X-Ray 6	November 8th , 2005	9:08am	9:37am	29
X-Ray 7	November 8th , 2005	10:50am	11:02am	12
X-Ray 8	November 8th , 2005	11:04am	11:27am	23
X-Ray 9	November 8th , 2005	1:02pm	1:17pm	15
X-Ray 10	November 8th , 2005	1:21pm	1:34pm	13
CT-1	November 8th , 2005	8:44am	9:52am	68 *
CT-2	November 8th , 2005	10:05am	10:43am	38 *
CT-3	November 8th , 2005	10:49am	11:43am	54 *
CT-4	November 8th , 2005	1:06pm	1:48pm	42 *
CT-5	November 8th , 2005	2:29pm	3:19pm	50 *

*** Waiting Time more than 30 Minutes**

DISCUSSION

Benefits of LTVS

Based on the initial data collected at HCCII, we observe several benefits from the implementation of the LTVS:

Patients can be clearly identified and tracked through their course of examinations to ensure that patients through a photograph taken during the patient registration and a Wi-Fi tag for the patient to wear. It allows users to understand the operational bottlenecks at HCCII and recommend an improved workflow.

Healthcare providers can know the patient location and the overall time a patient spent during the overall examination. Prompts can be put in place when the patient has remained in the waiting room for more than a specific amount of time to decrease the waiting time as to track workflow inefficiencies throughout the time the patient is within the department.

From a security standpoint, facial recognition will provide instantaneous and highly reliable biometric identity information, to be certain that the examination was being performed on the right patient. It helps to prevent misidentification of patients undergoing a radiological procedure.
It improves the overall clinical management of policies and procedures in a clinical environment in order to partially fulfill HIPAA requirements for patient electronic data security.
In addition, the tracking and biometrics verification application has the potential to provide other benefits to a healthcare center. For example, the active Wi-Fi tag can be useful in keeping track of expensive assets such as wheelchairs and other portable medical equipment. The tracking technology can be used by the administrator to locate staff members to improve productivity.

Cost Analysis

The prototype Location Tracking and Verification system for a clinical environment was designed and developed within the Image Processing and Informatics laboratory (IPI), USC. The LTVS was then evaluated at an out patient imaging center Healthcare Consultation Center II (HCCII) with 13,000 square feet. Table 4 shows the cost of LTVS including hardware and software installed at HCCII, excluding system design, implementation, and evaluation. The potential additional cost of LTVS includes five thousand dollars annual license fees for facial identification biometric system.

Table 4 -- The cost of the Location Tracking and Verification System (LTVS) evaluated at HCCII including the cost of hardware and software (excluding design, development and implementation costs).

Item		Qty	Unit Cost	Sub-Total
Hardware				
	Wireless Access Points	6	$35	$210
	Active Tags	15	$80	$1200
	FRS Cameras	6	$80	$480
	Server (Computer)	1	$700	$700
Software				
	Web Server (Apache)		Free	Free
	Database (PostGreSQL)		Free	Free
	Facial Recognition SDK			$5,000 license fees per year
	Wireless Location Tracking			$5,000 for 15 tags
Total				$12,590

Alternative Identification devices

We are evaluating other biometric verification solutions including fingerprint, and iris identification. The next steps are 1) to continue to test and collect more data for a longer period at HCCII to prepare for actual clinical implementation. 2) to change the facial biometric system to a different biometrics system, by evaluating and comparing them with the following criteria, including cost, ease of use, accuracy, reliability and user acceptance; and, 3) document the advantages and disadvantages of each biometric technology in the clinical environment.
After we complete the evaluation of the new biometric system, it can be easily integrated within the LTVS, since the LTVS was designed in modular fashion. The cost of LTVS would also be relatively cheaper than the facial biometrics system because it does not require annual license fees. Initial estimates indicate that the use of the fingerprint identification technology can be

about one half of the cost described in Table 4. With continuous feedback from the HCCII evaluation, we will continue to implement the LTVS at HCCII for clinical operations.

References:

[1] HIPAA, http://www.hhs.gov/ocr/hipaa/ 2006
[2] Thomas P, Evans C. An identity crisis? Aspects of patient misidentification. Clinical Risk 2004; 10:18-22
[3] Joint Commission on Accreditation of Healthcare Organizations (JCAHO), http://www.jointcommission.org/ 2006
[4] Ekahau Inc., http://www.ekahau.com/ 2006
[5] NevenVision, http://www.nevenvision.com/ 2006
[6] Vissers J.M.H. Patient flow-based allocation of inpatient resources: a case study. European Journal of Operational Research 1998, 105:356-370.
[7] Bing G, Jorge D, Jasper L, et al. A tracking and verification system implemented in a clinical environment for partial HIPAA compliance, Proceedings of SPIE 2006, 6145:184-191
[8] Bing G, Jorge D, Nelson K, Patient tracking and facial biometrics integrated in a clinical environment for HIPAA security compliance, Presented at the 91st Scientific Assembly and Annual Meeting of RSNA, (Inforad Exhibit), 2005

Eosinophilic enteritis: CT Features*

X. Zheng[1], J. Cheng[1], K. Pan[1], K. Yang[1], H. Wang[1], E. Wu[1]

[1]Department of Radiology, The First Affiliated Hospital of Wenzhou Medical College, Wenzhou 325000, China

* *Paper accepted to be published in Journal of Abdominal Imaging*

ABSTRACT

We report CT features of four cases of Eosinophilic enteritis. The disease involves the jejunum in one case, the ileum in two cases, and the colon in the remaining case. Two cases demonstrate a predominantly mucosal type of eosinophilic enteritis, while the other two cases demonstrate a predominantly subserosal type. CT findings include bowel wall thickening in four cases, bowel fold thickening in two cases, layering of the bowel wall in two cases, luminal narrowing without obstruction in three cases, an intraluminal granuloma mimicking a huge polyp in one case, an extra- luminal irregular granuloma markedly enhancing and slightly necrosing in one case, mesenteric lymphadenopathy with peripheral rim-like enhancement and marked necrosis in one case and ascites in one case. CT findings are more characteristic of an inflammatory disease rather than of a tumor, and these findings are helpful for assessing the extent and location of the disease. Moreover, combined with its typical clinical manifestations, CT findings may lead to the correct diagnosis.

Keywords: *Eosinophil, gastroenteritis, bowel, abdomen, CT, Radiology.*

1. INTRODUCTION

Eosinophilic enteritis is a rare inflammatory disease of unknown etiology characterized by focal or diffuse eosinophilic infiltration of the intestinal tract, with clinical and radiographic manifestations related to the location and layer of tissue involvement [1-4]. There have been some reports that predominantly describe clinical, pathological, therapeutic and even traditional radiographic features of the disease [1-7]. However, there are very fewer reports on the CT features of the disease, and these reports are so far entirely limited to case reports [8-13]. CT findings of the disease vary depending on the layer of tissue involved, and these findings can be valuable for evaluating the degree and extent of eosinophilic infiltration of the disease, as well as guiding the endoscopic transmural biopsy [8-13].

We retrospectively report four cases of eosinophilic enteritis and review the literature, with the aim at recognizing more specific CT features and avoiding the morbidity associated with the delay in diagnosis of this rare disease.

2. MATERIALS AND METHODS

We collected CT and clinical information of four cases of eosinophilic enteritis, diagnosed at our hospital from 1996 to 2002.

2.1 Clinical manifestations

The four cases, aged 23, 35, 61, 62 years, including two males and two females, all complained of an intermittent abdominal pain for one month to two years. Other symptoms include nausea and vomiting in two patients, bloody stool in two patients, diarrhea in one patient, constipation in one patient, diarrhea alternating with constipation in one patient, marked weight loss in one patient and fever in one patient. One patient had a history of recurrent allergic dermatitis. Physical examination revealed rebound tenderness in two cases and a palpable mass in one case. Laboratory data revealed peripheral blood eosinophilia in two cases with up to 21% and 8% of WBC, iron-deficiency anemia in one case, and an increased level of IgA and C-reactive protein in one case.

2.2 CT Methods

Prior to CT examinations, the patients took an oral contrast agent of 1000- 1800 ml of 3% iodine solution, to prepare the bowel. CT protocol of our four cases was first a routine unenhanced CT scan, followed by an enhanced CT scan with IV administration of 100 mL of contrast material (Omnipaque 350 mgI/L).

3. RESULTS

On CT, our four cases demonstrate specific abnormalities within the intestine at the level of the jejunum in one case, the ileum in two cases and the colon in one case. The most common feature was bowel wall thickening, found in all four cases, with thicknesses ranging from 6-12 mm. In two cases, there was also layering of the bowel wall as well as mucosal fold thickening (Fig. 1a). The presence of mucosal fold thickening is recognized by hyper-attenuation of contrast within the sinuses between mucosal folds, which we call an ‘araneid-limb-like’ sign (Fig. 1b). This sign can be visualized by CT image of a longitudinal axial-section of bowel. Luminal narrowing is found in three cases, but none of these developed obstruction. In contrast, another case demonstrated slight dilatation of the proximal bowel with a small air-fluid level, but no lumimal narrowing at the location of the lesion, which can be explained by a functional hypotonic state. An ovoid, well-defined, homogeneous soft-tissue attenuation mass measuring 30×25×20 mm, was found within the lumen of the ileum in one case with muscosal disease (Fig. 2). The other two cases with subserosal disease demonstrated another kind of mass outside of the bowel. One case demonstrated multiple mesenteric lymph nodes with peripheral rim-like enhancement and marked central necrosis (Fig. 3). Another case demonstrated an irregular, markedly enhanced mass with less necrosis, localized between the ileum and retroperitoneum (Fig. 4). Little ascites is found in this case.

Due to our relative inexperience with cases of peripheral eosinophilia, our pre-pathology CT interpretations did not entertain this rare disease, but rather suggested diagnoses of Crohn’s diseases, lymphoma, tuberculosis, and non-specific inflammation, respectively in these four cases. Nonetheless, while the specific disease interpretations were incorrect, the correct identification of the location and extent of the disease was useful for surgical or endoscopic localization.

The final diagnoses of eosinophilic enteritis in our series are pathologically proven by surgical and/or endoscopic biopsy, which revealed a predominantly muscosal disease in two cases (Fig. 1c) and a predominantly subserosal disease in the other two cases. In our four cases, two patients underwent exploratory laparotomy and were treated by curative resection of the affected intestine and/or the masses, clinically improving in the following two years with medical care. One patient

received steroid therapy and recovered rapidly. Another patient who mainly manifested with high fever and lower digestive tract bleeding had undergone two colonoscopic biopsies and an exploratory laparotomy with partial resection of the mesenteric nodes, followed by continued postoperative steroid therapy. Although the patient demonstrated mild improvement, he suffered a severe refractory episode eight months after the original onset and expired.

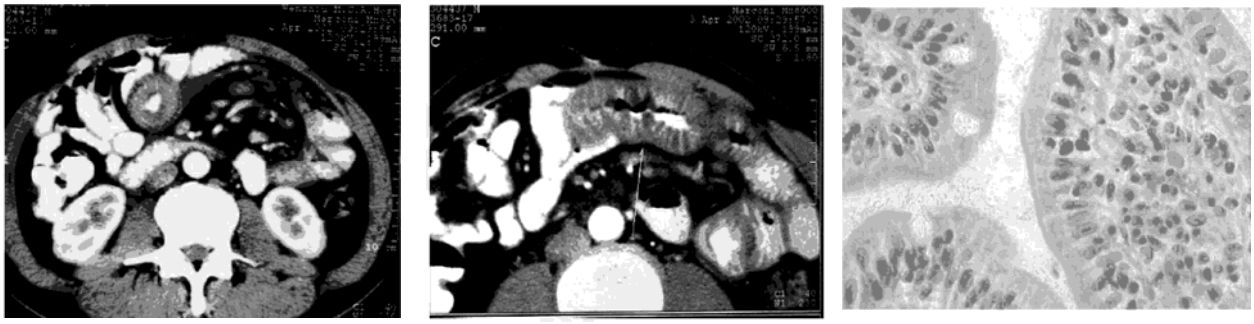

Fig. 1a-1c—35-year-old man with a predominantly mucosal eosinophilic enteritis of the jejunum, an enhanced CT (1a) shows bowel wall thickening with a halo sign and luminal narrowing without obstruction (arrow), CT image of a longitudinal axial-section of bowel (1b) shows fold thickening known as 'araneid-limb-like' sign (arrow), and histological examination of an endoscopic biopsy (1c) exhibits a great deal of eosinophilic infiltration within the villus of the jejunum.

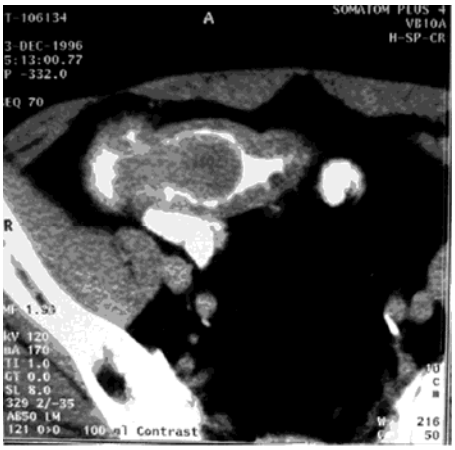

Fig. 2—62-year-old woman with a predominantly mucosal eosinophilic enteritis of the ileum. A delayed enhanced (at 5 minutes) CT shows a huge intraluminal 'polyp' (arrow), bowel wall (folds) thickening (short arrow) and luminal narrowing.

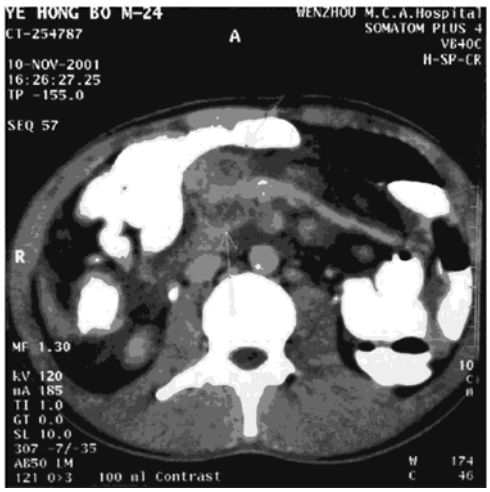

Fig. 3—23-year-old man with a predominantly subserosal eosinophilic enteritis of the colon, an enhanced CT shows necrotic mesenteric multiple nodes with peripheral rim-like enhancement (arrow), the colonic wall thickening with slight luminal narrowing (short arrow) and ascites (black arrow).

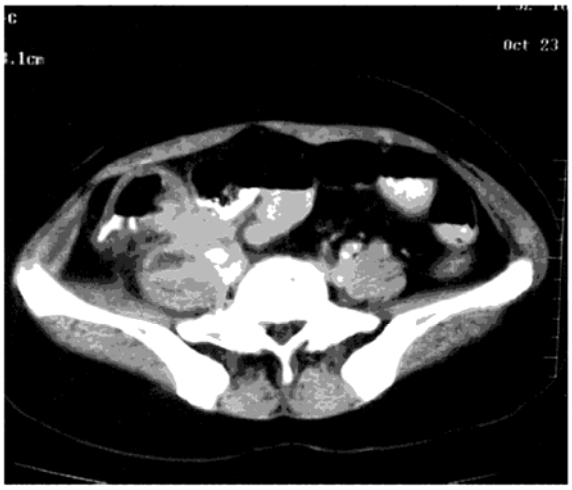

Fig. 4—61-year-old man with a predominantly subserosal eosinophilic enteritis of the ileum. An enhanced CT shows an irregular markedly enhanced mass (arrow) with little necrosis (black arrow), localized between the ileum and retroperitoneum, with the adjacent bowel wall thickening and the presence of a halo sign (short arrow).

4. DISCUSSION

Eosinophilic gastroenteritis, first reported in 1937, is a rare inflammatory disease characterized by focal or diffuse eosinophilic infiltration of the gastrointestinal tract [1-4]. According to the predominant layer of eosinophilic infiltration, Klein [2] classified the disease as predominantly mucosal, muscular, or subserosal. A review of 61 cases in the literature shows predominantly mucosal disease is the most common type (54%), followed by predominantly muscular disease (31%), and finally predominantly subserosal disease (15%) [1, 3]. Our four cases reveal a predominantly muscosal disease in 2 and a predominantly subserosal disease in 2 cases. The disease may occur within any part of the gastrointestinal tract, with an incidence of approximately 40% at the level of the stomach, 50% at both the stomach and small bowel with predominance at the distal stomach and proximal small bowel [1, 4, 8]. In our series, however,

three of the cases only affected the small bowel and the fourth cases affected colon. Although the definite etiology is unknown, there is evidences revealing that an allergic or immunologic disorder may be the most likely cause of this disease[1-4]. An allergic disorder has been reported to be present in 14 of 25 cases (56%) [1] and in one of our four cases. The other evidences include a peripheral eosinophilia varying from 20% to 96% of the reported cases [1,4,5] and in two of our four cases, a relief of symptoms with corticosteroid therapy in most of patients [1,4] , elevated IgE and symptomatic response to specific food [6].

The disease may have a series of clinical manifestations relating to the location and layer of tissue involvement, including abdominal pain, diarrhea, nausea, vomiting, weight loss, bleeding, obstructive symptoms, and occasionally complications of obstruction such as perforation and ascites [1-5]. Although these symptoms themselves are not specific, a chronic clinical course characterized by exacerbations and remissions, with steroids providing a rapid relief of symptoms may be characteristic of the disease [1,4,5]. The disease usually has a relatively benign clinical course and even self-limited recurrence [1]. Nevertheless, there have been four deaths due to the disease, three of these following complications of surgery [1]. Our series adds another case of mortality due to the disease with no complications from surgery.

So far, CT features of the disease have seldom been reported and all are limited to case report [8-13]. As reported, CT features may be different owing to the different types of the disease. Bowel wall thickening usually is the most common finding in all types of the disease on CT [5-13], as well as in our four cases. Furthermore, in our series, we find much more detail of the thickened bowel wall with either a layered bowel wall sign or a ‘araneidlimb-like’ sign. The sign of the layered bowel wall, also known as a halo sign, has been recognized as submucosal edema and represents a benign bowel pathology [8]. The ‘araneid-limb-like’ sign results from mucosal fold thickening, which has been described as a common feature of the disease by radiography [1]. We consider that both of these signs are characteristic of an inflammatory disease, and are valuable for distinguishing this disease from a malignant tumor of the bowel, such as lymphoma or adenocarcinoma. Polyp has been reported in one case with mucosal disease on CT [9]. One case in our series also presents a single, well-defined, homogeneously attenuating intraluminal granuloma with slight enhancement, mimicking a huge polyp. However, by carefully appreciating the concurrent bowel wall thickening with the ‘araneid-limb-like’ sign, we can easily distinguish the disease from either benign or malignant tumor or a simple polyp. Luminal narrowing is another common feature on CT [7, 11, 12], found in three of the four cases. Luminal narrowing may be caused by functional hypertonicity or spasm of the bowel, and it is this distinction which differentiates it from intestinal stenosis which has been recognized as the main characteristic of muscular disease by radiography [1]. Unfortunately, CT usually can not distinguish this difference as easily as radiography. As in two cases of our series, because of the presence of luminal narrowing without any obstruction, we suggest it may represent hypertonicity or spasm. These two cases are finally confirmed as mucosal disease by pathological diagnosis. On the other hand, a luminal narrowing with obvious obstruction tends to be a stenosis, which may be caused by the disease with muscular involvement [12]. Ascites is the most common CT finding of subserosal disease [7, 12, 13], which is the presentation in one of our two subserosal disease. Although ascites is nonspecific alone, an eosinophilic ascites detected by laboratory definitively suggests the diagnosis of the disease [1, 7]. Abdominal eosinophilic lymphadenopathy may present in subserosal disease [1, 13], but CT features of abdominal eosinophilic lymphadenopathy have only been reported in one case [13]. One case of our series with subserosal disease shows mesenteric multiple lymph nodes mimicking lymphoma on unenhanced CT. After contrast administration, however, these multiple lymph nodes actually more closely resemble tuberculosis rather than lymphoma due to their peripheral rim-like enhancement. Due to our lack of experience and unfamiliarity with the diagnosis of peripheral

eosinophilia, this case had been misdiagnosed as tuberculosis for almost a month. Pathology of the node revealed an eosinophilic lymphadenopathy with marked necrosis. Another case of subserosal disease shows an irregular mass with marked enhancement and little low-density outside the bowel on CT, which was proven to be eosinophilic granuloma with little necrosis by pathology.

5. CONCLUSION

We report our experience of CT features in four cases of eosinophilic enteritis. The characteristic CT features include bowel wall thickening with halo sign or 'araneid-limb-like' sign or intra-luminal granuloma, extraluminal lymphadenopathy or granuloma with necrosis and luminal narrowing without obstruction, All of these CT features suggest an inflammatory disease rather than either a malignant or benign neoplasitc process. Moreover, CT features combined with the typical clinical features, including an allergic history, peripheral eosinophilia and a rapid relief of symptoms by steroid therapy will likely lead to the correct diagnosis. In addition, CT is valuable for evaluating the location and extent of eosinophilic infiltration of the disease.

References

1 Vitellas KM, Bennett WF, Bova JG, et al. Radiographic manifestations of eosinophilic gastroenteritis. Abdom-Imaging.1995, 20: 406-413.
2 Klein NC, Hargrove RL, Sleisenger MH, Jeffries GH. Eosinophilic gastroenteritis. Medicine 1970;49:299-319
3 Talley NJ, Shorter RJ, Philips SF, Zinsmeister AR. Eosinophilic gastroenteritis: a clinicopathological study of patients with disease of the mucosa, muscle layer, and subserosal tissues. Gut 1990;31:54-58
4 Naylor AR, Pollet JE. Eosinophilic colitis. Dis Colon Rectum 1985; 28: 615-618.
5 A. Charalabopoulos, K. Charalabopoulos, M. Avuzuklidou. Eosinophilic gastroenteritis: presentation of two patients with unusual affect of terminal ileum and caecum with manifestations of acute abdomen and literature review. International Journal of Clinical Practice. 2004, 58: 413.
6 Pfaffenbach B, Adamek RJ, Bethke B, et al. Eosinophilic gastroenteritis in food allergy. Z Gastroenterol. 1996;34(8):490-493.
7 To Y, Ogawa C, Otomo M, et.al. A case of eosinophilic gastroenteritis. Complicated with ileus and ascites collection. Arerugi.1999,48:50-55. 8 Horton KM, Corl FM, Fishman EK. CT of nonneoplastic diseases of the small bowel: spectrum of disease.J-Comput-Assist-Tomogr.1999,23:417-428.
9 Frohlich H, Buttner D, Manago GB. Computed tomographic detection of a polypous form of eosinophilic gastroenteritis in the duodenum. Rontgenblatter. 1990;43(11):478-80
10 Van HL, Vanghillewe K, Baert AL, et al. CT findings in nonmucosal eosinophilic gastroenteritis. J-Comput-Assist-Tomogr.1994,18:818-820.
11 M. J. B Stallmeyer and Felixs. Chew. Eosinophilic gastroenteritis. AJR. 1993, 161:296.
12 Wiesner W, Kocher T, Heim M, et al. CT findings in eosinophilic enterocolitis with predominantly serosal and muscular bowel wall infiltration. JBR-BTR. 2002;85(1):4-6.
13 Smith TR, Schmiedeberg P, Flax H, et al. Nonmucosal predominantly serosal eosinophilic enteritis. A case report. Clin Imaging. 1990 Aug;14(3):235-8.

Wireless Remote Control of Clinical Image Workflow: Using a PDA for Off-Site Distribution and Disaster Recovery

Jorge Documet[a], Brent J. Liu[a], Luis Documet[b], H. K. Huang[a]

This paper describes a picture archiving and communication system (PACS) tool based on Web technology that remotely manages medical images between a PACS archive and remote destinations. Successfully implemented in a clinical environment and also demonstrated for the past 3 years at the conferences of various organizations, including the Radiological Society of North America, this tool provides a very practical and simple way to manage a PACS, including off-site image distribution and disaster recovery. The application is robust and flexible and can be used on a standard PC workstation or a Tablet PC, but more important, it can be used with a personal digital assistant (PDA). With a PDA, the Web application becomes a powerful wireless and mobile image management tool. The application's quick and easy-to-use features allow users to perform Digital Imaging and Communications in Medicine (DICOM) queries and retrievals with a single interface, without having to worry about the underlying configuration of DICOM nodes. In addition, this frees up dedicated PACS workstations to perform their specialized roles within the PACS workflow. This tool has been used at Saint John's Health Center in Santa Monica, California, for 2 years. The average number of queries per month is 2,021, with 816 C-MOVE retrieve requests. Clinical staff members can use PDAs to manage image workflow and PACS examination distribution conveniently for off-site consultations by referring physicians and radiologists and for disaster recovery. This solution also improves radiologists' effectiveness and efficiency in health care delivery both within radiology departments and for off-site clinical coverage.

Key Words: PACS, wireless 802.11b/g, PDA, disaster recovery, image workflow

J Am Coll Radiol 2006;3:520-527.

PURPOSE

This paper presents a web-based picture archiving and communication system (PACS) management tool that can be used with personal digital assistant (PDA) [1], which in conjunction with a wireless network provides a mobile tool for distributing medical examinations. First, we describe the basic ingredients of this tool, including design considerations, clinical workflow needs, and the PDA server. The disaster-recovery design using this tool on the basis of a particular disaster-recovery scenario is presented. Finally, we provide some statistics acquired during the past 2 years at the Saint John's Health Center (SJHC) in Santa Monica, Calif. Because the tool is a web-based application, it also can be used from any PC or Tablet PC, as long as these devices have access to a PDA server and a web-based browser. In this paper, a destination is defined as a Digital Imaging and Communications in Medicine (DICOM) node that has been already registered at the PDA server and the PACS archive to which the clinical examinations will eventually be sent. A local PACS is a PACS at a local site; thus, a local PACS archive is an archive at a local PACS. A local workstation is a workstation connected to a local PACS network, and so on.

Although the basic design of the PDA tool is quite simple, its use spreads into a significant range of needs within the clinical environment. For this reason, we broadly classify its applications into the following 2 major categories:

- Image distribution from a local PACS archive: this is the most common application, which sends examina-

[a]Image Processing and Informatics Laboratory, Department of Radiology, University of Southern California, Marina del Rey, Calif.

[b]Department of Radiology, Saint John's Health Center, Santa Monica, Calif.

Corresponding author and reprints: Jorge Documet, University of Southern California, Department of Radiology, 4676 Admiralty Way, Suite 601, Marina del Rey, CA 90292; e-mail: documet@usc.edu.

0091-2182/06/$32.00 • DOI 10.1016/j.jacr.2006.03.015

Table 1. List of the clinical requirements and the key technical features that result in the decision process of designing a wireless PDA server tool

Clinical Requirements	Technical Features
Need ad hoc image and report retrieval	Platform independent (HTTPS and DICOM compliant)
Need secure, flexible, and mobile solution	Fully wireless (IEEE 802.11 locally, EDGE/3G/UMTS nationally)
Need relevant clinical information	Secure (WEP, SSL)
Easy-to-use, all-purpose device	Text and graphics capable
PDA applications	Scalable implementation/thin client
Reference/education	
Mobile medical image display	
Workflow/disaster management	

Note: DICOM = Digital Imaging and Communications in Medicine; EDGE = Enhanced Data Rates for Global Evolution; HTTPS = secured hypertext transfer protocol; IEEE = Institute of Electrical and Electronic Engineers; PDA = personal digital assistant; SSL = secure socket layer; UMTS = Universal Mobile Telecommunications System; WEP = wired equivalent privacy.

tions from a local PACS archive to specific destinations, which could be any DICOM node, such as display workstations or CD-ROM-burning devices connected to the same PACS networks.

- Disaster recovery: in this application, a local PDA queries and retrieves images from a backup archive located at a remote facility to be sent to a local PACS during a disaster. For example, in application service provider (ASP) model [2-4] using a fault tolerant backup archive, a PDA requests examinations from a remote backup archive to be sent to a local PACS workstation. The characteristics of this application are that the PDA device, the PDA server, the backup archive, and the final destination could be in different locations. The section "Disaster-Recovery Design," below, describes the design of the disaster-recovery application in more detail.

The advantage of this application in a PACS environment are its simplicity to access different DICOM nodes using the same user interface in a PDA. First, the Web server manages the necessary configuration, specifically, in terms of DICOM entity title information. An end user can focus on the study management workflow. Another advantage is the granularity of privileges, which provides to users access only to a set of preauthorized servers and destinations. This provides flexibility, security, and simplicity all at once.

In the following, the section "Methods" describes the clinical needs and the architecture design of the applications. The section "Results" provides some statistics from the clinical data collected at SJHC.

METHODS

This section describes the clinical need assessment, the design of the PDA server and image query and retrieval operations, and its use for disaster recovery.

Clinical Needs Assessment

The practices for delivering health care have changed over the years, and one of the factors that contributes most is technology. However, technology itself cannot solve a particular need in the clinical environment. Thus, it is very important to find areas in common where there exist clinical requirements to be improved and at the same time where current technology is capable of offering feasible solutions. In our case, the PDA server provides some technical features that fulfill the PACS clinical expectations, making it an excellent tool to address the clinical workflow needs. Table 1 summarizes the technical features of a PDA device that satisfy certain PACS clinical needs.

PDA Server and Graphical User Interface Development

A PDA server is the key component of this application. It serves as a gateway between users and the DICOM nodes. A PDA server is a Web server combined with a DICOM query-and-retrieval tool that allows easy and fast translations of Web requests to DICOM commands. The PDA server was implemented on a Red Hat 8.0 server (with a Pentium 4 central processing unit operating at 2.8 GHz and 512 MB of random-access memory) running Apache 2.0 as the Web server and using the Perl programming language for server-side coding. The server was secured using the secure hypertext transfer protocol standard, which encrypts communications between the server and clients. In addition, a valid username and password are required to access the application, so only authorized users can use it. The application also provides auditing logs to conform to the requirements of the Health Insurance Portability and Accountability Act of 1996. Because this application uses wireless infrastructure, special care was needed to avoid vulnerabilities in

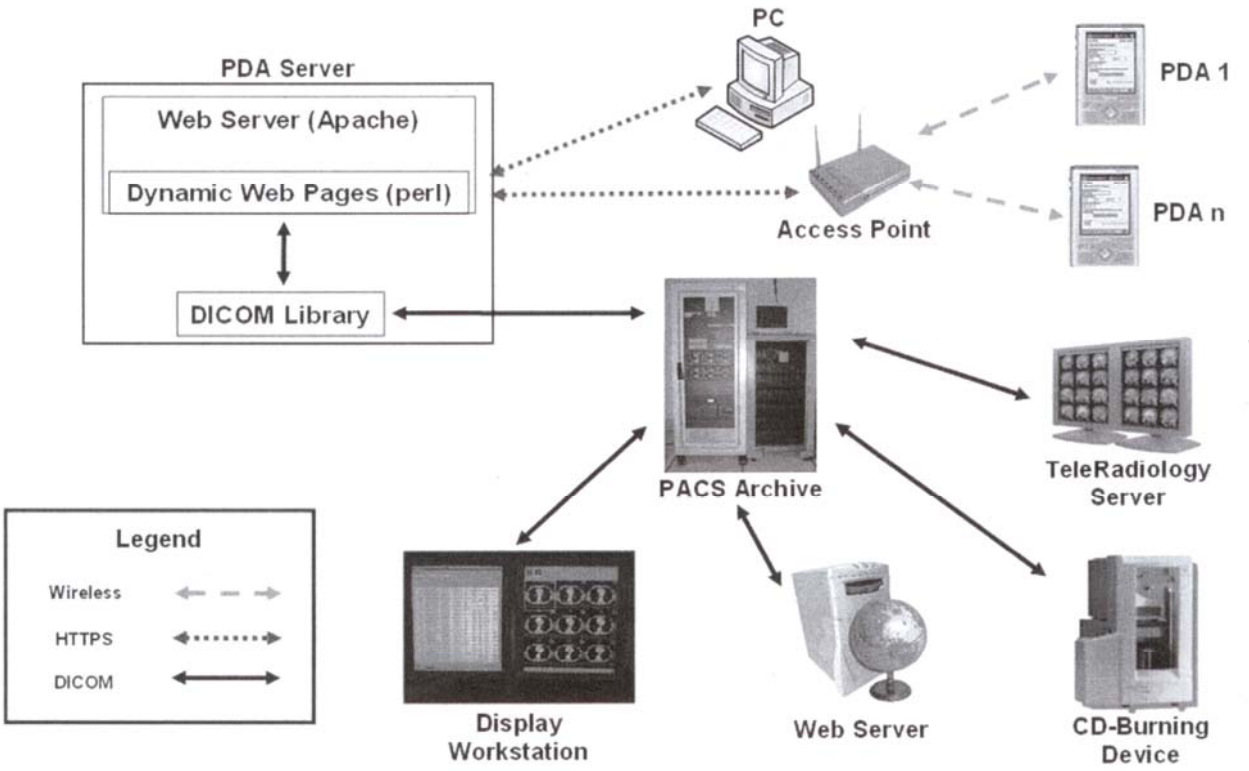

Fig 1. The use of the personal digital assistant server tool for remote management of the picture archiving and communication system at Saint John's Health Center.

the security of the application and the hospital's internal network as well. For this reason, we used the wired equivalent privacy protocol to allow the users connect to the wireless network.

Whenever a user uses the Web client to navigate through the PDA application, the input is passed to the PDA server, which will properly convert to the DICOM format and communicate to the designated DICOM node. Because the DICOM standard does not enforce a single manner of implementation, we have developed the PDA server to successfully interact with different PACSs. The current version of the application has been successfully tested against the following DICOM-compliant off-the-shelf vendor nodes: the DatCard PacsCube (DatCard Systems Inc., Irvine, Calif), the Siemens PACS (Siemens Medical Systems, Erlangen, Germany), the Image Processing and Informatics Laboratory (IPI) PACS controller (Image Processing and Informatics Laboratory, University of Southern California, Marina del Rey, Calif), the Stentor Web application (Global PACS Business Unit, Koninklijke Philips Electronics NV, Brisbane, Calif), and Cedara I-View 5.0 (Cedara Software, Mississauga, Canada). Figure 1 shows the system diagram at SJHC for the PDA application.

Because the DICOM query-and-retrieval application requires easy access from a PDA, one of the key requirements was to keep the graphical user interface as simple as possible. For this reason, this application provides the only needed steps to distribute an examination to the destined node. The screenshots in Figures 2 to 5 show the following 4 steps, described in the figure captions:

- step 1 (Figure 2): the user performs a query;
- step 2 (Figure 3): the PDA displays the query results;
- step 3 (Figure 4): the user selects studies from query results for retrieval; and
- step 4 (Figure 5): the PDA displays the retrieved results.

Disaster-Recovery Design

In the event of a disaster, the need for PACS data may not necessarily be at the local PACS site where the disaster occurred. Therefore, a key building block is to establish network connectivity between multiple sites at which PACS data can be transferred. Figure 6 shows one implementation in which 3 separate sites are connected. The primary site is a community hospital, the secondary site is a nearby academic hospital, and the third site is where the backup clinical images are ar-

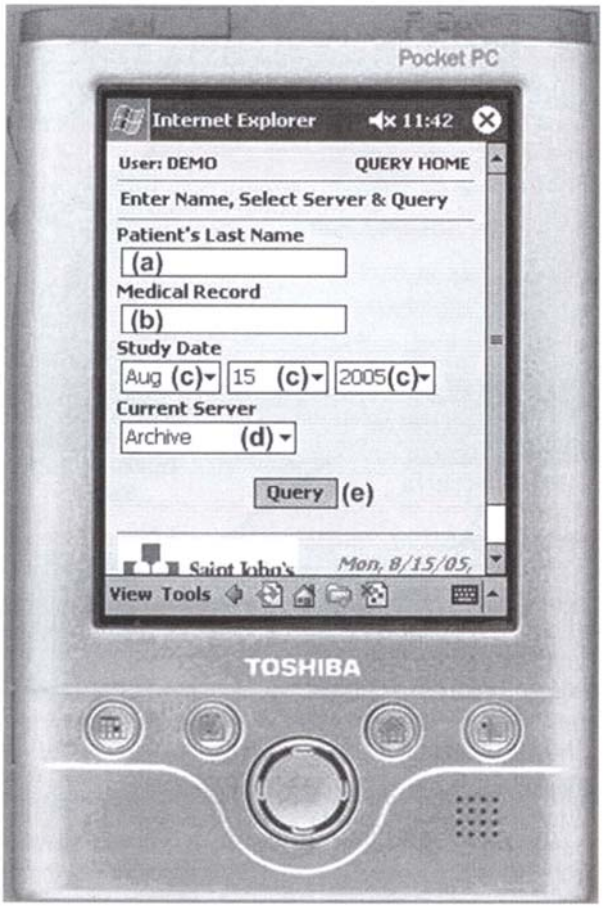

Fig 2. Step 1: to query the server, a user can enter a patient's last name in field (a) or enter the medical record in field (b). A logical "and" operation is performed when both inputs are presented. If both are blank, the study date (c) can be used for the query. The user then uses the current server (d) to select the input server on which the query will be performed. Finally, the user clicks the "query" button (e) to activate the query request. (In this example, a Toshiba personal digital assistant was used, but any other brand with similar capability can be used as well.)

Fig 3. Step 2: this screen shows the list of patients who matched the input search criteria from the previous step. The user can sort the results by using either "patient name" (a) or "patient ID" (c). The date of birth (b) is also shown as a reference but is not sortable. To obtain the list of studies for a particular patient, the user can tab the patient name of any of the results. In this example, the patient "Testing, Sample" (d) is selected. Field (e) shows the current server from which the query was obtained.

chived, the IPI at the University of Southern California. Because the PACS at each site could be different, the types of network connections can vary between sites. Also, it is important for each of the 3 sites to have an internal wireless network (for wireless PDA applications) as well as an internal high-speed local area network for its own PACS operation.

Once all the key building blocks are implemented, the disaster management tool can be designed and evaluated by creating disaster scenario drills. This is an important step not only to evaluate the success of the overall application but also to fine-tune any components or network connectivity issues. A disaster scenario is created first, and the drills are then designed accordingly. Assuming that all the building blocks are in place, the following is an example disaster:

1. The primary site encounters a disaster event that cripples the site.
2. The clinical PACS archive is destroyed.
3. Patients are transferred to nearby secondary site.
4. Historical PACS examinations from the primary site are needed at the secondary site.

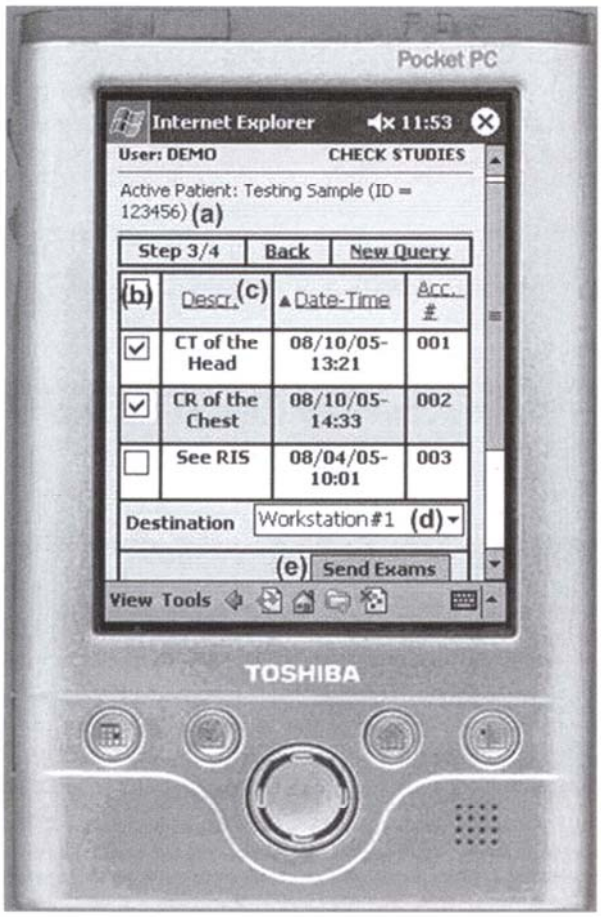

Fig 4. Step 3: this screen shows the list of studies available for the selected patient. Field (a) displays the patient's name and ID as a reference to the user. The check-box (b) allows the user to select all studies or each study at the appropriate check-boxes. The user can also sort by study description, study date and time, or accession number; all those columns are shown in (c). The user then selects where to send the selected examinations to by checking the "destination" list (d). Finally, clicking the "send exams" button (e) completes the retrieval process.

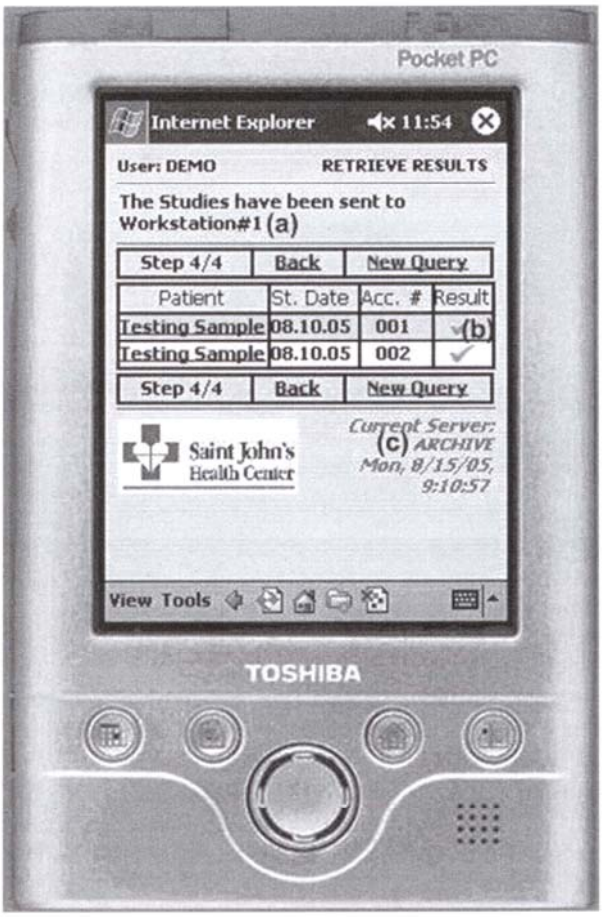

Fig 5. Step 4: this screen shows the results after the retrieval has been completed. Field (a) shows the destination, in this example, workstation 1. The check marks at (b) depict that all selected studies from the previous step were successfully sent, and the information shown includes "patient," "study date," and "accession number." The server from which the studies were retrieved is shown in (c); in the example the server was chosen in step 1 and stayed the same for all other steps. The user can always go back to the previous page to resubmit the query or can go back to the first page.

5. A physician or radiologist needs to view a PACS examination immediately at the secondary site.
6. Second copies of the PACS examinations at the primary site have been stored off site in the ASP back-up archive at IPI.

Having all the building blocks available allows us to create a real-life scenario for this architecture, which we call the "mobile transit scenario," in which a user of the PDA application is in transit in a metropolitan area but is still capable of remotely sending examinations to the chosen destination (in this scenario to the secondary site).

The workflow for this scenario is as follows:

1. During normal operation, a copy of the PACS examination is stored off site at the ASP back-up archive at IPI [2-4].
2. The user, while in transit to the secondary site, connects to the IPI network using a virtual private network connection. It is assumed that the user has access to the Internet from the PDA. Now, the user will be able to connect to a preconfigured PDA server especially for disaster-recovery scenarios.

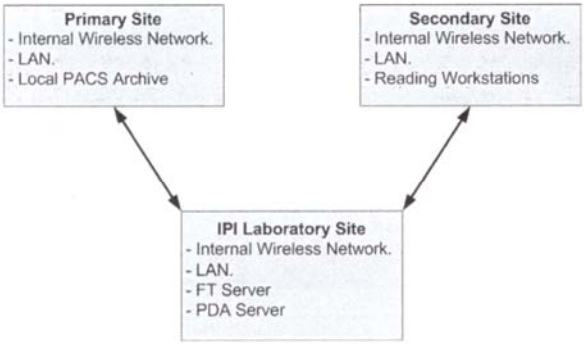

Fig 6. The disaster-recovery scenario requirements and connectivity for multiple sites. The primary site is a community hospital, the secondary site is a nearby academic hospital, and the third site is where the backup clinical images are stored at Image Processing and Informatics Laboratory at the University of Southern California.

3. Once the examination is located, a retrieval request is made for the ASP backup archive to forward the examination for viewing when the user eventually arrives at the secondary site.

This scenario is challenging to implement because it uses wireless mobile technologies integrated with the multiple sites. Current technology should allow using the same PDA for local wireless access and for broadband wireless access.

RESULTS

Clinical Statistics Gathered at SJHC

For nearly 2 years, SJHC has successfully implemented the PDA server tool to query and retrieve its clinical PACS archive with the flexibility of being mobile and portable. From a PDA, studies can be transferred without interrupting the normal workflow functions of SJHC's PACS workstation or other different DICOM nodes. Table 2 demonstrates that the average number of queries per month is 2,021, with 816 C-move retrieve requests. In this context, a retrieval is defined as a single study with a varied number of images.

Table 3 displays the number of retrievals (remote distributions) grouped by destination. Only the most representative DICOM destinations are included in the table. The 4 most frequently used destinations are CD-ROMs, the file room workstation, the emergency room/outpatient node, and teleradiology, which are described here. CD-ROM distribution has an average of 123 retrievals per month. This node is used to give patients their radiology examinations burned digitally on CD-ROMs. With 176 retrievals per month, the file room workstation ranks as the third most frequent destination. This workstation's main function is to reprint hard-copy requests. According to the workflow analysis, this behavior was expected because some of the users of the PDA tool are indeed film clerks, file clerks, or imaging managers, who are typically at the center of study workflow management and in charge of these tasks. The emergency room/outpatient DICOM node has the second largest number of retrievals. Using this tool allows staff members to send the previous examinations of patients in the emergency room without physically being in the location. The highest average is 231 examinations per month, and those examinations are sent to teleradiology servers for off-site reading and diagnosis. This node has only 5 months of activity, because it was added to the PDA application recently, but it is this destination that performs the greatest number of retrievals on average. This demonstrates the usefulness of the PDA server in teleradiology.

Table 2. Number of monthly queries and retrievals from the statistics obtained at Saint John's Health Center

Month	Queries	Retrievals	Total
Feb 2004[a]	408	179	587
Mar 2004	1,991	1,038	3,029
Apr 2004	2,113	1,489	3,602
May 2004	1,995	1,146	3,141
Jun 2004	2,841	1,666	4,507
Jul 2004	1,957	933	2,890
Aug 2004	2,024	904	2,928
Sep 2004	1,552	687	2,239
Oct 2004	1,449	642	2,091
Nov 2004	1,316	510	1,826
Dec 2004	1,213	501	1,714
Jan 2005	1,919	848	2,767
Feb 2005	1,468	679	2,147
Mar 2005	2,605	837	3,442
Apr 2005	2,905	595	3,500
May 2005	4,158	977	5,135
Jun 2005	2,482	600	3,082
Jul 2005[b]	1,978	449	2,427
Total	**36,374**	**14,680**	**51,054**
Average	**2,021**	**816**	**2,836**

[a]Only 7 days of data were collected.
[b]Only 26 days of data were collected.

DICOM Transfer Performance Results for Disaster-Recovery Scenarios

Above, we presented a disaster-recovery design for 3 sites that use the PDA application. For the sake of comparison and to give an idea of transfer speeds for various medical image types, Tables 4 and 5 show the DICOM throughput obtained for a dedicated point-to-point T1 line and a giga-

Table 3. Most common DICOM destinations selected at Saint John's Health Center when using the PDA application (including the total number of retrievals to each destination, the number of months the destination has been used, and the average number of retrievals proportional to the month's activity)

Destination	Total	Average/Month	Number of Months
Teleradiology	1,158	231.6	5
Emergency room/Outpatients	3,477	193.2	18
File room workstation	3,174	176.3	18
PacsCube (CD-ROM distribution)	2,225	123.6	18
CT/MR body	1,640	91.1	18
CT/MR neurologic	913	50.7	18
Inpatients	733	45.8	16
Outpatient tower imaging center	330	30.0	11
Review workstation 2	187	20.8	9
Radiation oncology reading station	207	14.8	14
Review workstation 1	135	9.6	14
Offsite distribution (Stentor)	77	7.7	10

Note: CT = computed tomography; DICOM = Digital Imaging and Communication in Medicine; MR = magnetic resonance; PDA = personal digital assistant.

bit fiber connection through a shared network. As can be seen, the maximum throughputs are 176 and 2,330 KB/s for the T1 line and the gigabit connection, respectively [5,6]. The differences in the performance numbers are due to higher performance connectivity between IPI and the University of Southern California Health Science Campus. It is also appreciated that the transfer speeds per modality are kept invariant no matter the different connection types; this was an expected behavior because of the DICOM overhead.

CONCLUSIONS

The PDA server and the study management tool have been shown to be a low-cost and flexible solution, with fast turnaround time, for the distribution of PACS examinations in clinical environments. This tool allows the distribution of studies to multiple DICOM nodes at the fingertips of users. On the basis of our workflow analysis results, this tool enables a user to avoid querying and retrieving the same study at every DICOM node at which the study is needed. This complements the fact that such users tend to be mobile and at the center of workflow management.

At SJHC, this tool has significantly modified the way studies are sent to a variety of DICOM destinations. It has become the first choice for querying information about PACS examinations for users who are in charge of image management workflow. We have shown in this paper that this tool works very well for the remote distribution of examinations both for local or off-site delivery and for disaster-recovery scenarios.

For PACS workstations, in either stand-alone or client-server architecture, physicians' primary function

Table 4. This table shows the throughput obtained from a point-to-point T1 line for various types of modalities (measured data are for a 20-mile T1 connection between the former location of IPI at the Children's Hospital of Los Angeles and Saint John's Health Center)

Modality Type	File Size	Throughput
MRI	130 KB	150 KB/s
CT	512 KB	165 KB/s
CR	7 MB	175 KB/s
Mammography	400 MB	176 KB/s

Note: CR = computed radiography; CT = computed tomography; IPI = Image Processing and Informatics Laboratory; KB = kilobytes; MB = Megabytes; MRI = magnetic resonance imaging.

Table 5. Throughput obtained for a gigabit connection through a shared network (measured data are between the IPI and Healthcare Consultation Center II, both located in Los Angeles, with about 20 miles in distance)

Modality Type	Average File Size	Average Throughput
MRI	276 KB	179 KB/s
Ultrasound	358 KB	575 KB/s
CT	512 KB	644 KB/s
CR	6.67 MB	2330 KB/s

Note: CR = Computed radiography; CT = computed tomography; IPI = Image Processing and Informatics Laboratory; MRI = magnetic resonance imaging.

should be to perform diagnoses or review PACS studies, not to perform study management tasks. On the basis of the workflow analysis, this tool has freed physicians from performing such tasks as query and retrieval as much as possible and allows users to perform multiple PACS study distributions to various DICOM nodes, all at their fingertips through PC or mobile technology. Also, for some DICOM devices that do not feature DICOM query and retrieval, this tool is even more effective.

In addition, because the tool is web-based, it can be used wherever there is a PC or mobile technology device supporting a web-based browser, thus making it useful throughout the hospital enterprise. With all these features and capabilities, this tool fulfills some of the clinical workflow needs in a low-cost, powerful, easy-to-use package. [7,8,9]

REFERENCES

1. Moore L, Richardson BR, Williams RW. The USU medical PDA initiative: the PDA as an educational tool. Proc AMIA Symp 2002:528-32.
2. Liu BJ, Huang HK, Cao F, Zhou MZ, Zhang J, Mogel G. A complete continuous-availability (CA) PACS archive server solution. RadioGraphics 2004;24:1203-9.
3. Huang HK, Cao F, Liu BJ, et al. Fault-tolerant PACS server design. SPIE Med Imaging 2001;4323:83-92.
4. Liu BJ, Huang HK, Cao F, Documet L, Muldoon J. Clinical experiences with an ASP model backup archive for PACS images. Radiology 2002; 225(P):313.
5. Huang HK, Huang C. Imaging and the Internet 2. Adv Imaging Oncol Admin 2003;13:52-58.
6. Liu BJ, Chao S, Documet J, et al. Implementation of an ASP model offsite backup archive for clinical images utilizing Internet 2. SPIE Med Imaging 2005;5748:224-31.
7. Yaghmai V, Salehi SA, Kuppuswami S, Berlin JW. Rapid wireless transmission of head CT images to a personal digital assistant for remote consultation. Acad Radiol 2004;11:1291-3.
8. Andrade R, Wangenheim A, Bortoluzzi MK. Wireless and PDA: a novel strategy to access DICOM-compliant medical data on mobile devices. Int J Med Informatics 2003;71:157-63.
9. Ratib O, McCoy M, McGill R, Li M, Brown A. Use of personal digital assistants for retrieval of medical images and data on high-resolution flat panel displays. RadioGraphics 2003;23: 267-72.

ENCYCLOPEDIA OF

MEDICAL DEVICES AND INSTRUMENTATION

Second Edition
Volume 6

Radiotherapy, Heavy Ion – X-Rays, Production of

Edited by

John G. Webster
University of Wisconsin–Madison

The *Encyclopedia of Medical Devices and Instrumentation* is available online at http://www.mrw.interscience.wiley.com/emdi

WILEY-INTERSCIENCE

A John Wiley & Sons, Inc., Publication

TEETH, PROPERTIES OF. See BONE AND TEETH, PROPERTIES OF.

TELEMETRY. See BIOTELEMETRY.

TELERADIOLOGY

H.K. HUANG
University of Southern California
Los Angeles, California

INTRODUCTION

Telemedicine and teleradiology have become increasingly important as our country's healthcare delivery system gradually changes from fee-for-service to managed, capitated care. During the past several years, we have seen the trend of primary care physicians joining health maintenance organizations (HMOs). These HMOs purchase smaller hospitals and form hospital groups under the umbrella of HMOs. Also, academic institutions form consortia to compete with other local hospitals and HMOs. This consolidation allows the elimination of duplication and the streamlining of healthcare services among hospitals. As a result, costs are reduced, but at the same time because of the downsizing, the number of experts available for service also decreases. Utilization of telemedicine and

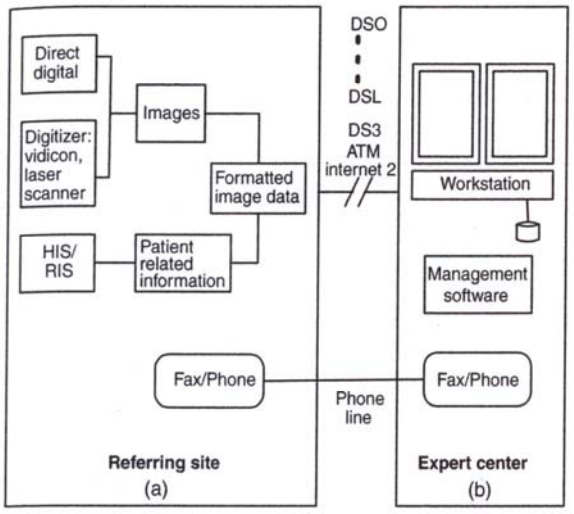

Figure 1. A generic teleradiology setup. (a) Referring site, (b) expert center.

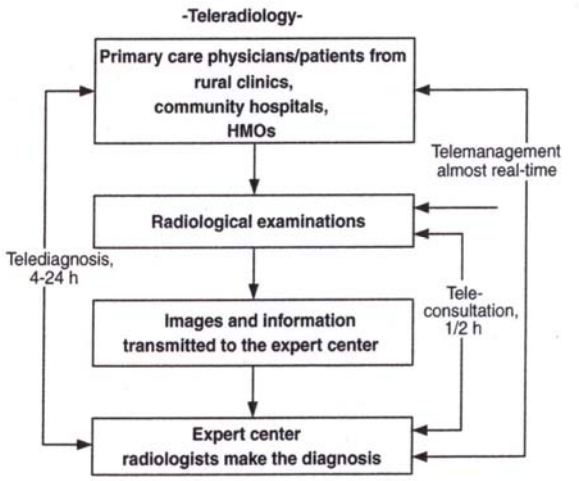

Figure 2. The expert center in teleradiology with three reading modes: telediagnosis, teleconsultation, and telemanagement. These three reading modes dictate the image communication requirements.

teleradiology is a method to alleviate the diminishing of experts, streamline the diagnosis process, and save healthcare costs.

Teleradiology is a subset of telemedicine operation focusing in remote diagnosis of medical images. Teleradiology utilizes computer, display, and telecommunication technologies for radiologists to make remote diagnosis from radiological images generated at distant examination sites. The diagnostic report is sent to the examination site where a primary physician can provide proper treatments to the patient immediately. Figure 1 shows a generic teleradiology set-up illustrating that teleradiology is not a single medical device or an instrument, instead, it is a system integration of various imaging devices using communication technology and system software connecting multiple imaging centers and expert centers together (1–3). Dependent on the required turn around time in obtaining the diagnosis from the examination site, the expert center has three reading modes: telediagnosis, teleconsultation, and telemanagement, which are shown in Fig. 2. These reading modes dictate the communication requirements of transmitting the images between the sites. Teleradiology operation can be very simple or extremely complicated. In the simple case, a radiology resident may send an image set from a CT (computed tomography) scanner using low quality teleradiology equipment and slow speed communication technology in the evening to the radiologist's home for a second opinion. This type of teleradiology operation does not require highly sophisticated equipment. A conventional telephone and simple desktop personal computer with modem connection and display software are sufficient to perform the teleradiology operation. This type of application originated in early 1970.

The complicated teleradiology operation can have different models starting from simple to complicated in ascending order as shown in Table 1. The complications occur when the current examination requires historical images for comparison, and when the radiologist needs information from the radiology information system (RIS) to make a diagnosis. In addition, complications arise when the images and the corresponding diagnosis report are required to be archived to the patient data file. Teleradiology is relatively simple to operate when neither retrieval nor archive of previous information and images is required. However, when both archive and retrieval are required, the operation becomes extremely complicated.

TELERADIOLOGY AND PACS

Picture Arching and Communication System (PACS) is a hospital integrated imaging management system developed in the early 1990s (Fig. 3) (4). The infrastructure of PACS is shown in the upper three rows. Two types of servers in the bottom of the figure are for various PACS applications. When teleradiology service requires patient's historical images as well as related information, technologies used in both teleradiology and PACS become very similar. Table 2 shows technologies used in teleradiology and PACS, the major differences are in image capture, communication, and storage. Some current teleradiology operations still use a film digitizer as the primary method of converting a projection film image-to-digital format, although the trend is moving toward direct digital capture. In PACS, direct digital image capture using Digital Imaging Communication in Medicine (DICOM) standard format is mostly used. In networking, teleradiology uses slower speed wide area networks (WAN) compared with the higher speed local area network (LAN) used in PACS.

Table 1. Four Models of Teleradiology Operation According to Its Complexity

	Historical Images/RIS	Archive
Most simplistic	No	No
Simplistic	Yes	No
Complicated	No	Yes
Most complicated	Yes	Yes

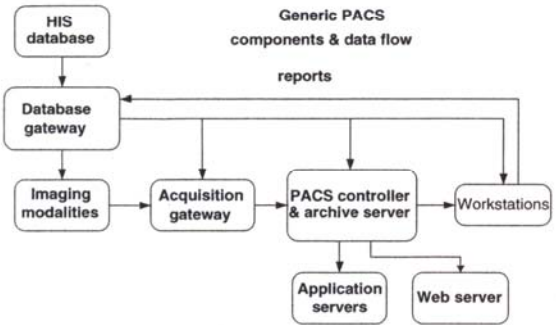

Figure 3. A generic PACS components and data flow. The upper three rows are the infrastructure, the bottom row is PACS applications.

Table 2. Differences in Technology Used between Teleradiology and PACS

Function	Telerad	PACS
Image capture	Digitizer	DICOM
Display technology	Same	Same
Networking	WAN	LAN
Storage	Short	Long
Compression	Yes	May be

In teleradiology, image storage is mostly short term, whereas in PACS it is long term. Teleradiology relies heavily on image compression, whereas PACS may or may not.

PACS and teleradiology use medical images shown in Table 3 for radiologists to make diagnosis. In Table 3, the first and second columns give types and sizes of some common medical images. In clinical applications, one examination is composed of many images of different views and anatomical emphasis, since a single image is generally not sufficient for making the proper diagnosis. In general, a typical examination generates between 10 and 20 MB, although some current CT and MR imaging modalities can generate up to 3000 images per examination. The fourth column shows an average size of one typical examination in each of these image modalities. The high extreme is in digital mammography, which routinely requires 160 MB. To transmit 160 MB of images through WAN for teleradiology requires a very high bandwidth communication technology.

WHY DO WE NEED TELERADIOLOGY?

The managed care trend in healthcare delivery expedites the formation of teleradiology expert centers. However, even without the healthcare reform, teleradiology is still an extremely important component in radiology practice for the following reasons: First, teleradiology secures images for radiologists to read so that no images will be accidentally lost in transit. Second, teleradiology reduces the reporting cycle time after the image is generated. Third, since radiology is subdivided into many subspecialties, a general radiologist requires a specialist's second opinion on occasion. The availability of teleradiology will facilitate seeking a second opinion. Fourth, teleradiology increases radiologists' income since no images would accidentally be lost and subsequently not reported. The healthcare reform adds two more reasons. (1) It saves healthcare costs since an expert center can serve multiple sites reducing the number of radiologists required. (2) It improves the efficiency and effectiveness of healthcare because the report turn-around time would be reduced and there would be no loss of image (5).

TELERADIOLOGY COMPONENTS

A generic schematic of teleradiology depicted in Fig. 1 shows teleradiology components and their connections. Modalities generating images in teleradiology applications include CT, MR, CR, DR, US, NM, DSA–digital fluorography (DF), and film digitizer. Their respective image and examination file sizes Images are shown in Table 3. These acquisition devices are first generated from the examination site and then sent through communication networks to the expert center if they are already in digital format. Or, if these images are stored on films, then they need to be digitized by a film scanner at the examination site.

Table 3. Data Size of Some Common Medical Images and Examinations

Instrument	One Image, bits	No. of Images/Exam	One Examination
Nuclear medicine (NM)	$128 \times 128 \times 12$	30–60	1–2 MB
Magnetic resonance imaging (MRI)	$256 \times 256 \times 12$	60–3000	8 MB up
Ultrasound (US)[a]	$512 \times 512 \times 8(24)$	20–240	5–60 MB
Digital subt. Angiography (DSA)	$512 \times 512 \times 8$	15–40	4–10 MB
Digital microscopy	$512 \times 512 \times 8$	1	0.26 MB
Digital color microscopy	$512 \times 512 \times 24$	1	0.79 MB
Color light images	$512 \times 512 \times 24$	4–20	3–15 MB
Computed tomography (CT)	$512 \times 512 \times 12$	40–3000	20 MB up
Computed/digital radiog (CR/DR)	$2048 \times 2048 \times 12$	2	16 MB
Digitized X rays	$2048 \times 2048 \times 12$	2	16 MB
Digital mammography	$4000 \times 5000 \times 12$	4	160 MB

[a]Doppler US with 24 bit color images.

Image Capture

In image capture, if the original image data are on film, then either a video frame grabber or a laser film digitizer is used to convert them to digital format. A video frame grabber produces low quality digital images, but is faster and cheaper. On the other hand, laser film digitizers produce very high quality digital data, but take longer and cost more compared to the video frame grabber. During the past several years, direct Digital Imaging and Communication in Medicine (DICOM) standard output images from CR, DR, CT, and MR have been used extensively in teleradiology.

Data Reformatting

After images are captured, it is advantageous to convert these images and related data to industry standards because multiple vendors' equipment can be used in the teleradiology chain. The two common standards used in medical imaging industry are the DICOM (6) for images and Health Level 7 (HL7) (7) for textual data. The DICOM standard includes both the image format as well as the communication protocols based on the standard TCP/IP. Health level 7 is the standard for textual data, it uses the TCP/IP communication protocols.

Image Storage

At the expert center, a local storage device is used before images are displayed. The capacity of this device can range from several hundred megabytes to many gigabytes. A long-term archive, such as a small DLT (digital linear tape) library, is used for teleradiology applications that require historical images and diagnostic reports, related patient information, and current images and diagnosis.

Display Workstation

For an inexpensive teleradiology system, a low cost 512-line single monitor can be used for displaying images. However, high resolution multimonitor display workstations are needed for the primary diagnosis.

Table 4 shows the specifications of a 2000- and a 1600-line workstation used for teleradiology primary readings. These state-of-the-art technology diagnostic workstations, use two monitors with over 2 GB of local storage, and can display images and reports from the local storage in 1–2 s. A 2000-line LCD monitor workstation costs from $20,000 to 30,000, and a 1,600 line costs from $15,000 to $20,000. User-friendly image display software is necessary for easy and convenient use by the radiologist at the workstation.

Table 4. Specifications of High-End 2000 and 1600 Line Workstations for Teleradiology

Two LCD Monitors
1–2 week local storage for current + previous exams
1–2 s display of images and reports from local storage
HL7 and DICOM conformance
Simple image processing functions

Table 5. Transmission Rate of Current Wide Area Network Technology

DS-0	56 kbits/s
DS-1	56 to (24 × 56) kbits/s
DSL	144 kbits/s – 8 Mbits/s
DS-1 (T1)	1.5 Mbits/s
ISDN	56 kbits/s to 1.5 Mbits/s
DS-3 (T3)	28 DS-1 = 45 Mbits/s
ATM (OC-3)	155 Mbits/s and up
Internet-2	100 Mbits/s and up

Communication Networks

An important component in teleradiology is communication networks used for the transmission of images and related data from the acquisition site to the expert center for diagnosis. Since most teleradiology applications are not within the same hospital complex, but through inter-healthcare facilities in metropolitan areas or at longer distances, the communication technology involved requires wide area network (WAN) technology. Wide area network can be wireless or with cables. In wireless WAN, some technologies available are microwave transmission and communication satellites. Wireless WAN has not been used extensively in teleradiology due to its higher cost. Table 5 shows cable technology available in WAN from the low communication rate DS-0 with 56 kb/s, to DSL (Digital Subscriber Line, 144 kb/s to 8 Mb/s, depending on data traffic and the subscription), T-1 and T-3 lines starting from 1.5 Mb/s, to very high broadband communication DS-3 with 45 Mb/s (8). These WAN technologies are available through either a long distance or local telephone carrier, or both. The cost of using WAN is a function of transmission speed and the distance between sites. Thus, within a fixed distance, for a DS-0 line with low transmission rate, the cost is fairly low compared to DS-3, which is much faster, but very expensive. Most of the private lines, for example, T-1 and T-3, are point-to-point and the cost depends on the distance between connections. Table 6 gives an example showing the relative cost of the DSL and the T-1 between University of Southern California and St. John's Health Center ~ 15 miles apart in the Greater Los Angeles Metropolitan Area.

Table 6 demonstrates that the initial investment for the DSL is minimal since the WAN carrier pays for the DSL Modem for the network connection. The lowest

Table 6. WAN Cost Using DSL (144 kB/s–8 MB/s) and T-1 (1.5 MB/s) between USC and St. John's Health Center—20 miles

DSL		T-1	
Up front Investment	Minimal	Up Front Investment	$ 5000
Modems (2)	None	T1 DSU/CSU[a] WAN interface (2)	
		Router (2)	$ 4000
Installation (2)	Minimal	T-1 Installation	$ 1000
Monthly charge: (the lowest rate)	$40	T-1 Monthly Charge:	$600

[a]DSU/CSU: Data service unit/ Channel service unit as of June, 2003.

monthly cost is ~$40/month. On the other hand, for T-1 service, the up front investment is $4000 for the two T-1 routers and $1000 for installation. The monthly cost is $600. The up-front investment for the T-1 is much higher than DSL, and for longer distances, its monthly charge is expensive. For example, the charge between Los Angeles and Washington, D.C. for a T-1 line could be as high as $10,000/month. However, T-1 is a point-to-point private line, and it guarantees its 1.5 MB/s specification, and provides communication security. The disadvantages of DSL are (1) it is through shared networks, and hence has no security; (2) its performance depends on the load of the DSL carrier at that moment; and (3) it is not available everywhere. Using T-1 and DSL for teleradiology is very popular. Some larger IT (Information Technology) companies lease several T-1 lines from telephone carriers and sublease portions of them to smaller companies for teleradiology applications.

Another wide area network listed in Table 5, Internet 2 (I2) technology, is ideal for teleradiology application because of its speed of transmission and low cost of operation after the site is connected to the I2 backbone (9). The I2 network is a national infrastructure of high speed communication backbones [> 10 GB/s using gigabit switches and Asynchronous Mode Technology (ATM)] supported by the National Science Foundation (NSF), currently consisting of the vBNS (very high performance Backbone Network Service), the CalREN-2 (California Research and Education Network), and the Abilene. In the global level, vBNS, Abilene and CalREN-2, provide readily available high speed backbones and administrative infrastructure. In the local level, the users have to learn how to connect the hospital and clinic environments to these backbones. Table 7 shows the current performance of the I2 between some sites in the United States. The advantages of using Internet 2 for teleradiology are its high speed and low operational cost once the local site is connected to the backbones. The disadvantages are (1) the local site has to upgrade its conventional Internet infrastructure to be compatible with the high speed I2 performance, which is costly; (2) not enough experts know how to connect from the radiology department to the backbone; and (3) I2 is not yet open for commercial use.

Table 7. Current Internet 2 Performance between Sites in the United States

Test Sites	Response Time (32 Bytes)	Throughput*
CHLA/USC LAN (Childrens Hospital/ U Southern California)	<1 ms	9.8 MBytes/s
CHLA/USC-UCLA	4 ms	2.7 MBytes/s
CHLA/USC-Stanford U	23 ms	900 KBytes/s
CHLA/USC-UCSF	24 ms	700 KBytes/s
CHLA/USC-NLM (National Library of Medicine)	67 ms	320 KBytes/s
CHLA/USC –U Hawaii	76 ms	700 KBytes/s

*units used are MBytes/s and KBytes/s which are different from those used in Table 5.

User Friendliness

User friendliness includes both the connection procedure of the teleradiology equipment at both the examination site and the expert center, and the simplicity of using the display workstation at the expert center.

User friendliness means that the complete teleradiology operation should be as automatic as possible requiring only minimal user intervention. For the image workstation to be user friendly requires three criteria:

1. Automatic image and related data prefetch.
2. Automatic image sequencing and hanging protocol at the monitors.
3. Automatic look-up table, image rotation, and unwanted background removal from the image.

Image and related data prefetch means that all necessary historical images and related data required for comparison by the radiologist should be prefetched from the patient folder at the imaging sites and send to the expert center. When the radiologist is ready to review the case, these prefetched images and related data are already available at the expert center. Automatic image sequencing and hanging protocol at the display workstation means that all these images and related data are sequentially arranged so that at the touch of the mouse, properly arranged images and sequences are immediately displayed on the monitors. Prearranged data minimizes the time required for the searching and organizing of data by the radiologist at the expert center. This translates to an effective and efficient teleradiology operation. The third factor, automatic look-up table, rotation, and background removal, is necessary because images acquired at the distant site might not have the proper look-up table set up for optimal visual display, images might not be generated in the proper orientation, and might have some unwanted white background in the image due to radiographic collimation. All these parameters have an effect on the proper and efficient diagnosis of the images. Figure 4 shows an example of automatic splitting of a CT examination of both the chest and the abdomen into a chest and an abdomen sequence for automatic display using the concept of presentation of grouped procedures (PGP) in IHE (Integrating the Healthcare Enterprise) profile technology (10).

Image Compression

Teleradiology requires image compression because of the slow speed and high cost of using WAN. For lossless image compression, current technology can achieve between 3:1 and 2:1 compression ratios, whereas in lossy compression using cosine transform based MPEG and JPEG hardware or software, 20:1–10:1 compression ratios can be obtained with acceptable image quality. The latest advance in image compression technology is the wavelet transform (11 and JPEG 2000), which has the advantages over cosine transform for higher compression ratio and better image quality, however, hardware wavelet compression is not yet available. Some Web-based teleradiology systems use progressive wavelet image compression techniques. In this

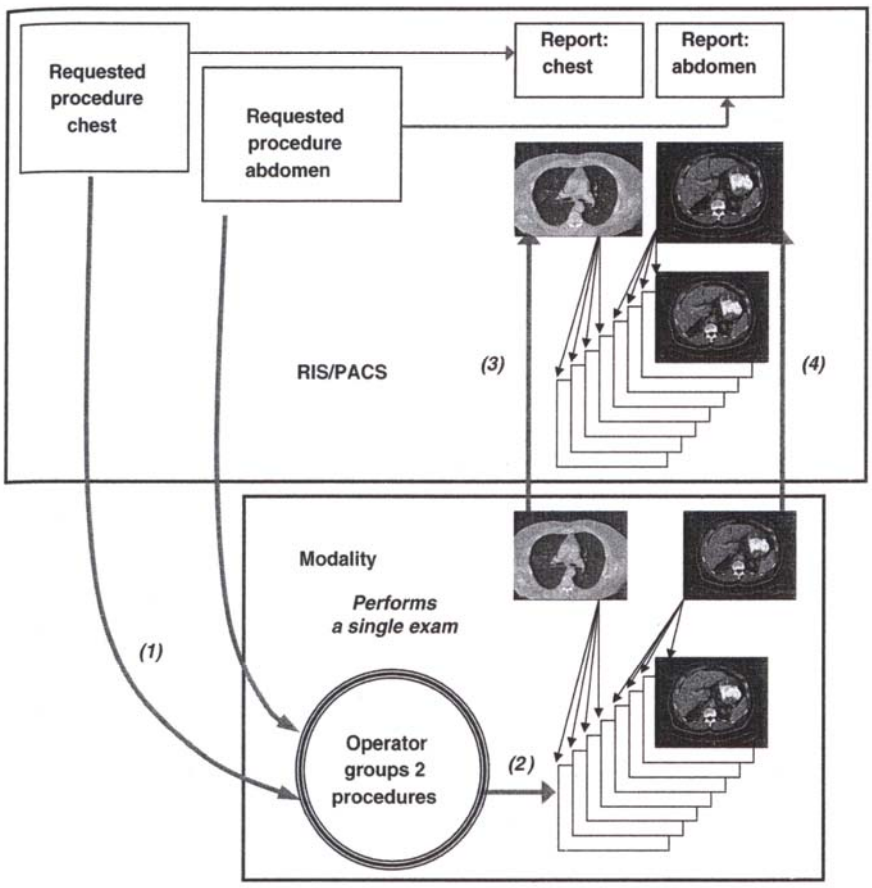

Figure 4. Integrating the Healthcare Enterprise (IHE) Presentation of Grouped Procedures (PGP) Profile. Example shows a single CT acquisition procedure is used to acquire both chest and abdominal scans. The scheduled workflow profile provides information for the PGP to split the acquired images into two subsets, one for the chest and the other for the abdomen (10). Numerals represent the workflow steps in the IHE PGP.

techniques, image reconstruction from the compressed file is in a progressive manner in that a lower resolution image is first reconstructed almost instantaneously and displayed upon request. The user would have the psychological effect that the image is transmitted through the network in real-time. Higher quality images are continuously reconstructed to replace the previous ones until the original image is reconstructed and displayed.

Image Data Privacy, Authenticity, and Integrity

Image transmission in teleradiology is mostly through public networks, for this reason, trust in image data becomes an important issue. Trust in image data is characterized in terms of privacy, authenticity, and integrity of the data. Privacy refers to denial of access to information by unauthorized individuals. Authenticity refers to validating the source of the image. Integrity refers to the assurance that the image has not been modified accidentally or deliberated during the transmission. Privacy and authenticity are the responsibility of the public network provider based on firewall and password technologies, whereas integrity is the responsibility of the end user.

Imaging integrity is mostly done based on the concept of public and private keys digital signature encrypted with mathematical algorithms during the process of image generation. In general, the public and private keys digital signature concept consists of seven steps (12):

1. Private and Public Keys: Set up a method in assigning public and private keys between the examination site and the expert center.
2. Image preprocessing: To segment the object of interest in the image from the background (e.g., the head in a CT image is the object of interest), and extract patient information from the DICOM image header at the examination site while the image is being generated.
3. Image digest: To compute the image digest (digital signature) of the object of interest in the image based on its characteristics using mathematical algorithms.
4. Data encryption: To produce a digital envelope containing the encrypted image digest and the corresponding patient information from the image header.
5. Data embedding: To embed the digital envelope into the background of the image as a further security. The background is used because the embedding would not alter the image quality of the object of interest. In cases where the image has no background, such as a chest radiograph, a more involved lossless embedding technique can been used.
6. The image with the embedded digital envelope is sent to the expert site.

7. The expert center receives Item 6, decrypts the image and the signature. It compares the two digital signatures. One comes with the image, the second is computed from the received image to validate the image integrity.

TELERADIOLOGY OPERATION MODELS

In this section, we discuss four teleradiology operation models that are common in current practice.

Off-Hour Reading

An off-hour reading model is to take care of the off-hour reviewing of the images including evenings, weekends, and holidays when most radiologists are not available at the examination sites. In this set up, image acquisition devices at different examination sites including hospitals and clinics are connected to an off-hour reading center with medium or low grade transmission speed (like the DSL) because the turn around time is not critical except for emergency cases. The connections are mostly direct digital with the DICOM standard. The reading center is equipped with network switches and various types of workstations compatible to the images generated by imaging devices at examination sites. The staffing includes technical personnel taking care of the communication networks and workstations, and radiologists who come in during the evening, weekend, and holiday shifts and perform on-line digital reading. They provide preliminary impression of the exam and transmit it to the examination site instantaneously after reading. The regular radiologists at the examination sites verify the readings and sign off the report the next day. This type of teleradiology set up is low technology but it serves its purpose of solving the shortage of radiologists during off hours.

ASP Model

Application Service Provider (ASP) model is a business venture taking care of the radiological image diagnosis for examination sites where on site radiology interpretations are not available. This model can be for supplying equipment only or for both equipment and radiologists. In the former, an ASP entity sets up a technical center housing network equipment and workstations. It also provides turnkey connectivity for the examination site where images would be transmitted to the center. The examination site can hire its own radiologists to perform reading at the center. In the latter, the center provides both technical support as well as radiologists for reading.

Web-Based Teleradiology

Web-based teleradiology is mostly used by hospital or larger clinics to distribute images to various parts of the hospitals or clinics, or outside of the hospital. A web server is designed where filtered images from PAC systems are either pushed from the PACS server to, or pulled by the Web server. Filtered images mean that the Web server has a predetermined directory to manage the image distribution based on certain criteria like what types of images to where and to whom, and so on. The clients can view these filtered images from the client workstation through the web server. The clients can be referring physicians who just want to take a look at the images or for radiologists to make a remote diagnosis. Web-based teleradiology is very convenient and low cost to set up because most technologies are readily available, especially within the hospital intranet environment. The drawback is that since Web is a general technology, the viewing capability and conditions are not as good as that in a regular PACS workstation where the set up is geared for radiology diagnosis. In order to have full DCIOM image resolution for visualization and manipulation at the clients, modifications have to be made at the Web Server to receive full 12 bits/pixel data from the PACS server, and additional display software at the clients.

PACS and Teleradiology Combined

Teleradiology can function as a pure teleradiology operation shown in Fig. 5. In this operation, the teleradiology management center serves as the operation manager. It receives images from different imaging centers, 1,..., N, keeps a record, but not the images, routes images to different expert centers, 1,..., M according to need for reading. Reports comes back to the management center, it records the reading reports, forwards reports to the appropriate imaging centers. The management center is

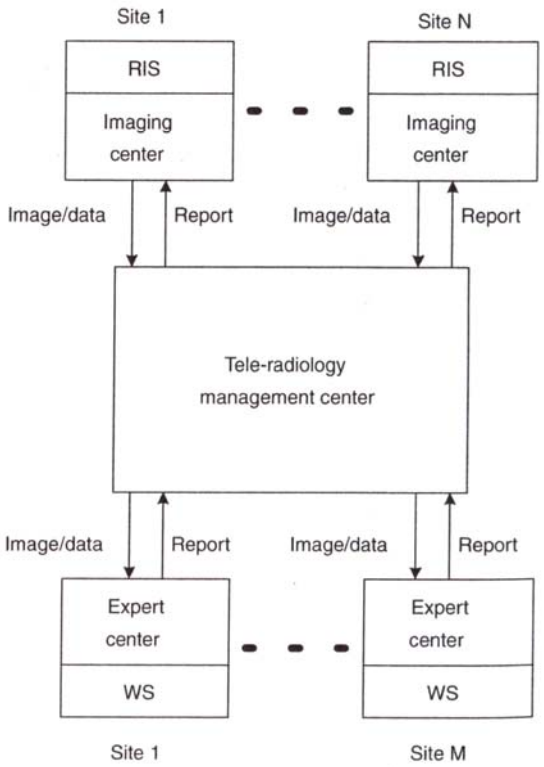

Figure 5. Pure teleradiology model. The management center monitors the operation to direct workflow between imaging centers and expert centers.

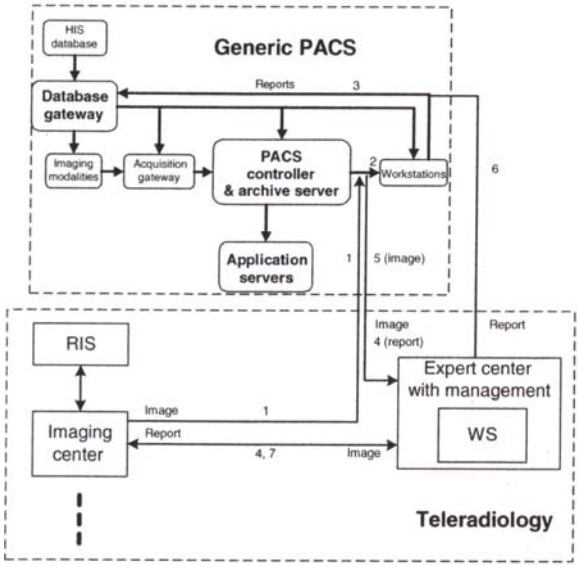

igure 6. PACS and Radiology Combined Model: The PACS ıpports either the imaging centers, or PACS and Teleradiology ıpport each other. See text for explanation of workflow steps in ımerals.

lso responsible for the billing and other administrative ınctions like image distribution and workload balancing. he networks used for connection between image centers, ıe management center, and expert centers can be mixed ith various performances dependent on the requirements ıd costs.

Teleradiology can be combined together with PACS as a ealthcare enterprise operation, as shown in Fig. 6. The vo major components in the combined model are the ACS (see Fig. 3) shown inside the upper dotted rectangle, ıd the pure teleradiology (see Fig. 5) model shown in the wer dotted rectangle. The workflow of this combined odel is as follows:

1. The image center can send images to the expert center for reading as in the pure teleradiology model (7).
2. Radiologists at PACS workstations can read exams from outside imaging centers as well (1).
3. After reading by in-house radiologists from its own workstations (2), reports are sent to the database gateway for its own in-house record (3), or to the expert center from where the report is also sent to the imaging center (4).
4. The PACS can also send exams directly to outside expert center for reading (5). The expert center then returns report to the PACS database gateway (6).

ıe combined Teleradiology and PACS model is mostly ed in a large enterprise level healthcare center with tellite imaging centers, or in back-up radiology coverage tween the hospital and imaging centers.

Enterprise Level PACS and Teleradiology Combined with Grid Computing

The PACS and teleradiology combined model described in the last section can be extended to the enterprise level using the grid computing infrastructure. The enterprise level PACS and teleradiology combined model is for very large-scale PAC systems and teleradiology applications. This large-scale model is becoming more and more popular in today's enterprise healthcare delivery system (13).

Grid computing is the integrated use of geographically distributed computers, networks, and storage systems to create a virtual computing system for solving large-scale, data-intensive problems in science, engineering, and commerce (14). A grid is a high performance hardware and software infrastructure providing scalable, dependable, and secure access to the distributed resources. Unlike distributed computing and cluster computing, the individual resources in grid computing maintain administrative autonomy and are allowed system heterogeneity; this aspect of grid computing guarantees scalability and vigor. Therefore, the grid's resources must adhere to agreed-upon standards to remain open and scalable. A popular standard grid computing toolkit is called Globus 3.0 (15). The grid computing provides the user with the following services: computational, data, application, and knowledge. For these reasons, grid computing infrastructure is the ideal technology for large-scale enterprise PACS and teleradiology combined model implementation.

Using the concept of grid infrastructure along with the DICOM standards and IHE workflow profiles, the PACS and teleradiology combined model shown in Fig. 6 can be extended to an enterprise level model conceptually shown in Fig. 7. Grid computing is still in its infancy for medical imaging application. The concept shown in Fig. 7 would require several years before it can materialize.

SOME IMPORTANT ISSUES IN TELERADIOLOGY

Relationship between Teleradiology Technologies and Operation

There are two sets of trade-off parameters in teleradiology. The first set relates to the operation consisting of image quality, reading turn-around time, and cost; and the second set relates to technologies used in the operation including image capture, workstation, compression, communication, and data security requirements. Table 8 shows the relationship between these two sets of parameters.

Image Data Security

In image data security, the patient confidentiality as well as image integrity are important. Since teleradiology uses a public communication method to transmit images that have no security, the question arises as to what type of protection one should provide to assure the patient's confidentiality, and the authentication of the sender. The second issue is the image integrity. After the image is created in digital form, can we assure that the image created has not been altered either intentionally or unintentionally during the transmission? To guarantee patient

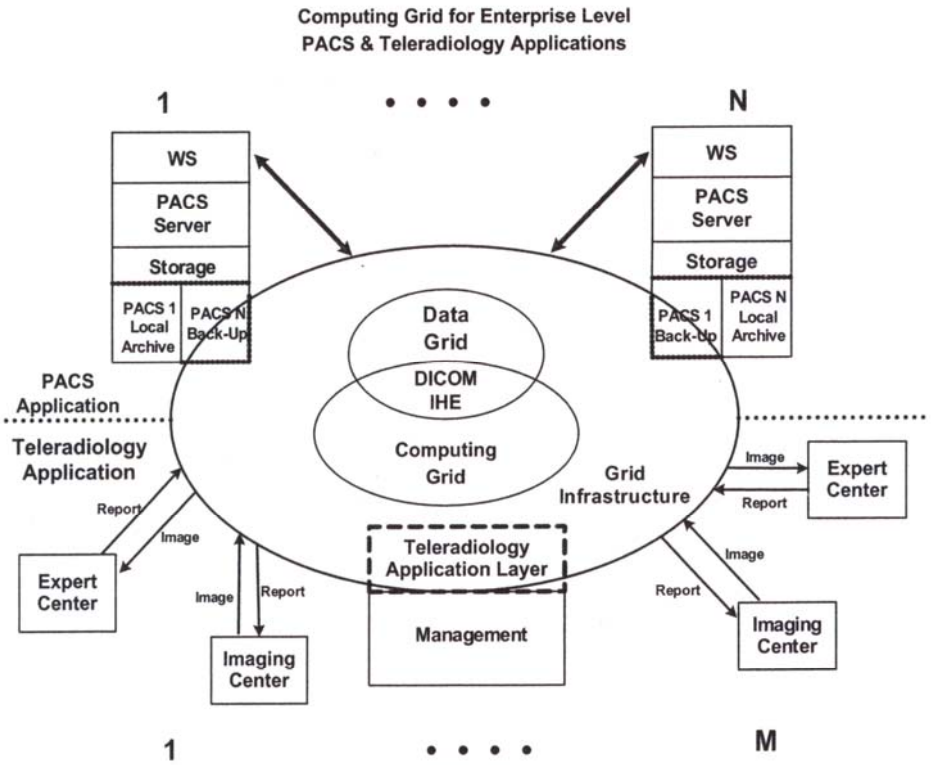

Figure 7. Enterprise level large-scale PACS and teleradiology combined model using the grid computing technology. The center ellipse of the figure is the grid computing infrastructure consisting of the data and computation grid with the DICOM standard and IHE workflow profiles. The data grid handles the image data, and the computational grid takes care of the workflow and management (see Chapter Section 19.2.2.4, Ref (4) for the concept of grid computing and the functions of the data grid.) The top row above the dotted line is the enterprise PACS, which consists of several PAC systems 1,..., N rectangles under numerals. The bottom row under the dotted line is the pure teleradiology model described in Fig. 5. The connection between PACS and teleradiology in the enterprise is not a straight line of data communication, instead it goes through the grid computing infrastructure for resource allocation and management, as well as image data acquisition and distribution.

confidentiality and image authenticity, methods such as hardware and software firewalls used routinely in information technology can be set up. To protect image integrity, data encryption and digital signatures can be used. These techniques have been in the domain of defense research for many years, which can be modified for teleradiology application. If high security is imposed on image data, it will increase the cost of decryption and decrease the easy access due to many layers of passwords. The trade-off between cost and performance, confidentiality, and reliability has become a major socioeconomic issue in teleradiology. Since altering a digital image is fairly easy in today's computer technology, developing methods to protect the integrity of image data is essential in teleradiology applications.

Table 8. Relationship between Technologies and Teleradiology Operation

	Image Capture	WS	Compression	Communication	Image Integrity
Image quality	X	X	X		
Turn-around time	X	X	X	X	X
Cost	X	X	X	X	X

Medical–Legal Issues

There are four major medical–legal issues in teleradiology: privacy, licensure, credentialing, and malpractice liability. The ACR (American College of Radiology) Standard for Teleradiology adopted in 1994 defines guidelines for "qualifications of both physician and nonphysician personnel, equipment specifications, quality improvement, licensure, staff credentialing, and liability. Guidelines to these topics, although much is still uncertain, have been discussed extensively by others (16–19). It is important that these issues should be considered thoroughly before a teleradiology operation is set up.

TRENDS IN TELEMEDICINE AND TELERADIOLOGY

The concept of telemedicine and teleradiology originated in the 1970s, however, technology was not ready for real clinical applications for teleradiology until several years ago. As teleradiology is being integrated into daily clinical service, the associated socioeconomic issues discussed also surface. The trends in teleradiology are to balance the cost with the requirements of image quality, and turn-around time for the service. Costs are affected by technology used in image capture, workstation, image compression, communication, and image security. We see that teleradiology will become a necessity in medical practices of the twenty-first century, and will be an integral component of telemedicine as the not so distant method for healthcare delivery.

Teleradiology uses the Web and Internet technologies. Issues that must be resolved immediately are how to lower the communication cost and to bundle textual with image information effectively and efficiently to assure efficient operation, and image security. For the former, Internet 2 appears to be an excellent candidate, and for the latter, ePR (electronic Patient Record) will evolve as a potential winner. [4, Ch 21].

BIBLIOGRAPHY

1. Stahl JN, Zhang J, Zeller C, Pomerantsev EV, Lou SL, Chou TM, Huang HK. Tele-conferencing with dynamic medical images. IEEE Trans Inform Tech Biom 2000;4(1): 88–96.
2. Zhang J, Stahl JN, Huang HK, Zhou X, Lou SL, Song KS. Real-time teleconsultation with high resolution and large volume medical images for collaborative health care. IEEE Trans Inform Tech Biom 2000;4(1):178–185.
3. Stahl JN, Zhang J, Chou TM, Zellner C, Pomerantsev EV, Huang HK. A new approach to tele-conferencing with intravascular ultrasound and cardiac angiography in a low-bandwidth environment. RadioGraphics 2000;20: 1495–1503.
4. Huang HK. March, PACS and Imaging Informatics: Principles and Applications. Hoboken, NJ: John Wiley & Sons; 2004.
5. Huang HK. Teleradiology technologies and some service models. Volume 20, Computerized Medical Imaging and Graphics. 1996. p 59–68.
6. DICOM Standard 2003, http://www.dclunie.com/dicom-status/status.html#BaseStandard2001
7. HL7 Version 3.0: Preview for CIOs, Managers and Programmers, http://www.neotool.com/company/press/199912_v3.htm#V3.0_preview
8. Stahl JN, Tellis W, Huang HK. Network latency and operator performance in teleradiology applications. J Digital Imag 2000;13(3):119–123.
9. Huang HK. 2003, Research trends in medical imaging informatics. In: Hwang NHC, Woo SLY, editors. Frontiers in Biomedical Engineering based on the Proc WCCBME (World Congress for Chinese Biomedical Engineers Proceedings), Chapt. 17, New York: Kluwer Academic Publisher; 2002; p. 269—281.
10. Carr C, Moore SM. IHE: A model for driving adoption of standards. Comp Med Imaging Graphics 2003;Issues 2–3: 137–146.

11. Wang J, Huang HK., Three-dimensional image compression with wavelet transform. In: Bankman IN, editor-in-chief, Rangayyan RM, Woods RP, Robb RA, Huang HK, editors. Hanbook of Medical Imaging. Academic Press; 2000; Chapt. 52, p. 851–862.
12. Zhou X, Huang HK. Authenticity and integrity of digital mammography image. IEEE Trans Medical Imaging 2001; 20(8):784–791.
13. Huang HK. Enterprise PACS and image distribution. Comp Med Imaging Graph 2003;27(2–3):241–253.
14. Bernman F, Fox G, Hey T. Grid Computing. Hoboken, NJ: John Wiley & Sons; 2003.
15. GlobusToolkit 3 Core White Paper, http://www-unix.globus.org/toolkit/documentation.html
16. James AE, Jr, James E, III, Johnson B, James J. Legal considerations of medical of medical imaging. Leg Med 1993; 87–113.
17. Berger SB, Cepelewicz BB. Medical-legal issues in teleradiology. Am J Roentgenol 1996;166:505–510.
18. Berlin L. Malpractice issue in radiology-teleradiology. Am J Roentgenol 1998;170:1417–1422.
19. Kamp GH. Medical-legal issues in teleradiology: A commentary. Am J Roentgenol 1996;166:511–512.

See also COMPUTER-ASSISTED DETECTION AND DIAGNOSIS; RADIOLOGY INFORMATION SYSTEMS.

A Data Grid Model for Combining Teleradiology and PACS Operations*

H.K. Huang, Brent J. Liu, Z. Zhou, Jorge Documet

Image Processing and Informatics Laboratory, Department of Radiology, Keck School of Medicine, University of Southern California, 4676 Admiralty Way, Suite 601, Marina del Ray, California 90292

* *Paper accepted to be published in Journal of Medical Imaging Technology*

ABSTRACT

The use of teleradiology for X-ray image communication and display was introduced as early as 1972 [1] and the PACS concept was conceived in 1982 [2, 3]; after more than twenty years of technological advancement and refinement, both teleradiology and PACS have become indispensable components in today's healthcare delivery system. Although both teleradiology and PACS share many common technological components and workflow profiles, these two imaging-based systems are operated independently and are not readily integrated. This paper compares the commonalities and differences between these two systems, and suggests a method for their integration in terms of image archival, reporting, and workflow using a Data Grid model.

Keywords: *PACS, teleradiology, Data Grid, DICOM, IHE*

1. INTRODUCTION

Teleradiology is a subset of telemedicine operations focusing on remote diagnosis of medical images. Teleradiology utilizes computer, display and telecommunication technologies for radiologists at workstations (WSs) to make diagnosis from clinical images generated from remote examination sites. The diagnostic report is sent back to the examination site where a primary physician can provide proper treatments to the patient immediately. Teleradiology operation can be very simple or extremely complex as shown in Table 1. Three factors contribute to the complexity: 1) Historical images are required for comparison; 2) Information from the radiology information system (RIS) is needed; and 3) Image archive is necessary. Teleradiology is relatively simple to operate when neither image and information retrieval, nor archival of images and reports are required. However, when both archival and retrieval are required, the operation becomes extremely complex. In this paper, we try to address the issue "How to combine images and reports from teleradiology with those from an outside archive, like a PACS?" as a means to systematically analyze the "most complex teleradiology operation" model shown in Table 1. We first define the pure teleradiology model, then the combined teleradiology and PACS model. The former model allows us to appreciate the workflow and workload of multiple sites teleradiology operation. The latter model addresses the global issue related to the earlier question.

Table1. Four Modes of Teleradiology Operation According to Their Complexity

	Historical Images/RIS	Archive
Most simplistic	no	no
Simplistic	yes	no
Complex	no	yes
Most complex	yes	yes

2. MATERIALS AND METHODS

The Pure Teleradiology Model with Multiple Sites

Teleradiology can function as a pure teleradiology operation shown in Fig. 1. In this operation, the teleradiology management center serves as the operations manager. It receives images from different imaging centers, 1,…, N, keeps a record but not the images, routes images to radiologists at different expert centers, 1,…, M for reading based on the "Supply and Demand" criterion. Reports come back to the management center, the transactions are recorded, and the reports are forwarded to appropriate imaging centers. The management center is also responsible for the billing and other administrative functions like image distribution and workload balancing.

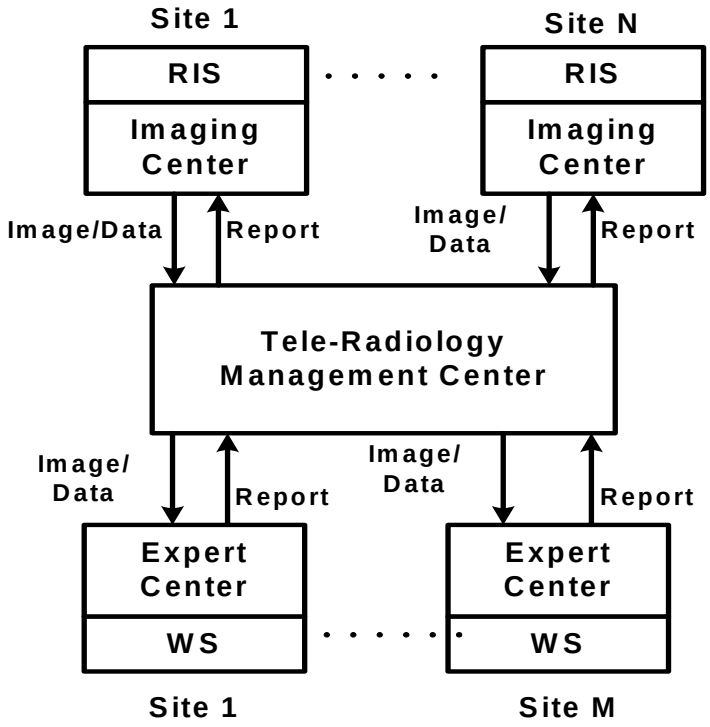

Fig. 1. A Pure Teleradiology Model with N Imaging Centers producing images and M Expert Centers with radiologists for reading. The management Center administrates the data flow and operation.

PACS and Teleradiology Combined Model

Teleradiology applications and PACS can be combined together as a unified healthcare enterprise operation with workflow shown in Fig. 2 [3]. Two major components in the combined model are the PACS (upper rectangle), and the pure teleradiology model (lower rectangle).

Pure Teleradiology Model: Image center sends images to the expert center for reading as in the pure teleradiology model shown in Fig. 1. The workflow step is depicted as No. 7 in Fig. 2.
PACS Radiologists assist Teleradiology Reading: Outside imaging centers (1) send exams to PACS WSs (2) for PACS Radiologists to read. Reports are sent to the database gateway for PACS record (3), and/or to the expert center (4).
Expert Center radiologists assist PACS reading: PACS sends exams to expert center radiologists to read (5). The expert center returns report to the PACS database gateway (6).

The combined Teleradiology and PACS model is mostly used in an enterprise level Healthcare system with satellite imaging centers, or in back-up radiology coverage for a hospital by imaging centers. In this model, PACS and each imaging center keep its own images; but the reports can be shared. This model addresses the sharing and archival of reports, but not image archival.

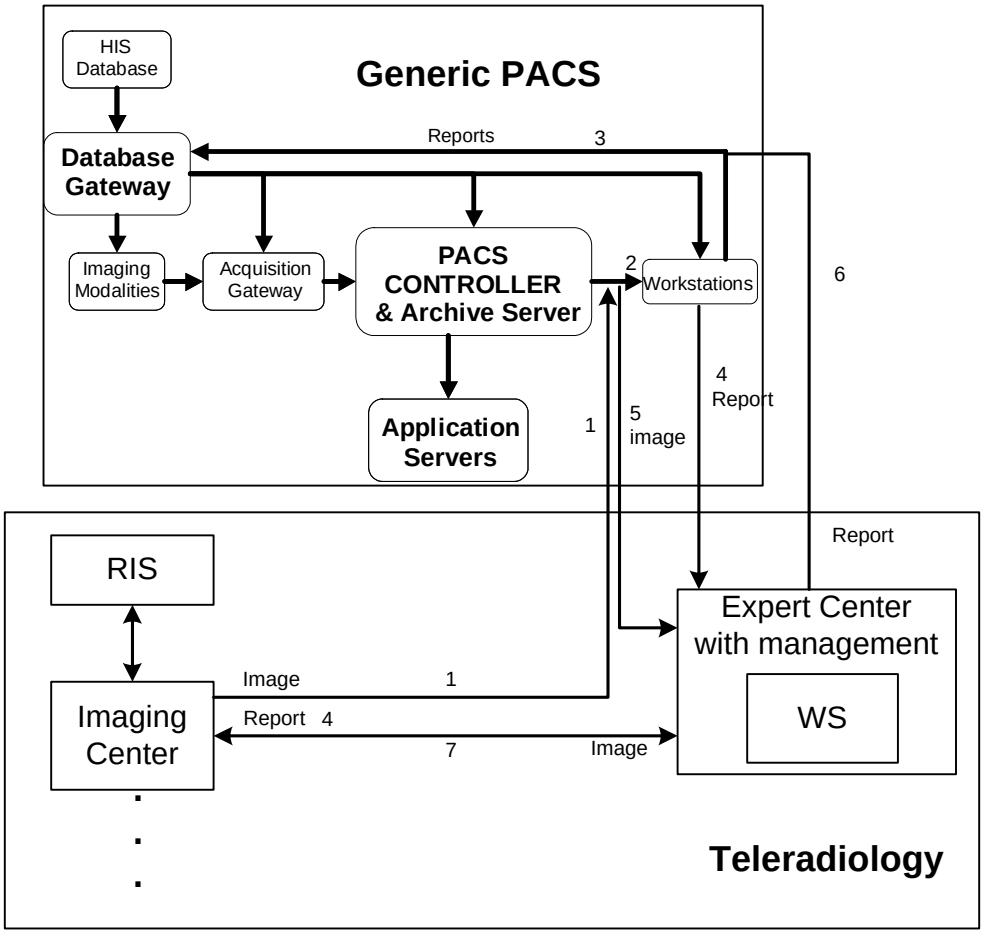

Fig. 2. PACS (top) and Teleradiology (bottom) Combined Model: Radiologists at PACS and at imaging centers can support each other [3].

A Data Grid for Medical Imaging Applications

Data Grid is a service of the Grid Computing technology. [4] A Data Grid [5, 6, 7] specifically designed for clinical image backup and disaster recovery was developed at IPI (Image Processing & Informatics Laboratory) using the Globus Toolkit 4 (GT4). [8] This Data Grid shown in Fig. 3 was designed to utilize the strengths of grid technology along with PACS (Picture Archiving and Communication Systems)/ DICOM (Digital Imaging and Communications in Medicine) technology for storing and distributing clinical images. In particular, some PACS/DICOM resources are embedded within the GT4 five layer grid architecture (Fig. 4) developed by IPI. These include Storage service, Query service, and Retrieve service, which are integrated with the DICOM standard protocols in addition to the use of other Data Grid Services. We use this Data Grid model to discuss the workflow of a combined PACS and Teleradiology Operations at the enterprise level.

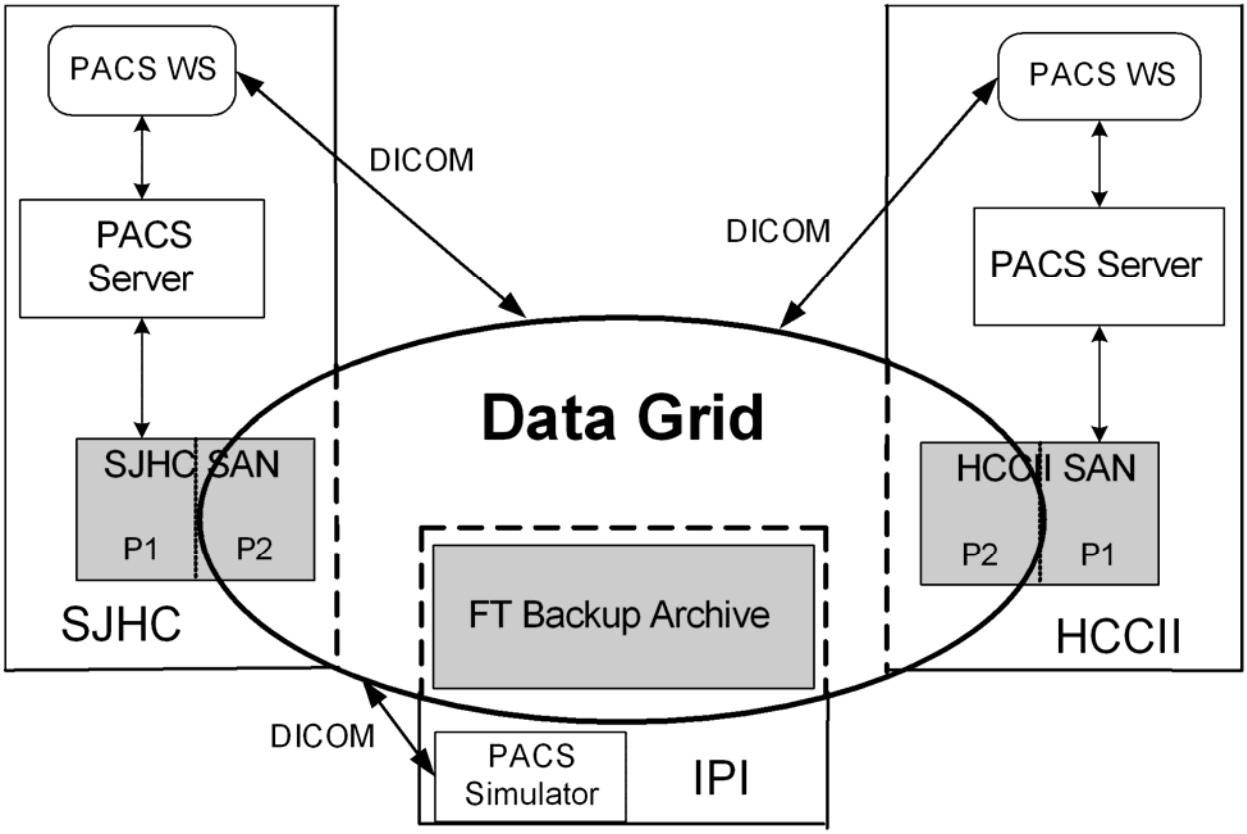

Fig. 3. Configuration of three PACS sites data storage systems (shaded boxes) that comprise of image data storage resources in the Data Grid. The SAN (Storage Area Network) partition P1 at each site is used for its own PACS images, whereas P2 becomes a shared resource of the Data Grid. Workstations outside of the Data Grid can access the grid for particular services, like image query/retrieve. SJHC: Saint Johns Healthcare Center, HCCII: Healthcare Consultation Center II, University of Southern California (USC), IPI: Image Processing and Informatics Laboratory, USC [6].

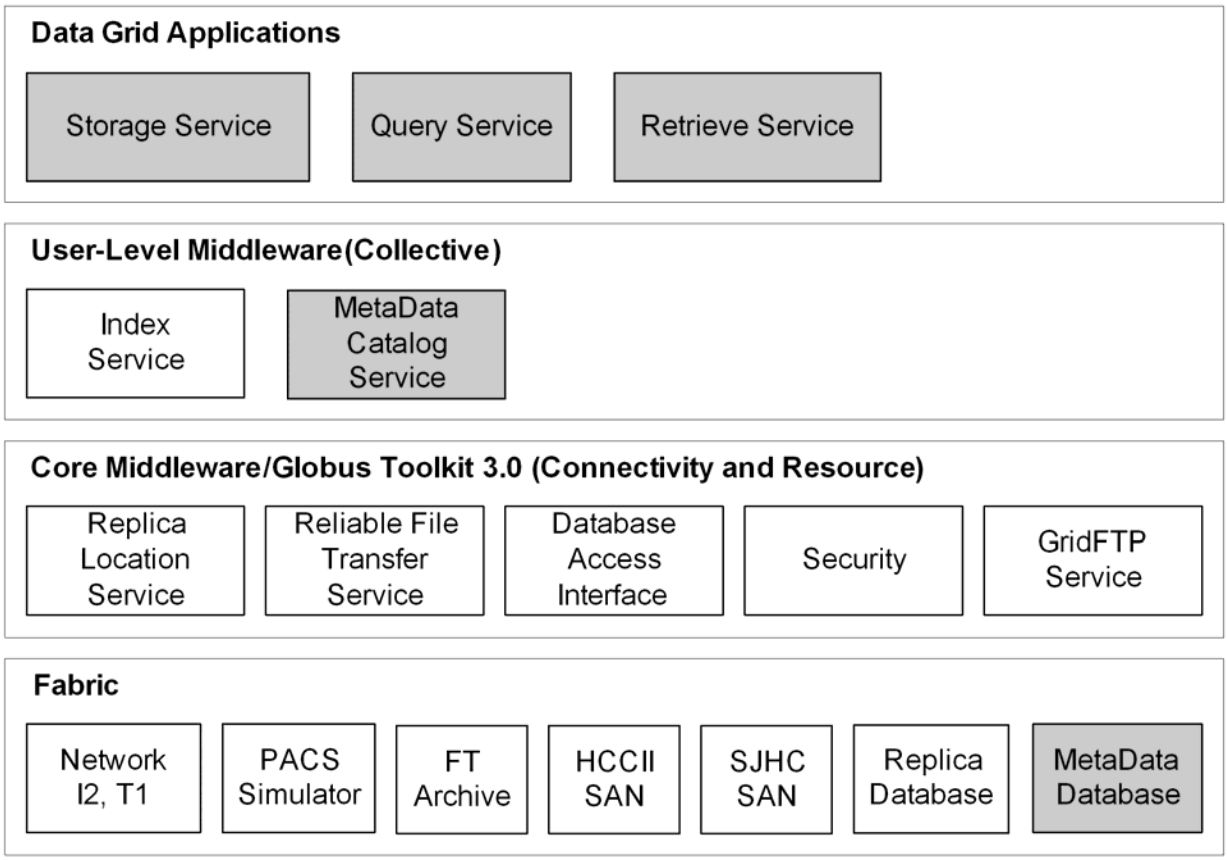

Fig. 4. Five-layer architecture (Fabric, connectivity, resource, collective, and application) of the Globus Toolkit 4, and contents of the Data Grid, shaded areas are integrated with DICOM services developed at IPI. Application Layer software is designed for clinical image data recovery. See also Fig. 3 caption [6].

3. RESULTS

PACS and Teleradiology in an Enterprise Level Operation Using the Data Grid Model

PACS and teleradiology combined model described in Fig. 2 can be extended to the enterprise level PAC systems and teleradiology operation. This model becomes popular in today's enterprise healthcare delivery system. Data Grid concept can be used to consolidate images/data obtained from both PAC systems and teleradiology operations into one unified image/report archive system for storage and distribution shown in Fig. 5 [9]. We use the Data Grid Model to address the global question raised earlier: "How to combine images and reports from teleradiology with those from outside archive?" Several PAC systems would be treated in this context as images and reports from outside archive.

Each PACS in the model has a shared storage contributed to the Data Grid as described in Fig. 3. In addition to P2 partition of the SAN storage in each PACS (See Fig. 3), the Data Grid has a major software module, Teleradiology DICOM, which directs the image and report workflow of teleradiology. Refer to Fig. 5, Telerardiology DICOM has three components: the Manager, Tele Rad Arch, and Tele Rad Backup. One function of the Manager is to determine if images from an Image Center need to be archived in the Tele Rad Arch storage. If this is the case, a backup copy would also been sent to the Data Grid, which would then create two backup copies strategically saved in the Grid (Fig. 3). The Tele Rad Backup architecture and functions

are the same as one of the PACS Back-up storages (See P2 in Fig. 3) which becomes a share resource of the Data Grid.

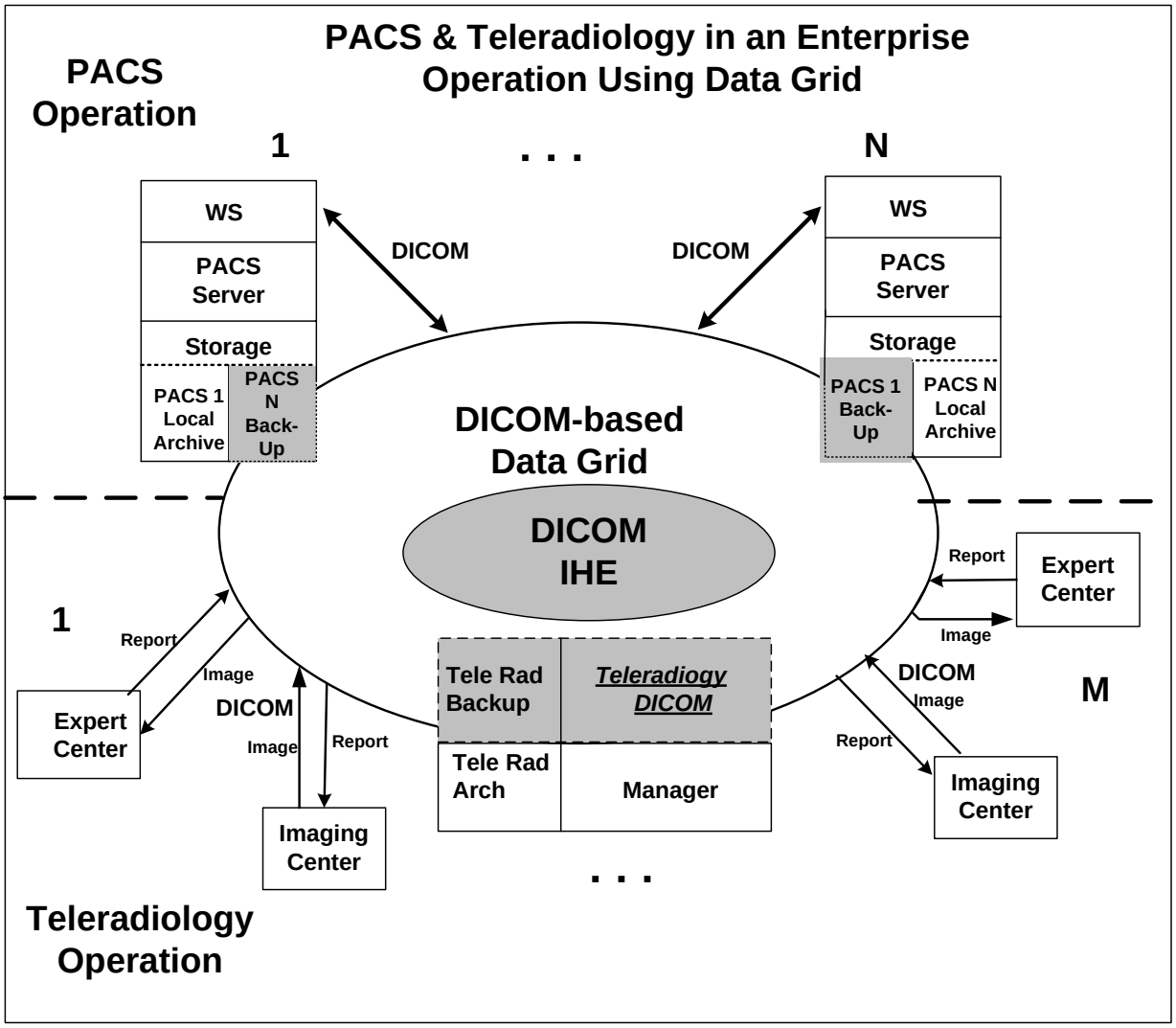

Fig. 5. Enterprise level large-scale PACS and teleradiology combined model using the Grid Computing technology. The center of the figure is the grid computing infrastructure consisting of the Data Grid with the DICOM standard and IHE workflow profiles. The Data Grid handles the image and reports storage, and other grid computing resources take care of the workflow and management. The top row is the enterprise PACS consists of 1,…, N PAC systems. The bottom row depicts the pure teleradiology model with 1,…, M operations. Each PACS in the model has a shared storage contributed to the Data Grid as described in Fig. 2. The Data Grid has a major component, Teleradiology DICOM, to direct the image and report workflow. Shaded areas represent the data storage contribution of PAC systems and Teleradiology to the Data Grid [9].

Workflow in the Enterprise PACS and Teleradiology Operation

The workflow of images, reports, and radiologist's readings are similar to that described in Fig. 2 except Item B in Section 2.2 where images from each Imaging Center to be archived would be determined by the Teleradiology DICOM Manager. A copy would also be sent to the Data Grid which creates two backup copies in the Grid (Fig. 5). Two new software packages would be necessary: 1) The Teleradiology DICOM to handle the image archive as well as its backup in the Data Grid, and 2) The Application Layer (Top Layer in Fig. 4) for PACS and Teleradiology operation which would be different from that listed in Fig. 4.

4. CONCLUSIONS

Following the combined PACS and teleradiology model, we design a Data Grid model to handle the integration of the image archive and reports in an enterprise operation. Although the Data Grid model is defined, due to the complexity of its implementation, development of using the Grid Computing technology for Enterprise level PACS and teleradiology combined model is still in its infancy.

Acknowledgements

Research has been partially supported by the National Institutes of Health, USA: NIH R01 EB 00298, NIH R01 LM 07606, T32 EB00438; and MI2.

References

[1] Steckel, R.J., Daily X-Ray Rounds in a Large Teaching Hospital Using High-Resolution Closed Circuit Television. Radiology, Vol 105, 1972, pp. 319-321.
[2] Duerinckx, A., Ed. Picture Archiving and Communication systems (PACS) for Medical Applications. First International Conference and Workshop, Proc SPIE Vol 318. Part 1 and 2, 1982.
[3] H.K. Huang, PACS and Imaging Informatics: Basic Principles and Applications, Wiley & Sons, NJ, 2004.
[4] A. Chervenak, I. Foster, C. Kesselman, C. Salisbury and S. Tuecke, The Data Grid: Towards an Architecture for the Distributed Management and Analysis of Large Scientific Datasets, Journal of Network and Computer Applications 23 (2001), 187-200.
[5] B.J. Liu, M.Z. Zhou and J. Documet, Utilizing data grid architecture for the backup and recovery of clinical image data, Computerized Medical Imaging and Graphics 29 (2005), 95-102.
[6] H.K. Huang, A. Zhang, B. Liu, Z. Zhou and etc, Data Grid for Large-Scale Medical Image Archive and Analysis, Proc. 13th ACM International Conference on Multimedia 2005, 1005-1013.
[7] B.J. Liu, F. Cao, M.Z. Zhou, G. Mogel and L. Documet, Trends in PACS Image Storage and Archive, Computerized Medical Imaging and Graphics 27 (2003), 165-174.
[8] I. Foster, Globus Toolkit Version 4: Software for Service-Oriented Systems, IFIP International Conference on Network and Parallel Computing, Springer-Verlag LNCS 3779, 2005, 2-13.
[9] H.K. Huang, Teleradiology, in Webster J.G., 2nd Ed., Encyclopedia of Medical Devices and Instrumentation, Wiley & Sons, NJ, 2006. Vol 6, 302-311.

Computer Aided Detection of Small Acute Intracranial Hemorrhage on Computer Tomography of Brain*

Tao Chan

Department of Health Technology and Informatics, The Hong Kong Polytechnic University, Hong Kong SAR, China
Department of Radiology, Princess Margaret Hospital, Hong Kong SAR, China

** Paper accepted to be published in Journal of Computerized Medical Imaging and Graphics*

ABSTRACT

Introduction:

Detection of acute intracranial hemorrhage (AIH) is a primary task in image interpretation of computer tomography (CT) of brain for patients suffering from acute neurological disturbance or head injury. Although CT readily depicts AIH, interpretation can be difficult especially when the lesion is inconspicuous or the reader is inexperienced.

Objective:

To develop a computer aided detection system that improves diagnostic accuracy of small AIH on brain CT.

Materials and Methods:

Intracranial contents are first segmented by thresholding and morphological operations, which are then subjected to denoising and adjustment for CT cupping artifacts. The brain is then automically realigned into normal position. AIH candidates are extracted based on top-hat transformation and left-right asymmetry. AIH candidates are registered against a normalized coordinate system such that the candidates are rendered anatomical information. True AIH is differentiated from mimicking normal variants or artifacts by a knowledge based classification system incorporating rules that make use of quantified imaging features and anatomical information.
A total of 186 clinical cases, including 62 CT studies showing small (< 1cm) AIH, and 124 controls, were retrospectively collected. 40 positive cases and 80 controls were used for the training of the CAD. Twenty-two positive cases and 44 controls as validation cases were used in the validation of the CAD system. Regions of AIH identified by two experienced radiologists were used as gold standard. The size of individual AIH volume was recorded.

Results:

On a per patient basis, the system achieved sensitivity of 95% (38/40) and 88.8% (71/80) in the training dataset. The sensitivity and specificity were 100% (22/22) and specificity of 84.1% (37/44) for the diagnosis of AIH in the validation cases.

Individual cases contained variable number of AIH volumes. There were 77 lesions in the 40 training cases and 46 lesions in the 22 validation cases. On a per lesion basis, the sensitivities were 84.4% (65/77) and 82.6% (38/46) for all lesions 10mm or smaller for the training and validation datasets respectively. False positive rates were 0.19 (23/120) and 0.29 (19/66) false positive lesion per case for the training and validation datasets respectively.

Conclusion:

This study demonstrated that CAD is valuable for detection of small AIH on brain CT.

INTRODUCTION

AIH literally means recent bleeding inside the confine of the skull. It comprises bleeding inside or outside the brain substance, which are termed intraaxial and extraaxial hemorrhage respectively. Intraaxial hemorrhage can be further specified as to the exact anatomical location of bleeding, e.g. cerebral hemorrhage and brainstem hemorrhage, and intraventricular hemorrhage (IVH). Extraaxial hemorrhage is classified according to the anatomical layer of meninges where bleeding occurs, namely extradural hemorrhage (EDH), subdural hemorrhage (SDH), subarachnoid hemorrhage (SAH).

AIH can be an important cause of acute neurological disturbance, e.g. cerebral hemorrhage causing hemiplegia, or consequence of head injury, e.g. extradural hemorrhage.

Identification of AIH is of crucial clinical significance, because this dictates very different management strategies; however, neither symptoms and signs nor other clinical parameters is accurate in differentiating AIH from other causes of neurological disturbance [1, 2]. CT has been the primary modality for detection of AIH because it is widely available, quick to perform, and readily depicts AIH [3, 4].

Visualization of an acute clot on CT depends on its intrinsic physical properties including the density, volume, location, and relationship to surrounding structures, and technical factors including scanning angle, slice thickness, and windowing [5]. It is conceivable that AIH can become difficult to identify when it is small. Although no formal classification of the size of AIH exist. The long axis diameter and thickness in the transverse plane represent the conventionally measured dimensions of intraaxial hematomas and extraaxial hematomas respectively. The current study defines a lesion as small if it is (a) intraaxial hemorrhage having a long axis diameter equal or less than 1cm, or (b) extraaxial hemorrhage having a thickness equal or less than 1cm. All the sizes quoted in the following discussions refer to either the long axis diameter for intraaxial hematomas or the thickness of extraaxial hematomas measured in the transverse plane.

It is obvious that diagnosis of AIH requires correct interpretation of the demonstrable AIH on CT. This can become difficult when the lesion is inconspicuous, e.g. small or being masked by normal structures, or when the reader is inexperienced.

In most parts of the world, acute care physicians, including emergency physicians, internists, or neural surgeons, are the only ones to read the CT images at odd hours, when radiologists' expertise may not be immediately available. However, the skill of acute care physicians regarding interpretation of brain CT has been shown to be imperfect [6]. Another study has shown that radiology residents can, albeit infrequently, overlook hemorrhage on brain CT [7].\

Even for the best human observers, it has long been recognized that errors in image interpretation, including erroneous perception or analysis, are inevitable [8]. It is envisaged that CAD may help to improve the accuracy in detection of AIH and hence decrease the risk of misdiagnosis and mismanagement. One system has been developed to detect acute middle

cerebral artery (ischemic) stroke [9], but there has been no published work in the CAD of AIH to the best of the authors' knowledge. A few systems have been reported recently by Hodgson et al., Yang et al., and Goto et al. [10-12]. Yet none of these systems have reported success in detecting small AIH, which are the problematic lesions that could present as challenge to both human observers and computer systems. Success in tackling the small lesions will therefore produce the greatest impact in clinical practice.

The current system has been built for the diagnosis of small AIH. It differs from existing CAD products, e.g. malignancy detection in mammography and nodule detection in chest radiograph or CT, in that the system is intended to be used by clinicians other than radiologists and that the system rates the authenticity of candidate lesions in different portions of the image dataset differently, depending on their anatomical positions and imaging features.

Therefore the objective of this research is to develop a CAD system that identifies small AIH to help in the management of patients suffering from head injury or acute neurological disturbance in an emergency setting.

As noted before, in emergent settings, expert radiologists may not be readily available to provide the often crucial image interpretation. Therefore the duty is shifted to clinicians who may not be best equipped for the task. It is therefore believed that CAD may become useful in these situations, in addition to its proven value for screening examinations. Special considerations need to be made because observers of less expertise may not be confident or knowledgeable enough to judge the correctness of CAD outputs. Therefore CAD systems targeted for non-radiologists need to minimize the false positive rates.

During the development stage of the system, it was found that the myriad combinations of imaging features of AIH in different parts of the brain could not be adequately described without reference to the anatomical positions where the lesions are found. But when the candidate lesions are divided up based on the anatomical position, classification between genuine AIH and mimicking variants or artifacts become feasible. This contrasts against target lesions of many CAD systems which are well-described with relatively little variation in their configurations, which are hence less dependent on the anatomical information in comparison to the local imaging features.

MATERIALS AND METHODS

Materials

One hundred and eighty-six brain CT studies, including 62 cases showing AIH and 124 cases showing no AIH, were retrospectively retrieved from the CT archive of the Princess Margaret Hospital in Hong Kong. All were cases performed on an emergency setting for evaluation of head injury or acute neurological disturbance. The studies were anonymized apart from the sex and age. Institute review board approval has been obtained for this study.

All studies were acquired with a single detector CT scanner (HiSpeed CT, GE Medical Systems, Milwaukee, WI, USA). All images were axial images obtained parallel to the orbito-meatal line (OML), at 120kV and 80-200mA. Most (159) of the examinations comprise 10mm thick sections throughout the brain, the standard protocol used in the authors' institution for emergency studies. Nineteen of the examinations comprise 5mm sections through posterior fossa and 10mm sections through the rest of the head, performed for patients with suspected lesions in the posterior fossa. Eight were 5-7 mm sections obtained for small children.

All emergent brain CT studies performed within a 6 month period that show small acute intracranial hemorrhage were retrospectively collected. It is noteworthy that studies containing AIH larger than 1cm or follow-up cases were excluded. In total, 62 cases were collected. Of

these, 40 cases were collected at the first phase of data collection, which constitute the training dataset of the CAD system. The remaining 22 cases were collected at the second phase and used for validation of the system.
The 22 cases were not included initially because they were not available in the temporary archive in the CT suite during the scheduled time of collection, probably being deleted from the workstations as routine housekeeping procedures between the intervals of the scheduled visits. They were subsequently retrieved from the permanent archive. Although the training and validation cases were not randomly allotted, we believe there were no plausible systemic biases involved in the process.
124 emergency CT cases, twice the number of positive cases, were selected randomly and used as controls. Final radiological diagnoses in this group included normal (88), chronic ischemia (23), acute ischaemic stroke (10), and tumor (3).
The radiological diagnoses in all the cases were established by consensus of two radiologists, who had 7 years and 11 years of experience in reading brain CT respectively. In addition, dimensions, locations, and type of individual disjoint AIH volumes were measured and recorded by radiologists for each study. One blood clot that spans across several axial sections is counted as one volume in this study, rather than considered as several separate lesions. Altogether there were 123 contiguous volumes of small AIH, 77 in the training cases and 46 in the validation dataset, with well represented samples of each different type of AIH and different sizes.

CAD System

Overview of the Scheme

All the anonymized DICOM CT images were transferred from the CT archive to a Pentium based PC running the Windows XP operating system. The CAD has been developed using MATLAB (The MathWorks, Inc., Natick, MA, USA). The system is programmed to read DICOM images in their indigenous format and file structure. All images in a series folder are automatically sorted, scaled, and adjusted to the desirable contrast according to information residing in DICOM headers of individual images.
The flow chart of the CAD algorithm is illustrated in figure 1. The image processing and analysis methods used in the scheme are listed in table 1. Intracranial contents are segmented by global thresholding and morphological operations, followed by contiguity analysis. Noise reduction using median filter and adjustment for CT cupping artifacts were performed. The intracranial contents are realigned into the conventional orientation after automatic localization of mid sagittal plane and boundaries of the series of images. Then, high attenuation components are segmented as candidate AIH from each of the axial sections based on top-hat transformation and subtraction between the two sides of the images. Image features of the candidates are quantified. The candidate AIH are given anatomical context by registration against a normalized coordinate system purposely developed for this project. The features and coordinates are then used in the rule based classification system to reduce false positives due to normal variants and artifacts.

Segmentation of Intracranial Contents

Intracranial contents, including both the brain and cerebral spinal fluid (CSF) containing spaces, are first segmented. This is done by 1. global thresholding that removes bones, which are high in attenuation; 2. morphological erosion that removes tiny remaining portions of the bones; and 3. removal of scalp tissues and structures in the orbits and paranasal sinuses by removing pixels separated from the largest central intracranial components by bones of the skull.

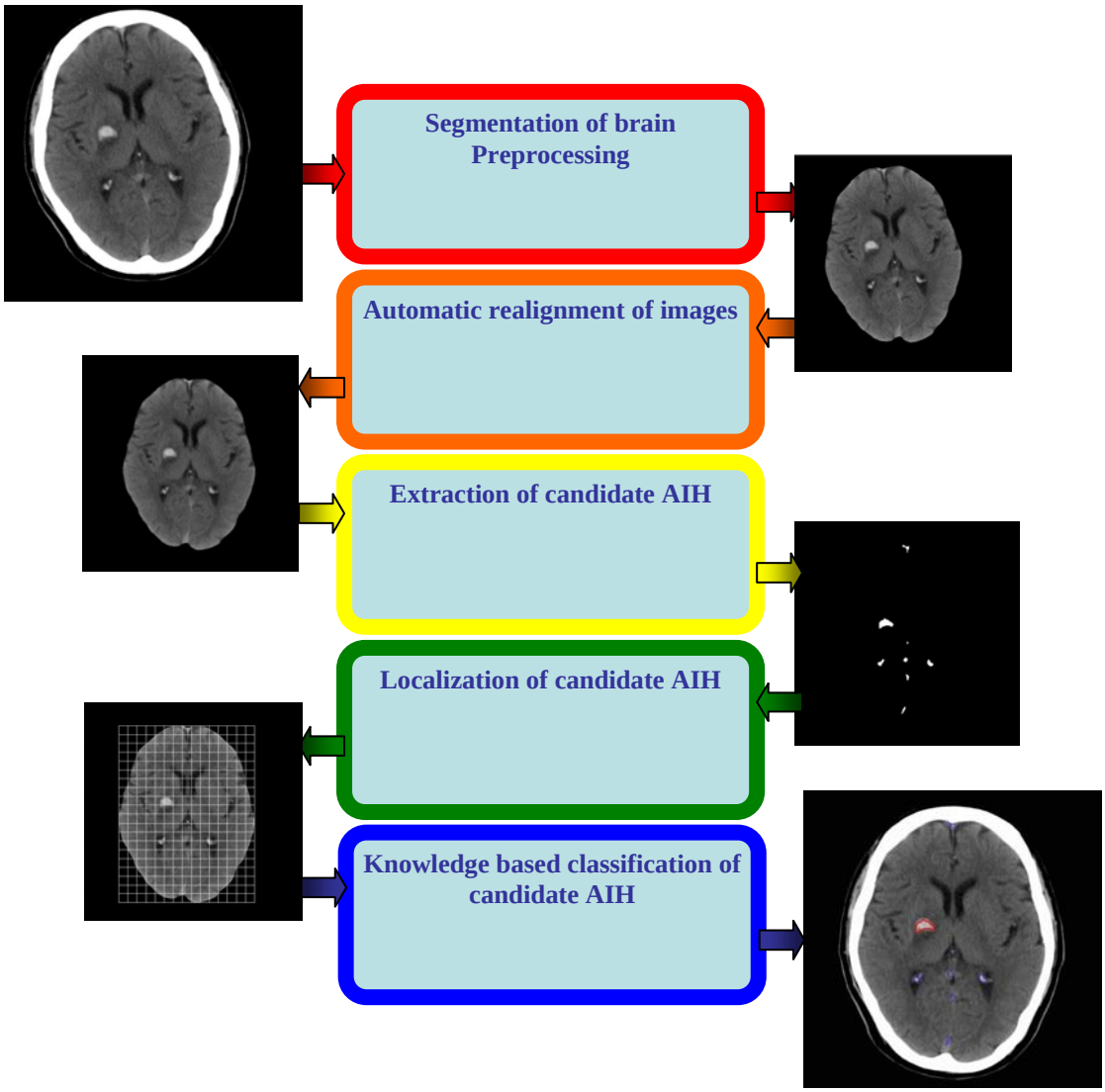

Figure 1 - Schematic diagram of the CAD system. Intermediary outputs of an image showing right basal ganglia hemorrhage illustrate the effect of individual steps. Details of individual steps are outlined in Table 1.

Table 1 Details of individual image processing and analysis steps of in the CAD algorithm as outlined in Figure 1.

Steps	Methods	Purposes
Segmentation of intracranial contents	Global thresholding and morphological operations Remove structures not contiguous with the main central bulk of intracranial contents	Remove bones of skull and face Remove scalp, orbits, and other head and neck soft tissues

Steps	Methods	Purposes
Preprocessing of intracranial contents	Median filtering Adjustment of intensity according to distance from the skull	Denoising Correction for CT cupping artifacts
Automatic realignment of images	Automatic localization of limits of brain, ventricles, floor of anterior intracranial fossa, mid-sagittal plane	Align the brain into the normal position
Extraction of candidate AIH	Top hat transformation Subtraction between the two sides	Highlight local high density regions Extract asymmetrically high density regions
Localization of candidate AIH	Registration of the brain in question against a normalized coordinate system	Render the candidate AIH anatomical information
Knowledge based classification of AIH	Rule based system with inputs of image features and anatomical coordinates of the extracted candidates	Distinguish genuine AIH from false positives resulting from noises, artifacts, and normal variants

Realignment of Images

Because CT studies obtained in an emergency setting as in this study tend not to be perfectly positioned. The images need to be properly realigned such that subsequent anatomical labeling process can take place. To do this, location and orientation of the brain need to be determined.

Boundaries of the Brain

The superior and both lateral limits are easily located by finding the margins of the segmented brain.

The landmark for the inferior limit of the cerebral hemisphere is at the lowest level of temporal lobes; however, during the development of the system, it was found that the floor of the anterior cranial fossa correlates more consistently with the location of most of the relevant internal structures. The level of the anterior cranial fossa can be accurately identified as the plane where there is significant 1. decrease in cross sectional area of the segmented intracranial contents; and 2. decrease in relative area of the segmented intracranial content to its convex hull, going from superior to inferior axial sections.

Location of Mid Sagittal Plane by Symmetry

There were several reports of midline location based on symmetry of brain parenchyma, but the proposed approaches were not suitable for brains containing pathologies which alter the symmetry such as AIH [13-15]. Our system locates the midline based on the assumption of symmetry of CSF spaces, predominantly the ventricular system.

The image of the brain that contains the main bulk of the lateral ventricles is selected by locating the section that contained the highest ratio of CSF containing space to solid brain substance. This particular plane is chosen because this is usually where the bulk of the lateral ventricles are located, which are sizable structures usually situated symmetrically about the midline, thus allowing the comparison of the two sides for locating the midline. This section is then binarized with a threshold such that CSF containing regions take on the value of zero whilst the brain parenchyma takes on the value of one. The binarized image is then rotated about its centroid to a range of angles. The absolute difference between the rotated image and its mirror image are obtained. The angle of the midline is the one that produces the least difference between the two halves of the rotated brain thus obtained. This process is illustrated in figure 2.

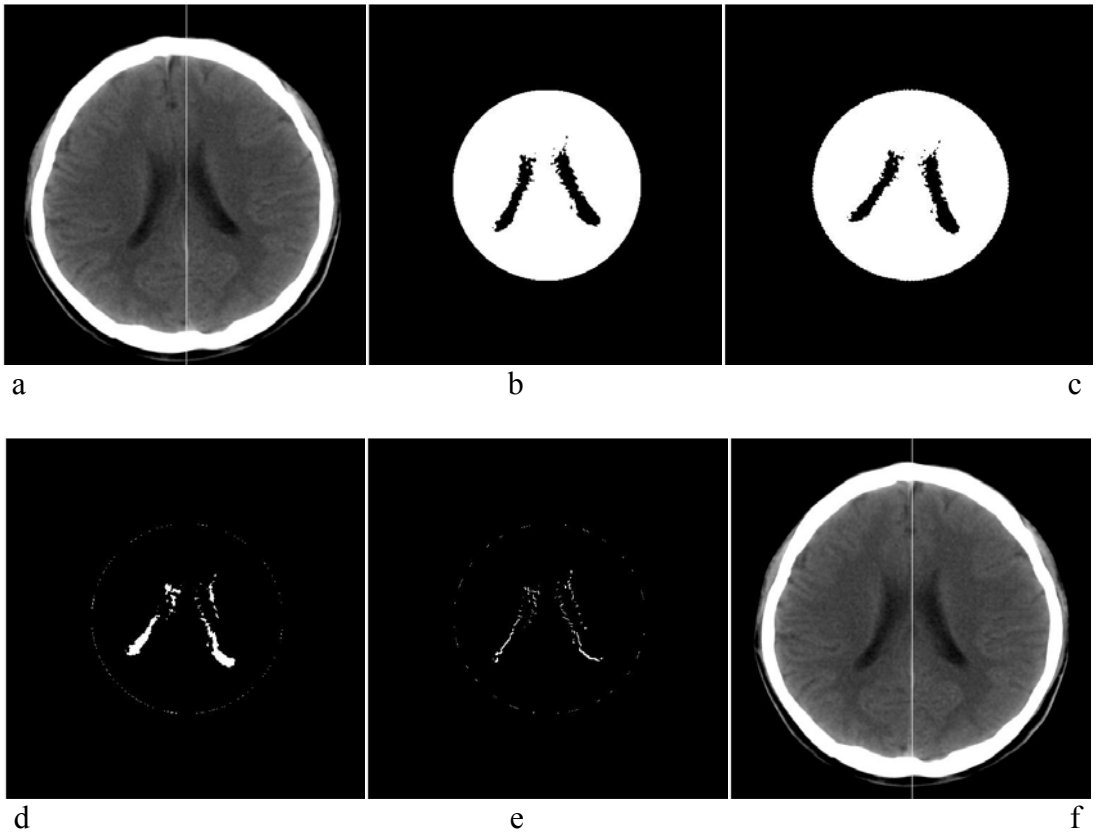

Figure 2 - The angle of the mid-sagittal plane is obtained by finding the line of symmetry of the body of lateral ventricles. The section containing the body of lateral ventricles (a) is automatically selected as described in text. The central portion of the image is binarized with threshold at CSF attenuation. It is rotated over a range of angles. The differences between the rotated image (b) and its mirror image (c) are obtained (d). The angle which gives the least difference (e) is the angle of the mid sagittal plane (f).

Manual Readjustment

Since automatic localization of the mid sagittal plane may be inaccurate due to exaggerated asymmetry in some normal subjects or distortion of anatomy due to pathological conditions, human intervention, although infrequently, may be required such that subsequent analysis can proceed. The system provides for this by incorporating an intermediary step when the observer can check and adjust the computer deduced mid sagittal plane.

After the midline and level of upper boundary of anterior cranial fossa are obtained, both are displayed for the user to decide if the localization is satisfactory. If not, an interactive tool is available for the user to manually align the images.

We believe identification of basic anatomical structures is a task that emergency physicians can comfortably perform. In fact, during development of the system, 7 emergency physicians had taken part in an informal trial of the manual adjustment tool. All were able to accurately localize the mid-sagittal plane and lowest section of anterior cranial fossa in randomly selected image datasets.

Preprocessing of Intracranial Contents

Median Filtering

To reduce noise, median filtering using a 3-by-3 square kernel was applied. Median filter was chosen because it is less sensitive to extreme values and able to remove outliers without reducing sharpness of the image.

Adjustment for Cupping Artifacts

CT cupping artifacts [16], which increase intensity over regions subjacent skull, inversely proportional to distance from the soft tissue-bone interface, has been recognized problem for intensity based thresholding of intracranial structures [17]. In the current application, these artifacts are particularly troublesome because immediately subjacent to skull are the locations where thin extraaxial hemorrhage are found. Therefore regions closer to skull are identified as abnormal only if they show intensity significantly higher than the regions at a similar distance from the skull. The average intensity as a function of distance from skull is obtained as a reference against which abnormal regions are compared. A series of successive morphological erosions is performed on the binarized image of the intracranial contents. The difference between the image after the nth erosion and the n+1th erosion yields the ring like mask at a distance proportional to n from the skull. Then average intensity of this ring can then be obtained by the multiplication of this mask with the original image and divided by number of pixels in the mask. The process is illustrated in figure 3.
The median filtered image with reduced cupping artifacts (I) is then ready for subsequent segmentation processes.

Segmentation of Candidate AIH

AIH is distinguished by its increased attenuation relative to normal intracranial structures. Its CT no. ranges from 40-100, whereas gray matter and white matter show CT no. in the range of 30-50 and 20-40 respectively. However, it is readily appreciated that simple thresholding would not work because the wide range of attenuation of AIH overlaps those of normal parenchyma. The problem is especially important for small AIH because the smaller lesions are more affected by partial volume averaging, which reduces the contrast and blurs the edge between the lesion and its adjacent parenchyma. Therefore global thresholding cannot effectively segment AIH. In this system, two parameters in addition to actual intensity value of the preprocessed image I(x,y) are obtained: 1. the intensity of a pixel above that of its immediate surroundings, obtained using image top-hat transformation; 2. its intensity difference above that of its contralateral anatomical region, obtained by subtraction of the flipped image from the original image.

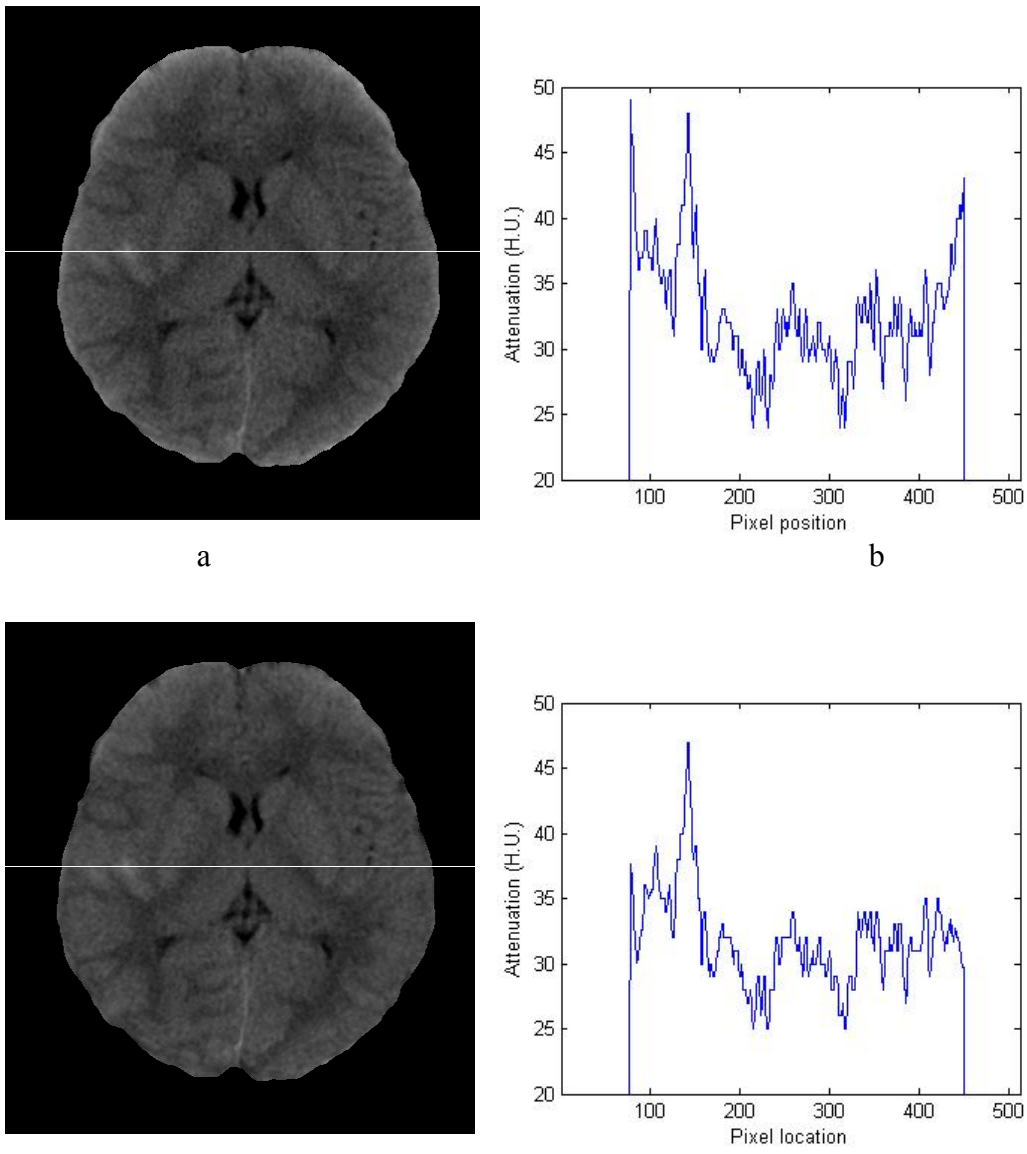

a b

c d

Figure 3 - The original image with artifactual increase in signal intensity towards the brain skull interface is shown in (a). The horizontal line indicates the position from where the intensity profile (b) is obtained. The image after correction of cupping artifacts is shown in (c). The intensity profile along the same horizontal line is shown in (d). It can be appreciated by comparison of (b) and (d) that the peak intensity at the pixel position of around 140 due to AIH is more prominent after correction of cupping artifacts.

Top-hat Transformation

Top-hat by opening or white top-hat transformation is the difference between the original image and its opening [18]. It extracts signal peaks on background of variable intensity levels, which do not fit the structuring element used for morphological opening. For the current application, as visualization of AIH depends primarily on the difference of attenuation between the lesion and its surrounding brain parenchyma that are of variable attenuation values, top-hat transform using a relatively large disk shaped structuring element is performed to extract the regions which show higher attenuation than adjacent brain parenchyma. This generate the first parameter for the segmentation F(x,y).

$F(x,y) = I(x,y) - \text{opening of } I(x,y)$

Extraction of Asymmetrical High Intensity Region

In addition, regions which are brighter than their presumably normal contralateral anatomical regions are more likely to be abnormal. It is especially important for small extraaxial hematomas, which are only of marginally increased signal intensity that the adjacent gray matter, but are much brighter than the contralateral CSF containing space. The brain is inverted along the mid sagittal plane. Minor asymmetry between the two sides of the brain is adjusted by elastic transformation of the flipped image. Control points for the transformation are obtained by intersections of 1. diagonals crossing the centroid of the mid sagittal plane and 2. the perimeter of the brain. This produces the elastically transformed mirror image J(x,y). Then difference G(x,y) between the original image and the morphological closing transformation of J(x,y) is obtained for individual pixels. This procedure is illustrated in figure 4.

$G(x,y) = I(x,y) - \text{closing of } J(x,y)$

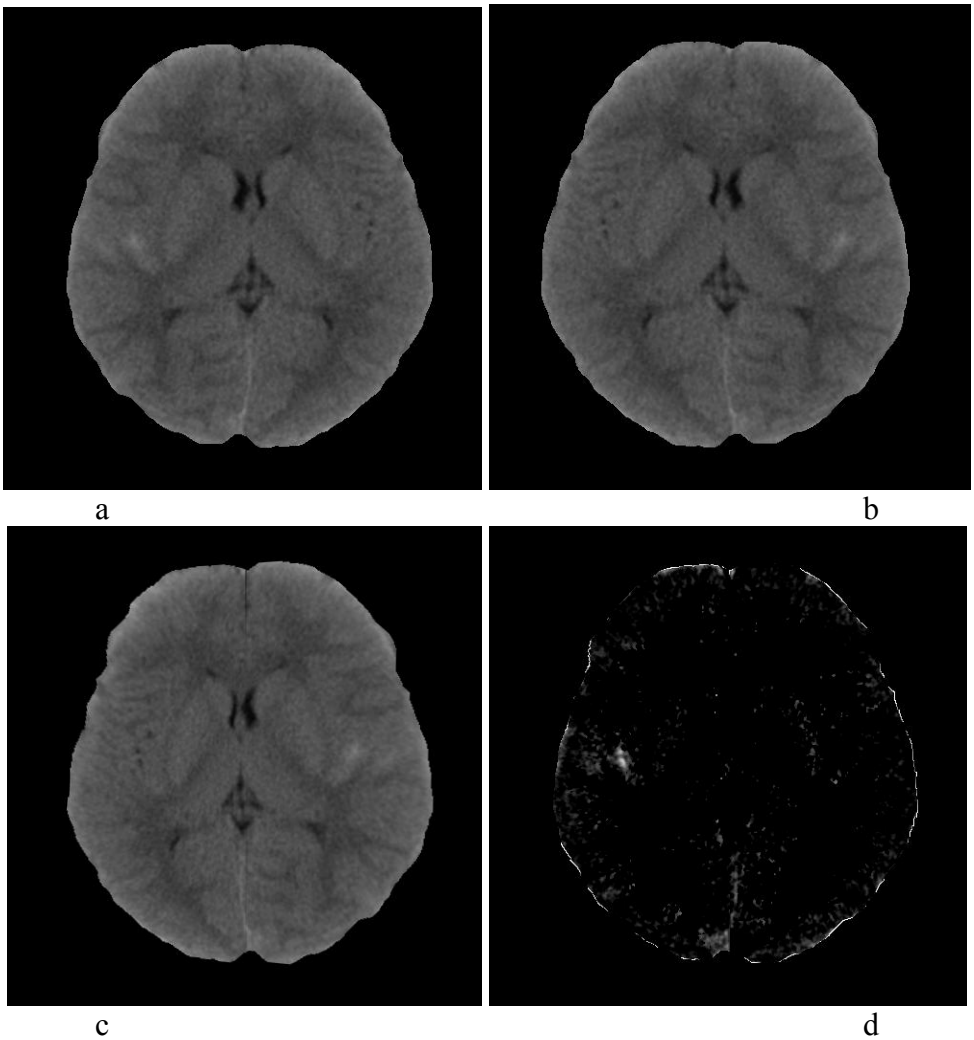

Figure 4 - The procedure of highlighting asymmetrical high density region is illustrated by the intermediary outputs of the CAD scheme. The original is shown in (a). The flipped image (b) is elastically transformed to reduce the normal structural asymmetry between the two sides of the brain (c). The difference between (a) and the morphological closing transformation of (c) highlights AIH within the right Sylvian fissure is of higher signal than CSF in the left contralateral Sylvian fissure (d).

With these, a pixel, p(x,y) of an axial image is segmented as candidate AIH if the weighted average of the pixel values in the aforementioned transformation images, exceeds a predefined threshold T (figure 5).

p(x,y) is a candidate AIH if w1F(x,y) + w2G(x,y) > T

where w1 and w2 are the weightings of F and G respectively

After thresholding, the cluster of AIH regions that are smaller than a predefined size are removed, to reduce artifacts due to noise. Then the sizes of candidate AIH lesions can be better approximated using intensity based region growing method. Subsequently, various descriptors, including intensity, size, eccentricity, orientation, etc. are extracted from individual candidate AIH region, which form the basis of subsequent knowledge based analysis.

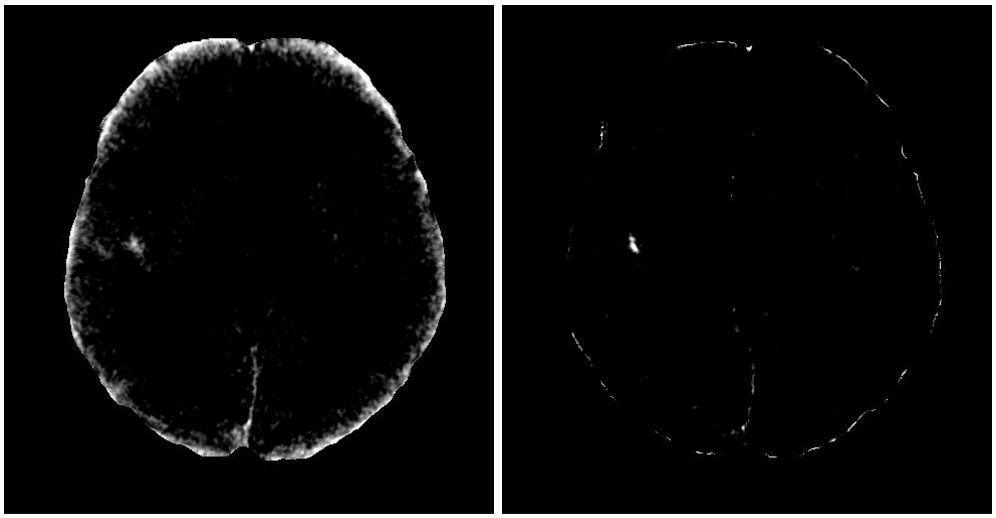

Figure 5 - Comparison of global thresholding of original image after removal of skull and extracranial tissues (Left), and thresholding of the combined processing steps including correction of cupping artifacts, image top hat transformation, and left-right comparison (Right) as discussed in the text. It is evident that the result of (Right) is much cleaner and manageable for subsequent processing.

Localization of Candidate AIH

In order to render the candidate AIH anatomical positional information such that subsequent classification can be performed in light of anatomical context, the brain need to be registered against a coordinate system in which anatomical information of a normalized brain model is embedded. Construction of the coordinate system is outlined in the following section. The control points for registration are sizable structures which are hence feasible to be automatically obtained. After registration by local weighted mean transformation, candidate AIH can be checked against the positions where AIH or mimics frequently appear.

Development of the Coordinate System

Since the current project is designed for images obtained by relatively thick axial sections prescribed in clinical protocols, anatomical labeling based on existing coordinate systems, e.g. Talairach atlas [19], is unreliable. Therefore a coordinate system that is applicable for clinical brain CT images has been purposely developed.

It was observed from a large number of images that the anatomical structures relevant for the current application can be adequately localized with reference to anatomical landmarks that can be automcally extracted from thick axial sections, including the mid sagittal plane, the boundaries of the brain, the level of anterior cranial fossa, and the boundaries of the lateral ventricles.
Based on these landmarks, the brain can represented by a coordinate system composed of a 15 x 20 x number of axial section (left-right x anterior-posterior x superior-inferior) matrix. The mid-sagittal plane is put into the central column of the coordinate. The cross-correlation between a coordinate position and the actual anatomical label is obtained by normalization using 65 of the training cases which show normal findings. The normalization process involved registration of the coordinate system to the training cases based on the automically extracted control points from individual case. The matrix was displayed as grids overlaid onto the original images, a radiologist then recorded the coordinates of the relevant structures after visual inspection of the composite images. After normalization process, relative frequency of occurrence of particular structure at each coordinate was transferred to the coordinate system.

Knowledge Based Classification

Genuine AIH can be identified from the candidates of suspected AIH, based on both imaging features and anatomical location. Despite the fact that AIH can take on a myriad of different size and shape, there are certain definable patterns that AIH may follow. For example, subarachnoid hemorrhage produces blood clots that match the configuration of subarachnoid spaces, which are located at the basal cisterns, Sylvian fissures, and sulcal spaces. Therefore if a candidate AIH volume matches these descriptions, e.g. a AIH volume with high eccentricity and vertically oriented (image features) and is located at the coordinate that corresponds to right Sylvian fissure (anatomical context), it would be rated a higher probability of being a genuine lesion by the rule-based classification system.
On the other hand, there are known constellations of imaging features and anatomical positions for different confounding normal variants, e.g. basal ganglia calcifications and venous sinuses, rules that lower probability of calling those suspected AIH as genuine were invoked when the criteria were met. For example, unusually high density regions smaller than a predetermined area and located symmetrically at the expected anatomical positions of bilateral basal ganglia would be rated a low probability for AIH, because they very much satisfies the rule for excluding basal ganglia calcification. Likewise, there are artifacts with some specific combinations of imaging and anatomical features, e.g. straight linear beam hardening artifacts between bones in posterior fossa, which are taken into account by another set of rules. In addition, correlation between different image planes have also been built in, e.g. partial volume artifacts are considered when a high density region lies immediate above bones, especially over petrous temporal bone and anterior cranial fossa.

Generally the rules that incorporate anatomical information take the following form:

$P \rightarrow Q$
$Q \rightarrow \Delta$ probability of AIH

Where P are the set of rules which check for the anatomical locations of the candidate AIH and Q are the corresponding rules which subsequently evaluate the imaging features of the candidate appropriate for the particular anatomical positions. When the imaging features satisfy some

defined pattern, probability of AIH is increased or decreased for the candidate. Some sample rules are listed in table 2

Table 2 Sample rules used in the knowledge base classification system. P are the set of rules which check for the anatomical locations and Q are the rules which evaluate the imaging features appropriate for some particular anatomical positions. A candidate AIH is first checked for the anatomical position. If the position is one that satisfies a particular P, the corresponding Q will be invoked to evaluate the image features of the candidate AIH. If an appropriate pair of P and Q is satisfied, the probability of AIH for the candidate is adjusted accordingly.

Anatomy rules (P)	Imaging feature rules (Q)	Interpretation	Probability of AIH
Rules that lower probability of AIH for candidates that conform to calcifications or normal high density structures			
mid sagittal plane, supracranial fossa	vertically aligned, ↑attenuation, ↑eccentricity, ↑ long axis length ↓short axis length	falx calcification	↓
mid sagittal plane, supracranial fossa periphery	intermediate attenuation, intermediate eccentricity, ↓convex hull	superior sagittal sinus	↓
medial portion of basal ganglia	↑attenuation (↑ if area ↑), ↓area (↑ if symmetrical), symmetrical	basal ganglia calcification	↓
central portion of cerebellum	↑attenuation (↑ if area ↑), ↓area (↑ if symmetrical), symmetrical	dentate nuclei calcification	↓
Rules that lower probability of AIH for candidates that conform to artifacts			
posterior cranial fossa	↑ eccentricity, ↑ long axis length ↓ short axis length	beam hardening artifact	↓
above anterior cranial fossa above temporal bone periphery near vertex	↑ attenuation ↓ area beyond adjacent bone in contiguous section	partial volume averaging	↓
Rules that increase probability of AIH for candidates that conform to particular type of AIH			
sylvian fissure	vertically aligned, intermediate attenuation, ↑ eccentricity, intermediate long axis length ↓ short axis length	sylvian fissure subarachnoid hemorrhage	↑
periphery	perpendicular to perimeter of brain ↓ long axis length ↓ short axis length	sulcal space subarachnoid hemorrhage	↑
anterior portion of posterior cranial fossa	horizontally alighed, intermediate attenuation, ↓ area	basal cistern subarachnoid hemorrhage	↑

Display of Output

The outlines of the genuine AIH as classified by the CAD are overlaid onto the original images. The original images without and with color coded outlines of AIH are displayed side by side, such that the user can compare the output of the system with the original images to better appreciate the results and make the clinical decision of whether to call the lesion a genuine AIH and act upon it. A screen capture of the graphical interface is shown in figure 6.

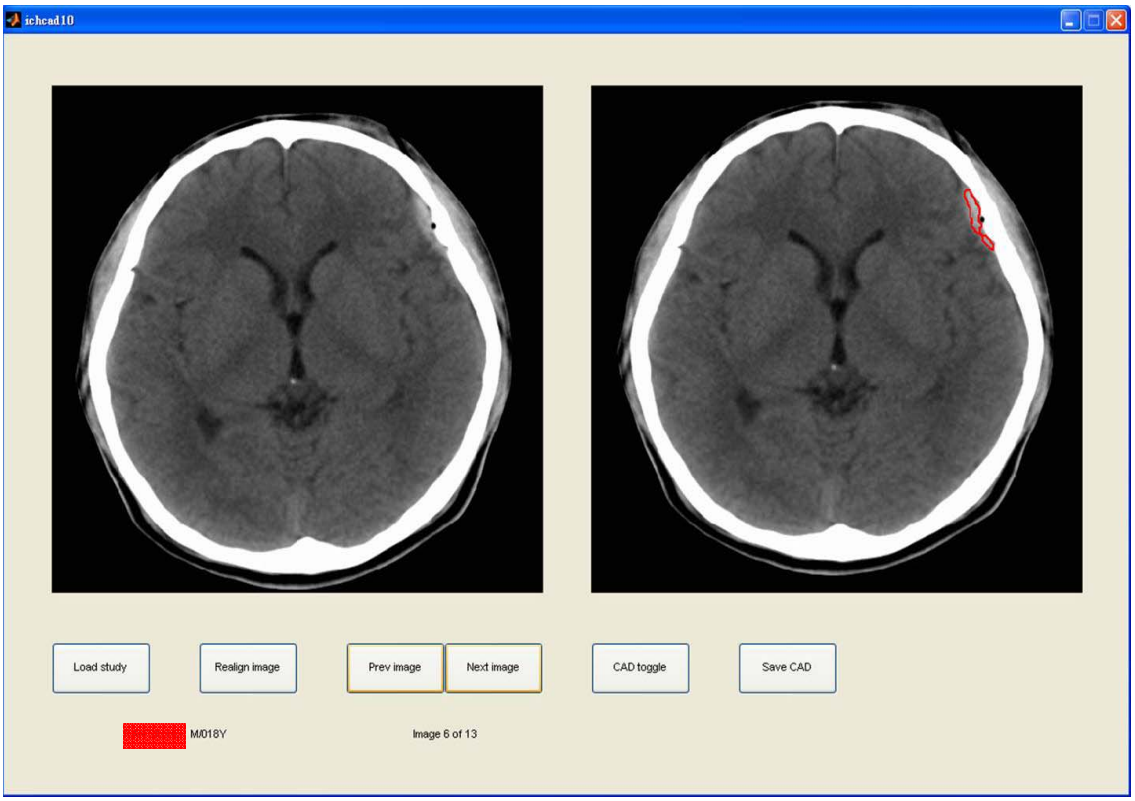

Figure 6 - Screen capture of the CAD system graphical user interface. The original images are displayed on the left window, whilst the output images with overlay of the outlines of AIH are displayed on the right. The original and output images are displayed in stripe mode and linked such that they can be scrolled in synchrony for review of the whole series.

RESULTS

Performance in Anatomical Localization

This method correctly located the level of the floor of middle cranial fossa in 97.5% (117/120) and 95.3% (61/64) of the training and validation cases respectively. All the other cases were off by one axial section only.

The mid sagittal planes (MSP) were accurately localized in 69.1% (83/120) and 65.6% (42/64) of the training and validation dataset respectively, which are defined as system output that is within 1mm of displacement and 1 degree of rotation from the genuine MSP. In 22.5% (27/120) and 25% (16/64) of the cases, the MSP were satisfactorily localized, off by within 3mm of displacement and 3 degrees of rotation, such that subsequent analysis was not adversely affected.

Altogether the system was successful in automatically putting the brain into the reference frame in 90.8% (109/120) and 85.9% (55/64) of the training and validation cases respectively, such that subsequent anatomical labeling was satisfactory. For the rest of the cases, the brain can be

readily realigned by the user through the interactive interface such that subsequent analysis can be performed satisfactorily.
Summary of the aforementioned results in anatomical localization is provided in table 3.

Table 3 Summary of success rate in identification of middle cranial fossa, mid sagittal plane, and putting the brain into the reference frame for anatomical localization. Manual intervention is required when the system fails to automatically put the brain into the reference frame.

	Training	Validation
Middle cranial fossa	97.5%	95.3%
Mid sagittal plane	91.6%	90.6%
Reference frame	90.8%	85.9%

Performance in Diagnosis of AIH

The performace of the system was described by sensitivity and specificity pairs on both per lesion and per case bases. The per lesion basis descriptors are more informative when number or size of lesions need to be quantified, or when the performance of detecting some particular type of lesion, e.g. SAH between 2.5mm and 5mm, is of interest. They are also independent of the number of lesion in each case. On the other hand, the performance on a per patient or per case basis is of more clinical relevance than the performance on a per lesion basis for the diagnosis of AIH. It is because the management options depend on the presence or absence of lesions rather than the quantity of lesions.
In the following section, a CAD output is counted as true positive if it overlaps at least part of the genuine blood clot as determined by radiologists. It is counted as false positive if it does not overlap any of the genuine blood clots. The sensitivity and specificity on a per (AIH) lesion basis are calculated accordingly.
Since classification of the results on a per patient/case basis may not be immediately apparent, its definition as used in the current study are elaborated in the following section. If any one of the CAD outputs for a particular patient is a true positive, then the case is counted as true positive, disregarding whether the other outputs are true or false positives. If there are one or more CAD output(s), but none of which is a true positive, then the patient is considered false positive. On the contrary, if there is no CAD output for a particular patient, but there is a genuine blood clot, the case is considered a false negative. If there is no CAD output for a patient in whom no blood clot existed, the case is counted as a true negative.
For the training cases, there were 77 contiguous AIH volumes in the 40 patients. The overall sensitivity was 84.4% (65/77). This increased significantly with increase in size of the lesion. The system correctly identified all AIH lesions larger than 5mm (28/28). Sensitivity dropped to 90% (27/30) for lesions between 2.5mm and 5mm, and 52.6% (10/19) for lesions smaller than 2.5mm (Table 4).
Forty-six contiguous AIH volumes were present in the 22 positive validation cases, averaging more than 2 lesions per case. The sensitivity on a per lesion bases was 82.6%(38/46). This increased significantly with increase in size of the lesion (Table 5). The sensitivity were 57.1% (4/7) for lesions 2.5mm or smaller, 84.2% (16/19) for lesions between 2.5mm and 5mm, 91.7% (10/11) for lesions between 5mm and 7.5mm, and 87.5% (7/8) for lesions 10mm or smaller.
There were altogether 23 false positive lesions detected in all the training cases, including both positives and controls. False positive rate was 0.19 (23/120) per case. For the validation cases, the false positive rate was 0.29 (19/66) per case.

Table 4 Summary of CAD result in the training cases according to type and size of individual AIH vol on a per lesion basis. IPH – intraparenchymal hemorrhage, IVH – intraventricular hemorrhage SAH – subarachnoid hemorrhage, SDH – subdural hemorrhage, EDH – extradural hemorrhage, AIH vol – number of contiguous AIH volumes, CAD+ - number of AIH vol correctly identified by the CAD.

Training Cases	IPH		IVH		SAH		SDH		EDH		All Types	
	AIH vol	CAD +	AIH vol	CAD +	AIH vol	CAD +	AIH vol	CAD +	AIH vol	CAD +	AIH vol	CAD +
0-2.5mm	0		1	1	17	9	1	0	0		19	10
>2.5-5.0mm	0		2	0	11	10	13	13	4	4	30	27
>5-7.5mm	1	1	0		6	6	3	3	1	1	11	11
>7.5-10.0mm	4	4	0		5	5	7	7	1	1	17	17
All Sizes	5	5	3	1	39	30	24	23	6	6	77	65

Table 5 Summary of CAD result in the validation cases according to type and size of individual AIH vol on a per lesion basis. IPH – intraparenchymal hemorrhage, IVH – intraventricular hemorrhage SAH – subarachnoid hemorrhage, SDH – subdural hemorrhage, EDH – extradural hemorrhage, AIH vol – number of contiguous AIH volumes, CAD+ - number of AIH vol correctly identified by the CAD.

Validation Cases	IPH		IVH		SAH		SDH		EDH		All Types	
	AIH vol	CAD +	AIH vol	CAD +	AIH vol	CAD +	AIH vol	CAD +	AIH vol	CAD +	AIH vol	CAD +
0-2.5mm	0		0		7	4	0		0		7	4
>2.5-5.0mm	0		3	2	12	10	3	3	1	1	19	16
>5-7.5mm	2	2	1	1	6	5	2	2	1	1	12	11
>7.5-10.0mm	1	0	1	1	2	2	4	4	0	0	8	7
All Sizes	3	2	5	4	27	21	9	9	2	2	46	38

On a per patient basis, the sensitivity and specificity were 95% (38/40) and 88.8% (71/80) respectively for the training cases (Table 6). The system achieved sensitivity of 100% (22/22) and specificity of 84.1% (37/44) for the diagnosis of AIH for the validation cases (Table 7).
The current system, although not optimized in terms of speed, takes an average of approximately 15 seconds per image to produce the output. Actual time varies substantially for each case, depending on number of image and number of candidate AIH produced to be evaluated by the classification system.

Table 6 Summary of CAD results on a per patient basis for training cases.

	Validation Positive	Validation Negative
AIH present	38	2
AIH absent	9	71

Sensitivity = 95.0%, Specificity = 88.9%, Accuracy = 90.8%, Positive Predictive Value = 80.8%, Negative Predictive Value = 97.3%

Table 7 Summary of CAD results on a per patient basis for validation cases.

	Validation Positive	Validation Negative
AIH present	22	0
AIH absent	7	37

Sensitivity = 100.0%, Specificity = 84.1%, Accuracy = 89.3%, Positive Predictive Value = 75.9%, Negative Predictive Value = 100.0%

DISCUSSION

Detection of Small AIH

There is no objective method of classifying AIH according to its size. The target size of detecting AIH smaller than 10mm is arbitrarily chosen. The width rather than the length is chosen for extraaxial hemorrhage because it is the dimension which is clinically relevant and customarily reported. Although it does imply that 10mm extraaxial AIH would be larger in area/volume than a 10mm intraaxial AIH described in this study, it is believed that this convention better reflect the radiologists' assessment and reporting standard.
Small AIH often shows ill-defined boundaries, variable configurations, and little contrast difference with adjacent structures. This presents challenges to the development of CAD based on low level processing alone. Furthermore, for a system to be clinically useful, it must be able to detect small lesions. The approach adopted in the current system is to be oversensitive in locating candidate AIH volumes using image processing techniques such that the vast majority of abnormal foci are extracted; however, this necessarily generates too many false positives. The average number of false positives generated by this CAD system based on the aforementioned processes alone is 62.1 per set of images or 4.2 per image in the training set. We believe it is especially important for a CAD system intended for use by non-radiologists, who may not be highly competent in telling the difference between genuine lesion and false positives, to be highly specific. It was found that genuine AIH may not be all that different from false positives considering simple image features. But with the input of anatomical information, classification

becomes feasible. It is because the candidates with similar image features may mean AIH at one particular location, or artifact if situated at another. With the knowledge based classification system in place, the false positive per case was dramatically reduced to 0.18.

Usage of Anatomical Information

There are different sets of rules for different parts of the brain because the probability of having a particular type of AIH or certain variant and artifact depends on anatomical position. For example subdural hemorrhage can be present over the convexity of the brain, along the falx cerebri or tentorium, but not within the brain or ventricular system. Also, the configuration of the same type of hematoma may depend on the anatomical location, e.g. along some well-defined planes which is present only at specific locations in the brain. Therefore rules for identifying typical image feature of SDH can only be applied at the appropriate regions. Likewise, calcifications are usually present in basal ganglia, pineal gland, and dentate nuclei and tend to be symmetrical. Accordingly rules for identifying normal calcifications are applied over the said regions with additional criteria of symmetry. With these rules in place, the false positive rate has been kept at an acceptable level.

There are several established methods to map digital images to standard brains. The most well known are the brain Talairach atlas and the Montreal Neurological Institute (MNI) brains. Software packages are available for mapping to these brains [20, 21]. However, these available systems cannot be effectively utilized in this project because the thick (5-10mm) sections used in clinical protocols preclude the accurate localization of landmark structures, especially the anterior commisure (AC) and posterior commisure (PC) required to define the AC-PC plane. In addition, the images are acquired along the orbital canthal – meatal plane (OM) conventionally used for clinical brain CT imaging, which lies at a variable angle of around 9 degrees from the AC-PC plane [22]. The thick axial sections thus obtained cannot be consistently converted to the AC-PC plane.

The current system maps the individual images to a coordinate system specifically developed based on axial sections along the OM plane, which is readily applicable to images obtained using standard clinical protocols for brain CT imaging. Although it lacks definition of the AC and PC, such that anterior-posterior relationship of some internal structures may be less accurate, the system does contain additional control points that modify the registration process according to the configuration of the lateral ventricles. It was observed that this significantly reduces the variability of coordinate positions for some relevant internal structures, especially the choroids plexus and basal ganglia. It is postulated that inclusion of control points based on the lateral ventricle positional information more accurately reflects the change in relative position of internal structure resulting from age-related brain atrophy. On the other hand, a more accurate age corrected coordinate system may be developed using the aforementioned scheme, with collection of a large sample containing enough number of sample for each age group. It is also hoped that inclusion of more information in addition to the ones which have been included may make the coordinate system valuable for other applications.

It is recognized that the accuracy of the anatomical labeling process in the current project is limited by the relatively large size represented by each coordinate position, which is about 1cm3 for a normal sized adult brain. In addition, tilt and yaw in the coronal and sagittal plane cannot be effectively corrected because the axial sections are thick. However, it must be understood that pinpoint accuracy in brain mapping is a daunting task on its own, and is impractical for images obtained using present day clinical protocols. Adding to the problem is that the current CAD deals with abnormal brain, which makes accurate mapping to a normalized atlas error prone and

counter productive. It is believed that the simple coordinate system generating relatively rough estimate of anatomical position is more efficient and reliable for the current application.

Limitation of the Study

The results in the training cases show lower sensitivity than those of the validation cases on per patient basis, 95% versus 100%. This was probably a chance occurrence because all the missed lesions in the validation cases are present in cases where at least one other lesion was detectable. The very similar overall sensitivity on per lesion basis of 84.4% and 82.6% for the two groups might be affected by the different distribution of size of lesions in individual patients.
It is admitted that the allocation of training and validation cases were not randomized in the strict sense. But we believe the collection process was not systemically biased, as the allocation into each group was essentially decided by the independent schedule between data collection by the investigator and housekeeping clearance of the temporary CT archive. However, there does seem to be difference in the composition of the lesions in the two datasets regarding the size of lesions, the training cases contain a lower proportion of larger (>5mm) lesions, 36.4% (28/77), as compared against the validation cases, 43.5% (20/46). This might have elevated the apparent overall sensitivity on per lesion basis for the validation cases. Therefore, we believe the results of sensitivity by size best represent the performance of the system. A similar trend of increase from 50-60% for lesions 2.5mm or smaller to 90-100% for lesions larger than 5mm was observed for both the validation cases and training cases.

Future Development

The CAD system has been designed to work on conventional axial sections obtained from an old machine. The authors are currently working on adapting the system to images obtained from multidetector row CT machine. Initial results were promising. The impression was that more accurate results could be achieved because the images are less prone to artifacts and contrast between AIH and normal parenchyma is higher, mainly because thinner sections make volume averaging less of a problem even for small lesions.
As a result, correction of CT cupping artifact can be less aggressive, so that sensitivity for very thin (< 2mm thick) extra-axial hemorrhage is increased. Also, a lower threshold of attenuation difference can be used such that smaller candidate lesions with lower attenuation can be detected. In addition to the techniques already implemented in the current project, AIH can be better characterized by 3 dimensional morphology or interrelation. For example, disc like lesions that span across different sections would make extra-axial hemorrhage far more likely than the linear beam hardening artifacts that tend to be different even in contiguous plane. Such differentiation can be difficult on axial sections alone because both would appear as peripherally located linear hyperdensity.
The concept of diagnosis based on anatomical information is well-recognized by clinicians. The component of anatomical labeling developed in the current project can be used for systems aiming to detect other types of intracranial lesions. A very useful application that may also complement the current system would be CAD of acute infarct. Of course, the target lesion would be ill-defined low density regions rather than high density foci, but a similar scheme of initial oversensitive extraction of candidate lesion, followed by classification based on anatomical correlation can be readily adopted. Even tumor diagnosis can utilize the concept, because different kinds of tumors tend to affect different anatomical regions.
Unlike tumor detection in mammography, chest radiography and CT, expert radiologists can diagnose AIH at very high accuracy. But this does not preclude the current system from

becoming a clinical useful tool. It is because emergency brain CT often need to be interpreted by acute care physicians to guide immediate management of patients, when radiologists are not readily available. The acute care physicians, however, may not possess the same interpretation skills to detect small or difficult AIH, or to distinguish genuine AIH from mimicking variant/artifact.

It is believed that the system can detect lesions that can be difficult for acute care physicians or even radiology residents. Some such lesions are shown in figure 7. Still, a formal observer study based on receiver operating characteristic curve comparing the diagnostic performance of acute care physicians and radiologists with and without the aid of the CAD need to be conducted in order to determine if there is significant benefit.

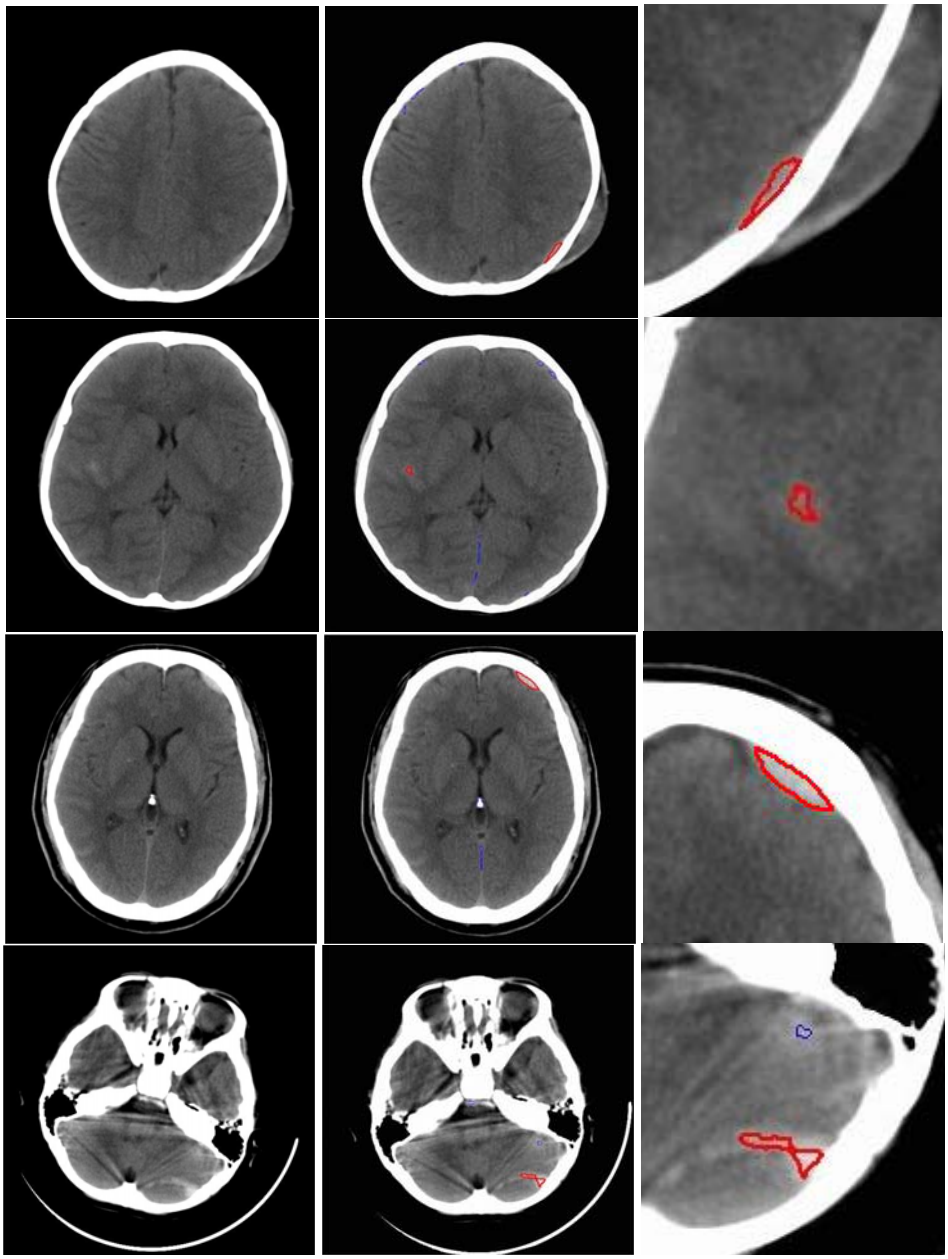

Figure 7 - AIH can be difficult to detect if they are small, of similar attenuation to adjacent structures, or confused with normal variant and artifact. Examples of some difficult cases (the left column) with their CAD results (the middle column) and magnified views (the right column) are shown. The system outlines AIH with red perimeters. High density regions which are segmented but subsequently classified as unlikely to be AIH are outlined with blue perimeters.

Another issue that needs to be considered before such system can be put into clinical practice is integration into the workflow of acute care physician or the emergency room. It is different from most of the current CAD systems designed for screening or routine reporting purpose, for which speed is of less concern. For applications to be useful for immediate management, immediate availability without significant additional cost of time is of utmost importance. Possible ways of integration include setting up an application server that connects with the PACS system, or better still, direct incorporation of the system into clinical PACS.

We envisage that the CAD system can be implemented into daily clinical practice in the emergency room. It is believed that the system can be used as a triage tool for patients suffering from minor neurological disturbance or head injury. After CT is performed, clinicians can read the images with help from the system. If AIH has been excluded, the patients may be safely observed for a shorter period of time before discharge. Also, patients may be admitted to neurosurgical units or other units based on the presence of absence of AIH.

CONCLUSION

A CAD system capable of identifying small intracranial hemorrhage has been developed. It classifies genuine AIH from mimicking normal variants or artifacts based on both image features and anatomical information, which is made possible by construction of a coordinate system that incorporates positional information of normal brain structures. It is expected that this system can benefit patient care especially in emergency situations when timely management decision need to be made by acute care physicians

References

1. Perry, J.J., et al., Attitudes and judgment of emergency physicians in the management of patients with acute headache. Acad Emerg Med, 2005. 12(1): p. 33-7.
2. Mader, T.J. and A. Mandel, A new clinical scoring system fails to differentiate hemorrhagic from ischemic stroke when used in the acute care setting. J Emerg Med, 1998. 16(1): p. 9-13.
3. Diehl, J.T., CT scanning in traumatic and emergency patients. Comput Tomogr, 1978. 2(3): p. 183-7.
4. Bagley, L.J., Imaging of neurological emergencies: trauma, hemorrhage, and infarction. Semin Roentgenol, 1999. 34(2): p. 144-59.
5. Cohen, W. and L. Wayman, Computed tomography of intracranial hemorrhage. Neuroimaging Clinics of North America, 1992. 2: p. 75-87.
6. Schriger, D.L., et al., Cranial computed tomography interpretation in acute stroke: physician accuracy in determining eligibility for thrombolytic therapy. Jama, 1998. 279(16): p. 1293-7.
7. Wysoki, M.G., et al., Head trauma: CT scan interpretation by radiology residents versus staff radiologists. Radiology, 1998. 208(1): p. 125-8.
8. Erickson, B.J. and B. Bartholmai, Computer-aided detection and diagnosis at the start of the third millennium. J Digit Imaging, 2002. 15(2): p. 59-68.
9. Maldjian, J.A., et al., Automated CT segmentation and analysis for acute middle cerebral artery stroke. AJNR Am J Neuroradiol, 2001. 22(6): p. 1050-5.
10. Hodgson, R., et al. CAD System for Detecting Haemorrhage in CT of Stroke. in RSNA 2004. 2004.
11. Goto, H., et al. CAD System in the Emergency Medical Care for Abdominal and Head Trauma. in RSNA 2005. 2005. Chicago.

12. Yang, G.L., et al. A Practical Computer-aided Diagnosis System for Intracranial Hemorrhage Detection in Acute Stroke. in RSNA 2005. 2005. Chicago.
13. Junck, L., et al., Correlation methods for the centering, rotation, and alignment of functional brain images. J Nucl Med, 1990. 31(7): p. 1220-6.
14. Minoshima, S., et al., An automated method for rotational correction and centering of three-dimensional functional brain images. J Nucl Med, 1992. 33(8): p. 1579-85.
15. Ardekani, B.A., et al., Automatic detection of the mid-sagittal plane in 3-D brain images. IEEE Trans Med Imaging, 1997. 16(6): p. 947-52.
16. Barrett, J.F. and N. Keat, Artifacts in CT: recognition and avoidance. Radiographics, 2004. 24(6): p. 1679-91.
17. Ruttimann, U.E., et al., Fully automated segmentation of cerebrospinal fluid in computed tomography. Psychiatry Res, 1993. 50(2): p. 101-19.
18. Soille, P., Morphological image analysis : principles and applications. 2nd ed. 2003
19. Talairach, J. and P. Tournoux, Co-planar stereotaxic atlas of the human brain : 3-dimensional proportional system : an approach to cerebral imaging. 1988
20. MEDIC. Available at http://medic.rad.jhu.edu/download/public/.
21. SPM 5. Available at www.fil.ion.ucl.ac.uk/spm/.
22. Weiss, K.L., et al., Clinical brain MR imaging prescriptions in Talairach space: technologist- and computer-driven methods. AJNR Am J Neuroradiol, 2003. 24(5): p. 922-9.

CHAPTER 2

AUTOMATIC METHODS TO ANALYZE AND QUANTIFY CARDIAC LEFT VENTRICLE PARAMETERS BY MEANS OF SPECT*

MARCO A. GUTIERREZ†, SÉRGIO S. FURUIE‡, MARINA S. REBELO§ and JOSÉ C. MENEGHETTI

Heart Institute (InCor), University of São Paulo Medical School,
Av. Dr. Enéas de Carvalho Aguiar, 44, São Paulo, SP, 05403-000, Brazil
†*Tel:+55-11-3069-5385*
†*marco.gutierrez@incor.usp.br*
‡*Sergio.Furuie@incor.usp.br*
§*marina.rebelo@incor.usp.br*

Single photon emission computed tomography (SPECT) is a non-invasive technique used in the visualization and analysis of the distribution of radioactive counts, for instance within the myocardium and surrounding structures. In the last two decades, a number of techniques have been developed to aid in the classification of the SPECT images. The strength and availability of these quantitative tools have in many ways provided a competitive advantage to nuclear cardiology, compared with other higher-resolution non-invasive imaging modalities for the detection of coronary artery disease (CAD). The first efforts in this area involved the quantification of planar images of patients with low probability of CAD. It allowed the construction of normality databases and the definition of mean and variance limits for normal patients. With the definition of these values, objective abnormality thresholds were defined. These tools were continuously expanded providing LV perfusion and function parameters in 2D, 3D and 4D. Some of them were incorporated and commercially offered with the scanners available nowadays. In such scenario, the comparison of the different techniques is a difficult task due to the diversity of approaches, image acquisition protocol and the lack of a "gold standard" to compare the results. Therefore, the search for robust methods to analyze automatically the complete series of images is yet an open study area.

Keywords: Single photon emission computed tomography; medical image processing; cardiology; image resolution; image sequences; image classification; image motion analysis; data visualization.

1. Introduction

It is a fundamental goal of many modalities of cardiac imaging and image analysis methods to measure the regional function of the left ventricle (LV), through LV wall motion, thickening, and strain measurements, in an effort to isolate the location, severity and extent of ischemic or infarcted myocardium.[1] However, most existing methods present severe shortcomings in making accurate and reliable quantitative regional LV function measurements over the entire cardiac cycle due to

*Portions adapted, with permission, from *Journal of Electronic Imaging*, **12**(1) (2003) 118–124.

the fact that the heart is a non-rigid moving object that rotates, translates, and deforms in 3D space, whereas most standard approaches rely on sequences of 2D images. Furthermore, most of these approaches often use only the end-diastolic and end-systolic image frames, while the LV actually goes through a temporal wave of twist, contraction and expansion. The asynchrony of surface motion or LV thickening from time to time, as well as from region to region, may be an indicative of ischemia.

Radionuclide imaging is a common non-invasive technique used in the evaluation of cardiac function and disease. The process to obtain images in this modality involves the detection of the radiation emitted from a patient's organ or region after the injection of a radiopharmaceutical such as thallium-201 (^{201}TI) and technetium-99m sestamibi (^{99}Tc^{m}-MIBI). Using a gamma camera, part of the emitted radiation can be used to produce an image indicating the distribution of the radionuclide in the myocardium.[1,2]

Temporal changes in the spatial distribution of radiopharmaceuticals can be obtained by taking multiple images over periods of time that may vary from milliseconds to hundred of seconds. Since the resulting image, known as planar image, contains information of the projection of a radioactive volume over the detector's face, it is often difficult to determine clearly the function of tissue deep in the body. Tomographic studies obtained by taking multiview acquisitions of the object overcome most problems caused by the superposition of information in a single planar view. The technique of single-photon emission computerized tomography (SPECT) provides the clinician a set of images that permits the visualization of the distribution of radioactive counts within the myocardium and surrounding structures. Defects on the distribution of some radionuclides such as ^{201}TI and ^{99}Tcm-MIBI in the myocardium indicate a muscle hypoperfusion due to the obstruction of the coronary arteries (Fig. 1).

Due to the capability to acquire myocardial perfusion, the SPECT studies gated to the electrocardiogram signal (ECG) provide the potential to extract additional

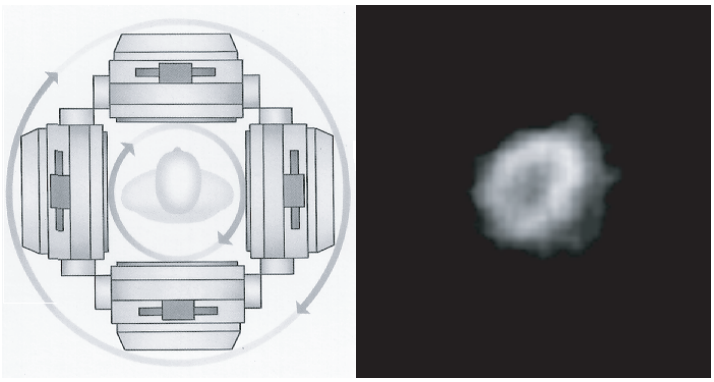

Fig. 1. A rotating gamma camera for emission tomography (left). By using reconstruction algorithms it is possible to estimate the LV transaxial image.

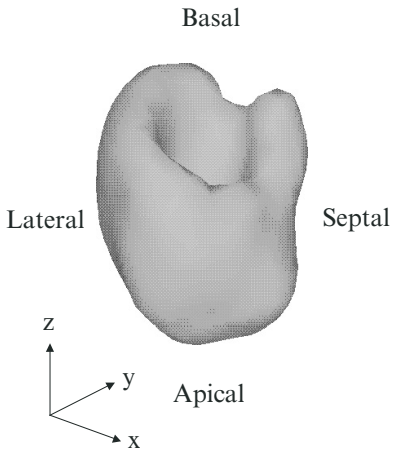

Fig. 2. Three-dimensional rendering of a normal cardiac left ventricle.

quantitative information about cardiac function from the time-dependent motion of the myocardium. While gated SPECT studies are usually interpreted as series of two-dimensional (2D) images, there is an increasing interest in the presentation of the data in a more realistic three-dimensional (3D) form. These new displays provide an overview of the many slices in a single image, and enhance the perception of spatial relationships. On the other hand, the visualization of the gated SPECT studies is complicated by the fact that 3D density images cannot be directly presented using common display devices that produce only 2D pictures. In general, some kind of transformation must be performed to the image sequence which introduces reduction of information.

Typically, there are two approaches: 2D sequence images or 3D surface rendering. The first approach preserves most of the intensity information. However, 3D relations between each slice are only implicit. Moreover, a typical 3D gated SPECT study produces hundreds of images, which are usually analyzed in a time consuming procedure. The second alternative makes 3D information explicit (Fig. 2), but density is represented indirectly through the shape of the surface.

2. Automatic Analysis of Cardiac Nuclear Images

A number of techniques, most of them concerned with visualization, have been developed to aid in the classification of the images. Perfusion abnormalities or defects were visually interpreted with the knowledge that normal myocardium displayed different radioactive distributions than those of abnormal myocardium.[4–8] However, it has been shown that interpretation of images by strictly visual techniques is subject to errors and inconsistencies due to variation in the size and orientation of the heart, the low contrast of planar imaging, photon absorption and scatter. For these reasons, assistance in diagnosis can be improved only through the development of automatic or semi-automatic methods to analyze and to quantify

medical image parameters with the expectation of a significant reduction in intra-observer variability.[9,10]

2.1. *Planar imaging analysis*

To solve the problem of interobserver variability, several methods of quantitative analysis of the radiotracer distribution have been described.[11–15] Watson[11,12] co-registered the serial images and reduced the 2D images to a series of linear radiotracer intensity profiles. Relative perfusion were then extracted from an analysis of these profiles as a function of time. Garcia[13,14] replaced the co-registration step by using a circumferential profile that reduced the 2D image into a line profile. The construction of the circumferential profile began with the manual definition of the center of the heart in the image. From that definition, the algorithm[13,14] sampled the myocardial tracer uptake along rays emanating from the user defined center. At 6° steps circling clockwise about the left ventricle, myocardial intensity profiles were recorded. From the myocardial intensity profiles along each ray, the maximum myocardial intensity was recorded as a function of angle, reducing the 2D images to a line profile.

The advances in quantification methods by imaging patients with low likelihood for coronary artery disease allowed the construction of normal databases and the definition of mean and variance limits for normal patients. With the definition of mean and variance limits for normal perfusion, objective abnormality thresholds were defined. The use of these quantification tools and normal databases improved the diagnostic sensitivity for detecting disease in individual coronary arteries and significantly reduced the intraobserver variability for the patient's classification.[15]

2.2. *SPECT imaging analysis*

The advances in camera technology in the late 80s allowed single-photon emission computed tomography (SPECT) to be used routinely. With its inherently better image contrast, SPECT imaging gradually replaced several exams usually carried out by conventional planar imaging. Typically, a gamma-camera SPECT acquisition may consist of 64 planar views, or projections, each containing 64×64 image pixels and acquired at 64 discrete angles covering 360° around the patient. By the use of reconstruction algorithms, it is possible to estimate transaxial, sagittal and coronal sectional images, creating 3D volumes or stacks of short-axis images that served as input to the quantitative software.

Although the objective of defining regional myocardial perfusion abnormalities with SPECT imaging did not change from that of planar imaging, the complexity of the problem increased significantly with the myocardium represented as a 3D volume rather than planar images.

The first effort to address this problem was carried out by Tamaki *et al.*[16] This quantitative tomographic analysis was assessed by the circumferential profile curves of the three short-axis sections (apical, middle and basal) of the left ventricle. To assess the apical region, the most central long-axis section cutting through the

apex was also selected. From these images, circumferential maximal count profiles of myocardial distribution were obtained in a manner similar to that of Meade[17] and Burow.[18] The center of the left ventricle cavity was manually determined and each tomographic image was divided into 36 radial segments at 10° intervals. The distribution of the radionuclide was determined by calculating the highest activity per pixel along each radial segment, normalizing the data to the segment with the highest counts to display a circumferential profile curve in each image. Perfusion defects were classified by use of uptake and washout distributions similar to the methodology used to quantify planar images. The results from theses studies showed better sensitivity for the detection of diseased coronary vessels than qualitative analysis.

Garcia *et al.*[19–21] extended the method proposed by Tamaki[16] to the entire SPECT volume by introducing the polar map, or bull's-eye displays, for viewing circumferential profiles. The polar maps allow a quick and comprehensive overview of the circumferential samples from all slices by combining them into a single color-coded image. The points of each circumferential profile are assigned a color based on normalized count values, and the colored profiles are shaped into concentric rings. The most apical slice processed with circumferential profiles defines the center of the polar map, and each successive profile from each successive short-axis slice is displayed as a new ring surrounding the previous. The most basal slice of the LV makes up the outermost ring of the polar map. Additional maps such as standard deviation map that shows the number of standard deviations below normal of each point in each circumferential profile can aid in evaluation of the study by indicating the severity of any abnormality.

In addition to tabulated defect extent values, various bull's-eye displays were developed to aid in the interpretation of the tomographic slices. The blackout polar map set those sectors in the polar map that where abnormal to the color black while maintaining the intensity of normal sectors. The blackout map provided a visual representation of the defect location and size. A second map, the defect severity map, mapped the defect abnormality in units of standard deviation below the normal mean. Both maps in combination with the vascular overlay template provided extent and severity values in each vascular region.

To account for differences among patients in the axial dimension of the heart, the slice thickness or polar map ring width was normalized so that each patient's polar map consisted of the same number of sampling points. With this technique, the polar map became the standard template for representing the 3D volume of the LV (Fig. 3). By eliminating the anatomic variations of the LV, the polar map provided the construction of normal databases as a pattern to compare 3D perfusion distribution from patients under study.

2.3. *Gated SPECT imaging analysis*

Commercial SPECT systems nowadays have the capability of acquiring and reconstructing electrocardiogram (ECG) gated myocardial perfusion studies. This feature

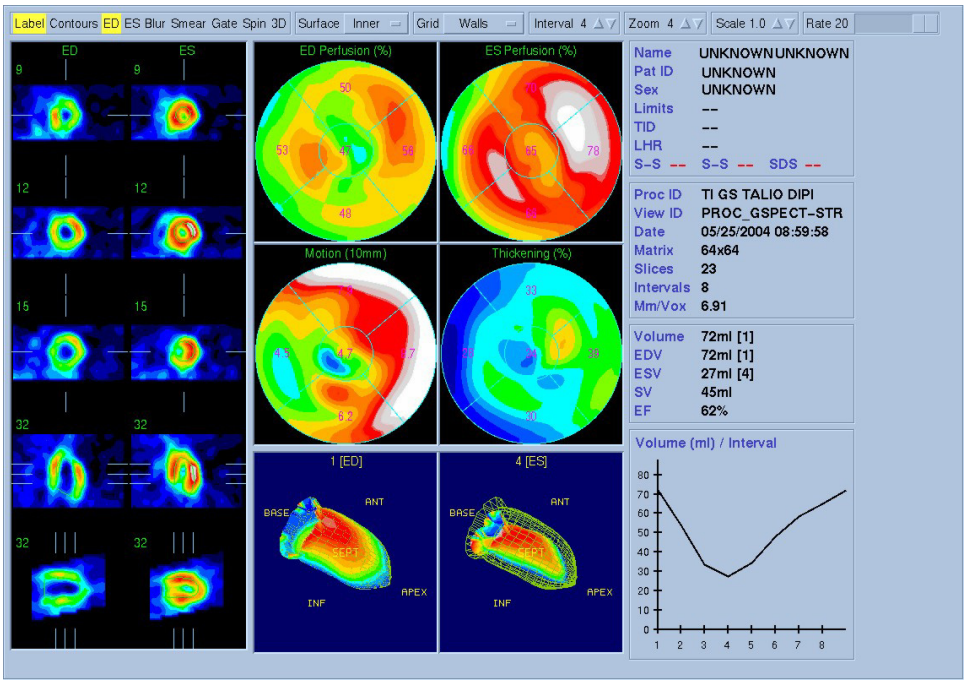

Fig. 3. Screenshot from the result page of a cardiac SPECT study. Some slices are shown on the left part of the screen. The polar maps (bull's eye) are shown on the upper middle and below, the three-dimensional surfaces in diastole and systole. (Screenshot taken from QGS – Guido Germano.)

requires ECG triggering, where the *R*-wave signal (Fig. 4), indicating the beginning of the contraction of the LV of the heart, is used to align the acquisition data from different cardiac cycles. A gated SPECT study will supply information about the cardiac function averaged over many heart beats during a period when the radiopharmaceutical ($^{99}\mathrm{Tc}^{\mathrm{m}}$ and $^{201}\mathrm{TI}$) is uniformly distributed.

This feature has promoted the use of SPECT for the total automatic assessment of myocardial perfusion and for global and regional function, including the assessment of LV ejection fraction, LV end-diastolic (ED) and end-systolic (ES) volumes and LV myocardial wall motion and thickening.

However, the quantification of global and regional LV parameters requires knowledge of the endocardial and, depending on the parameters being determined, the epicardial surface throughout the cardiac cycle. These surface determination may be manually assigned or automatically detected. Manual methods are subjective and time consuming. The automated methods use either boundary detection or geometric modeling.

A large effort has been devoted to the analysis and segmentation of cardiac images by methods guided by prior geometric knowledge. In general they can provide, with a limited number of global parameters, a rough shape approximation.

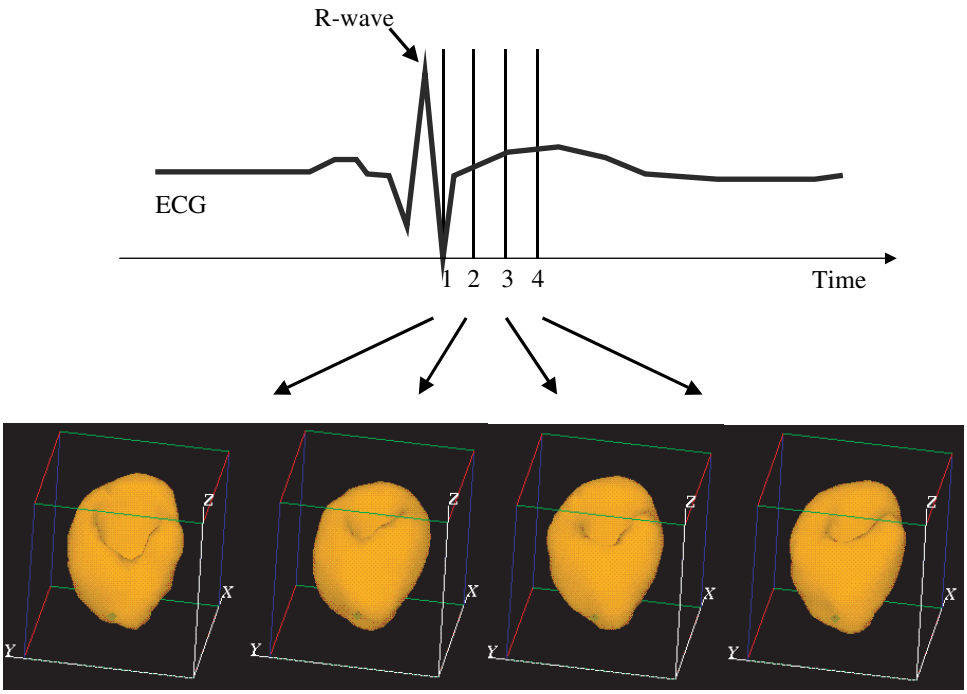

Fig. 4. The use of an ECG signal to provide gating for the SPECT study.

Faber *et al.*[22] developed a general model-based surface detector for finding the four-dimensional (three spatial dimensions plus time) endocardial and epicardial left ventricular boundaries for both perfusion and blood-pool SPECT studies. The model encoded LV shape, smoothness, and connectivity into the compatibility coefficients of a relaxation labeling algorithm. From the surface estimates, volumetric data were extracted to estimate the LV ejection fraction and regional wall motion was determined using a modified version of the centerline method. The final surfaces were visualized in a 3D rendering in which the displayed perfusion information could be presented with regional wall motion.

Cauvin *et al.*[23] modeled the LV as a truncated bullet, a combination of an ellipsoid and a cylinder, that is fitted to the morphological skeleton of the LV. Faber *et al.*[24] used a combination of cylindrical and spherical coordinate systems to build a discrete model of the LV in SPECT perfusion images. A radius function defined in a discrete space of longitudinal and circumferential coordinates describes the LV. For each orientation, the radius is determined by finding the position of maximal perfusion. After low-pass filtering to remove outlier radii, the radius function is mapped back to Cartesian space where the surface is represented using triangular meshes.

Germano *et al.*[25–29] introduced a fully automated algorithm that determined the LV surfaces from gated perfusion SPECT. In this approach, automatic border definition is done using thresholds of a Gaussian function precalibrated to a phantom.

Although the spatial resolution of SPECT is too low to actually measure the edges of the endocardial surface, the precalibration to a phantom and the high tolerance of the ejection fraction calculation provided highly reproducible volumetric estimates that correlated well with LV ejection fraction from other imaging modalities. This method has become popular and commercially available because it was the first to offer a fully automatic processing for gated perfusion. Figure 3 shows the patient's myocardial endocardial surface at end-diastole and end-systole depicted on an arbitrary orientation calculated by this method. This display may be viewed in a dynamic fashion to visually assess wall motion showing excursion and thickening of the wall as changes in color. The color is a function of both myocardial perfusion and myocardial thickness. A myocardial segment that increases in color brightness indicates thickening, and thus viable myocardium.

Garcia *et al.*[30] proposed an expert system called PERFEX as a tool for computer-assisted diagnosis of stress/rest myocardial perfusion SPECT studies. This approach has the potential for standardizing the image interpretation process. After reviewing hundreds of studies from patients with coronary artery disease, heuristic rules were derived that best correlated the location of perfusion defects in SPECT studies. Two sets of gold standards were used to define the rules: the interpretation by human experts and the results of coronary angiography studies. These rules operate on data that is input to the PERFEX from the SPECT quantification process, which identifies defects as portions of the myocardium where normalized perfusion falls below a predetermined number of standard deviation when compared to a normal file.

3. Motion Analysis in SPECT

A number of techniques have been used in order to describe and quantify the motion of the cardiac structures. They can be divided into three main categories: (1) detecting endocardial motion by observing image intensity changes; (2) determining the boundary wall of the left ventricle and tracking it; (3) attempting to track anatomical implanted or induced myocardial landmarks. There are few problems involved with each of these techniques.[31] Assumptions must be made about the motion model in the first two categories in order to obtain a unique point-wise correspondence between frames. To this end, optical flow methods[32–35] and phase contrast Magnetic Resonance[36–39] have been applied for (1) and curvature-based matching[40–44] has been applied to find point correspondence in (2). Landmark-based methods[45–52] provide information on material point correspondence. However, this information is mostly sparse and assumptions on the type of motion have to be made in order to regularize the problem of finding a dense displacement field. The use of implanted markers adds the extra complication of being invasive. Although implanted markers are usually regarded as the gold standard, there are some concerns about their influence on both image quality and modifications of motion patterns.

In gated SPECT, Bardinet *et al.*[53,54] extended a geometric model based on superquadrics[55] with the use of a free-form deformations (FFD), a technique introduced in computer graphics by Sederberg and Parry,[56] to estimate LV wall motion. This is accomplished by deforming the full model (superquadric and FFD) in the first frame, and modifying only the FFD in the subsequent frames. By tracking points with the same parametric coordinates along the cardiac cycle, a number of dynamic parameters like wall thickening and twisting motion can be computed.

Declerck *et al.*[57] have introduced a spatio-temporal model to segment the LV and to analyze motion from gated SPECT sequences. The model relies on a planispheric transformation that maps endocardial points in one time frame to the corresponding material points in any other frame. First, endocardial edge points are detected in all frames using a Canny-Deriche edge detector[58] in spherical coordinates. Selected points in subsequent frames are matched to the current frame using a modification of the Iterative Closest Point algorithm.[59] Based on corresponding point pairs, the parameters of a planispheric transformation are retrieved by least square approximation. This transformation allows to describe motion parameters such as radial motion, twisting motion and long-axis shortening.

Gutierrez *et al.*[60,61] proposed the combination of optical method with a multiresolution technique to estimate the myocardial Kinetic Energy (KE) obtained directly from gated SPECT images. Specifically, the method quantifies the 3D LV motion by a series of 3D velocity vector fields computed automatically for each voxel on the sequence of cardiac volumes. The velocity estimation for each voxel is used to compute the corresponding kinetic energy and the results are presented in a compact 2D form. The method was validated with a synthetic phantom and applied to groups of 30 volunteers and 29 patients. With the method, the cardiac condition of each subject can be studied taking the relation between the maximum and minimum values of kinetic energy observed during the cardiac cycle.

Meyering *et al.*[62] proposed a method to automatically estimate the velocity vector field based on the study of variation in frequency content in a time series of 2D gated SPECT images. The frequency analysis is performed by computing the Wigner–Ville and the Choi–Williams distributions[63,64] for each image pixel, yielding the corresponding 3D-frequency spectrum. From this 3D spectrum, the local velocity of each pixel is calculated by employing a multiple linear regression model. Experimental validation was carried out using synthetic phantoms that simulate translation and rotation between successive frames.

3.1. *Computing velocity vector field*

The tracking of structures in time series images has been studied by the computer vision community, especially in the areas of non-rigid motion, segmentation and surfacing mapping.[65] The goal is to obtain a displacement field that establishes a correspondence between certain points in the structure at time t and time $t + 1$.

Generally speaking, the common methods to obtain velocity vector fields lie within feature matching, gradient, frequency and spatio-temporal based techniques. The matching technique is very sensitive to ambiguity among the structures to be matched. This will be particularly true in the considerations of deformable structures where the geometrical relationships between object points may be distorted. Moreover, the correspondence method can be beset with combinatorial explosions of matching possibilities between two time-varying images.

3.1.1. *Gradient-based approach*

The gradient-based method or the differential method was introduced by Fennema and Thompson[66–68] and developed by Horn as the Optical Flow (OF) equation.[69] This method is based on the assumption that the intensity of image elements is conserved between the images. The equation formulated in the continuum is the well-known motion constraint equation:

$$E_x u + E_y v + E_t = 0 \tag{1}$$

where, E_x, E_y and E_t are the image derivatives in x, y and t directions, u and v are the components of the local velocity vector $\vec{v}$ along the directions x and y, respectively.

In cardiac SPECT images using a radionuclide such as ^{201}TI and ^{99}Tc^{m}-MIBI, the principal structure is the myocardium, therefore it is a reasonable assumption that the total intensity of voxels within the ventricle is conserved between successive frames, and that the motion of connected tissue within the myocardium should be smooth.[70,71]

Equation (1) is usually called the OF constraint (OFC) and to evaluate the flow velocity, Horn and Schunck[69] have introduced a "smoothness" constraint in addition to the fundamental constraint. Using the Horn and Schunck method and the extension to three dimensions, the velocity flow field can be obtained by minimizing the functional:

$$\min \int\int\int \left[\begin{array}{l} (E_x u + E_y v + E_z w + E_t)^2 \\ \quad + \alpha^2 \left(u_x^2 + u_y^2 + u_z^2 + v_x^2 + v_y^2 + v_z^2 + w_x^2 + w_y^2 + w_z^2 \right) \end{array} \right] dx\, dy\, dz \tag{2}$$

where the first term is the OFC, the second is a measure of the Optical Flow field smoothness, and α is a weighting factor that controls the influence of the smoothness constraint. The functionally Eq. (2) is minimized by using the calculus of variations,[72] which leads to a system of three coupled differential equations from the Euler–Lagrange equations:

$$\begin{aligned} \nabla^2 u &= \frac{E_x}{\alpha^2} \left(E_x u + E_y v + E_z w + E_t \right) \\ \nabla^2 v &= \frac{E_y}{\alpha^2} \left(E_x u + E_y v + E_z w + E_t \right) \\ \nabla^2 w &= \frac{E_z}{\alpha^2} \left(E_x u + E_y v + E_z w + E_t \right). \end{aligned} \tag{3}$$

These equations can be easily decoupled, and an interactive solution can be defined using discrete approximation of the Laplacian operator with a finite difference method. Therefore, the following set of equations is used to estimate the 3D OF components at each time instant

$$\begin{cases} u^{n+1} = \bar{u}^n - \dfrac{E_x\left(E_x\bar{u}^n + E_y\bar{v}^n + E_z\bar{w}^n + E_t\right)}{\alpha^2 + E_x^2 + E_y^2 + E_z^2} \\ v^{n+1} = \bar{v}^n - \dfrac{E_y\left(E_x\bar{u}^n + E_y\bar{v}^n + E_z\bar{w}^n + E_t\right)}{\alpha^2 + E_x^2 + E_y^2 + E_z^2} \\ w^{n+1} = \bar{w}^n - \dfrac{E_z\left(E_x\bar{u}^n + E_y\bar{v}^n + E_z\bar{w}^n + E_t\right)}{\alpha^2 + E_x^2 + E_y^2 + E_z^2} \end{cases} \tag{4}$$

where n is the iteration index; E_x, E_y, E_z are the partial derivatives of the image intensity in the directions x, y and z, respectively; E_t is the partial derivative in time; $\bar{u}, \bar{v}$ and $\bar{w}$ are the mean velocities in each direction, for the voxels in a neighborhood of a given voxel; and α is a weighting factor. Velocity components in the x, y and z directions for each voxel are computed as the solution of a linear algebraic system of equations whose coefficients are determined by the spatial and temporal derivatives given by Eq. (4). The linear system described in Eq. (4) can be solved by methods like Conjugate Gradient methods[73] or Algebraic Reconstruction techniques.[74]

As can be noted, the asymptotical complexity of the method on a sequential machine is a function of the number of iterations, n, that are needed to obtain the final solution and of the image dimensions, which is $O(n^3 D_x D_y D_z)$. It should be noted that, in the iterative solution presented, the initial value for OF estimation is set to zero (i.e. $\bar{u}^{n=0} = \bar{v}^{n=0} = \bar{w}^{n=0} = 0$) and the guessed value at time t is obtained from the previous time-step (i.e. $\bar{u}^n = u^{n-1}; \bar{v}^n = v^{n-1}; \bar{w}^n = w^{n-1}$, where $n-1$ is the number of iterations executed at the previous time-step). This reduces the number of iterations needed to obtain the OF estimation, as well as the computational effort.

The estimation of velocity components using OF approach depends on derivative approximations from discrete data. Numerical derivative is ill-posed in the sense of Hadamard theory.[75] A problem is well-posed in the sense of Hadamard if its solution: (1) exists, (2) is unique, and (3) depends continuously on the initial data. Digital images are always "dirty" in the differential geometric sense. In theory, $E(\vec{x})$ may be everywhere discontinuous. Some algorithms for differentiation try to avoid this problem by regularizing the data, for instance, by blurring the original data. Nevertheless data should not be modified, and a regularization of the operand must be found.

Ill-posedesness of numerical differentiation can be modified into a well-posed problem by using filters in the form of scaled convolution operators.[76] The result was obtained from the scale space theory, whose basic idea consists in generating from a given image a set of derived images with decreased resolution. It has been established that for front-end vision systems (in which no knowledge about the

observed scene is present) the unique linear scale space constructor is the Gaussian function:

$$G(\vec{x}, \sigma) = \frac{1}{\sqrt{2\pi\sigma^2}^D} e^{-\frac{\|\vec{x}\|^2}{2\sigma^2}} \tag{5}$$

where D denotes the dimension of the input domain. A blurred replica of the original image is obtained by convolution with $G(\vec{x}; \sigma)$ for a specific σ. The stack of images as a function of increasing scale parameter σ is coined a linear scale-space.

Equivalently, this set can be generated by the solution to the heat diffusion equation:

$$\frac{\partial L(\vec{x}, s)}{\partial s} \equiv \sum_{i=1}^{D} \frac{\partial^2 L(\vec{x}, s)}{\partial x_i^2} \tag{6}$$

where L is the pixel intensity located at $\vec{x}$, s is the continuous scale parameter ($\sigma^2 = 2s$) and the original image $L(\vec{x}; 0) \equiv E(\vec{x})$ is the initial condition for the linear second order differential Eq. (6).

One of the most useful results of scale space theory is that the derivatives of the Gaussian function are also solutions to the diffusion equations, and together with the 0th order Gaussian they form a complete family of differential operators. The 0th order kernel is a scalar, all higher order kernels are tensorial quantities as, for example, the first order kernel, the gradient, is a vector.

A scaled image $E(\vec{x}; \sigma)$ is a smooth function for all $\sigma > 0$ making scaled differentiation well-posed by nature. Taking the following identity:

$$\partial \{E(\vec{x}) \otimes G(\vec{x}, \sigma)\} = \partial E(\vec{x}) \otimes G(\vec{x}, \sigma) = E(\vec{x}) \otimes \partial G(\vec{x}, \sigma). \tag{7}$$

It follows that to obtain well-posed Cartesian partial derivatives of order n of a re-scaled image $L(\vec{x}; \sigma)$ it is only necessary to convolve the original image $E(\vec{x})$ with the corresponding partial derivatives of the 0th order Gaussian $G(\vec{x}; \sigma)$. This result enables the extraction of any order of derivative for discrete data. There is, however, a close relation between the order of differentiation, the scale of the operator and the accuracy of the result. This leads to the important concern about what should be the best scale to a specific problem. The issue can be addressed theoretically, and criteria for best scale selection was suggested by Lindeberg.[77] However, in practice we are interested in some specific objects and, in this case, some scales are better suited than others and can be determined experimentally.

3.1.2. *Frequency-based approach*

This method is most appropriate for determining the motion of a single object moving across a uniform background. The method takes advantage of the shift property of the Fourier transform.

Assume one is given two images, denoted $f(x, y)$ and $g(x, y)$, that are related by a pure translation $(\Delta x, \Delta y)$. Since the phase functions of their Fourier transforms $F(u, v)$ and $G(u, v)$ respectively, are given by:

$$\phi_F(u, v) = \arg\{F(u, v)\}$$

and

$$\phi_G(u, v) = \arg\{G(u, v)\} = \arg\{F(u, v)\} - (u\Delta x + v\Delta y) \tag{8}$$

and

$$\phi_G - \phi_F = [\arg\{F(u, v)\} - (u\Delta x + v\Delta y)] - \arg\{F(u, v)\}.$$

If ϕ_G and ϕ_F are known at two distinct frequencies (u_0, v_0) and (u_1, v_1), then Eq. (8) defines a system of two equations in two unknowns which can be solved for $(\Delta x, \Delta y)$. This method is clearly more restrictive than the gradient approach since only a single non-localized velocity vector is obtained for each image frame.

3.1.3. *Spatio-temporal frequency-based approach*

The spatio-temporal frequency (STF) based approach to optical flow derivation encompasses all methods which are based upon some underlying spatio-temporal frequency image representation. The major motivation for considering the use of the STF image representation as a basis for computing optical flow comes from the literature on mammalian vision. In particular, recent investigations have demonstrated that many neurons in various visual cortical areas of the brain behave as spatio-temporal frequency bandpass filters.[78–80]

In the field of non-stationary signal analysis, the Wigner–Ville Distribution (WVD) has been used for the representation of speech and image. Jacobson and Wechsler[81,82] first suggested the use of the WVD for the representation of shape and texture information. In particular, they formulated a theory for invariant visual pattern recognition in which the WVD plays a central role. Meyering *et al.*[62] extended this concept to analyze motion in gated SPECT images.

Given a time-varying image $f(x, y, t)$, its WVD is a 6-dimensional function defined as:

$$W_f(x, y, t, w_x, w_y, w_t) = \int_{-\infty}^{+\infty} \int\int R_f(x, y, t, \alpha, \beta, \tau) \mathrm{e}^{-j(\alpha w_x + \beta w_y + \tau w_t)}\, d\alpha\, d\beta\, d\tau \tag{9}$$

where

$$R_f(x, y, t, \alpha, \beta, \tau) = f(x + \alpha, y + \beta, t + \tau) \cdot f^*(x - \alpha, y - \beta, t - \tau) \tag{10}$$

is the pseudo-correlation function, where * denotes complex conjugation.

For the special case where a time-varying image is uniformly translating at some constant velocity (u, v), the image sequence can be expressed as a convolution between a static image and a translating delta function.

$$f(x, y, t) = f(x, y) * \delta(x - ut, y - vt). \tag{11}$$

Using the convolution and windowing properties of the WVD, we obtain:

$$W_f(x, y, t, w_x, w_y, w_t) = \delta(uw_x + vw_y + w_t) W_f(x - ut, y - vt, w_x, w_y). \tag{12}$$

The WVD of a linearly translating image with constant velocity is everywhere zero except in the plane defined by $\{(x, y, t, w_x, w_y, w_t) : uw_x + vw_y + w_t) = 0\}$, for fixed (u, v). Equivalently, for an arbitrary pixel at x, y and t, each local spatial and temporal frequency spectrum of the WVD is zero everywhere except on the plane defined by $\{(w_x, w_y, w_t) : uw_x + vw_y + w_t) = 0\}$.

From Eq. (9), the WVD assigns a three-dimensional spatio-temporal frequency spectrum to each pixel over which the image is defined. However, the WVD assigns a 3D spectrum with interference due to cross correlation when more than one frequency is present.[63]

In order to smooth the spectrum of WVD a filter must be introduced. Meyering *et al.*[61] adopted a Hanning filter to smooth the spectrum.

$$h = 0,5 * \left[1 - \cos\left(\frac{2\pi n}{N}\right)\right] \quad \text{for } 0 \leq n \leq N - 1. \tag{13}$$

They also used the Choi–Williams distribution (CWD) to reduce the effects of the cross-terms. The CWD was introduced with the aim of controlling the cross-terms encountered in Wigner–Ville distribution. The exponential kernel introduced by Choi and Williams is defined as:

$$cw = \frac{1}{\sqrt{4\pi\tau^2\sigma}} \exp\left(\frac{-(\mu - t)^2}{4\tau^2\sigma}\right). \tag{14}$$

From the Eq. (14), if a small σ is chosen, the Choi–Williams distribution approaches the Wigner–Ville distribution, since the kernel approaches to one. On the other hand, for large σ more cross-terms are suppressed and auto-terms are affected.

The spatial orientation of the smoothed 3D frequency spectrum is completely governed by the pixel velocity, whose components can be obtained through a simple multiple linear regression model:[83,84]

$$w_t = b + uw_x + vw_y + e. \tag{15}$$

Equation (15) is a linear regression extension where w_t is a linear function of two independent variables w_x and w_y. The values of the coefficients b, u and v are achieved by solving the following linear system:

$$\begin{bmatrix} n & \sum_{k=1}^{n} w_{x_k} & \sum_{k=1}^{n} w_{y_k} \\ \sum_{k=1}^{n} w_{x_k} & \sum_{k=1}^{n} w_{x_k}^2 & \sum_{k=1}^{n} w_{x_k} w_{y_k} \\ \sum_{k=1}^{n} w_{y_k} & \sum_{k=1}^{n} w_{x_k} w_{y_k} & \sum_{k=1}^{n} w_{y_k}^2 \end{bmatrix} \cdot \begin{bmatrix} b \\ u \\ v \end{bmatrix} = \begin{bmatrix} \sum_{k=1}^{n} w_{t_k} \\ \sum_{k=1}^{n} w_{x_k} w_{t_k} \\ \sum_{k=1}^{n} w_{y_k} w_{t_k} \end{bmatrix} \tag{16}$$

where n is the number of pixels, w_{x_k}, w_{y_k} and w_{t_k} are the frequency components in each direction and u and v are the velocity components on x and y directions, respectively.

3.2. *Kinetic energy estimation*

The techniques described on the previous section allow the determination of the velocity vector for each voxel at each time frame of the cardiac cycle. Figure 5 shows the LV 3D velocity vector field estimated by the gradient method. In this figure, the complex deformation observed in the LV, during the systole, can be explained by observing the principal fiber paths in a dissected LV as reported by Torrent-Gausp.[85] Figure 6 shows a SPECT slice at systole and diastole, superimposed by their velocity vector fields calculated employing the spatio-temporal frequency based approach using WVD and CWD.

Observing Figs. 5 and 6, one can easily notice that the analysis of the velocity field from all voxels is extremely complex, due to the high amount of information presented simultaneously. To make this bunch of information useful for diagnostic purposes, it is necessary to find a compact form of presenting it. From the velocity vector information, it is possible to estimate a scalar quantity, the Kinetic Energy (KE), for each voxel in the 3D image:

$$KE = \frac{1}{2} m \left(v_x^2 + v_y^2 + v_z^2 \right) \tag{17}$$

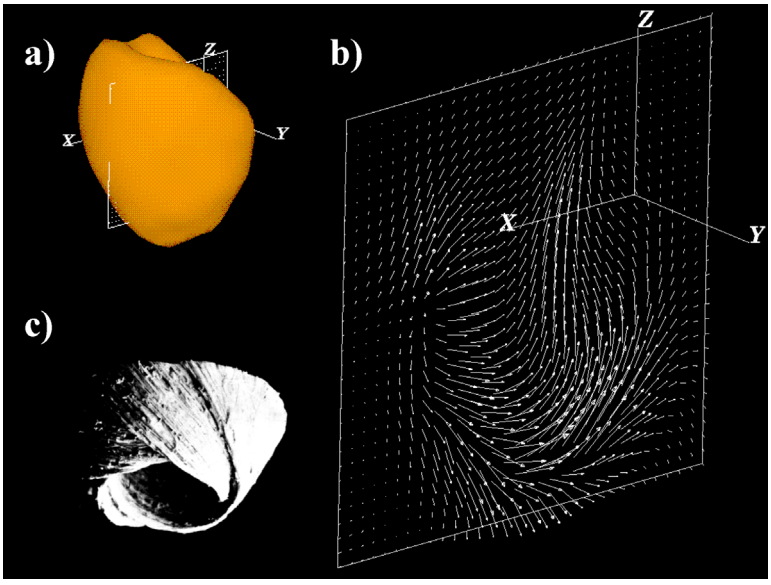

Fig. 5. (a) A view of the 3D left ventricle image of a normal heart; (b) the corresponding velocity vector field in a coronal slice at systole estimated by the gradient-based approach; (c) the principal fiber pathways of a cow's LV (Torrent-Gausp[85]).

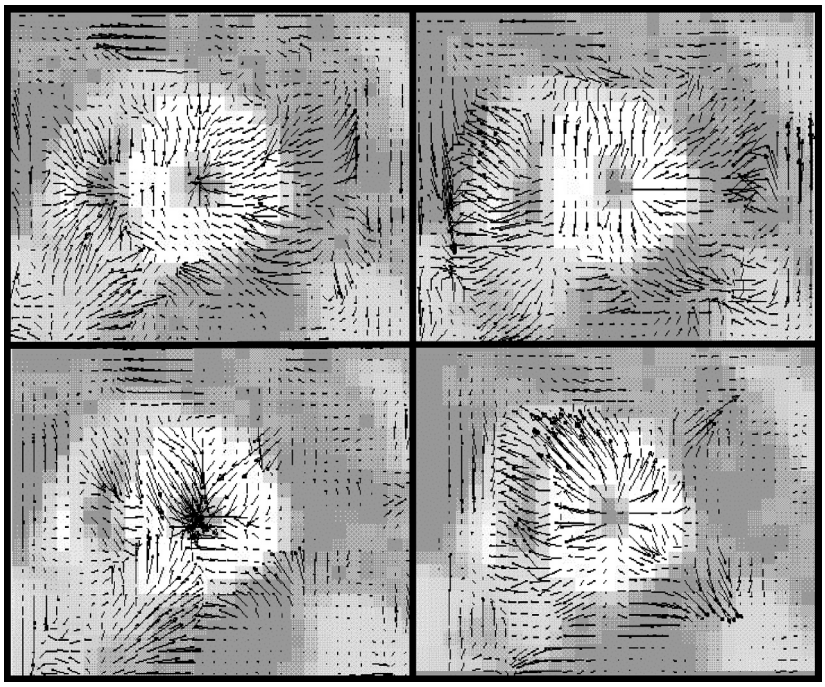

Fig. 6. Oblique SPECT slice at systole (left) and diastole (right), superimposed by their velocity vector fields calculated employing the frequency-based approach using WVD (upper row) and CWD (under row).

where m is the voxel mass, v_x, v_y and v_z the components of the velocity vector in the x, y and z directions. The voxel mass was approximated by the voxel intensity obtained directly from the image since in SPECT images the image count is proportional to the perfused myocardium mass. Moreover, a voxel volume may contain several muscle cells with different contraction (density) states. The integration of this scalar quantity over the cardiac muscle gives the total muscle KE. This quantity can be obtained for all cardiac volumes from the gated acquisition and displayed as a time curve. Discussions with physicians lead to the description of an index that allows the quantification of the cardiac condition, based on the relation between maximum and minimum values of these curves. This index was coined "KE index" and is estimated by Eq. (18):

$$KEf = \frac{KE_{\max} - KE_{\min}}{KE_{\max}} \tag{18}$$

where $KE_{\max}$ and $KE_{\min}$ are the maximum and minimum values of the kinetic energy function. To find the normality values for this new parameter, Gutierrez *et al.*[60] applied the methodology to a set of normal subjects.

3.3. *Experimental evaluation*

3.3.1. *Numerical phantom simulations*

The velocity vector along three frames of 3D images was computed by the gradient and frequency-based methods at each voxel of a mathematical phantom. The phantom consists of a cylinder with the dimensions $74 \times 74 \times 5$ in the directions x, y and z respectively. Each cylinder's cross-section comprises voxels with intensity function described below:

$$E(x, y, z) = \alpha + \beta[\sin(\omega_1 x) + \sin(\omega_2 y)] \tag{19}$$

where $E(x, y, z)$ is the intensity of the voxel in the spatial position x, y, z of the voxel space, α and β are constants, and ω_1 and ω_2 are the spatial frequencies. Figure 7 shows a cross-section of the cylinder with respect to the z direction.

The cylinder was submitted to translation and rotation with known velocities. The velocities were estimated by the proposed method and the results compared with the real velocities. The Root Mean Square Error (RMSE) was used as a measure of error between the estimated and the real velocities. In the computation of Eq. (4), setting the value 10 to the α parameter produced the results with lower RMSE. The value of α was maintained for the experiments with real images. Tables 1 and 2 show the results obtained after applying translation to the cylinder using different velocities between each image frame. In these Tables, u and v are the actual velocities (pixels/frame) in x and y directions respectively, $\hat{u}$ and $\hat{v}$ are the mean estimated velocities (pixels/frame) and ε_{rms} is the RMSE expressed as percentages.

$$RMSE = 100 \frac{\sqrt{\sum_i^M \sum_j^N (u_{i,j} - \hat{u}_{i,j})^2 + (v_{i,j} - \hat{v}_{i,j})^2}}{\sqrt{\sum_i^M \sum_j^N (u_{i,j})^2 + (v_{i,j})^2}}. \tag{20}$$

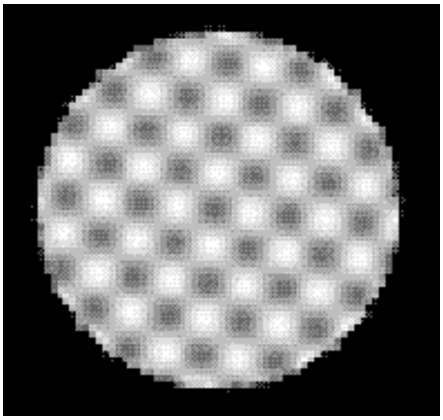

Fig. 7. Cross-section of the cylinder (numerical phantom). The light voxels simulate regions with high intensity values in SPECT images.

Table 1. Results obtained after translation movement in a section of the cylinder using the gradient-based method.

u	v	$\hat{u}$	$\hat{v}$	$\varepsilon_{rms}(\%)$
1	0	0.9308	0.0002	7.13
2	0	1.9741	0.0012	11.10
1	1	0.9747	0.9585	6.86
1	2	1.1635	1.9095	14.13

Table 2. Results obtained after translation movement in a section of the cylinder using the frequency-based method and two different distributions (Wigner–Ville and Choi–Williams).

		Wigner–Ville			Choi–Williams		
u	v	$\hat{u}$	$\hat{v}$	$\varepsilon_{rms}(\%)$	$\hat{u}$	$\hat{v}$	$\varepsilon_{rms}(\%)$
1	0	0.9012	0.0000	11.87	0.9482	−0.0007	7.12
2	0	1.8022	−0.0004	12.29	1.8874	0.0002	8.21
1	1	0.9018	0.8562	15.32	0.9448	0.9266	8.96
1	2	0.9050	1.7209	16.39	0.9467	1.87149	8.73

Table 3. Results obtained after rotation movement in a section of the cylinder by the gradient and frequency based methods and two different distributions (Wigner–Ville and Choi–Williams).

Gradient-Based Method			Frequency-Based Method			
			Wigner–Ville		Choi–Williams	
ω	$\hat{\omega}$	$\varepsilon_{rms}(\%)$	$\hat{\omega}$	$\varepsilon_{rms}(\%)$	$\hat{\omega}$	$\varepsilon_{rms}(\%)$
2	1.9441	8.09	1.7900	23.80	1.8600	25.97
5	5.1011	9.56	4.4500	21.45	4.8050	14.71
7	6.9944	20.27	6.1950	20.94	6.8200	12.43

Table 3 shows the results obtained after applying rotation to the same phantom using the gradient and frequency-based methods. In Table 3, ω and $\hat{\omega}$ are the real and estimated angular velocities (degree/frame), respectively, and ε_{rms} is the RMSE expressed as percentages. These results show that the method has a satisfactory performance (errors lower than 10%) for translation and rotation when the velocities applied to the phantom are less than 2 pixels per frame, corresponding to speeds around 200 mm/s which are higher than typical heart wall speeds.

The gated three-dimensional mathematical cardiac torso phantom (3D gMCAT) was used to simulate cardiac deformation.[86,87] The 3D gMCAT phantom uses simple geometric representations (ellipsoids and cylinders) to model the heart, other organs, and the body outline. Contraction, rotation and cardiac motion resulting from respiration are included in the model. Figure 8 shows the transversal slices of the gMCAT phantom at systole and diastole superimposed by the velocity

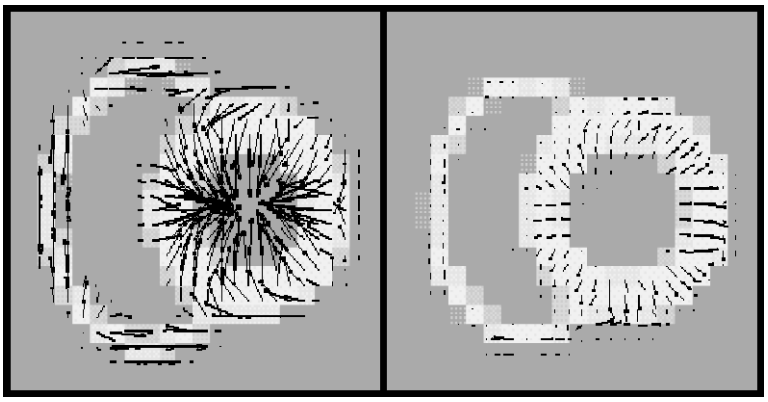

Fig. 8. Transversal projections of the gMCAT phantom at systole (left) and diastole (right) superimposed by the velocity vector field calculated employing the Wigner–Ville distribution.

vector field calculated using the frequency-based method with the Choi–Williams distribution.

3.3.2. *Real images*

The method was applied to 3D gated perfusion studies $^{99}Tc^{m}$-MIBI obtained from 30 healthy and 28 patients diagnosed as having severe cardiomyopathy.[a] All acquisitions were performed by a dual-head rotating gamma camera (ADAC VertexPlus with a LEAP Collimator). The acquisition process is synchronized with the electrocardiogram and the cardiac cycle can be divided into 8 or 16 frames per cycle. A total of 64 projections were obtained over a semi-circular 180-deg orbit. All projection images were stored using a 64×64, 16 bits matrix. All transverse tomograms were reconstructed with a thickness of 1 pixel/slice (6, 47 mm). The volume of transverse tomograms was re-oriented, and sets of slices perpendicular to the long axis (oblique) and of slices parallel to the long axis (coronal and sagittal) were created.

The velocity vector field is estimated by means of Eq. (4), where spatial and temporal derivatives were calculated using the multiresolution approach provided by the scale-space theory. For this specific study we found, empirically, $\sigma = 1.42$ as the best value to the Gaussian function. Figure 9 shows the results of applying the procedure to estimate the numerical differentiation in space and time domains.

After the estimation of the velocity vector for each voxel in the image sequence and using Eq. (16), it is possible to estimate the KE for each voxel. The time to compute the KE curve for a series of 304 images with a 64×64 matrix (16 cardiac volumes with 19 images in each one) is 750 s (Intel Pentium III-450 MHz running Linux Kernel 2.2.14). Figure 10 shows the KE obtained for one orthogonal slice to

[a]The two population involved in this work were part of two research protocols at Heart Institute involving gated-SPECT and MRI.

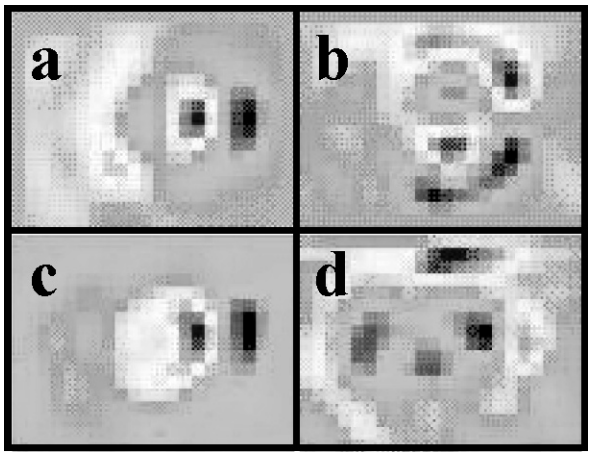

Fig. 9. Spatial and temporal scale-space derivatives ($\sigma = 1.42$) obtained from a 2D cross-section of a 3D gated-SPECT image of human heart. Spatial resolution is 30×30, temporal resolution 16 frames/cardiac cycle. a), b), c) and d) are the derivatives images in x, y, z and time directions, respectively.

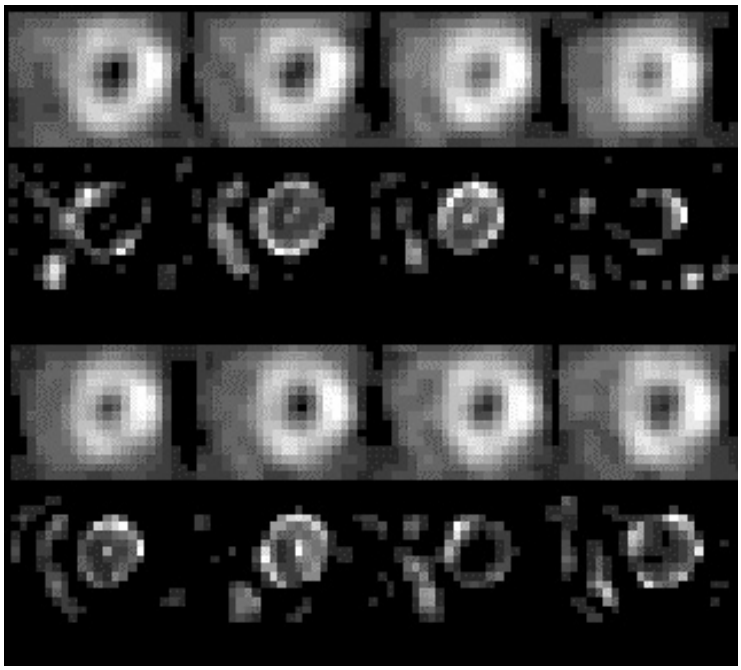

Fig. 10. Sequence of a 2D cross-section of a 3D gated SPECT image of human heart during the cardiac cycle (1st and 3rd rows — bright voxels represent high intensity values) and the correspondent 2D cross-section of the 3D Kinetic Energy values (2nd and 4th rows — bright voxels represent high values of KE).

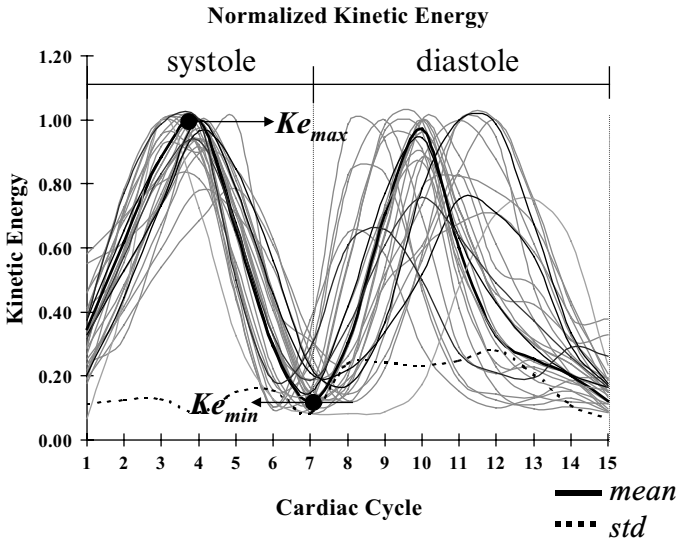

Fig. 11. Normalized kinetic energy obtained from normal subjects ($n = 30$). The continuous black curve indicates the mean curve obtained from the population. The dashed curve indicates the standard deviation from the mean.

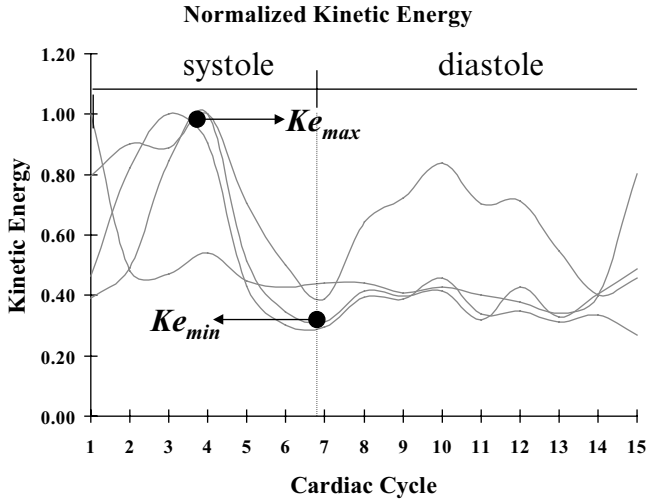

Fig. 12. Normalized kinetic energy obtained from patients with heart disease ($n = 4$).

the long axis. In this figure, the gray scale indicates low and high kinetic energy for black and white pixels, respectively.

The integration of this quantity over the cardiac muscle gives the total muscle KE. Figures 11 and 12 show the KE curves in a cardiac cycle obtained from the

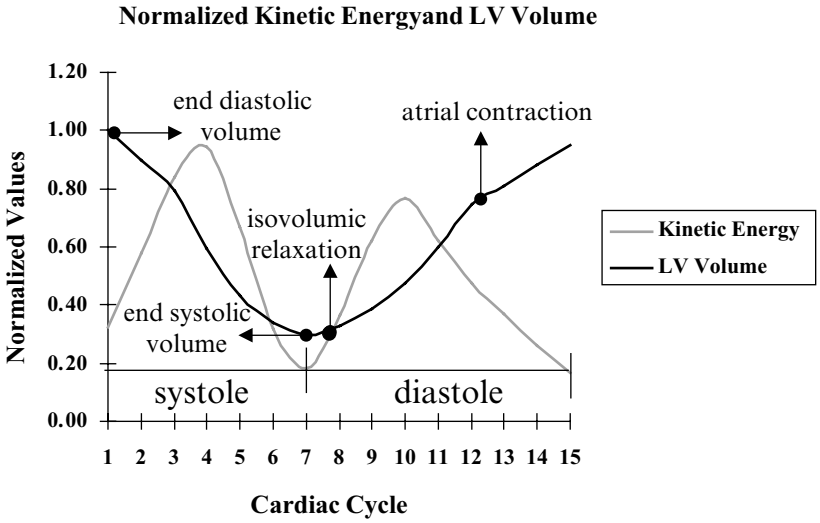

Fig. 13. Mean kinetic energy curve and the left ventricle volume through the cardiac cycle obtained from the normal volunteers.

normal subjects and from patients, respectively. For this specific study, Gutierrez *et al.*[61] measured a $KEf = 0.8582 \pm 0.0365$ for the normal subjects ($n = 30$) and a $KEf = 0.4455 \pm 0.1444$ for the patients ($n = 28$). The null hypothesis was rejected because there is a significant difference between the two populations ($t = 19, p \ll 0.01$).

Figure 13 shows the superimposition of the mean KE curve and the LV volume through the cardiac cycle obtained from the normal volunteers ($n = 30$). The LV volume was measured by a specialist based on a manual segmentation of the cavity. The end diastolic volume, end systolic volume, isovolumic relaxation, atrial contraction, and their relationship with the KE curve are depicted in this figure and represent important events that occur during the contraction and relaxation of the LV.

4. Conclusions and Outlook

In this chapter, we have reviewed the techniques to analyze and quantify LV parameters by means of SPECT proposed in the last two decades. The strength and availability of these quantitative tools have in many ways provided a competitive advantage to Nuclear Cardiology compared with other higher-resolution noninvasive imaging modalities for the detection of coronary artery disease. During the 80s, the planar imaging of patients with low probability of coronary artery disease allowed the construction of normality databases and the definition of mean and variance limits for normal patients. With the definition of mean and variance limits for normal perfusion, objective abnormality thresholds were defined. These tools were expanded for gated SPECT, providing LV perfusion and function parameters

in 2D, 3D and 4D. Although a number of techniques have been developed to aid the classification of the SPECT images, the search for robust methods to analyze automatically the complete series of images is yet an open study area. Moreover, the comparison of the different techniques is a difficult task due to the diversity of approaches, image acquisition protocol and the lack of a "gold standard" to compare the results.

The validation of the presented techniques can be classified in three areas: (1) with no validation or only qualitative analysis; (2) with quantitative validation on patients; (3) with quantitative validation on phantoms, normal subjects and patients. Table 4 shows the comparison of some techniques reported in the last twenty years.

The group (1) includes papers presenting technical or methodological aspects of advanced modeling techniques.[23,54,57] The group (2) the evaluation was performed on human volunteers and patients,[16,19,22,24,30] including qualitative results in terms of cardiac functional parameters. Finally the last group (3) includes studies performed on numerical or physical phantoms, normal subjects and patients. They have the advantage to assess the accuracy and reproducibility of the techniques.[25,61,62] The size of test population in most cases was small. In only five of them,[16,19,25,30,61] the studies were conducted on more than fifty volunteers or patients.

The methodology and validation of two distinct approaches to quantify the myocardial motion in SPECT images were also described in deep. The first method adopted the gradient based approach to compute OF in 3D. The derivatives estimation, a fundamental step in any OF implementation, was improved by a multi-resolution technique. In the second method a spatio-temporal frequency based approach was used to OF derivation. The majors motivations for considering this

Table 4. Overview of automatic methods to analyze and quantify cardiac LV parameters by means of SPECT

			Validation	
Reference	Year	LV Parameters	Phantom	Patients or Volunteers
Tamaki	1984	2D Segmental Analysis		104
Garcia	1985	3D Segmental Analysis		53
Faber	1991	Volume		38
Cauvin	1993	Volume		—
Germano	1995	Volume, Ejection Fraction	1	65
Bardinet	1996	Volume, Wall Thickness, Motion Field		1
Declerck	1998	Motion Field		4
Faber	1999	Volume, Mass, Ejection Fraction		10
Garcia	2001	3D Segmental Analysis		655
Meyering	2002	Motion Field	1	1
Gutierrez	2003	Motion Field, Kinetic Energy	1	58

kind of motion representation were: (1) in non-rigid motion, the image frequency components change with time; (2) some investigations on mammalian vision have demonstrated that many neurons in various visual cortical areas of the brain behave as spatio-temporal frequency band-pass filters.

From synthetic phantom experiments it was found that the errors associated with velocity measurement were less than 10% for velocities lower than 2 pixels/frame, which makes the proposed methods suitable for Nuclear Cardiology studies. A qualitative analysis of the 3D gMCAT phantom movement and its corresponding velocity vector field has shown that the spatio-temporal frequency approach could detect complex motion such as contraction and rotation.

However, in both methods, it was necessary to find a compact form of presenting the myocardial velocity information in order to make it useful for diagnostic purposes. From the velocity vector information, it was possible to estimate a scalar quantity, the myocardial KE, and a new physiologic parameter was introduced. The clinical evaluation of this parameter showed that the curve patterns for 28 patients with myocardial perfusion abnormalities were substantially different from 30 normal subjects. Moreover, discussion with physicians led to the description of an index that allowed the quantification of the cardiac condition based on the relation between maximum and minimum values of those curves.

The main features of the presented methods were: (1) the motion estimation was based on automatic analysis of all images presented in a series of gated SPECT study; (2) the myocardial 3D motion was presented as a kinetic energy curve rather than a set of sequential images given global information of the cardiac condition;

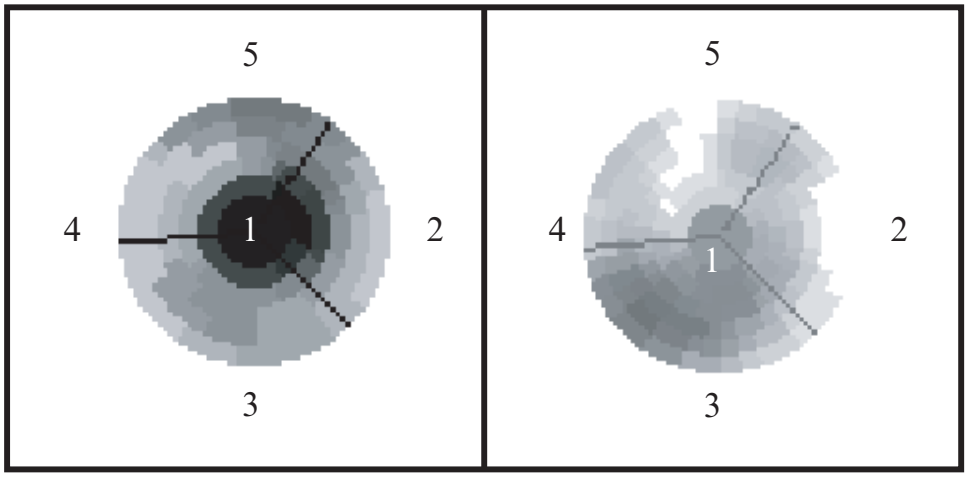

Fig. 14. Left: the kinetic energy polar map obtained from a normal subject, at systole. The regions are: (1) Apex; (2) Lateral Wall; (3) Inferior Wall; (4) Septum; (5) Anterior Wall. Right: the polar map from a patient with heart disease.

(3) although the estimation of myocardial KE shows an important global information about the cardiac condition, the study of this quantity in specific regions of the myocardium may improve the classification process. This goal can be achieved by the construction of kinetic energy polar map (bull's-eye) using the same methodology proposed by Garcia *et al.*[19–21] (Fig. 14).

Acknowledgments

This work was supported in part by the National Council for Scientific and Technological Development (CNPq) Grants 471143/2001-4 and 303664/2002-9 and Zerbini Foundation. The authors would like to acknowledge Dr. Benjamin M.W. Tsui and his group at the Department of Biomedical Engineering, University of North Carolina (Chapel Hill), for providing the 3D gMCAT phantom used in our simulations, and Drs. Agda Cecilia Leite Munhoz and Rubens Abe for assisting in setting up the protocol to SPECT acquisition in volunteers and patients.

References

1. R. J. Ott, M. A. Flower, J. W. Babich and P. K. Marsden, in *The Physics of Medical Imaging*, ed. S. Webb (Institute of Physics Publishing, Bristol and Philadelphia), Chap. 6, pp. 214–226.
2. E. V. Garcia, T. L. Faber and J. R. Galt *et al.*, *IEEE Eng Med Bio* **5** (2000) 21–33.
3. I. K. Baily, L. S. C. Griffith, J. Rouleau, H. W. Staruss and B. Pitt, *Circulation* **55** (1977) 79–87.
4. J. L. Ritchie, G. B. Trobaugh and G. W. Hamilton *et al.*, *Circulation* **56** (1977) 66–71.
5. G. W. Hamilton, G. B. Trobaugh, J. L. Ritchie, D. L. Williams, W. D. Weaver and K. L. Gould, *Am J Cardiol* **39** (1977) 347–354.
6. E. H. Botvinick, M. R. Taradash, D. M. Shames and W. W. Parmley, *Am J Cardiol* **41** (1978) 43–59.
7. G. B. Trobaugh, F. J. Wackers, E. B. Sokole, T. A. DeRouen, J. L. Ritchie and G. W. Hamilton, *J Nucl Med* **19** (1978) 359–363.
8. R. C. Meade, V. S. Bamrah, J. D. Horgan, P. P. Ruetz, C. Kronenwetter and E. L. Yeh, *J Nucl Med* **19** (1978) 1175–1178.
9. R. D. Burow, M. Pond, A. W. Schafer and L. Becker, *J Nucl Med* **20** (1979) 771–781.
10. E. P. Ficaro and J. R. Corbett, *J Nucl Cardiol* **11,** 1 (2004) 62–70.
11. D. D. Watson, N. P. Campbell, E. K. Read, R. S. Gibson, C. D. Teates and G. A. Beller, *J Nucl Med* **22** (1981) 577–584.
12. B. C. Berger, D. D. Watson and G. J. Taylor *et al.*, *J Nucl Med* **22** (1981) 585–593.
13. E. V. Garcia, J. Maddahi, D. S. Berman and A. Waxman, *J Nucl Med* **22** (1981) 309–317.
14. J. Maddahi, E. V. Garcia, D. S. Berman, A. Waxman, H. J. C. Swan and J. Forrester, *Circulation* **64** (1981) 924–935.
15. K. F. Van Train, D. S. Berman, E. V. Garcia, H. J. Berger, M. J. Sands, J. D. Friedman, M. R. Freeman, M. Pryzlak, W. L. Ashburn, S. L. Norris, A. M. Green and J. Maddahi, *J Nucl Med* **27** (1986) 17–25.
16. N. Tamaki, Y. Yonekura, T. Mukai, S. Kodama, K. Kadota, H. Kambara, C. Kawai and K. Torizuka, *J Am Coll Cardiol* **4** (1984) 1213–1221.

17. R. C. Meade, V. S. Bamrah, J. D. Horgan, P. P. Ruetz, C. Kronenwetter and E. L. Yeh, *J Nucl Med* **19** (1978) 1175–1178.
18. R. D. Burow, M. Pond, A. W. Schafer and L. Becker, *J Nucl Med* **20** (1979) 771–781.
19. E. V. Garcia, K. F. Van Train, J. Maddahi, F. Prigent, J. Fredman, J. Areeda, A. Waxman and D. S. Berman, *J Nucl Med* **26** (1985) 17–26.
20. E. Depasquale, A. Nody, G. DePuey, E. V. Garcia and G. Pilcher, *Circulation* **77** (1988) 316–327.
21. E. V. Garcia, C. D. Cooke, K. F. Van Train, R. D. Folks and J. W. Peifer, *Am J Cardiol* **66** (1990) 23–31.
22. T. L. Faber, E. M. Stokely, R. M. Peshock and J. R. Corbett, *IEEE Trans Med Imag* **10** (1991) 321–329.
23. J. C. Cauvin, J. Y. Boire, M. Zanca, J. M. Bonny, J. Maublant and A. Veyre, *Comp Med Im Graph* **17,** 4 (1993) 345–350.
24. T. L. Faber, C. D. Cooke, R. D. Folks, J. P. Vansant, K. J. Nichols, E. G. DePuey, R. I. Pettigrew and E. V. Garcia, *J Nucl Med* **30** (1999) 638–649.
25. G. Germano, H. Kiat, P. B. Kavanagh, M. Moriel and M. Mazzanti *et al.*, *J Nucl Med* **36,** 11 (1995) 2138–2147.
26. G. Germano, P. B. Kavanagh, J. Chen, P. Waechter, H.-T. Su, H. Kiat and D. S. Berman, *J Nucl Med* **36,** 6 (1995) 2127–2132.
27. G. Germano, P. B. Kavanagh and J. D. S. Berman, *Int J Card Imag* **13,** 4 (1997) 337–346.
28. G. Germano, J. Erel, H. Kiat, P. B. Kavanagh and D. S. Barman, *J Nucl Med* **38,** 5 (1997) 749–754.
29. G. Germano and D. S. Berman, *Clinical Gated Cardiac SPECT* (Futura Publishing Co., Armonk, NY, 1999).
30. E. V. Garcia, C. D. Cooke, R. D. Folks, C. A. Santana, E. G. Krawczynska, L. De Braal and N. F. Ezquerra, *J Nucl Med* **42,** 8 (2001) 1185–1191.
31. A. F. Frangi, W. J. Niessen and M. A. Viergever, *IEEE Trans Med Imag* **20,** 1 (2001) 2–5.
32. J. L. Prince and E. R. McVeigh, *IEEE Trans Med Imag* **11,** 2 (1992) 238–249.
33. T. S. Denney and J. L. Prince, *IEEE Trans Imag Proc* **3,** 2 (1994) 178–191.
34. T. S. Denney and J. L. Prince, *IEEE Trans Imag Proc* **4,** 9 (1995) 1324–1327.
35. L. Dougherty, J. C. Asmuth, A. S. Blom, L. Axel and R. Kumar, *IEEE Trans Med Imag* **18,** 4 (1999) 359–363.
36. S. M. Song and R. M. Leahy, *IEEE Trans Med Imag* **10,** 3 (1991) 295–306.
37. S. M. Song, R. M. Leahy, D. P. Boyd, B. H. Brundage and S. Napel, *IEEE Trans Med Imag* **14,** 2 (1994) 386–397.
38. J. M. Gorce, D. Friboulet and I. E. Magnin, *Med Imag Anal* **1,** 3 (1996) 245–261.
39. F. G. Meyer, R. T. Constable, A. J. Sinusas and J. S. Duncan, *IEEE Trans Med Imag* **15,** 4 (1996) 453–465.
40. A. A. Amini and J. S. Duncan, *Imag Vis Comp* **10,** 6 (1992) 418–430.
41. S. Benayoun and N. Ayache, *Int J Comput Vision* **26,** 1 (1998) 25–40.
42. D. Friboulet, I. E. Magnin, C. Mathieu, A. Pommert and K. H. Hoehne, *Comp Med Im Graph* **17,** 4 (1993) 257–262.
43. C. Kambhamettu and D. B. Goldgof, *Comp Vis Graph Im Proc* **60,** 1 (1994) 26–43.
44. S. K. Mishra, D. B. Goldgof, T. S. Huang and C. Kambhamettu, *Int J Image Syst Tech* **4** (1992) 214–225.
45. S. C. Amartur and H. J. Vessele, *Magn Res Med* **29,** 1 (1993) 59–67.
46. L. Axel and L. Dougherty, *Radiology* **172,** 2 (1989) 349–350.
47. T. S. Denney and J. L. Prince, *IEEE Trans Med Imag* **14,** 4 (1995) 1–11.

48. S. E. Fischer, G. C. McKinnon, M. B. Scheidegger, W. Prins, D. Meier and P. Boesiger, *Magn Res Med* **31,** 4 (1994) 401–413.
49. W. S. Kerwin and J. L. Prince, *Med Imag Anal* **2,** 4 (1998) 339–353.
50. S. Kumar and D. Goldgof, *IEEE Trans Med Imag* **13,** 1 (1994) 122–132.
51. A. A. Young, D. L. Kraitchman, L. Dougherty and L. Axel, *IEEE Trans Med Imag* **14,** 3 (1995) 413–421.
52. A. A. Young and L. Axel, *Radiology* **185** (1992) 241–247.
53. E. Bardinet, N. Ayache and L. D. Cohen, *Med Image Anal* **1,** 2 (1996) 129–150.
54. E. Bardinet, L. D. Cohen and N. Ayache, *Comp Vis Image Underst* **71,** 1 (1998) 39–54.
55. A. H. Barr, *IEEE Comp Graph & Appl* **1,** 1 (1981) 11–23.
56. T. W. Sederberg and S. R. Parry, *SIGGRAPH'86* **20** (1986) 151–160.
57. J. Declerck, J. Feldmar and N. Ayache, *Med Image Anal* **2,** 2 (1998) 197–213.
58. O. Monga, R. Deriche and J.-M. Rocchisani, *Comp Vis Graph & Im Proc: Imag Underst* **53,** 1 (1991) 76–87.
59. J. Declerck, J. Feldmar, M. L. Goris and F. Betting, *IEEE Trans Med Imag* **16,** 6 (1997) 727–737.
60. M. A. Gutierrez, S. S. Furuie, L. A. Moura and J. C. Meneghetti, *Comput Cardiol* **22** (1995) 75–78.
61. M. A. Gutierrez, M. S. Rebelo, S. S. Furuie and J. C. Meneghetti, *J Elec Imag* **12** (2003) 118–123.
62. W. I. Meyering, M. A. Gutierrez and S. S. Furuie, *SPIE Medical Imaging* **3,** 21 (2002) 176–185.
63. L. Cohen, *Time-Frequency Analysis* (Prentice Hall PTR, New Jersey, 1995).
64. H. I. Choi and W. J. Williams, *IEEE Trans Acous Speech, Sig Proc* **37,** 6 (1989) 862–871.
65. J. M. Fitzpatrick, *Comp Vis Graph & Im Proc* **44** (1988) 155–174.
66. C. Fenema and W. Thompson, *Comp Vis Graph & Im Proc* **9** (1979) 301–315.
67. P. A. Laplante and A. D. Stoyenko, *Real-time Imaging: Theory, Techniques and Applications* (IEEE Press, New York, 1996).
68. S. S. Beauchemin and J. L. Barron, *ACM Comput Suerveys* **27,** 3 (1995) 427–433.
69. B. K. P. Horn and B. G. Schunck, *Artificial Intelligence* **17** (1981) 185–203.
70. G. J. Klein, B. W. Reutter and R. H. Heusman, *IEEE Trans Nucl Sci* **44,** 4 (1997) 1509–1512.
71. E. Debreuve, M. Barlaud, G. Aubert, I. Laurette and J. Darcourt, *IEEE Trans Med Imag* **20,** 7 (2001) 643–659.
72. H. Sagan, *Introduction to the Calculus of Variations* (Dover Publications, New York, 1969).
73. O. Axelsson, *Iterative Solution Methods* (Cambridge University Press, Cambridge, 1996).
74. G. T. Herman, *Medical Imaging Systems Techniques and Applications: Computational Techniques*, ed., C. T. Leondes (Gordon and Breach Science Publishers, Amsterdam, 1998).
75. J. Hadamard, *Princeton University Bulletin* **13** (1902).
76. J. J. Koenderink, *Biological Cybernetics* **50** (1984) 363–370.
77. T. Lindeberg, *J Math Imag Vis* **3** (1993) 349–376.
78. E. H. Adelson and J. R. Bergen, *J Opt Soc Am A* **12** (1985) 284–299.
79. H. Gafni and Y. Y. Zeevi, *Biol Cybern* **28** (1977) 73–82.
80. H. Gafni and Y. Y. Zeevi, *Biol Cybern* **32** (1979) 165–173.
81. L. D. Jacobson and H. Wechsler, *Comp Vis Graph Im Proc* **38** (1987) 29–65.

82. L. D. Jacobson and H. Wechsler, *Signal Proc* **14** (1988) 37–68.
83. S. C. Chapra and R. P. Canale, *Numerical Methods for Engineers with Programming and Software Applications* (McGraw-Hill, New York, 1998).
84. D. G. Kleinbaum, L. L. Kupper and K. E. Muller, *Applied Regression Analysis and Other Multivariable Methods* (PWS-KENT Publishing Company, Boston, 1988).
85. F. Torrent-Gausp, *The Cardiac Muscle* (Fundacion Juan March, Madrid, 1942).
86. P. H. Pretorius, W. Xia, M. A. King, B. M. W. Tsui, T. S. Pan and B. J. Villegas, *J Nucl Med* **38** (1997) 1528–1535.
87. P. H. Pretorius, M. A. King, B. M. W. Tsui, K. J. LaCroix and W. Xia, *Medical Physics* **26,** 11 (1999) 2323–2332.